UNIVERSITÉ DU LUXEMBOURG

PhD-FSTM-2021-028
The Faculty of Sciences, Technology and Medicine

# DISSERTATION

Defence held on 04/06/2021 in Esch-sur-Alzette, Luxembourg

to obtain the degree of

# DOCTEUR DE L'UNIVERSITÉ DU LUXEMBOURG

# EN CHIMIE

by

Sabrina GUILLEMOT (WACK)
Born on 26 January 1993 in Thionville (France)

# CHEMICAL VAPOR-PHASE DEPOSITION OF NANOSTRUCTURED SILVER LAYERS

## Dissertation defence committee

Dr. Renaud Leturcq, dissertation supervisor
*Luxembourg Institute of Science and Technology*

Dr. Alex Redinger, Chairman
*Professor, Université du Luxembourg*

Dr. Emmanuel Scolan
*European Space Resources Innovation Centre*

Dr. Christophe Detavernier
*Professor, Ghent University*

Dr. David Muñoz-Rojas
*Laboratoire des Matériaux et du Génie Physique, INP-CNRS, Université Grenoble Alpes*

# Acknowledgment

Let's switch to my native language to acknowledge, in the best possible manner, people with whom I have collaborated all along my PhD thesis and those who have contributed to its good progress.

L'écriture de cette partie de la thèse marque, pour chaque étudiant doctorant, la fin de plusieurs années de travail. Dans mon cas, elle représente la concrétisation d'un long et riche voyage chargé en souvenirs, de presque 4 années, qui n'a pas toujours été un long fleuve tranquille mais au cours duquel j'ai pu me développer à la fois en tant que scientifique ainsi que sur le plan personnel. Bien que cette partie ne traite aucunement de résultats expérimentaux ou de science, elle occupe à mes yeux une place primordiale dans le manuscrit de thèse. Ce travail n'aurait pas pu aboutir sans l'aide et le soutien de nombreuses personnes qui y ont contribué de façon directe ou indirecte, et qui me tient à cœur de remercier.

Mes travaux de recherches ont été effectué au sein du *Luxembourg Institute of Science and Technology* (LIST), situé à Belvaux au Luxembourg et plus précisément dans le département *Materials Research and Technology* (MRT), unité *Nanomaterials and Nanotechnologies* (NN) et groupe *Transparent and Optically Tuneable Materials and Nanostructures* (TOTE), dans le cadre d'un projet en collaboration avec un partenaire industriel, ainsi qu'au sein de l'Université du Luxembourg, à l'école doctorale *Science and Engineering* (DSSE), dans le programme *Physics and Materials Science* (DPPM).

Tout d'abord, je tiens à remercier infiniment mon superviseur de thèse, Renaud Leturcq. Merci pour la confiance que tu m'as accordée à la fois lors de mes précédents stages et dans l'étude de ce projet de thèse. Je te remercie de m'avoir offert cette opportunité unique qu'est le doctorat. Merci pour ton encadrement sans faille et pour ta disponibilité en toute circonstance. Ton haut niveau scientifique et ton large éventail de connaissances m'ont permis à la fois d'améliorer ce travail de thèse et de le présenter fièrement aujourd'hui mais aussi de m'améliorer en tant que scientifique. Ce doctorat est un mérite partagé. Merci pour tout Renaud !

Mes remerciements se tournent également envers Damien Lenoble, directeur du département MRT et leader de l'unité NN pour m'avoir accueilli au sein de l'institut de recherche mais aussi pour son aide pour l'après PhD. Merci également à Emanuele Barborini, leader du groupe TOTE, pour avoir régulièrement veillé au bon déroulement de ma thèse.

Je tiens à remercier les membres de mon comité d'encadrement de thèse, Emmanuel Scolan et Alex Redinger, pour avoir accepté de suivre mon travail au cours de ces années ainsi que pour les retours pertinents qu'ils m'ont donné suite à nos différentes réunions d'avancée de thèse. Je remercie également les membres de mon jury, Christophe Detavernier et David Muñoz-Rojas, pour avoir accepté d'évaluer mes travaux et me faire l'honneur de leur présence lors de ma soutenance.

Je souhaite aussi exprimer toute ma gratitude à l'ensemble des chercheurs et ingénieurs du LIST, plus spécialement les personnes avec qui j'ai pu collaborer majoritairement au sein du département MRT, soit pour analyser des échantillons ou par qui j'ai été formé sur les différents équipements, mais aussi pour les enrichissantes discussions (extra)professionnelles.

La jeune padawan que je suis remercie Sir Petru Popa Lunca, mon awesome acolyte de projet, pour avoir pris le temps de répondre à bons nombres de mes questions sur la physique, à s'en arracher les cheveux (c'est peut-être pour cela que tu n'en as plus d'ailleurs ;)). Merci pour ta bienveillance, pour la bonne humeur quotidienne que tu as apporté avec tes blagues (pas toujours drôles mais qui vont quand même me manquer :p), pour les bêtises qui nous ont tant fait rire mais qui nous laissent maintenant des beaux souvenirs et bien évidemment pour ton aide précieuse au niveau scientifique. Merci, mon ami.

Une attention toute particulière envers Bianca Rita Pistillo et Kévin Menguelti, mes « parents du LIST », ou plutôt grande sœur et grand frère (sinon ça vieillit, askip). C'est avec vous deux que tout a commencé, avec mon premier stage au sein du LIST en 2015 et au cours duquel j'ai développé mon goût pour la recherche. Je faisais déjà face aux caprices de la science (sacrée PRODOS !) mais j'ai énormément appris au travers de cette expérience. Je vous remercie aussi pour vos qualités humaines très rares de nos jours.

Merci à l'expert ALD, Noureddine Adjeroud et l'expert SEM Didier Arl. Merci aussi aux membres de la plateforme de caractérisation sans qui bon nombre d'analyses n'auraient pas pu être effectué : Patrick Grysan, l'expert AFM (je ne pourrai plus t'embêter avec le réglage du laser), les professionnels des analyses XPS, Jérôme Guillot et Christèle Vergne, le binôme de choc et voisins de bureau Jean Luc Biagi et Jérôme Bour (vos 'tu es encore là toi' résonnent encore dans ma tête), les spécialistes SIMS and cie Gille Frache, Nathalie Valle et Brahime El Adib et Monsieur XRD, Yves Fleming. Merci aussi à Corinne Lavorel (ma Coco), Alexis De Col, Guillaume Lamblin, Asma El Moul, Kamal Baba, pour nos discussions (extra)professionnelles au travers des couloirs ou autour d'un café, qui ont toujours été un plaisir ! Je remercie également toutes les personnes qui ont contribué à l'obtention de certains résultats présentés dans cette thèse, notamment Tony Schenk, Delphine Collard et Régis Vaudemont.

Un grand merci aux actuels doctorants ou fraîchement docteurs avec qui j'ai partagé mon bureau F1.14 où j'ai pu passer de bons moments au cours de ma thèse (mais aussi en dehors quand c'était encore possible !): Team France avec Raoul et Antoine versus le reste du monde avec Tai, Shiv, Joao, Nikhar, Rutuja, Hameeda et Rishabh. Un remerciement particulier à Dominique (aka mon fry), une amitié née durant cette thèse (Fadadi bientôt ton tour !). Merci aussi aux anciens PhD et actuels postdocs : Jonathan (non je ne suis toujours pas copine avec les équations que tu aimes tant), Vincent (vive la photocat !), Nohora, David, Serena, Sunil et mon ancienne voisine de bureau Divya, pour ne citer que les derniers. Bon courage à vous tous pour la suite !

Enfin, mes plus sincères remerciements à ma famille, plus particulièrement ma mère et ma sœur, ma belle-famille bordelaise ainsi que ma meilleure amie Fanny et mes vrai(e)s ami(e)s, qui ont su me rebooster quand cela était nécessaire et qui m'ont toujours encouragée durant ces 4 années de thèse.

A mon mari, Thomas, merci pour ton soutien indéfectible au cours de ce doctorat. J'espère que les sacrifices de ces derniers mois et l'obtention de mon diplôme nous ouvriront la voie vers nos futurs projets tant attendus ! The world is ours, je t'aime !

# Abstract

**Keywords:** silver, metals, ultra-thin metallic films, nanoparticle films, chemical vapor-phase deposition, atomic layer deposition, conformal deposition, large-scale deposition.

Among the noble metals, silver (Ag) presents the lowest electrical resistivity at low thickness, the highest reflectance from visible to infrared spectra and the lowest thermal conductivity. Consequently, it is used in a large range of applications, either as nanoparticle (NP) films, e.g. in devices based on localized surface plasmon resonance, or as continuous thin films for highly reflective optical mirrors or as infrared reflecting coatings. Although copper (Cu) is widely used in the field of microelectronics, Ag is a good candidate as a potential replacement of Cu for interconnects in integrated circuits (ICs) thanks to its lower residual stress and the absence of considerable increase of resistivity when downscaling. Among the non-line-of-sight vacuum deposition method, atomic layer deposition (ALD) is known for its ability to produce an accurate and precise thickness control giving uniform and conformal film growth thanks to the sequential and self-limiting surface reactions of precursors. However, the ALD of silver is still weakly understood, and the uniform deposition over large scale is often not demonstrated. It is also very challenging to obtain an ultra-thin continuous Ag films due to the growth mechanism leading to islands films rather than continuous layer.

One part of this thesis work is dedicated to take advantage of the nanoparticle morphology and overcome the challenge of the good control of the morphology of Ag nanostructures on large-scale surfaces by an understanding of the growth mechanism. The uniformity of the deposition of silver NPs by plasma-enhanced ALD (PE-ALD) is quantified in terms of film morphology as well as chemical composition and crystalline structure over an 8-inch surface area. After a careful investigation of the PE-ALD parameters and their impact on the Ag deposition, we prove the self-saturated regime required for obtaining good control of the deposition and large-scale uniformity. An empirical model which explains the silver NPs growth mechanism correlated with the experimental results obtained is also proposed. This fine control of the Ag NP morphology opens the way for interesting applications requiring precise NP dimensions.

The thesis also reports a new approach relying on an original two-step plasma-enhanced chemical vapor-phase deposition as an alternative process regime which might be more promising for obtaining the challenging continuous and highly conductive ultra-thin films deposition. After reviewing the influence of the deposition conditions, we prove that the first step provides a uniform new morphology made of compact Ag NPs that is usually not achieved at low thickness with CVD or ALD. Based on the experimental results obtained, a proposed model for the growth mechanism of this peculiar Ag morphology is discussed and suggests that the chemical reaction occurs not only on the surface but also in the gas phase. After the second step of plasma post-treatment of silver made of compact nanoparticles, the sintering of the Ag NPs enhances the electrical conductivity of silver films by increasing the connectivity between particles due to the presence of higher density of energetic radicals. This is highlighted by a rigorous investigation of the influence of the post-processing conditions on the film morphology and its electrical properties. Therefore, we manage to reach the electrical performances of silver films obtained by physical approaches, i.e. by achieving a critical thickness as low as 15 nm and an electrical conductivity of $3.9\times10^5$ S/cm for a 40-nm thick Ag film. The described method can also be extended to other noble metals, in particular copper and gold, for which the deposition using chemical vapor-based methods is a very active field.

The two different processes developed in this work, i.e. standard PE-ALD and the novel two-step approach, are compared on complex substrates. The later path demonstrates a high film conformality on complex lateral high aspect ratio structures (LHAR with AR of 100), with better coverage than the one reported up to now for ALD of Ag. Moreover, the quasi-substrate-independency of silver films chemical-vapor phase deposited using both approaches confirms the weak influence of the underlayers known in the literature for Ag. On the other hand, we show that the study of the optical behavior of Ag films gives information about their morphology. Indeed, the presence of an absorbance visible peak is a signature of metallic NP morphology causing localized surface plasmon resonance. By following the film reflectivity spectrum of Ag NP films, a 'continuous-like' behavior understood by the Drude model is found at low wavelengths whereas higher wavelengths highlight a 'particle-like' behavior sticking to the oscillator model. This evolution of the optical properties is very similar for separated NPs using standard PE-ALD and film made of compact NPs obtained by the novel approach, except a stronger and broader absorbance peak typical for a film of aggregated NPs in the last case. On these compact NPs, a plasma post-processing gives strong increase of the infrared reflectance up to 97% and a strong decrease of near infrared transmittance as low as 3% for a 40-nm-thick film. Due to the wide ranges of applications of thin metal films, and the challenge to provide methods for conformal deposition, this work is interesting for the whole community of material scientists and could inspire many investigations.

"N'ayez *pas peur de recommencer.*
*Cette fois, vous ne partez pas de zéro.*
*Vous partez de l'expérience.*"

Denzel Washington

# Table of contents

# Glossary

## Chemicals

| | |
|---|---|
| acac | *Acetylacetonate* |
| Ag | *Silver* |
| Ag(fod)($PEt_3$) | *2,2-dimethyl-6,6,7,7,8,8,8-heptafluorooctane-3,5-dionato)silver(I)-triethyl-phosphine* |
| ALO/$Al_2O_3$ | *Aluminum oxide* |
| Al-O-Al bridges | *Aluminium* |
| ATMS | *Allyltrimethylsilane* |
| Au | *Gold* |
| AZO | *Aluminum-doped zinc oxide* |
| BDMESA | *Bis(dimethyl)ethylsilylacetylene* |
| $BH_3(NHMe)_2$ | *Dimethylamineborane* |
| Bi | *Bismuth* |
| bipy | *Bipyridine* |
| Btfac | *1-phenyl-4,4,4-trifluoro-1,3-butanedionato* |
| BTMSA | *Bis(trimethylsilyl)acetylene* |
| BTMSE | *Bis(trimethylsilyl)ethene* |
| Bu | *Butyl* |
| Carbo. | *Carboxylates* |
| Carbo. P add. | *Carboxylates phosphine adducts* |
| CDO | *Carbon-doped oxide* |
| $CH_3CH_2CH_2OH$ | *Propan-1-ol* |
| CO | *Carbon monoxide* |
| Co | *Cobalt* |
| COD | *1,5-cyclooctadiene* |
| Cu | *Copper* |
| $Cu_2O$ | *Copper(I) oxide or cuprous oxide* |
| DEZ | *Diethyl zinc* |
| DI | *De-ionised* |
| dpm | *Dipivaloylmethanato* |
| Et | *Ethyl* |
| F Carbo. | *Fluorocarboxylates* |
| F Carbo. P add. | *Fluorocarboxylates phosphine adducts* |
| Fe | *Iron* |
| fod | *2,2-dimethyl-6,6,7,7,8,8,8-heptafluoro-3,5-octanedionato* |
| GaAs | *Gallium arsenide* |
| GaOx | *Gallium oxide* |
| Ge | *Germanium* |
| $H_2$ | *Dihydrogen* |
| HCHO | *Formalin* |
| $HCO_2H$ | *Formic acid* |
| hfac | *1,1,1,5,5,5-hexafluoro-2,4-pentanedionato* |
| hfacNchex | *1,1,1,5,5,5-hexafluoro-4-(cyclohexylimino)-2-pentanedionato* |
| hfacNhex | *1,1,1,5,5,5,hexafluoro-4-(n-hexylimino)-2-pentanedionato* |
| $HfO_2$ | *Hafnium oxide* |
| hmds | *Bis(trimethylsilyl)amine or hexamethyldisilazane* |
| HMTA | *Hexamethyl-tetramine* |
| In | *Indium* |
| InOx | *Indium oxide* |
| IPA | *Isopropanol* |
| Ir | *Iridium* |
| MB | *Methylene blue* |
| Me | *Methyl* |
| MgO | *Magnesium oxide* |
| Mo | *Molybdenum* |
| $MoO_3$ | *Molybdenum trioxide* |

| | |
|---|---|
| $N_2$ | *Nitrogen* |
| $Nb_2O_5$ | *Niobium pentoxide* |
| $NH_3$ | *Ammonia* |
| NHC | *N-heterocyclic carbene-based* |
| Ni | *Nickel* |
| $O_2$ | *Dioxygen* |
| OH | *Hydroxyl* |
| Os | *Osmium* |
| Pd | *Palladium* |
| PF | *Perfluoro-1-methylpropenyl* |
| Pt | *Platinum* |
| Rh | *Rhodium* |
| Ru | *Ruthenium* |
| $Ru(thd)_3$ | *Tris(2,2,6,6-tetramethyl-3,5-heptanedionato)-ruthenium* |
| $RuCp_2$ | *Bis(cyclopentadienyl)ruthenium* |
| Si | *Silicon* |
| Si-H | *Hydrogen terminated silicon* |
| SiNx | *Silicon nitride* |
| $SiO_2$ | *Silicon dioxide or silica* |
| Si–OH | *Hydroxyl-terminated (oxidized) silicon* |
| $SnO_2$ | *Tin oxide* |
| Ta | *Tantalum* |
| $Ta_2O_5$ | *Tantalum(V) oxide or tantalum pentoxide* |
| TaN | *Tantalum nitride* |
| TBH | *Tertiarybutyl hydrazine* |
| TDMASn | *Tetrakis(dimethylamino)tin(IV)* |
| TDMATi | *Tetrakis(dimethylamido)titanium(IV)* |
| TEMAHf | *Tetrakis(ethylmethylamido)hafnium(IV)* |
| tfac | *1,1,1-trifluoro-2,4-pentanedionato* |
| THF | *Tetrahydrofuran* |
| Ti | *Titanium* |
| TiN | *Titanium nitride or tinite* |
| $TiO_2$ | *Titanium oxide* |
| TMA | *Trimethyl aluminium* |
| tmeda | *N,N,N',N'-tetramethylethylenediamine* |
| Ttfac | *1-(2-thienyl)-4,4,4-trifluoro-1,3-butanedionato* |
| VTES | *Vinyltriethylsilane* |
| W | *Tungsten* |
| $ZnCl_2$ | *Zinc chloride* |
| ZnO | *Zinc oxide* |
| ZnS | *Zinc sulfide* |
| $ZrO_2$ | *Zirconium dioxide or zirconia* |
| β-dik | β *-diketonates* |
| β-dik P add | β *-diketonates phosphine adducts* |
| β-diketoim | β *-diketoiminates* |
| β-diketoim P add. | β *-diketoiminates phosphine adducts* |

## Abbreviations

| | |
|---|---|
| 2D | *Two dimensions* |
| 3D | *Three dimensions* |
| AA-CVD | *Aerosol assisted chemical vapor deposition* |
| AFM | *Atomic force microscopy* |
| ALD | *Atomic layer deposition* |
| AP-CVD | *Atmospheric pressure chemical vapor deposition* |
| APP-ALD | *Atmospheric pressure plasma-enhanced atomic layer deposition* |
| AR | *Aspect ratio* |
| BE | *Binding energy* |
| BEOL | *Back-end-of line* |
| CVD | *Chemical vapor deposition* |
| DLI-CVD | *Direct liquid injection chemical vapor deposition* |
| DRAM | *Dynamic random-Access Memory* |
| DTA | *Differential thermal analysis* |
| EDX/EDS/EDXS | *Energy dispersive X-ray spectroscopy* |

| | |
|---|---|
| EPMA | *Electron probe microanalysis* |
| FA-CVD | *Flame assisted chemical vapor deposition* |
| GIXRD | *Grazing incidence X-ray diffraction* |
| GPC | *Growth per cycle* |
| HR | *High resolution* |
| IR | *Infrared* |
| IRR | *Infrared reflective* |
| LHAR | *Lateral high-aspect-ratio* |
| LI-CVD | *Laser-induced chemical vapor deposition* |
| LIST | *Luxembourg Institute of Science and Technology* |
| LP-CVD | *Low pressure chemical vapor deposition* |
| LSPR | *Localized surface plasmon resonance* |
| MFP | *Mean free path* |
| MO-CVD | *Metal organic chemical vapor deposition* |
| n.a. | *Not available* |
| NIR | *Near infrared* |
| NP(s) | *Nanoparticle(s)* |
| NR | *Nanorods* |
| OR | *Ostwald ripening* |
| PE-ALD | *Plasma-enhanced atomic layer deposition* |
| PE-CVD | *Plasma-enhanced chemical vapor deposition* |
| PSD | *Particle size distribution* |
| PVB | *Polyvinyl butyral* |
| PVD | *Physical vapor deposition* |
| QCM | *Quartz crystal microbalance* |
| RE-ALD | *Radical-enhanced atomic layer deposition* |
| RF | *Radio frequency* |
| rms | *Root mean square* |
| RT | *Room temperature* |
| SC | *Semiconductor* |
| SEM | *Scanning electron microscopy* |
| SERS | *Surface-enhanced Raman scattering* |
| SFT-CVD | *Supercritical fluid transport chemical vapor deposition* |
| SoA | *State-of-the-art* |
| SPR | *Surface plasmon resonance* |
| SR | *Smoluchowski ripening* |
| TAMS | *Total Absolute Measurement System* |
| TCO(s) | *Transparent conductive oxide(s)* |
| TGA | *Thermogravimetric analysis* |
| Th-ALD | *Thermal atomic layer deposition* |
| Th-CVD | *Thermal chemical vapor deposition* |
| TOA | *Take-off angle* |
| ToF-SIMS | *Time-of-flight secondary ion mass spectrometry* |
| TSK | *Terrace-step-kink* |
| UHV-CVD | *Ultrahigh vacuum chemical vapor deposition* |
| UV | *Ultraviolet* |
| VASE | *Variable Angle Spectroscopic Ellipsometry* |
| VHAR | *Vertical high-aspect-ratio* |
| Vis | *Visible* |
| VM | *Volmer-Weber* |
| WCA | *Water contact angle* |
| XPS | *X-ray photoemission spectroscopy* |
| XPS | *X-ray photoelectron spectroscopy* |
| XRD | *X-ray diffraction* |
| XRR | *X-ray reflectivity* |

## Symbols

| | |
|---|---|
| *%A* | Absorbance |
| *%at.* | Atomic percentage |
| *%R* | Reflectance |
| *%T* | Transmittance |
| $\gamma_{material}$ | Surface energy of the material |
| $k_B$ | Boltzmann constant |

| | |
|---|---|
| $\gamma_{interface}$ | Interface energy between the material and the substrate |
| $\gamma_{metal-oxide}$ | Surface energy of the oxide/metal interface |
| $\gamma_{metal-v}$ | Pure surface energies of the metal film |
| $\gamma_{oxide-v}$ | Pure surface energies of the oxide substrate |
| $\gamma_{substrate}$ | Surface energy of the substrate |
| $\nu_a$ | Adsorption frequency |
| $Ar_{pl}$ | Argon flow in the plasma head |
| $Ar_{pr}$ | Argon flow in the process lines (from the precursor boat to the reactor) |
| $d$ | Distance substrate-grid |
| $h$ | Gap height |
| $H_{2pl}$ | Hydrogen flow in the plasma head |
| $l$ | Gap lateral width |
| $P_{dep}$ | RF plasma power during deposition |
| $P_{post}$ | RF plasma power during post-treatment |
| $R_s$ | Sheet resistance |
| $T_b$ | Boiling point temperature |
| $T_{ch}$ | ALD chamber temperature |
| $T_d$ | Decomposition temperature |
| $T_{hs}$ | Hot source temperature (for the precursor evaporation) |
| $T_m$ | Melting point temperature |
| $T_p$ | Precursor temperature (related to $T_{hs}$) |
| $t_{pl}$ | Pulse time 2 of plasma |
| $t_{post}$ | Time of post-treatment |
| $t_{pr}$ | Pulse time 1 of Ag precursor |
| $t_{pu1}$ | Purge time 1 after Ag pulse |
| $t_{pu2}$ | Purge time 2 after plasma pulse |
| $T_s$ | Substrate temperature (related to $T_{ch}$) |
| $W$ | Opening width |
| $\alpha'$ | Modified Auger parameter |
| $\lambda$ | Mean free path |
| $\rho$ | Resistivity |
| $\sigma$ | Conductivity |
| $Ea$ | Adsorption energy of the atoms |
| $\gamma$ | Surface energy or surface tension |

# List of figures

# List of tables

# General Introduction

A brief introduction of the context and challenges of the thesis work is presented. The aim of the research and the objective are described. The PhD structure with an overview of the content of each chapter and the main conclusions is outlined.

# Context

Noble metals are transition metals presenting outstanding resistance to oxidation and corrosion even at high temperatures, which confers them their more noble character as compared to other metals. [1] In a more inclusive list, noble metals include coinage metals gold (Au), silver (Ag) and copper (Cu) as well as platinum group metals ruthenium (Ru), rhodium (Rh), palladium (Pd), osmium (Os), iridium (Ir), platinum (Pt). [2] They present very good conduction of heat and electricity and have a higher melting point than usual metals, which justifies the interest in this type of material for making nanostructures.

The downscaling of these materials to the nanometer scale size confers them specific and unique physico-chemical properties compared to those of larger sized particles and counter bulk materials. [3] The decrease in size of the nanoparticles leads to a large surface-to-volume ratio which plays a preponderant role in the properties involving exchanges at the interface between the object under consideration and its environment. The amount of atoms or molecules present at the surface increases with a decrease of the particle size. This higher amount of surface atoms creates more surface area and thus more surface energy which can potentially enhance the NPs materials reactivity from a chemical point of view, but also create the possibility to tune the optical, magnetic and conducting properties. [4]

Nowadays, several applications in diversified areas of our daily life use these metallic nanomaterials, ranging from personal care commercial products in cosmetics, packaging for food, [5] to textiles [6] or integrated circuits of mobile phones. [7] This leads to the breakneck development of nanotechnologies. [8] Thanks to their low resistivity and high optical reflectance over a wide optical spectrum, the metallic thin films play also an important role in several technologies. In most applications, the control of the metallic film morphology represents a key factor in order to achieve either a continuous smooth film or discrete particles with well-controlled size. [9] In a non-exhaustive way, we can mention applications for nanoparticles in heterogeneous catalysis with Pt and Pd nanoparticles being the mostly used, [10] in biology with Au NPs as fluorescent markers for imaging [11] or in medicine with the use of gold nanoparticles for the treatment of cancers, [12, 13] and applications for noble metal continuous films in microelectronics with Cu films as interconnects, [14] in optical sensors applications thanks to the apparition of surface plasmon resonance [15] or as anticorrosion, self-cleaning or anti-fouling smart coatings. [16]

In particular, metallic silver nanometer-scale coatings are of great interest for a number of applications. Ag presents the lowest electrical resistivity (1.59 μΩ.cm), the highest reflectance from visible to infrared (IR) spectra as compared to other metals [17] and a plasmonic frequency being located in UV region ($\lambda_p$ = 140 nm [18]). It has a face-centered cubic (fcc) crystal structure, a density of 10.5 g/cm$^3$ and a melting point of 962°C. In the fabrication of microelectronic devices, which include Dynamic Random-Access Memory (DRAM) capacitors, transistors, and back-end-of line (BEOL) interconnects, copper films are widely studied. However, in this field, silver is of particular interest due to its low electrical resistivity and low residual stress compared to Cu. Moreover, a downscaling to less than 100 nm is possible without a considerable increase in resistivity. [19] All these arguments impose Ag as a potential replacement of Cu for contacts and interconnects. Besides microelectronics field, its visible and infrared reflectivity make it a good choice for optical instruments including highly reflective mirrors [20] or optical coatings for lenses or windows. [21] In particular, the actual high

demand on the smart windows market in the field of automotive or smart buildings requires ultra-thin coatings with specific optical and electrical properties. Optically transparent infrared reflective (IRR) or low-emissivity coatings play an important role in the heat management of glazing products by avoiding heat to be transferred to the interior. [22] Currently used IRR coatings involve several thin continuous silver layers embedded in a complex stack of metal oxide multilayers in order to achieve maximum reflection in the IR optical spectrum, while preserving high transmission in the visible range. Thanks to its chemical reactivity, Ag is also used as antibacterial surfaces and has been applied as coatings on particular medical devices such as indwelling catheters, wound dressings and stainless steel orthopaedic devices. [23] Ag has also been extensively examined in the form of nanoparticles (NPs) for their broad-spectrum antimicrobial activities in pharmaceutics, medicine, and dentistry fields. [3, 24] Owing to their plasmonic properties, Ag NPs are used in functional optical coatings [25, 26] with applications in surface-enhanced Raman scattering (SERS), biosensing and plasmon circuitry, [27] coherent light sources, sensors and photovoltaic devices based on localized surface plasmon resonance (LSPR). [28]

For commercial devices, [29, 30] applications of Ag both NPs and continuous thin films require good control of the morphology and chemical composition of the Ag layers on large-scale surfaces. Thin films based on Ag NPs are usually produced using a chemical approach, which is carried out in a wet environment using a reduction of metal ions in solution. It favors the formation of metal clusters or aggregates with well-controlled size. [31] Line-of-sight methods such as physical vapor deposition (PVD), including evaporation, sputtering, or laser ablation, [32] are commonly used for ultra-thin silver films deposition. These techniques exhibit the best quality of ultra-thin continuous films with high conductivity, i.e $1.02\times10^5$ S/cm by magnetron sputtering, [17] and a percolation threshold as low as 11 nm by e-beam evaporation without the use of a wetting layer. [33] However, these methods do not allow conformal deposition on complex morphology structures which represents a crucial criterion in the microelectronics industry, where the miniaturization of semiconductor devices introduces complex three-dimensional structures with high aspect ratio.[2, 34] One of the main challenges is to be able to uniformly fill the metallic films into these structures. Non-line-of-sight vacuum deposition methods such as chemical vapor deposition (CVD), including thermal or plasma-enhanced CVD (PE-CVD), [35, 36, 37, 38] allow a large-scale deposition of films on the substrate with complex geometries, such as structured or bent substrates. A very interesting CVD method is atomic layer deposition (ALD), including thermal or plasma-enhanced ALD (PE-ALD), which has demonstrated a very high control of the film thickness and morphology at the atomic level due to the use of self-limiting surface reactions. [39] Moreover, it leads to uniform and conformal films which are often needed for commercial applications.

However, there are still challenges to reach when it comes to ALD of Ag. Although the ALD of Ag layers has been demonstrated, this method is still at an early stage owing to the tricky deposition conditions, that is, a narrow process window and the challenge involved in developing volatile and stable enough Ag precursor as well as efficient reducing agent. Moreover, the exact deposition mechanism of Ag is not yet fully understood. This could explain why ALD of Ag has only been investigated from 2007, [40] and why there are relatively few reference works in the literature. One major difficulty in producing ultra-thin continuous silver or other noble metals on oxide substrates is the formation of separated clusters due to the higher surface energy of metallic materials as compared to oxide surfaces. The deposition follows the islands growth mechanism and furthermore leads to an NP morphology rather than a continuous layer. [19, 40, 41] Therefore, non-electrically-conductive Ag

films are obtained for low thickness. [2] The reduction of the critical thickness of conductive films is one of the major research activities in the deposition of metal films, and several techniques have already been investigated but mainly for PVD methods (see [42] and [43] and references therein). The reduction of the critical thickness has been attempted for PE-ALD of silver through which the use of highly reactive species enables to work at low temperature at which diffusion of silver on the surface is strongly reduced and a critical thickness down to 22 nm has been reached. [41] Although PE-ALD usually gives a higher coverage with a lower critical thickness than thermal ALD, [40, 41, 44, 45] a critical thickness down to 9 nm was reported by thermal ALD using a specific co-reactant. [46] However, these two works are not reflecting the entire state-of-the art of Ag by ALD as they are isolated results. While ALD is the most promising technique for conformal deposition, the PE-ALD of Ag thin film suffers from the recombination of plasma species (radicals) on the surfaces, which prevents the growth deeper into lateral high aspect ratio structure. [2, 47] On the other hand, by means of the use of a wetting layer, only non-continuous films [48] with a slight enhancement of the coverage but still non-continuous morphology [19] were observed when chemical vapor-phase methods were engaged. A two-step approach consisting of the deposition of a metal-containing film subsequently reduced to a metallic state was proved for copper thin layers. [2, 47] However, this will be difficult to transfer to silver coatings, as $Ag_2O$ decomposes itself at moderate temperatures (around 120°C in vacuum [273]). Although ALD is a surface-dependent technique, presenting chemical requirements for the self-limiting reactions behavior, the growth of silver is more complex than an ideal “layer-by-layer” deposition. Thus, when it comes to Ag NPs, there is still a lack of control of the nanostructure morphology on a large-scale surface area. [49]

## Aim of the research

The thesis is dealing with chemical vapor-phase deposition of nanostructured silver layers. Three main challenges are expected to be addressed during the thesis. The first one deals with the growth of continuous metal thin films by a highly conformal and uniform deposition technique. The second one is related to the control of the morphology of nanostructured metal thin films. The last one is focused on understanding the growth mechanism of metal films in order to tailor adequately their physical properties. Therefore, the first objective is to achieve self-limiting ALD with a fine control of the morphology, mainly the size and shape of NPs, and chemical composition of the Ag nanostructures on large-scale surfaces. The second objective is to manage to reduce the critical thickness of continuous Ag layers in order to obtain conformal ultra-thin conductive and continuous Ag films. The mastering and understanding of the chemical vapor-phase deposition of silver films, either nanostructured or continuous, is highlighted. The tuneable functional properties, mainly optical and linked to film conformality, confirm the practical interest of the obtained thin films.

## Outline of the thesis

In the **first chapter** of this thesis, a description of the principle of chemical vapor-phase deposition is given by differentiating CVD from ALD. The growth mechanisms of metallic films on a substrate are reviewed. These mechanisms are illustrated by a literature review on noble metals particle size distribution (PSD) which give reliable information about the diffusion processes. This overview is incremented by a more extensive state-of-the-art on silver film deposited by chemical vapor-phase methods in terms of film morphology and electrical properties. One of the main challenges in the deposition of metal films being the reduction of the critical thickness of conductive films, several solutions for improving the continuity of ultra-thin noble metal films are highlighted. The continuity of the metallic films can also be studied by their optical properties, which are thus presented and linked to theoretical models existing in the literature.

**Chapter 2** intends to first present the processing methods and experimental tools employed for depositing silver films as well as the substrates and precursors handled. The second part reports the characterization techniques used all along the thesis work. Among the structural and morphological investigation, in addition to the use of *grazing incidence X-ray diffraction* (GIXRD) for film crystallinity determination and *atomic force microscopy* (AFM) for film topography determination, a focus is made on two original analyses, i.e. silver thin films thickness measurement by *energy-dispersive X-ray spectroscopy* (EDS) and film morphology characterization and quantification by *scanning electron microscopy* (SEM). The elemental and chemical composition is investigated by *X-ray photoelectron spectroscopy* (XPS) and *time-of-flight secondary ion mass spectrometry* (ToF-SIMS). Regarding the functional characterization, we use four-point probe measurement for the study of the electrical properties of the films, UV-Visible-NIR spectroscopy for determining the optical properties of the film and PillarHall© structures to investigate the film conformality.

The next two chapters 3 and 4 discuss the Ag nanoparticle films obtained by standard plasma-enhanced ALD. **Chapter 3** investigates the deposition process development with the aim to prove the ALD self-saturated regime. The experimental results are quantitatively compared based on the film thickness evolution as a function the ALD parameters and the film thickness uniformity over a large surface area (8-inch substrate). As usually observed for most of ALD processes, the more relevant parameters are found to be the temperatures, both of the chamber to control the precursor decomposition on the substrate, and of the precursor to ensure a good control of its evaporation, the ALD sequence times (pulse and purge times of the precursors) in order to ensure a saturation of the substrate surface, the argon flows, both in the process lines to control the amount of precursor exposed into the chamber and in the plasma head to regulate the exposure of radicals created by the plasma, and finally the plasma conditions where reactive hydrogen radical species are found to be mandatory in order to obtain pure silver in metallic state. **Chapter 4** presents in more details the correlation between the large-scale deposition depending on the process parameters and the growth mechanism of silver nanoparticles. A deeper investigation of the uniformity of the deposition is quantified in terms of film morphology using an original methodology. We report both the value at the center position and, more originally, the gradient over a 10 cm distance on the substrate. Relying on the dependence of the silver nanostructures on the deposition parameters, an empirical model is proposed with a view to understanding the Ag NP growth mechanism. The results suggest that the Ag thin films mainly evolve following a material transfer. Two potential mechanisms are in competition: the migration of the particles and their further coalescence through the Volmer–Weber growth mode

or a “surface Ostwald ripening”-like process. Under certain conditions, this last mechanism could explain the non-uniformity of the deposition.

**Chapter 5** demonstrates an alternative two-step process regime which is more promising for continuous ultra-thin silver film deposition. This process relies on a first pulsed plasma-enhanced CVD, giving a peculiar compact nanoparticle morphology that is usually not achieved at low thickness with CVD or ALD. A further plasma post-treatment sinters the compact NPs and forms a quasi-continuous and electrically conductive ultra-thin silver film. In order to understand the growth mechanism of silver compact films, the influence of the deposition parameters is investigated, and a proposed qualitative model is discussed. We observe that, by exposing the precursor during the plasma pulse, we can deposit a silver thin film made of dense and compact nanoparticles, by using mild plasma conditions, i.e. low RF power or high distance between the grid and the sample. Higher deposition temperatures and argon flows show to strongly improve the morphology and uniformity of the deposition. Based on these observations, the model highlights that, during the first deposition step, the precursor is exposed to the chamber also during the plasma pulse, thus making the reaction not only on the surface but also in the gas phase. The chapter ends with a deeper study on the post-processing of this peculiar film morphology, resulting in a highly conductive ultra-thin film. The presence of higher density of energetic radicals is created by an increase of plasma power and prolonged plasma exposure time and leads to a higher degree of coalescence of the particles.

In the last **chapter 6**, we compare the two different silver deposition processes, i.e. standard plasma-enhanced ALD versus two-step process, in terms of functional properties. The deposition on complex substrates using complex lateral high aspect ratio structures (LHAR) as well as the influence of the underlayer are presented in a first part. With the standard PE-ALD process, a poor film uniformity is obtained, due to the recombination of radical species with the walls of the trench. With the new two-step approach, we succeed in reaching a high conformality of the Ag deposited film on LHAR with better coverage than the one reported up to now for ALD of silver. Interestingly, for both processes, a weak influence of the underlayers is obtained. This represents a key factor for the synthesis of metal films in a broad range of applications requiring weakly-interacting film/substrate systems, e.g. in optoelectronic and catalytic devices. The second part of the chapter focuses on the influence of the silver film morphology on the optical properties in visible and near infrared ranges. The localized surface plasmon resonance absorbance peak is obtained as a first feature of Ag films made of NPs. The second one is the transition from high reflectance/low transmittance at low wavelength to low reflectance/high transmittance at higher wavelength. The same signature is obtained for the compact NP morphology synthetized by the novel two-step approach but in this case, an absorbance peak typical for a film of aggregated nanoparticles is highlighted. When a post-processing is performed on this peculiar film morphology, a strong increase of IR reflectance and strong decrease of both NIR absorbance and transmittance are achieved.

Finally, a last part focuses on concluding the thesis regarding the challenges described in this introduction. Future perspectives of this PhD work are presented and, based on preliminary experiments that have been performed and give encouraging results, potential applications of our Ag films are discussed.

# Chapter 1

## State-of-the-art

The thesis is dealing with chemical vapor-phase deposition of nanostructured metal layers and more precisely silver. Therefore, in this chapter, the first part is dedicated to explaining the general principles of the chemical vapor-phase deposition, i.e. by differentiating atomic layer deposition (ALD) from chemical vapor deposition (CVD). The parameters influencing the film's growth rate are then highlighted. In a second part, we review the main underlying physical mechanisms taking place in the nucleation and growth of thin films of materials on solid surfaces by gas-phase deposition. The thin film growth modes, the atomistic processes and the material transfer mechanism via ripening occurring on the surface are presented. We illustrate this study by a literature review on noble-metal particle size distribution (PSD) which gives reliable information about the diffusion processes. In a third part, the different CVD techniques mainly used for Ag deposition are first described, and we then exhibit a general overview of the quite challenging Ag films deposition by this method. The state-of-the-art of the ALD of silver, which is a more recent technique, is then reviewed. Based on data from the literature, both insights (CVD and ALD) of the results are outlined in terms of morphology and electrical properties. Since the major issue in depositing ultra-thin noble metals is the formation of separated clusters rather than continuous film, we bring to light solutions used by different synthesis methods to obtain continuous noble metal films that are potentially transferrable to ALD. We then focus the overview on Ag films deposited by different methods. Finally, we spotlight the optical properties of metal films as an indicator of the film morphology.

## I.1. Principe of chemical vapor-phase synthesis

### I.1.1. Introduction

Thin films based on metallic NPs, are usually produced by three different methods. [50] The first one is a chemical approach, which is carried out in a wet environment using a reduction of metal ions in solution (see section I.4.). It favors the formation of metal clusters or aggregates with well-controlled size. [31] The second method is physical vapor deposition (PVD), including evaporation, sputtering or laser ablation. [32] The third method is chemical vapor deposition (CVD), including thermal or plasma CVD. [35, 38] As a non-line-of-sight vacuum deposition method, CVD enables a large-scale deposition of films on substrate with complex geometries, such as structured or bent substrates. A very interesting CVD method is atomic layer deposition (ALD), which has demonstrated a very high control of the film thickness and morphology at the atomic level due to the use of self-limiting surface reactions. [39] Moreover, it leads to uniform and conformal growth, as shown in the first subsection. [1]

### I.1.2. Principle

The aim of this part is to introduce the principle of chemical gas-phase synthesis of metallic films, including standard CVD and ALD.

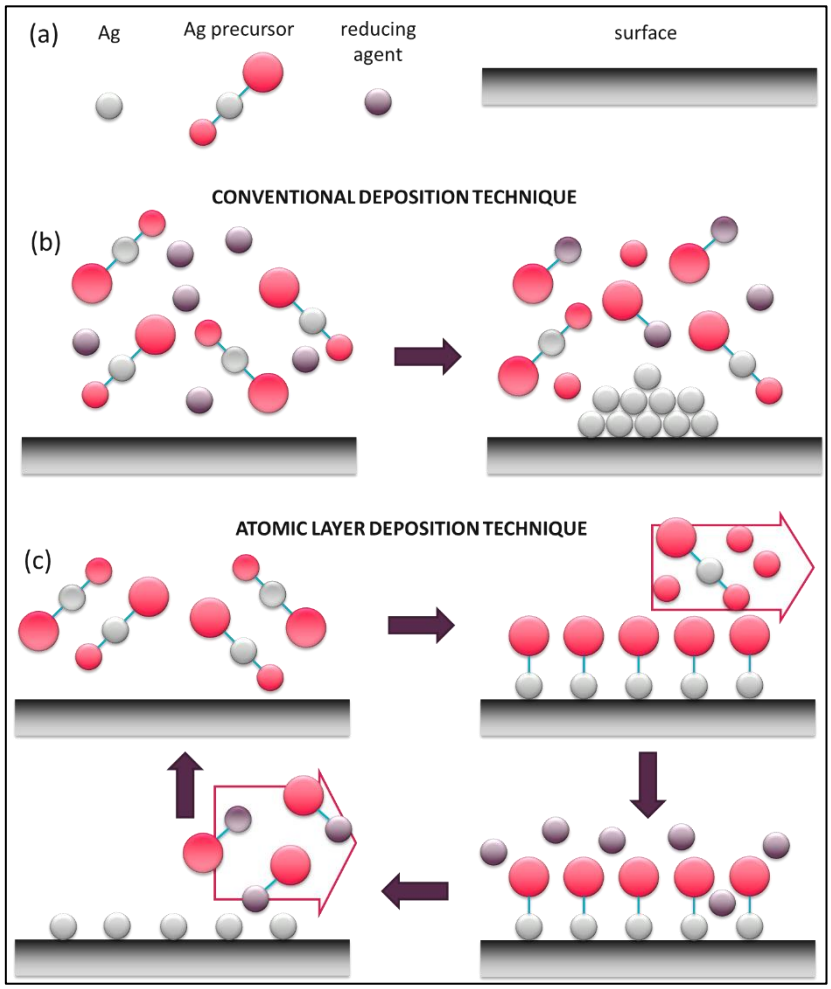


Figure 1: Schematic representation of the chemical reactions involved in (b) a conventional chemical vapor deposition process and (c) in the ALD process (two half-reactions realized in a cycling way). (a) Legend of the schemes.

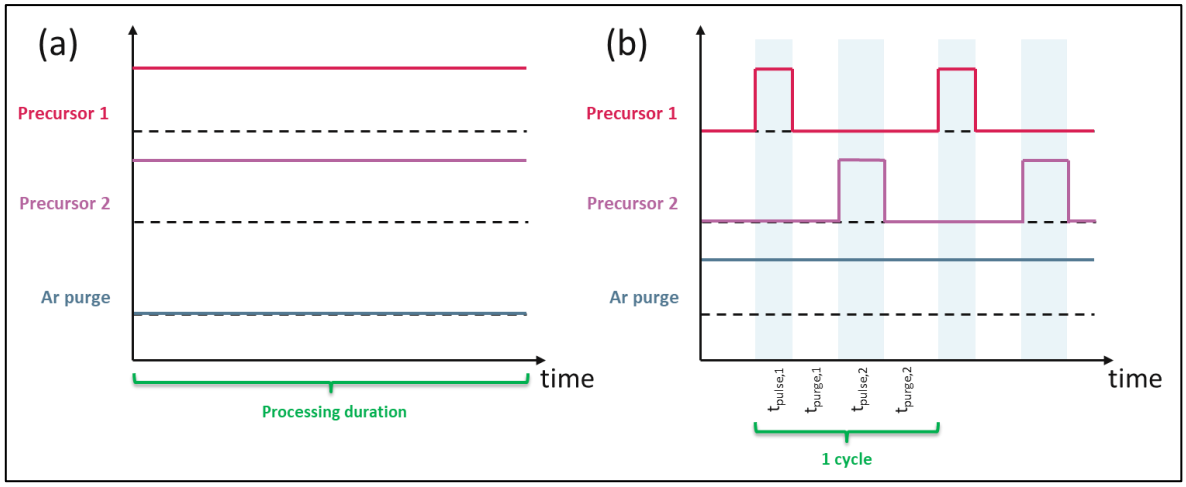

Figure 2: Pulse sequence for (a) standard CVD and (b) standard thermal ALD process with two precursors.

In a conventional chemical vapor deposition technique (Figure 1 (b)), the precursor and the reducing agent are exposed at the same time in the reactor, as shown in the pulse sequence in Figure 2 (a). The type of growth is then mainly determined by the reactor conditions (temperature, reactor pressure, precursors partial pressure, etc.), which control the equilibrium between the gas phase and the solid phase. The film thickness is thus determined by the process duration. [51, 52]

In the ALD (Figure 1 (c) and Figure 2 (b)), the precursor is first pulsed during $t_{pulse,1}$ and is left for some time in order to react with the surface, then the left-over is purged during $t_{purge,1}$. In a second step, the reducing agent is exposed ($t_{pulse,2}$) in order to react with the precursor condensed on the surface, and it is purged ($t_{purge,2}$), leaving a thin layer of metal atoms. Here the growth can be controlled by the cycling of precursor and reducing agent in a periodic way. These sequential self-limiting surface reactions of precursors enable not only a uniform and conformal film growth but also an accurate and precise thickness control. [1]

The chemical reactions involved in the deposition of metal (M) take place as follows:

**CVD Global reaction**

$$M^{+I} - ligand + Surface + Red \rightarrow Surface - M^{0} + ligand - Red$$

**ALD ½ reactions**

$$M^{+I} - ligand + Surface \rightarrow Surface - M^{+I} - ligand$$
$$Surface - M^{+I} - ligand + Red \rightarrow Surface - M^{0} + ligand - Red$$

The next section highlights the importance of the deposition parameters used for ALD process on the film growth per cycle or growth rate (GPC), focusing on the temperature, the pulse/purge length times and the number of ALD cycles.

### I.1.3. Parameters influencing the growth per cycle in ALD

An essential result allowing to inform about the growth regime, and in particular whether the reaction is self-limited (ALD regime) or occurs in bulk (CVD regime), is the growth rate, measured by the "growth per cycle" (GPC), i.e. the amount of material deposited for each reaction cycle. This

quantity is either measured by the film thickness (GPC in units of nm.cycle$^{-1}$) or by the mass of deposited material (GPC in units of g.m$^{-2}$.cycle$^{-1}$). In the ALD regime, the GPC is expected to be weakly dependent on the deposition conditions due to the self-limited surface reaction. In the CVD regime, the GPC is expected to strongly depend on parameters influencing the amount of precursor arriving on the substrate.

#### I.1.3.1. Effect of the temperature on the GPC

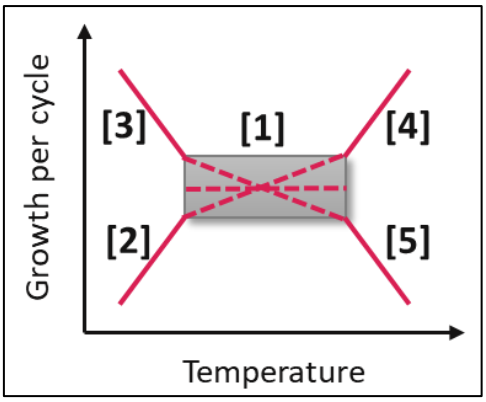


Figure 3: Influence of the deposition temperature on the growth per cycle, depicted as a function of the different regions (represented by the numbers).

One of the main parameters influencing the deposition conditions is the deposition temperature, as it influences directly the rates of the chemical reactions (precursor with the surface, and reduction) and the mobility of the reactants on the surface. Thus, the ALD temperature plays a critical role in the process and influences the growth per cycle, as depicted in Figure 3. One can distinguish five different regions of the dependence of the GPC and the temperature [39, 53, 54, 55, 56, 57]:

- At low temperature, either an increased GPC **[2]** or a decreased GPC **[3]** takes place.
    - the increased GPC **[2]** indicates that the reactions are not complete due to the limited reaction kinetics. It reveals also a slow reaction speed and that the time needed for the reaction to occur is longer than the time of one cycle;
    - the decreased GPC **[3]** indicates that the precursor species condensate physically on the substrate surface if the temperature is too low to maintain the precursor in the gas phase.
- At high temperature, either an increased GPC **[4]** or a decreased GPC **[5]** takes place.
    - the increased GPC **[4]** indicates that the precursor molecule decomposes on the surface. This results in a higher growth rate than the saturated growth.
    - the decreased GPC **[5]** indicates that the precursor molecule desorbs or the sticking constant of the precursor decreases, the surface species reduces or the deposited material sublimates.
- The temperature range **[1]** where we have saturation of the surface. This temperature range is called ALD window. In this regime, the GPC is controlled by the adsorbed species, either through steric hindrance of the ligands or by the number of available reactive surface sites, or by the reaction process, which might depend on the temperature. [39] It represents a key factor to determine if a process satisfies the requirement of ALD self-limiting reaction.

At a specific deposition temperature, the main factor influencing the saturation of the surface reaction is the sequence times, i.e. the pulse and purge time length.

### I.1.3.2. Effect of the sequence times on the GPC

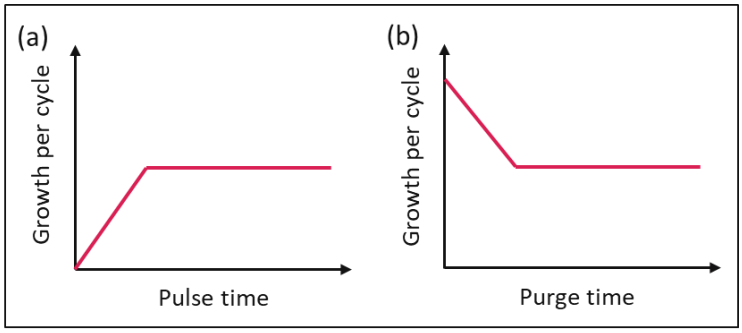


Figure 4: Influence of the sequence times, i.e. pulse time of the precursor and purge time after the precursor exposure, showing the saturation growth of ALD process.

Figure 4 illustrates the typical saturation growth curves with influence of the pulse and purge times on the GPC. The pulse time needs to be long enough in order to saturate the surface and the purge time influences the type of deposition, with a too-short purge time leading to an excess precursor overlapping as some reactants remain in the reactor and thus to a CVD-type reaction. When proceeding to the optimization of the sequence times on the GPC, it is important to notice that, for each studied time, the other times are kept constant and need to be chosen in order to be sure to have a self-saturated regime.

In general, the GPC increases with the pulse time (Figure 4 (a)) due to a preliminary under-saturated regime and becomes constant under surface saturation. When it comes to purge time (Figure 4 (b)), for short times, the reactor is not completely purged, and some precursors might remain inside (CVD like) before reaching a plateau which ensure an efficient reduction reaction and efficient evacuation of non-reacted precursor potentially left in the reactor.

### I.1.3.3. Effect of the number of ALD cycles on the GPC

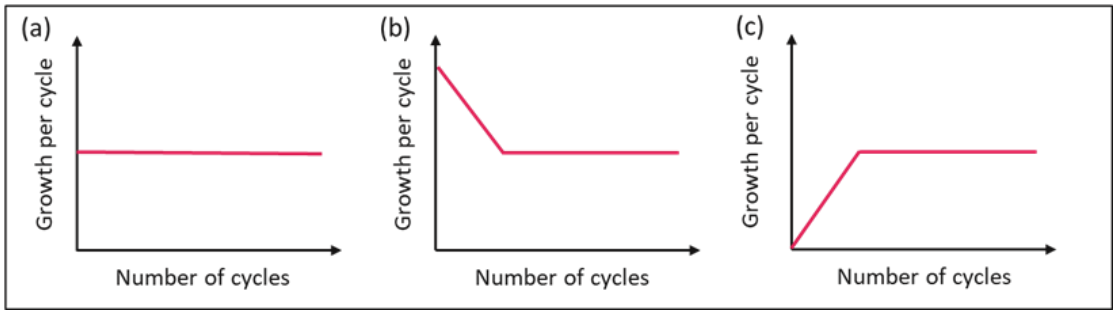


Figure 5: Influence of the number of ALD cycles on the growth per cycle in different types of ALD growth regime: (a) linear growth, (b) substrate-enhanced growth (c) substrate-inhibited growth.

The ALD film growth occurs successively on the substrate surface during the first cycles, on a surface containing both the deposited material and the substrate during the subsequent cycles and lastly on a surface composed exclusively of the deposited material (depending on the growth mode and the GPC). This leads to a variation of the surface chemical composition with the number of ALD cycles and hence, of the GPC. [39, 53]

In the saturated regime, each new ALD cycle is equivalent to the previous one in terms of the amount of deposited material, and a linear increase of the thickness is expected. [58] The GPC is thus an important parameter to help understanding the deposition regime and in particular the linear deposition regime. [39] During ALD growth regime, three cases can be distinguished based on how the GPC varies with the number of ALD cycles and for each, after a sufficient number of ALD cycles, the GPC is expected to reach a constant value, as depicted in Figure 5 [39, 53]:

- The **linear growth regime**, where the GPC is constant as early as the first cycle, and in the steady state. This takes place for a process where the number of adsorption sites is constant, or a process where steric hindrance of the ligands of the adsorbed species governs saturation (Figure 5(a));
- The **substrate-enhanced growth regime**, where the GPC is greater than the steady state during the first ALD cycles. This occurs if the number of adsorption sites is higher on the substrate rather than on the deposited material (Figure 5 (b));
- The **substrate-inhibited growth regime**, where the GPC is lower than the steady state, during the first ALD cycles. This takes place due to a weaker number of adsorption sites on the substrate than on the deposited material. (Figure 5 (c)). This is the most common regime proceeding during ALD process where island growth occurs, as discussed in the next section below.

## I.2. Growth mechanisms of metals film by chemical vapor-phase synthesis

ALD is a non-equilibrium process ruled by a competition between thermodynamics and kinetics which is at the origin of thin film growth from atoms synthetized from the gas phase. In this part, we are focusing on the thin film growth by chemical vapor phase methods, and more particularly, ALD extended to noble metals. The initial stage of thin film deposition includes the atoms arrival and accommodation on the surface (adsorption) and their migration all along the surface (diffusion). Then, their aggregation into adatom islands (nucleation and growth) takes place. [59] This is the object of sections I.2.2. and I.2.3.

The growth of metals on oxide substrate starts with the formation of isolated island due to surface energies discrepancy between the material deposited and the substrate, as explained below.

### I.2.1. Thin film growth modes

This part aims to describe the basic physical mechanisms involved in the nucleation and growth of thin films of materials on solid surfaces by vapor deposition.

Under thermal equilibrium, the initial stage of film deposition occurs by one of the three growth mechanism models depicted in Figure 6, leading to different thin film morphologies. [60, 61] The occurrence of one of the growth modes rather than another is governed by the bond strength between atoms of the layer and the atom/substrate bond strength.

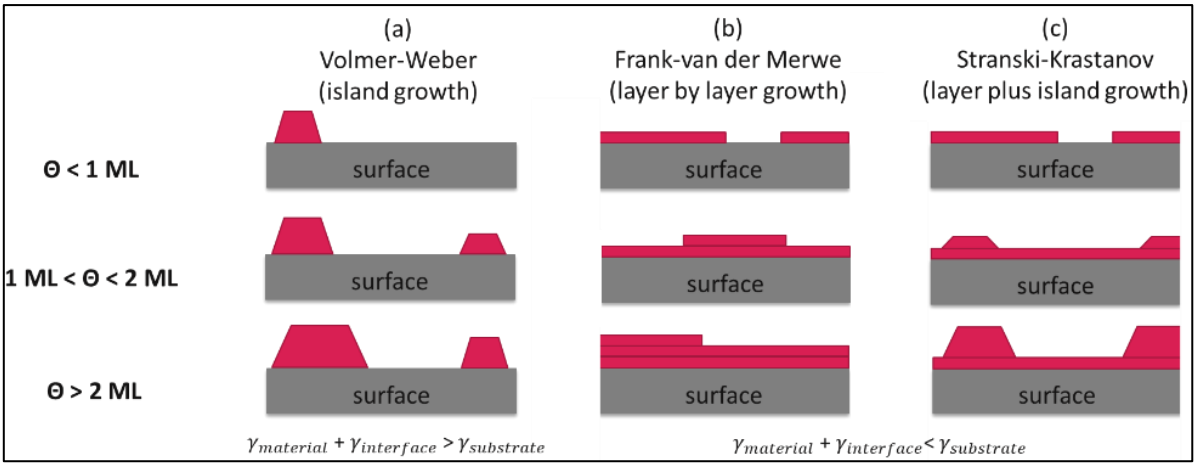


Figure 6: Schematic representation of the different thin film growth mechanism models. (a) Volmer-Weber model (island growth); (b) Frank-van der Merwe model (layer by layer growth and (c) Stranski-Krastanov model (layer plus island growth). Θ represents the overlayer coverage in monolayers (ML). $\gamma$ refers to the surface energy: of the substrate ($\gamma_{substrate}$), of the material ($\gamma_{material}$) and of the interface between the substrate and the material ($\gamma_{interface}$).

In the **Volmer-Weber** (VM) growth mode or island growth (Figure 6 (a)), three-dimensional growth occurs when the adatoms of the deposit have a strong affinity to each other rather than to the substrate. The nucleation of small clusters directly on the substrate surface which further coalesce, latter leads to a continuous film. It is often the case for metal films on insulators substrates. In the **Frank-van der Merwe** growth mode or layer by layer growth (Figure 6 (b), two-dimensional growth occurs when the adatoms of the deposit have a strong affinity to the substrate rather than to each other. An homogeneous film is formed prior to the growth of any subsequent layer. This is the case for metal/metal (e.g. Cu/Cu), metal/semiconductor (e.g. Fe/GaAs) and semiconductor/semiconductor (e.g. GaAs/GaAs) systems. The **Stranski-Krastanov** growth mode or layer plus island growth (Figure 6 (c), is a mix of the first two models. This mixed model occurs when the initially two-dimensional growth switches into three-dimensional, after one or more monolayers. It takes place when further layer growth becomes energetically unfavorable and 3D islands form, that is the case for Ge/Si or In/Si systems.

The occurrence of a growth mode rather than another and thus the film morphology may be understood qualitatively in terms of surface energy γ (or surface tension). [62] At thermal equilibrium, the driving force is the minimization of the surface free energy of the system film/substrate. When a material is deposited on a substrate, the model of growth depends on the energy balance between the surface energy of the substrate ($\gamma_{substrate}$), the one of the deposited material ($\gamma_{material}$) and the interface energy between the two materials ($\gamma_{interface}$). These free energies enter into their minimization. If $\gamma_{material} + \gamma_{interface} > \gamma_{substrate}$, the deposited material does not wet the substrate, the growth occurs by island nucleation (Figure 6 (a)). If $\gamma_{material} + \gamma_{interface} < \gamma_{substrate}$, the deposited material wets completely the substrate. Two possibilities occur, depending on the interface energy. If the initially two-dimensional growth becomes three-dimensional, Stranski-Krastanov growth occurs (Figure 6 (c)). On the other hand, if the growth remains two-dimensional, Frank-van der Merwe mode takes place (Figure 6 (b)).

For the deposition of metal film on an oxide substrate, the same analogy can be used. The complete wetting of the oxide substrate by the metal, i.e. the formation of a continuous film, is only taking place when, at equilibrium: $\gamma_{metal-oxide} = \gamma_{oxide-v} - \gamma_{metal-v}$ , where $\gamma_{metal-oxide}$ is the

surface energy of the oxide/metal interface, $\gamma_{\mathrm{oxide-v}}$ and $\gamma_{\mathrm{metal-v}}$ are the pure surface energies of the oxide substrate and the metal film, respectively, in vacuum. [19] The surface free energy of metals is usually larger than that of oxides, [63] thus the wetting of metal film on oxide substrate surface is only possible when the metal surface energy is lowered by minimizing its own surface area during growth, i.e. by forming nanoparticles in which atoms are closely packed together. This explains why the growth of metal on oxide substrate leads to island growth mode. By replacing the oxide substrate with a substrate exposing higher surface energy than the metal film, one could expect, in theory, the formation of a continuous metal film. The study of the wetting layer as a potential solution to obtain metallic ultra-thin films is exposed in section I.4.

### I.2.2. Atomistic processes on surfaces

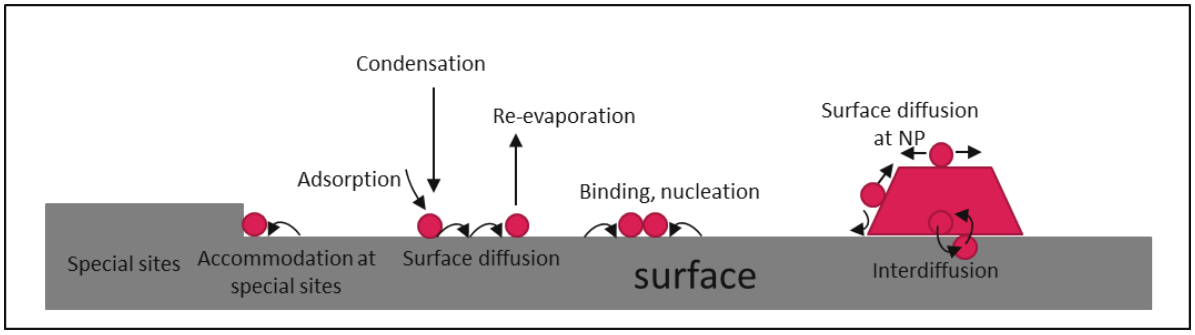


Figure 7: Schematic diagram of typical atomistic processes occurring during nucleation and growth on surfaces.

The typical atomistic processes taking place during film growth are schematically illustrated in Figure 7. During nucleation and growth, three steps are differentiated: first the production of atomic species in the gas phase, then the transport through a carried medium of the species to the surface substrate and finally the condensation of these species onto the substrate directly or by chemical reaction.

During chemical vapor phase deposition, the vapor containing the precursor atoms is deposited on the substrate surface. This creates single atoms on the substrate. According to the energy of the atoms and the location at which they collide with the substrate, the hitting atom can adsorb to it and becomes an adatom or re-evaporate (at higher temperature).

The adsorption rate of the adatoms to the surface follows an Arrhenius-type of equation and is roughly proportional to $\nu_a . exp\left(-\frac{E_a}{k_B T}\right)$, where $\nu_a$ is the adsorption frequency, $E_a$ the adsorption energy of the atoms, $\mathrm{k_B}$ the Boltzmann's constant and $\mathrm{T}$ the substrate temperature. [64, 65, 66]

For silver, $E_a$ of the atoms is in the range of 0.5-0.9 eV which is much lower than the binding energy of pairs of Ag atoms in free space of 1.65 eV. This explains why we have island growth (as proved in above section) during Ag growth and why the critical nucleus size is nearly always a single atom. The single Ag adatoms re-evaporate easily above room temperature (highly mobile due to low $E_a$) while they form a stable nucleus growing by adatom capture in the case that they meet another adatom. [64]

The formation of van der Waals bond with the surface atom is typical of physisorption whereas covalent or ionic bond with the surface atom is the signature of chemisorption. Due to the week intensity of the bond in physisorption, the atoms may migrate on the substrate (diffusion) and interact

with each other as well as with the surface atoms (interdiffusion). Adatoms may also meet other adatoms to form a dimer or attach to existing islands. Once adatoms are attached to an island, they may detach from the island edge or diffuse along the island edge. Deposition of adatoms on top of islands may also take place. [67] The single atoms diffusing over the surface may also nucleate of 2D/3D clusters by binding of atoms, be captured by existing clusters or at special defect sites like kinks, vacancies or steps. [59, 60] The terrace-step-kink (TSK) model of a surface has been widely used to describe the atomistic processes of growth. [65]

Overall, during the growth of the film, atoms from the precursor adsorb on the surface and rapidly diffuse hitting into each other and nucleate 2D islands. As adatoms are added, the islands continue to get bigger, but the system remains in a far-from-equilibrium state. (see [68] and references therein) In order to obtain an in-equilibrium system, the surface free energy is decreased by reducing the density of islands and thus increasing their size via ripening, as described in the sub-section below.

### I.2.3. Material transfer mechanism via ripening

Once the initial NPs have been formed, their growth continues through different mechanisms.

Firstly, the growth from adatoms may occur by adding freshly deposited atoms either on the surface of the NPs or nearby them via adatoms diffusion towards the NPs. Secondly, the NPs may expand their size via merging process by meeting each other and combining. [66]

The NPs growth may also take place by their own diffusion onto the surface. The material transfer from single atoms, section of cluster or entire cluster may cause the ripening of NPs. This material transfer may involve the competition between two potential mechanisms: Ostwald ripening (OR) or Smoluchowski ripening (SR), [69, 70] as depicted in Figure 8.

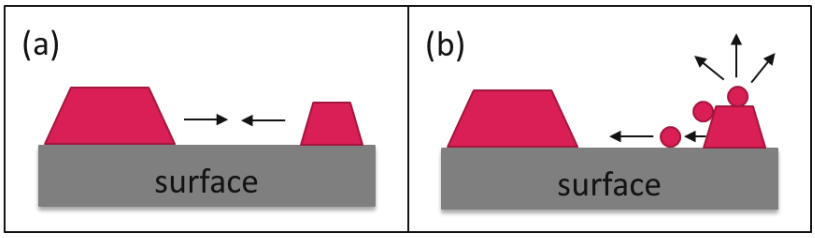


Figure 8: Schematic illustration of ripening processes: (a) Smoluchowski ripening (SR) or particle migration and coalescence and (b) Ostwald ripening (OR) or atom migration.

In the event of SR mechanism or particle migration and coalescence (Figure 8 (a)), smaller particles, which generally diffuse faster, [71] migrate onto the substrate surface and then coalesce with larger particles. [72] In this case, the whole NP diffuses onto the surface. The OR process or atom migration[73] (Figure 8 (b)) is defined as a process in which larger particles grow at the expense of smaller ones either by surface diffusion along the substrate or by vapor phase diffusion due to the difference in the chemical potentials between smaller and larger particles. [72, 74, 75] In this case, the atoms are diffusing from small NPS to larger ones. Several steps which are kinetically limited due to energy barriers must take place: detachment of atoms from small clusters, diffusion onto the substrate surface or via vapor phase, and then attachment to bigger NPs. [69, 76] These both ripening processes are driven by the minimization of the surface energy and support the formation of bigger NPs.

In the field of the ALD of noble-metal NPs, the synthesis of size-selected NPs presents a real topic of interest for applications in the field of microelectronics, since ALD enables atomic-level precision of material being deposited. However, there is a lack of understanding of the fundamental mechanisms leading to diffusion processes since the major part of these studies are dealing with the surface chemistry behind the deposition of the atoms on an oxide substrate. [49, 76] The study of the evolution of the NPs density and particle size distribution (PSD) leads to reliable information about the diffusion processes but this has been investigated to a less extent. [49, 76, 77] Consequently, the correlation between PSD and growth mechanisms leading to ALD of NPs is still under debate. [49, 76, 77, 78, 79]

The most common thermal ALD processes for noble metal deposition are $O_2$-based processes. [52] The shape and size of the NPs of the noble metals are controlled by a growth mechanism based on the cyclic combustion of organic ligands and NP formation through metal aggregation. This is the case for Ru, Os, Rh, Pt, Pd and Ir, [49, 80]when oxygen is used as the co-reactant. This has been widely observed for the synthesis of Pt NPs by several groups. [76, 77]

The conditions used for ALD processes influence the surface diffusion mechanisms. Indeed, in the study of Grillo *et al.* [81] the influence of the oxygen co-reactant partial pressure on the deposition of Pt has been investigated. At high $O_2$ exposure, which is linked to the partial pressure and the pulse time, the combustion of the organic ligands remaining on the surface after Pt precursor chemisorption promotes Smoluchowski ripening by unpinning and displacing NPs, even at temperature not adequate for NPs mobility. The high oxygen partial pressure reduces also the aggregation of NPs at high exposure. Indeed, a broader clusters size distribution with less dense but bigger NPs are obtained at low partial pressure while smaller but more dense clusters leading to a spikier behavior of the PSD at high $O_2$ partial pressure is achieved. In this case, a better pinning with a quick removal of the ligand leads to less mobile Pt NPs. In the work of Mackus *et al.* [82], a much larger PSD was found for the Pt thermal ALD process using $O_2$ co-reactant while a narrow PSD shifted to greater sizes with ALD cycles was observed for Pd and Pt PE-ALD processes (using either hydrogen plasma or a three-step process with oxygen and hydrogen plasma). The explanation was a difference in mobilities of Pd or Pt atoms on the substrate. Their diffusion is limited in the case of thermal ALD of Pt because unreacted ligands are present on the substrate. Dendooven *et al.* [83] also observed differences in Pt deposition either using $O_2$ or $N_2$ plasma as a co-reactant. In the latter case, surface diffusion process seems to be suppressed inducing constant density whereas with plasma oxygen-based process, ripening of NPs due to atom or NPs mobility takes place promoting coalescence by increase of NPs size and decrease of their density. Solano *et al.* [84] noticed Ostwald ripening in different oxygen atmospheres and starting above 500°C in most cases. For Pt NPs with oxidized surfaces in a reductive environment, ripening was noticed at room temperature which seems to come from very mobile species (PtO or $Pt_2O_3$) created by the reduction of $PtO_2$. Overall, for the combustion of organic ligands processes, the oxidizer partial pressure affects the surface chemistry as it is based on adsorption reaction, i.e. the amount of metal deposited and thus the average NP size. The choice of the co-reactant in the process also influence the catalytic properties of the deposited nanoparticles.

The mobility plays also a role when it comes to the temperature used during deposition. Grillo *et al.* [76] shows that at low temperature, the mobility of the clusters on the surface is very dependent of their size and close to zero which gives a very narrow spiky peak in the PSD (see Figure 9) whereas at

higher temperature, the mobility of clusters is no longer size-dependent. In this case, even big NPs are moving on the surface and a quick coalescence of NPs explaining a broader PSD with the presence of a tail is observed (see Figure 9). These observations are in agreement with the work of Mackus *et al.* [77] during Pt ALD on oxides, where Pt NPs grow not only due to ALD surface reactions, but also through Ostwald ripening via volatile $PtO_2$. Pt ALD in the works of Goulas *et al.* [78] and Sun *et al.* [79] support the features of high-temperature PSDs as well. The study of Van Bui *et al.* [49] for ALD of Pd NPs resulting in broad right-skewed PSD with a reduction in the NPs density with the number of cycles, is consistent with NPs sintering via Smoluchowski ripening.

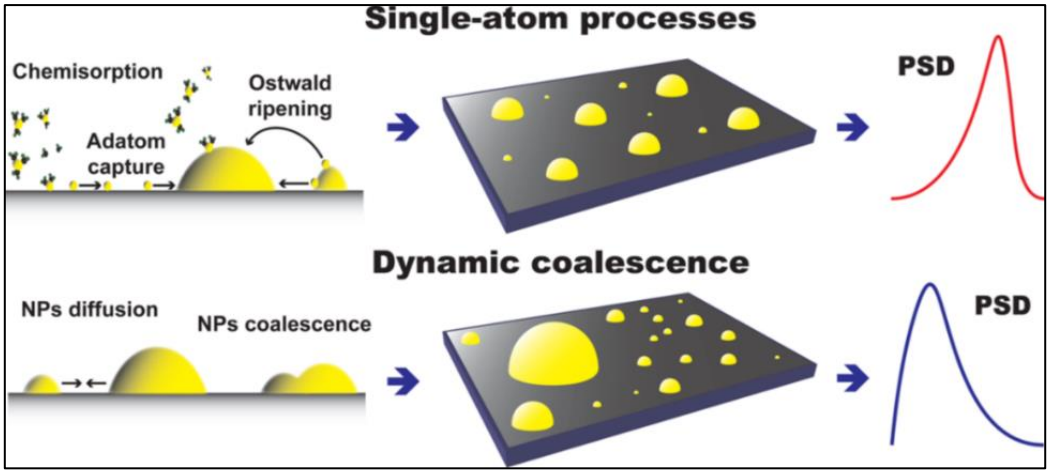


Figure 9: Schematic representation of the atomistic processes relevant to ALD of NPs and their effect on the shape of the PSD. From [76].

The process temperature is also important in ALD of Ag films. Van den Bruele *et al.* [85] investigated the island growth regime and found that the surface island morphology is dependent on surface diffusion. The PSD shows a log-normal distribution with a decrease of density of island nuclei and an increase of islands size with increasing temperature. The Ag growth mechanism in the PE-ALD regime in terms of ripening has only been reported by Golrokhi *et al.* [29]. They prove the occurrence of surface Ostwald ripening by studying the NPs morphology while increasing ALD cycles. As the agglomeration takes place, they noticed a reduction of the NPs density, an increase of their size and gap between particles while the PSD started to broaden. Overall, the deposition temperature plays a critical role in the surface diffusion processes and a significant repercussion on the evolution of the shape of the PSD with the number of cycles.

Outside the field of ALD, Smoluchowski ripening is said to occur for homoepitaxial growth of metal on metal (100) substrate. This is the case for Ag/Ag(100) system at 295K and Cu/Cu(100) at the same temperature. In contrast, Ostwald ripening occurs for Ag/Ag(111) at 295 K, for Cu/Cu(111) between 300 and 355 K, and for Cu/Cu(100) at 343 K. (see [68] and references therein)

Among the few works on the effect of plasma treatment on metallic NPs, Tang *et al.* [74] brought to light the fact that with plasma treatment, the Ag NPs deposited by the DC magnetron sputtering process started to aggregate and their size increased due to the Ostwald ripening process. This process was more pronounced for denser particle samples as bigger nanoparticles have been deposited. An article studying the influence of oxygen plasma treatment on the morphology of Ag film deposited via a metalorganic silver precursor demonstrated that highly covered film promoted the Ostwald ripening process and that oxygen plasma is an efficient way to tune the Ag nanoparticles. [86]

However, it remains some difficulties to clearly discriminate between OR and SR from PSD due to the fact that similar lognormal distribution can be found in both cases even if either the whole NPs or a single atom species participate to the growth mechanism. [87] Zhang *et al.* [87] differentiate the contribution of each mechanisms and found, by in situ electron microscopy study of Pt nanoparticles, that OR had a larger effect on the particle coarsening. [84]

### I.2.4. Conclusion

In this section, thin film growth modes have been presented and the influence of the surface energy has been demonstrated. Several physical and chemical processes play a role in the noble metal growth mechanism by chemical vapor-phase method: the atoms arrival from the precursor and their adsorption, their diffusion engendering NPs formation and growth, and the creation of an in-equilibrium system by decreasing the NPs surface energy via ripening processes. The substrate has also an influence on the diffusion process and represents an alternative route for continuous thin film deposition. This is the object of section I.4. Before that, the next part reviews the chemical vapor-phase deposition of silver films.

## I.3. Chemical vapor-phase synthesis of silver films

The aim of this part is to review the state-of-the-art (SoA) of Ag film by chemical vapor deposition and atomic layer deposition techniques.

### I.3.1. Chemical Vapor Deposition

#### I.3.1.1. Introduction

This section describes first the chemical vapor deposition (CVD) techniques mainly used for Ag deposition, with their pros and cons. A general overview of the SoA of CVD of Ag films in terms of morphology and electrical properties are then reviewed.

| | | | Principle | Advantages / Purpose | Disadvantages / Requirements |
|---|---|---|---|---|---|
| **Classical CVD** | **Conventional CVD** *Chemical Vapor Deposition* | | • Substrate placed in a reaction chamber and is heated to a high temperature.<br>• A chemical carrier gas composed of the coating material passes around the part and deposits the coating metal or compound on the part surface through a chemical reaction from the vapor phase. | • Avoid the line-of-sight.<br>• High deposition rate.<br>• Production of thick coating layers. | • Requires high temperatures: increase process cost and limit use of compounds/substrates due to their thermal instability.<br>• Precursors exhibiting high vapor pressure, high volatility and high thermal stability, reacting on a heated substrate at temperature low enough to avoid decomposition but high enough to provide the energy necessary for chemical reaction. |
| | | **MO-CVD** *Metal Organic CVD* | CVD processes using metalorganic precursor (attaching metal to organic compound that has a very high vapor pressure). | • Use the property of high vapor pressure of precursor.<br>• Evaporation and decomposition of the precursor at low temperature.<br>• Increase in the reactivity of the precursors and allows high deposition rates to be obtained at low temperatures. | • Contamination of deposit by carbon derived from the ligands. |
| | | **AP-CVD** A*tmospheric Pressure CVD* | CVD processes undergone at atmospheric pressure. | • Lower equipment cost since use of simple experimental setup without the need of a vacuum system.<br>• Use of precursors with moderately high vapor pressures.<br>• High deposition rate, high throughput. | • Poor uniformity.<br>• Undesired contamination.<br>• Gas flow dynamics difficult to control. |
| | | **LP-CVD** *Low Pressure CVD* | CVD processes undergone at sub-atmospheric pressure. | • No carrier gases required.<br>• Reduced pressures to reduce undesired gas-phase reactions and particle contamination: high purity material.<br>• Lower reaction temperature than AP-CVD and less dependence on gas flow dynamics.<br>• Improve film uniformity along substrates. | • Lower deposition rate than AP-CVD (but reasonable).<br>• Expensive cost. |
| | | **UHV-CVD** *Ultrahigh Vacuum CVD* | LP-CVD processes undergone at a very low pressure, i.e. below $10^{-8}$ Torr. | | |
| | **DLI-CVD** *Direct Liquid Injection CVD* | | • Precursors in a liquid state (liquid or solid dissolved in a suitable solvent).<br>• Liquid solutions injected into a spray chamber by means of injectors.<br>• Precursors transported to the substrate as in conventional CVD. | • Suitable for the use of liquid or solid precursors.<br>• Allows the utilization of low vapor pressure and thermally unstable chemical precursors.<br>• High growth rates. | • Requires precursor solubility in a solvent that does not decompose on the substrate surface during deposition. |
| | **AA-CVD** *Aerosol Assisted CVD* | | Involves producing a very fine mist of a liquid precursor (or a solution of the precursor)<br>• Precursor first dissolved in a solvent. | • Suitable for non-volatile precursors.<br>• Enables high mass-transport rate of precursor to the substrate.<br>• Does not require high precursor vapor pressure at room temperature or long-term thermal stability of the precursor at | |

| | | | | |
|---|---|---|---|---|
| | | • Solution passed through an aerosol generator where micron-sized droplets are generated in an inert carrier gas and passed into a preheating zone where both the solvent and the precursor evaporate.<br>• Gas flow reaches heated substrate surface where thermally induced reactions occurs to produce films | elevated temperatures (allow transport of thermally sensitive compounds).<br>• Higher deposition rates than conventional delivery method.<br>• Reproducible deposition of binary materials. (operated under conditions where the precursor delivery rate and the composition of precursors in solution and droplets do not change with time) | |
| | **PE-CVD** *Plasma-Enhanced CVD* | • CVD processes using plasmas in a vacuum to ionize and dissociate the chemical carrier gas, enhancing the chemical reaction and providing heat. | • Operate at lower temperatures since chemical reactions in PECVD not ignited by heat, thus reducing stress/thermal expansion mismatch.<br>• Better uniformity.<br>• Improve deposition rates.<br>• Suitable for both organic/inorganic precursors. | • Desorption of by-products incomplete because of low temperature and gases (particularly hydrogen) remain as inclusion in the deposit.<br>• Plasma damage. |
| **Non- classical CVD** | **FA-CVD** *Flame Assisted CVD* | • Flame used as the heat source in an open atmosphere chamber to provide required energy to crack precursor species into fragments and subsequently forms the film upon the substrate. | • Use of low hazard aqueous precursors, which are in many cases very soluble, and of relatively low toxicity (environmental impact).<br>• A low-cost, relatively simple atmospheric pressure CVD technique.<br>• Compatible with small volume, batch, and high-volume continuous coating processes. | • Control of the flame temperature.<br>• Poor film coverage. |
| | **LI-CVD** *Laser-induced CVD* | • Focused laser beam provides the localized heat source on the part.<br>• The carrier gas undergoes a thermally induced chemical reaction, depositing the coating on the part. | • Operates at lower temperature than thermal CVD, but with higher deposition rates.<br>• Resulting chemical gas-phase reactions very specific, leading to highly pure film deposits | • Generally difficult to remove light element impurities formed during the deposition. |
| | **SFT-CVD** *Supercritical Fluid Transport CVD* | • CVD process in which precursors is dissolved in supercritical fluids.<br>• Then solution, under high pressure, pass through a restrictor into a deposition chamber where rapid expansion of supercritical fluid causes vaporization of the solutes.<br>• Vaporized precursor compounds then induced to react at or near the substrate surface to form a thin film | • Suitable for non-volatile precursors.<br>• If aerosols rather than vapors formed, aerosol particles smaller than those formed by nebulization of ordinary liquid solutions | • Requires precursors solubility in common supercritical fluids ($CO_2$, $N_2O$). |
| | **Powder flash evaporation MOCVD** | • Powder of precursor is kept at room temperature in an inert atmosphere during the deposition and steadily delivered by small portions into an evaporator.<br>• Small beads of an inert material are added to the powder in order to dilute the mixture and make the slow powder delivery process more reliable.<br>• Flash-evaporation of precursor from the beads' surface assures controlled and constant in-time composition of the precursor vapor. | • Facilitates the use of temperature unstable precursors, more particularly suitable for use of precursors with a big difference in sublimation/evaporation temperatures. | • Temperature required for evaporation precursor is at least equal to the decomposition temperature which generates product losses and poor yield. |
| | **Powder feed method-CVD** | • Reagent powders is slowly fed and pneumatically transported by argon flow directly into the chemical vapor deposition furnace. | • Allows lower vapor pressure materials to be used.<br>• Because vaporizers are not used, the number of process parameters that must be controlled is greatly reduced.<br>• Deposition rates are at least an order of magnitude greater than those achieved by reagent sublimation. | • technological problem concerns the control of the powder feeding rate |

Table 1: Chemical vapor deposition (CVD) methods used to deposit metallic films.[88, 89, 90, 91]

| Technique | Refs. | General formula | Ag precursor | Solvant | $T_{Deposition}$ (°C) | $T_{Precursor}$ (°C) | Reagent | Resistivity (µΩ.cm) | Thickness (nm) |
|---|---|---|---|---|---|---|---|---|---|
| **DLI-CVD** *Direct Liquid Injection CVD* | [92] | Carbo. P add. | $(n\text{-}Bu_3P)_2AgOOCC(CH_3)CCH_3H$ | THF | 152-402 | 152 | - | Max. 1500 Post-treated: 15 | 200-600 |
| | | | $(n\text{-}Bu_3P)_2AgOOC(CH_2)C_6H_5$ | | | | | Max. 2600 Post treated: 550 | 200-600 |
| | [38] | β-dik P add. | $Ag(fod)(PEt_3)$ | - | 250-350 | 80 | $H_2$ | N.A. | |
| | | | | | | | - | 1.9-3 | N.A. |
| | [36] | β-dik | Ag(hfac)(1,5-COD) | ethanol, methanol or monoglyme | 150-400 | 220 | - | 3 | > 150 |
| | | Inorganic salt | $AgNO_3$ | | | | - | 2 | > 900 |
| | [93] | Carbo. | $AgOOCC(CH_3)_3$ | Mesytilene diisopropylamine | 250 | | $O_2$ | 2-4 | >200 |
| | | | | | 300 | 150 | $H_2$ | | |
| **CVD** *Chemical Vapor Deposition* | [94] | β-dik P add. | $Ag(fod)(PEt_3)$ | - | > 230 | 80 | - | 1.92 | N.A. |
| | | β-dik | Ag(hfac)(1,5-COD) | - | 180-350 | 80 | - | No film obtained | |
| | | | Ag(hfac)(VTES) | | >180 | | | 1.83 | 720 |
| | [95] | β-dik | Ag(hfac)(tmeda) | - | 300-450 | 65-75 | $N_2/H_2O$ or $H_2$ | N.A. | |
| | | | Ag(hfac)(bipy) | | N.A. | | | N.A. | |
| | [96] [a] | Carbo. | $AgOOCC(CH_3)_3$ | - | 250-510 | 250 | - | 2-4 | 1000-3000 |
| | [97] | β-dik P add. | $Ag(hfac)(PMe_3)$ | - | 250-350 | 80-100 | - | 6.5 | 1100 |
| | | | $Ag(hfac)(PEt_3)$ | | | 50-70 | - | N.A. | |
| | [35] | β-dik P add. | $Ag(hfac)(PMe_3)$ | - | 250-350 | 80-100 | - | 6.5 | 1100 |
| | | | $Ag(hfac)(PEt_3)$ | | 250-350 | 50-70 | - | N.A. | |
| | | | $Ag(fod)(PMe_3)$ | | 300 | 50-80 | Dry/wet $H_2$ | N.A. | |
| | | | | | 370-380 | | - | | |
| | | | $Ag(fod)(PEt_3)$ | | 230-320 | | Dry/wet $H_2$ | 2.6-2.8 | 2000 |
| | | | | | 370-380 | | - | | |
| | [98] | β-dik | Ag(hfac)(VTES) | - | 160-280 | 30 | - | < 5 [d] | 1000 |
| | | | Ag(tfac)(VTES) | No deposition performed | | | | | |
| | | | Ag(fod)(VTES) | | | | | | |
| | [99] | β-dik | Ag(hfac)(BTMSA) | - | 150-250 | 30 | $H_2$ | < 6.5 [d] | N.A. |
| | | | | | | | - | | |
| | | | Ag(Ttfac)(BTMSA) | No deposition performed | | | | | |
| | | | Ag(Btfac)(BTMSA) | | | | | | |
| | | | Ag(fod)(BTMSA) | | | | | | |
| | [100] | F Carbo. P add. | $Ag(OOCC_2F_5)(PMe_3)$ | - | 210-290 | 180 | - | N.A. | |
| | | F Carbo. | $Ag(OOCC_2F_5)$ | | 270-350 | 240 | | | |
| | [101] | β-dik | Ag(hfac)C=NMe | - | 250-280 | 80-90 | Dry/wet $H_2$ | N.A. | |
| | | | | | 320 | | - | | |
| | [102] | Carbo. P add. | $Ag\{OOCC(CH_3)_3\}(PMe_3)$ | - | 180-200 | 160 | - | 113 | 20 |
| | | | | | | | | 67 | 58 |
| | | | $Ag\{OOCC(CH_3)_3\}(PEt_3)$ | | | | | N.A. | |
| | [103] | F Carbo. | $Ag(OOCC_2F_5)$ | - | 280 | 240 | - | N.A. | |
| | [104] | Carbo. | $Ag_2(CH_3CH_2C(CH_3)_2COO)_2$ | No deposition performed | | | | | |
| | | | $Ag_2(CH_3CH_2C(CH_3)_2COO)_2(PMe_3)_2$ | | | | | | |
| | | | $Ag_2(CH_3CH_2C(CH_3)_2COO)_2(PEt_3)_2$ | - | 200-280 | 170 | - | N.A. | |
| | [105] | F Carbo. P add. | $Ag(OOCC_2F_5)(PMe_3)$ | - | | 165 | - | N.A. | |

| | | | | | | | | | |
|---|---|---|---|---|---|---|---|---|---|
| | | | $Ag(OOCC_3F_7)(PMe_3)$ | | 190-220°C | 180 | | N.A. | |
| | | | $Ag(OOCC_8F_{17})(PMe_3)$ | | | 160 | | N.A. | |
| | [106] | β-dik | Ag(COD)(hfac) | - | 160-240 | 80-150 | $H_2$ | N.A. | |
| | [107] [b] | Inorganic salt | AgI | - | 800-900 | - | $H_2$ | N.A. | |
| | | | | | < 700 | | $H_2$/no $H_2$ | No film obtained | |
| | | F Carbo. | $Ag(OOCCF_3)$ | - | 600 | - | $H_2$ | N.A. | |
| | | | | | 300-900 | | ≤ 0.05 l/min | ∞ | N.A. |
| | | Ag(PF) | $Ag[CF_3CF=C(CF_3)]$ | - | 300-700 | - | $H_2$ | N.A. | |
| | | | | | | | ≤ 0.01 l/min | No film obtained | |
| | [108] [c] | Inorganic salt | AgF | - | 80-600 | N.A. | - | N.A. | |
| | [109] | Ag(PF) | $[AgCF_3CF=C(CF_3)]_4$ | - | 275 | 110 | - | N.A. | |
| | [110]** | β-dik P add. | $Ag(fod)(PEt_3)$ | - | 230-260 | 67 | $H_2$ | N.A. | |
| | [111] | β-dik P add. | $Ag(hfac)(PMe_3)$ | | 200-425 | 20-50 | - | No film obtained | |
| | | | | - | 200-425 | | $H_2$ | N.A. | |
| | | | $Ag(hfac)(PMe_3)_2$ | | | | | | |
| | [112] | β-dik | Ag(hfac)(BTMSE) | - | 180-220 | 80 | - | 1000 | N.A. |
| **LI-CVD** *Laser-induced CVD* | | | No deposition performed with: Ag(hfac)(BDMESA) Ag(hfac)(ATMS) | - | 80-220 | 80 | - | 1 | N.A. |
| | [113]*** | Carbo. | $Ag(OOCCH_3)$ | - | 380 | - | - | 200-6000 | 1000 |
| | [114]*** | Carbo. | $Ag(OOCCH_3)$ | - | 380 | - | - | N.A. | |
| **PE-CVD** *Plasma-Enhanced CVD* | [37] | Ag(PF) | $Ag[CF_3CF=C(CF_3)]$ | - | 120, 150 | N.A. | $H_2$ | ≤ 2 [d] | 20-500 |
| | | | | | | | - | ≥ $2\times10^8$ [d] | |
| **AA-CVD** *Aerosol Assisted CVD* | [115]* | β-dik P add. | $Ag(acac)(PPh_3)$ | THF | 310 | - | - | only faint transparent films | |
| | | | $Ag(dpm)(PPh_3)$ | | | | | only faint transparent films | |
| | | | $Ag(tfac)(PPh_3)$ | | | | | 7.04 | 32 |
| | | | $Ag(hfac)(PPh_3)$ | | | | | 569.16 | 30.6 |
| | | | $[Ag(fod)]_3(PPh_3)_5$ | | | | | ∞ | 16.7 |
| | | β-diketoim P add. | $Ag(hfacNhex)(PPh_3)$ | | | | | 3.245 | 29.5 |
| | | | $Ag(hfacNchex)(PPh_3)$ | | | | | 414.16 | 24.8 |
| | [116] | Carbo. | $Ag(OOCCH_3)$ | THF | 310 | - | - | No deposition performed | |
| | | | $Ag[OOC(CH_3)_3]$ | | | | | No film obtained | |
| | | | $Ag(OOCC_6H_2Me_3)$ | | | | | No deposition performed | |
| | | F Carbo. | $Ag(OOCC_3F_7)$ | | | | | 3.78 | 9 |
| | | | $Ag(OOCC_6F_{13})$ | | | | | 37.7 | 26 |
| | | | $Ag(OOCC_7F_{15})$ | | | | | 5490000 | 22 |
| | | Carbo. P add. | $Ag(OOCCH_3)(PMe_3)_2$ | | | | | 48960000 | 28.8 |
| | | | $Ag\{OOCC(CH_3)_3\}(PMe_3)_2$ | | | | | 458.64 | 27.3 |
| | | | $Ag(OOCC_6H_2Me_3)(PMe_3)_2$ | | | | | ∞ | 9.1 |
| | | | $Ag(OOCCH_3)(PPh_3)_2$ | | | | | ∞ | N.A. |
| | | | $Ag\{OOCC(CH_3)_3\}(PPh_3)_2$ | | | | | ∞ | 8 |
| | | | $Ag(OOCC_6H_2Me_3)(PPh_3)_2$ | | | | | ∞ | N.A. |
| | | | $Ag(OOCCH_3)(PPh_3)_3$ | | | | | ∞ | N.A. |
| | | F Carbo. P add. | $Ag(OOCC_3F_7)(PPh_3)_2$ | | | | | ∞ | 6.5 |
| | | | $Ag(OOCC_6F_{13})(PPh_3)_2$ | | | | | ∞ | 9 |

| | | | | | | | | | |
|---|---|---|---|---|---|---|---|---|---|
| | | | $Ag(OOCC_7F_{15})(PPh_3)_2$ | | | | | ∞ | 9.5 |
| | [117] | Carbo. | $Ag(OOCCH_2CN)$<br>$Ag(OOCH_2C{=}CH)$<br>$Ag(OOCH_2C{=}CHCH_2CH_2]$<br>$Ag[OOCMe(H)C{=}C(Me)]$<br>$Ag[OOCPh(H)C{=}CH]$ | No deposition performed | | | | | |
| | | Carbo. P add. | $Ag[OOCH_2C{=}CH(PPh_3)_2$ | | | | | | |
| | | | $AgOOCCH_2CN(PPh_3)_2$ | THF | 300-546 | - | - | No film obtained | |
| | | | $Ag[OOCH_2C{=}CHCH_2CH_2\ (PPh_3)_2]$ | | 300 | | | 238 | 170 |
| | | | $AgOOCPh(H)C{=}CH(PPh_3)_2$ | | 200-398 | | | Only ultra-thin film obtained | |
| | | | $Ag(OOC(Me)C{=}C(H)Me)(PPh_3)_2$ | | 300 | | | 268.8 | 168 |
| | | 1,2-bis(phenylthio) ethane add. | $AgOOCH_2C{=}CHCH_2CH_2(PhSCH_2CH_2SPh)_2$ | | 250-300 | | | N.A. | 89 |
| | | | $AgOOCMe(H)C{=}C(Me)(PhSCH_2CH_2SPh)_2$ | Ethanol or methanol | 200-348 | | | N.A. | 84 |
| | [118] | Aryloxide-triphenylphosphine complexes | $Ag(OC_6H_2Cl_3\text{-}2,4,6)(PPh_3)_2$ | THF | 300-596 | - | - | poor quality of the films, resistivities not measured | |
| | | | $Ag\{OC_6H_2(CH_2NMe_2)_3\text{-}2,4,6\}(PPh_3)_2$ | | 300 | | | | |
| | | | $[Ag(OC_6H_4Me\text{-}2)(PPh_3)_3].2\text{-}MeC_6H_4OH.C_6H_5CH_3$ | | 250-398 | | | | |
| | | | $Ag(OC_6H_4Me\text{-}2)(PPh_3)_2]$ | No deposition performed | | | | | |
| | | | $[Ag(OPh)(PPh_3)_3].PhOH$ | | | | | | |
| | [119]* | β-dik | $Ag(hfac)(SEt_2)$ | Toluene | 120-300 | 65-85 | - | 2 | N.A. |
| **FA-CVD** *Flame Assisted CVD* | [120]* | Inorganic salt | $AgNO_3$ | Water | 300 | - | - | N.A. | |
| | [121]* | Inorganic salt | $AgNO_3$ | Water | 300 | - | - | N.A. | |
| | [122]* | Inorganic salt | $AgNO_3$ | Water | 300 | - | - | 8.1 | 250 |
| | | | | | 100 | | | ∞ | N.A. |
| **SFT-CVD** *Supercritical Fluid Transport CVD* | [123] | Inorganic salt | AgI | Acetone | 600 | N.A. | - | N.A. | |
| | | Ag triflate | $AgCF_3SO_3$ | Diethyl ether | 600 | | | | |

Table 2: Summary of achievements reported of the CVD of silver thin films

* AP-CVD: Atmospheric Pressure CVD; **: UHV-CVD: Ultrahigh vacuum CVD; ***: Laser-Induced Thermal Decomposition;

[a]: powder-flash evaporation; [b]: powder feed method; [c]: ion-pumped 12 in; [d]: critical thickness;

N.A.: Not available; RT: room temperature;

No deposition performed: No CVD was performed either based on previous analyses (TGA, MS,…) or just not selected for the study;

No film obtained: tentative of depositing Ag films failed;

PF: perfluoro-1-methylpropenyl; THF: tetrahydrofuran; Et: ethyl; Me: methyl; Bu: butyl; Carbo.: Carboxylates; F Carbo.: Fluorocarboxylates;

Carbo. P add.: Carboxylates phosphine adducts; F Carbo. P add.: Fluorocarboxylates phosphine adducts;

β-dik: β-diketonates; β-dik P add.: β-diketonates phosphine adducts;

β -diketoim: β -diketoiminates; β-diketoim P add.: β -diketoiminates phosphine adducts.

### I.3.1.2. Chemical vapor deposition methods for silver film deposition

Table 1 summarizes the main chemical vapor deposition (CVD) processes investigated to deposit metallic films, more precisely the one used for Ag films. Conventional thermal CVD method requires to use precursors exhibiting high vapor pressure, high volatility and high thermal stability in order to react on a heated substrate at temperature low enough to avoid decomposition but high enough to provide the energy necessary for chemical reaction.

One of the most important challenge associated with CVD of metal films is the insufficient volatility of several metal-containing compounds. To circumvent this aspect, metal organic CVD (MO-CVD) is employed. Its particularity is due to the use of organometallic precursors, i.e. precursors containing one metal atom and several hydrocarbon bonds. These precursors have two main advantages: a high vapor pressure and an evaporation and decomposition at reduced temperatures. This increases the reactivity of the precursors and makes it possible to obtain high deposition rates at lower temperatures than classical CVD. However, in this case, contamination by non-metallic impurities remained the major issue, although the use of a reagent like $H_2$ can reduce their amount.

Playing with the working pressure may also improve the film quality: atmospheric pressure CVD (AP-CVD) causes undesired contamination level which may be reduced by diminishing the pressure using low pressure CVD (LP-CVD) or ultrahigh vacuum CVD (UHV-CVD), even though these two last methods engender lower deposition rate.

Another way to improve the deposition process is to use an alternative way of transporting precursors by more sophisticated methods. Direct liquid injection CVD (DLI-CVD) uses precursor in a liquid state (liquid or solid dissolved in a suitable solvent) which is brought to the reactor in liquid form and is vaporized before being transported to the substrate as in conventional CVD. Aerosol assisted CVD (AA-CVD) is a variant of DLI-CVD, the main difference is that the precursor is sprayed in liquid form on the substrate and not vaporized in the chamber as in DLI-CVD. These two methods allow the use of low vapor pressure and thermally unstable chemical precursors while they require precursor solubility in a solvent.

Plasma-enhanced CVD (PE-CVD) is also a promising method to produce pure metallic films. Using plasmas in a vacuum to ionize and dissociate the chemical carrier gas, it operates at reduced temperatures since chemical reactions are not ignited by heat. However, due to low temperature process, impurities coming from gases (particularly hydrogen) remain as inclusion in the deposit.

In addition to these methods, non-classical CVD techniques have been also developed. Flame assisted CVD (FA-CVD) is an environmentally-friendly technique with the ability to use aqueous salts rather than organic precursors or solvents, where a flame provides the energy to ignite the chemical reaction at atmospheric pressure. The control of the flame temperature and the poor film coverage remain the major drawbacks. Laser-induced CVD (LI-CVD) operates at lower temperature than thermal CVD since a carrier gas undergoes a thermally induced chemical reaction by means of a focused laser beam which generally produce light element impurities during deposition and difficult to remove.

Other exotic methods are employed to circumvent the necessity for high precursor vapor pressure and high thermal stability. This is the case of supercritical fluid transport CVD (SFT-CVD) which, though, requires precursors solubility in common supercritical fluids. Precursor transported by powder feed method CVD enables the low vapor pressure reactant powder transport directly into the chemical vapor deposition furnace, but the major problem concerns the control of the powder feeding rate. Precursor transported by powder flash evaporation MOCVD enables to work at reduced temperature and pressure to improve thermal stability of the precursor. It is well suitable for use of precursors with a big difference between sublimation and evaporation temperatures. However, the

temperature required for evaporating the precursor is at least equal to the decomposition temperature which generates product losses and poor yield.

It is also possible to combine different techniques in order to obtain the combined merits of the respective techniques, e.g. DLI-MOCVD and AA-CVD/AP-CVD.

### I.3.1.3. Results for chemical vapor deposition of silver films

Table 2 gives a general overview of the state-of-the-art of Ag films regarding the CVD techniques used, the selected Ag precursors (only the general formula and the precursor name are given in this table, the correspondence between general and structural formulae is given in Annex 1), the process conditions and the results obtained in terms of electrical properties. These electrical properties have been summarized in the plot of the resistivity as a function of the film thickness in Figure 10, when data are available in the publication. The morphologies of the obtained films are compared using SEM images in Figure 11.

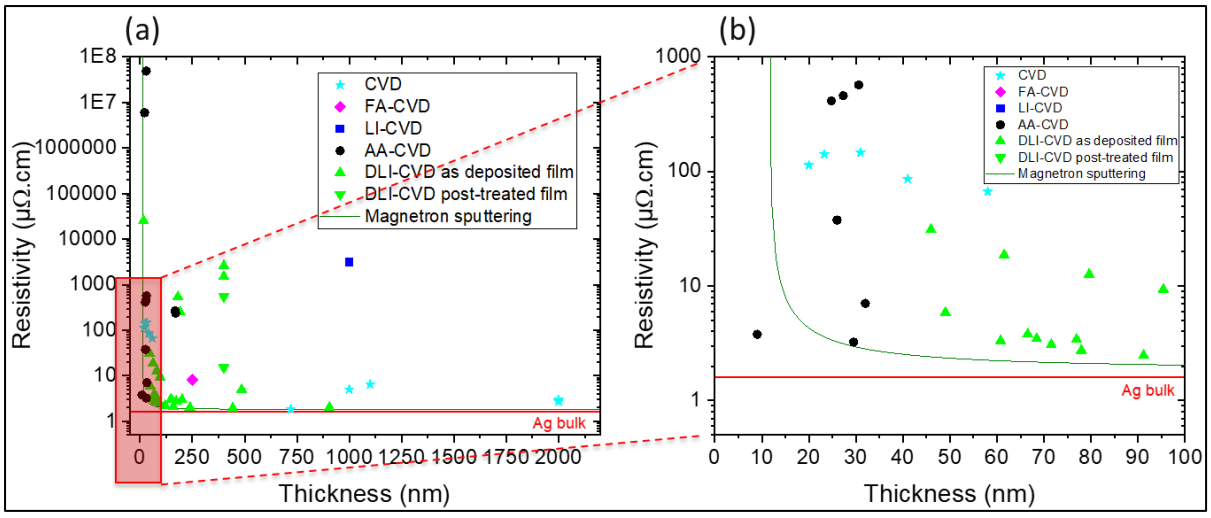


Figure 10: (a) Resistivity of silver films plotted as a function of the film thickness based on commonly used CVD techniques by various authors to grow Ag films (see Table 2 for references and zoom in in (b). The green curve has been plotted as a reference for the Ag thin film deposited by magnetron sputtering, following the publication of Hauder *et al.* [17].

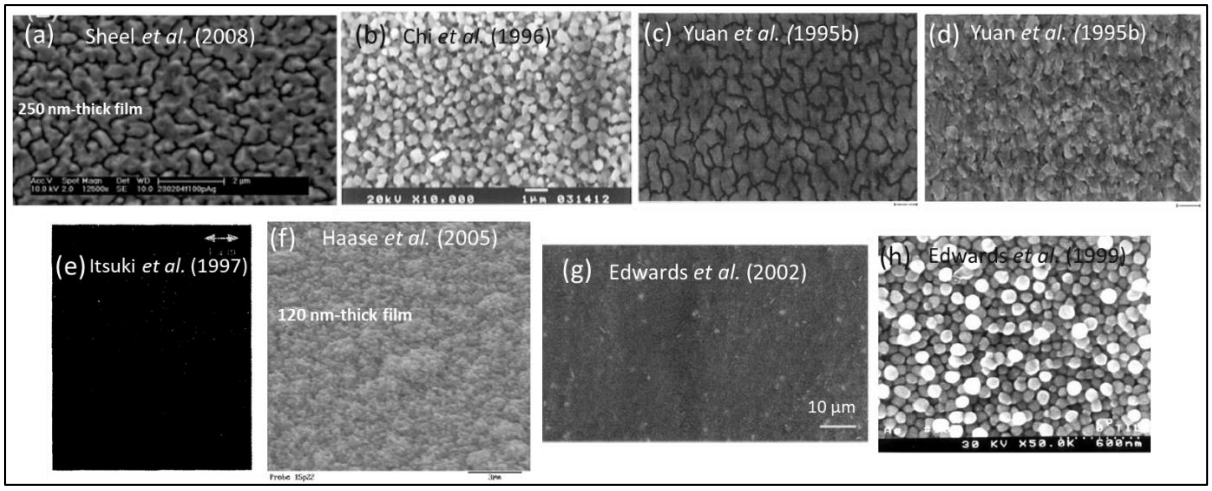


Figure 11: Scanning electron micrographs of typical silver films obtained by CVD using different approaches: (a) FA-CVD [122]; (b) standard CVD [98]; (c) and (d) standard CVD [101] using (c) high temperature and no carrier gas and (d) low temperature in the presence of carrier gas; (e) LI-CVD [112]; (f) DLI-CVD [92]; (g) and (h) AA-CVD using different type of silver precursor (g) fluorocarboxylates [116] and (h) β-diketoiminates phosphine adducts [115]. The references are indicated on the pictures, and the related conditions are reported in Table 2.

In this part, we are focusing on Ag films obtained by CVD using Ag precursors and not on the study of the Ag compounds available and their potential use as Ag precursors for CVD. Indeed, this has already been the aim of several reviews (e.g. [2, 8, 124, 125, 126, 127]), and scientific articles (e.g. [128, 129, 130, 131, 132, 133, 134]), mainly focused on the chemical point of view.

Several precursors have been investigated in order to obtain Ag thin films. Due to the requirement of CVD mentioned above, it is quite challenging to find a suitable Ag precursor exhibiting high vapor pressure and also reacting at low deposition temperature in order to form a high-purity films. For example, Ngo *et al.* [135] investigated 17 Ag complexes and none of them was suitable because of the ligands' dissociation. Haase *et al.* [92] studied 15 Ag complexes and only one of them was appropriate for the CVD of silver.

Based on Table 2, there is no general correlation between the deposition method and the film quality. As expected for a deposition at equilibrium, silver tends to form islands rather than a uniform film on oxide surface. This is due to the weak wettability of oxides by metals, and the high mobility of silver, even at low temperatures. An increase in film thickness promotes coalescence of these islands.

This is the case for **FA-CVD** [120, 121, 122] using widely silver salts ($AgNO_3$) which gives continuous conductive film (Figure 11 (a)) at high thicknesses, i.e. 250 nm-thick Ag film gives a resistivity of 8 µΩ.cm. [122] (Figure 10) This is also the case for **standard CVD** processes for which resistivities close to Ag bulk are obtained at very high thicknesses, [35, 96, 97, 98] e.g. 1.83 µΩ.cm for a 720-nm-thick Ag film [94] and high resistivities are obtained for thinner films, e.g. 110 µΩ.cm for 20 nm [102] (Figure 10). Typical morphology of the films consists of continuous grains (Figure 11 (b)). The use of hydrogen as a reagent could enhance the deposition and reduce the processing temperature. [35, 99, 101] In the study of Yuan *et al.* [101], using simple thermal CVD, Ag films deposition were performed at 320°C (deposition at 250°C being inefficient) and a high level of contamination of carbon and oxygen were found. At 250°C, with the use of either dry or moist hydrogen as carrier gas, films had a shiny mirror-like appearance with no detectable impurities. SEM images reveal amorphous islands with diameter of 1 µm for high temperature with no carrier gas (Figure 11 (c)) and crystalline film with grain size of 0.2–0.4 µm for low temperature in the presence of hydrogen (Figure 11 (d)).

Using **PE-CVD** technique, Oehr *et al.* [37] proved that $H_2$ is essential for the deposition of Ag, otherwise the films became polymeric. They found a resistivity lower than 2 μΩ.cm and greater than $2\times10^8$ μΩ.cm, with and without $H_2$, respectively. Although the Ag(PF) complex has been useful, growth rates have been relatively slow due to the modest vapor pressure of the complex.

Itsuki *et al.* [112] compared **thermal CVD** versus **LI-CVD** using a β-diketonate silver complex [(BTMSE)Ag(hfac)]. The laser CVD results were far better than the thermal CVD ones. In addition to make deposition possible at lower temperature (80°C for LI-CVD vs. 200°C for thermal CVD), LI-CVD exhibits film resistivity of the order of 1 μΩ.cm with finer and more evenly distributed morphology (Figure 11 (e)) versus 1 mΩ.cm with unevenly distributed granular islands of silver for standard CVD process. The explanation was that photoactivation by the excimer laser confined the absorption to around 308 nm, so any species components present in the precursor did not affect the film purity. In another study Lu *et al.* [113] exposes film with high thickness and still very high resistivity, but it is difficult to extract a trend since this is a unique value and no set of data is available.

Modifications such as **DLI-MOCVD** reduces the volatile requirements of precursors, allowing the use of less volatile non-fluorinated Ag precursors such as Ag carboxylates (due to a tendency to dimerize in the gas phase, thus making gas-phase transport quite difficult). [136] The work of Bahlawane *et al.* [36] confirmed that pure silver films may be produced using the metal-organic precursor Ag(hfac)COD in the presence of alcohols at low pressure (15 mbar). They observed an improvement of the growth rate and of the film quality in the presence of alcohols, which was attributed to the occurrence of a dehydrogenation reaction on the substrate surface. At thicknesses between 50–60 nm, resistivities of 3–6 μΩ.cm have been obtained using specific conditions. The resistivity decreases with the film thickness and a near bulk resistivity is reached at thickness higher than 150 nm. The reagent can also play an important role in DLI-CVD. In their study, Abourida *et al.* [93] obtained the best performances using Ag carboxylate either with medium hydrogen flow rate at high temperature or high oxygen flow rate at low temperatures, with a resistivity of 2–4 μΩ.cm for an Ag film of 300 nm. Gao *et al.* [38] used a β-diketonate [Ag(fod)($PEt_3$)] precursor and they found that Ag films have a higher conductivity at lower deposition temperature (less than 300°C), typically 1.9–3 μΩ.cm. Their explanation is that the contamination level decreases with the decrease of temperature and at higher temperature (higher than 300°C), a poor connectivity between grains is obtained. However, contrary to the standard CVD process, the effect of the reagent gas (hydrogen) results in larger resistance but the reason for this change has not been clearly understood. An interesting result is also obtained by Haase *et al.* [92] using tri-$^n$butylphosphine silver carboxylate and giving a smooth structure with compact nanocrystallites (Figure 11 (f)). For a film thickness of 200–600 nm, a resistivity of 1.5 mΩ.cm is achieved and then reduced to 15 μΩ.cm by means of an air plasma treatment in open atmosphere which removes surface carbon impurity. Another modification to reduce the volatility requirement of precursor is to use **SFT-CVD** but very few works for Ag films have been performed with this technique. [123]

As seen in Figure 10, the thinner Ag films with the lower resistivities are obtained by **AA-CVD** technique. Even though it enables higher deposition rate than standard CVD, the technique is highly precursor dependent. Indeed, Edwards *et al.* [118] obtained very disappointing results with poor quality silver films using silver(I) aryloxide triphenylphosphine complexes. In two other studies of the same group, [116, 117] they found only 2 silver carboxylates out of 28 suitable as CVD precursors. Employing Ag($OOCC_3F_7$) precursor, a resistivity as low as 3.8 μΩ.cm has been obtained for a silver film

thickness as low as 9 nm, which is by far better than Ag films obtained by PVD techniques. Even though the very rough surface and the presence of non-identified crystalline material was observed embedded into the film (Figure 11 (g)), EDXS analysis revealed the presence of carbon impurities but the absence of fluorine contaminants, contrary to the other fluorocarboxylates precursors investigated in this study. In another investigation, [115] working at atmospheric pressure and employing β-diketoiminates phosphine adduct as silver precursor [Ag(hfacNhex)($PPh_3$)], a 30-nm thick film exhibits a resistivity of 3.3 μΩ.cm. At low magnification, the film appears fairly uniform and smooth and at higher magnification, the film is made up from several layers of loosely packed spheres of silver. (Figure 11 (h))

#### I.3.1.4. Conclusion

We have given a broad overview on the current state-of-the-art of the CVD of silver films. No general correlation between the deposition method and the film quality have been extracted. In most cases, due to the growth mode of metals, Ag tends to form islands rather than a uniform film on oxide surface and the coalescence of the nanoparticles is promoted by an increase in film thickness. Employing Ag($OOCC_3F_7$) precursor and AA-CVD, the lowest resistivity of 3.8 μΩ.cm has been obtained for a silver film thickness as low as 9 nm. [116] This method is however highly precursor dependent.

Mixed ligand stabilized Ag(I) complexes containing either a fluorinated carboxylate or fluorinated and non-fluorinated β-diketonate have been widely synthesized and employed for the CVD of Ag. [137] They appear to be promising precursors since they combine criteria such as thermal stability, high vapor pressure and low sensitivity to light and air. Szlyk *et al.* [100] compared silver fluorocarboxylates precursors with and without phosphine and found that the phosphine containing complex can be evaporated at lower temperatures and also reacted at lower temperatures. The type of carboxylate group plays also a role on the morphology of deposited silver layers and the way of the grain packing on the substrate surface. [8] A special attention is paid to fluorinated β-diketonates coordinated with low molecular weight tertiary phosphines complexes, like Ag(hfac)($PEt_3$) or Ag(fod)($PEt_3$), the latter exposing the best volatility and stability of β-diketonates complexes. These precursors could be very effective as silver precursor in atomic layer deposition with gas injection thanks to their low melting point (45–46 and 26–28°C, respectively) giving high vapor pressure and allowing to work at lower deposition temperatures.

### I.3.2. Atomic Layer Deposition

#### I.3.2.1. Introduction

This section describes the SoA of the atomic layer deposition of silver thin films. It is first important to note that the ALD technique is a recent technique, mainly developed in the 1990's and 2000's, and the ALD of silver has only been investigated from 2007, due to the lack of appropriate precursors. This novelty of the subject explains the relatively low number of reference works in the literature.

As a reminder (see section I.1.), the main characteristics of ALD as compared to other deposition techniques (physical or chemical) is the self-saturation of the involved surface reactions. This self-saturation can ensure a very high control over the thickness, and a highly conformal coating. The principle of ALD consists in sequentially separating the global chemical reaction into two half-reactions, thus avoiding uncontrolled surface reaction that could occur when all reactants are available in the chamber. The half-reactions are kept separated by pulsing sequentially the first reactant (here the silver precursor) and the second reactant (here the reducing agent).

Beyond the reaction conditions, the main parameters to be selected concern the first and second reactants, which are investigated in the two next sections for the ALD of silver films. After that, we review the SoA of ALD of silver films in terms of morphology and electrical properties.

### I.3.2.2. Choice of the silver precursor

In the ALD process, one of the main parameters influencing the deposition, is the process temperature. The main characteristic temperatures appearing in the choice of precursor and ALD process are described in Table 3.

| | Label |
|---|---|
| **Precursor physical properties** | |
| Decomposition temperature | $T_d$ |
| Boiling point temperature | $T_b$ |
| Melting point temperature | $T_m$ |
| **Process conditions** | |
| Precursor temperature | $T_p$ |
| Substrate temperature | $T_s$ |

Table 3: Main characteristic temperatures for the choice of a metal precursor.

As for CVD (see previous section), two types of injections may be performed for the precursor. For precursors with sufficiently high vapor pressure, a gas injection may be performed, i.e. the precursor is evaporated and transported by the carrier gas to the reaction chamber. In case the precursor has very low vapor pressure, the main technique relies on the dissolution of the precursor in a solvent, and then the direct injection of the liquid in the reaction chamber, with vaporization due to the lower pressure. This process is called direct liquid injection-atomic layer deposition (DLI-ALD).

The three main criteria for the choice of a metal precursor for the ALD process with gas injection are:

- Sufficient volatility in order to be evaporated towards the deposition chamber ($T_m$ or $T_b < T_p < T_s$);
- Absence of self-decomposition at the used deposition temperature ($T_s < T_d$);
- Sufficient reactivity towards surface groups formed by other precursors.

The criteria are similar for the liquid injection, although in this case, the volatility is not relevant since the precursor is diluted in a solvent.

The analysis of commercial silver precursors volatility has been performed by Kariniemi *et al.* [41] by means of thermogravimetry analysis (TGA), as described in Figure 12. From this analysis, the most promising silver precursor for ALD is Ag(fod)($PEt_3$). Other precursors with higher decomposition

temperature unfortunately exhibit a larger amount of residues, which shows their incomplete decomposition.

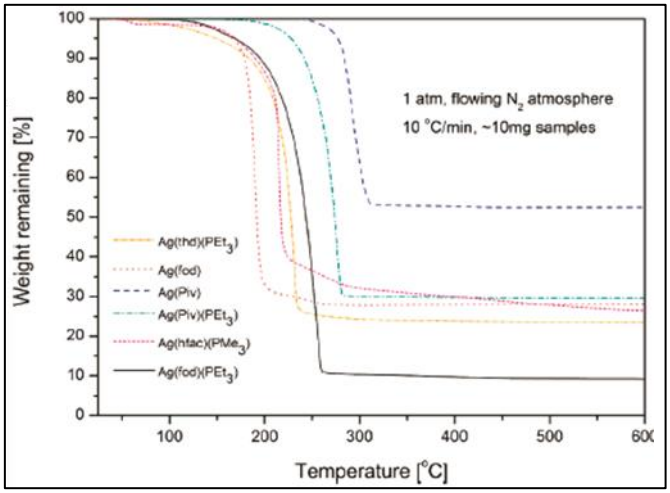


Figure 12: Thermogravimetry analysis of commercial silver precursors envisioned for ALD. From [41].

Following this analysis, several precursors have been investigated for the ALD of silver films. As it is seen in the next section I.3.2.3., two types of ALD modes are distinguished depending on the reducing agent: plasma-enhanced ALD (PE-ALD) and thermal ALD (Th-ALD). The use of precursors is classified using these two modes in Table 4. As seen from the references, PE-ALD has been more widely investigated than Th-ALD. For the former, a gas injection is employed while for the latter, either gas or liquid injection is used, depending on the vapor pressure of the precursor.

| | | Ag precursor | | | | |
|---|---|---|---|---|---|---|
| | | **Name** | **Formula** | **$T_m$ (°C)** | **$T_b$ (°C)** | **Injection** |
| **PE-ALD** | Niskanen *et al.* (2007) [40] | Ag(piv)($PEt_3$) | $C_{11}H_{25}AgO_2P$ | n.a. | n.a. | gas |
| | Boysen *et al.* (2018) [138] | Ag(NHC)(hmds) | $C_{17}H_{40}AgN_3Si_2$ | 116 | 225 | |
| | Cleveland *et al.* (2012) [139] | Ag(fod)($PEt_3$) | $C_{16}H_{25}AgF_7O_2P$ | 26 | > 230 | |
| | Kariniemi *et al.* (2011,2012) [41, 140] | | | | | |
| | Prokes *et al.* (2012,2013,2014) [141, 142, 143, 144] | | | | | |
| | Van den Bruele *et al.* (2015) [85] | | | | | |
| | Amusan *et al.* (2016) [19] | | | | | |
| | Caldwell *et al.* (2011) [145] | | | | | |
| | Mameli *et al.* (2016) [146] | | | | | |
| | Ko *et al.* (2015) [147] | | | | | |
| | Compton *et al.* (2014) [148] | | | | | |
| | Minjauw *et al.* (2017) [26] | | | | | |
| **Th-ALD** | Mäkelä *et al.* (2017) [45] | Ag(fod)($PEt_3$) | $C_{16}H_{25}AgF_7O_2P$ | n.a. | n.a. | gas |
| | Masango *et al.* (2014) [48] | Ag(hfac)($PMe_3$) | $C_8H_{10}AgF_6O_2P$ | 141 | 95(*) | gas |
| | Devlin-Mullin *et al.* (2017) [149] | Ag(hfac)(1,5-COD) | $C_{13}H_{13}AgF_6O_2$ | 123 | n.a. | liquid |
| | Chalker *et al.* (2010) [44] | | | | | |
| | Golrokhi *et al.* (2016,2017) [29, 46] | | | | | |

Table 4: List of precursors used in ALD of silver, classified vs. the choice of the reduction mode for the ALD process, i.e. plasma-enhanced (PE) or thermal (Th) ALD (see section I.3.2.3). n.a.: not available. (*) Sublimation temperature.

### I.3.2.3. Choice of the reducing agent

The oxidation state in the silver precursors mentioned in the previous section is +1, which is the most common oxidation state of silver. In order to obtain metallic silver, a reducing agent is required to reduce the oxidation degree of Ag +1 to Ag 0. Several reducing agents have been proposed for the ALD of silver films, as described in Table 5. These reducing agents are classified in two types, as they may either be activated using a plasma in the plasma-enhanced ALD mode (PE-ALD), or they may be thermally activated in the thermal ALD mode (Th-ALD).

| | | Ag precursor | | Reducing agent | |
|---|---|---|---|---|---|
| | | **Name** | **Formula** | **Name** | **Formula** |
| **PE-ALD** | Niskanen *et al.* (2007) [40] | Ag(piv)($PEt_3$) | $C_{11}H_{25}AgO_2P$ | $H_2$ plasma* | |
| | Boysen *et al.* (2018) [138] | Ag(NHC)(hmds) | $C_{17}H_{40}AgN_3Si_2$ | | |
| | Cleveland *et al.* (2012) [139] | Ag(fod)($PEt_3$) | $C_{16}H_{25}AgF_7O_2P$ | | |
| | Kariniemi *et al.* (2011,2012) [41, 140] | | | | |
| | Prokes *et al.* (2012,2013,2014) [141, 142, 143, 144] | | | | |
| | Van den Bruele *et al.* (2015) [85] | | | | |
| | Amusan *et al.* (2016) [19] | | | | |
| | Caldwell *et al.* (2011) [145] | | | | |
| | Mameli *et al.* (2016) [146] | | | | |
| | Ko *et al.* (2015) [147] | | | | |
| | Compton *et al.* (2014) [148] | | | | |
| | Minjauw *et al.* (2017) [26] | | | $H_2$ or $NH_3$ plasma* | |
| **Th-ALD** | Mäkelä *et al.* (2017) [45] | Ag(fod)($PEt_3$) | $C_{16}H_{25}AgF_7O_2P$ | Dimethylamine borane | $BH_3(NHMe)_2$ |
| | Masango *et al.* (2014) [48] | Ag(hfac)($PMe_3$) | $C_8H_{10}AgF_6O_2P$ | Formalin | HCHO |
| | | | | trimethylaluminum + water | $(AlMe_3)_2$ + $H_2O$ |
| | Devlin-Mullin *et al.* (2017) [149] | Ag(hfac)(1,5-COD) | $C_{13}H_{13}AgF_6O_2$ | Propan-1-ol | $CH_3CH_2CH_2OH$ |
| | Chalker *et al.* (2010) [44] | | | | |
| | Golrokhi *et al.* (2016) [29] | | | | |
| | Golrokhi *et al.* (2017) [46] | | | tertiary butyl hydrazine | $C_4H_{12}N_2$ |

Table 5: List of reducing agents used in the ALD of silver, classified vs. the choice of ALD mode for the reduction process. *Diluted with inert gas (Ar or $N_2$).

It has been demonstrated that molecular hydrogen ($H_2$) cannot directly act as a reducing agent for the mentioned silver precursors. [150] For this reason, it is necessary to activate hydrogen radicals ($H^{\bullet}$) by using a plasma source. In PE-ALD, two plasma configurations can be used, the direct plasma configuration, where the sample is directly inserted in the plasma chamber, or the remote plasma configuration, where the radicals are generated in a separate plasma chamber and transported to the sample using the gas flow. The plasma is ignited using only gases (hydrogen or oxygen), but it is more commonly ignited using inert gas (e.g. Ar) with dilute gas.

In the thermal ALD configuration, the main challenge relies in finding a sufficiently strong reducing agent able to reduce silver at a temperature well below the decomposition temperature of

the precursor, and that has a sufficiently high vapor pressure in order to be vaporized at the same temperature. As already mentioned for CVD processes (see previous section), Ag precursor in the liquid state (dissolved into a solvent) may be used to overcome low vapor pressure and thermally unstable chemical precursors. This DLI-ALD has been used for Ag(hfac)(1,5-COD) precursor in several works. [29, 44, 46, 149] Several reducing agents have been attempted for Th-ALD. In DLI-ALD, propan-1-ol is commonly used. [29, 44, 149] One study substitutes alcohol with tertiary butyl hydrazine which presents a more favorable reactivity due to its more acidic character (lower value of pKa). [46] Dimethylamine borane is another exotic reducing agent selected not only for its very low sublimation temperature (32°C in the study) enabling the use of various deposition temperature but also because it does not contain oxygen which making it attractive for noble metal deposition. [45] Besides alcohol, formalin has also been used as mild reducing agent thanks to its functional organic group and an alternative three-step Th-ALD process has also been reported using trimethylaluminum and water. [48]

#### I.3.2.4. Film structure – electrical conduction correlation for atomic layer deposition of silver films

In this part, the results obtained for ALD of Ag films are reviewed. The main goal is to demonstrate continuous (or at least connected) silver films with a finite electrical conduction, as compared to films made of disconnected nanoparticles that are insulating.

Table 6 summarizes the main results using PE-ALD of silver in terms of film structure and electrical properties and the corresponding film morphologies are exposed in Figure 13 and Figure 14. Table 7 and Figure 15 exposes the results obtained for thermal ALD of Ag. As indicated by the references, the former method has been more widely studied than the latter. In both cases, the growth leads to an NP structure for low thickness but PE-ALD of Ag gives higher coverage and mainly continuous film with a lower critical thickness. [1, 2, 8, 54] Although ALD is a surface-dependent technique, which presents chemical requirements for the self-limiting reactions behavior, the growth of metals, and more specifically silver, is more complex than an ideal “layer-by-layer” deposition. As with most noble metals, the deposition occurs through cluster formation, referred to the islands or Volmer-Weber growth mode (see section I.2.). For Ag deposition, the detailed deposition mechanism is still weakly understood and leads to a lack of control of the nanostructure morphology over large scales.

Indeed, SEM images show that most films grown by PE-ALD achieve a connected structure for sufficiently high thickness and is thus appropriate for investigating continuous silver films. We mainly observe two types of structures (Figure 13), either made of disconnected grains but forming a compact film, [40, 148] or made of flat interconnected islands. [19, 41, 85, 138, 139, 141, 142] These morphologies lead to electrically conductive films, except for the works of Compton *et al.,* [148] Ko *et al.* [147] and Minjauw *et al.* [26] (Figure 14) which demonstrate nanoparticle Ag films due to the initial stage deposition of a few ALD cycles. However, the aim of these studies was to investigate applications of Ag NPs in plasmonic and photocatalysis. Most presented works use the remote plasma configuration where the ion bombardment remains low at the substrate level with an important rate of active radicals resulting from the dissociation of molecules (e.g. H from $H_2$). [57, 151, 152] An exception is made for the work of Niskanen *et al.* [40] with the use of radical-enhanced atomic layer deposition (RE-ALD) where a deported plasma is used to avoid any direct contact between the plasma

and the substrate. Due to the higher mean free path of radicals compared to the charged particles of a plasma (which can be a source of defects), only the radicals will survive long enough to be still active on the substrate. [57, 151, 152] In both configurations (remote plasma or RE-ALD), plasma enhancement creates very reactive species also at low temperatures and ensures high quality films with a better removal of impurities combined with an improvement of the deposition rate, even at temperature where Th-ALD processes are not possible. [57, 151, 152] The nanoparticle morphology leading to insulating films is also observed in most cases by thermal ALD, [29, 44, 45, 48, 149] except for the study of Golrokhi *et al.* [46] when using tertiary butyl hydrazine (TBH) as reducing agent (Figure 15 and Table 7).

As mentioned before, due to the lack of appropriate Ag precursors and reducing agent, there are relatively few reference works in the literature and the ALD of Ag has only been investigated for the first time in 2007 by Niskanen *et al.* [40]. They used Ag(piv)($PEt_3$) and $H_2$ plasma as a reducing agent. A conformal deposition but not on large surface area has been achieved with a high growth per cycle (0.12 nm/cycle) at 140°C but the quite-grainy films exposed significant impurity content (10 %at. of oxygen, 5 %at. of hydrogen, 4 %at. of phosphorus and 1 %at. of carbon). However, a 40-nm-thick film exhibited surprisingly a quite low resistivity of only 6 µΩ.cm. The mainly used deposition process employs Ag(fod)($PEt_3$) as silver precursor due to its high vapor pressure and good thermal stability (see section I.3.2.2.) combined with $H_2$ plasma as a reducing agent. [19, 26, 85, 139, 141, 142, 143, 144, 145, 146, 147, 148] The best results have been obtained by Kariniemi *et al.* [41] with a saturated growth at a temperature range of 120–140°C and a GPC of 0.03 nm/cycle, allowing larger area uniformity as compared to Niskanen *et al.* [40], even if the growth rate was lower. This low GPC was explained by the steric hindrance of Ag precursor molecules, which caused high distance between chemisorbed molecules. Despite a low amount of impurities (7% at. of hydrogen, 3% at. of oxygen, 3% at. carbon and less than 1% at. of phosphine, nitrogen and fluorine), the film exposed a critical thickness as low as 22 nm, corresponding to a resistivity of 6 µΩ.cm. Based on these promising results, several groups have used the same deposition process. [19, 26, 85, 139, 141, 142, 143, 144, 145, 146, 147, 148] Although using the same chemistry, a large panel of resistivities have been obtained (see Table 6). However, a recent study demonstrated spatial APP-ALD (atmospheric pressure plasma-enhanced atomic layer deposition) of Ag(NHC)(hmds) and Ag(fod)($PEt_3$), both reduced by hydrogen plasma. [138] At 100°C, they obtained a higher deposition rate (0.036 nm/cycle vs. 0.014 nm/cycle) and a higher surface coverage showing some degree of coalescence after 1200 ALD cycles (85% vs. 62%) using phosphine-free Ag precursor. The hypothesis given by the researchers was a higher reactivity of the carbene-based Ag precursor but further investigations regarding percolation thresholds and growth modes were planned. On the other hand, similar GPC values have been obtained in APP-ALD of Ag(fod)($PEt_3$) in the work of Mameli *et al.* (0.015 nm/cycle at 120°C) [146] whereas a higher GPC of 0.03 nm/cycle at 120°C has been obtained at low pressure process in [41]. This two times lower GPC is due to the growth in under-saturation regime caused by limitations of their spatial-ALD reactor configuration leading to inaccessibility of higher precursor exposures times. In another APP-ALD using the same precursor, by doing a statistical particle size distribution of Ag NPs grown at different deposition temperatures, Van den Bruele *et al.* [85] proved that the chamber temperature controls the islands size and density since it is a surface-diffusion dependent parameter: larger island size and a lower island density have been obtained at 120°C compared to 100°C, due to difference in GPC values. However, they also performed deposition at undersaturated regime as a function of the pulse times and obtained a varying GPC in the studied temperature range (100–120°C).

Very high number of ALD cycle (4500) were needed in order to obtain electrically continuous films with a quite high resistivity of 18 μΩ.cm. In the literature of Ag ALD, the study of the number of ALD cycles, which allows the coalescence and continued nucleation, controls the particle size distribution. The fingerprint is an increase of both the NP size, with irregular shapes, and the gap between islands, with a decrease of their density. [19, 29, 45, 48, 144, 146] However, the growth mechanism is still little understood at the initial stage of the film synthesis.

Using the same silver precursor as Kariniemi, Minjauw *et al.* [26] have studied the influence of the reducing agent via PE-ALD using either $H_2$ or $NH_3$ plasma (Figure 14). $NH_3$* is giving smaller Ag NPs with higher densities by combining an enhanced nucleation with a six-times-larger growth rate as compared to $H_2$* process (0.24 ± 0.03 nm/cycle vs. 0.04 ± 0.02 nm/cycle).The authors explained this result by a difference in reactive groups present on the surface after the plasma pulse. Stable and more reactive NHx surface groups produced after $NH_3$-plasma pulse saturate the surface, whereas the surface is saturated by non-stable Ag–H surface groups after $H_2$-plasma pulse. Therefore, after the next pulse of Ag precursor, more Ag(fod)($PEt_3$) molecules will react with NHx groups as compared to Ag–H groups. This explanation was highlighted by the high N concentration in the bulk for film grown with the $NH_3$ process (7 %at. vs. 2% for $H_2$ process). Mäkelä *et al.* [45] used the same Ag precursor and dimethylamine borane ($BH_3$-($NHMe_2$)) as co-reagent in Th-ALD at 110°C. They hypothesized that dimethylamine borane adsorbed on the surface converted to ($Me_2N$-$BH_2$)$_2$ and $H_2$, acted afterwards as reactive sites for Ag deposition in metallic state. They found a similar growth rate (0.03 nm/cycle) than the work of the same group using PE-ALD, [41] even if no linear increase of the film thickness vs ALD cycles was confirmed due to the formation of even more reducing species than dimethylamine borane itself when reacting with Ag on the surface (0.035 nm/cycle after 1500 ALD cycles). However, even after many ALD cycles (2500), the film was very granular and not continuous even if it exhibited a lower level of contamination (1.6 % at. of oxygen, 0.8 % at. of hydrogen, and 0.7 % at. carbon.) due to a better handling of the sample after deposition. This highlights the fact that, in this case, the growth leading to low deposition rate depends mainly on the Ag precursor used, i.e. Ag(fod)$PEt_3$ in both thermal or plasma-enhanced ALD, and not the way it is adsorbed after dissociation of the phosphine adduct or molecularly.

The influence of the reducing agent has also been studied with Th-ALD using other silver precursor. Masango *et al.* [48] used (Ag(hfac)($PMe_3$) combined with either formalin in an AB-type process (200°C) or trimethylaluminum (TMA) and $H_2O$ in an ABC-type process (at 110°C). With increasing number of ALD cycles, the ABC-type process leads to a nearly constant particle size with an increasing metal loading whereas the AB-type process provided small particles in addition to bigger ones. They explained this result by an enhancement of the adsorption of the Ag precursor by the presence of nucleation sites which have been created after several cycles for the three-step process. On the contrary, the two-step process presented a surface diffusion of small NPs which agglomerate to form bigger one and the researchers group explained the mixing in particles size by the need of a catalytic step. However, in both cases, a very poor growth per cycle (below 0.01 nm/cycle) has been obtained due to surface poisoning with hfac ligands. It was also mentioned that ABC-type process suited for low temperatures (110°C) while AB-type process was more suitable for high temperature processes (higher than 200°C). Indeed, at 100°C, the two-step process was impossible due to the high nucleation time needed to remove the adsorbed hfac ligand.

The work of Chalker *et al.* [44] was the first thermal study which have exploited in details the properties of the silver nanoparticles and they used sequential doses of Ag(hfac)(1,5-COD) and propan-1-ol to produce nanoparticle films of silver via a catalytic oxidative dehydrogenation of the metal precursor by the co-reactant. Just like Devlin-Mullin *et al.* [149], they used direct liquid injection ALD in order to enhance the transport of the low vapor pressure and insufficient thermal stable precursor. However, they did not prove the self-limiting character of the deposition (very narrow temperature window between 122 and 127°C) and achieved NPs rather than film morphology. Golrokhi *et al.* of the same group [46] managed to broaden the ALD window to lower temperatures (105–128°C) thanks to the use of tertiary butyl hydrazine (TBH) rather than propan-1-ol (123–128°C) [29] with quite similar growth rate (0.018 nm/cycle vs 0.016 nm/cycle). They obtained a better surface coverage and interconnection between particles, a larger NPs size and a wider ALD window (23°C) with TBH rather than alcohol (5°C). The different morphologies were explained by the authors to come from the enhanced decomposition of silver precursor and bonding of Ag layer with the substrate thanks to the reaction of hydrogen with the substrate in the case where TBH was used in contrast to the oxidative dehydrogenation catalyzed by Ag particles from the metal precursor.

| | **Ag precursor** | | **Reducing agent** | **Structure** | **Electrical properties** | |
|---|---|---|---|---|---|---|
| | **Name** | **Formula** | | | **Resistivity (μΩ.cm)** | **Thickness (nm)** |
| Niskanen *et al.* (2007) [40] | Ag(piv)($PEt_3$) | $C_{11}H_{25}AgO_2P$ | $H_2$ plasma | rough thick film | 6 | 40 |
| Boysen *et al.* (2018) [138] | Ag(NHC)(hmds) | $C_{17}H_{40}AgN_3Si_2$ | | continuous percolated layer | 10 | 111 |
| | Ag(fod)($PEt_3$) | $C_{16}H_{25}AgF_7O_2P$ | | nanoparticles | insulating | |
| Cleveland *et al.* (2012) [139] | | | | coalesced mosaic-like structure | n.a. | 58 |
| Kariniemi *et al.* (2011,2012) [41, 140] | | | | large grain, continuous film | 6 | 22 |
| Prokes *et al.* (2012,2013,2014) [141, 142, 143, 144] | | | | mosaic-like micro-structures | < 10 | 49 |
| Van den Bruele *et al.* (2015) [85] | | | | small islands, coalesced together | 18 | 50 |
| Amusan *et al.* (2016) [19] | | | | large islands, interconnected | 5.7 | 97 |
| Caldwell *et al.* (2011) [145] | | | | mosaic-tile | n.a. | 45 |
| Mameli *et al.* (2016) [146] | | | | continuous film | n.a. | 35 |
| Ko *et al.* (2015) [147] | | | | nanoparticles | insulating | |
| Compton *et al.* (2014) [148] | | | | nanoparticles | insulating | |
| Minjauw *et al.* (2017) [26] | | | $H_2$ or $NH_3$ plasma | nanoparticles | insulating | |

Table 6: SoA of PE-ALD of silver in terms of film structure and electrical properties. The thickness corresponds to the film used for measuring the resistivity. n.a.: not available.

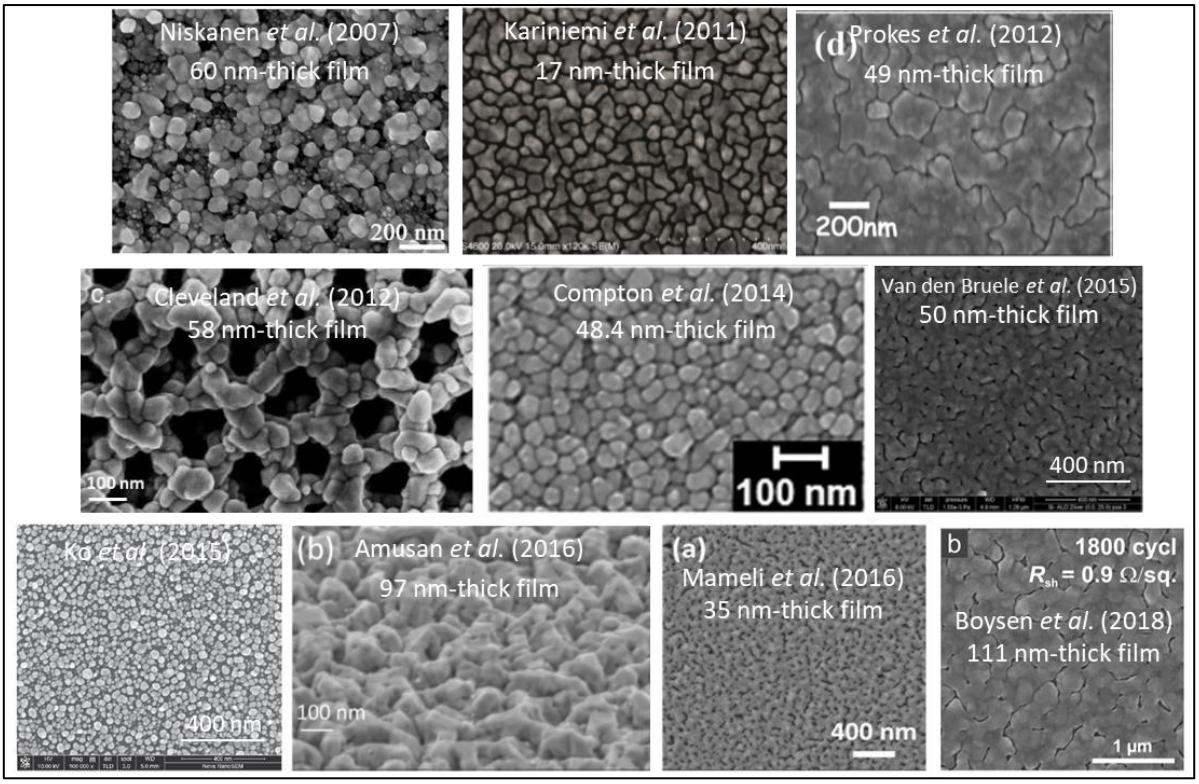


Figure 13: Scanning electron micrographs of typical silver films obtained by PE-ALD. The references are indicated on the pictures, and the related conditions are reported in Table 6.

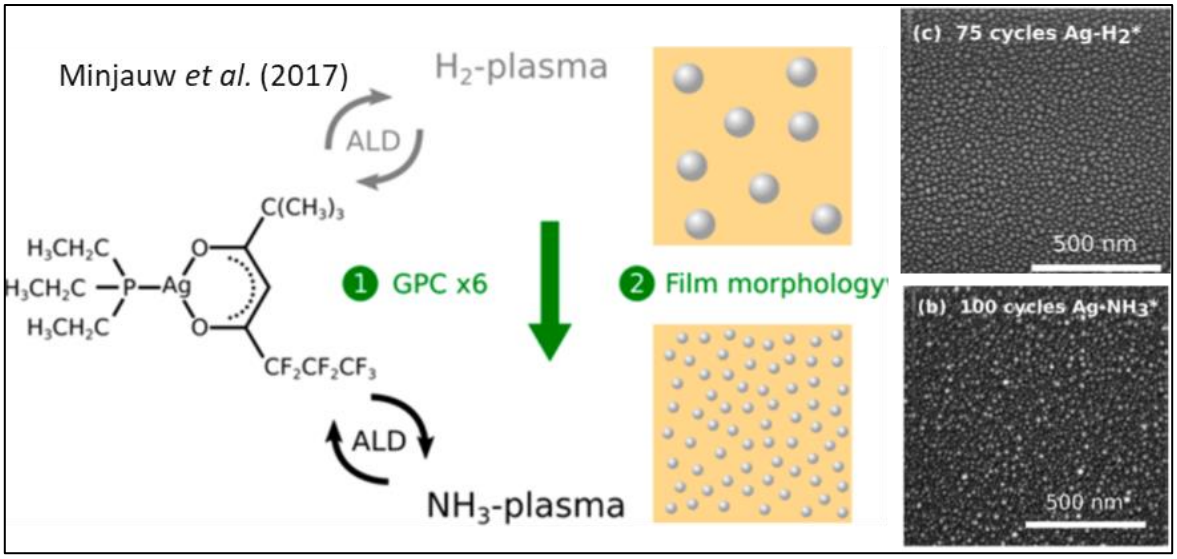


Figure 14: Scanning electron micrographs of Ag films obtained by PE-ALD using either $NH_3$-plasma or $H_2$-plasma as reducing agent. From [26].

| | Ag precursor | | Reducing agent | | Structure | Electrical properties | |
|---|---|---|---|---|---|---|---|
| | Name | Formula | Name | Formula | | Resistivity (μΩ.cm) | Thickness (nm) |
| Mäkelä *et al.* (2017) [45] | Ag(fod)($PEt_3$) | $C_{16}H_{25}Ag\ F_7O_2P$ | dimethylamine borane | $BH_3(NHMe)_2$ | NPs | Insulating | |
| Masango *et al.* (2014) [48] | Ag(hfac)($PMe_3$) | $C_8H_{10}Ag\ F_6O_2P$ | formalin | HCHO | NPs | | |
| | | | TMA + water | $(AlMe_3)_2$ + $H_2O$ | NPs | | |
| Devlin-Mullin *et al.* (2017) [149] | Ag(hfac)(1,5-COD) | $C_{13}H_{13}Ag\ F_6O_2$ | propan-1-ol | $CH_3CH_2CH_2OH$ | NPs | | |
| Chalker *et al.* (2010) [44] | | | | | NPs | | |
| Golrokhi *et al.* (2016) [29] | | | | | NPs | | |
| Golrokhi *et al.* (2017) [46] | | | tertiary butyl hydrazine | $C_4H_{12}N_2$ | planar film-like morphology | 10 | 27 |

Table 7: SoA of thermal ALD of silver in terms of structure and electrical properties. The thickness corresponds to the film used for measuring the resistivity.

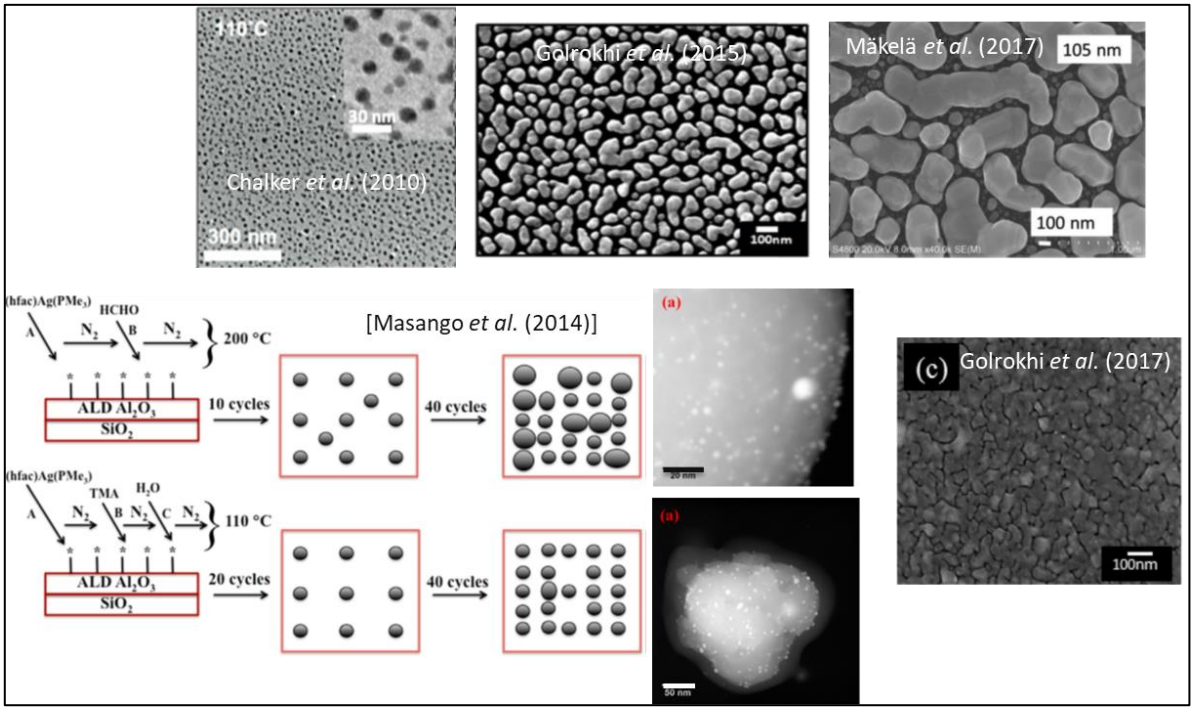


Figure 15: Scanning electron micrographs of typical Ag films by thermal ALD, including the proposed mechanism by Masango *et al.* [48]. The references are indicated on the pictures, and the related conditions are reported in Table 7.

### I.3.2.5. Conclusion

According to the SoA, we have proven that there are still challenges to reach when it comes to ALD of Ag. The process represents a challenge by itself due to the need to find suitable Ag precursor and reducing agent. In addition, whether the synthesis is made by plasma-enhanced ALD or thermal ALD, the growth of the metallic film leads to a NP structure for low thickness due to the island growth mode of metals. Although PE-ALD usually gives a higher coverage with a lower critical thickness than

thermal ALD, we note that one thermal ALD route has shown fair results for the deposition of connected films. [46] Although this result has not been reproduced yet, the easiest processing conditions of thermal ALD as compared to PE-ALD presents several advantages that could be investigated in the future. Several recent works have successfully demonstrated the reduction of the critical thickness, down to 22 nm for PE-ALD performed at a low temperature, at which diffusion of silver on the surface is strongly reduced thanks to the presence of highly reactive radical species. [41] The most promising route towards silver continuous thin films by ALD remains the use of the precursor Ag(fod)($PEt_3$) with $H_2$ plasma as reducing agent (i.e. PE-ALD). The critical thickness for continuous films using this path has been demonstrated to approach 20-30 nm, and the resistivity of these films can be as low as 6 μΩ.cm, against 1.6 μΩ.cm for bulk Ag and typically > 2.5 μΩ.cm for Ag thin films of thickness less than 50 nm obtained by sputtering. This PE-ALD approach have been reproduced by several groups and is thus the route that has been naturally chosen for this thesis work.

## I.4. Solutions for ultra-thin metallic film deposition

As highlighted in section I.2, one major challenge in depositing ultra-thin continuous silver films or other noble metals on oxide substrates, is to find a solution to overcome the formation of separated clusters caused by the higher surface energy of metallic materials as compared to oxide surfaces. The deposition follows the Volmer-Weber growth mode and further leads to an NP morphology rather than a continuous layer. This has been demonstrated for Cu films [2, 14, 153, 154] and for Ag films. [19, 40, 41] However, studies on the ALD of metal Ag are much less common than those of Cu since the exact deposition mechanism is not yet fully understood.

The reduction of the critical thickness of conductive films is one of the major research activities in the deposition of metal films, and several techniques have already been investigated, mainly for PVD methods (see [42] and [43] and references therein).

### I.4.1. Wetting layer

In this section, we investigate the influence of the wetting layer on the morphology of noble metals in general deposited by ALD. We then focus the overview of Ag films deposited by different methods. Among the several works performed on the study of the influence of the sublayer, no clear trends could have been extracted. Therefore, we choose to expose case per case investigation and establish correlation between them when possible.

#### I.4.1.1. Atomic layer deposition of noble metals

It is well-known that ALD of noble metals displays nucleation difficulties for producing continuous thin layers. [2, 49] It is worth noting that reaction mechanisms during the nucleation differ from those during the steady-state growth. As shown previously, noble metal precursor reacts with the substrate only during the first ALD cycles (i.e. nucleation) and on the deposited material during the subsequent cycles, once the critical thickness has been reached. One way of reducing the island

formation in order to deposit ultra-thin continuous metallic film is to use a wetting layer, i.e. a layer with large surface energy on which the metal will grow as film rather than islands. Therefore, this parameter is a strong indication of the regime change during ALD deposition.

For instance, Shrestha *et al.* [155] found a critical thickness of 15 nm when depositing Pt films and improved adhesion on oxidized silicon substrate as compared to bare Si. Before this threshold, the growth followed the Volmer-Weber growth mechanism and after, the classical layer-by-layer growth regime occurred. Choi *et al.* [156] proved that Ir deposition is highly affected by the sublayers during the first ALD cycles (first 150 cycles) with a poor nucleation and island growth of Ir on Si, $SiO_2$ and very thin TaN seed layers but smooth and uniform Ir film on 3-nm-thick TaN. However, when increasing the number of cycles (up to 300), the adsorbed Ir precursor acts as the seed layer for all substrates which leads to smooth and uniform Ir films on all the film substrates.

For the investigation of the influence of the sublayer, we thus focus exclusively on the nucleation phase.

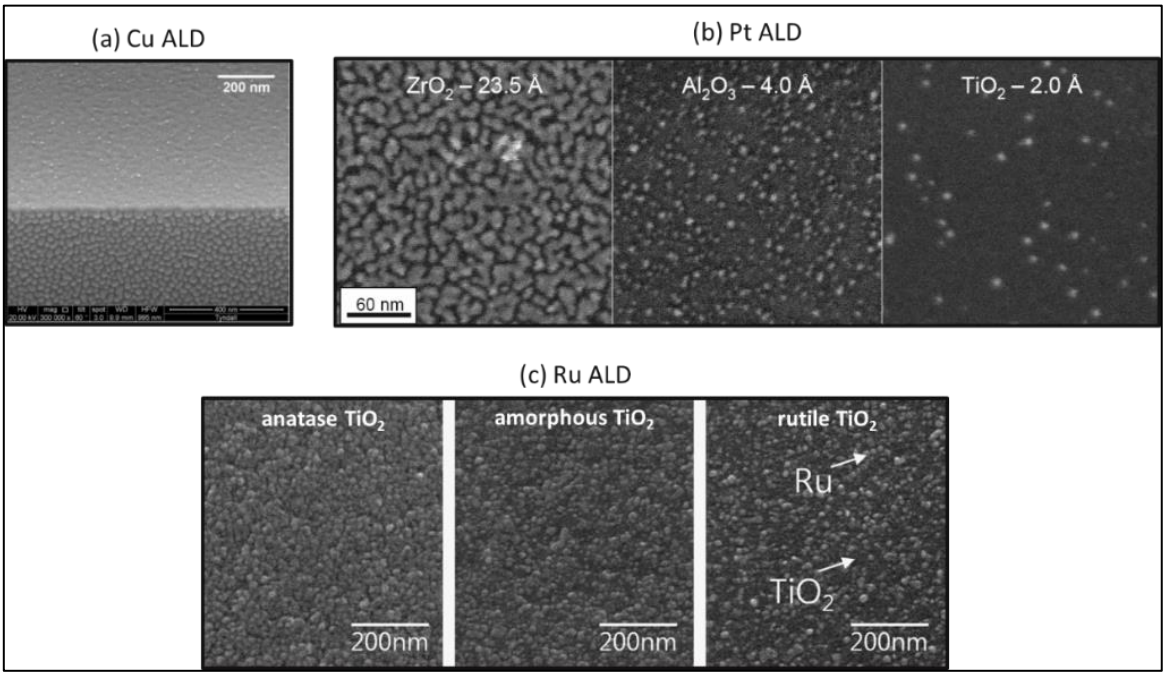


Figure 16: Scanning electron micrographs showing the wetting layer influence on the morphology of noble metal films deposited by ALD. (a) and (b): Influence of the nature of the substrate (oxide vs. metal) (a) Cross section image of Cu film deposited on Ru coated $SiO_2$/Si substrate (from [14]) and (b) Top views images of Pt films deposited on different metal-oxide substrates: $ZrO_2$, $Al2O_3$, $TiO_2$ (from left to right) (from [9]). The indicated Pt film thicknesses were determined using optical absorption measurements on glass substrates. (c) Influence of the crystallinity of the substrate: Top views images of Ru deposited on anatase, amorphous and rutile $TiO_2$ substrates (from left to right) (from [157]).

Nucleation delay of metallic films on inert substrate model has been elaborated by Puurunen *et al.* [158]. Except of this work, investigations to develop nucleation mechanism applicable to metal ALD using concepts established by other thin-film depositions like PVD, are very rare. [14] It is important to notice that, apart some exceptions, all the noble metals grown by ALD require an incubation period. [52] However, the incubation time may differ from one noble metal to another. For example, the small absorption coefficient of Ir film leading to a low nucleation density engenders a longer nucleation delay for Ir layer than other noble metals, e.g. Ru. [156]

Kim *et al.* [159] studied also the substrate-dependence for the ALD of Ru with $O_2$ as reactant. The strong interaction between the Ru precursor and the metallic substrates (Au and Pt) lead to a negligible incubation time (10 cycles) bringing to a continuous smooth Ru layer, even at a film thickness of 1 nm. On the contrary, the weak interaction of Ru precursor with covalent bonds in TiN and $SiO_2$ sublayers lead to a long incubation time (180 cycles on TiN) which was lower in Ru deposited on $TiO_2$ (90 cycles). In this case, the ionicity of the substrate (examined in terms of electronegativity) played a significant role and may affect the adsorption of precursor molecules. Indeed, $TiO_2$ has more ionic character than TiN and $SiO_2$ since the difference in electronegativity of $TiO_2$ is larger than that of TiN and $SiO_2$. When comparing metal oxides substrates, Elam *et al.* [9] suggested different reactivity of the metal precursor for ALD of Pt using oxygen reagent. After 40 Pt ALD cycles, they obtained a quasi-continuous Pt film on $ZrO_2$ sublayer (5 cycles), a high density of particles on $Al_2O_3$ surface (after 30 cycles) while almost no Pt deposition on $TiO_2$ surface after 80 cycles (see Figure 16 (b)). For the latter sublayer, they suggested a surface poisoning of residual ligands from Pt precursor to explain the absence of reactivity of Pt.

Yim *et al.* [160] showed that the nucleation of Ru deposited by ALD with $O_2$ as reactant was substrate-dependent. They developed a model which included mechanisms as surface diffusion of atoms and release and reabsorption of atoms by large islands. Different dielectric surfaces (thermally grown $SiO_2$, $NH_3$ plasma-treated $SiO_2$, and CVD SiNx) have been tested and Ru nucleation was much enhanced on the nitride substrates while the overall nucleation kinetics followed a similar mechanism: a slow nucleation rate at initial stage becoming high during the second stage and at last a coalescence mechanism. This enhanced nucleation was due to the higher density of adsorption sites for Ru precursor on nitride surfaces ($1.2\times10^{12}$ $cm^{-2}$ on SiN*x* at 160 ALD cycles, and $2.3\times10^{12}$ $cm^{-2}$ on $NH_3$ plasma-nitrided $SiO_2$ at 110 ALD cycles versus $5.7\times10^{10}$ $cm^{-2}$ on the $SiO_2$ surface at 500 ALD cycles) although the mechanism of adsorption remains not clear. Indeed, the initial nucleation density of the noble metal is crucial for the formation of metallic films: a high nucleation density leads to a short nucleation delay and thus faster formation of a continuous film with a smoother surface as compared to low nucleation density. [80]

The crystallinity of the sublayers plays also a critical role on the incubation delay and thus the morphology of the deposited metal. Kim *et al.* [157] observed a long incubation time for Ru deposited on amorphous and rutile $TiO_2$ (approximately 330 and 100 cycle number at 230°C and 250°C, respectively,) whereas a noticeably shorter incubation time was found on anatase $TiO_2$ sublayers (∼260 and 70 cycle number at 230°C and 250°C, respectively). The explanation was the high catalytic activity of the anatase structured $TiO_2$ which promoted the adsorption of the Ru precursor, lowering the nucleation delay leading to continuous Ru films rather than island-shape Ru grains before coalescence obtained for the amorphous and rutile $TiO_2$. (see Figure 16 (c)). Kukli *et al.* [161] also found continuous and rougher Ru films on anatase (Ru thickness of 6.6 nm) as compared to amorphous $TiO_2$ (Ru thickness of 5.0 nm) with rms roughness of 1.9 versus 0.32 nm, respectively, but less resistive (26–36 versus 30–70 μΩ.cm, respectively).

The surface preparation is also a factor to consider when depositing material on a surface. Egorov *et al.* [162] proved that the growth rate of Ru is a strong function of the morphology of the substrate. The nucleation delay has been significantly reduced when $NH_3$/Ar plasma pre-treatment have been performed on $HfO_2$ surfaces. This further promoted the nucleation density and allowed to obtain continuous and smooth Ru ultra-thin films up to 2 nm. Wu *et al.* [163] obtained a poor-adhesive

Cu separated islands on Ta layer but an enhanced-quality film on Ru. A further improvement of the film quality has been obtained by performing an $H_2$-plasma precleaning to remove the native oxide present on the surface of Ru, which was much more readily removed than that of Ta. [164] Indeed, as-deposited film presented a resistivity of 307 μΩ.cm which drastically decreased to 19 μΩ.cm after 4 min plasma pre-treatment for a 20-nm thick Cu film, which was attributed to a reduction of interfacial O contamination.

Several other factors affect also the nucleation delay for noble metal ALD deposition, like the deposition temperature, the selected metal precursor (e.g. $RuCp_2$ and $Ru(thd)_3$ for Ru deposition [165, 166]) and reducing agent (e.g. air instead of $O_2$ for Pt deposition [165, 167] or $H_2$, $NH_3$, $O_2$ plasma for plasma-enhanced Pd ALD [168]) and ALD parameters (e.g. reducing agent and exposure time for Pd deposition [9]). As the object of this thesis work was not to study the influence of the wetting layer on these factors, the reader can refer to previous published results. [1, 2, 51, 52, 169, 170]

Interestingly, Hagen *et al.* [14] did not observed nucleation delay for Cu PE-ALD (using $H_2$ as reducing agent) on Si samples coated with tantalum nitride (TaN), carbon-doped oxide (CDO), and Ru. Alternately, after only some cycles, mainly for TaN and CDO, the island density was already very high and subsequently reduced during next cycles due to coalescence which described a lognormal distribution. The deposition on Ru surfaces was different due to lattice-matched substrate and a continuous film has been obtained while islands have been formed on $Si/SiO_2$ surface (edge of the cross section sample) (see Figure 16 (a)). Similarly, Li *et al.* [153] have also revealed substrate to which the lattice of Cu matches well. Cu atoms ALD-deposited using molecular $H_2$ as co-reactant performed on metallic surfaces such as Co and Ru, presented a strong surface-adherence and a slow diffusion leading to a low GPC. This was due to the fact that further reactions were inhibited because chemisorbed precursor blocked access to contiguous sites. This gave dense and smooth films which were continuous even for films as thin as four atomic layers. On the contrary, on oxide surfaces, Cu atoms showed a weak adherence with a rapid diffusion, giving rough films. In this case, an initial rapid GPC (close to one monolayer) was obtained, resulting from the agglomeration of Cu atoms and chemisorbed precursor to form larger Cu nuclei, and more reactive sites (most likely –OH groups) were available to react with Cu precursor. They also studied Cu growth on HF–ended Si surfaces leading to Si–H surfaces and proved that almost no deposition was obtained in this case, highlighting the importance of hydroxyl groups. The studies of Aaltonen *et al.* for the deposition of Ru [171] and Ir [172] proved also that OH–groups uniformly covering the surface enhanced the nucleation of the noble metal, while no sublayers used lead to non-uniform films with macroscopic defects. Ru ALD on Si–H, $SiO_2$, and $HfO_2$ surfaces studies by Park *et al.* [173] also confirms these results. Interestingly, Chaukulkar *et al.* [174] proved that hydroxyl groups are not required for plasma-enhanced Cu deposition on oxide substrate but the precursor chemisorption on the Al–O–Al bridges in the case of $Al_2O_3$ sublayer was the dominating mechanism.

#### I.4.1.2. Particular case of silver

In the case of Ag films**,** the use of a wetting layer has demonstrated strong improvement for the growth of ultra-thin continuous films only in particular cases (see detailed review in [2, 43]). Although good results were obtained in case of line-of-sight techniques, [32, 33, 42, 175, 176, 177, 178, 179, 180, 181, 182] only non-continuous films [48] with potentially a slight enhancement of the

coverage but still non-continuous morphology [19] were observed when chemical vapor-phase methods were engaged.

| Ag deposition method | Wetting layer | Result | Reference |
|---|---|---|---|
| DC magnetron sputtering | AZO | critical thickness down to 10nm, AZO reduces islanding | [175] |
| | Cu (1 nm) | percolation thickness reduced from 6 nm to 3 nm | [180] |
| High-power impulse magnetron sputtering (HIPIMS) | ZnO | smoother coating surfaces, film density improved | [176] |
| RF magnetron sputtering | Cu, ZnS, Ge | for all, low surface roughness with no island formation<br>Cu: improved reflectance (%R) in infra-red range<br>Ge: very high %R<br>ZnS: helps Ag to form smooth film, but deteriorates the optical performances | [177] |
| Evaporation | $\alpha$-$Al_2O_3$, Ti, O-rich ZnO | $\alpha$-$Al_2O_3$: poor wetting by Ag<br>Ti: improved as compared to $\alpha$-$Al_2O_3$<br>O-rich ZnO: improved as compared to $\alpha$-$Al_2O_3$ | [178] |
| | ZnO, $SnO_2$ | Ag shows better coverage on ZnO than on $SnO_2$, despite the larger roughness of ZnO | [181] |
| Thermal evaporation | $MoO_3$ | continuous Ag film 10 nm thick | [32] |
| Electron beam evaporation | Ge | ultra-low critical thickness (down to 3 nm) and decreased roughness | [33] |
| | Ge (1 nm) | reduction of the Ag surface roughness down to 0.2 nm for a 10 nm-thick film | [179] |
| Thermal process | $SiO_2$, Si–H, Si–OH | no deposition when absence of –OH groups | [183] |
| PE-ALD | Co, Ni, Ti, TiN, Ti/TiN, $SiO_2$, W | among the tested surfaces, all except W give a similar result (critical thickness of 47 nm)<br>Ag shows the poorest adhesion properties on W due to presence of $WO_3$ native oxide | [19] |
| PE-ALD | Si, $MoO_3$/Mo, Mo | native $MoO_3$ blocks Ag coalescence, need to be removed by plasma pre-treatment | [146] |
| Th-ALD | $Al_2O_3$ | $Al_2O_3$ acts as seedlayer for Ag NPs by providing –OH groups | [48] |

Table 8: Examples of wetting layers (list is non-exhaustive) investigated for the deposition of Ag thin films using various methods.

Several materials have been suggested as wetting layers, in particular other metals (Ti, Ge, etc.), but also oxides (ZnO, $Ta_2O_5$, $Nb_2O_5$, $TiO_2$, $SnO_2$, GaOx, InOx, MgO, etc., or mixture of them), with ZnO as usually preferred material. Some examples of wetting layers investigated for the deposition of Ag thin films by various methods are presented in Table 8. Most of the works concern PVD (sputtering or evaporation), and only very few CVD or ALD due to the much more recent development of metal layers deposited by these techniques.

The morphology of the surface also shows strong influence of the wetting of the Ag layer. Kato *et al.* [184] have investigated the influence of the structure of ZnO and $SnO_2$ underlayer on the electrical resistivity of sputtered Ag films. They showed a linear increase of the resistivity vs. roughness of the underlayer, with the curve for $SnO_2$ shifted to higher resistivity as compared to ZnO. Moreover, the Ag film on $SnO_2$ is less crystallized than on ZnO, showing that ZnO promoted the crystallization of Ag films and its reduced resistivity.

Interestingly, Amusan *et al.* [19] have investigated several wetting layers using the same PE-ALD process as the one investigated in this thesis work (i.e. PE-ALD with Ag(fod)($PEt_3$) as silver precursor and $H_2$-based plasma). They demonstrated that Ag grows faster on metallic substrates (Co and Ni) which present high surface energy. Similar adhesion properties on Co, Ni, Ti, TiN, Ti/TiN and $SiO_2$ with relatively smooth deposition have been obtained (see above Figure 13) while poor adhesion properties on W with quite rough deposition have been shown. The authors explained this result by

the presence of the low surface energy of the native tungsten oxide that could not be removed by a $H_2$-plasma exposure prior to deposition.

Mameli *et al.* [146] proved that the presence of native $MoO_3$ on Mo blocked the coalescence of Ag. Therefore, it was necessary to remove it by a $H_2/N_2$ plasma pre-treatment which enhanced Ag wetting on the surface and reduced the nucleation delay observed on $MoO_3$. A 15-nm thick Ag deposition exhibited a fully percolated film.

Duan *et al.* [183] deposited Ag from Ag(hfac)($PMe_3$) precursor and thermal reduction on silicon-based substrates including silica, H–terminated Si(100), and OH–terminated (oxidized) Si(100). They proved the existence of preferential reaction sites for Ag growth. Basically, no deposition (few particles founded at defect sites) has been highlighted on Si–H substrates, proving that the surface was very inert to Ag precursor. However, on Si–OH and silica, similar morphology of Ag NPs has been formed showing that the O atoms of the hydroxyl groups played a critical role leading to attractive surfaces for Ag precursor. The importance of the –OH adsorption sites for the Ag precursor chemisorption has also been demonstrated in the work of Masango *et al.* [48] by using $Al_2O_3$ as a seed layer which provides hydroxyl groups. From these two works, different surface reaction mechanisms have been proposed based on the experimental results (mainly XPS). Duan *et al.* suggested that after Ag(hfac)($PMe_3$) deposition, a removal of the hfac ligand by forming hfacH group desorbing from the surface and let the Ag($PMe_3$) moiety on it. On the other hand, the chemical reactions of the same Ag precursor reacting on $Al_2O_3$ surfaces have been proposed by Masango et *al.* as followed:

$$Al - O^* + (hfac)Ag(PMe_3) \rightarrow Al - O - Ag(hfac)^* + PMe_3$$

with the asterisks represent the surface species.

After HCOH precursor exposure:

$$Al - O - Ag(hfac)^* + HCOH \rightarrow Al - O - Ag - H_x^* + H(hfac) + CO + 0.5\,(1 - x)H_2$$

And in the linear regime:

$$Al - O - Ag - H^* + (hfac)Ag(PMe_3) \rightarrow Al - O - Ag - Ag(hfac)^* + PMe_3$$

$$Al - O - Ag - Ag(hfac)^* + HCOH \rightarrow Al - O - Ag - Ag - H_x^* + Hfac + CO + 0.5(1 - x)H_2$$

As we can see in this case, contrary to the work of Duan *et al.*, it is the moiety Ag(hfac) which remains on the surface and the group $PMe_3$ which is removed. This set of reactions was also suggested for the ALD of Pd. [185] Moreover, by using Ag(hfac)(1,5-COD) combined with propanol, Golrokhi *et al.* [29] affirms that the 1,5-COD ligand is weakly bonded to silver and easily dissociated when the precursor is volatilized. Therefore, the author assumes the chemisorption onto the surface of the Ag(hfac) intermediate and its reaction with the hydroxyl surface groups, as suggested by Masango *et al.* [48].

In order to provide a wide overview of the strategies for the deposition of ultra-thin metal films, we mention here three alternative routes that have been envisioned and could provide good opportunities for films deposited by ALD as well.

### I.4.2. Two-step approach: Oxide deposition and further reduction to metal layer

One way to circumvent the island growth of noble metal is to use a two-step approach consisting in the deposition of a metal-containing film subsequently reduced to a metallic state. Due to the much easier deposition of ultra-thin oxide films, this method may open to the deposition of ultra-thin metal films. This was proved mainly for copper thin layers. [2, 47]

Dhakal *et al.* [47] have demonstrated ALD of ultra-thin Cu films on $SiO_2$ by deposition of Ru-doped $Cu_2O$ from $[(^nBu_3P)_2Cu(acac)]$ and $O_2$, and subsequent reduction in formic acid ($HCO_2H$) or CO. The reduction process with formic acid was performed at 110°C and allowed reduction of $Cu_2O$ films up to 4.7 nm- thick. The reduction process with CO was performed at 145°C and allowed reduction of $Cu_2O$ film up to 3 nm- thick.

The same combination of Cu precursor and reduction agent for $Cu_2O$ deposition has been previously reported by Waechtler *et al.* on different substrates, including $SiO_2$, TaN, and Ru. [186] On TaN, a linear two-dimensional growth was obtained whereas island growth with further coalescence and continuous film formation took place on $SiO_2$. [187] This process has been then used in the work of the same author [188] to deposit Cu seed layer for electrochemical Cu deposition by further reduction of $Cu_2O$ in $HCO_2H$ between 110–120°C. A more effective reduction reaction has been found for $Cu_2O$ deposited on Ru ($Cu_2O$ thickness of 12 nm) rather than TaN ($Cu_2O$ thickness of 5 nm), due to a stronger activity with respect to formic acid decomposition for Ru.

Li *et al.* [189] first deposited copper(I) nitride $Cu_3N$ by ALD at 160°C from $[Cu(^sBu\text{-}Me\text{-}amd)]_2$ precursor and ammonia as reducing agent. Electrically continuous Cu layers as low as 0.8 nm-thick (about 3 monolayers) was then obtained by reduction of $Cu_3N$ film with molecular $H_2$ gas.

To our knowledge, this two-step method has however not been reported for silver films up to now. Indeed, this will be difficult to transfer to silver coatings, as $Ag_2O$ decomposes itself at moderate temperatures (around 120°C in vacuum [273]).

### I.4.3. Doping agent for silver films

One alternative way to obtain smooth ultra-thin metal films is performed by doping. Al and Cu doping have demonstrated strong reduction of the Ag film roughness and critical thickness of films deposited by sputtering, [42, 43, 182, 190] although similar attempt has not yet been reported for ALD or CVD.

By depositing a small amount of aluminum during the co-sputtering deposition of silver (around %4 at. Al in Ag), Gu *et al.* [42] and Zhang *et al.* [182] have demonstrated that the resulting film was much smoother (see Figure 17) and presented a high resilience against dewetting. They could then obtain a critical thickness of 6 nm with a conductivity of $2.3\times10^4$ S/cm. The role of Al in suppressing the usual Volmer-Weber growth mode of Ag layers on oxide substrate was not fully understood, but could be related to the increase of nuclei density with larger energy of the Al–O bound as compared to the Ag–O bound, and the resulting lower diffusion length of Al on the surface.

Cu-doped Ag thin films showing a percolation threshold as low as 6 nm and a sheet resistance of 14.1 Ω/□ have been obtained through magnetron sputtering by Huang *et al.* [190]. This was also attributed to an enhancement of the nuclei density caused by smaller diffusion distance of Cu atoms conducting to the immobilization of Cu atom on the substrate which finally suppressed the 3D cluster growth.

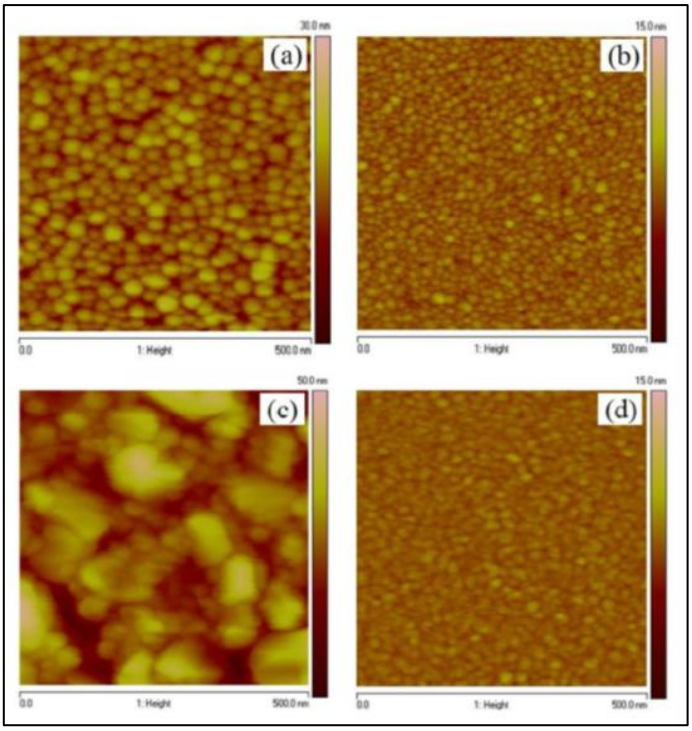

Figure 17: AFM images of (a) 3 nm pure Ag films, (b) 3 nm Al-doped Ag films, (c) 15 nm pure Ag films, and (d) 15 nm Al-doped Ag films on $SiO_2$/Si(100) substrates. From [42].

### I.4.4. Plasma post-treatment of silver nanoparticles

In order to make the deposit conductive and thus continuous, plasma post-treatment has been demonstrated for solution processed Ag nanoparticles, mainly for inkjet-printed process. [191, 192, 193, 194] However, it is worth noting that the starting film is composed of compact nanoparticles, and not islands. Post-treatment of islands leads to even more separation, as discussed in the I.2.3. section. Interestingly, Ma *et al.* [195] used argon gas post-treatment to sinter Ag NPs of different diameters (23 nm and 77 nm with assumed thicknesses of 46 nm and 154 nm, respectively) synthetized by wet chemistry and investigated the plasma power and time effects on the morphology and electrical conductivity of Ag nanoparticle film. For 23 and 77 nm Ag NPs size, the lowest resistivities of the sintered film have been obtained with a plasma post-treatment of 900 W during 60 min, respectively 5 times (8.73 μΩ.cm) and 12 times (18.7 μΩ.cm) higher than bulk Ag resistivity (1.59 μΩ.cm). The morphology of the obtained films is exposed in Figure 18, both in top view and cross section. Morphologically continuous films and a densification of the uppermost layer are obtained in both cases after plasma processing.

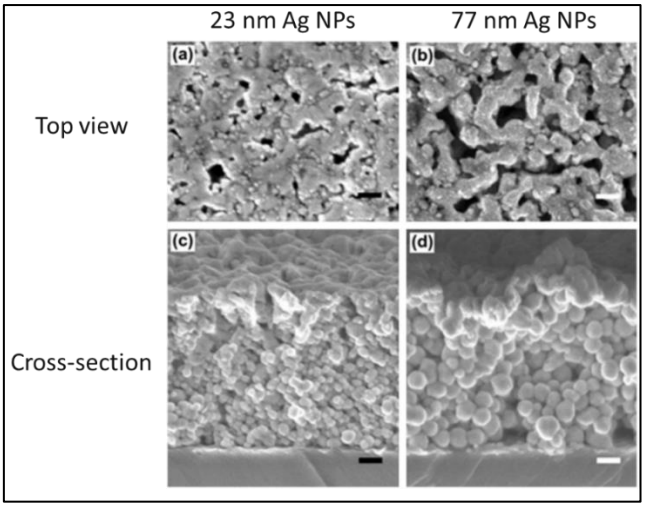


Figure 18: SEM top view (a,b) and cross-section (c,d) of plasma sintered AgNP films after a plasma-post treatment of 900 W during 60 min performed on the 23 (left column) and 77 nm (right column) AgNP films. The scale bars are 100 nm. From [195]

### I.4.5. Conclusion

In this section, alternative routes that have been envisioned for ultra-thin metal films deposition have been described and including the use of a wetting layer, the doping by another metal (e.g. Al, Cu) in order to enhance the interaction of the metal film with the oxide surface and the deposition of the metal oxide followed by a reduction step. Post-treatment processes also enhance the sintering of NPs, giving electrically continuous films, although not applicable for films made of discrete islands. These routes could provide good opportunities for metal films deposited by chemical gas-phase synthesis (CVD and ALD), more particularly Ag films which gives mainly nanoparticular films, as showed in the previous parts.

## I.5. Specific case of metal films optical properties

### I.5.1. Optical constants

From a macroscopic point of view, the optical response of a metal can be described by the interaction between the solid represented by its dielectric function and the light represented by an electromagnetic wave. [196] The dielectric function ε thus appears as the relevant physical quantity to characterize the optical response of a material. This quantity is complex, i.e. it has both real and imaginary parts, defined as $\varepsilon_1$ and $\varepsilon_2$, respectively and depends on the frequency $\omega$. Therefore:

$$\varepsilon(\omega) = \varepsilon_1(\omega) + i\varepsilon_2(\omega) \quad (1)$$

The refractive index $n(\omega)$ corresponds to the real part of the square root of the complex dielectric function while the extinction coefficient $K(\omega)$ corresponds to the imaginary part. The complex index of refraction $\hat{n}(\omega)$ is defined as:

$$\hat{n}(\omega) = n(\omega) + iK(\omega) \equiv \sqrt{\varepsilon(\omega)} \quad (2)$$

With

$$\sqrt{\varepsilon(\omega)} = Re\sqrt{\varepsilon(\omega)} + iIm\sqrt{\varepsilon(\omega)} \quad (3)$$

At the interface between two media, the refractive index $n$ is linked to the reflection of the electric field, and the extinction coefficient $K$ to its absorption. [196] The reflectance of a thin film can be directly correlated with the values of $n$ and $K$. If we assume that the first medium is air ($n_1 = 1$), the second medium a metal with a refractive index $n$ and an extinction coefficient $K$, the Fresnel's equation [196] at the normal incidence gives the following expression for the reflectance $R$:

$$R = \frac{(n-1)^2 + K^2}{(n+1)^2 + K^2} \quad (4)$$

## I.5.2. Theories of free and bound charge carriers

The dielectric function can be calculated analytically in specific limiting cases. Based on equations of motion for the charge carriers, two classical models for the dielectric function are extracted: the Drude model (free electron) and the Lorentzian oscillator theory (bound electron). [196]

### I.5.2.1. Drude model or free charge carriers theory

The objective of the Drude's model is to explain the large variety of electrical and thermal properties observed for different metals by using the simple microscopic model of free electrons. In this model, metals are represented by a cloud of free electrons which are not bound to a particular atomic nucleus but are free to move through the metal lattice. [197] In the Drude (or free electron) model, the dielectric function can be directly calculated as follows [196]:

$$\varepsilon\,(\omega) = 1 - \frac{\omega_p^2}{\omega^2 + 2i\gamma\omega} \quad (5)$$

where $\omega_p$ corresponds to the plasma frequency of the material (a constant for each material) and $\gamma$ the damping constant necessary to consider the damping of the electron's movement.

Figure 19 (a) illustrates the evolution of the real part and imaginary part of the dielectric function, based on equation (5). In order to calculate $n$ and $K$, both the real part and the imaginary part must be extracted from the square root of equation (5). The results of this calculation are illustrated in Figure 19 (b).

When $\omega < \omega_p$, the real part $n$ is very weak with respect to $K$. According to Fresnel's equation (4), when $n \ll K$, a value of 1 is obtained for $R$, that corresponds to total reflection. This explains why a high reflectance is observed in the reflectivity spectrum of metals at high wavelength (Figure 19 (c)). On the contrary, in the region where $\omega > \omega_p$, we have optical constants satisfying $n \gg K$. If $n$ is close to 1, it results in a low reflectance and a high transmittance. Thus, at lower wavelength (higher frequency), the drop of the reflectance is obtained in the optical spectra for the different metals (Figure 19 (c)). When passing from high reflectance/low transmittance ($\omega < \omega_p$) to low reflectance/high transmittance ($\omega > \omega_p$), the plasmonic resonance where $\omega = \omega_p$ takes place at the intersection of these two curves giving a certain absorbance. According to equation (4), $n$ and $K$ are very weak compared to 1 leading to almost no reflectance. This means that all the electrons oscillate in phase throughout the material propagation length.

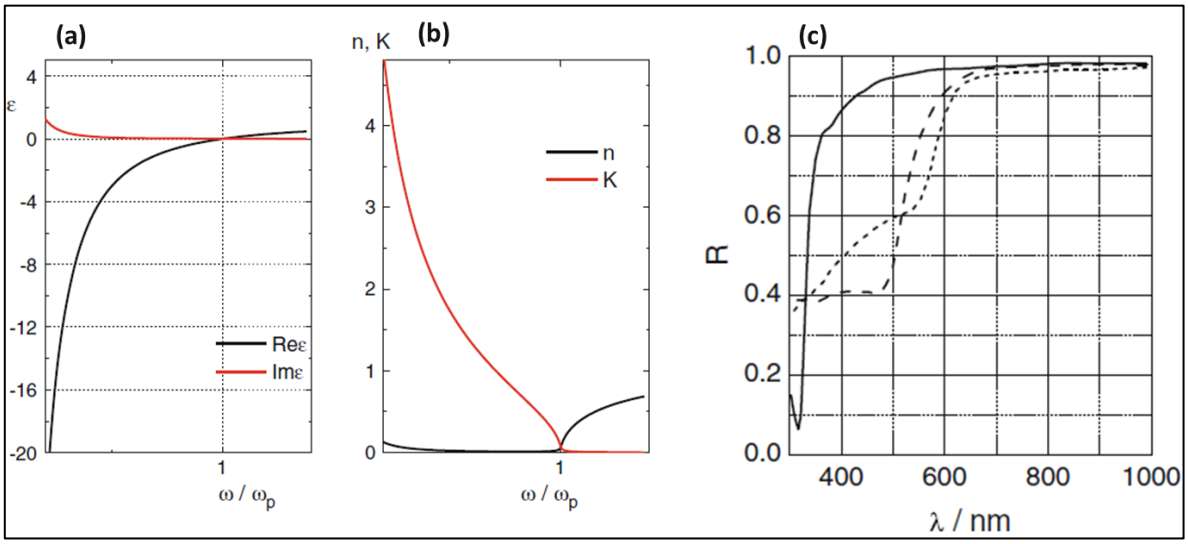


Figure 19: Dielectric function (a) and optical constants (b) according to equation (5) (c) Normal incidence reflectance of silver (solid line), gold (dash), and copper(short dash) surfaces. From [196].

### I.5.2.2. Lorentzian oscillator model or bound charge carriers theory

In the Drude model, the electron-electron and electron-nucleus interactions are neglected and only the oscillation of the electron gas constituted by free electrons close to the Fermi level is taken into account. The Lorentzian oscillator model was proposed to provide a more accurate prediction of the permittivity. This model includes the one of the bound charge carriers in the material through harmonic oscillators. [197] Using this theory, the dielectric function can be directly calculated as follows [196]:

$$\varepsilon(\omega) = 1 + \frac{\omega_p^2}{\omega_0^2 - \omega^2 - 2i\gamma\omega - \frac{\omega_p^2}{3}} \equiv 1 + \frac{\omega_p^2}{\tilde{\omega}_0^2 - \omega^2 - 2i\gamma\omega} \qquad (6)$$

With $\tilde{\omega}_0^2 = \omega_0^2 - \frac{\omega_p^2}{3}$

where $\omega_p$ corresponds to the plasma frequency of the material and $\gamma$ the damping constant necessary to consider the damping of the electron's movement, as for Drude's theory. $\omega_0$ is the resonance frequency and $\tilde{\omega}_0^2$ corresponds to the resonance frequency valid for the dielectric function.

Figure 20 (a) illustrates the evolution of the real part and imaginary part of the dielectric function, based on equation (6). In order to calculate $n$ and $K$, both the real part and the imaginary part must be extracted from the square root of equation (6). The results of this calculation are illustrated in Figure 20 (b).

When $\omega < \tilde{\omega}_0$, contrary to Drude's model, the real part $n$ tends to 1 while $K$ is very weak. According to Fresnel's equation (4), this corresponds to an absence of reflection. Similarly, at high frequency $\omega > \tilde{\omega}_0$, we have optical constants satisfying $n \gg K$ which results again in the absence of reflectance. Therefore, far from the plasmonic resonance where $\omega = \tilde{\omega}_0$, the material is completely transparent and the refractive index $n$ is modified only close to the plasmonic resonance.

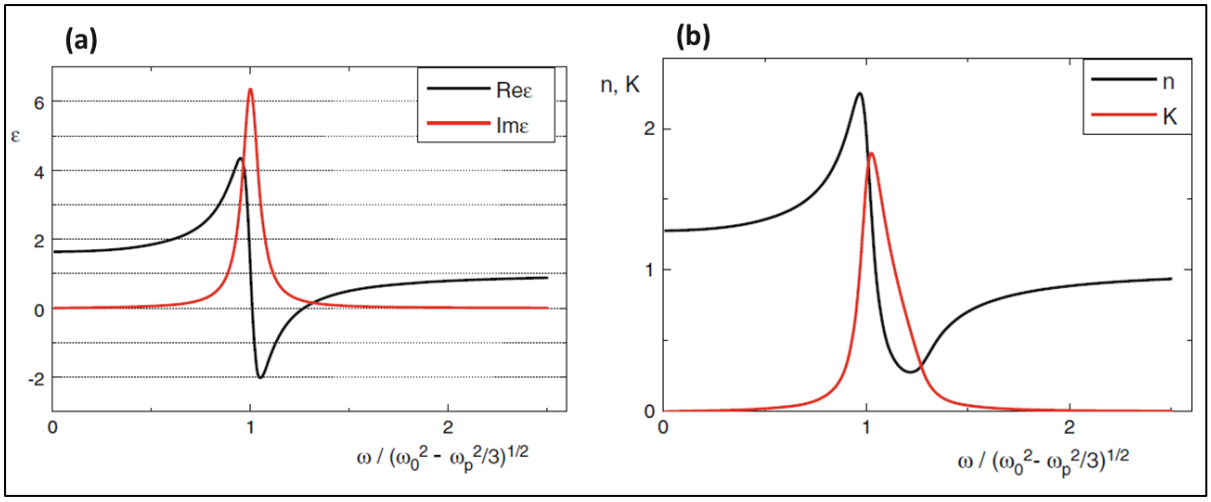

Figure 20: Dielectric function (a) and optical constants (b) according to equation (6). From [196].

### I.5.2.3. Correlation between reflectivity spectrum and film morphology

Information about the metallic films' morphology can be obtained by studying their optical properties. For example, the continuity or the nanoparticular structure can be determined by studying the reflectance (%R) spectrum. [198] Figure 21 shows the evolution of the measured reflectivity spectra during the deposition process of Ag layer for discontinuous (Figure 21 (a)) and continuous (Figure 21 (b)) film and the corresponding SEM images (Figure 21 (b) and Figure 21 (d), respectively).

For an ideal continuous film (simulation, dotted red curves), the signature is a high infrared reflectance increasing with the thickness, as a result of longer deposition time. The high %R and its increase with the wavelength is predictable by the Drude's theory. In the case of discontinuous film, a reflectance peak is expected in the visible range due to the Drude model again followed by a drop at higher wavelength (Figure 21 (a)), understood by the oscillator theory.

The explanation is that, in metals, for low wavelength/high frequency, when electrons, that have a proper speed, are excited by an electric field from incident light, they change their direction very quickly and are not moving over a long distance but oscillate over a small distance. On the contrary, for high wavelength/low frequency, the lower the frequency, the longer the path covered by the electrons.

In the presence of a nanoparticle metallic film, there is a transition between low wavelength/high frequency and high wavelength/low frequency. At low wavelength/high frequency, the movement of electrons is included in a particle, their traveled distance being less than the size of the particle, the particle behaves as a bulk metal. This could be referred as a 'continuous-like' behavior and understood by the Drude model. The plasmonic frequency of silver being located in UV region ($\lambda_p$ = 140 nm [18]), we are in the case where $\omega < \omega_p$ which justified the high reflectance. (see section I.5.2.1.) At high wavelength/low frequency, the more the frequency will decrease, the more the path/distance traveled by the electrons will be long. In this case, the electrons are confined in a restricted space which corresponds to the dimension of the particle and the oscillation of the electrons polarizes the particles, as it is explained in the next subsection I.5.3. This particle then behaves not like a bulk metal but like an atom, with bound electrons. This could be referred as a 'particle-like' behavior

and understood by the oscillator model. This justifies the high transparency and low reflectance of the metal at high wavelength far from the plasmonic resonance frequency. (see section I.5.2.2.)

By replacing the heterogeneous system (NP/ surrounding medium) by a homogeneous medium with an effective dielectric function, the Maxwell-Garnett theory quantitatively reproduces this transition from free electron model to bound electron model, [199] but this analysis goes beyond the scope of the thesis work.

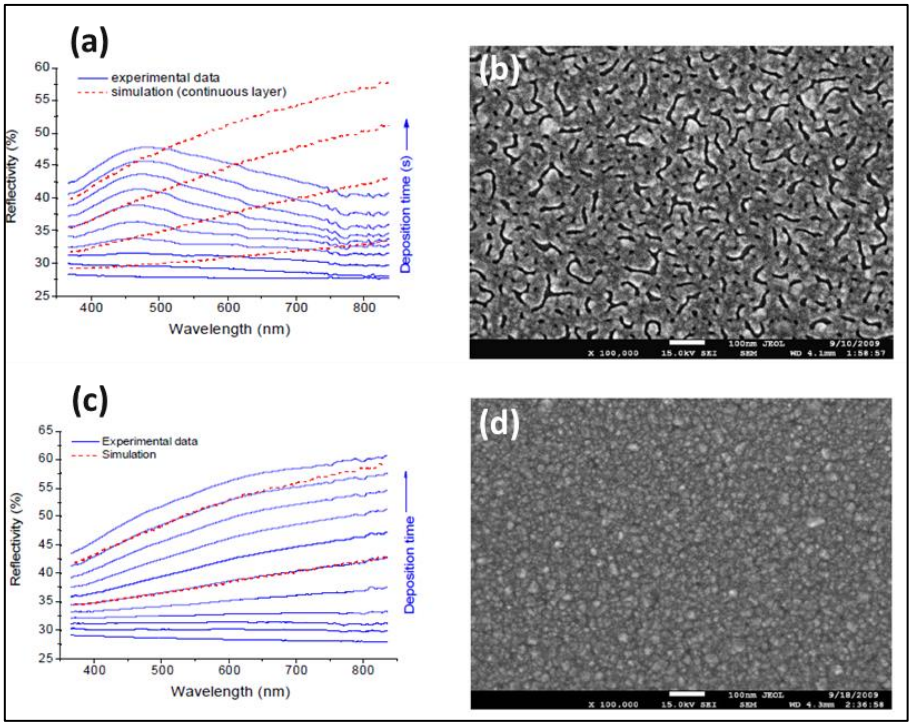


Figure 21: (a) and (c) Evolution of the measured reflectivity spectra during the deposition process of (a) discontinuous Ag layer and (c) continuous Ag layer with a growth mode influenced by $AgO_x$ coating prepared on the substrate before the deposition. The blue lines correspond to experimental data and the dotted red curves exhibit a simulation of the reflectivity of ideal continuous silver layer. (b) and (d) Corresponding scanning electron micrographs of ultra-thin silver layers corresponding to, respectively, spectra (a) and (d). From [198].

### I.5.3. Specific case of metallic nanoparticles

In the case of metallic nanoparticles, the interaction of the free electrons with the incident light leads to apparition of the localized surface plasmon resonance (LSPR). (Figure 22 (a)) When light irradiates a metallic particle, the oscillation of the electric field engenders the free electrons to oscillate coherently. Surface plasmons (SPs) are collective oscillations of a set of delocalized coherent electrons of a metal existing at the interface of two materials (metal-dielectric). This oscillation of the free electron induces an oscillating dipole inside a particle, that furthermore induces an electrical polarization of the particle.

The result of the confinement of SP in a nanoparticle of size comparable to or smaller than the wavelength of light used to excite the plasmon is called localized surface plasmon (LSP). This is responsible of two effects: a local exaltation of the electric field close to the surface of the particle and a maximum absorbance peak at the plasmon resonance frequency.

In the case of well-defined geometrical shaped and well-separated particles, the Mie theory predicts the LSPR peak at a well determined frequency which does not depend on the size and the shape of the particle but only on the type of material and the medium. [25] However, it was found in the literature that the LSPR optical response (spectral position, intensity and width of the absorbance peak) depends on the morphology of the nanoparticle and the covered area. [25] As shown in (Figure 22 (b)), a red-shift of LSPR peak in the absorbance spectrum is generally observed with the increasing size of Ag particles. Several theoretical and experimental works have been performed on metallic particles of different shape in order to find the optimum Ag nanoparticles' morphology to enhance the sensitivity of the plasmon resonance response. The option to modulate the LSPR response presents a huge interest for a lot of application, including surface-enhanced Raman spectroscopy or other optical effects where localized plasmons are used.

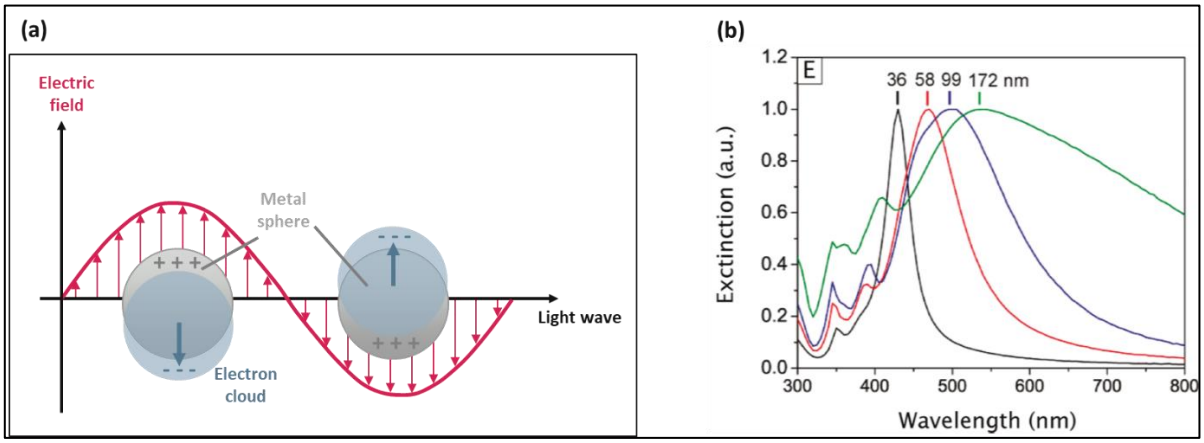


Figure 22: (a) Schematic of the interaction of an electric field from incident light on a metallic nanoparticle. (b) Extinction (absorbance) spectrum of Ag nanocubes of different edge length where LSPR peak of the nanocubes red-shifts with the increased of edge length. From [25].

## I.5.4. Conclusion

In this part, we have seen that the optical behavior of thin metallic films can be understood by two theories. The first one is related to the free charge carriers theory or Drude model. It is used to explain the 'continuous like' optical behavior of the nanoparticle film at low wavelength translated by a high reflectance and a low transmittance. This model is also used to explain these features in the infrared region spectra of an ideal continuous film as well as the reflectance decrease in the UV/visible range. The second theory is the bound charge carriers or oscillator model. It describes the 'particle-like' behavior of the nanoparticle film at higher wavelength exhibiting low reflectance and high transmittance. We have also shown the optical response of the specific metallic nanoparticle with the apparition of a localized surface plasmon resonance (LSPR) leading to a maximum absorbance peak at the plasmon resonance frequency of the metal which depends on the nanoparticle morphology, i.e. size and shape.

## I.6. Conclusion

In this first chapter, we have described the principle of chemical vapor-phase deposition techniques by differentiating CVD from ALD. As non-line-of-sight depositions, these methods enable a uniform and conformal film growth on substrate with complex geometries. More specifically, ALD has demonstrated an accurate and precise thickness control due to the use of sequential self-limiting surface reactions of precursors. In order to determine if a process satisfies the requirement of ALD self-limiting reaction, the impact on the GPC of the synthesis temperatures, the sequences times of the precursors (pulse and purge times) and the number of ALD cycles needs to be controlled. The aim is to find a constant GPC that does not depend on these parameters.

The **growth of metals on oxide substrates** by chemical vapor depositions starts with the formation of **isolated island** due to surface energies discrepancy between the material deposited and the substrate. This is the result of Volmer-Weber type growth. The atomistic processes taking place on surfaces are the interaction of the metal precursor molecules on the substrate surface, the surface diffusion of the atoms leading to the formation of NPs and their further growth via ripening. The study of the evolution of the NPs density and particle size distribution (PSD) has shown reliable information about the diffusion processes but this has been investigated to a less extent. Consequently, the correlation between PSD and growth mechanisms leading to ALD of NPs is still under debate.

We have reviewed the **state-of-the-art of chemical gas-phase processing** of **silver films** for which the major challenge is to find a suitable metal precursor combining a high thermal stability, a high vapor pressure and a high volatility. The main goal was to demonstrate continuous (or at least connected) silver films with a finite electrical conduction, as compared to films made of disconnected nanoparticles that are insulating. When it comes to the **CVD of silver films**, one of the most important challenge is the insufficient volatility of several metal-containing compound and several techniques have been developed to circumvent this aspect. Due to the Volmer-Weber mode, Ag islands are obtained at low film thickness and their coalescence is promoted with increasing thickness. No direct correlation between the deposition method and the film quality has been extracted. The different techniques used are very precursor-dependent. The most promising Ag precursors appeared to be mixed ligand stabilized Ag(I) complexes containing either a fluorinated carboxylate or fluorinated and non-fluorinated β-diketonate. The best volatility and stability of β-diketonate complexes have been obtained for fluorinated β-diketonates coordinated with low molecular weight tertiary phosphines complexes and particularly Ag(fod)($PEt_3$). Due to recent development of the ALD technique and the lack of appropriate Ag precursors, the **ALD of silvers films** has been only investigated from 2007 and thus quite few investigations are available in the literature. Moreover, ALD of metal nanoparticles, and in particular silver, is still weakly understood. Using this method, we have highlighted two types of ALD processes depending on the reducing agent, i.e. plasma-enhanced ALD (PE-ALD) and thermal ALD (Th-ALD). We have seen that it was quite challenging to obtain continuous Ag films in both cases, also due the islands growth of metals, and non-electrically-conductive Ag films are obtained for low thickness. Among the different works, we have shown that PE-ALD gives higher coverage with a lower critical thickness as compared to thermal processes due to the presence of highly reactive species enabling to work at lower temperatures at which the diffusion of Ag is decreased. In these conditions, the most promising result have been obtained with the use of high vapor pressure Ag(fod)($PEt_3$) precursor exhibiting a low melting point of 26–28°C. This PE-ALD approach have been also reproduced by several groups.

**Consequently, the route that has been naturally chosen for this thesis work towards silver continuous thin films by ALD is the use of the precursor Ag(fod)($PEt_3$) with $H_2$ plasma as reducing agent (i.e. PE-ALD).**

On the other hand, the **reduction of the critical thickness** of conductive films remains one of the major research activities in the deposition of metal films, and we have demonstrated that several techniques have already been investigated for this purpose, mainly for PVD methods. For **atomic layer deposited noble metal**, the influence of the wetting layer exhibits a large panel of results and no clear trends could have been extracted due to the high number of parameters needed to be taken into account, e.g. the wetting layer crystallinity, the surface preparation, the deposition temperature, the metal precursor and reducing agent… When it comes to Ag, although a strong improvement for the growth of **ultra-thin Ag continuous films** have been obtained with line-of-sight techniques, only non-continuous films or a slight enhancement of the coverage but still non-continuous morphology were noticed when chemical gas-phase synthesis were used. In such conditions, we have seen that the surface hydroxyl groups are mandatory for Ag precursor adsorption. The other alternative routes that have been envisioned for ultra-thin metal films deposition seems to be relatively hard to be transferred to Ag, due to its much more noble character as compared to other noble metals, leading to non-stable Ag complexes.

At last, we have also highlighted that the investigation of the **optical properties** is a powerful method to get information about the morphology of the metallic films. One signature of films made of separated metal island is the presence of localized surface plasmon resonance absorbance peak in the visible region. The other feature is the transition from a 'continuous like' optical behavior at low wavelengths, understood by Drude's model and highlighted by a high reflectance/low transmittance, to the 'particle-like' behavior at higher wavelengths, understood by the oscillator model and highlighted by a low reflectance/high transmittance. For an ideal continuous film, the signatures are a high reflectance and a low transmittance in the infrared region spectra while a decrease reflectance in the UV/visible range.

# Chapter 2

# Experimental methods

In this chapter, we intend to describe the experimental techniques which are used all along this thesis work. The first part presents the deposition methods and experimental tools employed as well as the substrates and precursors handled for the synthesis of silver thin films. The second part is dedicated to reference the characterization techniques used to investigate the structural, morphological, chemical and physical properties of the grown thin films. A brief description of the principle and the main characteristics of each, as well as the experimental parameters used, are presented.

Some results of the chapter are taken from the publications:

*S. Wack, P. Lunca Popa, N. Adjeroud, J. Guillot, B. R. Pistillo, R. Leturcq,* Large-Scale Deposition and Growth Mechanism of Silver Nanoparticles by Plasma-Enhanced Atomic Layer Deposition, *J. Phys. Chem. C*, **2019**, 123, 44, 27196-27206.

*J. Crêpellière, K. Menguelti, S. Wack, O. Bouton, M. Gérard, P. Lunca Popa, B. R. Pistillo, R. Leturcq, M. Michel*, Spray Deposition of Silver Nanowires on Large Area Substrates for Transparent Electrodes, *ACS Appl. Nano Mater.*, **2021**, 4, 2, 1126–1135.

## II.1. Atomic layer deposition reactor and film growth

### II.1.1. Atomic layer deposition reactor

#### II.1.1.1. Plasma-enhanced atomic layer deposition of silver films

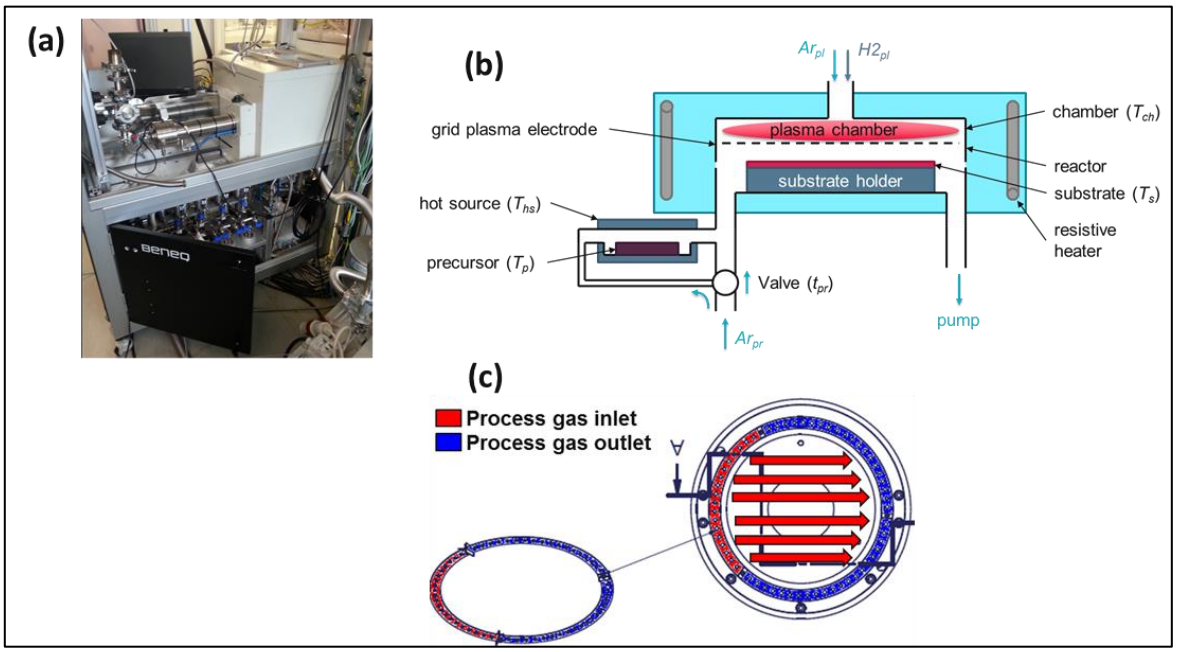


Figure 23: (a) Photography of the ALD TFS 200 system from Beneq. (b) Simplified scheme of the Beneq TFS 200 ALD system with the remote plasma and the hot source HS500 with open boat for the precursor and (c) Top view scheme of the reactor showing the cross-flow precursor delivery system.

The experiments for the deposition of silver layers have been performed on a Beneq TFS 200 atomic layer deposition (ALD) system, equipped with an open-boat hot source HS500 for the silver precursor and the remote plasma option ($Ar/H_2$ plasma). A photography and a simplified scheme of the reactor is shown in Figure 23.

The substrate is placed in the reactor of the ALD, which is heated by heating resistors placed in the chamber to control its temperature ($T_{ch}$). The chamber temperature $T_{ch}$ is measured close to the reactor and is assumed to be representative of the sample. The substrate temperature ($T_s$) depends directly on the chamber temperature but is not controlled independently nor monitored. (see Figure 23 (b)). The silver precursor is loaded into an open quartz boat and heated using the HS500 precursor cell at the temperature $T_{hs}$. The precursor temperature ($T_p$) depends directly on the hot source temperature but is not directly controlled. By punctual in-situ measurements, we have observed that $T_p$ is systematically 0 to 10°C above $T_{hs}$, and $T_s$ systematically 5 to 15°C above $T_{ch}$. However, these differences, related to the geometries of the parts, the gas flows or the plasma ignition, may change from one process to the other, and for this reason only $T_{hs}$ and $T_{ch}$ are reported in the following studies. Moreover, the exposure of the precursor is regulated by the process argon flow ($Ar_{pr}$) and a gas valve. In the default position, the valve drives the flow directly to the reactor. When it is activated (during the precursor pulse time $t_{pr}$), the valve drives the flow to the hot source, which carries the precursor into the reactor.

For film deposition, we have used a remote capacitively coupled plasma (radio frequency (RF), 13.56 MHz) placed on top of the reactor. A grid serves as a ground electrode and defines the plasma chamber, allowing radical flows into the reactor. In order to promote the glow discharge ignition, a mix of argon ($Ar_{pl}$) and hydrogen ($H_{2pl}$) is injected. This mixture flows continuously to avoid deposition of the Ag precursor in the plasma head. We have checked that no reaction occurs between the precursor and molecular hydrogen when the plasma is turned off. ALD tool gas lines are equipped with Ar and $H_2$ purifier cartridges from Entegris. Both Ar, used as precursor carrier and process gas, and $H_2$ gases used during the process are respectively Alphagaz 1 and Arcal Prime from Air Liquide. Their flows are controlled using mass flow controllers. The plasma post-treatment was performed in the same reactor using a continuous plasma with glow discharges fed with a mix of hydrogen and argon. Some tests have also been performed using argon only. In this thesis work, two configurations of plasma post-processing have been tested. The first one is the remote or indirect plasma, the same as the one used for film deposition. In this case, the presence of the grid leads to a decrease of flux and energy of the ions towards the substrate but also to a somewhat reduced radical density flowing into the reactor. In order to enhance the efficiency of the plasma by promoting not only the hydrogen radical's density but also the ionic species, we have also studied the effect of removing the grid and thus creating a direct contact with the active plasma. The two configurations of plasma are named arbitrary along the thesis as "direct post-treatment" for post-treatment performed in the absence of the grid and "indirect or remote post-treatment" for post-treatment performed in the presence of the grid. It is worth mentioning that the denomination used during this thesis work is in agreement with the one employed previously by Kariniemi *et al.* [41]. However, in some other publications, [57, 152] the use of a capacitive discharge and thus of the reactor Beneq TFS 200, is classified as direct plasma even in the presence of the grid between the polarized electrode and the substrate.

Other parameters such as the reactor pressure or the plasma bias voltage are not directly controlled by the process, but are direct consequences of the parameters mentioned above. They have been recorded but are not discussed in the thesis. They then do not appear along the thesis.

All the terminology used in the previous paragraphs is summarized in Table 9.

| Symbol | Designation | Units |
|---|---|---|
| $Ar_{pl}$ | Argon flow in the plasma head | sccm |
| $Ar_{pr}$ | Argon flow in the process lines (from the precursor boat to the reactor) | sccm |
| $H_{2pl}$ | Hydrogen flow in the plasma head | sccm |
| $P_{dep}$ | RF plasma power during deposition | W |
| $P_{post}$ | RF plasma power during post-treatment | W |
| $T_{ch}$ | ALD chamber temperature | °C |
| $T_{hs}$ | Hot source temperature (for the precursor evaporation) | °C |
| $T_p$ | Precursor temperature (related to $T_{hs}$) | °C |
| $T_s$ | Substrate temperature (related to $T_{ch}$) | °C |
| $d$ | Distance between grid electrode and substrate | cm |

Table 9: Experimental parameters terminology used for the deposition performed with Beneq TFS 200 equipment.

The reactor of the TFS 200 enables deposition on samples up to 200 mm in diameter (8 inches) and up to few mm in thickness. The scheme top view of the reactor (Figure 23 (c)) shows the geometry of the silver precursor flow from the inlet part to the outlet part. We note that, in the plasma configuration, the maximum sample thickness is determined by the distance *d* of the plasma ground electrode (grid electrode) to the substrate, which can be adjusted.

### II.1.1.2. Thermal atomic layer deposition of oxides and nitrides

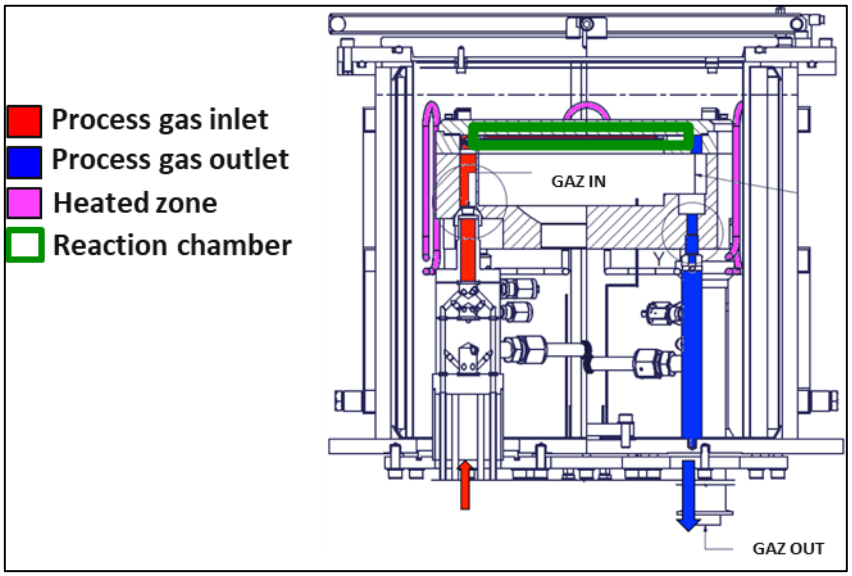


Figure 24: Drawing of the Beneq TFS 200 ALD deposition chamber in the planar reactor configuration, showing the gas inlet (in red), the gas outlet (in blue), the heated zone (in pink) and the delimitation of the reaction chamber (in green).

The thin oxide films investigated during the thesis were deposited using the same Beneq TFS 200 equipment as the one used for silver deposition, but in its planar configuration. A wide range of chemical precursors is indifferently applied, going from gas to low vapor pressure liquid or solid precursors (inorganic and organic). Depositions are carried out from room temperature (20°C) and up to 450°C. The planar reactor accepts samples up to 2 mm thick. Figure 24 shows a drawing of the chamber in the planar reactor configuration, along with the gas inlet and outlet. When depositions of oxides and nitrides were performed on thicker samples (e.g. 2.1 mm-thick flat glass), a higher reactor ("3D reactor") or directly the reactor in the plasma configuration were rather used.

## II.1.2. Selected Ag precursor and reducing agent

Following the state-of-the-art in section I. , it appears that the most favorable precursor and reducing agent in order to obtain continuous silver thin films are respectively (2,2-dimethyl-6,6,7,7,8,8,8-heptafluorooctane-3,5-dionato)silver(I)-triethyl-phosphine (Ag(fod)($PEt_3$)) and $H_2$ plasma. For this reason, these are the conditions that have been chosen for developing Ag thin films in the thesis. The silver precursor Ag(fod)($PEt_3$) was provided by Strem Chemicals, Inc. (ref. 47-3025) with minimum 98% purity.

In order to investigate the weight loss of the Ag precursor vs. temperature, we perform thermogravimetry analysis (TGA) and differential thermal analysis (DTA) is used to study the phase transition of the precursor, as shown in Figure 25. The test was carried out with 69.425 mg of Ag precursor, heated up to 400°C at a heating rate of 1°C/min using a Netzsch STA 409PC thermobalance.

The signals clearly show first the melting of the precursor at about 25-30°C (expected 26°C).Then, the precursor is thermally stable at least up to 230°C and a small amount of residues is left, meaning that it evaporates itself a large part of the compound.

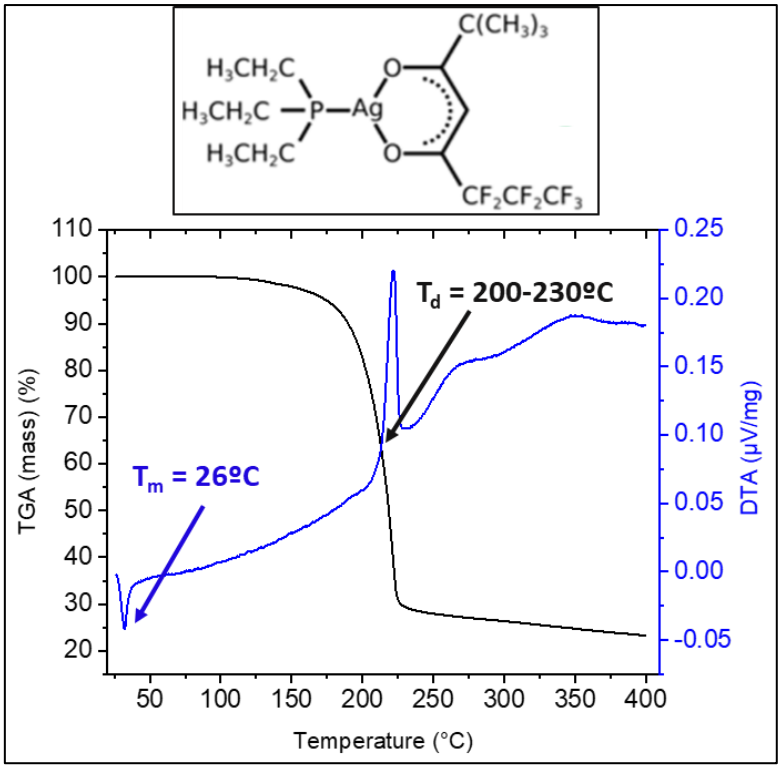


Figure 25: Thermogravimetry analysis of the precursor Ag(fod)($PEt_3$) (semi-developed formula on top of the graph). Both the thermogravimetry signal (TGA), representing the mass loss during the temperature ramp, and the differential thermal analysis signal (DTA), showing phase transition of the precursor, are shown.

### II.1.3. Distinction of the ALD-based processes

During the completion of the thesis, we use two different processing methods for depositing silver films. The two methods differ by the pulse sequence used during the ALD process. In order to explicitly describe the difference, we schematically reproduce in Figure 26 the pulse sequence for standard thermal ALD process (Figure 26 (a)) and for the standard PE-ALD process (Figure 26 (b)). In both standard processes, the pulse for the first precursor and for either the second precursor or the plasma are separated in time by purges where only non-reacting gas is injected. This enables a good separation of the two surface reactions occurring during the standard ALD processes. In the two-step process described in Figure 26 (c), the first step consists in continuously exposing the precursor and pulsing repeatedly the plasma source. This process is called pulsed PE-CVD. We see in the thesis that this first step provides a film made of compact silver particles. During the second step, the precursor is stopped, and a plasma post-processing is performed. Although this process deviates from the ideal ALD case, we will see that it is strongly beneficial for producing ultra-thin conducting films. Moreover, with the view to avoid the apparent finite depth treated by the post-processing step, which is expected since the post-treatment is a surface processing step, we develop a processing in which both two-step processing and plasma post-processing are gathered in one step called “super-cycle”.

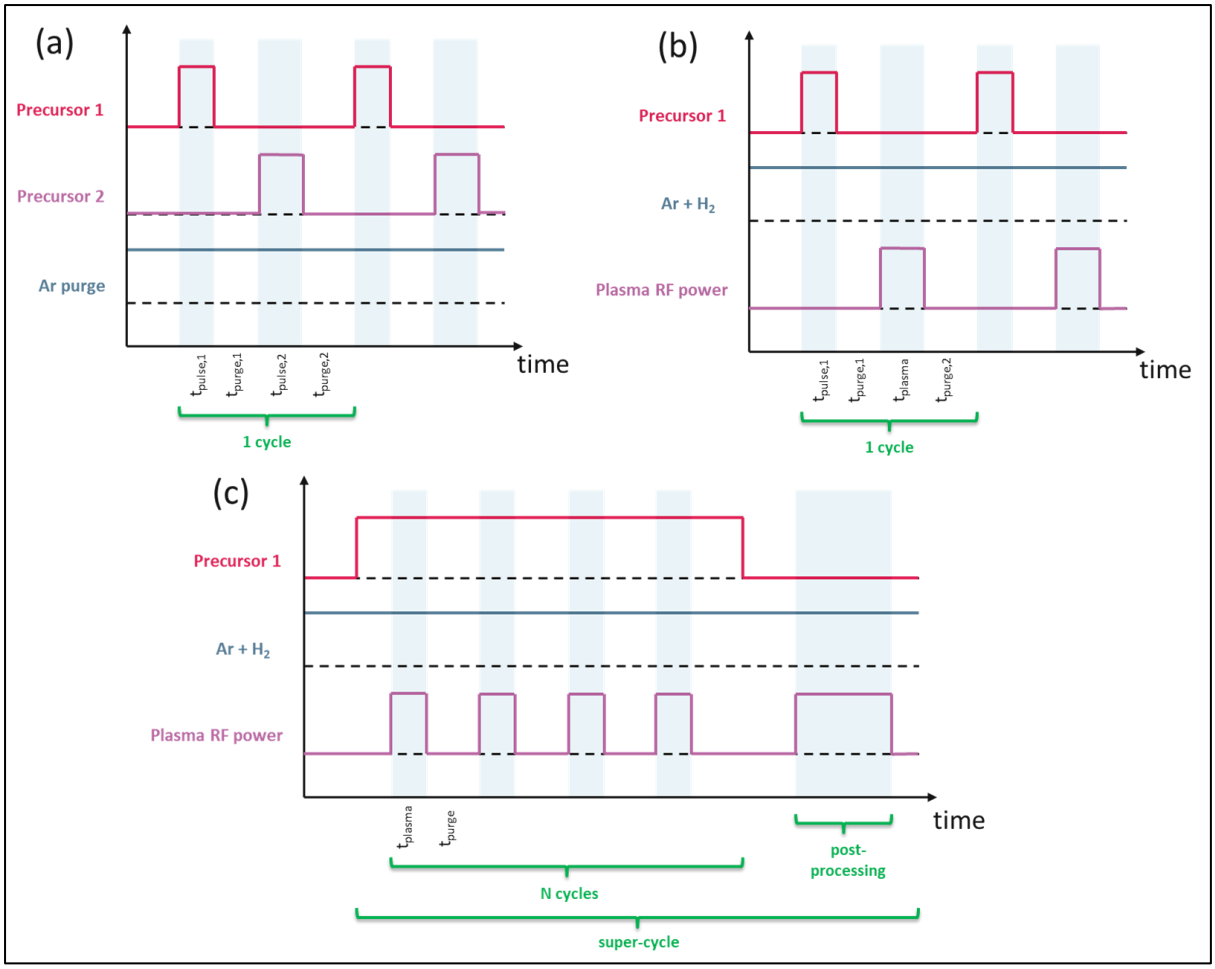


Figure 26: Pulse sequence for several types of ALD processes. (a) Standard thermal ALD process with two precursors. (b) Standard plasma enhanced ALD (PE-ALD) process with one precursor and a plasma source. (c) Two-step pulsed-PECVD process developed during the thesis for the deposition of continuous silver thin films.

### II.1.4. Substrates

During this thesis work, different substrates, flat or 3 dimensions, have been used for the development of Ag nanostructures. The choice of substrates was made according to the type of characterizations to be carried out but also motivated by the future functional applications and for the study of the influence of the sublayer on the morphology of Ag films. It is also worth mentioning that all substrates covered with different underlayers used in the following parts (II.1.4.3 and II.1.4.4.) were exposed to air before Ag deposition. The main reasons are that either their synthesis has been performed with other deposition techniques (wet chemistry for ZnO nanorods) or because the reactor was opened and vacuum cutted between their synthesis and the deposition of Ag in order to have the same experimental conditions for the metal deposition.

#### II.1.4.1. Silicon wafer

The depositions have been performed on 200 mm diameter silicon substrate with electronic grade (from Siegert Wafer), oriented according to the (100) plane ± 0.5°, with a resistivity 1-100 Ω.cm and with p-type (boron) doping. Their thicknesses are 725 ± 25 µm and the silica native oxide is 2-3 nm-thick. Single crystal silicon (100) is the reference substrate used for the majority of growths. It is conductive and enables all spectrometric techniques involving charged particles (XPS, SEM, SIMS) to be performed without serious charge accumulation problems on the substrate.

The face on which the deposits are made is single side "mirror polished" so as not to disturb the growth of the deposits during the process. The surface of these substrates is covered by a native amorphous $SiO_2$ layer (typically 1 to 3 nm thick). These substrates have high grade (in particular concerning the number of particles) and did not require specific cleaning prior to deposition. However, before deposition, an $Ar/H_2$ plasma of 1 min have been performed in order to remove organic compounds deposited during the handling of the sample.

In order to investigate the uniformity of the deposition on the substrates in the reactor, the position on the substrate is marked versus the distance from the inlet of the precursors in the reactor, as shown in Figure 27. The uniformity in the lateral direction (i.e. perpendicular to the precursor flow) has been shown to be very good, as demonstrated by the quantitative analyses determined regarding several morphological criteria deduced by the study of the SEM micrographs (Figure 27 (b-c) and see explanation of image treatment in section II.2.2.3.) . For this reason, no specific investigation along this direction was performed. The principle of the uniformity measurement is explained in more details in Section II.2.2.4.

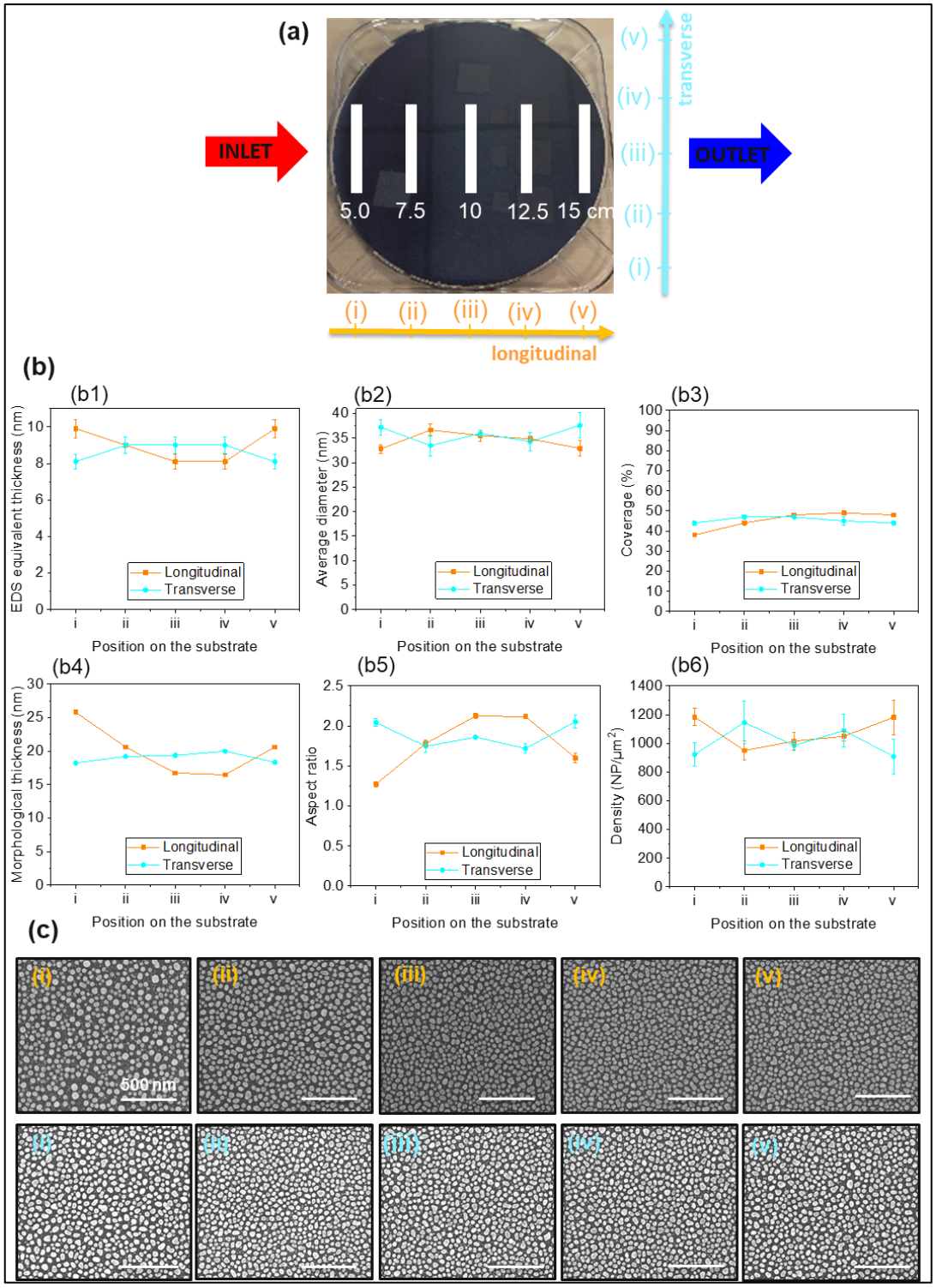


Figure 27: (a) Picture of a 200 mm substrate showing the labelling used for marking the position of the substrate (grey squares are due to presence of small samples during deposition) and the labelling used for the comparison between transverse and longitudinal direction variation. (b) Quantitative analyses performed for the comparison between longitudinal (in orange) and transverse (in blue) direction variation for (b1) the EDS equivalent thickness, (b2) average diameter of Ag NPs, (b3) coverage, (b4) morphological thickness, (b5) aspect ratio and (b6) density of NPs. (c) Scanning Electron Micrographs of Ag thin films deposited on silicon at different positions on the substrate regarding the longitudinal direction (in orange) and the transverse direction (in blue). The scale bars represent 500 nm.

The substrates listed in the next sub-sections have been placed on top of the silicon wafer, hence the presence of grey squares in Figure 27.

### II.1.4.2. Glass

The glass substrates are 2.1 mm thick flat glass pieces from Guardian (clear glass). Bottom side (tin side) was selected for the Ag deposition. The glass has been previously washed with brushes and DI water. The pieces are further cleaned using the following protocol:

1) 5 min. in acetone with ultrasounds;
2) 5 min. in isopropanol with ultrasounds;
3) 5 min. in DI water with ultrasounds;
4) Drying under $N_2$ flow.

Two other different cleaning procedures have also been investigated using different solvents: acetone/ethanol without ultrasounds and only water with ultrasounds. Figure 28 shows the influence of the cleaning protocols on the surface wettability by means of water contact angle (WCA) analysis measured within the first five minutes avec the cleaning. A high WCA of 35 ± 3° was found for cleaning with only acetone/ethanol procedure versus 7 ± 1° for washing with only water and ultrasounds protocol and lower than 5° for the acetone/isopropanol/water with ultrasounds cleaning procedure. This proves that, after the two last approaches, the glass substrate is highly hydrophilic, and the advantage of the last procedure was the removal of the residual organic compounds and forms sufficient hydroxyl –OH groups on the surface to react with the precursors in the reactions caused by the ALD method. That is the reason why the Acetone/Isopropanol/water protocol has been chosen.

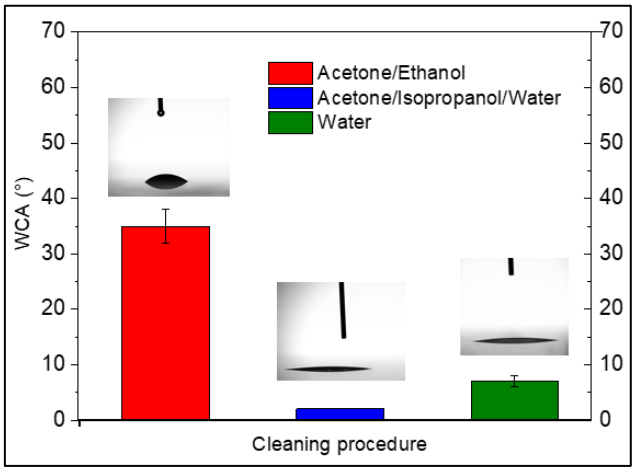


Figure 28: Water contact angle on glass surface cleaned by three protocols: acetone/ethanol without ultrasounds (in red), acetone/isopropanol/water with ultrasounds (in blue) and water only with ultrasounds (in green). From [200].

For the deposition on glass substrates, square pieces of glass with lateral dimension from 2.5 to 10 cm are placed on the Si substrate at various positions, labelled with the same convention as in Figure 27. As glass is an insulating substrate, it was used for measuring the resistivity of the Ag films deposited on top of it, in order to get rid of the leakage current influence in the case where conducting substrate is used.

### II.1.4.3. Oxides

All the oxides layers have been deposited via ALD process on silicon and/or glass substrate presented in previous subsection. Table 10 describes the precursor used for the deposition of ZnO, Al-doped ZnO (AZO), $Al_2O_3$, $TiO_2$, $SnO_2$, $HfO_2$ materials as well as the ALD sequences. All oxide depositions use basic sequences alternating two precursors, the metal precursor and $H_2O$ as the oxidant. For Al-doped ZnO, the goal was to introduce a small amount of Al in the ZnO matrix. For this purpose, the sequence uses a super cycle, with a certain number of ZnO cycles using DEZ and $H_2O$, separated by a single $Al_2O_3$ cycles, using TMA and $H_2O$. The consequence of this process is the deposition of Al-doped ZnO with a given percentage of Al doping of 3 % (30 cycles of ZnO, 1 cycle of $Al_2O_3$). This supercycle is then repeated in order to increase the deposited thickness.

| Material | Precursors | Cycle description |
|---|---|---|
| ZnO | Diethylzinc (DEZ)<br>Water ($H_2O$) | 1. **DEZ** pulse **150 ms**<br>2. Purge 10 s<br>3. **$H_2O$** pulse **200 ms**<br>4. Purge 10 s |
| $Al_2O_3$ | Trimethylaluminum (TMA)<br>Water ($H_2O$) | 1. **TMA** pulse **100 ms**<br>2. Purge 10 s<br>3. **$H_2O$** pulse **100 ms**<br>4. Purge 10 s |
| Al-doped ZnO (AZO) | Diethylzinc (DEZ)<br>Trimethylaluminum (TMA)<br>Water ($H_2O$) | 30:1<br>ZnO:$Al_2O_3$ |

Table 10: Description of the precursors and ALD cycle sequences used for each deposited material. Each cycle is repeated a given number of times in order to obtain the appropriate thickness. For AZO, the sequence is composed of a supercycle alternating a given number of ZnO cycles and one $Al_2O_3$ cycle.

### II.1.4.4. High aspect ratio substrates

High aspect ratio substrates have been used to study the conformality of Ag deposition and the influence of high rms roughness sublayers on the morphology of Ag films.

### Zinc oxide nanorods

The synthesis of zinc oxide nanorods (ZnO NRs) has been performed via hydrothermal growth method since the solution phase synthesis of NRs was carried out in aqueous solution (water). The procedure follows the one performed in the work of Caicedo *et al.*, except that we did not use polyethylene glycol was not used. [201] Briefly, the substrates were ZnO thick film (around 110 nm) deposited on $Si/SiO_2$ wafers using ALD, as presented in the previous section. Substrates were placed face down in a flask containing 100 mL de-ionised (DI) water (the face where film is grown is touching the water). The water was heated to 70°C. 1 mL of 1M zinc chloride ($ZnCl_2$) and 1mL 1M of Hexamethyl-tetramine (HMTA) was added and the temperature of the solution was increased to 85°C. It is to be noted that the solution was not stirred at any point during the growth. After 30 min, heating was turned off and the substrates were removed from the flask. They were washed with DI water and let dry naturally in air.

**Lateral and vertical high aspect ratio structures**

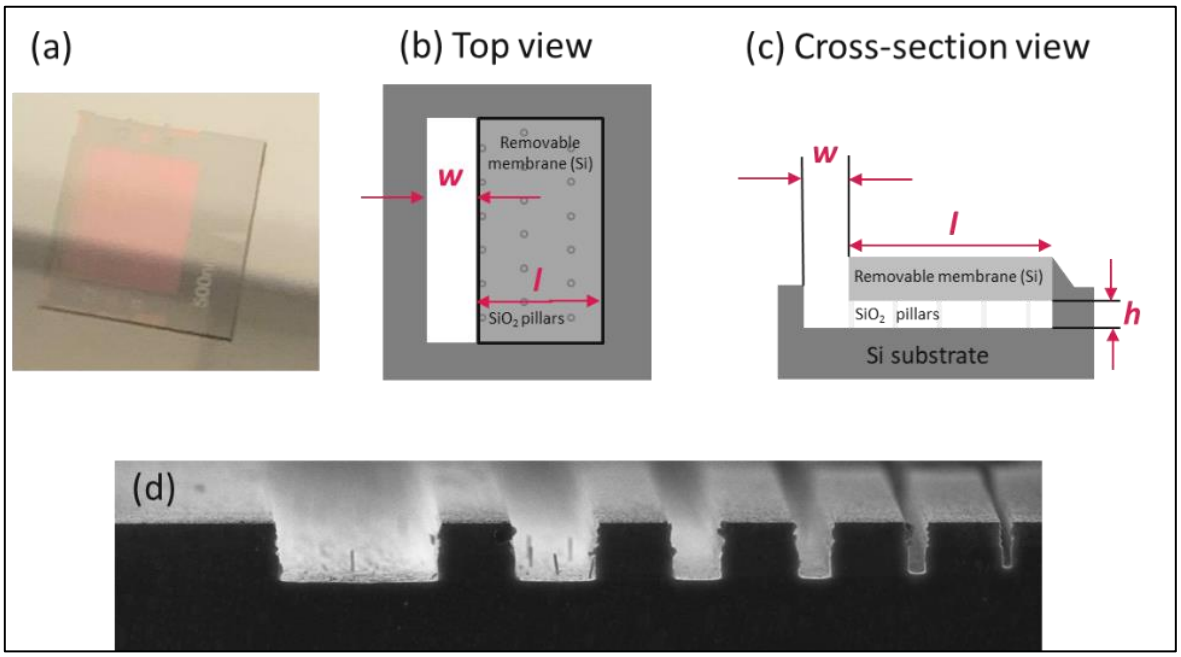


Figure 29: (a) Photography of the PillarHall® Test Chips. (b) and (c) Schematic illustration of the opening width (w), lateral gap width (l) and gap height (h) used to specify different lateral high-aspect ratio test structures in the PillarHall® Test Chips in (b) top view and (c) cross-section view. (d) SEM cross-section image of the vertical high-aspect ratio (VHAR) array test structures (with $Al_2O_3$ deposition on top).

Lateral- and vertical-high-aspect-ratio (LHAR, VHAR) trenches are PillarHall® Test Chips ($4^{th}$ generation advanced LHAR4-series test chips) fabricated in VTT Technical Research Centre of Finland (Figure 29). The main test structure area consists of 10 LHAR test structures. Each LHAR chip consists of several lateral structures, where the roof is formed by an easily removable, pillar-supported silicon membrane and each individual LHAR test structure has a different "opening width (*w*)" and a gap lateral width (*l*), as shown in Figure 29. The aspect ratio, which is the depth to width ratio, has been determined for the structure as the ratio of lateral gap width (*l*) over the gap height *h* (*h* of a constant value of 500 nm). The combination of *h* with *l* gives aspect ratios in the range 2:1 to 10045:1. The principle of the conformality measurements using these structures is described in the next section. The main test structure area contains also vertical high-aspect-ratio (VHAR) test structure array as shown in Figure 29 (c).

## II.2. Techniques for film characterization

The aim of this part is not to explain in detail the principles inherent to each technique, but to reference the tools used for the characterization of our films, describing briefly the principle and the main characteristics of each, as well as the parameters used. Table 11 provides an overview of the characterization techniques used along this thesis work and which are explained more deeply in the following sub-sections. We distinguish structural and morphological characterization from elemental/chemical composition characterization and functionalization characterization. A particular attention is paid to the measurement of the thickness, more particularly by energy dispersive spectroscopy (EDS).

| Characterization type | Characterization technique | Information |
|---|---|---|
| Structural and morphological | *Grazing incidence X-ray diffraction* (GIXRD) | - Crystallinity information<br>- Crystallite size determination |
| | *X-ray Reflectivity* (XRR) | - Thickness determination<br>- Interface and surface roughness<br>- Layer density |
| | *Scanning Electron Microscopy* (SEM) | - Topographical and morphological determination (sampled depth 1-2 nm)<br>- Thickness determination using cross section |
| | *Atomic Force Microscopy* (AFM) | - Topographical determination<br>- Root-mean-square roughness determination |
| | *Energy dispersive X-ray* Spectroscopy (EDS) | - Thickness determination |
| | *Profilometry* | - Thickness determination |
| | *Ellipsometry* | - Thickness determination<br>- Optical constants (refractive index *n*, extinction coefficient *k*) determination |
| | *Water contact angle* (WCA) | - Contact angle determination<br>- Wettability evaluation |
| Elemental and chemical composition | *X-ray Photoelectron Spectroscopy* (XPS) | - Analysis of the surface chemical composition (sampled depth 10-12 nm)<br>- Ion beam etching for depth analysis |
| | *Time-of-Flight Secondary Ion Mass Spectrometry* (ToF-SIMS) | - Surface elemental and molecular analysis (sampled depth 1-2 nm)<br>- Determination of the molecular structure<br>- Ion beam etching for depth analysis |
| Functional characterization | Four-point probe | - Electrical properties (electrical conductivity, mean free path) determination |
| | UV-Visible-NIR spectroscopy | - Optical properties (transmittance, reflectance, absorbance) determination<br>- Photocatalytic properties |
| | PillarHall© structures | - Conformality determination |
| | Antibacterial properties | - Antibacterial activity |

Table 11: Summary of the techniques used for film characterization and the information extracted from each technique used in the thesis work.

## II.2.1. Elemental & chemical composition characterization

### II.2.1.1. X-ray Photoelectron Spectroscopy (XPS)

The elemental and chemical composition of the samples has been investigated by X-ray photoelectron spectroscopy (XPS), on a Kratos Axis Ultra DLD system. The depth of analysis is much smaller than in the case of EDX analysis, around a few nanometers, which makes it possible to be extremely sensitive to the surface state of the sample studied. The sensitivity of the technique is of the order of the atomic percentage.

Basically, the surface sample is irradiated with a monochromatic Al $K_\alpha$ X-ray source (hν = 1486.7 eV) operating at 150W. If the X-ray photon has sufficient energy, it is absorbed by an atom on the surface and the electron, whose binding energy is less than the incident X-ray energy $h\upsilon$, is ejected as a photoelectron with a kinetic energy $E_{kin}$. The detection is done by quantifying this kinetic energy and the number of electrons re-emitted from the analysis surface. Since the energy of a photon at a particular wavelength is known, the ejected photoelectron will have a binding energy $E_B$ that can be calculated according to the relation $E_B = h\upsilon - E_{kin} - W$ where $E_{kin}$ is the measured kinetic energy, h$\upsilon$ the incident X-ray energy, $E_B$ the electron binding energy and $W$ the working function of the element. Therefore, by detecting and measuring the energy of this electron, which is unique for each chemical element, the composition of the sample can be determined according to the spectrum of electron intensity as a function of the measured energy.

An etching of the surface has been carried out with an $Ar^+$ ion beam operating at 2 kV to remove surface contamination. High-resolution (HR) Ag photoelectron (Ag 3d) and Auger (Ag MNN) spectra were acquired on a surface analysis of 300 × 700 $\mu m^2$ with a pass energy of 20 eV and a 0.05 eV step size. The quantification of the elemental composition of the samples is based on the survey spectra and acquired with a pass energy of 160 eV and a 1 eV step size. As there is almost no difference in the Ag 3d peak shape and position for silver in metallic Ag(0) and oxidized Ag(I) and Ag(II) forms, the Ag $M_4N_{4,5}N_{4,5}$ Auger line (calibrated at 357.6 eV) and Ag $3d_{5/2}$ photoelectron line were used to determine the silver chemical state from the modified Auger parameter (α'). Casa XPS software (2.3.15) was used for quantifications and peak analysis.

### II.2.1.2. Time-of-Flight Secondary Ion Mass Spectrometry (ToF-SIMS)

The elemental and chemical composition of the samples has been investigated by time-of-flight secondary ion mass spectroscopy (TOF-SIMS) in positive and negative mode of ions, on a system from ION-TOF GmbH fitted with a bismuth liquid metal ion gun delivering $Bi_n^{q+}$ bismuth cluster ions.

The principle of secondary ion mass spectrometry (SIMS) consists in a bombardment by a focused beam of primary ion (bismuth cluster ions, $Bi_3^+$), which irradiates the surface of the sample inducing the desorption/ionization of secondary ions. The latter is then separated according to the mass-to-charge ratio (m/z) in the time-of-flight (ToF) analyzer. The mass spectra obtained represent the intensity (number of secondary ions detected) as a function of the mass-to-charge ratio (m/z).

## II.2.2. Structural & morphological characterization

### II.2.2.1. X-ray diffraction (XRD)

The X-ray diffraction (XRD) consists in diffracting the monochromatic incident beam incident from the tube onto the different crystal planes of the grains that make up the material. The X-ray beams produced by the tube are sent to the sample in which they are deflected by the atoms. These diffracted beams interfere with each other, leading to the production of an intense signal in specific areas of space. This signal is collected by the detector and plotted as a curve (diffractogram) that has peaks at specific angles of diffraction. The position of these peaks represents the signature of the arrangement of the atoms inside a crystal (distance between intracrystalline planes). The Bragg's law, defined as ($2d_{hkl}sin\theta = n\lambda$) (where $d_{hkl}$ is the distance lattice plane (hkl), $\theta$ is the Bragg diffraction angle (°) and $\lambda$ is the source wavelength, relates the angles at which peaks are observed and the distances between atomic planes. In the $\theta - 2\theta$ geometry, only lattice planes (hkl) that are oriented parallel to the surface plane can contribute to Bragg diffraction. However, for thin films, a large fraction of the diffractogram in $\theta - 2\theta$ geometry comes from the substrate due to the X-ray penetration depth.

During the thesis work, as we study thin films deposition, we have performed grazing incidence XRD (GIXRD) at an angle of 0.5°, which is preferred to increase the thin-films diffraction and probe almost all diffractions planes of the polycrystalline thin films. We have used a Bruker D8 Discover diffractometer with a monochromatic Cu Kα radiation of 0.1542 nm operating at 40 kV and 40 mA in parallel beam configuration. The angle scanning has been typically performed between 20-80° and we have used a scanning step of 0.02°. The software DIFFRAC.EVA has been used for data treatment.

The crystallite sizes have been determined by the analysis of the peak width using first a pseudo-Voigt (PV) fitting function of the XRD diffractogram. [202, 203] This function is a linear combination of lorentzian (L) and gaussian (G) functions with a coefficient η:

$$\boldsymbol{PV = \eta L + (1 - \eta) G}$$

In the literature, it has been experimentally verified that a lorentzian function describes approximately the crystallite-size broadening while a gaussian function describes better the microstrain broadening. [202, 204] The integral breadth contribution of lorentzian ($\boldsymbol{\beta_L}$) to the integral breadth of the peak ($\boldsymbol{\beta}$, which is the ratio of the peak area over the peak maximum intensity) have been calculated by the empirical formula [203]:

$$\boldsymbol{\beta_L = (0.017475 + 1.500484\eta - 0.534156\eta^2)\,\beta}$$

The pseudo-Voigt fitting of our diffractogram is very closed to the lorentzian fitting (see Figure 30), then the major contribution of the XRD peaks comes from the crystallite size and the microstrain contribution can be neglected.

Since the function is assumed to be a pure Lorentzian, η=1, therefore:

$$\boldsymbol{\beta_L = (0.017475 + 1.500484 - 0.534156)\,\beta}$$

The crystallite size L have then been extracted (by taking into account the contribution of the instrumental error) [203]:

$$\langle L\rangle_V = K\lambda/(\beta_L \cos\theta)$$

Where $\langle L\rangle_V$ is the volume-weighted average crystallite size, $K$ is a constant ≈ 0.9, $\lambda$ is the X-ray source wavelength and $\theta$ the Bragg angle diffraction peak.

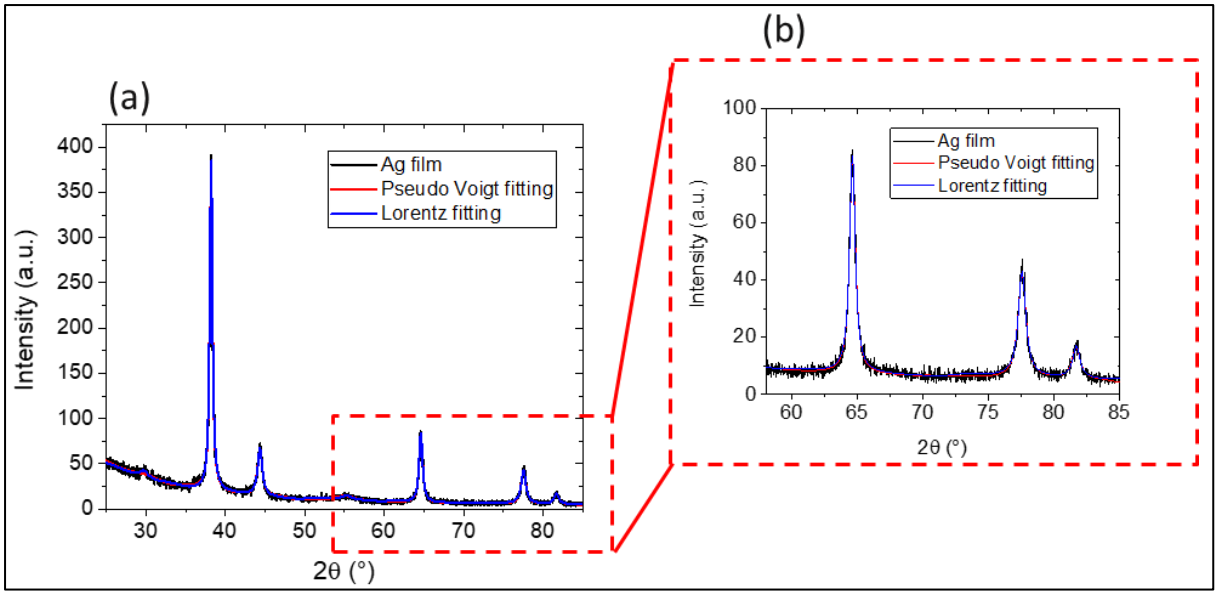


Figure 30: (a) Diffractogram of Ag thin films fitted with pseudo Voigt (in red) or Lorentz (in blue) function and zoom in in (b).

### II.2.2.2. Specular X-ray Reflectivity (XRR)

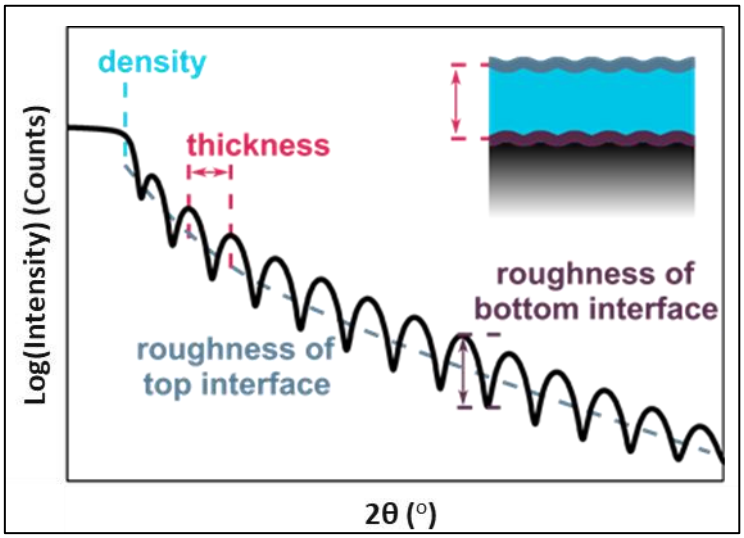


Figure 31: Schematic representation of an XRR spectra and information which can be extracted from it.

X-ray Reflectivity (XRR) can be used to measure the thicknesses of a film, but also gives access to the density and roughness (interface and surface) of layers or multilayers with high precision, regardless of the crystallinity of each layer (single crystal, polycrystalline or amorphous). This technique is based on the reflection of a monochromatic X-ray beam, sent to the surface of the sample

with a grazing angle θ. In reflectivity experiments, the X-ray reflection of a sample is measured around the critical angle. This occurs around grazing incidence angles. The electromagnetic X-ray, when it changes of medium, undergoes, like any electromagnetic wave, reflection and refraction phenomena, due to differences in optical index between the different media, which can be analyzed from the classical theory.

For incident angles lower than the critical angle, the beam is totally reflected on the material: it is from this that the density of the material is determined. This corresponds to the edge in Figure 31, which also gives information about the porosity of the material. For incident angles above the critical angle, at every interface where the electron density changes, and thus the refractive index of the material changes, a part of the X-ray beam is reflected. The interference of theses partially reflected X-ray beams, coming from the film surface and film-substrate interface, creates the oscillation pattern observed in the reflectivity curves (Figure 31). This pattern is composed of fringes, for which the period depends on the difference in optical path between two waves and thus on the optical thickness of the thin layer and its index: the lower the film thickness, the larger the period. When the surface roughness of the film is increasing, it leads to a decrease of the intensity of the reflected beam. Thus, the decay gives an information on the roughness of the top interface of the sample (Figure 31). However, for very rough surface, the thickness determination becomes impossible since the decrease of the intensity masks the oscillation pattern. The advantage of XRR in the film thickness determination is that it is an absolute measurement which directly gives the thickness of the layer. No prior knowledge or assumptions about the optical properties of the films are required, unlike optical ellipsometry. In addition, no reference samples or standards are needed, either.

We have used the PANalytical X'Pert ProMPD equipment and the knife edge collimator tool, which reduced the footprint of the beam, has been used to avoid inhomogeneity problem of the film. The angle scanning has been typically performed between 0.2 and 8° and we have used a scanning step of 0.01°. GenX 2.4.9 software has been used for fitting of the data.

#### II.2.2.3. Atomic Force Microscopy (AFM)

Atomic Force Microscopy (AFM) measurements have been performed on a commercial AFM Innova from Bruker in tapping mode. Topography was acquired by keeping the amplitude of the first resonant mode of the cantilever constant and recording the Z-piezo displacement. The AFM tip used was an OPUS 160AC-NA (Mikromasch, Bulgaria) with a typical first resonance frequency of 300 kHz, a cantilever stiffness of 26 N/m and a radius of curvature of 7nm. The surface topography of the sample is determined with a very high resolution less than 1 nm in depth. The tip radius (few nanometers) and the scan method set the lateral resolution. When the tapping mode is used, the surface is probed with a sharp tip attached to a cantilever. The system oscillates the cantilever at a frequency close to its resonance. The feedback loops is controlled by the reflection of a laser on the cantilever into a photodetector. When the surface of the sample is scanned by the tip, the topography of the samples is determined by the amplitude variation of the laser reflection. A scanner 512 × 512 pixel resolution, and a 0.25 Hz scan rate was used to measure the surface roughness average Sq. The AFM scans have been performed over 1 × 1 $\mu m^2$ areas. Data treatment has been analyzed with Gwyddion software.

### II.2.2.4. Scanning Electron Microscopy (SEM) and image treatment

The films have been imaged using a Scanning Electron Microscopy (SEM) on a FEI Helios NanoLab 650. It is a high-resolution imaging technique based on the electron-matter interaction. It enables the imaging of structures of nanometric size down to 10 nm. Basically, an electron beam produced by a cathode (electron probe) is projected onto the sample to be analyzed. The interaction between this electron beam and the sample generates low-energy secondary electrons (most common SEM mode used), which are accelerated towards a secondary electron detector that amplifies the signal. It is thus possible, by scanning the beam over the sample, to obtain a map of the scanned area. This phenomenon takes place in a vacuum in order to avoid both the oxidation of the source and the deceleration and deviation of the electrons by collision with molecules in air. Electromagnetic lenses focus the electron beam, which enables a high resolution to be obtained. The images obtained give access to topography and morphology information. Most imaging of deposition performed on silicon substrate have been performed with a voltage of 10 kV and a current 100 pA while 2kV and 25pA parameters have been mainly used for non-conductive depositions and the ones deposited on glass substrates. In order to avoid charging effect, carbon tape was sometimes used for highly resistive samples.

Based on the images recorded, different morphological parameters have been measured by means of Image J software.

- The **Ag NP size** corresponds to the equivalent diameter of the Ag NPs;
- The **coverage percentage** is the areas occupied by the Ag nanoparticles, calculated by the difference between the total sampled area and the void area;
- The **density** corresponds to the number of nanoparticles by unit of surface, here per $\mu m^2$.

The very small or not easy to distinguish Ag islands have been analyzed by measuring manually the different parameters over 100 nanoparticles. The related average and standard deviation values could have been then extracted and used as error bars in the following plots.

The well-separated Ag islands have been analyzed automatically using the ImageJ software. First, the scale of the image is fixed in order to establish the relation between the distance in pixels and the unit of length (typically we obtained a scale in pixels/nm). We applied the Gaussian blur function which is a plug-in filter using convolution with a Gaussian function for smoothing. At this stage, it is necessary to find a compromise between removing the background noise and keeping the sharpness of the image, this by playing on the sigma (radius in scaled units), i.e. the standard deviation sigma of the Gaussian. Typically, the radius was fixed to 2 nm. Figure 32 exposes SEM micrograph of Ag depositions and image treatment using or not this filter. A smoothing of the image with well-defined particles is obtained with the Gaussian blur function (Figure 32 (c)) as compared to blurred ones without (Figure 32 (b)).

Then, we have had to convert the image in 8-bit (256 shades of grey) in order to apply a threshold. This latter allows us to separate objects from each other according to their greyscale intensity, or objects with background noise. For that, we used the “Default” automatic threshold technique which has been recognized as the best one after testing several other techniques available in the software. This technique has been justified by comparing the measure of Ag NPs manually and automatically. Finally, after having selected a zone to study (referred as mask), the “analyze particles” function have

been used. This analysis gives automatically: the count of particles in the selected zone, the total area, the average particle size and the percentage area. For the last criteria, we chose to not exclude the particles on edges in order to obtain the real area occupied by Ag islands. The Ag NPs diameter have been extracted by assuming circular nanoparticles ($A = \pi r^2$). Three different zones were systematically measured so that the average value and standard deviation (error bars in the following plots) are used to statistical analysis.

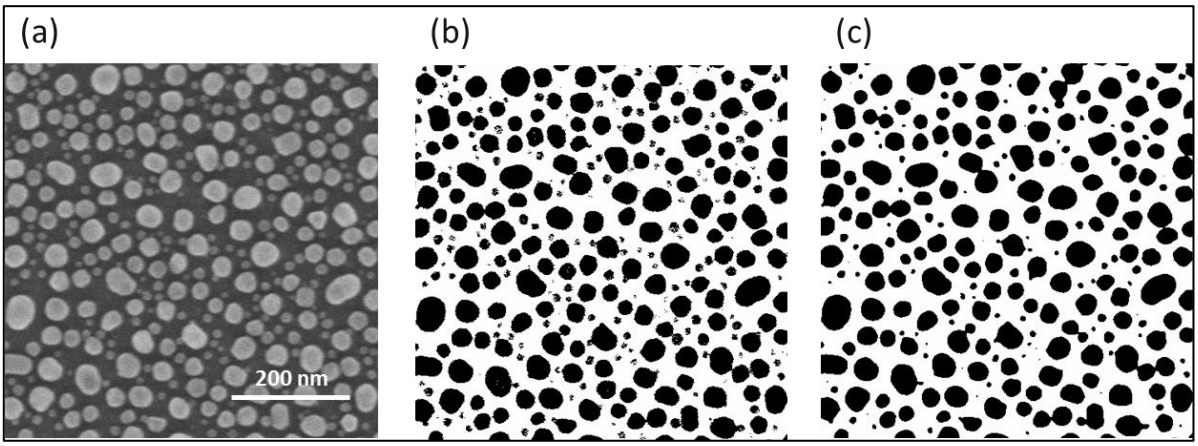


Figure 32: (a) Scanning electron micrograph of Ag nanoparticles deposited on silicon substrate. (b) and (c) Image treatments of the SEM micrograph in (a) without using Gaussian blur in (b) and using Gaussian blur with a radius of 2 nm showing the smoothing of the image in (c).

The effective thickness has been determined by energy dispersive spectroscopy (EDS), and corresponds to the quantity of deposited silver on the surface. The next sub-section II.2.3. is dedicated to the principle of the EDS measurement. Combining results of image treatment and equivalent thickness determination, the following morphological criteria have been determined:

- The **morphological thickness** corresponds to the vertical thickness or height of Ag islands, determined by the ratio of the EDS equivalent thickness over the coverage;
- The **aspect ratio** corresponds to the ratio of the Ag NP size and the morphological thickness or in other words, to the lateral growth over the vertical one.

### II.2.2.5. Principle of the measurement of uniformity of the deposition

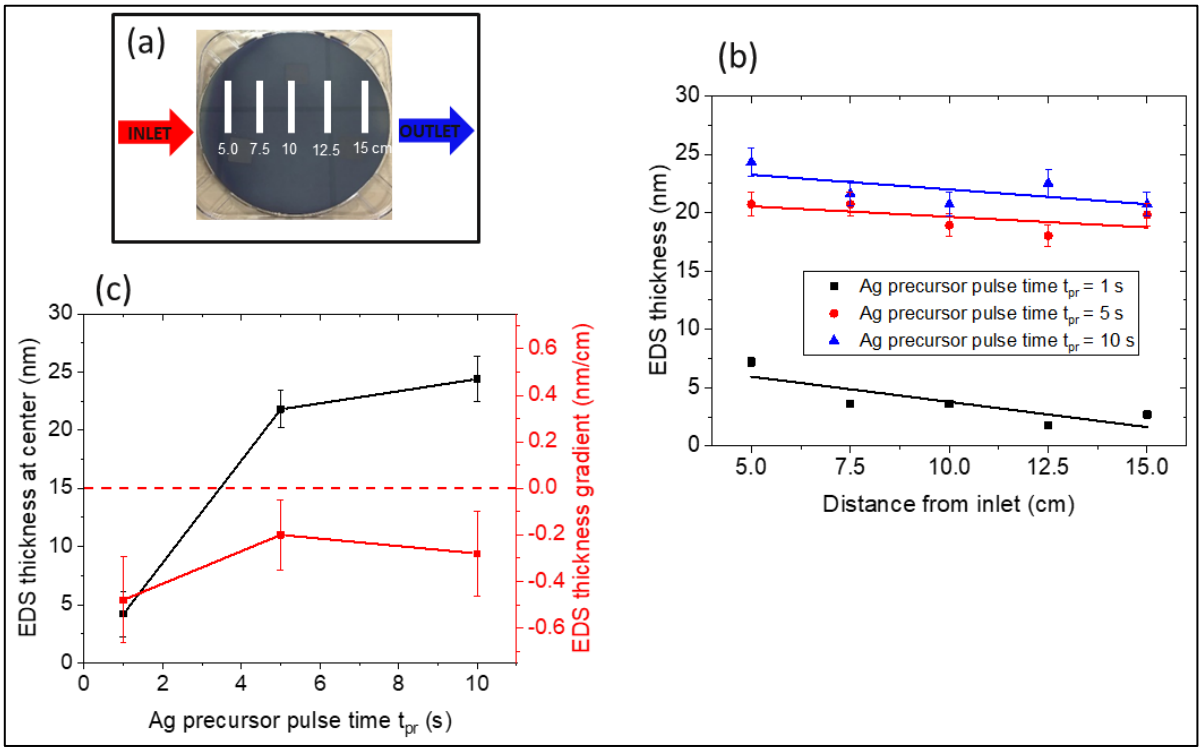


Figure 33: (a) Picture of a 200 mm Si substrate showing the labelling used for marking the position on the substrate. (b) and (c) Principle of the original quantification of the uniformity demonstrated on a specific example: (b) Plot of the EDS equivalent thickness for different Ag precursor pulse times $t_{pr}$ as a function of the distance from the inlet and the linear fit associated. (c) Plot of the EDS thickness at the center (black curves) and the associated gradient (red curves) as a function of the investigated parameter (here, the Ag precursor pulse time).

Most of the published research on ALD Ag films have investigated the influence of the deposition parameters on the film morphology at a given position, but the overall uniformity of the deposition is not often demonstrated quantitatively. [26, 41, 45, 48] During this thesis work, we have used an original methodology of quantifying the uniformity of the deposition regarding different morphological quantities by measuring them at 5 points, equally spaced on a 200 mm (8 inches) wafer along the gas flow in the reactor (Figure 33 (a)). The value at the center and the gradient of the quantities are calculated using a linear fit of each quantity as a function of the distance from the inlet. From the linear fit $y = a + b * x$ (Figure 33 (b)), the slope $b$ corresponds to the gradient of the value, while the value at the center is given by $y = a + b * 10\ cm$. Finally, the gradient $b$ and $y$ values have been plotted as a function of the investigated parameter (Figure 33 (c)). Both the absolute value of the gradient (related to the deposition uniformity) and its sign (important for the growth mechanism analysis) are extracted.

### II.2.2.6. Water contact angle (WCA)

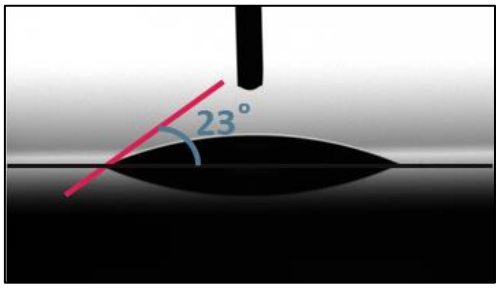


Figure 34: Principle of the water contact angle showing the tangent line (in pink) from the contact point along the liquid-vapor interface in the droplet profile applied my means of a microsyringe. In this case, the surface is hydrophilic.

The wettability of a surface, i.e. the ability of a liquid to maintain contact with a solid surface, is characterized and quantified by the value of the water contact angle $\theta$. When $\theta$ = 0°, the liquid spreads completely on the solid surface in the form of a film, the wetting is total. When $\theta$ = 180°, the wetting is zero. When 0° < $\theta$ < 180°, the wetting is partial and the surface is wetting or hydrophilic for $\theta$ < 90° and non-wetting or hydrophobic for $\theta$ > 90°.

Using a microsyringe, a drop of ultrapure distilled water is applied on the test sample. The contact angle is defined as the angle formed by the intersection of the liquid-solid interface and the liquid-vapor interface. It is geometrically acquired by applying a tangent line from the contact point along the liquid-vapor interface in the droplet profile. This angle is then measured from a photography taken with the camera of the instrument. (Figure 34) The water contact angle measurements have been done with Technex Theta 200 instrument. The experiments were performed with a drop volume of water of 2 µL and an experiment time of 5 s.

### II.2.2.7. Ellipsometer

Variable Angle Spectroscopic Ellipsometry (VASE) is a non-destructive optical measurement technique for measuring properties of thin films. A polarized beam of light is reflected off a sample at a given angle of incidence and the change in polarization state induced by the sample is measured. This measurement is presented in terms of the ellipsometric parameters Δ and Ψ. To extract information such as thicknesses and optical constants (refractive index *n*, extinction coefficient *k*), a model must be built to fit the optical data. The thicknesses of the various metal oxides and metal nitride films (see section II.1.4.) were estimated from a mathematical model of Cauchy type, for flat and homogeneous films deposited on silicon disks. The VASE M2000V J. A. Woollam ellipsometer has been used. Spectra are acquired at 3 different angles of incidence (65°, 70°, 75°), from 370 to 1000 nm (390 wavelengths) with a 1s acquisition time in high accuracy mode. Spectroscopic data have been treated with CompleteEASE software from J. A. Woollam.

### II.2.2.8. Profilometer

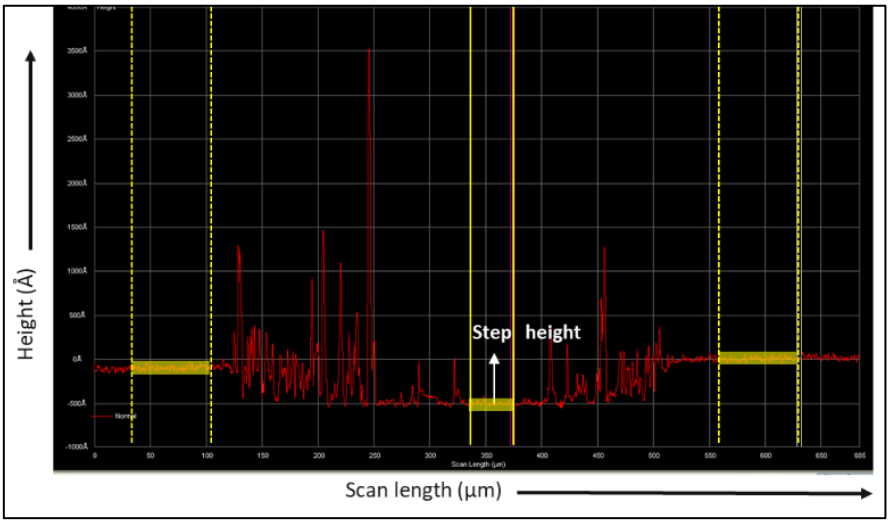


Figure 35: A step height profile over a scratch made by a metal tweezer across the Ag film.

The Ag film thickness has been first measured using P-7 Stylus Profiler instrument. A diamond tip with a scan speed of 50 µm/s, a sampling rate of 200 Hz and an applied force of 2 mg comes into physical contact with the surface to be measured and moves perpendicularly on either side of the step height which has been previously created by performing a scratch on the film using a metal tweezer. The height variation is then recorded with the help of profiler 7.45 software program. It is then possible to measure the difference in height and thus to deduce the thickness of the deposited film. (Figure 35). The thickness has been averaged over five measurements along the scratch and the error bars correspond to the standard deviation. We note that this measurement provides the maximum topographical thickness of the films, not taking into account surface roughness or non-continuity of the film. This method thus always leads to an overestimate of the real average thickness.

This technique differs from techniques relying in the measurement of the deposited mass, divided by the density of the deposited materials, such as the quartz microbalance (QCM) or the electron dispersion X-ray spectroscopy (EDS) techniques. We note that the latter technique requires an assumption on the density of the ideal material. Since the density of real materials is usually lower than the ideal material, these methods always lead to an underestimate of the thickness. EDS thickness determination of Ag films have been studied more deeply and presented in the following sub-section.

## II.2.3. Thickness measurement of silver thin films by electron dispersion X-ray spectroscopy

### II.2.3.1. Principle of the electron dispersion X-ray spectroscopy measurement

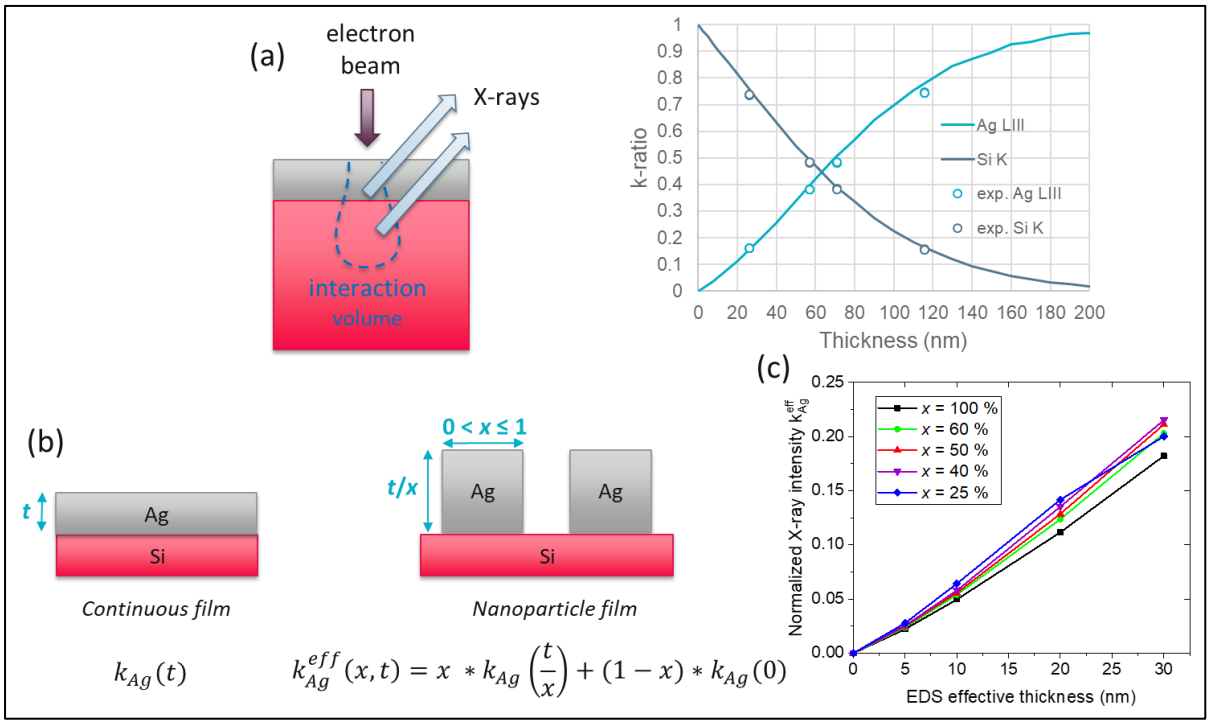


Figure 36: (a) Principle of the effective thickness measurement using energy dispersive X-ray spectroscopy, (b) and (c) Effect of the film coverage on the effective film thickness determination by EDS measurements, where t is the effective film thickness, x the film coverage, t/x the nanoparticle height, and $k_{Ag}$ the ratio of the X-ray intensity of a thin film of silver deposited on a substrate and the X-ray intensity of Ag as a bulk.

The principle of EDS for extracting the thickness is not usual. The electron beam interacts with the material up to a given depth. When electrons interact with the atoms in the material, they emit X-rays at a well-defined energy corresponding to the electronic transitions of the material. For a thin film deposited on a substrate, the interaction volume covers both the film and part of the substrate (Figure 36 (a)). The relative intensity of the signal coming from the film material vs. the substrate material can be related to the thickness of the film. However, an accurate determination requires a simulation. By comparing the intensity of the experimental signals coming from Ag (the film) and from Si (the substrate) to the one given vs. the thickness in the simulation, we extract the thickness of the film.

For Ag films deposited on silicon substrate, Xmax 50 $mm^2$ equipment from Oxford Instrument and connected to the above cited SEM has been used and the data have been analyzed by means of INCA software. For Ag films deposited on other substrates (glass, oxides), Quanta 200 10 $mm^2$ equipment from EDAX Inc. connected to FEI Quanta FEG 200 SEM have been used and the data have been analyzed via GENESIS software. The X-ray signal is measured with the sample perpendicular to the electron beam (tilt of 0°), with the X-ray detector at a take-off angle of 35° and with an electron energy of 10 keV. Indeed, at energy higher than 10 keV, the measurement is less sensitive to the low thickness of the film since thin film stops only weakly the electron. In the inverse, at lower energy than 10 keV, the measurement is less sensitive to high thickness. Moreover, it is needed to use an electron energy higher than the energy of characteristic X-ray of Ag $L_\alpha$ (2.894 keV) in order to detect Ag. Since we have studied Ag film of thickness ranging from 5 to 100 nm, for EDS measurements, we choose an intermediate value of the electron energy of 10 keV.

### II.2.3.2. Simulation

#### Method

The thickness determination follows the electron probe microanalysis (EPMA) method, [205] as already demonstrated for Ag thin films deposited by ALD. [41] We have performed the extraction by comparing the values of the experimental k-ratio of Ag $L_{III}$ lines, i.e. the ratio between the X-ray intensity measured on the sample and the X-ray intensity of a reference bulk material of the same element, with the one obtained by Monte-Carlo simulations, following the method described in [206, 207]. This method has demonstrated reliable thickness values as compared to Rutherford backscattering spectroscopy and quartz crystal microbalance within 5 %, even for film thickness below 10 nm. [208, 209] The Monte-Carlo simulations have been performed with the CASINO software (version 2.5.1), [210] using the Mott cross section obtained by interpolation, which has shown to be most accurate for metal thin films, [208, 210] the Casnati effective section ionization and the Joy and Luo ionization potential (see [211]).

We have assumed a uniform Ag film with the same density as the bulk, i.e. 10.5 g/cm$^3$. The resulting value of the thickness, called EDS equivalent thickness, corresponds thus to the amount of material deposited on the surface, rather than the height of the nanoparticles. [205, 212] For nanoparticle film, this effective thickness depends on the size and shape of the nanoparticles formed and in particular the film coverage. In the event of a continuous film (coverage $x = 1$), it is directly the thickness of the film. In the case of a nanoparticle film (coverage $x < 1$), we measure an effective thickness corresponding to the same amount of material distributed as a continuous film on the substrate.

#### Error bars related to the film thickness determination

For continuous film, the error bars are linked to the non-uniformity of the deposition and determined by the variation of EDS thickness of close points at the same position, typically 1 nm, and by a systematic error of the method evaluated to be of maximum 5%. [209] For nanoparticle films, it is also needed to add the film coverage uncertainty (up to 7%) due to the nanoparticle morphology with a coverage less than 100%, depending on the coverage value. The main error for nanoparticles comes from the fact that, when the electron beam interacts with the surface, it directly hits Ag nanoparticles and Si substrate, whereas in the case of continuous film, it directly hits Ag exclusively and then the Si substrate through the Ag material. For this reason, the intensity of the X-ray is different, and the quantification biased. We have studied this phenomenon using simulations (Figure 36 (b) and (c)). We assume that the normalized X-ray intensity (the k-ratio) of a nanoparticle film, $k_{Ag}^{eff}(x,t)$, is simply the weighted average between the k-ratio of an Ag film with thickness $t/x$, and the k-ratio of Si (see Equation in Figure 36 (b)). The results obtained as a function of effective film thickness are shown in Figure 36 (c). This figure shows that, by assuming that coverage $x = 1$, i.e. assuming $k_{Ag}^{eff}(x,t) = k_{Ag}(t)$, we overestimate the thickness of the film, something that has generally been done in previous works based on film thickness determination by EDS. [41] For example, if we assume a total coverage of the film ($x = 1$), and the real coverage is $x = 0.5$, we overestimate the thickness by 10% (for film thinner than 30 nm). To reduce this overestimation, it is necessary to directly correlate the coverage of the film and a calibration deduced by simulation. Therefore, a correction factor of 0.9 must be applied for a coverage of 50%, which is the average

coverage value obtained in our investigation. Typically, if we work with nanoparticle film with a coverage $0.4 < x < 0.6$. We have performed calibration by simulation for different coverage ($x$ = 0.4, 0.5, 0.6, 1) with the film thickness $0 < t \leq 30$. We have based our thickness determination on the calibration $x$ = 0.5 and have used the calibration $x$ = 0.4 and $x$ = 0.6 to assess the thickness error, which is estimated to be less than 3% for film thinner than 30 nm.

**Influence of the sublayer in the simulation**

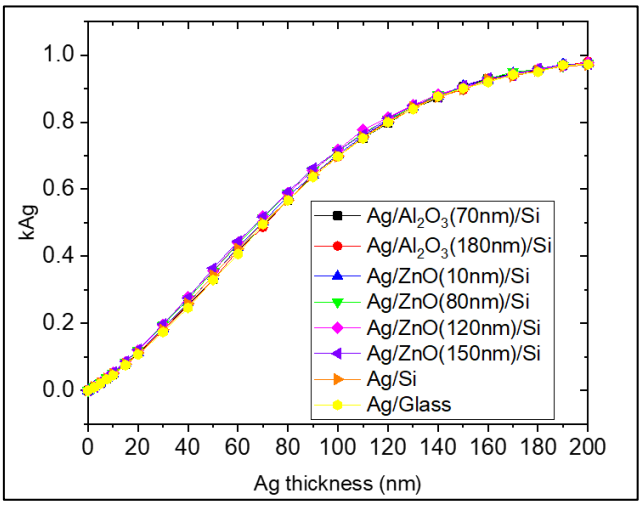


Figure 37: k-ratio of Ag extracted from simulation performed on different sublayers ($Al_2O_3$, ZnO, Si and glass) as a function of the Ag film thickness.

In order to study the influence of the sublayers on the k-ratio of Ag, we have simulated Ag films deposited on different kind of sublayers, i.e. $Al_2O_3$-coated Si, ZnO-coated Si, Si and glass. The composition of glass substrate used on the simulations is based on experimental EDX measurements by taking an average of the atomic percentage (%at.) of three measurements for each element: 27.27%at Si; 56.35 %.at O; 10.06%at. Na; 1.95%at. Mg; 3.18%at. Ca; 0.35%at. Al; 0.83%at. C. As seen in Figure 37, kAg is independent on the sublayers. Therefore, we need to base the Ag thickness determination on the k-ratio of this element only, without taking into account the k-ratios of the elements of the sublayers. For sake of simplicity, Ag on Si simulation is used as a model for thickness determination. We note that, during experimental measurements, we need to integrate all element present both in the film and the substrate, otherwise we under/overestimate one element compared to another.

### II.2.3.3. Comparison with other thickness measurement methods

Two different techniques, profilometer and EDS, were used to compare the data of films deposited as a function of the number of cycles, as shown in Figure 38(a,b). The thickness dependence on the number of cycles was linearly fitted; the slope, i.e. the growth per cycle (GPC), and the intercept on the y-axis (thickness offset) were then extracted. The GPC are compared in Figure 38(c). It clearly shows the overestimate of the thickness measurement by the profilometer. Interestingly, the GPC obtained by EDS is similar to the one published in [140], which is obtained by the same method. Therefore, this method is preferably used along the thesis work.

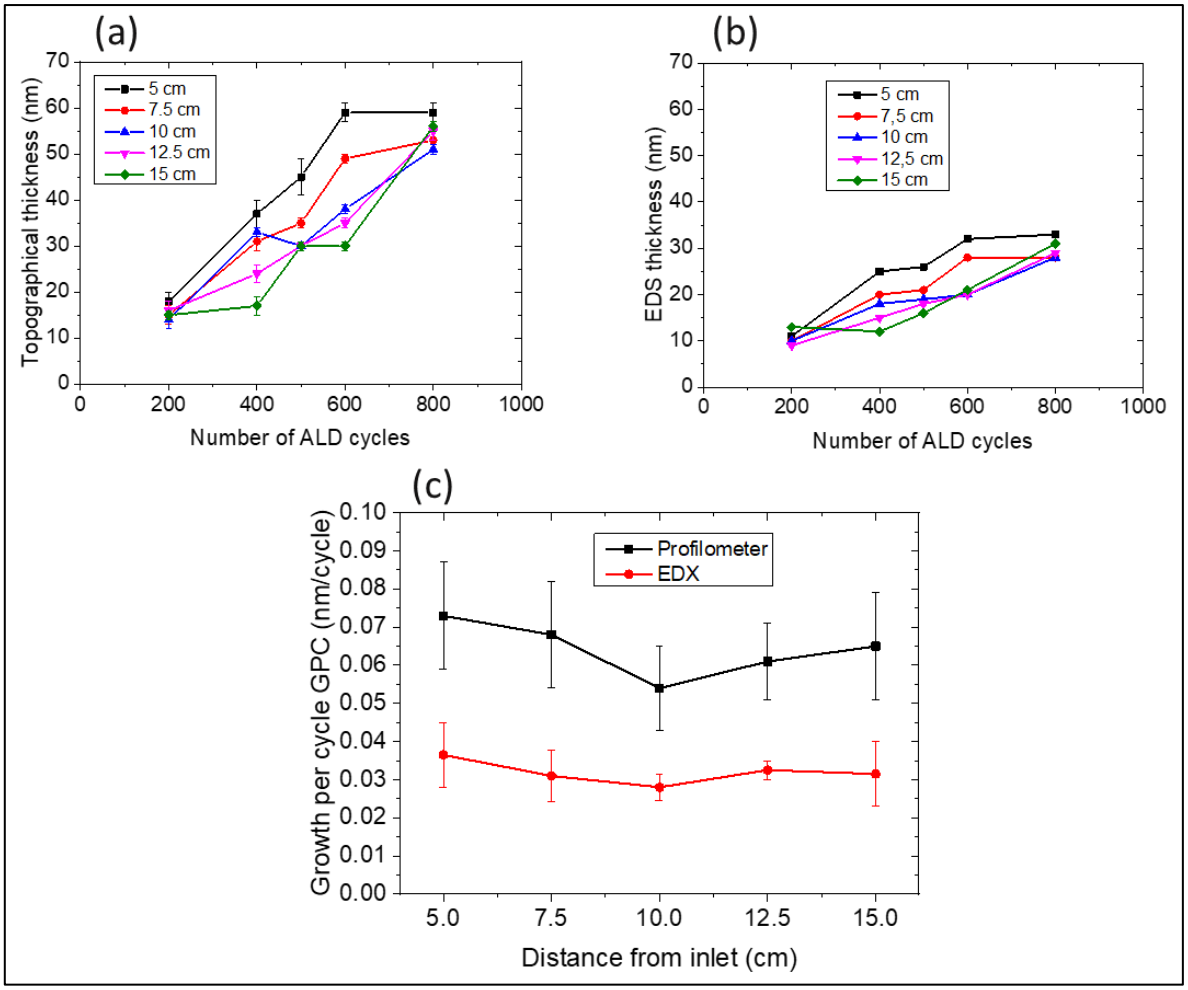


Figure 38: Thickness of Ag films obtained by ALD for different number of cycles and at different positions as compared to the inlet of the reactor, measured (a) using a profilometer and (b) using the EDS technique described here. (c) Comparison of the growth per cycle (GPC), obtained by a linear fit of the curves in panels (a) and (b).

A third thickness measurement method using XRR has also been performed and the preliminary results are shown in Figure 39. A 40-nm-thick silver film made of compact silver nanoparticles (Figure 39 (a)) has been measured and the experimental data were fitted using a model made of a single silver layer. As we can see in Figure 39 (b), this model does not match correctly with the experimental results. Therefore, a more complicated model had to be used. An hypothetical model including a double silver layer of different density has been tested and showed a better fitting with the experimental data (Figure 39 (c)). This model includes a first bottom silver layer made of less dense nanoparticle film and a top layer of more dense and rougher film which could be in agreement with the non-uniform film morphology presented in Figure 39 (a). However, even if this model matches well with the experimental data, it is certainly not the only one and a deeper investigation of a model which matches well with a film made of NPs is needed to draw a solid conclusion. That is the reason why we are not using this method for the rest of the thesis work.

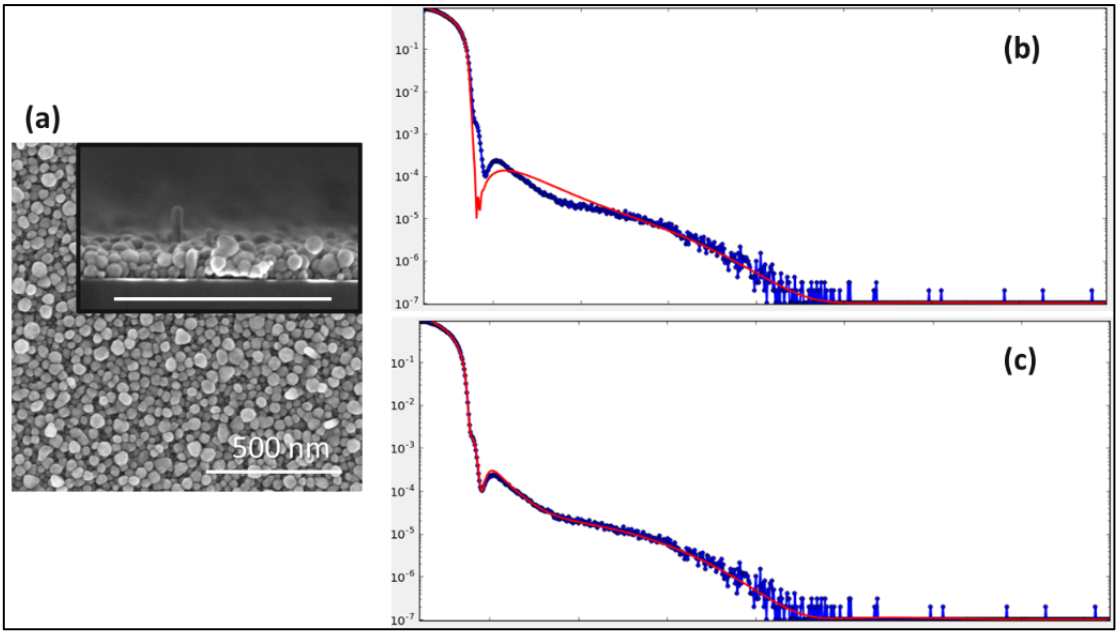

Figure 39: (a) Scanning electron micrographs in top view and cross section (inset) of a 40-nm-thick silver films deposited on Si (with native oxide). The scale bars represent 500 nm. (b-c) XRR spectra (in blue) corresponding to the analysis of the sample in (a) and fitted with a model (in red) (a) of a single silver layer and (c) of a double layer of silver of different density.

## II.2.4. Functional characterization

### II.2.4.1. Four-point probe resistivity measurement and mean free path determination

This method consists in placing four points on the surface of the layer to be characterized by aligning them and taking care to separate them by an equidistant value from each other. The sheet resistance is then measured by using in-line four-point-probe system from Jandel (probe spacing 1 mm, probe diameter 100 µm) by passing a current $I$ sent by a generator through the outside two points of the probe and measuring the voltage across the inside two points.

For a thin film (film thickness much below the probe spacing distance between points), the sheet resistance $Rs$ is then given by the relation:

$$Rs = \frac{\pi}{\ln(2)} * \frac{U}{I} \text{ with } \frac{\pi}{\ln(2)} = 4.53, \text{therefore Rs} = 4.53 * \frac{U}{I}$$

The sheet resistance of the films has been measured on films deposited on glass substrates in order to avoid artifacts that could come from parallel conduction from the substrate. The error bars were determined by the standard deviation of the values of sheet resistance measured at five different positions on the glass samples.

The resistivity $\rho$ is then calculated using the EDS thickness $t$ measured on the same glass substrate:

$$\rho = Rs * t$$

And the conductivity $\sigma$ is given by:

$$\sigma = \frac{1}{\rho}$$

The mean free path (MFP) of free electrons $\lambda$ is given by the relation [17]:

$$\frac{\rho_0}{\rho} = 1 - \frac{3\lambda}{8t}$$

where $\rho_0$ is the bulk resistivity (1.8 µΩ.cm), $\rho$ the film resistivity and $t$ the film thickness.

By plotting $\rho_0/\rho$ as a function of $1/t$, the slope $b$ can be extracted and used to determine the MFP by the relation:

$$\lambda = \frac{8 * b}{-3}$$

### II.2.4.2. UV/Visible spectroscopy

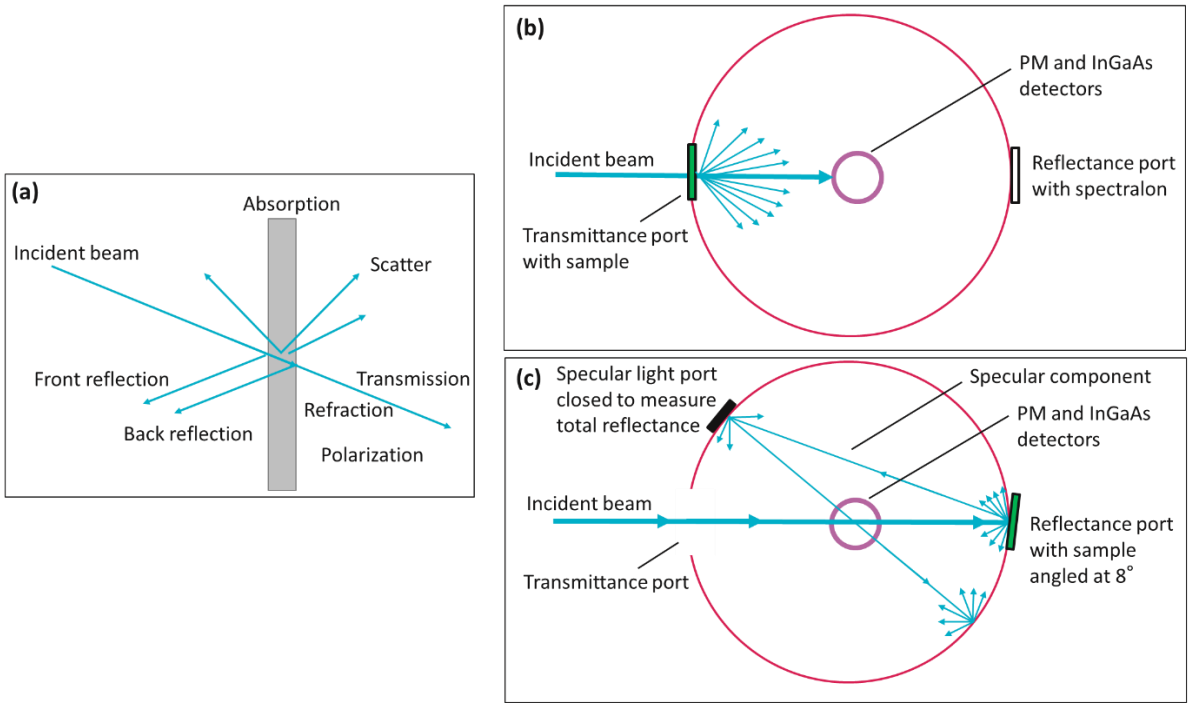


Figure 40: (a) Interaction of light with a solid. (b) and (c) Principle of the measurements with an integration sphere for (b) total transmittance measurement and (c) total reflectance measurement.

Upon interaction of electromagnetic radiation with a sample surface, the beam may undergo reflection, transmission, diffusion (due to scattering), or absorption, as shown in Figure 40 (a). The respective likelihood of these outcomes depends on the incident beam's angle of incidence with the solid. UV/Vis spectroscopy enables to measure the different percentages of light reflected, transmitted or absorbed by the sample. However, using a standard UV/Vis spectrometer with conventional detector arrangement, light is lost before it reaches the detector, resulting in significant photometric errors. The use of an integrating sphere thus permits to collect all the light which has passed through the sample.

For measuring transmittance of a solid sample, total transmittance, i.e. specular and diffuse transmittance must be considered. For that, the sample is placed in front of the sphere at the transmission port and the light passes through into the sphere (Figure 40 (b)). For measuring total reflectance, the sample is placed at the back of the sphere and the light is reflected back off the sample and collected by the sphere (Figure 40 (c)).

Optical transmittance %T and optical reflectance %R of the films used in the thesis work have been deposited on glass substrate and measured on a Perkin Elmer Lambda 1050 spectrophotometer in the wavelength range from 250 to 2500 nm, using a step of 5 nm. The beam is incident on the film side at 0° normal incidence for transmission measurements and 8° for reflection acquisition. The absorbance %*A* of the film has been deduced from %*T* and %*R* using the relation $\%A = 100\% - (\%R + \%T)$.
The spectrophotometer enables two measurements configuration:

1. 150 mm integrating sphere equipped with photomultiplier (UV-VIS) and InGaAs (NIR) detectors
2. Total Absolute Measurement System (TAMS) equipped with 49 mm integrating spheres and Si (UV-VIS) and InGaAs (NIR) detectors.

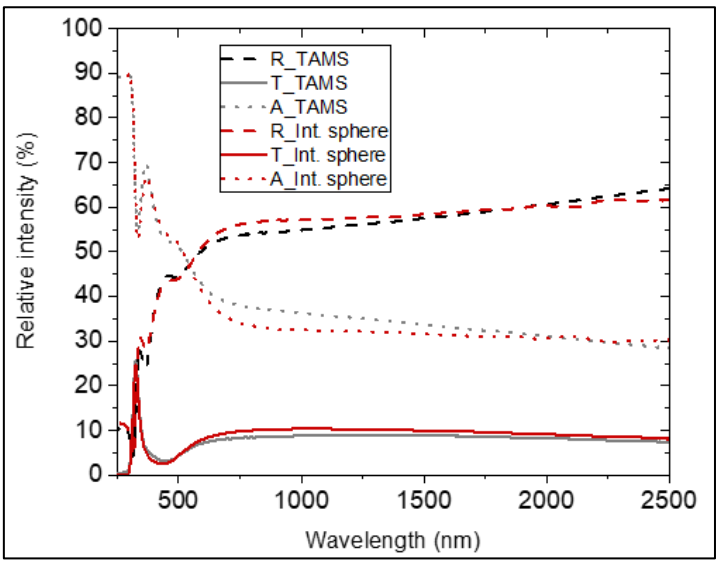


Figure 41: Optical properties (reflectance, transmittance and absorbance) of a continuous Ag films using the two different configurations available on the spectrophotometer: TAMS and 150 mm integrating sphere.

In both configurations, the set-up uses an integrating sphere. The diameter of the sphere is the surface area of the ports which is equate to a certain percentage of the internal reflective surface. The higher the diameter, the greater the precision. The advantage of using TAMS configuration is that it enables automatic measurements at different incident beam angles while the sphere diameter is smaller than the 150 mm integrating sphere meaning that only a fraction of diffuse reflectance/transmittance is measured. However, as seen in Figure 41 for the optical measurements of a sample with both configurations of the spectrometer, same results have been obtained in both cases, which means that the diffuse light part is negligible compared to the specular one.

### II.2.4.3. Conformality measurements

As already mentioned in section II.1.4., PillarHall® Test Chips have been used as a substrate to study the conformality of the deposition, mostly in lateral high-aspect ratio structures. Figure 42 illustrates the analysis concept.

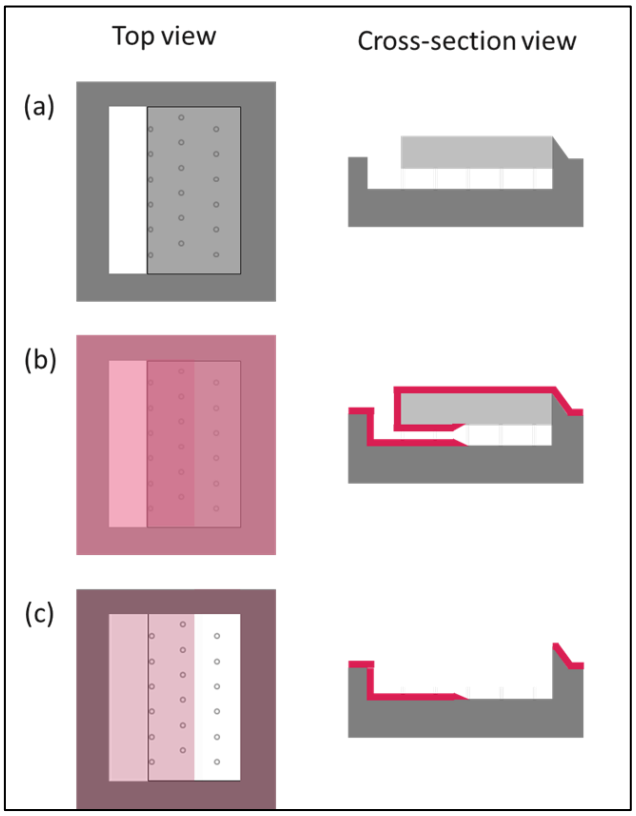


Figure 42: Schematic illustration of top view (left column) and cross section view (right column) of lateral high-aspect ratio test structures in the PillarHall® Test Chips analysis concept (a) before thin film deposition, (b) after thin film deposition and (c) after peeling off the top silicon membrane roof.

After the depositions process, the top membrane of the trench has been peeled with scotch tape (Figure 42 (c)). The penetration depth of the deposit into the cavity has been measured either by optical microscopy (Figure 43 (a)) or by scanning electron microscopy imaging (Figure 43 (b)). In order to quantify the degree of conformality, thickness profiles of the Ag film (determined by EDS) deposited into the 3D structures have been determined.

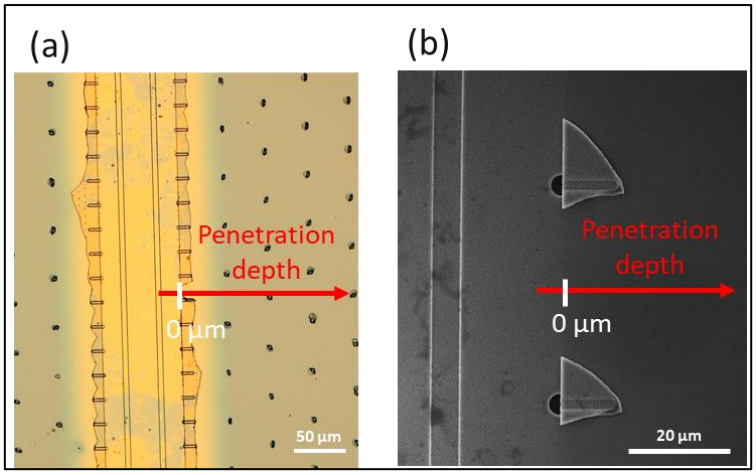

Figure 43: Penetration depth determination principle: (a) Top-view optical microscopy image of Ag deposited in LHAR structure (AR of 100) and (b) Top-view scanning electron micrograph of Ag deposited in LHAR structure (AR of 10048). In both images, the membrane has been peeled off, allowing thickness line scans to be recorded.

## II.3. Conclusion

All along the thesis work, for the silver deposition, the Beneq TFS 200 reactor is used. We employ (Ag(fod)($PEt_3$)) as silver precursor and $H_2$ plasma as reducing agent. We use two different ALD-based process types, i.e. a standard PE-ALD process and a two-step deposition with a first pulsed PE-CVD followed by a plasma post-treatment. For the structural and morphological investigation, in addition to the commonly used methods for crystallinity determination (GIXRD) and film topography determination (AFM), we focus on more original analyses, i.e. silver thin films thickness measurement by EDS and film morphology characterization and quantification through the study of SEM images. The elemental and chemical composition is investigated by the standard methods XPS and ToF-SIMS. In order to check the functional properties of Ag films, electrical conduction is determined by four-point probe measurement while the optical properties are investigated by UV-Visible-NIR spectroscopy. Uncommonly and originally, lateral high aspect ratio structures from PillarHall© technology are employed for film conformality investigation.

# Chapter 3

# Development of the silver film deposition process

This first chapter of results is meant to describe the development of Ag film deposited by standard PE-ALD. We study the influence of the ALD parameters (temperatures, argon flows, plasma conditions and sequence times) by assuming groups of parameters which are independent from each other. We further quantitatively compare the experimental results based on the film thickness evolution and its uniformity over a large surface area (8-inch silicon wafer). We see that a preliminary investigation highlights a deficiency of the precursor injection system, creating a leak and continuous exposure of Ag precursor. This is upgraded through modification of the geometry of the gas-valving system, producing a strong improvement of the uniformity of the deposition. Following the fixation of this issue, we prove the self-saturated regime as a function of the ALD parameters. We see that reactive hydrogen radical species are mandatory in order to obtain pure silver in metallic state. For film thickness below 60 nm, PE-ALD of Ag leads to the expected separated island morphology on the substrate. Under selected parameters and reducing temperatures, quasi-continuous layers are obtained. However, depositions made at such low temperatures are strongly non-reproducible due to the non-appropriate evaporation conditions of the Ag precursor.

This chapter is based on the publication *S. Wack, P. Lunca Popa, N. Adjeroud, J. Guillot, B. R. Pistillo, R. Leturcq,* Large-Scale Deposition and Growth Mechanism of Silver Nanoparticles by Plasma-Enhanced Atomic Layer Deposition, *J. Phys. Chem. C*, **2019**, 123, 44, 27196-27206.

## III.1. Strategy of optimization

In this chapter, we focus on the optimization of the silver deposition conditions depending on the ALD parameters. Due to the high number of ALD parameters, we have first simplified the statistical design of experiments by assuming different categories of parameters which have an influence on a common mechanism. We also make the hypothesis that each subset of parameters will be independent of another subset. These parameters are roughly classified into three categories:

1. Parameters influencing the injected amount of Ag precursor: mainly the hot source temperature ($T_{hs}$), Ar process flow ($Ar_{pr}$) for carrying the precursor to the reactor, and the precursor pulse time ($t_{pr}$);
2. Parameters influencing the reaction of the precursor on the surface: mainly the chamber temperature ($T_{ch}$) and the precursor pulse time ($t_{pr}$);
3. Parameters influencing the reduction reaction of the precursor: mainly the chamber temperature ($T_{ch}$), the plasma Ar and $H_2$ flows ($Ar_{pl}$ and $H_{2pl}$), the RF plasma power ($P_{dep}$), the distance between the grid-substrate ($d$) and the plasma pulse time ($t_{pl}$).

The studied parameters with their symbols, designations and units are reminded in Table 12. Although this chapter is focusing on the ALD process and is also used in chapter 4, the knowledge of the influence of each parameter has influenced the development of the two-step approach, both the precursor exposure and the post-treatment processing, as it is presented in chapter 5.

| Symbol | Designation | Units |
|---|---|---|
| $Ar_{pl}$ | Argon flow in the plasma head | sccm |
| $Ar_{pr}$ | Argon flow in the process lines (from the precursor boat to the reactor) | sccm |
| $H_{2pl}$ | Hydrogen flow in the plasma head | sccm |
| $P_{dep}$ | RF plasma power during deposition | W |
| $P_{post}$ | RF plasma power during post-treatment | W |
| $T_{ch}$ | ALD chamber temperature | °C |
| $T_{hs}$ | Hot source temperature (for the precursor evaporation) | °C |
| $T_p$ | Precursor temperature (related to $T_{hs}$) | °C |
| $T_s$ | Substrate temperature (related to $T_{ch}$) | °C |
| $d$ | Distance between grid electrode and substrate | cm |
| $t_{post}$ | Time of post-treatment | s |
| $t_{pr}$ | Pulse time 1 of Ag precursor | s |
| $t_{pl}$ | Pulse time 2 of plasma | s |
| $t_{pu1}$ | Purge time 1 after Ag pulse | s |
| $t_{pu2}$ | Purge time 2 after plasma pulse | s |

Table 12: List of ALD parameters studied for the optimization of the processes.

## III.2. Preliminary investigation of the plasma-enhanced atomic layer deposition of silver

The first step of optimization of our Ag deposition has been based on the more promising PE-ALD of Ag giving continuous silver films (see I. Background) i.e. the one developed by Kariniemi *et al.* [41]. They used Ag(fod)$PEt_3$ and plasma $H_2$ precursors and the same Beneq TFS 200 ALD-reactor. They found an ALD-type saturated growth at deposition temperatures of 120-140°C. The other parameters are reported in Table 13.

| $T_{ch}$ | $T_{hs}$ | $H_{2pl}$ | $P_{dep}$ | $Ar_{pr}$ | $Ar_{pl}$ | $t_{pr}$ | $t_{pu1}$ | $t_{pl}$ | $t_{pu2}$ | $d$ | Reactor pressure |
|---|---|---|---|---|---|---|---|---|---|---|---|
| (°C) | (°C) | (sccm) | (W) | (sccm) | (sccm) | (s) | (s) | (s) | (s) | (cm) | (mbar) |
| 120-150 | 106 | 20 | 100 | 170 | 140 | 1-4 | 5 | 3-5 | 3 | 4 | 5-8 |

Table 13: Parameters used in the work of Kariniemi *et al.* [41] which are used as reference in the thesis work.

Therefore, we have used the default parameters described in Table 14 as a basis and then have reoptimized them in order to obtain the best film quality. As a reminder, for our process, the reactor pressure is not directly controlled but is a direct consequence of the parameters mentioned above. On the other hand, the Ar flow in the chamber, $Ar_{ch}$, is only relevant for setting the average pressure in the chamber (controls that the chamber is at an overpressure as compared to the reactor) and was not directly influencing the deposition.

| $T_{ch}$ | $T_{hs}$ | $H_{2pl}$ | $P_{dep}$ | $Ar_{pr}$ | $Ar_{pl}$ | $Ar_{ch}$ | $t_{pr}$ | $t_{pu1}$ | $t_{pl}$ | $t_{pu2}$ | $d$ | Reactor pressure |
|---|---|---|---|---|---|---|---|---|---|---|---|---|
| (°C) | (°C) | (sccm) | (W) | (sccm) | (sccm) | (sccm) | (s) | (s) | (s) | (s) | (cm) | (mbar) |
| 140 | 100 | 20 | 100 | 170 | 140 | 100 | 5 | 2 | 7 | 2 | 1-4 | 3 |

Table 14: Default parameters used for the preliminary investigation of the relevant parameters.

The experimental results are first quantitatively compared based on the thickness evolution as a function the ALD parameters (Table 15) and the aim is to prove an ALD saturated regime. An added criterion is the film thickness uniformity which enable us to judge if this regime is controlled all along the Si wafer.

| Quantity | Usual units | Measurement method | Comment |
|---|---|---|---|
| Topographical film thickness | nm | Profilometer | Upper limit for the real film thickness |
| Film thickness uniformity | % | Profilometer | |

Table 15: Quantities compared during the experiments for the quantitative comparison of the results obtained during the first screening of the ALD parameters.

During this preliminary investigation of the PE-ALD of silver, we have observed a leak of the precursor occurred during the purging process, leading to precursor exposure also during the plasma pulse (see scheme in Figure 44 (a)). In the usual ALD cycle, the precursor must be exposed during a limited pulse time, after which it is purged using an inert gas before the second reactant (plasma) is exposed (see scheme in Figure 44 (b)). In order to solve the deficiency of the exposure of the silver precursor into the reactor, a major upgrade of the precursor injection system through modification of the geometry of the gas-valving system has been performed. One of the major consequences of this upgrade was the strong improvement of the uniformity of the deposition. The graph presented in Figure 44 (c) shows the thickness variation as a function of the position on the silicon substrate (measured from the inlet of the reactor) and the photos related to two silver depositions performed for constant ALD parameters before and after upgrade of the precursor injection system. We can see that, before the upgrade, we had a very non-uniform process. This is confirmed by the apparition of a halo on the silicon wafer. However, after having upgraded the gas-valving system, the deposition is more uniform in terms of thickness and more homogeneous. This observation proves the efficiency of the new upgraded process. This is the object of section III.3.

However, interesting results have been obtained before the upgrade with the continuous exposure of the precursor. Firstly, it enables us to study the more relevant ALD parameters as preliminary results (section III.2.), i.e. the temperatures of both the chamber $T_{ch}$ and the hot source $T_{hs}$ as well as the Ar flows used both in the process lines $Ar_{pr}$ and in the plasma head $Ar_{pl}$. Secondly, a remarkable new morphology made of highly covering compact Ag nanoparticles has been obtained in

some specific parts of the wafer, under non-appropriate conditions, even for ultra-thin layers. We report in chapter 5, results observed both before and after the upgrade, since the leak observed with the defective configuration has a weak influence on the conditions of the new process. Indeed, the development of the two-step approach has been inspired by some results obtained for deposition performed with the continuous exposure of the precursor and the pulse only of the plasma. Thirdly, the parameters obtained during the preliminary investigation of the PE-ALD of silver represent the ground of both processes, standard PE-ALD (chapters 3 and 4) and the new two-step approach (chapter 5).

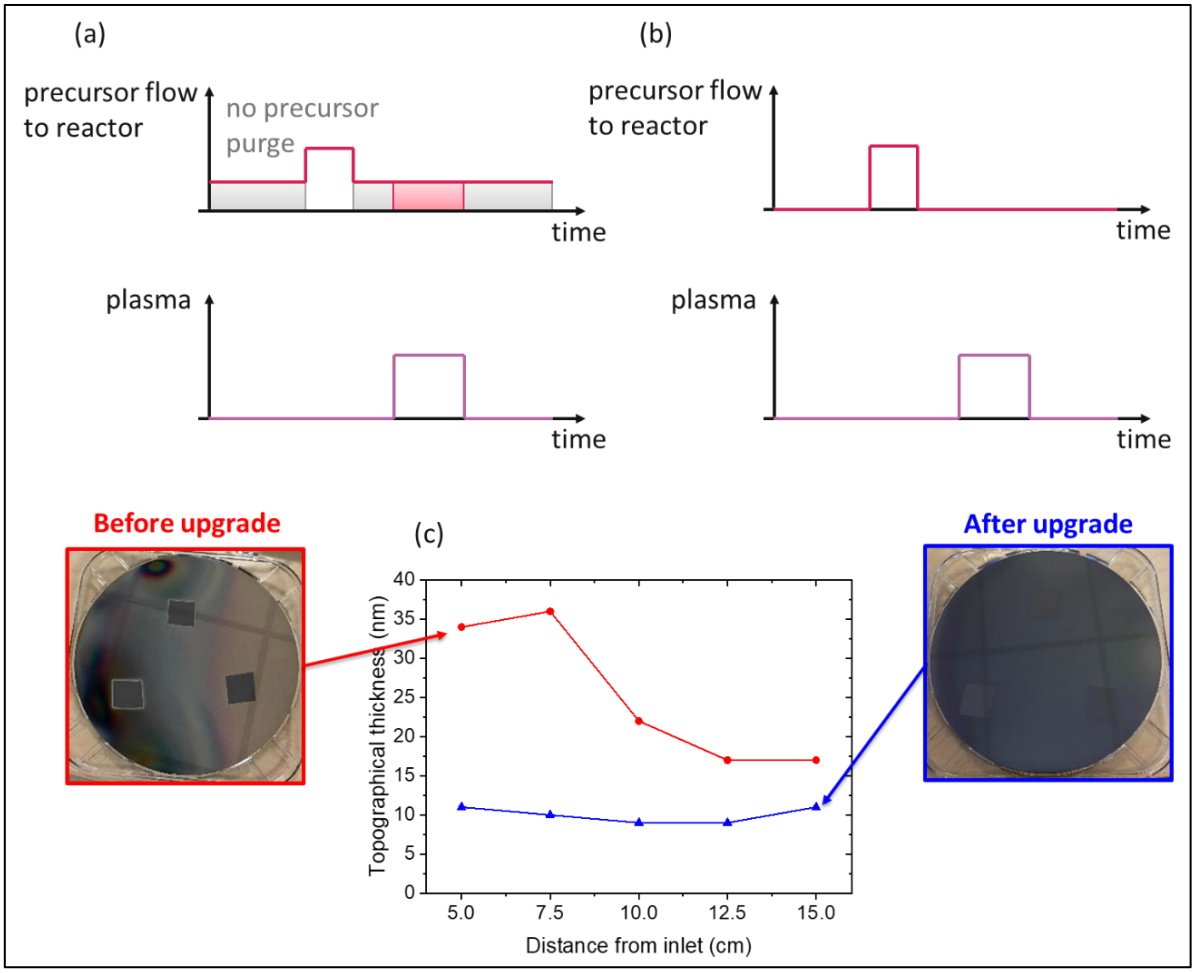


Figure 44: Comparison of different silver depositions before and after the upgrade of the precursor injection system. (a-b) Schemes representing the precursor flow to reactor correlated to the plasma pulse as a function of the deposition time (a) before upgrade and (b) after upgrade. (c) Thickness comparison of two silver depositions made at different periods, before upgrade (in red) and after upgrade (in blue), vs. the position on the Si substrate compared to the inlet and correlated to the photos of the Si 8'' wafer after silver deposition.

### III.2.1. Influence of the chamber temperature $T_{ch}$

One of the main parameters influencing the deposition conditions is the **chamber temperature $T_{ch}$**, as it influences directly the rates of the chemical reactions (precursor with the surface, and reduction) and the mobility of the reactants on the surface. Figure 45 shows the thickness as a function of the chamber temperature (Figure 45 (a)), and as a function of the position on the substrate (Figure 45 (b)) in order to investigate the uniformity of the deposition. The results obtained

are directly correlated with the I.1.3.1. section of the background. Indeed, we observe a plateau of the thickness vs. temperature from about 100 to 140°C, which corresponds to an optimum deposition, i.e. the ALD window. The deposition rate decreases at lower temperature than 100°C due the suppression of the reaction of the precursor with the surface, and eventually re-condensation of the precursor at the inlet of the reactor, since the reactor temperature becomes lower than the precursor evaporation temperature. This last point may also explain the strong non-uniformity of the deposition. At temperature higher than 140°C, the deposition starts to become strongly non-uniform with a thicker deposition on the inlet and a thinner deposition on the outlet. This behavior may be due to the decomposition of the precursor directly at the inlet, and lower amount arriving at the outlet.

From this analysis, we determine an optimum chamber temperature range between **100 and 140°C**, with the best uniformity obtained between 100 et 110°C (variation less than 30% over 10 cm).

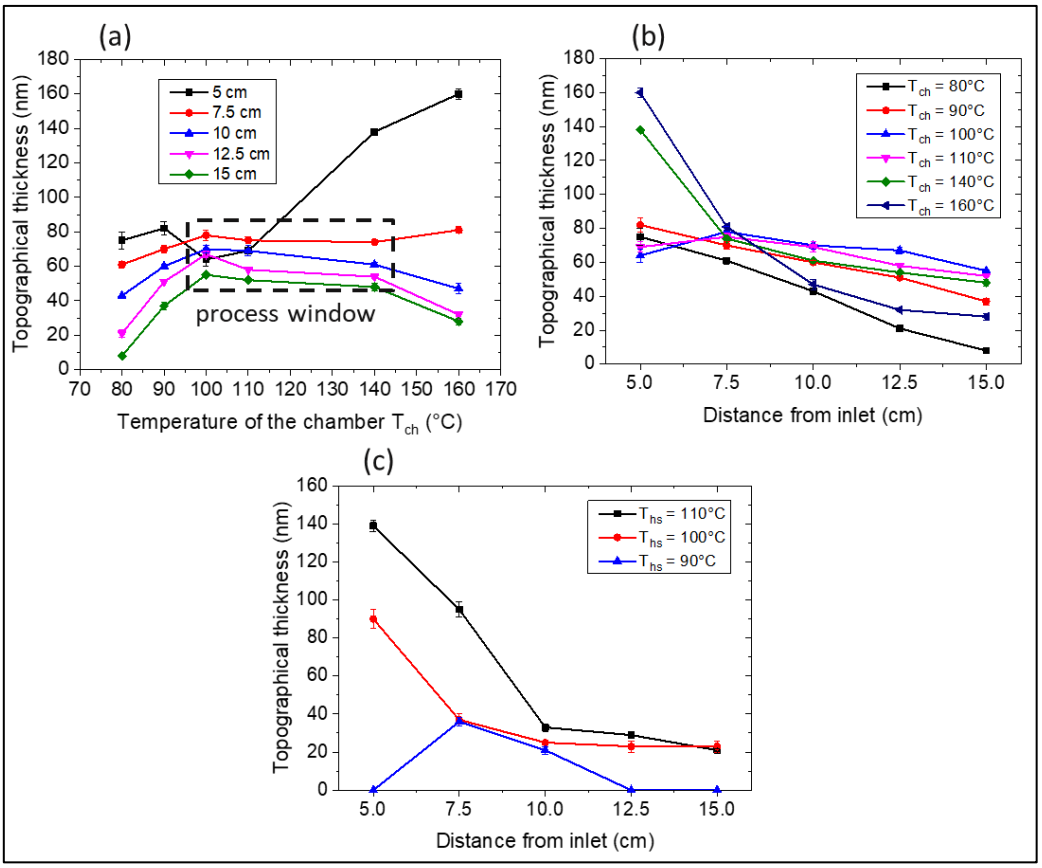


Figure 45: Preliminary investigation of the optimized temperatures. (a) and (b) Influence of the chamber temperature $T_{ch}$ on the topographical thickness of Ag films deposited on Si at different position, plotted (a) as a function of the chamber temperature $T_{ch}$ and (b) as a function of the positions on the Si substrate from the inlet. The used parameters are the default parameters described in Table 14, except for $t_{pl}$ = 3 s. Deposition for 800 cycles. (c) Influence of the hot source temperature $T_{hs}$ on the topographical thickness vs positions on the Si substrate from the inlet. The chamber temperature is kept at 140°C.

### III.2.2. Influence of the hot source temperature $T_{hs}$

The hot source temperature, $T_{hs}$ influences the amount of precursor exposed into the reactor as it is linked to the evaporation rate of the precursor. For the test of the **hot source temperature $T_{hs}$**, the $T_{ch}$ was set to 140°C in order to keep a sufficiently high gradient of temperature from the precursor

boat to the reactor, and thus avoiding spurious effect that could be related to re-condensation of the precursor before the reactor. We have nevertheless observed that, for a chamber temperature of 110°C or lower, a gradient of minimum 10°C between the hot source and the chamber is providing optimum deposition parameters. Figure 45 (c) shows the influence of the hot source temperature on the deposited thickness. This parameter is critical in the used configuration as a lowering of the temperature to 90°C resulted in parts of the substrate with no deposition, while an increase to 110°C showed a decrease of the uniformity. For this reason, the optimum hot source temperature is set to **100°C** at $T_{ch}$ of 140°C. Reducing further the temperature is moreover a challenge since it requires to reduce the precursor temperature, which is not favored for appropriate evaporation conditions.

### III.2.3. Influence of the argon flows: $Ar_{pr}$ and $Ar_{pl}$

Figure 46 shows the influence of the **Ar flows** used **in the process lines** $Ar_{pr}$ and **in the plasma head** $Ar_{pl}$, on the deposited thickness performed at $T_{ch}$ of 140°C and $T_{hs}$ of 110°C.

The **Ar process flow** $Ar_{pr}$ is expected to influence the amount of precursor carried to the reactor. This parameter mainly influences the deposition rate closer to the inlet, while almost no influence is observed close to the outlet (Figure 46 (a)). This observation may be explained by two different deposition regimes vs. the position, a CVD-type of deposition (i.e. not self-limited) close to the inlet, and an ALD-type of deposition close to the outlet. We however see in the next section that this parameter has a stronger influence at a lower chamber temperature.

The **Ar flow in the plasma head** $Ar_{pl}$ is expected to influence the amount of radicals arriving on the substrate for the reduction reaction. (Figure 46 (b)) shows the influence of this parameter on the deposited thickness. The deposited thickness is significantly lower at the lowest flow (70 sccm), which is attributed to a reduced number of hydrogen radicals able to reach the substrate. Above 140 sccm, no further evolution is observed, and the flow seems sufficient in order to ensure a saturation of the substrate surface with H radicals.

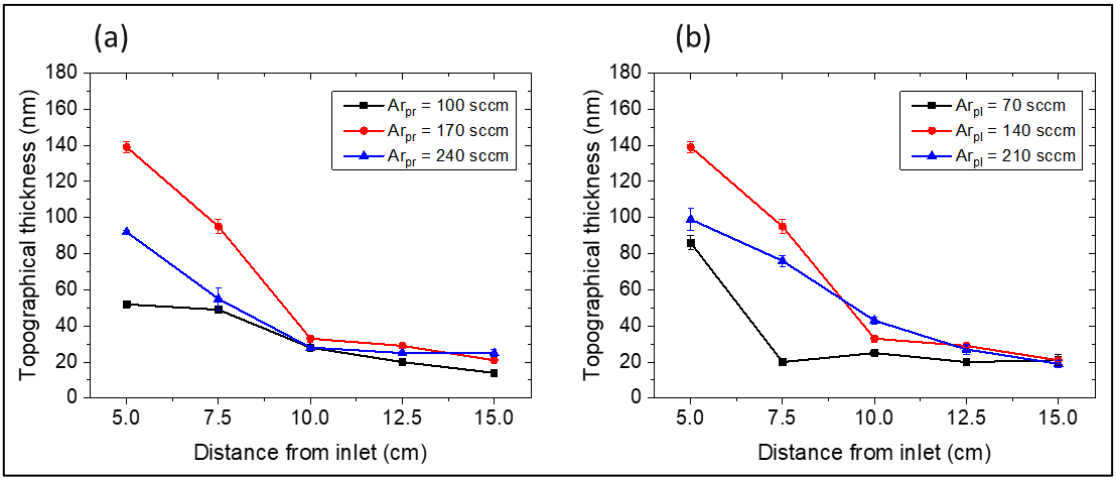


Figure 46: Preliminary investigation of the Ar flows: Influence of (a) the Ar process flow $Ar_{pr}$ at a constant Ar plasma flow of 140 sccm and (b) the Ar plasma flow $Ar_{pl}$ at a constant Ar process flow of 170 sccm on the topographical thickness as a function of the positions on the Si substrate from the inlet.

### III.2.4. Selected sets of experiments

Following previous screening of the main parameters influencing the deposition conditions, five sets of parameters have been selected and more carefully investigated here in terms of deposition regime and functional properties of conducting films. These sets of parameters are summarized in Table 16. The three parameters that have been varied during this investigation are:

- The chamber temperature $T_{ch}$, which influences the first precursor decomposition on the substrate (first half-reaction of the ALD process);
- The process argon flow $Ar_{pr}$, which mainly influences the amount of precursor exposed into the chamber;
- The argon flow in the plasma head $Ar_{pl}$, which influences the exposure of radicals created by the plasma.

| | $T_{ch}$ (°C) | $T_{hs}$ (°C) | $H_{2pl}$ (sccm) | P (W) | $Ar_{pr}$ (sccm) | $Ar_{pl}$ (sccm) | $Ar_{ch}$ (sccm) | $t_{pr}$ (s) | $t_{pu1}$ (s) | $t_{pl}$ (s) | $t_{pu2}$ (s) |
|---|---|---|---|---|---|---|---|---|---|---|---|
| Set 1 | **140** | 100 | 20 | 100 | **170** | **140** | 100 | 5 | 2 | 3 | 2 |
| Set 2 | **140** | 100 | 20 | 100 | **300** | **140** | 100 | 5 | 2 | 3 | 2 |
| Set 3 | **110** | 100 | 20 | 100 | **170** | **140** | 100 | 5 | 2 | 3 | 2 |
| Set 4 | **110** | 100 | 20 | 100 | **300** | **140** | 100 | 5 | 2 | 3 | 2 |
| Set 5 | **110** | 100 | 20 | 100 | **300** | **300** | 100 | 5 | 2 | 3 | 2 |

Table 16: Main parameters used for the five selected sets.

In order to investigate the GPC, we have performed several depositions varying the number of cycles, from 400 to 1800. The GPC based on the maximum topographical thickness ($GPC_t$) determined by profilometer measurement is investigated in this part. Figure 47 shows the plot of the topographical thickness as function of number of cycles for the five sets of parameters investigated here.

We observe in these graphs a major impact of the chamber temperature.

At $T_{ch}$ of 140°C, the thickness first increases as a function of the number of cycles from 400 to 800 cycles, and then saturates at positions close to the outlet of the reactor (position 15 cm). This effect is enhanced at lower $Ar_{pr}$ flow (Figure 47 (a)) than higher $Ar_{pr}$ flow (Figure 47 (b)). Moreover, the uniformity along the sample (i.e. thickness variation from the inlet to the outlet) strongly increases with the number of cycles. This behavior may be explained by a reaction driven by the decomposition of the precursor rather than a surface reaction at the inlet of the reactor, and/or an etching of the deposited film by the plasma close to outlet. It is however not the favored regime for a controlled deposition of thick films.

At a chamber temperature of 110°C, we observe a monotonic increase of the thickness as a function of the number of cycles, and this increase is uniform along the sample. This monotonic increase has been tested up to 2400 cycles in Figure 47 (e). This behavior is a strong indication of a deposition driven by surface reactions, as expected for ALD (see Background section I.1.3.3.)

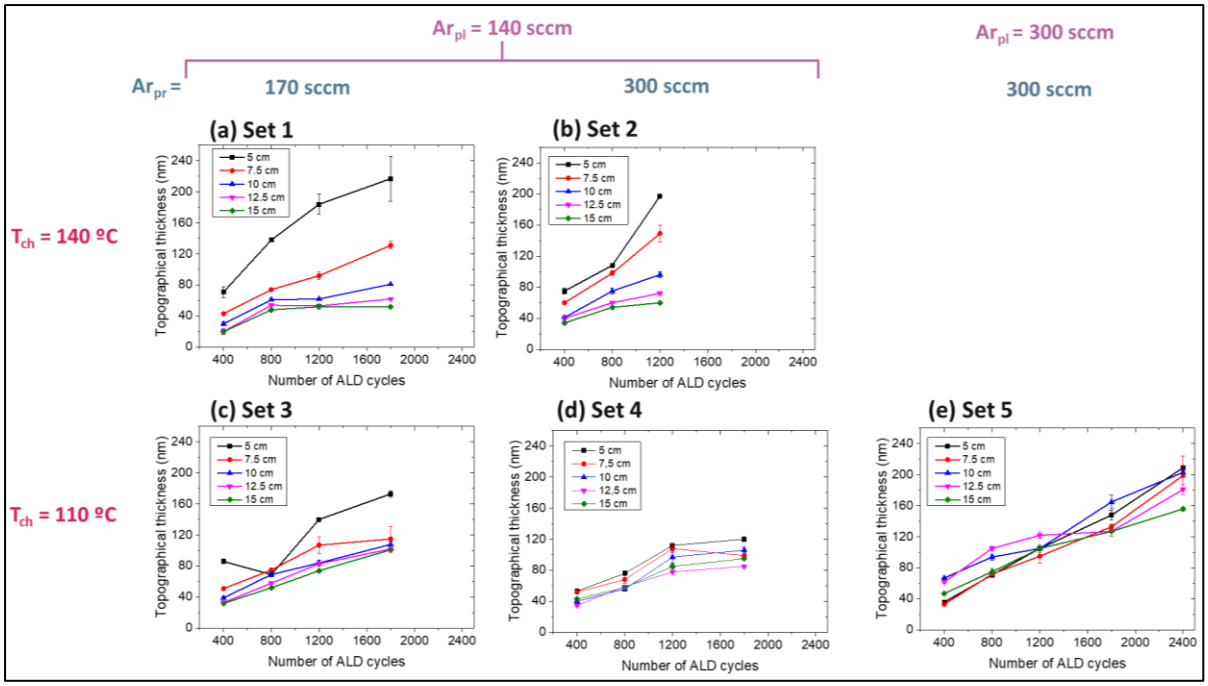


Figure 47: Topographical thickness as a function of the number of deposition cycles for the five identified sets of optimized parameters ($T_{ch}$ in red, $Ar_{pr}$ in blue, $Ar_{pl}$ in purple). The ALD parameters used for each set are described in Table 16.

In order to further compare the deposition regimes obtained at 110°C, we have fitted the dependence of the thickness as a function of number of cycles by a linear fit and extracted the slope, i.e. GPC. The results of the fit are represented in Figure 48. Due to the strong non-uniformity of the deposition at a position of 5 cm from the inlet, we have excluded the experimental data for the fit. The GPC varies from 0.04 to 0.07 nm/cycle, for the different gas flows. First, we note that this value is larger than the one reported by the literature, which is 0.03 nm/cycle. [41] We note however than the thickness measurement in our case, based on topographical thickness measured by profilometry, differs from most of the methods reported (based on electron dispersion X-ray spectroscopy (EDS) or quartz microbalance (QCM)), which rely rather on the total mass deposited, divided by the expected density of the material. The two methods differ strongly for non-uniform films, as it is obviously the case for the silver films, and in case the density of the films does not correspond to pure silver. That is the reason why EDS equivalent thickness is used in the optimization of the deposition parameters in the following sections III.3.

The influence of the flows on the GPC is remarkable closer to the inlet of the reactor, with an increased GPC with increasing Ar plasma flow, and a decreasing GPC with increasing Ar process flow (Figure 48). This behavior shows that the reactions are not fully self-limited as expected for ALD. This effect is however reduced closer to the outlet of the reactor, pointing out to a non-optimum reactor geometry.

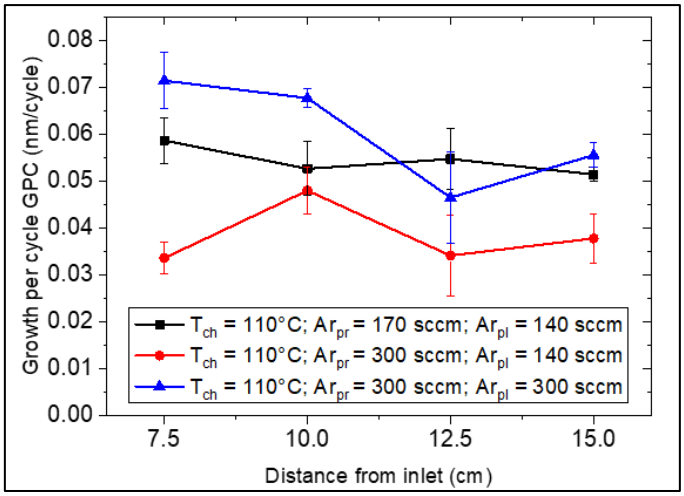


Figure 48: Growth per cycle GPC (from the topographical thickness determined by profilometry) as a function of the positions on the Si substrate from the inlet for the three sets of depositions performed at a chamber temperature $T_{ch}$ of 110°C.

At a chamber temperature of 110°C, quasi-continuous silver films have been observed under specific ALD conditions. Figure 49 shows typical SEM images comparing the different Ar flows (process and plasma) used. We observe that quasi-continuous films are obtained only with $Ar_{pr}$ = 300 sccm and $Ar_{pl}$ = 140 sccm at $T_{ch}$ of 110°C (Figure 49 (b)) whereas nanoparticle film morphology is produced at $T_{ch}$ of 140°C (Figure 49 (d)). Moreover, a critical thickness, above which the films are conductive, of about 60 nm is obtained for films deposited at $T_{ch}$ = 110°C with $Ar_{pr}$ = 170 sccm and $Ar_{pl}$ = 140 sccm, leading to a conductivity of $5.19\times10^3$ S/cm. This critical thickness increases with the Ar flow, with a value close to 110 nm for $Ar_{pr}$ = 300 sccm and giving a conductivity of $3.95\times10^3$ S/cm. The critical thickness is even higher for films deposited at higher temperature of 140°C with a value of $2.93\times10^3$ S/cm for a 133 nm-thick film. This effect might be related to the faster migration of the precursor on the substrate at higher temperature, with an island-limited growth. Indeed, during the deposition of metal films on oxide layers, the formation of disconnected particles is usually observed, and is believed to be due to the migration of metal atoms on the surface allowing them to form clusters, which is their most stable state. At low temperature, the migration is reduced and we expect a better coverage of the deposition, as it is the case as shown in Figure 49 (a-c) compared to Figure 49 (d).

Nevertheless, depositions performed at $T_{ch}$ of 110°C were non reproducible. The main reasons are the challenging control of the ALD parameters at this low temperature and the non-optimum parameters used for the process leading to reactions not fully self-limited, as expected for ALD. Indeed, when decreasing $T_{ch}$, we also have to decrease the temperature of the Ag precursor in the hot source leading to problem of evaporation of precursor but at the same time, we also have to avoid the re-condensation of the precursor at the inlet of the reactor, since the reactor temperature becomes closer to the precursor evaporation temperature.

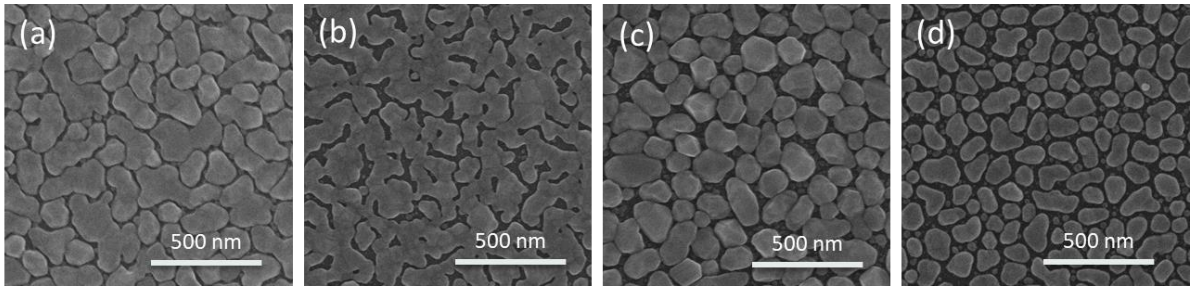

Figure 49: Scanning electron micrograph of typical results Ag films deposited at $T_{ch}$ = 110°C for 800 cycles (a) for $Ar_{pr}$ = 170 sccm and $Ar_{pl}$ = 140 sccm, (b) for $Ar_{pr}$ = 300 sccm and $Ar_{pl}$ = 140 sccm, (c) for $Ar_{pr}$ = 300 sccm and $Ar_{pl}$ = 300 sccm and (d) at $T_{ch}$ = 140°C for 800 cycles for $Ar_{pr}$ = 170 sccm and $Ar_{pl}$ = 140 sccm. The images are taken at the center of the substrate (10 cm from inlet). The scale bars represent 500 nm.

### III.2.5. Conclusion

In this part, a preliminary investigation has been performed in order to understand the influence of the ALD growth parameters. The most critical parameter is the chamber temperature, with a process window lying between 100 and 140°C. The hot source temperature, which controls the evaporation of the precursor, was also investigated, and it needs to be at least 10°C lower than the chamber temperature in order to avoid condensation of the precursor on the reactor. Other parameters, such as gas flows were also investigated and optimized. Under specific conditions, quasi-continuous films have been obtained. However, problem of reproducibility of the depositions due to the limited control of ALD parameters have been highlighted.

Following this previous investigation of the main parameters influencing the deposition conditions, a fine optimization of the deposition parameters have been then performed. In this next sub-section, we more focus on the analysis of the results for thin films and, as explained in the II. Experimental methods section, we mainly use the EDS film thickness and not profilometer anymore since it is a more reliable method for thickness determination.

## III.3. Optimization of the plasma-enhanced atomic layer deposition of silver

Following the fixation of the issue linked to the leakage of precursor, the full set of deposition parameters needed to be optimized again in order to obtain the highest uniformity. The ALD parameters, i.e. the sequence times, plasma conditions and temperatures, have been investigated in the range of values described in Table 17 below and the detailed experimental plans for each parameters are given in the dedicated sections.

| Parameters | Symbol | Units | Range |
|---|---|---|---|
| **Pulse time 1 of Ag precursor** | $t_{pr}$ | s | 0, 1, 5, 10 |
| **Pulse time 2 of plasma** | $t_{pl}$ | s | 0, 1, 3, 5, 10 |
| **Purge time 1 after Ag pulse** | $t_{pu1}$ | s | 2, 5, 10, 20 |
| **Purge time 2 after plasma pulse** | $t_{pu2}$ | s | 2, 5, 10 |
| **Distance substrate-grid** | $d$ | cm | 1, 2, 4 |
| **RF plasma power** | $P_{dep}$ | W | 50, 100 |
| **Chamber temperature at $T_{hs}$ = 100°C** | $T_{ch}$ | °C | 120, 130, 140, 150, 160 |
| **Chamber temperature at $T_{hs}$ = 90°C** | $T_{ch}$ | °C | 100, 110, 120, 140 |

Table 17: List of ALD parameters and investigated range studied for the optimization of the standard PE-ALD process.

The experimental results are first quantitatively compared by using the EDS equivalent film thickness corresponding to the quantity of material deposited and the film thickness uniformity over a large surface area (8-inch substrate). The measurable quantities are described in Table 18.

| Quantity | Usual units | Measurement method | Comment |
|---|---|---|---|
| Equivalent film thickness | nm | EDS | Quantity of material deposited |
| Film thickness uniformity | % | EDS | |

Table 18: Quantities compared for the quantitative comparison of the results obtained during the fine optimization of the ALD parameters.

## III.3.1. Optimization of the pulse and purge times

We give in Table 19 the list of ALD parameters studied in order to optimize the pulse and purge times needed for silver deposition process and the optimum values obtained. In these different studies, it is important to notice that, for each studied time, the other times were kept constant and have been chosen in order to be sure to have a self-saturated regime. The times have been optimized at $T_{ch}$ = 130°C / $T_{hs}$ = 100°C.

| Parameters | Symbol | Units | Range | Optimum |
|---|---|---|---|---|
| **Pulse time 1 of Ag precursor** | $t_{pr}$ | s | 0, 1, 5, 10 | 5 |
| **Pulse time 2 of plasma** | $t_{pl}$ | s | 0, 1, 3, 5, 10 | 3 |
| **Purge time 1 after Ag pulse** | $t_{pu1}$ | s | 2, 5, 10, 20 | 5 |
| **Purge time 2 after plasma pulse** | $t_{pu2}$ | s | 2, 5, 10 | 10 |

Table 19: List of ALD parameters studied for the optimization of the pulse and purge times needed for the silver deposition process.

### III.3.1.1. Silver precursor and plasma pulse times: $t_{pr}$ and $t_{pl}$

ALD is defined to be based on sequential and self-limited surface reactions of precursors. The aim of the study is thus to find a precursor dose as low as possible to save time and money but as high as needed for saturation of the surface.

Figure 50 illustrates the influence of the silver precursor exposure time and plasma pulse time on the deposited thickness. The plot of the silver films thickness as a function of the silver precursor pulse time for the different positions all along the silicon wafer (Figure 50 (a)) shows that, for silver precursor pulse time shorter than 5 s, the thickness increases with the pulse time and then, it reaches a plateau from 5 s to 10 s. This plateau is typical of a saturated growth and a proof that the surface is saturated by the precursor, as exposed in the background section (I.1.3.2.). Moreover, we see that at 5 s of silver pulse time, the deposition is more uniform in terms of thickness. This is observed in Figure 50 (b): below 5 s, we have an under-saturated regime with a very low silver thickness deposited and above $t_{pr}$ = 5 s, we are in the ALD regime with self-saturated reaction and higher thickness. Since the value of the thickness with 5 s and 10 s of silver pulse time is similar, **5 s** is found to be the optimum silver precursor exposure time.

The same analysis was performed for the plasma pulse time, as seen in Figure 50 (c) and Figure 50 (d). The plasma pulse time influences the number of radicals arriving on the substrate for the reduction reaction. The plot of the thickness of silver films as a function of the plasma pulse time for the different positions all along the silicon wafer (Figure 50 (c)) shows that for plasma pulse times shorter than 3 s, the thickness increases with the pulse time and then, it reaches a plateau from 3 s to 10 s. It appears also that 3 s plasma pulse time favors a more uniform film deposition. Figure 50 (d) highlights the fact that 3 s seems sufficient in order to ensure a saturation of the substrate surface. In conclusion, **3 s** is found to be the optimum plasma pulse time.

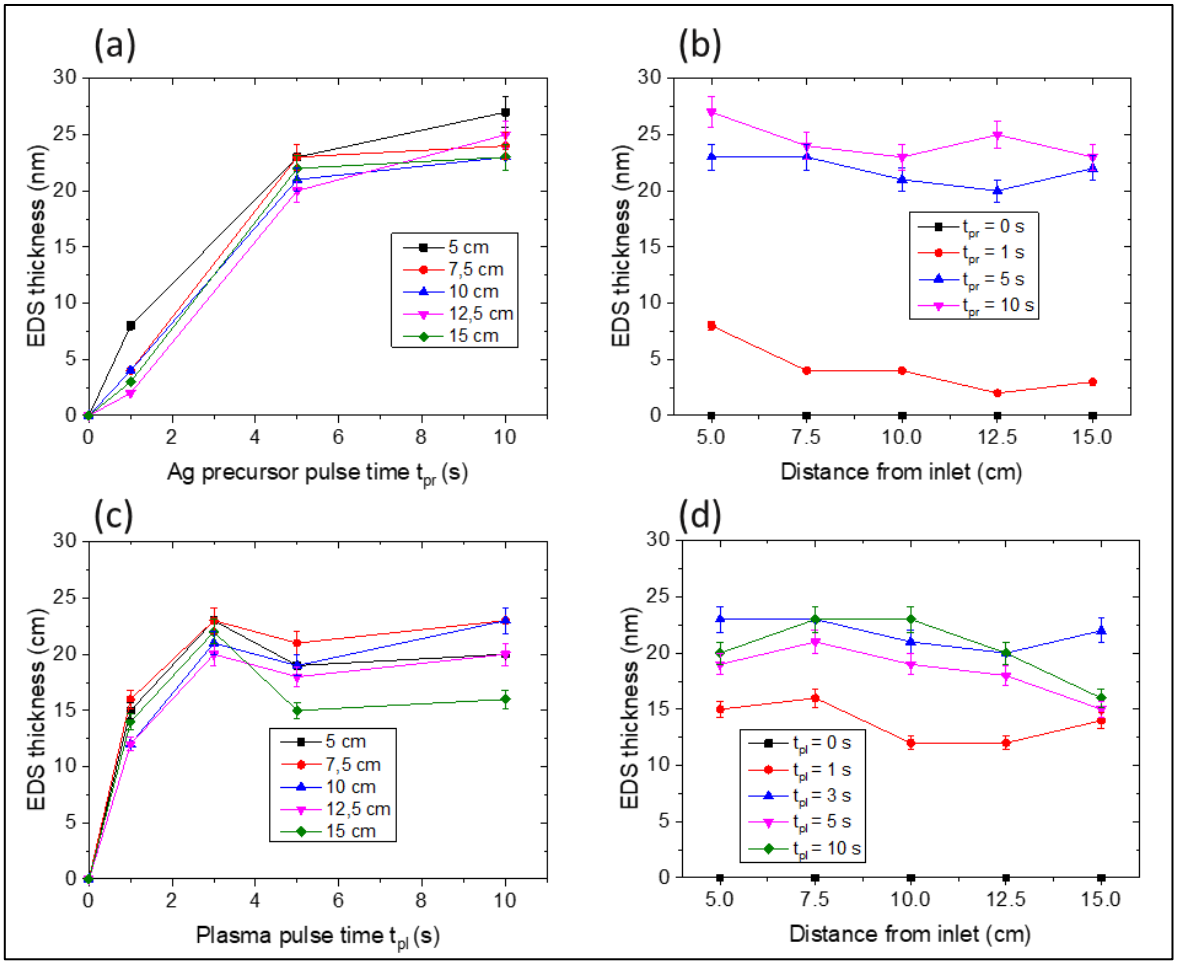


Figure 50: (a) and (b) Influence of the silver precursor pulse time on the thickness of the silver films determined by EDS vs. (a) the studied parameter (silver precursor pulse time) and (b) the position on the Si substrate compared to the inlet. (c) and (d) Influence of the plasma pulse time on the thickness of the silver films determined by EDS vs. (c) the studied parameter (plasma pulse time) and (d) the position on the Si substrate compared to the inlet. The chamber temperature is kept at 130°C and the hot source temperature at 100°C.

### III.3.1.2. Purge times after Ag precursor and plasma pulses: $t_{pu1}$ and $t_{pu2}$

The purge time is expected to have an influence on the type of deposition, leading to CVD-type with an excess precursor overlapping as some reactants remain in the reactor when the time is too short, or a waste of time and eventual thermal desorption when it is too long.

Figure 51 shows the influence of the purge times after the silver precursor pulse and after the plasma pulse on the deposited thickness.

As seen on the plot of the thickness as a function of the purge time after Ag precursor pulse for the different positions all along the wafer (Figure 51(a)), the thickness reaches a plateau from 5 s to 20 s: 5 s seems to be sufficient for evacuating the non-reacted silver precursor. This is confirmed by the better uniformity of the deposition at this purge time. Figure 51 (b) highlights the bad precursor elimination illustrated by a higher deposition thickness below 5 s and a similar and constant one for depositions performed above 5 s. To conclude, **5 s** is found to be the optimum purge time after pulse of silver precursor.

The same study was performed for the purge time after the plasma pulse as shown in Figure 51 (c) and Figure 51 (d). The higher deposited thickness for short purge time after plasma pulse (below 5s) indicates possible remaining H radicals in the reactor when the next precursor exposure is performed. Even if 5 s seems already sufficient, as confirmed by the uniformity of the deposited thickness, **10 s** was chosen for the purge time after plasma pulse in order to ensure efficient reduction reaction and efficient evacuation of non-reacted silver precursor potentially let in the reactor.

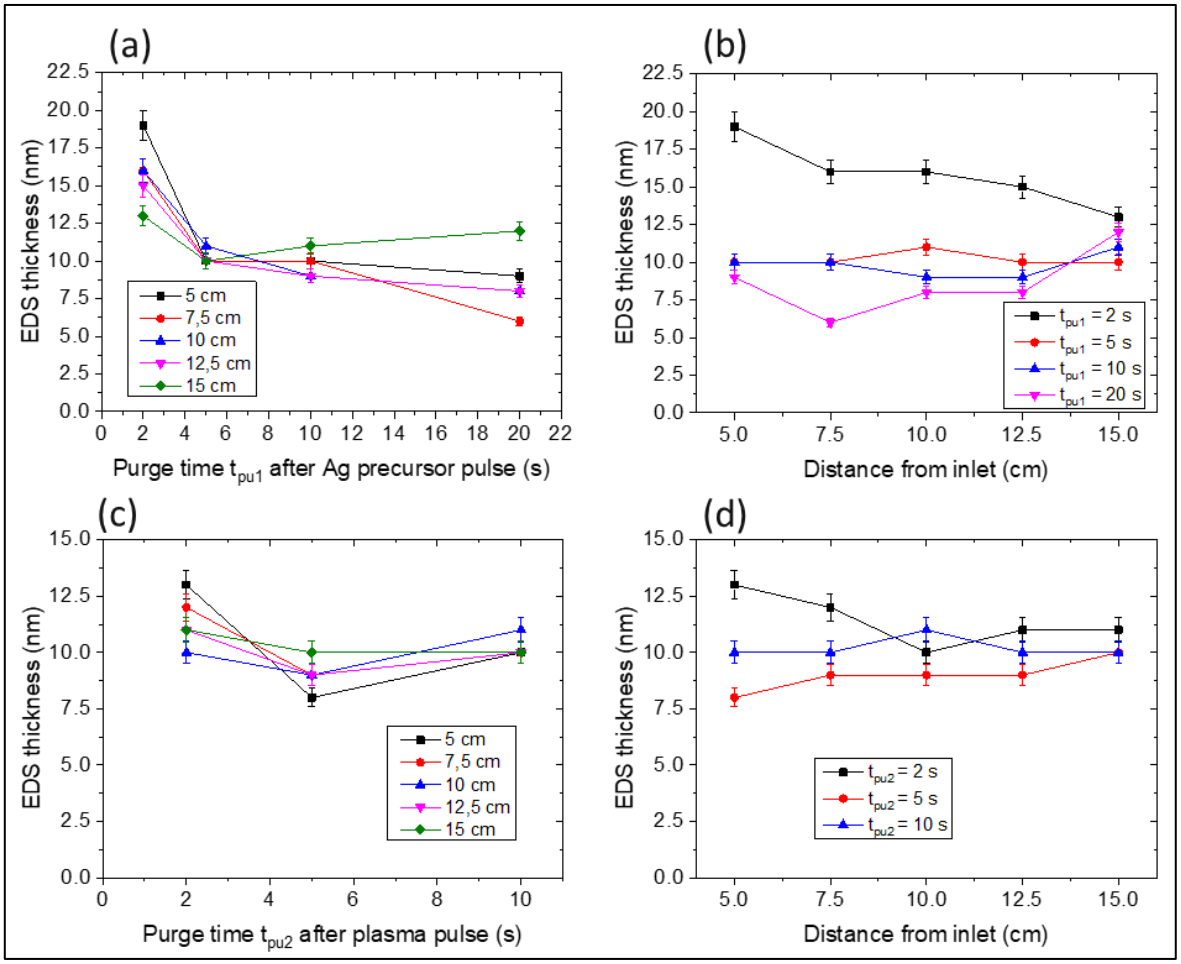


Figure 51: (a) and (b) Influence of the purge time after Ag precursor pulse $t_{pu1}$ on the thickness of the silver films determined by EDS vs. (a) the studied parameter ($t_{pu1}$) and (b) the position on the Si substrate compared to the inlet.
(c) and (d) Influence of the purge time after plasma pulse $t_{pu2}$ on the thickness of the silver films determined by EDS vs. (a) the studied parameter ($t_{pu2}$) and (b) the position on the Si substrate compared to the inlet. The chamber temperature is kept at 130°C and the hot source temperature at 100°C.

## III.3.2. Influence of the plasma conditions

### III.3.2.1. Nature of the plasma gas and plasma ignition

A first study has been performed to evaluate the influence of the hydrogen flow in the plasma head ($H_{2pl}$) and the use of the RF plasma power (Table 20). It has been demonstrated that molecular hydrogen ($H_2$) cannot directly act as a reducing agent for the mentioned silver precursors. [150] For this reason, it is necessary to activate hydrogen radicals ($H^{\bullet}$) by using a plasma source.

Quasi no deposition or very small NPs have been obtained in the absence of plasma (RF power set to zero), either with or without hydrogen flow (argon only), which means that reactive species created by the plasma source are mandatory in order to reduce Ag precursor and make the reaction happen. The depositions performed in the presence of plasma give more uniform films when a mix of $H_2$ and Ar is used rather than Ar alone. (Figure 52)

| | **$H_{2pl}$ / $Ar_{pl}$** | **$Ar_{pl}$** |
|---|---|---|
| **Plasma power ON** | Influence of $H_2$ and Ar in the plasma head: Ar and H radicals | Influence of only Ar in the plasma head: Ar radicals |
| **Plasma power OFF** | Test of precursor decomposition under $H_2$ atmosphere | Test of thermal decomposition of the precursor |

Table 20: Summary of the study on the influence of the hydrogen/argon flow in the plasma head ($Ar_{pl}/H_{2pl}$) and the use of the RF plasma power.

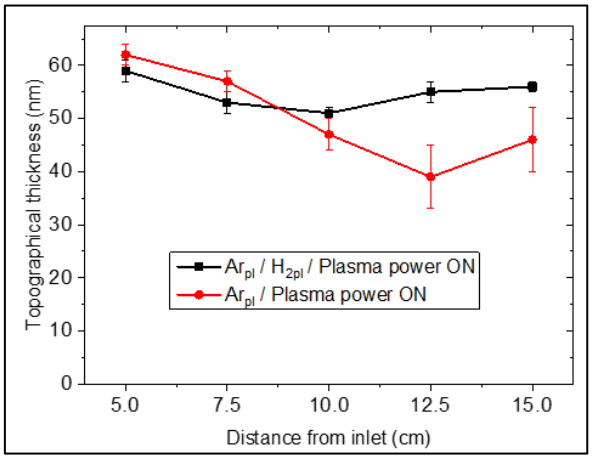


Figure 52: Influence of the gas flows in the plasma head: $Ar_{pl}$ and $H_{2pl}$ (in black) or only $Ar_{pl}$ (in red) on the topographical thickness of Ag films deposited on Si at different position from inlet.

We have performed XPS analyses in order to study the influence of the nature of the plasma, i.e. $H_2$/Ar gas versus Ar gas only. Figure 53 exposes the corresponding elemental composition of the samples. The spectra were acquired before and after argon sputtering (280 s) in order to determine the elemental composition in the first nanometers (10 nm) of the deposit.

For Ag film deposited with Ar/$H_2$ plasma, we observe the usual contaminants (carbon and oxygen) on the surface of samples exposed to air and the presence of Si may be attributed to the silicon and $SiO_2$ from the substrate due to the morphology made of islands (Figure 53 (c)). In both cases, fluorine and phosphorus suggest the presence of unreacted precursor on the particle surface, which also leads to additional carbon and oxygen amounts. However, a much lower Ag amount and higher contamination of carbon, fluorine and phosphorus are detected for layers deposited with Ar

plasma only. This suggests a higher quantity of remaining silver precursor on the surface and a less efficient reduction reaction by the Ar radicals created by means of plasma as compared to H radicals.

After etching, for $Ar/H_2$ plasma deposited film, we notice the almost complete decomposition of the silver precursor and the removal of surface contaminants suggested by the lower amount of carbon, oxygen, fluorine and phosphorus. Using only Ar plasma, the creation of poorly reactive Ar species generates a high level of carbon even in the bulk. The decrease of fluorine amount and the high increase of carbon might come from a better removal of inorganic species like fluorine than organic ones, and might be also due to the redeposition of carbon after etching of the precursor.

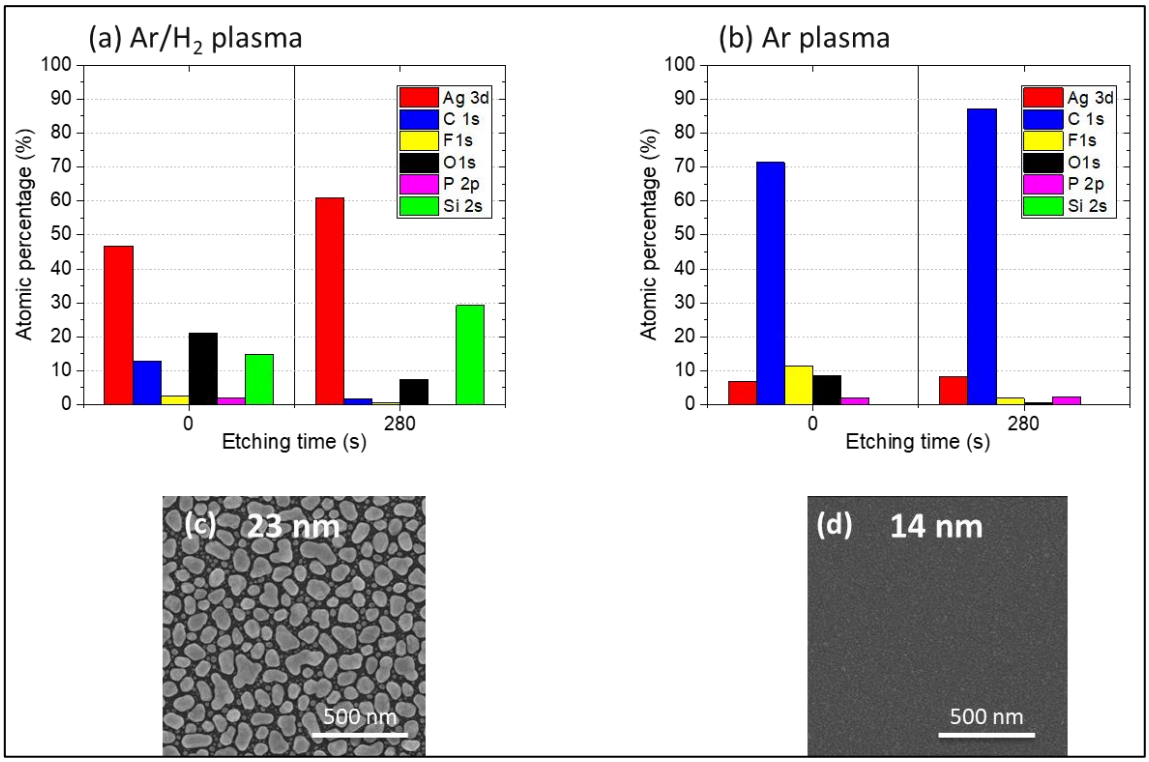


Figure 53: (a) and (b) Elemental composition (in at.%) of Ag thin films synthetized with (a) $Ar/H_2$ plasma and (b) Ar plasma on silicon substrate measured by XPS before (etching time 0 s) and after 280 s of Ar sputtering. (c) and (d) Scanning electron micrographs corresponding to Ag thin films deposited with (c) $Ar/H_2$ plasma and (d) Ar plasma. The values on the images refer to the thickness of the films determined by EDS and the scale bars represent 500 nm.

In addition to the study of the elemental composition of Ag thin films, the XPS spectra have been further investigated to determine the chemical state of Ag. According to the literature dealing with XPS of Ag [213, 214]:

- Ag 3d region has well separated spin-orbit components (Ag $3d_{5/2}$- Ag $3d_{3/2}$ splitting $\Delta_{metal}$ = 6.0 eV);
- Peaks have asymmetric peak shape for metal;
- Loss features are observed to higher binding energy side of each spin-orbit component for Ag metal. This energy loss corresponds to the plasmonic resonance. Indeed, the oscillation of electrons in metal under an electromagnetic field has a natural frequency of oscillation (the plasma frequency). In silver, this frequency corresponds to a wavelength of 320-350 nm which corresponds to an energy of 3.5-4 eV. In the XPS spectrum, this

resonance creates a satellite peak separated from the main peak of 3.5-4 eV. The surface plasmon has a lower energy than the volume plasmon, which may explain a peak shift; [214]

- Small binding energy shifts for compounds, such as oxides, are present and Ag 3d peaks are broaden with respect to metal peaks.

As there is almost no difference in the Ag 3d peak shape and position for silver in metallic Ag(0) and oxidized Ag(I) and Ag(II) forms, the Ag $M_4N_{4,5}N_{4,5}$ Auger line (calibrated at 357.6 eV) and Ag $3d_{5/2}$ photoelectron line were used to determine the silver chemical state from the modified Auger parameter (α'). [215] It is particularly effective in identifying the majority phases, as this parameter is insensitive to the variation of the peak positions due to charge phenomena. [216] We performed this study in order to check whether Ag is in a metallic state, i.e. in the oxidation state 0 (see Table 21). Indeed, the Auger parameter is effective to differentiate the metal form Ag (0) from the oxidized forms but non-effective for identifying other oxidation states. [217] However, the small BE and Auger parameter shifts reported in the literature as well as the inconsistencies between authors make it difficult to determine the exact oxidation state of silver. [215, 217, 218, 219, 220, 221]

| Oxidation number | Compound | Modified Auger parameter α' (eV) |
|---|---|---|
| Ag (0) | Ag | 726.0-726.4 |
| Ag (I) | $Ag_2O$ | 724.3-724.5 |
| Ag (II) | AgO | 723.5-724.8 |

Table 21: Modified Auger parameter α' of silver for different compounds, from [222].

Consequently, in order to determine the oxidation state of silver, three key parameters have been investigated:

1. The presence of a loss feature in the XPS binding energy (BE) spectra, i.e. in the high resolution (HR) Ag 3d peak;
2. The shape of the Auger peak, i.e. the Ag MNN peak;
3. The value of the modified Auger parameter α' which is calculated taking into account the maximum value of Ag 3d photoelectron peak (Ag $3d_{5/2}$) and Auger Ag $M_4N_{4,5}N_{4,5}$ peak.

In Figure 54, HR Ag 3d spectra of the two different samples are reported and each of them are compared with the Ag reference spectrum. The spectra were recorded at the surface level (t=0) and after an etching time of 280 s. In both cases, i.e. for Ag deposited with $Ar/H_2$ plasma and Ar plasma only, the observation of a similar asymmetric Ag 3d peak shape of the samples to Ag foil reference (red lines) suggests the presence of Ag in metallic state. The presence of loss features is well observable in the spectra corresponding to Ag deposited with $Ar/H_2$ plasma and matches very well with the silver reference after Ar sputtering (slight shift for as-deposited film due to surface contamination). For layers deposited without $H_2$ plasma, this satellite feature is almost absent. Moreover, in this case, we observe a shift as well as a broaden of Ag 3d peaks (highlighted in the zoom in of Ag $3d_{5/2}$) with respect to metal peaks, which will be highlighted by the calculation of the Auger parameter in the following part. These observations highlight that, in addition to metallic contribution linked to the line shape of the spectra, the contribution of silver oxide is higher for film deposition in the presence of Ar plasma only. This also suggests that hydrogen radicals created by the plasma are much more reactive to reduce the silver precursor in metallic state.

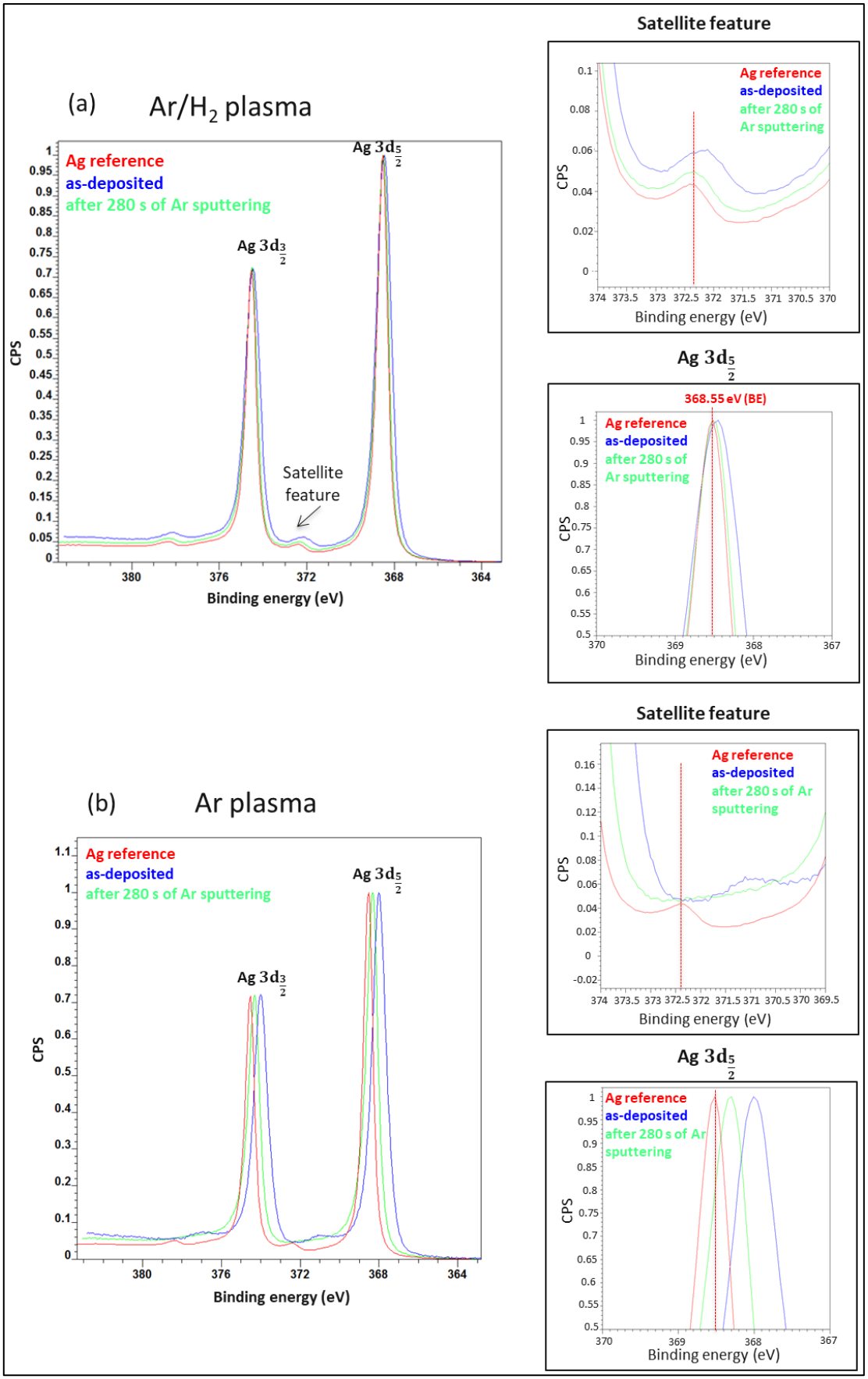


Figure 54: High resolution Ag 3d spectra of Ag thin films synthetized with (a) $Ar/H_2$ plasma and (b) Ar plasma. Each spectrum, compared with the Ag reference (red line), was recorded at t=0 (in blue) and after 280s of Ar sputtering (in green). A zoom of the satellite feature and the Ag $3d_{5/2}$ is also provided in both cases.

The shape of the Auger Ag MNN peaks (Figure 55) matches well the previous observations. Even if the intensity of the background for as-deposited films is higher due to surface contamination in both cases, we observe a much higher background intensity for Ag films synthetized with the presence of Ar plasma only. This suggests the existence of a higher amount of contaminant materials on the surface potentially explained by the presence of higher amount of unreacted monomer through higher amount of carbon for these films. In addition, the presence of a much more distorted peak for films deposited without $H_2$ plasma fits well with the higher contribution of silver oxidized phase in this case, in addition to Ag metal.

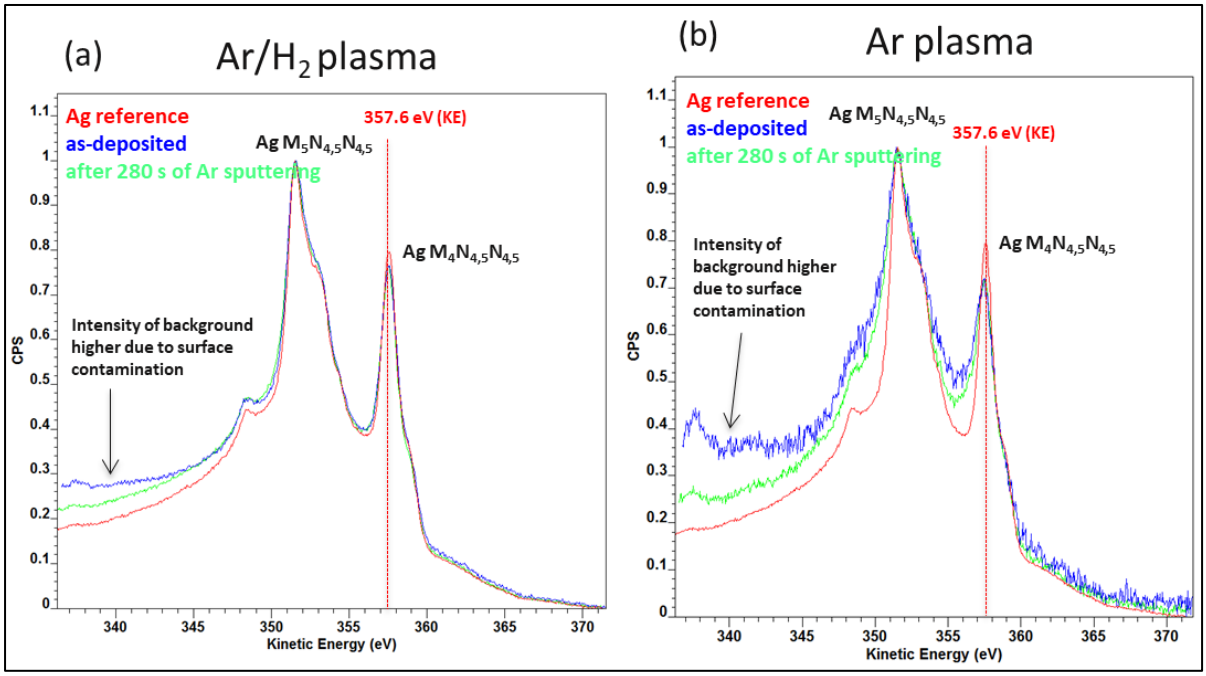


Figure 55: High resolution Ag MNN spectra of Ag thin films synthetized with (a) Ar/$H_2$ plasma and (b) Ar plasma. Each spectrum, compared with the Ag reference (red line), was recorded at t=0 (in blue) and after 280s of Ar sputtering (in green).

Finally, the third parameter investigated and calculated is the modified Auger parameter α'. Figure 56 presents all α' values calculated for the samples discussed above. When compared with the data from literature presented in Table 21, the low Auger parameter before sputtering is an indication of the remaining precursor, surface contamination or the oxidized silver surface for the as-deposited film. In the bulk, after 280 s of Ar etching, values closer to the Ag foil metallic reference are obtained for the two different depositions. However, Ag layer synthetized under the presence of Ar plasma alone presents a lower value of Auger parameter and the Ar/$H_2$ plasma enhances the metallic nature of Ag highlighted by a α' closer to the Ag foil reference. This highlights again the enhanced reduction reaction of silver precursor thanks to hydrogen species.

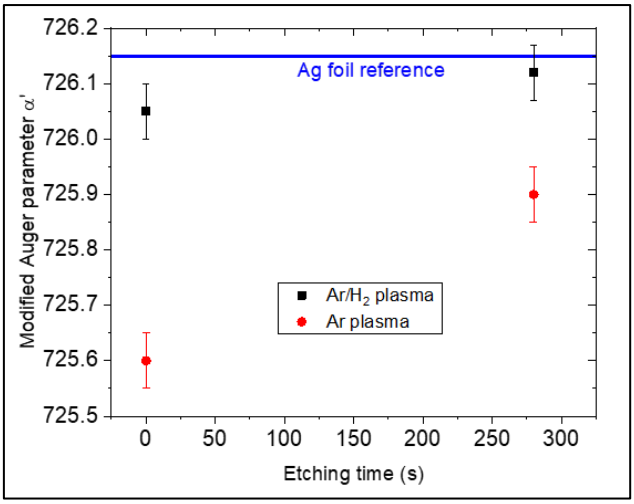


Figure 56: Modified Auger parameter (α') of Ag thin films synthetized with $Ar/H_2$ plasma (black square) or Ar plasma (red disks) for different etching times (0 and 280). The blue line corresponds to a reference Ag foil (oxidation state of 0). The error bars correspond to the experimental error linked to the spectra acquisition step size.

The main conclusion of the chemical investigation is that the presence of $H_2$ in the plasma is needed to enhance the reduction reaction of silver precursor molecule by lowering mainly the carbon amount in the film through the creation of high hydrogen radical reactive species compared to less reactive Ar radicals.

### III.3.2.2. Distance *d* grid-substrate and RF plasma power $P_{dep}$

The ALD parameters studied in order to optimize the plasma conditions needed for the silver deposition process are the **distance substrate-grid *d*** and the **RF plasma power $P_{dep}$**, as exposed in Table 22.

| Parameters | Symbol | Units | Range | Optimum |
|---|---|---|---|---|
| **Distance substrate-grid** | *d* | cm | 1, 2, 4 | * |
| **RF plasma power** | $P_{dep}$ | W | 50, 100 | * |

Table 22: List of ALD parameters studied for the optimization of the plasma conditions needed for the silver deposition process. *: these two parameters need to be correlated in order to have the same efficiency of the plasma source.

In order to have the same efficiency of the plasma source, it is obvious to correlate *d* and $P_{dep}$. They influence the quantity of radicals arriving on the substrate and needed for the reduction reaction of the precursor. Moreover, the grid is used as a bottom electrode and defines the plasma chamber.

Figure 57 illustrates the influence of the substrate-grid distance on the thickness of the silver films as a function of the position on the silicon substrate compared to the inlet for two RF plasma power values. For both RF plasma power $P_{dep}$, it appears that the grid-substrate distance *d* has a very slight influence on the deposition thickness. Indeed, at a $P_{dep}$ of 50 W, the thickness varies between 6 and 10 nm. We notice the same weak influence at a $P_{dep}$ of 100 W (variation between 8 and 11 nm). As a conclusion, the grid-substrate distance correlated to the RF plasma power are not parameters as significant as expected, but we decided to keep ***d* = 1 cm** and **$P_{dep}$ = 100 W** to generate a large enough amount of radicals. These conditions presumably favor a uniform cross-flow between the lateral flow of the Ag precursor and the vertical flow of H radicals.

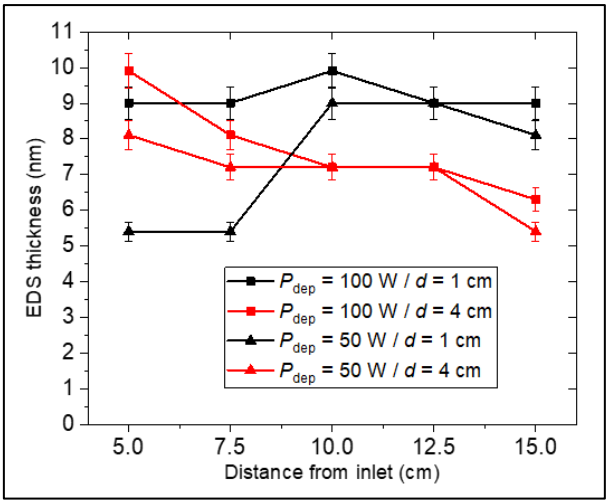


Figure 57: Influence of the distance *d* between the plasma grid and the substrate on the thickness of the silver films determined by EDS vs. the position on the Si substrate compared to the inlet for two different RF plasma power $P_{dep}$ 50 W and 100 W. The chamber temperature is kept at 130°C and the hot source temperature at 100°C.

### III.3.3. Influence of the chamber and hot source temperatures: $T_{ch}$ and $T_{hs}$

The chamber temperature $T_{ch}$ directly affects the number and type of reactive sites present on a surface and then the preferred reaction mechanism that occurs. During the deposition of metal films on oxide layers, as mentioned before, a high temperature engenders a formation of disconnected particles while a lower temperature, due to the reduction of the migration of metal atoms on the surface, is expected to lead to a more compact film. In order to investigate that, we have performed an optimization of the chamber temperature at two different hot source temperatures $T_{hs}$, 90 and 100°C, with the aim to decrease the chamber temperature by decreasing the one of the hot source. Table 23 gives the list of ALD parameters studied in order to optimize $T_{ch}$ at two hot source temperatures needed for the silver deposition process and the optimum values obtained.

| Parameters | Symbol | Units | Range | Optimum |
|---|---|---|---|---|
| **$T_{ch}$ at $T_{hs}$ = 100°C** | $T_{ch}$ | °C | 120, 130, 140, 150, 160 | 130 |
| **$T_{ch}$ at $T_{hs}$ = 90°C** | $T_{ch}$ | °C | 100, 110, 120, 140 | 110 |

Table 23: List of ALD parameters studied for the optimization of the chamber temperature needed for the silver deposition process.

#### III.3.3.1. Optimization of the chamber temperature $T_{ch}$ for the hot source $T_{hs}$ of 100°C

During the preliminary investigation of the PE-ALD of silver, exposed in previous section III.2., we have found a process window ranging from 100 to 140°C for the chamber temperature. Based on that, we have focused our study in a temperature range from 120 to 160°C with a fine variation of the temperature.

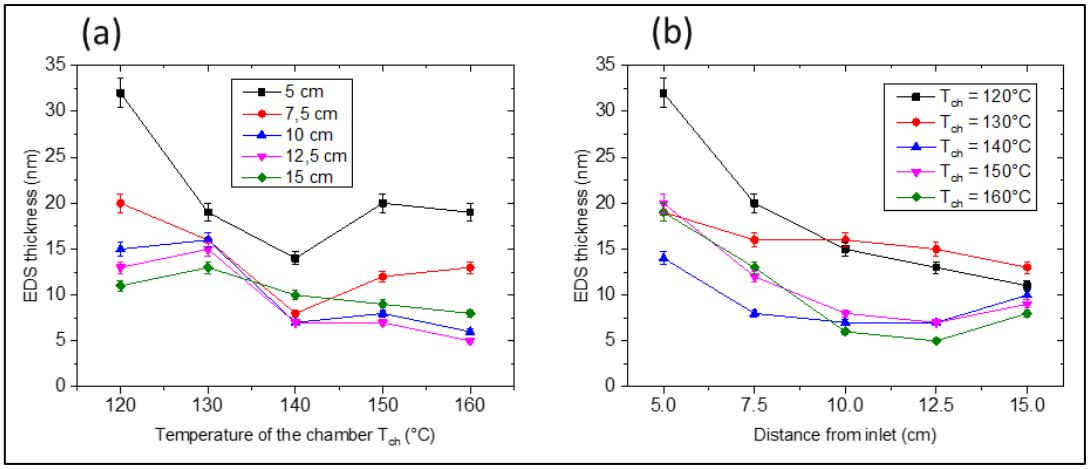


Figure 58: Influence of the chamber temperature $T_{ch}$ on the EDS thickness of Ag films deposited on Si at different position, plotted (a) as a function of the chamber temperature $T_{ch}$ and (b) as a function of the positions on the Si substrate from the inlet. The hot source temperature is kept at 100°C and the deposition corresponds to 400 ALD cycles.

Figure 58 shows that the EDS thickness is highly dependent on the chamber temperature. A better film uniformity (variation of less than 15% over 15 cm) has been obtained at a chamber temperature of 130°C. This temperature was determined as the optimum one for the chamber deposition temperature at a hot source temperature of 100°C.

At this optimum temperature, we have studied the thickness as a function of the number of deposition cycles, from 200 to 1800 (Figure 59).

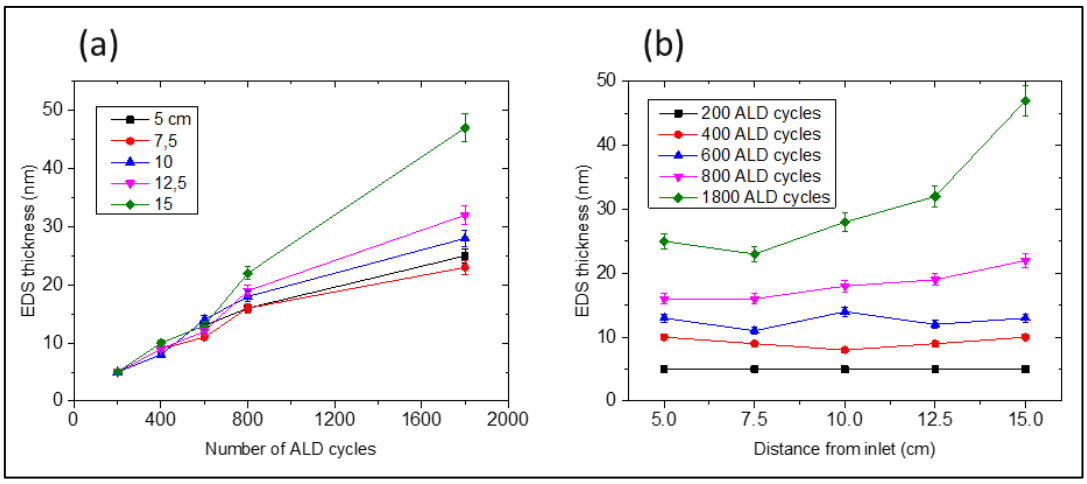


Figure 59: Influence of the number of ALD cycles on the EDS thickness of Ag films deposited on Si at different position, plotted (a) as a function of the number of cycles and (b) as a function of the positions on the Si substrate from the inlet. The studies were performed at the optimum temperatures $T_{ch}$ = 130°C/$T_{hs}$ = 100°C.

The thickness increases linearly with the number of deposition cycles but then presents a strong non-uniformity after 600 ALD cycles. This is probably due to a saturation of the precursor on the surface, maybe caused by its non-constant exposure in the reactor. Another explanation may be the decrease of the hot source fill level. [223] We have then extracted the GPC for cycles below 600, due to the non-linear behavior. The GPC varies slightly from 0.015 to 0.0225 nm/cycle as a function of the position all along the wafer which proves the uniform self-saturated ALD regime.

Figure 60 (a) to (d) shows the corresponding SEM images of silver thin films deposited after varying the number of deposition cycles from 200 to 800 at temperatures $T_{ch}$ = 130°C/$T_{hs}$ = 100°C. As we can see, after 200 cycles, the film is made of small and spaced nanoparticles and when we increase the number of cycles, the particles begin to get bigger and closer. A more detailed investigation of the nanoparticle morphology with a quantitative analysis is made in the next chapter 4.

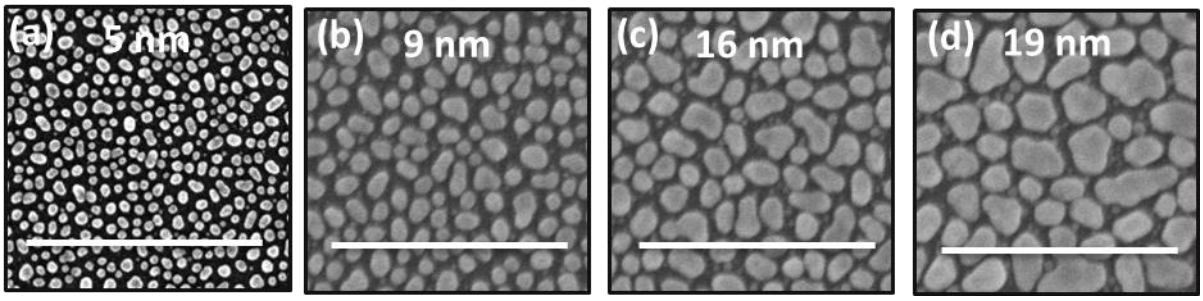


Figure 60: Scanning Electron Micrographs of Ag thin films deposited on silicon at the center of the substrate (10 cm from inlet) after a varying number of cycles (a) 200 cycles, (b) 400 cycles, (c) 600 cycles and (d) 800 cycles. The values on the images refer to the thickness of the films determined by EDS and the scale bars represent 500 nm. The studies were performed at the optimum temperatures $T_{ch}$ = 130°C/$T_{hs}$ = 100°C.

### III.3.3.2. Optimization of the chamber temperature $T_{ch}$ for the hot source $T_{hs}$ of 90°C

We have performed the same study of the optimal chamber temperature at a hot source temperature of 90°C. We have reduced this temperature compared to the previous study with the aim to avoid the migration of Ag atoms on the surface and obtain a more continuous film, as explained during the preliminary investigation in section III.2.1.

Figure 61 shows that the optimum chamber temperature seems to be 120°C since it presents a better uniformity at a hot source temperature of 90°C. However, as seen on the SEM images of silver films presented in Figure 62, we notice a better coverage and a more continuous film at a chamber temperature of 110°C instead of 120°C for a hot source temperature of 90°C.

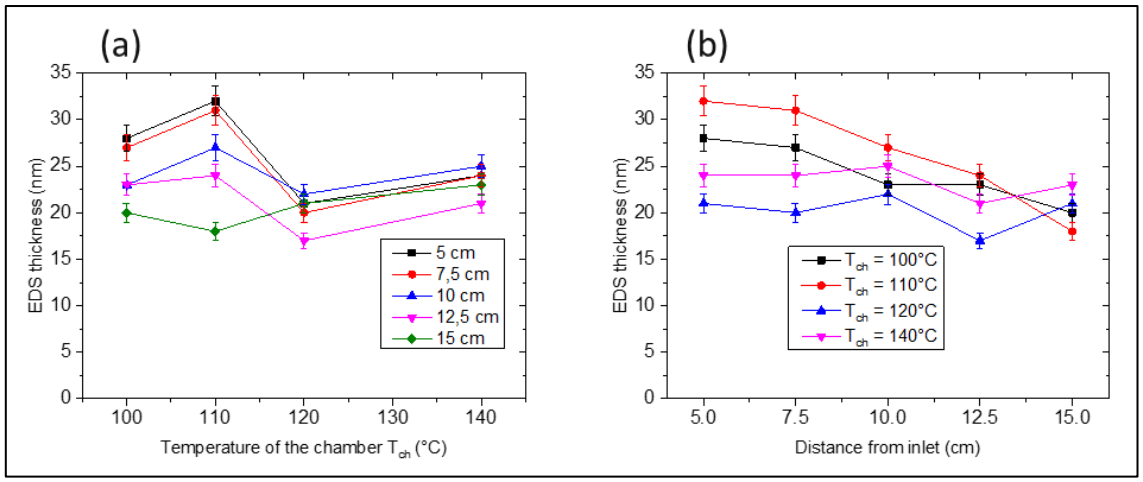


Figure 61: Influence of the chamber temperature $T_{ch}$ on the EDS thickness of Ag films deposited on Si at different position, plotted (a) as a function of the chamber temperature $T_{ch}$ and (b) as a function of the positions on the Si substrate from the inlet. The hot source temperature is kept at 90°C and the deposition corresponds to 400 ALD cycles.

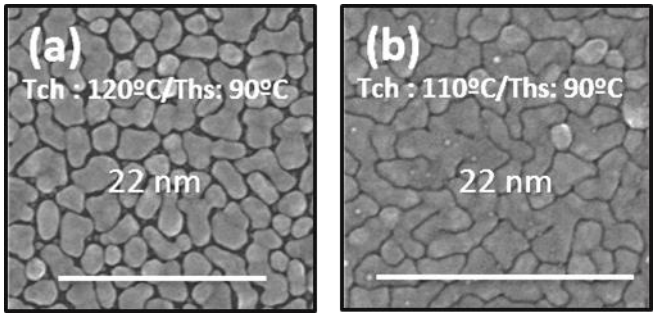


Figure 62: Scanning electron micrographs of silver films deposited on Si (with native oxide) after 400 ALD cycles at (a) $T_{ch}$ = 120°C/ $T_{hs}$ = 90°C and (b) $T_{ch}$ = 110°C/ $T_{hs}$ = 90°C measured at the same position on the wafer. The values on the images refer to the thickness of the films determined by EDS and the scale bars represent 500 nm.

At 110°C, we have studied the thickness as a function of the number of deposition cycles, from 200 to 600 (Figure 63). We observe a monotonic increase of the thickness as a function of the number of cycles, and this increase is uniform along the sample. This behavior is a strong indication of a deposition driven by surface reactions, as expected for ALD. Regarding the GPC, it varies from 0.065 to 0.040 nm/cycle. The GPC is remarkably higher at the inlet of the reactor and decreases when the distance from inlet increases. This GPC dependence on the distance on the wafer may be explained by a non-optimum reactor geometry.

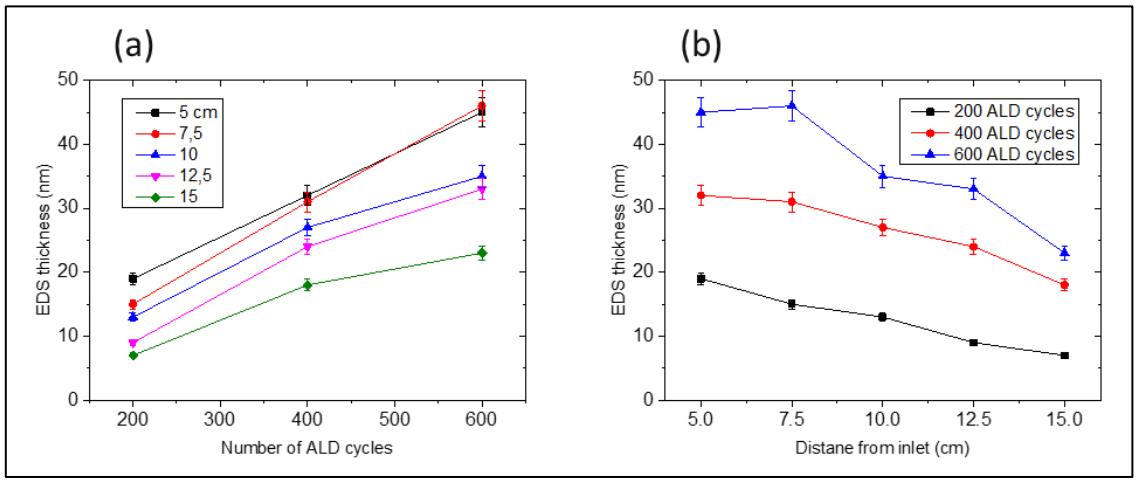


Figure 63: Influence of the number of ALD cycles on the EDS thickness of Ag films deposited on Si at different position, plotted (a) as a function of the number of cycles and (b) as a function of the positions on the Si substrate from the inlet. The studies were performed at the optimum temperatures $T_{ch}$ = 110°C/$T_{hs}$ = 90°C.

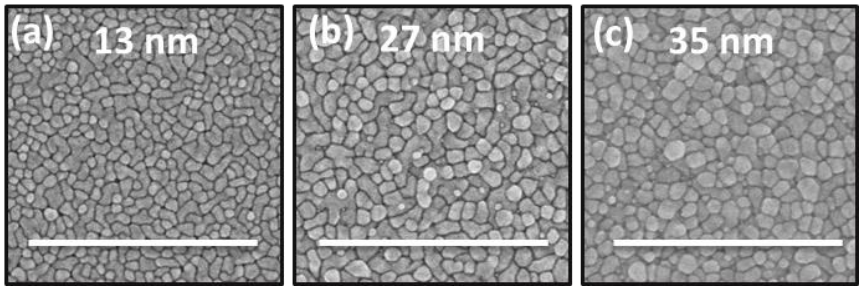


Figure 64: Scanning Electron Micrographs of Ag thin films deposited on silicon at the center of the substrate (10 cm from inlet) after a varying number of cycles (a) 200 cycles, (b) 400 cycles and (c) 600 cycles. The values on the images refer to the thickness of the films determined by EDS and the scale bars represent 500 nm. The studies were performed at the optimum temperatures $T_{ch}$ = 110°C/$T_{hs}$ = 90°C.

Figure 64 (a) to (c) illustrates the SEM images of silver thin films deposited after varying the number of deposition cycles from 200 to 600 at temperatures $T_{ch}$ = 110°C/$T_{hs}$ = 90°C. Already after 200 ALD cycles, the morphology of the film is made of dense islands and the film becomes more continuous when the deposition cycle number increases.

### III.3.3.3. Comparison of the two couples of temperatures $T_{ch}$ / $T_{hs}$ in terms of morphology and electrical properties

When comparing the two couples of temperatures $T_{ch}$ = 130°C / $T_{hs}$ = 100°C and $T_{ch}$ = 110°C / $T_{hs}$ = 90°C deposited at the same number of ALD cycles (Figure 60 (c) and Figure 64 (c), respectively), we see that the deposition performed at higher temperatures reveals a film made of nanoparticles which are separated, contrary to the film deposited at lower temperatures which is more uniform and dense. This observation confirms that the lower temperatures favored the formation of a more continuous film.

Regarding the **electrical properties**, for depositions performed at higher temperatures **$T_{ch}$ = 130°C/ $T_{hs}$ = 100°C** [1], the silver films show electrical conductivity after 1800 cycles, but the value is very week, $2.46\times10^{-5}$ S/cm for a thickness of 47 nm. This is due to the presence of nanoparticles which only begin to coalesce at very high number of ALD cycles at this high temperature.

If we decrease the temperatures, **$T_{ch}$ = 110°C/ $T_{hs}$ = 90°C**, we succeeded in improving the value of the critical thickness. Unfortunately, the conductivity is still very low, $7.12\times10^{-2}$ S/cm for a silver film of 22 nm. In contrast to the deposition made at higher hot source temperature, the percolation phenomenon does not occur in the same way with the number of cycles since the migration of the silver atoms is different. However, here again, as for section III.2.4., problem of non-reproducibility has been observed.

## III.3.4. Conclusion

We have seen that the couple of temperatures $T_{ch}$ = 110°C/ $T_{hs}$ = 90°C gives quasi-continuous films but with a very low conductivity. Moreover, the deposition made at such low temperature are strongly non-reproducible, which we attribute to a difficult precursor evaporation and exposure for such a low hot source temperature. At $T_{ch}$ = 130°C / $T_{hs}$ = 100°C, a very high number of ALD cycles is needed to give continuous and conductive films. In optimum conditions, the Ag precursor pulse length $t_{pr}$ is 5 s, while the hydrogen plasma pulse $t_{pl}$ is 3 s. The purge length after the metal precursor $t_{pu1}$ is 5 s and after the plasma exposure $t_{pu2}$ is 10 s. These parameters are then used in order to more carefully investigate and demonstrate the large-scale uniform deposition of Ag NPs. Moreover, a more detailed study of the growth mechanism based on the particle morphology is presented in chapter 4. The optimum parameters are given in Table 24 and are then used in the future experiments, except if define otherwise in the caption of the figures.

[1] Here we point out that the chamber temperature used in the preliminary investigation of the ALD parameters cannot be directly compared to the chamber temperature used in this section due to a change in the position of the temperature sensor between each set of experiments. We evaluate the difference in temperature between the current set of experiment and the one reported in the previous part to about 20°C

| $T_{ch}$ | $T_{hs}$ | $H_{2pl}$ | $P$ | $Ar_{pr}$ | $Ar_{pl}$ | $Ar_{ch}$ | $t_{pr}$ | $t_{pu1}$ | $t_{pl}$ | $t_{pu2}$ | $d$ | **Reactor pressure** |
|---|---|---|---|---|---|---|---|---|---|---|---|---|
| (°C) | (°C) | (sccm) | (W) | (sccm) | (sccm) | (sccm) | (s) | (s) | (s) | (s) | (cm) | (mbar) |
| 130 | 100 | 20 | 100 | 300 | 300 | 100 | 5 | 5 | 3 | 10 | 1 | 3 |

Table 24: Optimum parameters used for the study of the large-scale uniform deposition of Ag NPs in the next sections.

## III.4. Conclusion

In this chapter, the standard PE-ALD parameters and their impact on Ag film thickness and conductivity have been screened. We have confirmed the state-of-the-art of Ag ALD-deposited on oxide surfaces with the obtention of Ag films made of discrete islands for thickness lower than typically 60 nm. Due to a deficiency of the precursor injection system, a first upgrade through modification of the geometry of the gas-valving precursor injection system has been performed and enabled a strong improvement of the deposition uniformity. In a preliminary investigation, we have shown that the deposition temperatures, argon flows, plasma conditions and sequence times had a strong impact on the synthesis of Ag films. The study has been achieved by following the film thickness uniformity over a large surface area (8-inch substrate) with the aim to obtain an ALD self-saturated regime. The deposition temperature plays the more critical role on the film thickness uniformity and gives an optimum temperature range from 100°C to 140°C. In order to avoid condensation of the precursor, the Ag precursor temperature needs to be at least 10°C lower than the one of the chamber. The argon flows, both in the plasma head and in the process lines, had a stronger influence at lower temperatures due to the more challenging control of the ALD parameters. We have also seen that, under selected parameters and reduced temperatures, interesting transformation of the morphology, with more dense islands have been obtained. But, due to the non-appropriate evaporation conditions of the Ag precursor depositions made at such low temperatures, the depositions were strongly non-reproducible. A following fine development based on these preliminary results highlighted that the ALD sequence times played a major role in order to ensure a saturation of the substrate surface. The optimum ALD sequence times was found to be 5s/5s/3s/10s and a deviation of the times conducts to a decrease of film thickness uniformity. More precisely, this led to a CVD-like deposition when the purge times were too low and an under-saturated regime when the pulse times were not high enough. We have also proved that reactive hydrogen radical species created by the plasma are mandatory in order to obtain pure silver in metallic state. A film made of separated nanoparticles have been obtained at a chamber temperature of 130°C and a hot source temperature of 110°C and low electrical conduction was obtained for quite thick films (conductivity of $2.46\times10^{-5}$ S/cm for a thickness of 47 nm). We have also confirmed that reducing the chamber temperature from 130°C to 110°C leads to an interesting transformation of the morphology, with the formation of continuous and slightly conductive Ag thin films, probably due to the reduced migration of the metal atoms on the surface. The obtained resistivity for a film of 20 nm is however very high (10 Ω·cm or conductivity of $7.12\times10^{-2}$ S/cm), which is not matching with electrical properties required in the microelectronics field. Moreover, reducing further the temperature is a challenge since it requires to reduce the precursor temperature, which is not favored for appropriate evaporation conditions and lack of reproducibility has been highlighted.

Based on the above process optimization, the next chapter 4 focuses on Ag nanoparticle films and expose the large-scale deposition and understanding of the growth mechanism using standard PE-ALD process.

# Chapter 4

# Large-scale deposition and growth mechanism of silver nanoparticles by plasma-enhanced atomic layer deposition

In the previous chapter 3, a detailed screening of the ALD parameters have been performed. In this chapter, based on the optimized parameters, the uniformity of the deposition is investigated over a large surface area (8-inch substrate) in order to understand the underlying growth mechanism of silver films. Silver nanoparticles are of strong interest for plasmonic applications, which require a very good control of the size and shape of the particles. Most of the published research has investigated the influence of the deposition parameters on the film morphology at a given position, and the overall uniformity of the deposition is not often demonstrated quantitatively. Here we demonstrate that the full analysis of the morphology and the uniformity gradient provides more information than the more commonly investigated average thickness alone. This uniformity is quantified using different morphological criteria, i.e. morphological and EDS film thickness, size, density and aspect ratio of Ag NPs as well as film coverage, both at the center position of an 8-inch substrate and, more originally, the gradient over a 10 cm distance on the substrate. To the same end, the elemental composition and crystalline structure is determined. We also prove that the silver nanostructures can be tailored by the deposition parameters. For Ag deposition, the literature highlights that the exact deposition mechanism is not yet fully understood and leads to a lack of control of the nanostructure morphology on a large scale. In this part, in order to better understand the growth mechanism of Ag NPs, more detailed studies are undertaken within the first deposition stages (first 800 ALD cycles). An empirical model is finally proposed and directly compared with the experimental results with a view to understanding the Ag NP growth mechanism.

---

This chapter is based on the publication *S. Wack, P. Lunca Popa, N. Adjeroud, J. Guillot, B. R. Pistillo, R. Leturcq,* Large-Scale Deposition and Growth Mechanism of Silver Nanoparticles by Plasma-Enhanced Atomic Layer Deposition, *J. Phys. Chem. C*, **2019**, 123, 44, 27196-27206.

## IV.1. Demonstration of the large-scale uniform deposition of silver nanoparticles

Most of the published research have investigated the influence of the deposition parameters on the film morphology at a given position, but the overall uniformity of the deposition is not often demonstrated quantitatively. [26, 41, 45, 48] Here we analyze in detail the uniformity of the deposition in terms of deposition thickness, but also in terms of film morphology, in order to understand the deposition mechanisms and provide recipes for a higher control of the morphology.

As exposed in chapter 2, section II.2.2.3., the quantitative analyses have thus been performed with respect to the following morphological criteria determined by SEM image treatment or direct measurements:

- EDS equivalent thickness
- Ag NPs size
- Coverage percentage
- Density
- Morphological thickness
- Aspect ratio

The film quantitative analyses correspond to the longitudinal variation (i.e. in the precursor flow direction). We not consider the transverse variation (i.e. perpendicular to the precursor flow) since it showed a maximum variation of 5% for the thickness of the film and the nanoparticle diameter, independent of the deposition conditions. (see Figure 27 in chapter 2)

Based on these quantitative studies, we have used the method presented in chapter 2, section II.2.2.5. in order to quantify the uniformity of the Ag deposition. Basically, we have plotted the value at the center of the wafer and the gradient of the quantities as a function of the investigated parameter. We base our study on the results obtained in the optimization of the deposition parameters part (III.3.). Table 25 reminds the parameters that have been used for all the experiments presented in this chapter, except if defined otherwise in the captions of the figures.

| $T_{ch}$ | $T_{hs}$ | $H_{2pl}$ | $P$ | $Ar_{pr}$ | $Ar_{pl}$ | $Ar_{ch}$ | $t_{pr}$ | $t_{pu1}$ | $t_{pl}$ | $t_{pu2}$ | $d$ | Reactor pressure |
|---|---|---|---|---|---|---|---|---|---|---|---|---|
| (°C) | (°C) | (sccm) | (W) | (sccm) | (sccm) | (sccm) | (s) | (s) | (s) | (s) | (cm) | (mbar) |
| 130 | 100 | 20 | 100 | 300 | 300 | 100 | 5 | 5 | 3 | 10 | 1-4 | 3 |

Table 25: Optimum parameters used for the study of the large-scale uniform deposition of Ag NPs.

### IV.1.1. Influence of the precursors pulse and purge times on the uniformity of the deposition

The goal of this part is to investigate the influence of the precursors pulse and purge times on the uniformity of the morphology of the silver film and use this information for investigating the deposition mechanism.

#### IV.1.1.1. Influence of the pulse times

Figure 65 illustrates the influence of the Ag precursor exposure time $t_{pr}$ and Figure 66 the one of the plasma pulse time $t_{pl}$ on the quantitative morphological parameters determined by SEM image treatment. Regarding the EDS thickness, as already demonstrated in chapter 3, the substrate surface is saturated by the precursors after 5 s of Ag precursor exposure (Figure 65 (a)) and 3 s of plasma

exposure (Figure 66 (a)). This is highlighted by the presence of a plateau in both cases, typical of a saturated growth. Here, we confirm that these precursors pulse times favor a more uniform film deposition. A negative gradient, i.e. thicker film at the inlet rather than the outlet, but close to zero in both cases have been obtained. The morphological thickness follows the same trend than the EDS equivalent thickness when increasing $t_{pl}$ (Figure 66 (d)), even in terms of uniformity. For silver precursor exposure, it is both the morphological thickness ((Figure 65 (d)) and film coverage (Figure 65 (c)) which increases as the EDS thickness, with a more uniform film for higher exposure time and a saturated regime after 3 s of exposure leading to a constant aspect ratio (taking into account the error bars in Figure 65 (e)). The plot of the NP size at the center and gradient as a function of the silver precursor pulse time $t_{pr}$ (Figure 65 (b)) shows that not only the thickness but also the nanoparticle size is highly dependent on the silver precursor pulse time. Here we see that an exposure time shorter than 5 s strongly favors a smaller particle diameter, which confirms the under-saturated regime; after saturation, the nanoparticles become larger and more uniform in size. The exponential decrease of the density of Ag NPs (Figure 65 (f)) agrees the average NP diameter variation: a more uniform and less dense film is obtained due to the increase in size of the NPs and their sintering. When it comes to the influence of the plasma pulse time $t_{pl}$, on the NP size, more surprisingly, the nanoparticles become larger with longer pulse times, with no apparent saturation (Figure 66 (b)): between $3 \leq t_{pl} \leq 10$ s, there is a very slight variation of EDS thickness (less than 10%), i.e. the quantity of material, but a significant one in particle diameter (almost 45%). The expansion of the aspect ratio (Figure 66 (e)) and film coverage (Figure 66 (c)) follows the one of the particle size which means that flat NPs are produced. The NP density on the surface decreases with the increasing $t_{pl}$ (Figure 66 (f)). As discussed later (section IV.2.3.), these trends might be caused by a ripening process, due to the longer exposure of the film to the plasma. [29, 74, 86]

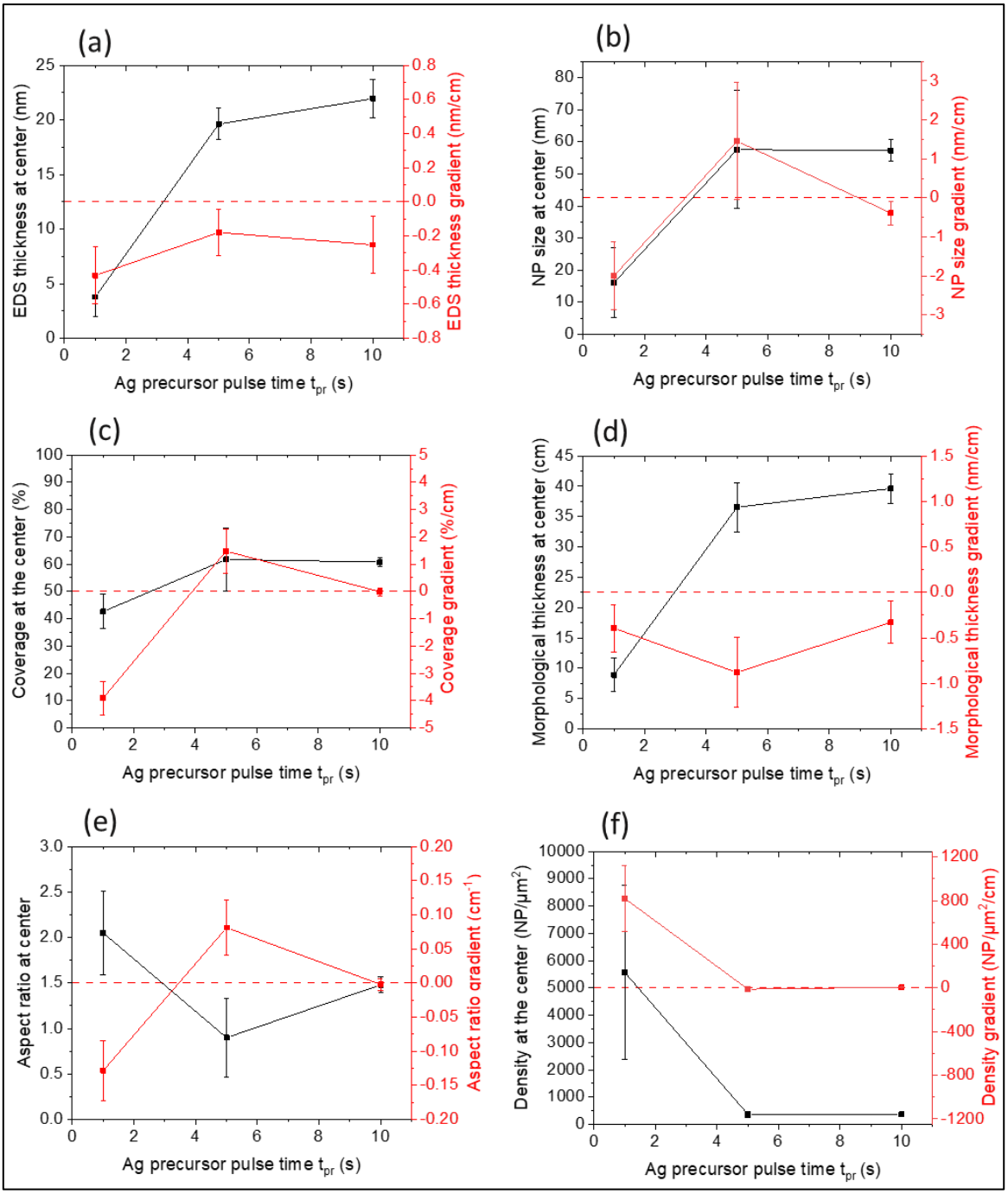


Figure 65: Plot of the quantitative parameter (a) EDS thickness, (b) NP size, (c) coverage in percentage, (d) morphological thickness, (e) aspect ratio and (f) density of NP vs. the silver precursor pulse time $t_{pr}$. For each case, we have plotted the average value at the center of the studied parameter (black) and the gradient associated (red). The values have been taken on the whole Si wafer from inlet to outlet in order to check the uniformity of the silver deposition.

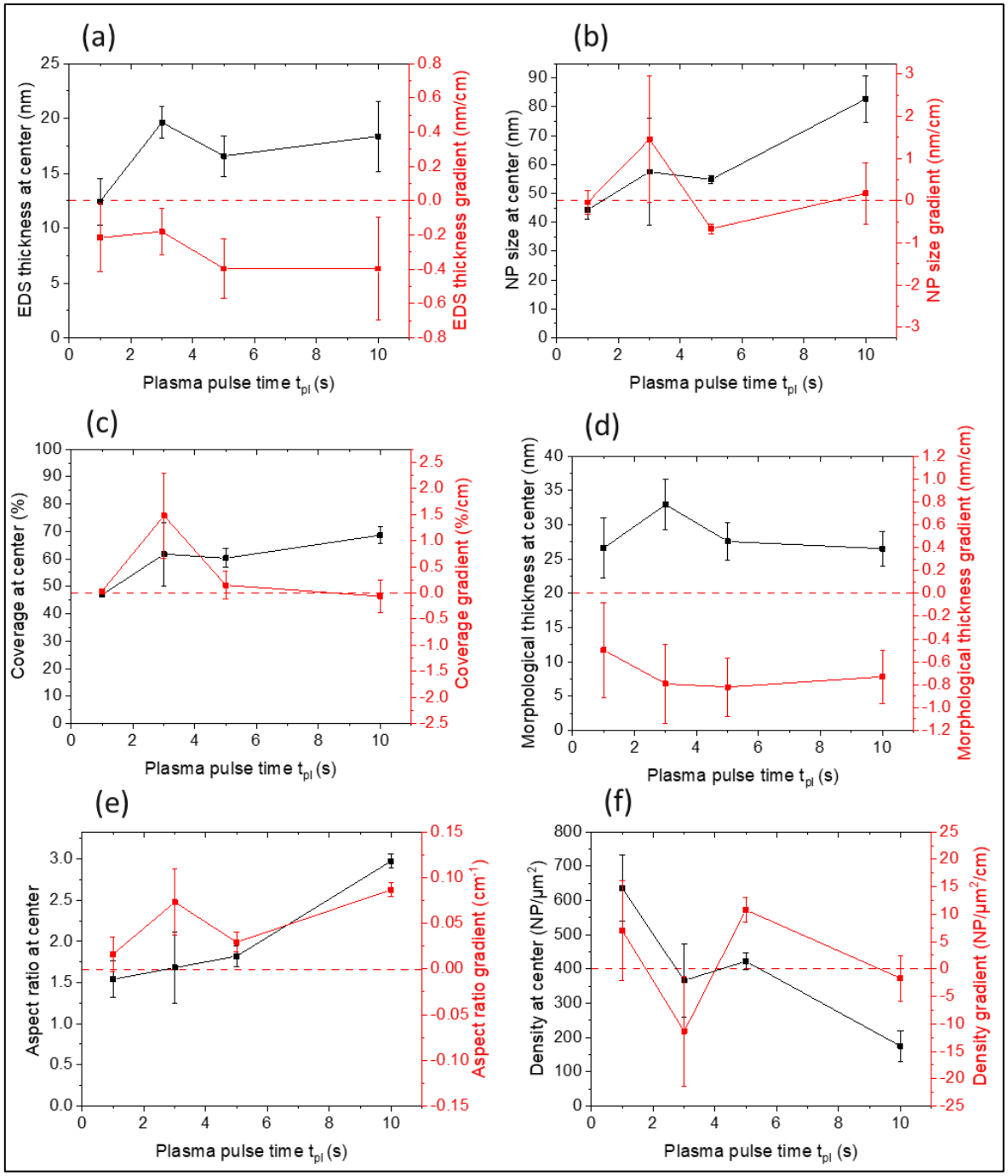


Figure 66: Plot of the quantitative parameter (a) EDS thickness, (b) NP size, (c) coverage in percentage, (d) morphological thickness, (e) aspect ratio and (f) density of NP vs. the plasma pulse time $t_{pl}$. For each case, we have plotted the average value at the center of the studied parameter (black) and the gradient associated (red). The values have been taken on the whole Si wafer from inlet to outlet in order to check the uniformity of the silver deposition.

### IV.1.1.2. Influence of the purge times

The purge times influence the type of deposition: ALD or CVD regime. Figure 67 and Figure 68 show the influence of, respectively, the purge time $t_{pu1}$ after silver precursor pulse and the purge time $t_{pu2}$ after plasma pulse, on the quantitative morphological parameters extracted from image treatment.

The EDS equivalent thickness variation confirms that a 5-s purge time after Ag pulse (Figure 67 (a)) and a 10-s purge time after plasma pulse (Figure 68 (a)) favors a more uniform film deposition, highlighted by a positive gradient closer to zero even if the film is thicker at the outlet. At higher $t_{pu1}$, a thinner and much less uniform film is obtained due to the probable thermal desorption occurring. The coverage remains constant from $t_{pu1}$ of 5 s (Figure 67 (c)) and $t_{pu2}$ of 2 s Figure 68 (c)) to higher purge times and more uniform at the optimum purge time. These two features lead to a morphological thickness following the one determined by EDS (Figure 67 (d) and Figure 68 (d)). NP size decreases when the purge time increases for $t_{pu1}$ > 5s and $t_{pu2}$ > 2s. The Ag deposition is less and less uniform in terms of NP size when both $t_{pu1}$ ((Figure 67 (b)) and $t_{pu2}$ (Figure 68 (b)) increase, as the gradient is much and much far from 0 and its positive sign suggests bigger particles at the outlet position at each purge time. This degradation of the uniformity with the purge time is also seen through the evolution of the NP density (Figure 67 (f) and Figure 68 (f)). The negative gradient suggests also less dense particle at the outlet independently of the purge time. The correlation between the morphological thickness (or particle height) and particle diameter leads to an aspect ratio with no specific variation as function of the times for $t_{pu1}$ (Figure 67 (e)) and a decrease of the value for $t_{pu2}$ (Figure 68 (e)). In both cases, the aspect ratio fluctuates between 1.6 and 2.2 and approaching 2, i.e. close to half-spherical particles, which is also consistent with the Volmer-Weber growth mechanism. This half-spherical morphology of the particles is seen in the inset of Figure 68 (e). For time shorter than 2 s, the higher EDS and morphological thicknesses and the slightly lower film coverage can be explained by the fact that the reactor is not completely purged, and some precursors, i.e. non-reactive Ag precursor and/or hydrogen radicals might remain inside (CVD like) after both $t_{pu1}$ and $t_{pu2}$.

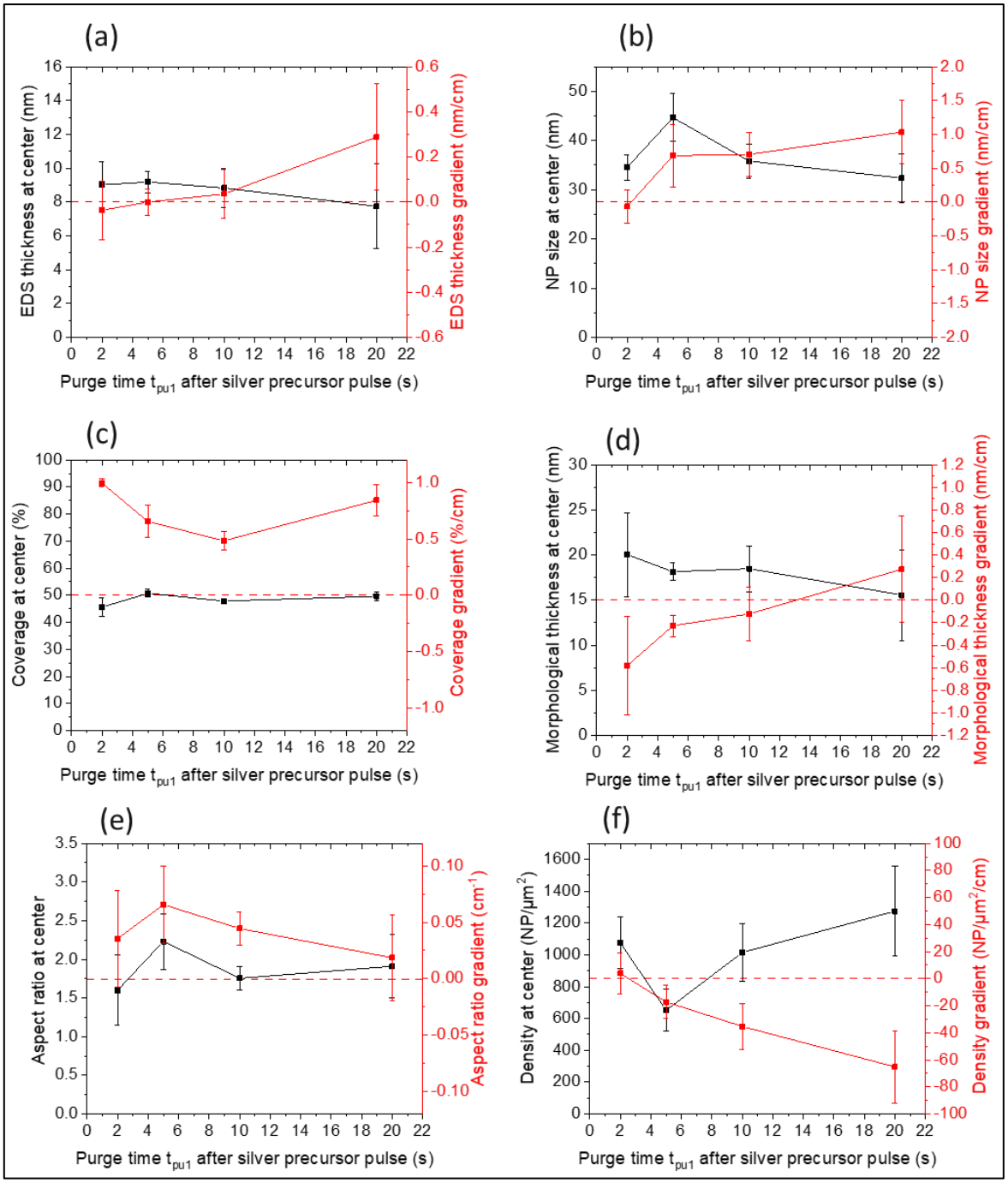


Figure 67: Plot of the quantitative parameter (a) EDS thickness, (b) NP size, (c) coverage in percentage, (d) morphological thickness, (e) aspect ratio and (f) density of NP vs. the purge times $t_{pu1}$ after silver precursor pulse. For each case, we have plotted the average value at the center of the studied parameter (black) and the gradient associated (red). The values have been taken on the whole Si wafer from inlet to outlet in order to check the uniformity of the silver deposition.

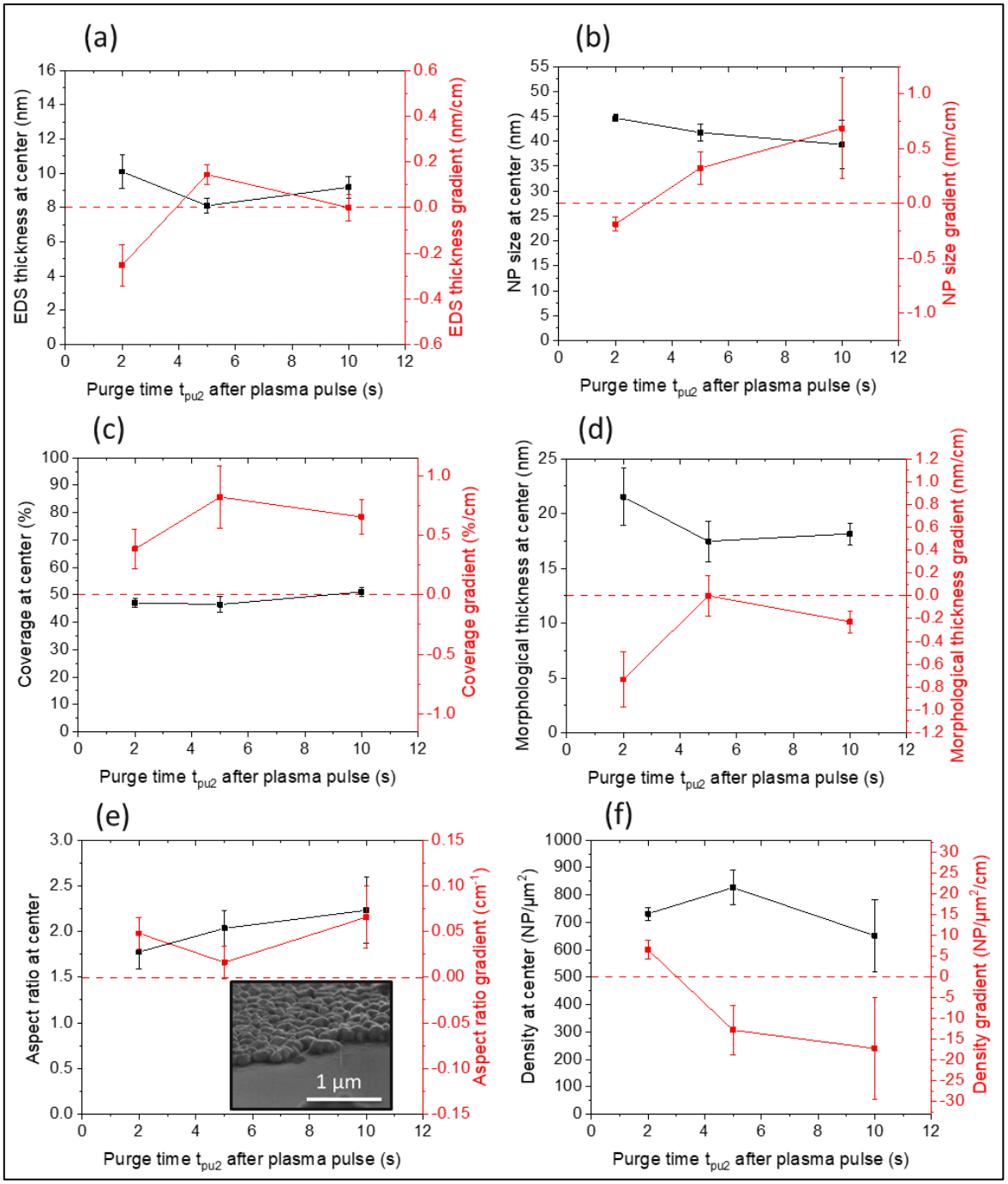


Figure 68: Plot of the quantitative parameter (a) EDS thickness, (b) NP size, (c) coverage in percentage, (d) morphological thickness, (e) aspect ratio and (f) density of NP vs. the purge times $t_{pu2}$ after plasma pulse. For each case, we have plotted the average value at the center of the studied parameter (black) and the gradient associated (red). The values have been taken on the whole Si wafer from inlet to outlet in order to check the uniformity of the silver deposition. The inset in (e) is a *cross*-section scanning electron micrograph of a typical sample with an aspect ratio approaching 2, showing the half-spherical morphology of the particles and the scale bar represents 1 µm.

### IV.1.2. Influence of the number of atomic layer deposition cycles

The uniform deposition of Ag by ALD on a large scale is often not demonstrated, despite requirements in many commercial applications. [26, 48] To the best of our knowledge, there is only one report [45] inspecting the uniformity of the deposition with a quantitative criterion, over a wider surface area (4 cm), but this was restricted to the deposited thickness. Here, we extend this analysis up to 10 cm and to other morphological and structural parameters (see section II.2.2.4.).

In the saturated regime, each new ALD cycle is equivalent to the previous one in terms of the amount of deposited material, and a linear increase of the thickness is expected. [58] The growth per cycle (GPC) is thus an important parameter to help understand the deposition regime and in particular, the linear deposition regime. [39]

In order to investigate the uniformity in terms of film morphology, after performing several depositions varying the number of cycles and based on the study of the SEM micrographs, we have plotted the morphological criterion at the center and the gradient as a function of the number of cycles (Figure 69). The analyses have been carried out on films deposited under saturated growth conditions, as exposed in chapter 3, section III.3.

From 200 to 600 cycles, a monotonic increase of the EDS thickness as a function of the number of cycles is observed along the sample (i.e. thickness variation from the inlet to the outlet). This behavior is a strong indication of a deposition process driven by surface reactions, as expected for ALD. However, after 600 cycles, the thickness is less uniform with a positive gradient. One explanation for this may be the effect of the migration of the atoms from the inlet to the outlet part of the substrate. The non-linear growth and film non-uniformity in ALD have already been noticed in other works. [223, 224] Similar analyses have been performed on the NP size, film coverage, morphological thickness, aspect ratio and density (Figure 69 (b) to (f) and see Figure 27 in chapter 2 for longitudinal direction). The NP size and morphological thickness show a sharp increase as for the EDS thickness, which leads to an increased aspect ratio. A less abrupt positive slope is observed for the film coverage. The nanoparticles density decreases exponentially suggesting the sintering of the Ag NPs. All these observations agree with the island growth or Volmer-Weber mode, as seen in the next sections. Regarding the uniformity of the depositions, the NP size gradient follows the same trend as the one of the EDS thickness. The film coverage gradient also increases which explains that the morphological thickness is much more uniform as a function of the number of cycles. The density is strongly non-uniform for 200 cycles and becomes much more uniform which is related to the merging of the NPs. Overall, the quantitative analyses show that a variation of between 5 and 20% over 10 cm is obtained depending on the morphological parameters in these conditions. This shows the very good uniformity achieved with optimally set parameters.

In order to further compare the deposition regimes achieved, the thickness dependence on the number of cycles is linearly fitted up to 600 cycles, which is the limit of the sample saturating surface reaction; the slope, i.e. the growth per cycle (GPC), and the intercept on the y-axis (thickness offset) is then extracted. The results are presented in Figure 70. The GPC fluctuates between 0.014 and 0.020 nm/cycle as a function of the position all along the wafer but remains close to the experimental error bars. The average value of 0.017 ± 0.004 nm/cycle is 1.8 times lower than that obtained previously

using the same precursors. [41] This discrepancy is not surprising given the challenging control of the deposition conditions of Ag by ALD. Considering the spacing between face-centered cubic (fcc) Ag(111) planes of 0.236 nm, the GPC value suggests the deposition of less than one monolayer of Ag atoms in each cycle. [26] For the future analysis, we focus our study on 400 ALD cycles in order to be well within the saturated surface reaction regime.

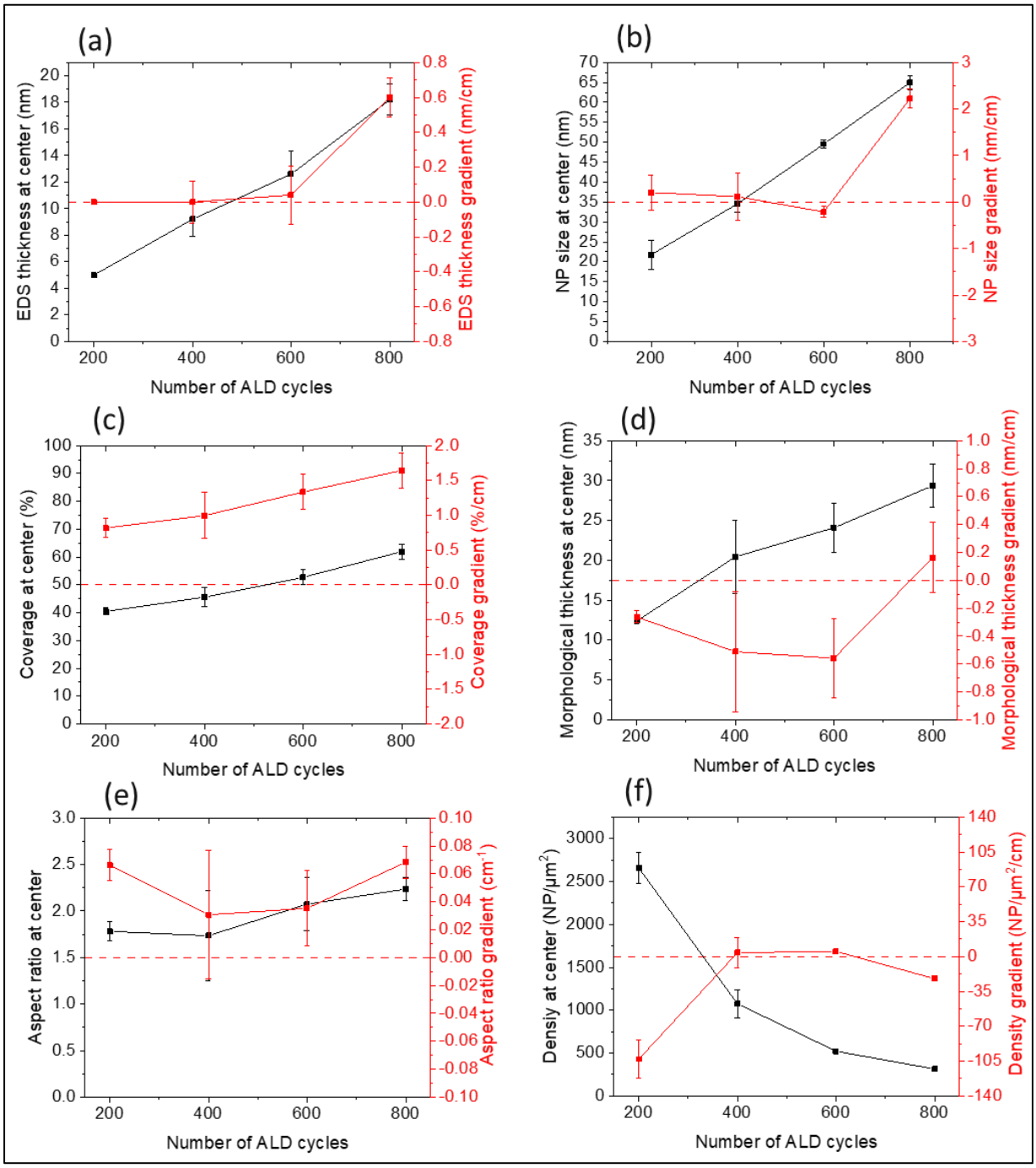


Figure 69: Plot of the quantitative parameter (a) EDS thickness, (b) NP size, (c) coverage in percentage, (d) morphological thickness, (e) aspect ratio and (f) density of NP vs. the number of ALD cycles. For each case, we have plotted the average value at the center of the studied parameter (black) and the gradient associated (red). The values have been taken on the whole Si wafer from inlet to outlet in order to check the uniformity of the silver deposition.

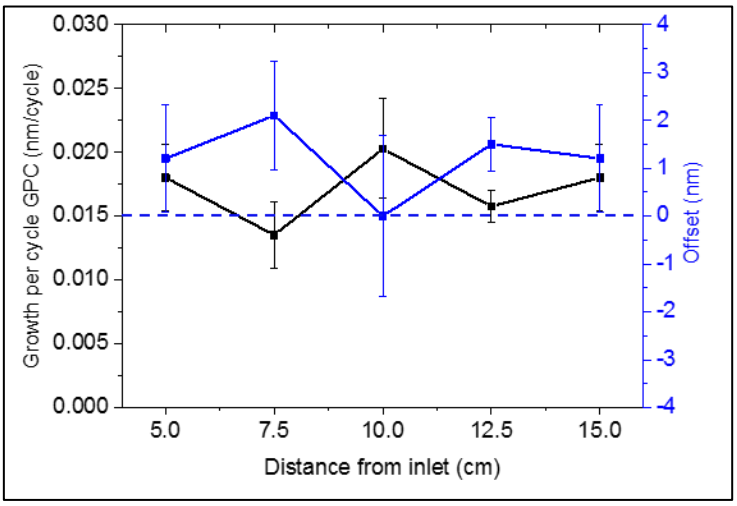


Figure 70: Plot of the growth per cycle rate (in black) and the offset (in blue) of the silver deposition processes for different positions on the Si substrate from the inlet.

### IV.1.3. Influence of the temperature and the plasma conditions on the uniformity of the deposition

In this section, we analyze the influence of the substrate temperature and the plasma conditions, both having a strong influence on the reaction efficiency. However, in an ideal ALD regime, both parameters should not significantly alter the deposition within a range usually called the "process window", i.e. range of temperature and/or plasma conditions where the ALD regime is achieved. Here, we demonstrate that the full analysis of the morphology and the gradients provides more information than the more commonly investigated average thickness alone (presented in section III.3.).

The chamber temperature directly influences the rates of the chemical reactions (precursor with the surface, and reduction) and the mobility of the reactants on the surface. This parameter is also important for the process window where self-limiting growth occurs. The influence of the chamber temperature on the nanoparticle morphology is described in Figure 71.

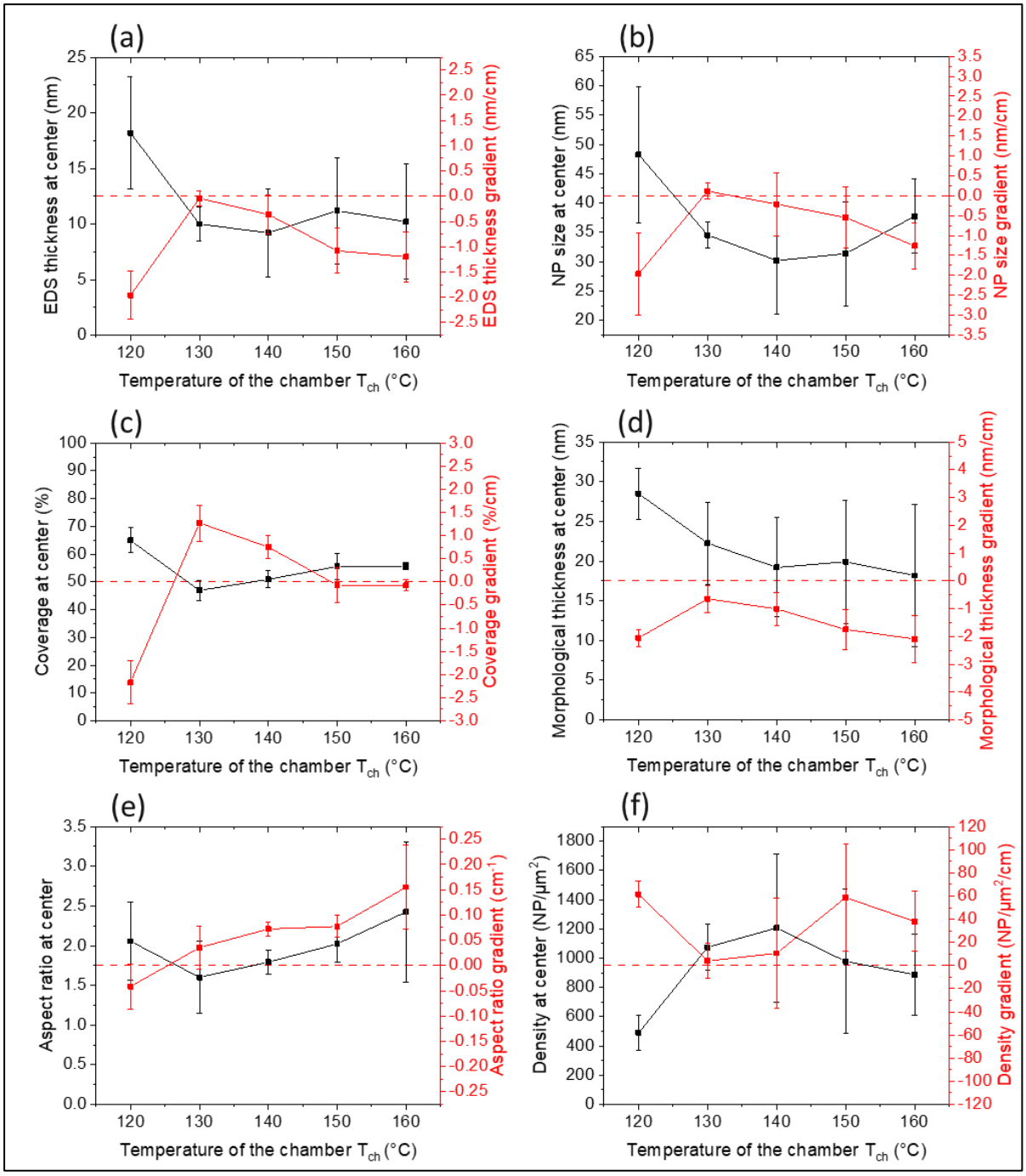


Figure 71: Plot of the quantitative parameter (a) EDS thickness, (b) NP size, (c) coverage in percentage, (d) morphological thickness, (e) aspect ratio and (f) density of NP vs. the temperature of the chamber. For each case, we have plotted the average value at the center of the studied parameter (black) and the gradient associated (red). The values have been taken on the whole Si wafer from inlet to outlet in order to check the uniformity of the silver deposition.

Figure 71 (a) shows that the EDS equivalent thickness of Ag films depends on the chamber temperature being below 130°C, and is then constant up to 160°C. However, at temperatures beyond 140°C, the deposition starts to become non-uniform, with a thicker deposition at the inlet and a thinner deposition at the outlet (negative gradient). This behavior may be due to the early decomposition of the precursor directly at the inlet, and lower amount arriving at the outlet. A negative gradient is also observed at a temperature lower than 130°C, probably due to the re-

condensation of the precursor at the inlet, since the reactor temperature becomes closer to the precursor evaporation temperature (see II. Experimental section). The analysis of the large-scale deposition, and in particular the gradient of the thickness, is thus useful here as it demonstrates the lower effective process window between 130-140°C, which is not anticipated by investigating the average thickness alone.

After doing a statistical particle size distribution of Ag NPs grown at different deposition temperatures, Van den Bruele *et al*. [85] proved that the chamber temperature controls the islands' size and their density, since it is a surface-diffusion dependent parameter. In the present case, the nanoparticle morphology (size and density) is also highly dependent on the chamber temperature (Figure 71 (b-f)). We however point out that the NP morphology is uniform only in the process window of 130-140°C, and the gradient of thickness outside the process window strongly influences the NP size. Indeed, outside this process window, the NP size shows a negative gradient (smaller particles towards the outlet) and the density a positive gradient (larger density towards the outlet). Both observations are consistent with a larger deposition rate at the inlet, as shown in next section, and make a direct correlation of the morphology with the temperature difficult.

One of the main parameters that we identify as critical for obtaining a uniform deposition is the "plasma density". In order to investigate the influence of the plasma conditions, we have varied both the RF power $P_{dep}$ and the distance $d$ between the grid and the substrate and then plotted the value of the quantitative parameter at the center and the associated gradient as a function of the plasma conditions (Figure 72).

The EDS equivalent thickness is slightly impacted by a change of the plasma conditions, as shown by the variation from 8 to 10 nm in Figure 72 (a)). However, as suggested by the gradient closer to 0, the best uniformity is obtained at higher power of 100 W and smaller distance of 1 cm. In these conditions, more uniform film made of bigger nanoparticles combined with higher morphological thickness (or particle height) are obtained (Figure 72 (b) and Figure 72 (d)) which leads to an aspect ratio close to 2, i.e. to half-spherical particle (Figure 72 (e)) and a uniform half-covering film (Figure 72 (c)). The particle density shows also the better uniformity (Figure 72 (f)) when high RF plasma power and low distance substrate-grid are used. Lowering $P_{dep}$ or increasing $d$ leads to a much less uniform film regarding the morphological criteria. This means that the maximum quantity of radicals arriving on the substrate and a reduced travelling distance give the higher plasma efficiency needed for the reduction reaction of the precursor. These conditions presumably also favor a uniform cross-flow between the lateral flow of silver precursor and the vertical flow of hydrogen radicals.

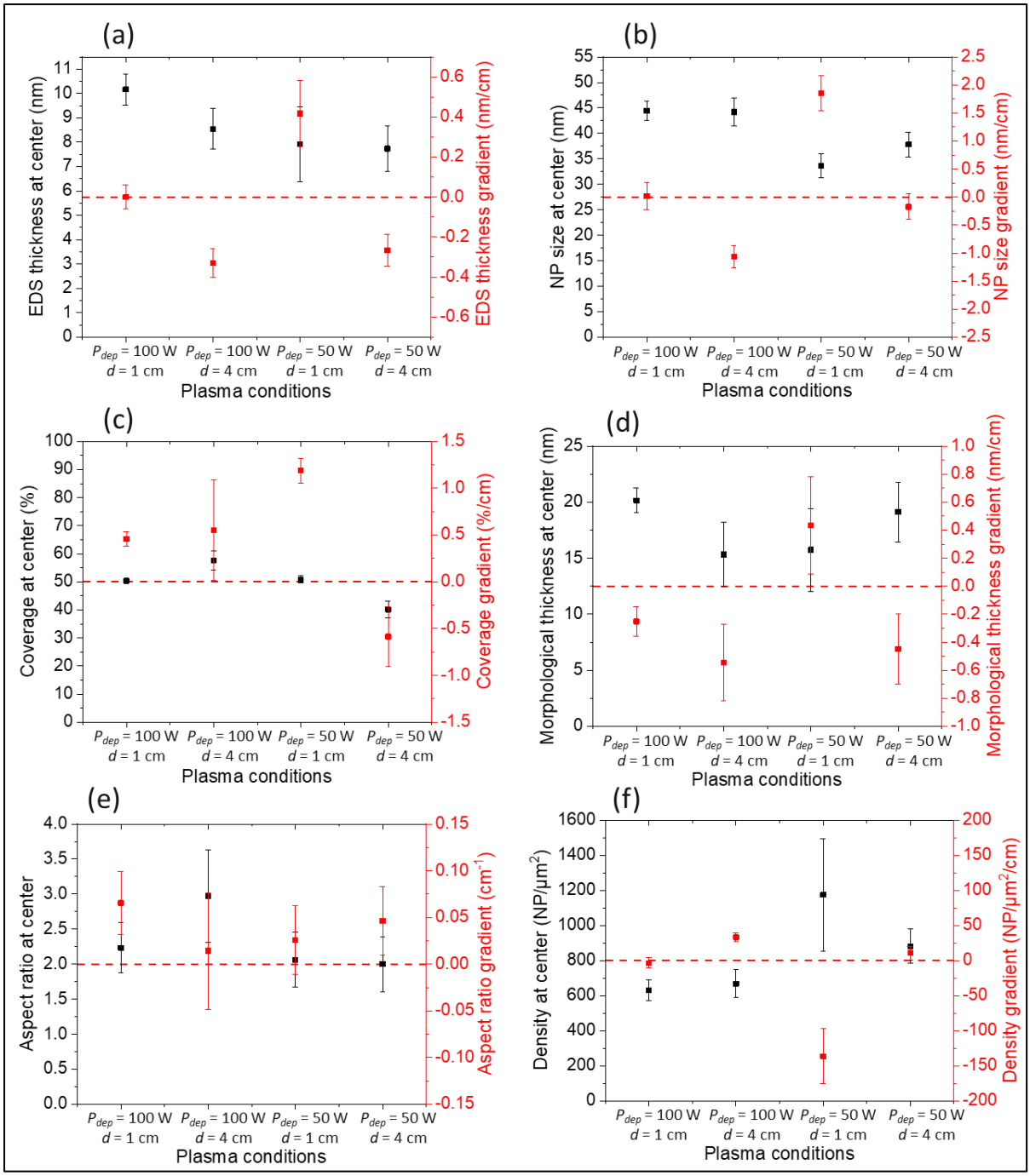


Figure 72: Plot of the quantitative parameter (a) EDS thickness, (b) NP size, (c) coverage in percentage, (d) morphological thickness, (e) aspect ratio and (f) density of NP vs. the plasma conditions. For each case, we have plotted the average value at the center of the studied parameter (black) and the gradient associated (red). The values have been taken on the whole Si wafer from inlet to outlet in order to check the uniformity of the silver deposition.

So far, we have demonstrated how the ALD of silver nanoparticles follow the saturated regime required for obtaining good control of the deposition and large-scale uniformity. We have shown that appropriate pulse and purge times produce films with less than 5% gradient of the thickness and NP size over 10 cm length.

### IV.1.4. Uniformity at the atomic scale

Here we also analyze the elemental composition and the crystalline structure of the film at different positions on the wafer in order to prove the uniformity of the structure at the atomic scale.

#### IV.1.4.1. Film composition

XPS analyses were used for investigating one important signature of the chemical reaction, namely the uniformity of the film's final composition. The spectra were acquired before and after argon sputtering (280 s) in order to determine the elemental composition in the first nanometers (10 first nm for as-deposited) of the deposit and in the bulk (after 280 s of etching). Figure 73 presents the survey spectra for as-deposited Ag film (Figure 73 (a)) and after Ar sputtering (Figure 73 (b)) and Figure 74 (a-b), the corresponding elemental composition.

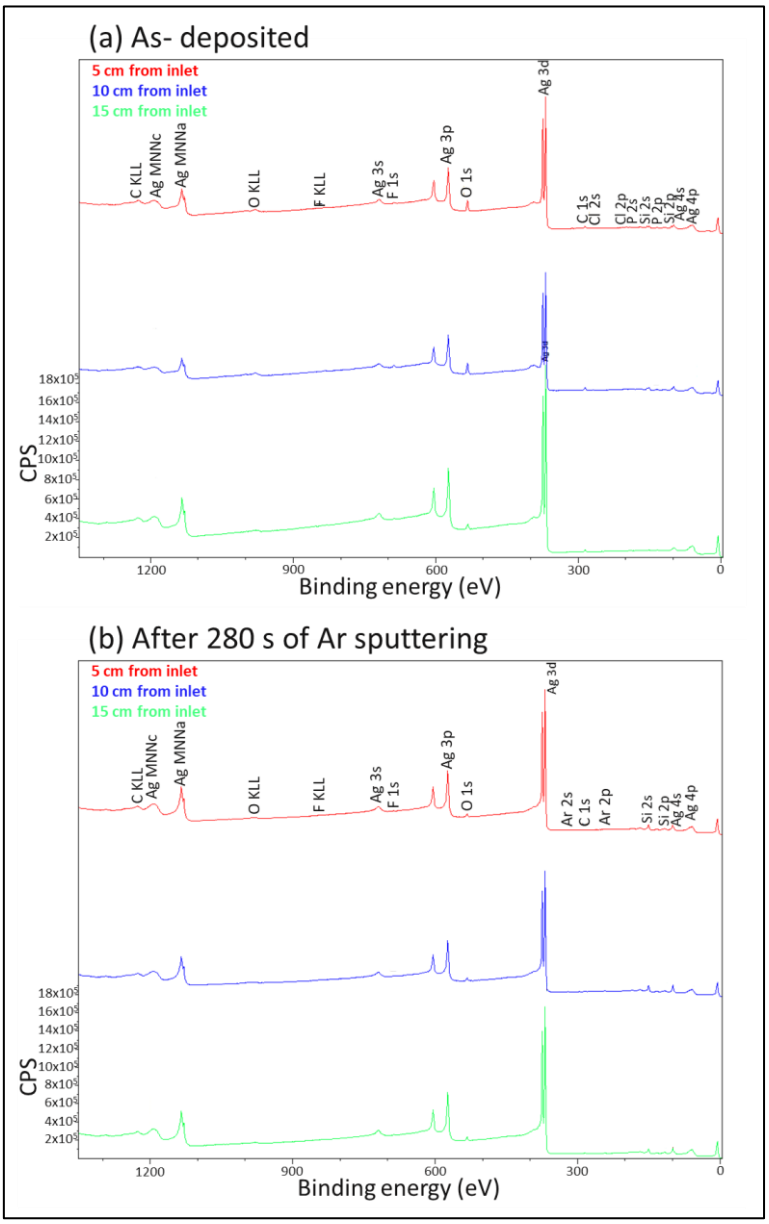


Figure 73: XPS survey spectra of Ag films deposited at three different positions on the Si substrate from the inlet (5 cm in red, 10 cm in blue and 15 cm in green), (a) as-deposited and (b) after 280 s of argon sputtering.

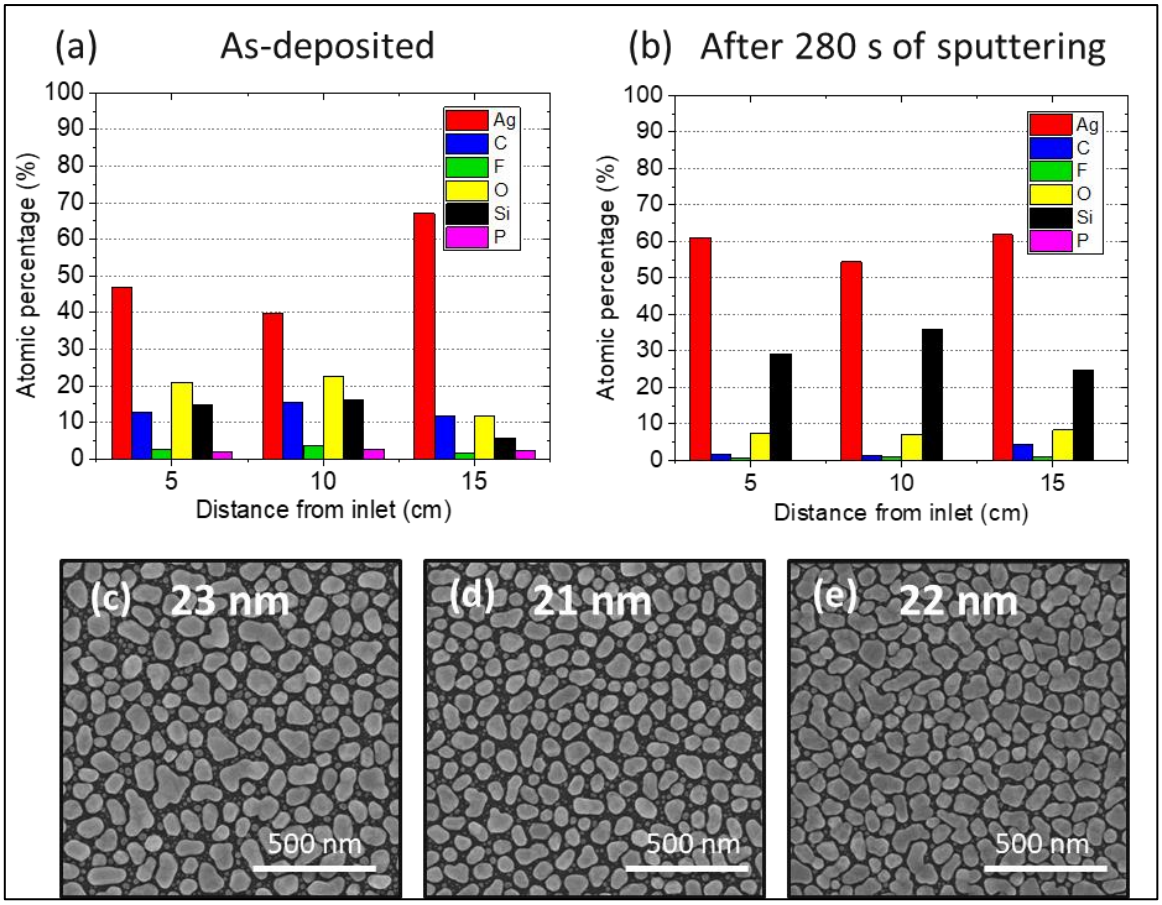


Figure 74: (a) and (b) Elemental composition (in at.%) of Ag films deposited at three different positions on the Si substrate from the inlet (a) as-deposited and (b) after 280 s of argon sputtering. (c) to (e) Scanning electron micrographs corresponding to the three positions from the inlet (c) 5 cm, (d) 10 cm and (e) 15 cm. The values on the images refer to the thickness of the films determined by EDS and the scale bars represent 500 nm.

On the surface, before the sputtering, carbon and oxygen are contaminants usually observed by XPS on the surface of samples exposed to air. The presence of fluorine and phosphorus can be attributed to the unreacted precursor after the last ALD cycle. The F 1s contribution at around 688 eV (see survey spectra in Figure 73) corresponds to organic fluorine and not to metal fluorides that should be present at a lower binding energy. This also leads to additional carbon and oxygen amounts. The granular film structure and its small thickness (see Figure 74 (c) to (e)) enable the detection of the silicon and $SiO_2$ from the substrate.

From the line shape of the Si 2s peak, the formation of silicide is not observed. Consequently, the Ag / Si ratio are altered by the different morphologies of the film in various positions of the samples in the reactor (from the inlet (5 cm) to the outlet (15 cm), see Figure 74 (c) to (e)). Indeed, even if the Ag equivalent film thickness remains constant, the island sizes and the coverage increase by 8.4% and 5.5%, respectively, whereas the density of particles on the surface decreases by 18.8%. The difference in the percentage of the Ag amount may also be attributed to the presence of less surface contamination in the outlet part, which is directly linked to the gas flow in the reactor.

In contrast to the analysis before etching, which shows a large non-uniform surface contamination, the elemental composition of the samples after etching is almost independent of the position in the reactor and suggests a good uniformity of the reaction in the reactor (Figure 74 (b)). In all cases, the lack of phosphorus confirms the potential Ag-P bond breakage. The low amount of oxygen, carbon and fluorine after etching also confirms the almost complete decomposition of the silver precursor.

The slight variations of Ag and Si contents between 5 cm and 15 cm might be correlated with a slight change in the film morphology.

In Figure 75, HR Ag 3d spectra of samples at three different positions from the inlet, are reported. Furthermore, each sample are compared with the Ag reference spectrum. The spectra were recorded at the surface level (t=0) and after an etching time of 280 s. The presence of loss features combined with the asymmetric peak shape in all spectra confirms the presence of Ag as metal, as required from the literature (see section III.3.2.1). The presence of less surface contamination and thus higher amount of Ag in the outlet part leads to results closer to the silver reference.

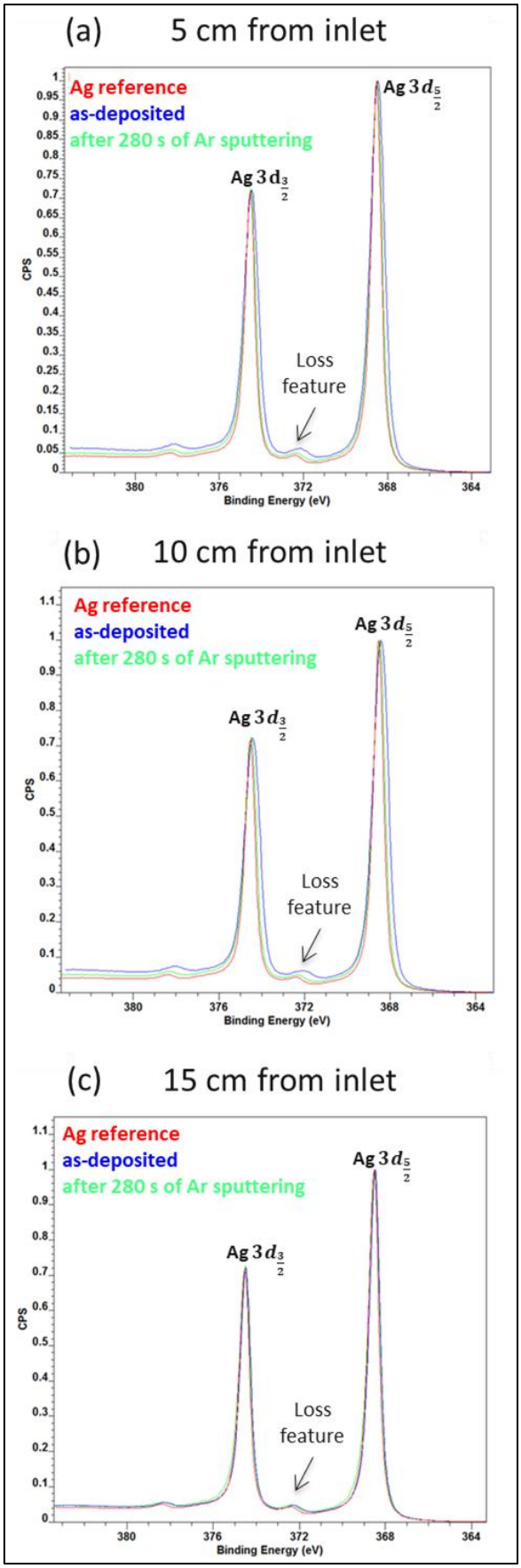


Figure 75: High resolution Ag 3d spectra of samples at different positions from the inlet (a) 5 cm, (b) 10 cm and (c) 15 cm, respectively. Each spectrum, compared with the Ag reference (red line), was recorded at t=0 (in blue) and 280 s (in green) of etching.

In Figure 76, all Auger Ag MNN peaks show a shape similar to that one of the Ag reference (red line) which suggests the presence of Ag in metallic state. The slight difference relies on the intensity of the background which is higher for the spectra recorded at the surface due to surface contamination.

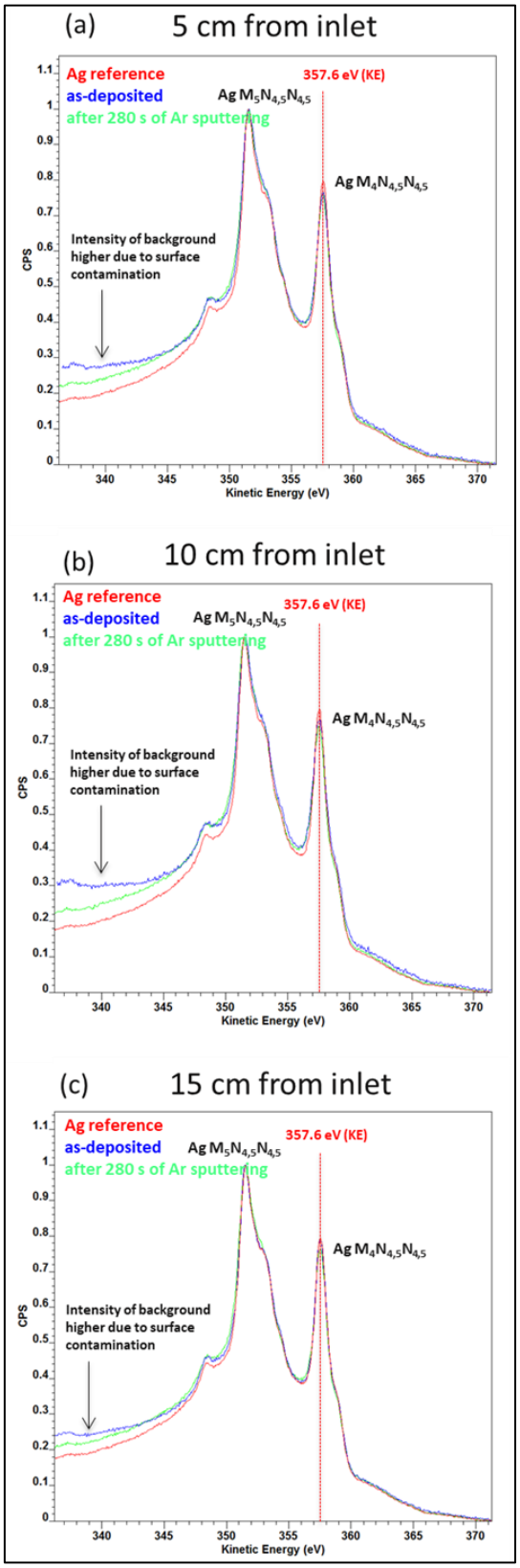


Figure 76: Auger Ag MNN spectra of samples at different positions from the inlet (a) 5 cm, (b) 10 cm and (c) 15 cm, respectively. Each spectrum, compared with the Ag reference (red line), recorded at t=0 (in blue) and 280 s (in green) of etching.

Finally, the third parameter investigated and calculated is the modified Auger parameter α' which is calculated taking into account the maximum value of Ag 3d photoelectron peak and Auger Ag $M_4N_{4,5}N_{4,5}$ peak.

Figure 77 presents all α' values calculated for the samples discussed above. When compared with the data from literature (see chapter 3, Table 21), the modified Auger parameter values suggest that silver in the films is mainly in the metallic state in all the samples. The slight increase of the modified Auger parameter after sputtering is characteristic of the presence of a low amount of silver oxide on pristine surfaces (black) and removed with argon etching (red).

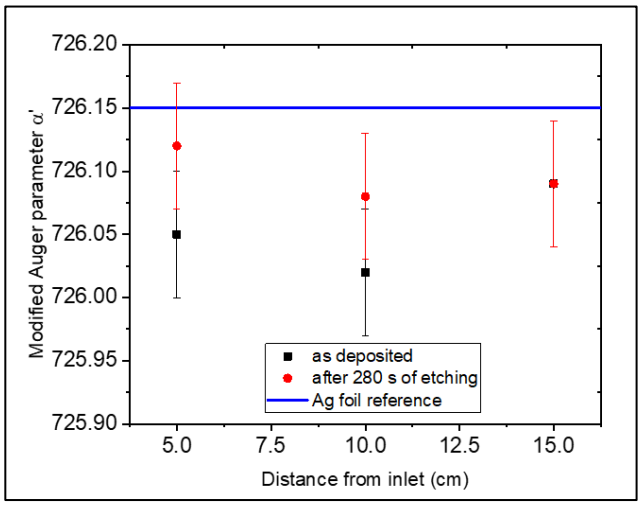


Figure 77: Modified Auger parameter (*α'*) of Ag for different points on the wafer (distance from the inlet): as-deposited in black and after 280 s of etching in red. The blue line corresponds to a reference Ag foil. The error bars correspond to the experimental error linked to the spectra acquisition step size.

In order to better understand the decomposition of the precursor on the substrate and the origin of the remaining impurities after the ALD reaction, we have performed ToF-SIMS analysis of a representative film on Si substrate at three different positions from gas inlet. The spectra recorded in the positive and negative modes, are shown in Figure 78. The results are compared to the silver precursor (chemical formula shown in the inset). We note here that the observed fragments result from recombination of ions and are not directly representative of the molecules present in the samples.

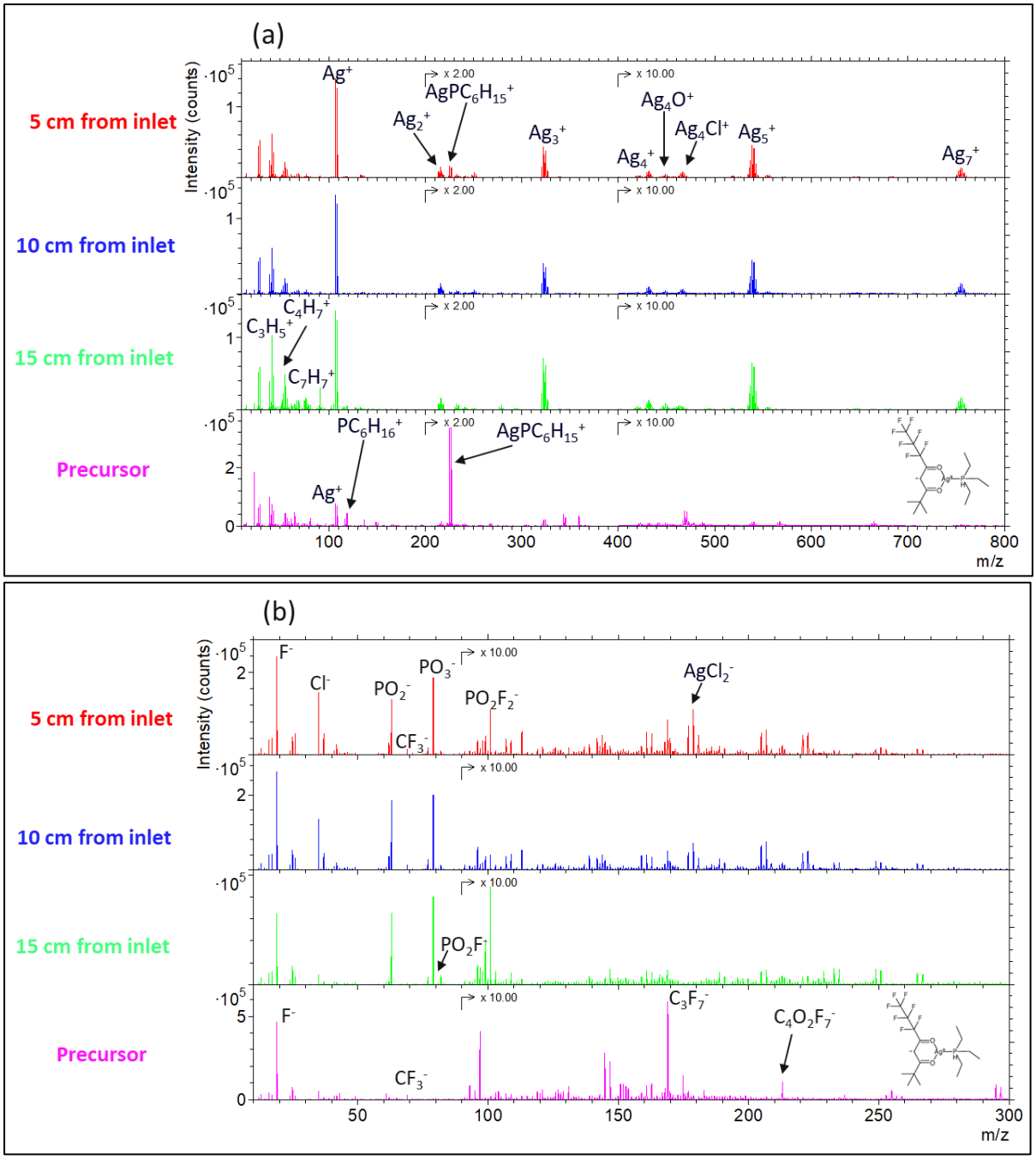


Figure 78: ToF-SIMS spectrogram (intensity as a function the atomic mass m/z) measured (a) in the positive mode (only positive ions are collected) and (b) in the negative mode (only negative ions are collected), at three positions from inlet (5 cm in red, 10 cm in blue and 15 cm in green) as well as for the silver precursor Ag(fod)($PEt_3$) (in magenta, chemical formula in the inset).

The main fragments observed in the precursor spectrogram in positive mode (Figure 78 (a)) are $AgPC_6H_{15}^+$ and $PC_6H_{16}^+$, which are directly associated with the chemical formula of the precursor. The absence of the contribution of the entire molecule suggests that it is easily fragmented due to the destructive analysis method used. For the films, the main observation is first, the strong decrease of these ions, $AgPC_6H_{15}^+$ decreasing with the increased distance from the inlet and second, an increase of silver in the form of several clusters ($Ag^+$, $Ag_2^+$, $Ag_3^+$, $Ag_4^+$, $Ag_5^+$ and $Ag_7^+$). These observations are a strong indication of the reduction reaction giving pure silver films, as proved with previous XPS analyses. This is also confirmed in the negative mode (Figure 78(b)), where $C_4O_2F_7^-$ and $C_3F_7^-$ are

fragments observed in the monomer spectrum while their strong decrease is exposed for Ag films with the increased distance from the inlet. The presence of anions $Cl^-$ and $AgCl_2^-$ in the Ag deposition spectrum confirms that it is coming from contamination of the ALD reactor since they are not present in the monomer spectrum. This contamination decreased with the distance from the inlet to the outlet of the substrate. XPS results did not highlight the presence of chlorine since, on the surface, the amount was close to the limit of detection of the analysis and absent after Ar sputtering. Organic fluorine and not metal fluorides found in XPS analyses is also confirmed by ToF-SIMS measurement.

#### IV.1.4.2. Crystalline structure

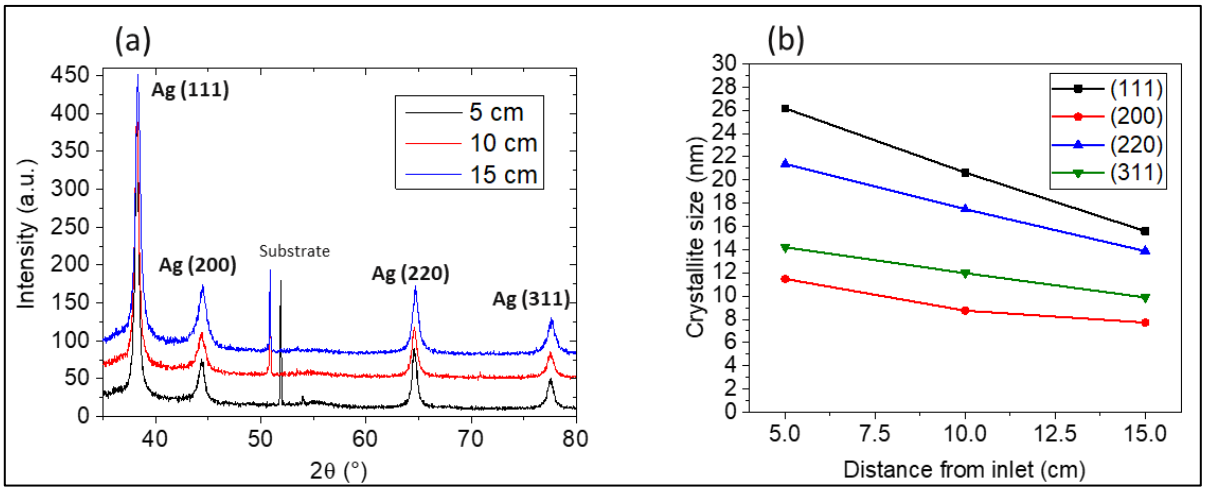


Figure 79: (a) X-ray diffraction spectrogram of 20 nm-thick Ag thin film deposited on silicon substrate at three positions in the reactor, close to the inlet, at the center and close to the outlet. (b) Crystallite size extracted from (111), (200), (220) and (311) diffraction peaks at three positions in the reactor, close to the inlet, at the center and close to the outlet.

The XRD diffractogram (Figure 79 (a)) shows that the films consist of polycrystalline face centered cubic (fcc) silver ($Fm\bar{3}m$) (JCPDS 04-0783) and exhibit (111), (200), (220) and (311) reflections for the three different positions in the reactor. No signature of other phases, such as silver oxide, are observed. The presence of all peaks for the three positions proves that the crystallinity of the films is independent of the position in the reactor. The crystallite size for the four diffraction peaks (Figure 79 (b)) decreases very slightly from the inlet to the outlet, independently of the diffraction plans. This decrease is interesting as it shows that, despite the good uniformity in terms of thickness and NP size, the microscopic crystalline structure is affected by the position.

## IV.2. Discussion of a proposed model for the growth mechanism of silver nanoparticles

Up to now, we have demonstrated that uniform Ag NPs film are produced on a large-scale using PE-ALD in the saturated regime. The uniformity has been analyzed in terms of morphology, growth rate, elemental composition and crystal structure, with less than 5% variation of the thickness and NP size over 10 cm length. We also pointed out that the averaged morphological quantities alone do not provide a full criterion for a perfect control of the deposition. The gradient of these quantities is a major criterion for choosing an accurate parameter. By analyzing this gradient, we have observed that

several mechanisms influence the deposition uniformity, and we have suggested that material transfer via precursor migration or ripening process might play an important role. In the following part, we analyze in more details the growth mechanism in order to confirm these hypotheses.

### IV.2.1. Morphology and crystal structure as a function of the number of atomic layer deposition cycles

In the literature, the study of the number of ALD cycles, which enables the coalescence and continued nucleation, controls the particle size distribution. The fingerprint is an increase of both the NP size, with irregular shapes, and the gap between islands, with a decrease of their density. [19, 29, 45, 48, 144, 146] However, the growth mechanism is still little understood at the initial stage of the film synthesis.

SEM micrographs were carried out on thin silver films deposited after varying the number of deposition cycles from 200 to 800 in order to investigate the growth mechanism. The analysis at a lower number of cycles did not enable a reliable analysis using SEM. All positions along the wafer have been studied and the results are comparable due to the high uniform deposition. For the sake of clarity, only the center position (10 cm from inlet) is presented here (based on Figure 69), and the related SEM micrographs are shown in Figure 80.

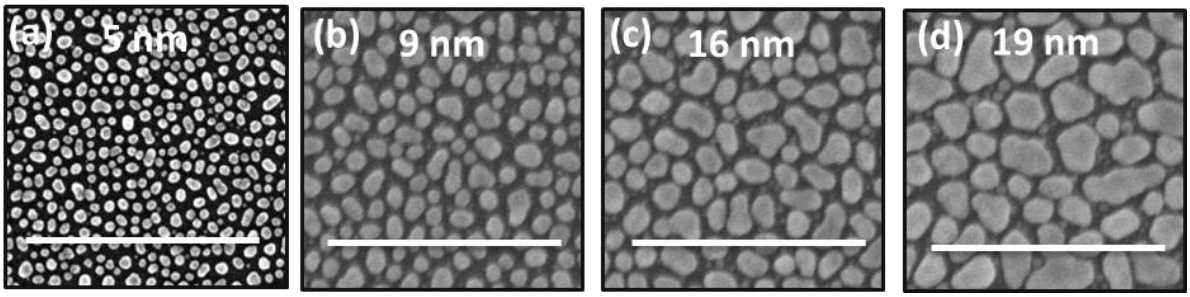


Figure 80: Scanning Electron Micrographs of Ag thin films deposited on silicon at the center of the substrate (10 cm from inlet) used in order to investigate the growth mechanism after a varying number of cycles (a) 200 cycles, (b) 400 cycles, (c) 600 cycles and (d) 800 cycles. The values on the images refer to the thickness of the films determined by EDS and the scale bars represent 500 nm. The studies were performed at the optimum temperatures $T_{ch}$ = 130°C/$T_{hs}$ = 100°C.

After 200 cycles, the film morphology is characterized by small and spaced nanoparticles. These particles get bigger, closer, and increasingly irregular in shape with increasing numbers of cycles. In order to quantify these observations, the influence of the number of cycles on different morphological parameters is examined in Figure 81. Ag NPs begin to coalesce at a critical thickness of 62 nm, but since we are focusing on tailoring Ag NPs, the data are not relevant here. The EDS equivalent thickness, the NP size and the morphological thickness increase linearly with the number of cycles (Figure 81 (a), (b) and (d)), something that is attributed to usual island growth. According to the literature, silver films present an island morphology before growing into a film. [19, 29, 48, 85] This is known as the Volmer-Weber growth mechanism: due to the high surface energy of metals (1.25 J/m$^2$ for silver [225]), the atoms have a strong affinity with each other instead of adhering to the substrate (0.75 J/m$^2$ for $SiO_2$/Si [226]). The experimental observations in Figure 81 strongly suggest that the growth occurs following the Volmer-Weber growth mode. Both NP diameter (Figure 81 (b)) and morphological thickness (Figure 81 (d)) increase, leading to the expansion of the aspect ratio (Figure 81 (f)). This proves the

anisotropic growth on vertical and lateral directions, with a flattened shape favored since the ratio is larger than one. The coverage shows a weaker linear increase (Figure 81 ((c)), which could also be attributed to this mechanism. This is however contradicted by the exponential decrease of the nanoparticle density with the number of cycles (Figure 81 (g)), presumably related to the merging of the NPs. The rms roughness (Figure 81 (e)) increases exponentially as a function of the ALD cycles and is directly associated to the NP size trend.

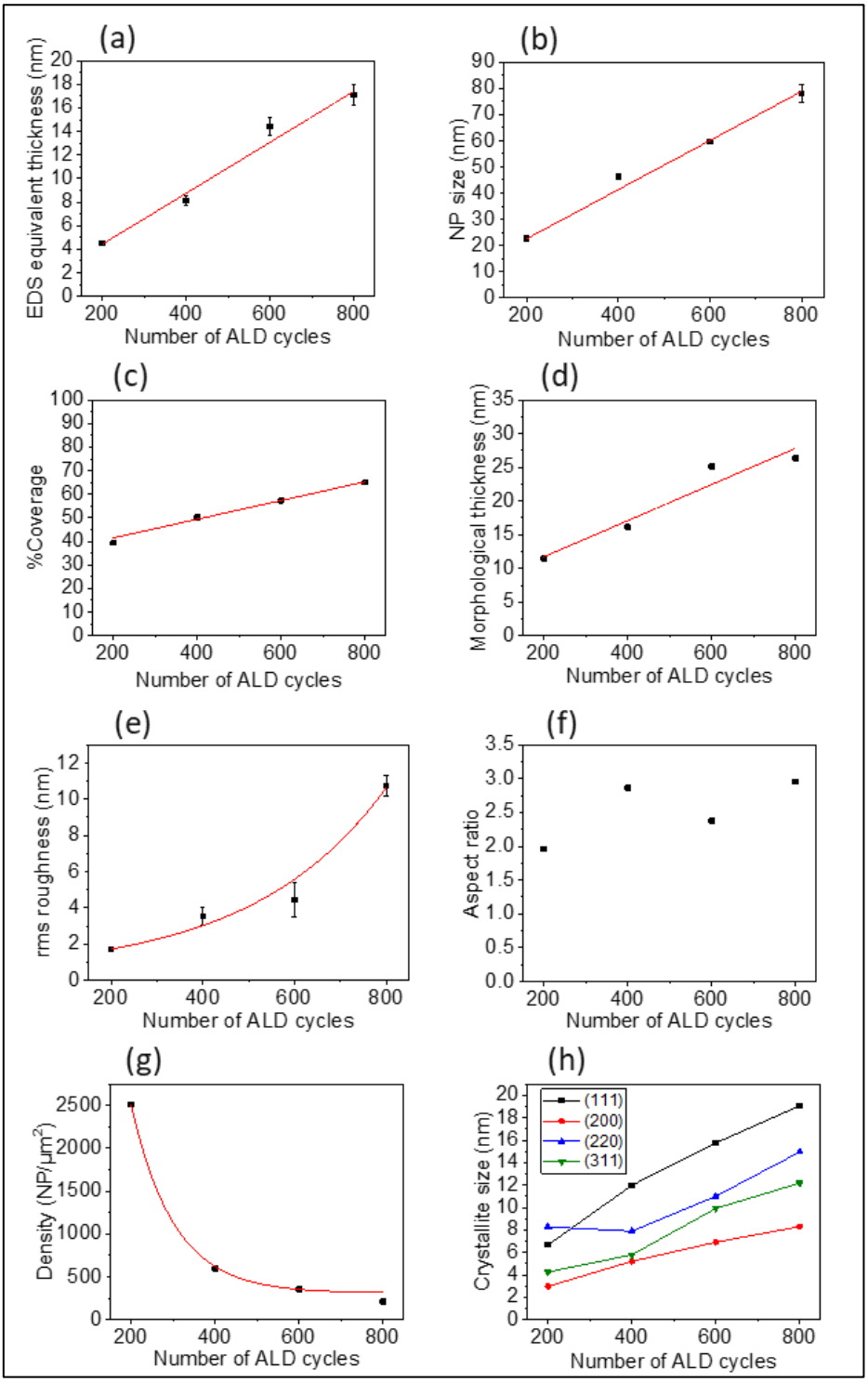


Figure 81: Influence of the number of cycles on (a) the EDS equivalent thickness, (b) the nanoparticle size, (c) the coverage, (d) the morphological thickness (vertical thickness), (e) the rms roughness determined by AFM, (f) the aspect ratio, (g) the density and (h) the crystallite size extracted from (111), (200), (220) and (311) diffraction peaks.

Finally, the crystallite size behavior was analyzed. A linear increase of the grain size with the number of cycles is observed (Figure 81 (h)). This implies that a better crystallization takes place during growth, showing a clear redistribution of the atoms rather than a simple condensation of crystallites. Moreover, the XRD diffractogram exposed in Figure 82, proves that the films consist of polycrystalline face centered cubic (fcc) silver ($Fm\bar{3}m$) (JCPDS 04-0783) and exhibit (111), (200), (220) and (311) reflections.

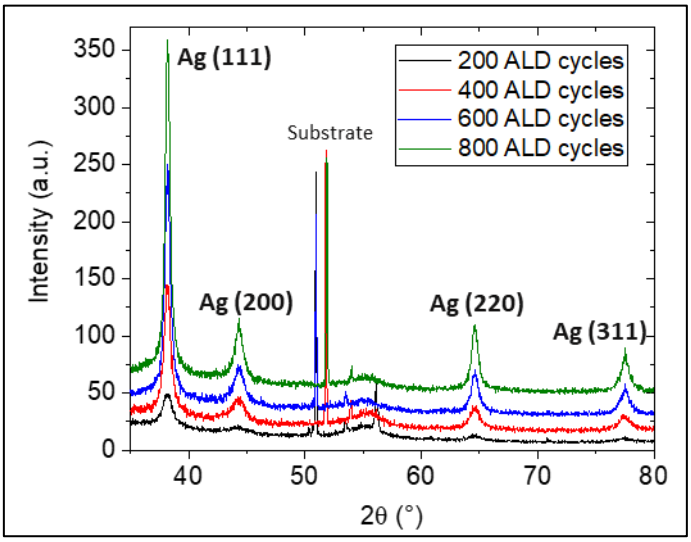


Figure 82: X-ray diffraction spectrogram of Ag thin film deposited on silicon substrate at four different numbers of cycles (200,400, 600 and 800)

### IV.2.2. Growth model for the deposition of silver nanoparticles

At the end of the first analysis, it is possible to conclude that the observed trends are not consistent with a single growth mechanism. In order to give a global picture of the deposition mechanism, we compare the results with a simple empirical model for the growth of a nanoparticle on a surface. We assume four main mechanisms involved for the deposition of silver atoms on the surface:

1. reaction and deposition on top of a silver nanoparticle already adsorbed on the surface;
2. reaction and deposition on the triple point, i.e. interface between substrate, deposited silver and gas;
3. reaction directly on the substrate (nucleation);
4. transfer of material between particles, either through migration, coalescence, or Ostwald ripening.

These mechanisms are illustrated in Figure 83 and the table summarizes how the main morphological parameters are expected to evolve as a function of the involved mechanism. Finally, it is possible compare these evolutions with the experimental results obtained in Figure 81.

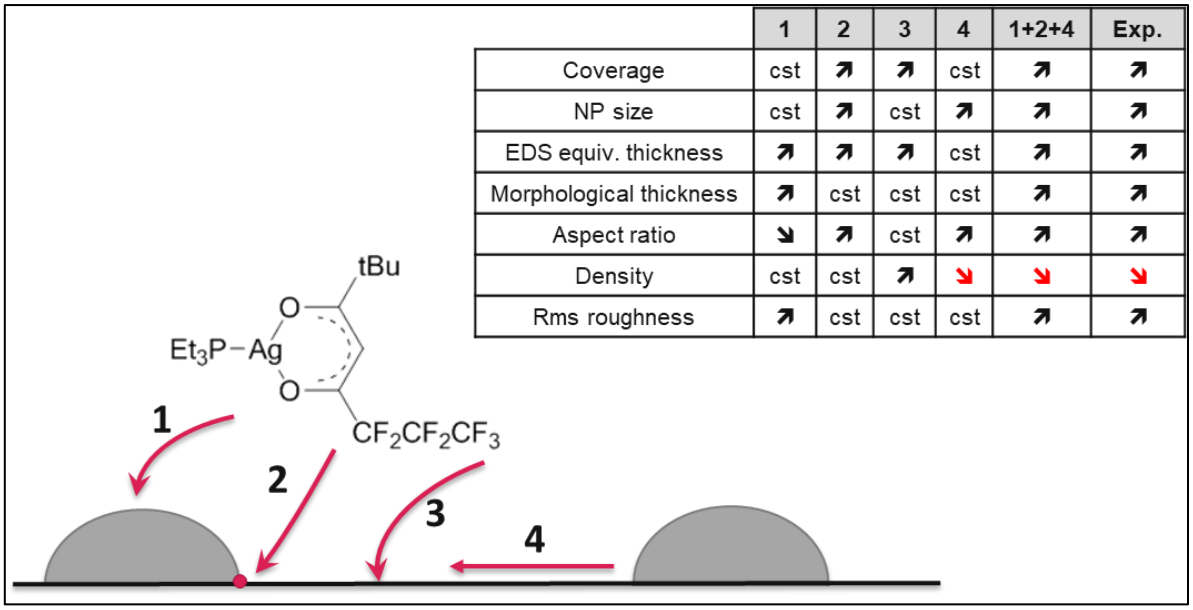


| | 1 | 2 | 3 | 4 | 1+2+4 | Exp. |
|---|---|---|---|---|---|---|
| Coverage | cst | ↗ | ↗ | cst | ↗ | ↗ |
| NP size | cst | ↗ | cst | ↗ | ↗ | ↗ |
| EDS equiv. thickness | ↗ | ↗ | ↗ | cst | ↗ | ↗ |
| Morphological thickness | ↗ | cst | cst | cst | ↗ | ↗ |
| Aspect ratio | ↘ | ↗ | cst | ↗ | ↗ | ↗ |
| Density | cst | cst | ↗ | ↘ | ↘ | ↘ |
| Rms roughness | ↗ | cst | cst | cst | ↗ | ↗ |

Figure 83: Scheme representing the different attachment mechanisms of a nanoparticle on a surface and the associated table summarizing the evolution of the nanoparticle size, the EDS equivalent film thickness, the coverage, the height of the NP, the rms roughness, the aspect ratio, the nanoparticle density regarding the simplistic model and comparison with the experimental results.

Interestingly, the combination of top deposition (1), side deposition (2) and material transfer (4) is the minimal combination that reproduces the experimental results. Surface nucleation (3) is excluded by the exponential decrease of the particle density. After this exclusion, we note that top deposition (1) is required for explaining the increase of morphological thickness and rms roughness. The side deposition (2) is required for explaining the coverage increase. The material transfer (4) is required for explaining the exponential decrease of particle density while the coverage shows a weak linear increase, i.e. we do not observe the simple merging of particles with increasing size.

### IV.2.3. Analysis of the material transfer mechanism

As exposed in section I.2.3., the material transfer (mechanism 4) involves the competition between two potential mechanisms: Ostwald ripening (OR) or particle migration and eventual coalescence (Smoluchowski ripening - SR). [69, 70]

In order to further investigate this mechanism, we have performed a plasma post-treatment on deposited NPs, with the same plasma conditions as those used for the deposition. Figure 84 (a) and Figure 84 (b) show SEM pictures of the particles before and after post-treatment, and the histograms of particle sizes are presented in Figure 84 (c) and Figure 84 (d). The observation of an increase of the NP size and a decrease of the NP density after plasma treatment is in line with the work done by Duan *et al.* [86] where the author strongly suggests an OR process. Moreover, point out that this mechanism is also consistent with the observation made on the influence of the plasma pulse time exhibited in previous sections. In Figure 66 (b), the continuous increase of the particle size with plasma pulse time is observed, even with a saturation of the deposition thickness (EDS equivalent thickness). This is full consistent with the study of Tang *et al.* [74] who observe a $t^{1/3}$ dependence between nanoparticle diameter and plasma post-treatment time which indicates an Ostwald ripening process. In addition, the dependence of the Ag NPs morphology with the number of ALD cycles where we observed an

increase of both the NP size, with irregular shapes, and the gap between islands, with a decrease of their density (Figure 80, Figure 81) fits the results of the previous published work of Golrokhi *et al.* [29] and the occurrence of material transfer via OR. Lastly, Ostwald ripening can take place either by surface diffusion along the substrate or by vapor phase diffusion. For our experiments, if this process occurred by vapor phase diffusion, the hypothesis would be bigger NPs in the outlet part of the wafer than in the inlet part. We observe a uniform deposition, consequently the surface diffusion along the substrate seems to be favored as it is expected to have a shorter range.

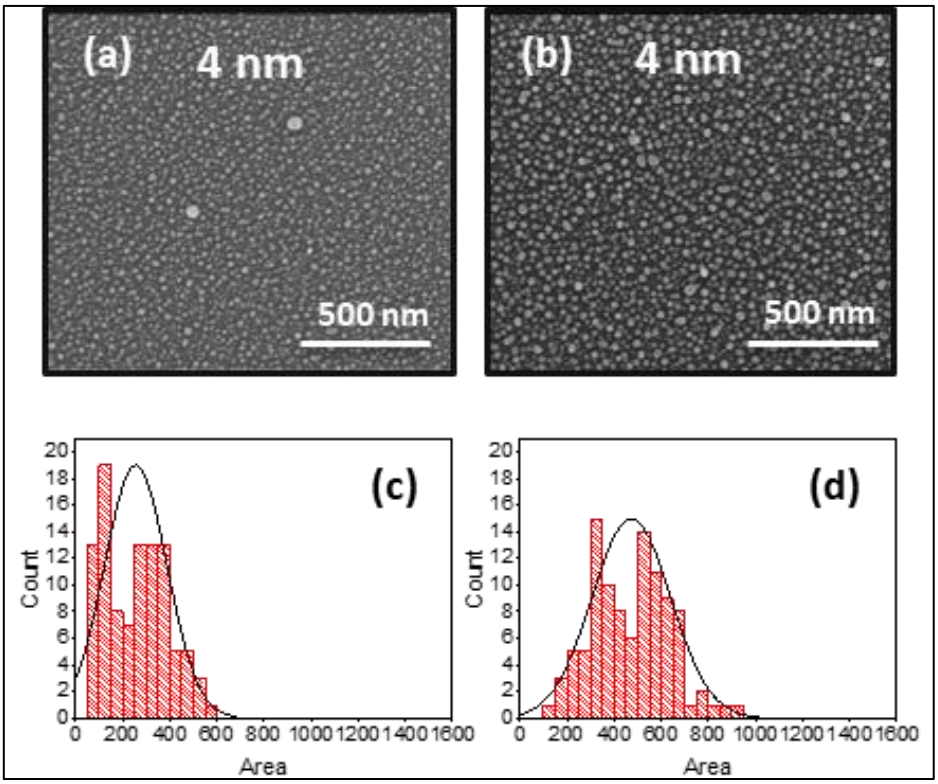


Figure 84: (a-b) Scanning electron micrographs of Ag thin films (a) as-deposited after 100 cycles and (b) after plasma post-treatment for 5 min. The EDS equivalent thickness is 4 nm in both cases, and the scale bare is 500 nm. (c-d) Particle size distribution histograms of Ag thin films (c) as-deposited and (d) after plasma post-treatment. Black line curves are lognormal fit.

## IV.3. Conclusion

This chapter has presented in more details the correlation between the large-scale deposition depending on the ALD process parameters and the growth mechanism of silver nanoparticles. A deeper investigation of the uniformity of the deposition has been quantified in terms of film morphology using an original methodology. We have reported both the value at the center position of an 8-inch silicon wafer and more originally, the gradient over a 10 cm distance on the substrate of different morphological criteria, i.e. morphological and EDS film thickness, Ag NPs size, density and aspect ratio and film coverage. We have demonstrated that this method gives more indications than the more commonly investigated average thickness alone. More precisely, we have found a limited process temperature window ranging from 130 to 140 °C, which is not anticipated by investigating the deposition rate alone. In this ALD window, less than 5% gradient of the thickness and NP size over

10 cm length have been obtained under appropriate pulse and purge times. The most efficient reduction reaction of the Ag precursor by hydrogen radical species was found with a high amount of reactive species and a reduced travelling distance. The completeness of the reduction reaction has also been demonstrated by chemical analyses which have shown an atomic scale uniformity and a film deposition made of polycrystalline pure metallic silver with a low amount of impurities. We have investigated the Ag growth mechanism by changing the number of ALD cycles within the first 800 cycles and studied more criterion, i.e. by adding the film roughness and its crystallinity. We have observed a linear increase of the EDS equivalent thickness, the Ag NP size, the morphological thickness and the films coverage with increasing ALD cycles which is fully consistent with the well-known Volmer-Weber growth mechanism occurring for metal film on oxide surfaces. This leads to an anisotropic growth on vertical and lateral directions, with an Ag NPs flattened shape favored, and the grain size has suggested a better crystallization taking place during growth. The exponential decrease of the nanoparticle density is however a signature of the merging of the particles and suggests that the observed trends were not consistent with a single growth mechanism. An empirical model has been established on four growth mechanisms taking place during the nucleation of a film on a substrate deposited by chemical vapor-phase method. The minimal combination that reproduces the experimental results was the reaction and deposition, on top of a silver nanoparticle already adsorbed on the surface, on the triple point (interface between the substrate, deposited silver and gas) and material transfer. But the material transfer mechanism dominates the NP morphology with a decrease of the roughness as the signature. We have shown that this material transfer mechanism mainly occurred during the plasma pulse, allowing us to tune the NP size while keeping the average thickness constant. Similar behavior has been found in the literature and have suggested ‘surface Oswald ripening’ like process, but a deeper investigation is still needed regarding this material transfer.

# Chapter 5

# Two-step approach for chemical vapor-phase deposition of ultra-thin conductive silver films

As reported in previous part, the deposition of silver films using the standard PE-ALD process did not demonstrate continuous ultra-thin silver films (i.e. continuous films with thickness below 20 nm). Here we demonstrate an alternative process regime which might be more promising for continuous ultra-thin films deposition.

In this chapter, the proof of concept of the novel approach is first demonstrated by presenting the principle of the Ag deposition and the electrical properties of the resulting film. This processing relies on a two-step process divided in, first, a chemical vapor-phase deposition giving almost insulating compact nanoparticle morphology and, second, a plasma post-treatment which sinters the nanoparticles and forms a quasi-continuous ultra-thin conductive silver film. By means of its chemical composition and crystallographic properties, we prove, in the second section, that the first product is already silver in metallic state with some Ag precursor remaining on the surface, even if it is electrically non-conductive. In the third section, we investigate the deposition parameters which allow us to obtain a compact NPs morphology in order to understand the occurring growth mechanism. Based on the obtained results, we discuss about a proposed qualitative model for the growth mechanism of Ag compact films. The last section is dedicated to a deeper study of the parameters used for hydrogen-based plasma post-treatment of Ag films made of compact nanoparticles and their influence on the film morphology and electrical properties.

---

This chapter is based on the publication *S. Wack, P. Lunca Popa, N. Adjeroud, C. Vergne, R. Leturcq,* Two-Step Approach for Conformal Chemical Vapor-Phase Deposition of Ultra-Thin Conductive Silver Films, *ACS Appl. Mater. Interfaces*, **2020**, 12, 32, 36329–36338.

## V.1. Proof of concept of the new two-step approach

### V.1.1. Principle and morphological properties

The two-step approach is based on the standard PE-ALD processing using the same silver precursor and $H_2$-based plasma reducing agent, in conditions similar to the ones demonstrated for standard PE-ALD regime (see Figure 85 (a)).

In order to obtain a conducting ultra-thin film, the main challenge is to obtain a dense and compact deposit. Both standard ALD and CVD rely on the reaction of the precursor with the surface, leading to a non-conducting island morphology (Figure 85 (c)), due to specific Volmer-Weber growth mechanism, as exposed in previous chapter. Electrical conduction is achieved only after the coalescence, characterized usually by high critical thickness. In order to circumvent this morphology, we have used a modified processing condition in order to favor gas-phase reaction before the surface reaction (see Figure 85 (b)). This is usually avoided in the ALD or CVD of thin film as it leads to a lack of control over the thickness and to deposition of nanoparticles. This regime has been referred to forced "pulsed-PE-CVD".

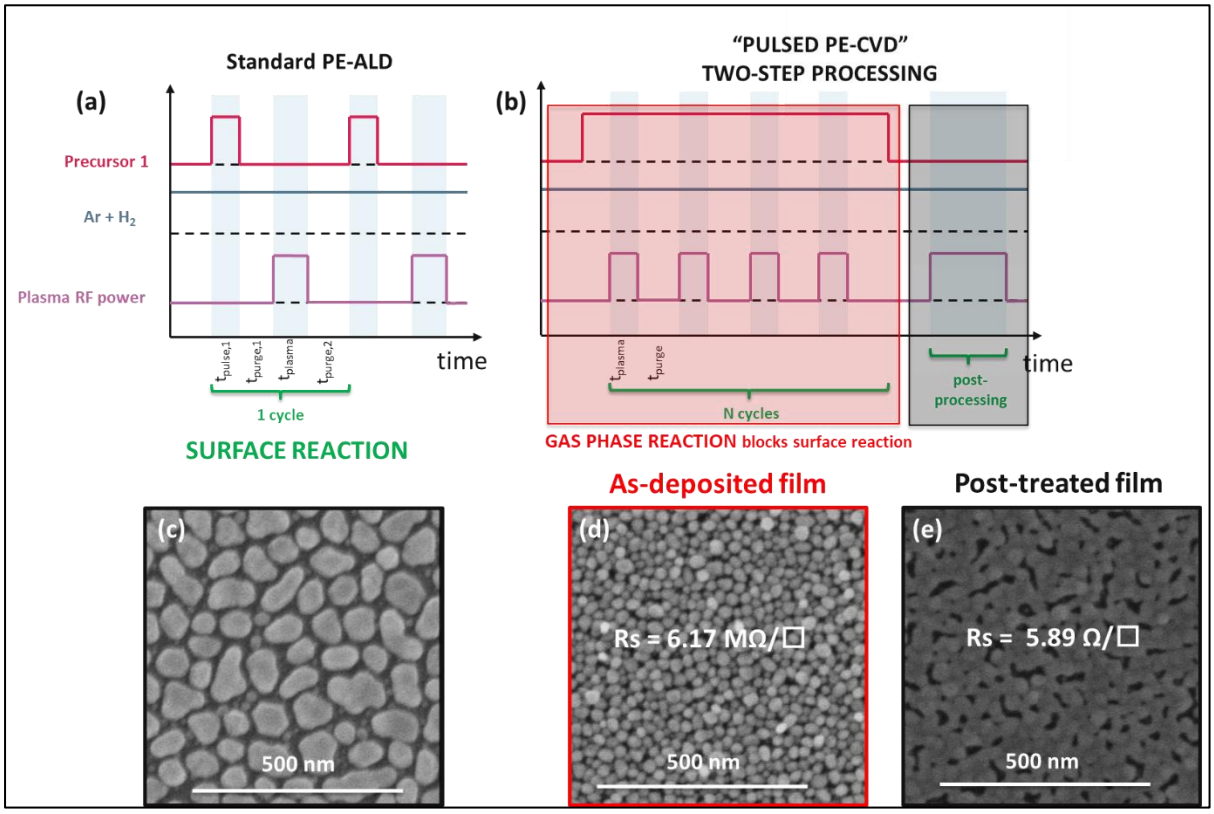


Figure 85: (a) and (b) Pulse sequence for (a) standard PE-ALD processing characterized by a surface reaction and (b) Two-step pulsed PE-CVD processing developed during the thesis for the deposition of percolated silver thin films. (c) to (e) Scanning Electron Micrograph of Ag thin films on glass substrates corresponding to (c) standard PE-ALD processing for an EDS film thickness of 19 ± 1 nm; (d) and (e) Two-step pulsed PE-CVD processing with (d) as-deposited and (e) post-treated films. The EDS equivalent thickness is 24 ± 2 nm in both cases. The values shown in the middle of the images correspond to the sheet resistance of the Ag layer.

This peculiar pulsed-PE-CVD regime was achieved by continuously exposing the metal-organic silver precursor in the reactor, while keeping the pulsed hydrogen-based plasma sequence from PE-ALD (Figure 85 (b)). This has been discovered with the deficient precursor injection system, as already

explained in chapter 3. The as-deposited film (Figure 85 (d)) is made of compact silver-based nanoparticles with a surface coverage close to 100 % that is usually not achieved at low thickness with CVD or ALD methods. The as-deposited film has a high sheet resistance (6 ± 5 MΩ/□) for the film in Figure 85 (d)), which we attribute to remaining precursor on the surface of the nanoparticles, as it is discussed in section V.4.

Figure 86 exposes the influence of the number of cycles on the thickness of the Ag film. As highlighted by the linear fit, the layer thickness is controlled in the new processing conditions by changing the number of deposition cycles. A thicker deposition is however obtained at the inlet probably due to the early decomposition of the precursor directly at the inlet, and lower amount arriving at the outlet. This process leads to a typical growth rate of 0.065 ± 0.02 nm/cycle.

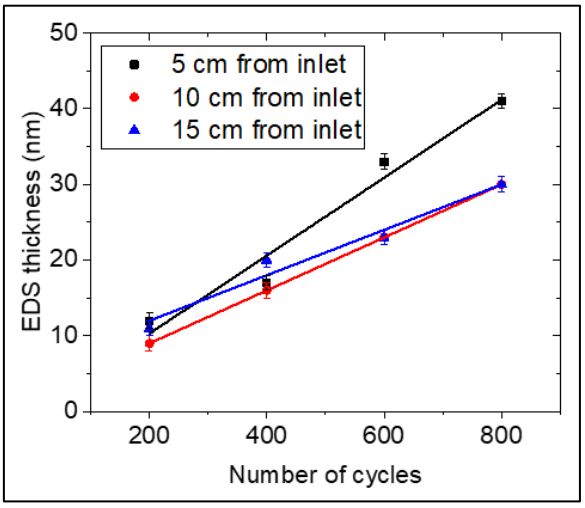


Figure 86: Influence of the number of cycles on the EDS thickness of Ag films deposited on Si at different position from the inlet.

In order to make the deposit conductive, a second step of post-treatment (PT) is performed, as already demonstrated for solution processed Ag nanoparticles, as exposed in I.4.4. Background. After a hydrogen-based plasma PT, the compact nanoparticles sinter and form a quasi-continuous ultra-thin silver film with a low sheet resistance (6 ± 1 Ω/□) for the film in Figure 85 (e)). This decrease of the sheet resistance by six orders of magnitude is remarkable, as previous reports for silver thin layers obtained by gas-phase synthesis suggest that post-processing steps usually increase the sheet resistance of silver films due to the dewetting effect. [227] This difference might be attributed to the very peculiar morphology of the as-deposited film.

The morphological properties of the Ag films have been investigated in Figure 87. As exposed above, as-deposited film is made of compact silver-based nanoparticles with a surface coverage close to 100 %, which sinter and form a quasi-continuous ultra-thin silver film after PT. However, a 40-nm-thick Ag as-deposited film presents a high rms roughness (Figure 87 (a)) which is slightly reduced after plasma post-treatment but still remains important (Figure 87 (b)). SEM cross-section has been performed on Ag film deposited on Si substrate, and as seen in Figure 87 (c), it demonstrates that the film is rather composed of multiple layers of particles.

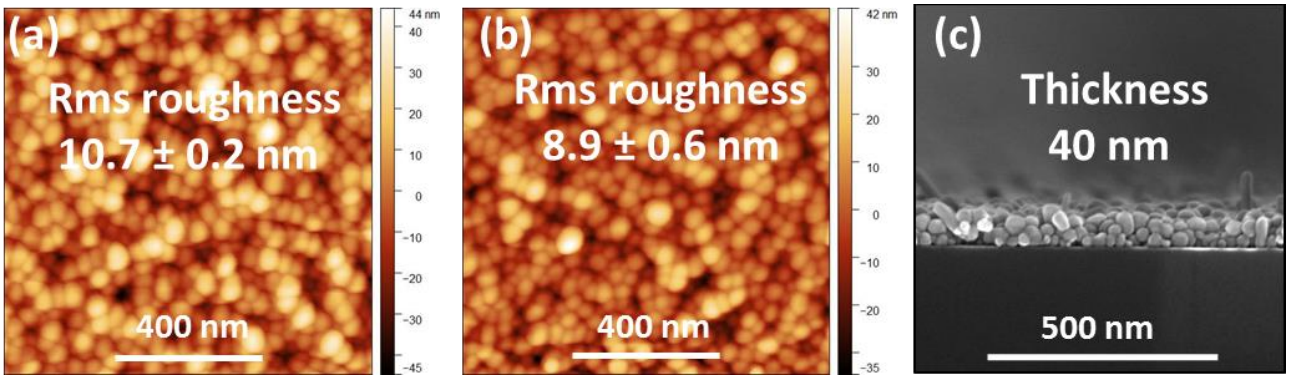


Figure 87: Morphological properties of Ag thin films. (a) and (b) Atomic Force Micrographs of Ag thin films on silicon substrates (a) as-deposited and (b) post-treated films. The EDS equivalent thickness is 40 ± 2 nm in both cases. The values shown in the middle of the images corresponds to the rms roughness of the Ag layer. (c) Scanning electron micrographs cross-section of as-deposited Ag thin film on silicon substrate. The value shown in the middle of the image corresponds to the EDS equivalent thickness of the Ag layer.

## V.1.2. Electrical properties

### V.1.2.1. Critical thickness

Owning its lowest bulk resistivity among the metals, Ag appears as a promising candidate for the replacement of aluminum or copper as interconnects in microelectronics. [17, 38] The small-scale devices used here impose the synthesis of highly uniform and conformal conductive films with low critical thickness as a crucial criterion. The effect of the plasma post-treatment processing on the electrical properties of the silver layers was furthermore investigated. The plot of the sheet resistance Rs as a function of the silver thickness is depicted in Figure 88.

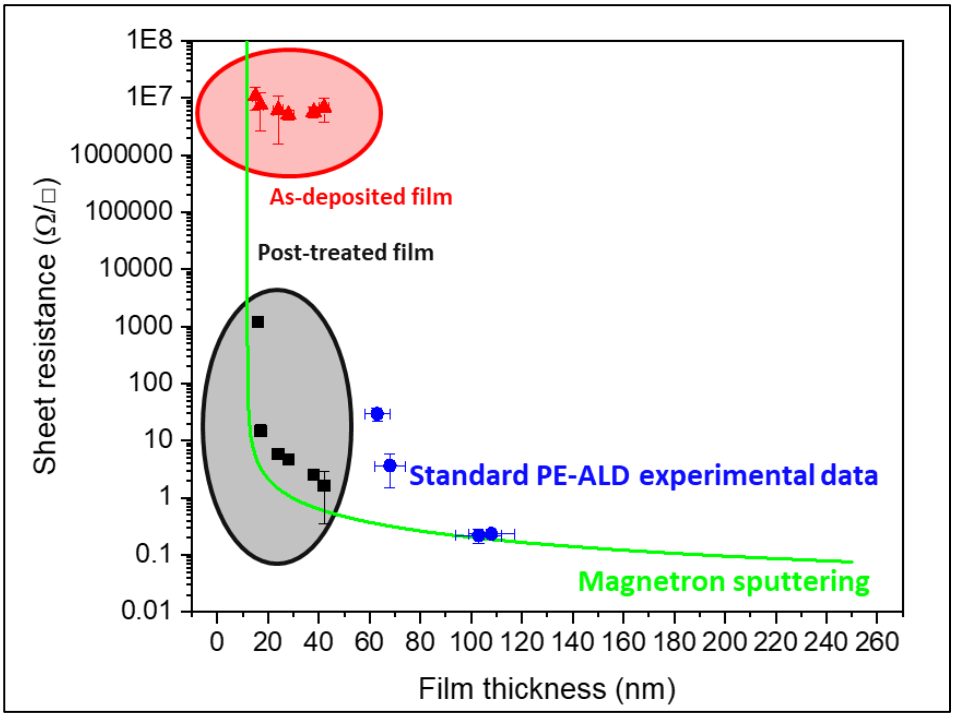


Figure 88: Sheet resistance as a function of EDS equivalent thickness of Ag thin films on glass substrates. The data have been referred for the as-deposited (red triangle symbols) and post-treated (black square symbols) films. The blue spots have been obtained by a standard ALD process, following our previous work presented in chapter 4. The green curve has been plotted as a reference for Ag thin film synthetized by magnetron sputtering, following the publication of Hauder *et al.* [17]

The as-deposited silver films (triangle symbols) present a very high sheet resistance, almost independent of the thickness. The PT strongly reduces this sheet resistance (square symbols), that becomes thickness-dependent, as expected for a uniformly conductive film. Those results match well with the precursor removal of on the surface after PT and its presence for as-deposited films, which is highlighted by chemical analyzes in the next sections. The critical thickness (above which the deposits are conducting) is lower than 15 ± 1 nm, for which the sheet resistance reaches a value of 1.2 ± 0.1 kΩ/□ after post-treatment. This is very close to the state-of-the-art values for sputter-deposited thin films for the same thickness (green curve [17]) and well below the 63 ± 5 nm (value in grey circles) for standard PE-ALD process using the same conditions as the one used in this work. It is also lower than 22 nm, the lowest value for PE-ALD reported by Kariniemi *et al.* [41].

We have also investigated the uniformity of the electrical properties of the coatings on 10 cm x 10 cm flat glass substrate. An average value of the sheet resistance of 3.5 ± 1.4 Ω/□, i.e. with a standard deviation of 40 % over the full sample, confirms the large-scale efficiency of the deposition performed in a standard non-optimized reactor with a diameter of 200 mm.

### V.1.2.2. Mean free path

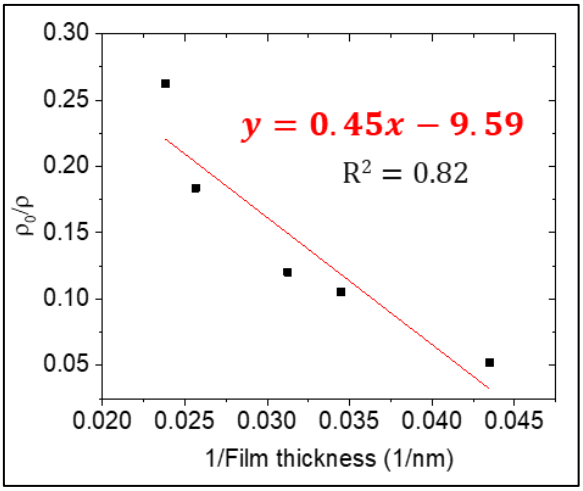


Figure 89: Plot of $\rho_0/\rho$ as a function of the inverse of the film thickness 1/t in order to deduce the mean free path of electrons $\lambda$.

The resulting electrical resistivity after plasma PT fits well to the scaling equation exposed in chapter 2:

$$\frac{\rho_0}{\rho} = 1 - \frac{3\lambda}{8t}$$

As seen in Figure 89, $\lambda$ is equal to 26 ± 2nm , which is very close to the 31 nm found for sputtered Ag films, based on the work of Hauder *et al.* [17]. This means that the conductivity is limited by the surface scattering rather than the grain boundaries and it proves the good quality of the film. The error of the fit ($R^2$ = 0.82) is related to the fact that we assume a continuous film whereas the morphology presents some gaps.

## V.2. Chemical composition and crystallographic properties

The chemical and crystallographic properties of the Ag films have been investigated in order to follow the evolution after deposition and after post-treatment.

### V.2.1. Film composition

Figure 90 presents the survey spectra for as-deposited (Figure 90 (a)) and post-treated Ag film (Figure 90 (b)) and Figure 91 ((a) and (b), the corresponding elemental composition.

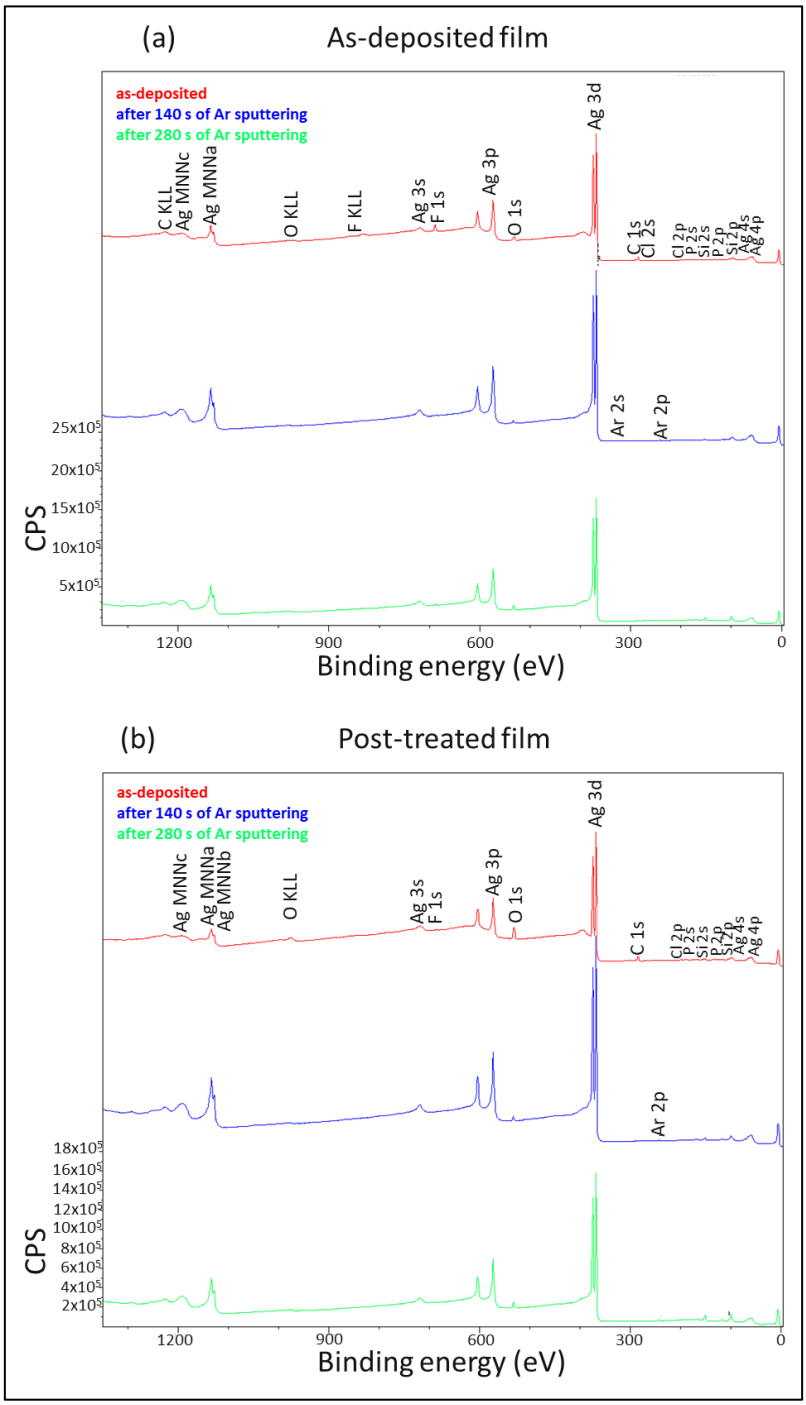


Figure 90: XPS survey spectra of (a) as-deposited and (b) post-treated Ag thin films. Each spectrum was recorded at t=0 (in red) and after Ar sputtering (two different times, t= 140 s in blue and t= 280 s in green).

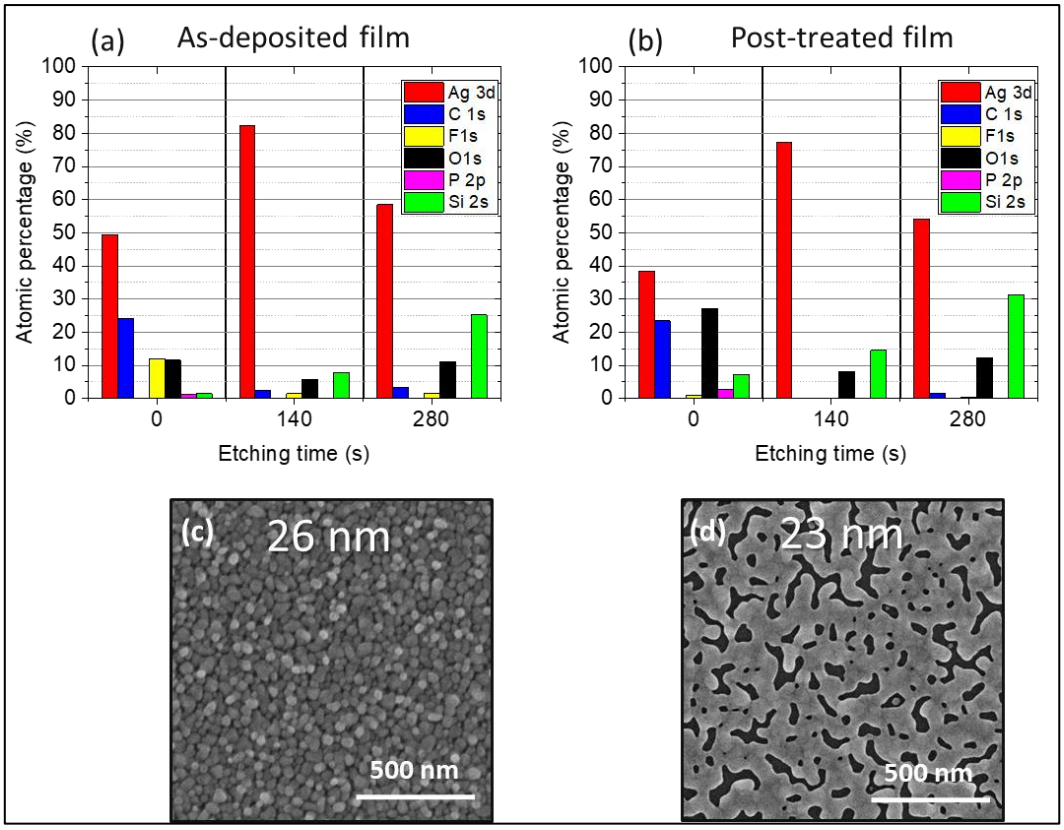


Figure 91: (a) and (b) Elemental composition (in at.%) of Ag thin films synthetized on silicon substrate using the new process (EDS equivalent thickness of 26 ± 2 nm) measured by XPS before (etching time 0 s) and after Ar sputtering (two different etching times, 140 and 280 s). (a) As-deposited and (b) post-treated Ag thin films. (c) and (d) Scanning electron micrographs of the corresponding 26-nm-thick (c) as-deposited and (d) post-treated Ag thin films. The scale bars represent 500 nm.

For the as-deposited film (Figure 91 (a)), the presence of usual contaminants (carbon and oxygen) on the surface of samples exposed to air is observed. Fluorine and phosphorus suggest the presence of unreacted precursor on the particle surface, which also leads to additional carbon and oxygen amounts, and explains the high sheet resistance of the as-deposited film. Due to the small thickness of the film (26 ± 2 nm), the presence of Si could be attributed to the silicon and $SiO_2$ from the substrate. The amount is however close to the detection limit of XPS which is in line with the compact film morphology (see Figure 91 (c) or Figure 85 (d) ). After 140s of etching, one might observe the removal of surface contaminants and unreacted precursor. The almost complete decomposition of the silver precursor is proven by the low amount of carbon, oxygen, fluorine and phosphorus (last two elements are close to the detection limit of XPS). The Ag atomic percentage is thus elevated. After 280s, the interface between the silicon substrate and the deposit is reached since we observe that the Ag amount diminishes whereas the silicon and oxygen amounts increase.

After post-treatment (Figure 91 (b)), the surface contaminants (carbon and oxygen) and the unreacted precursor (fluorine and phosphorus) observed before argon sputtering are still present. However, fluorine content is strongly reduced as compared to the film before post-treatment. The high O amount on the surface might indicate partial oxidation of silver or presence of OH groups at the surface, as the film is exposed to air after post-treatment. The non-100%-covering film structure evidencing the presence of gaps (see Figure 91 (d) or Figure 85 (e) ) and its small thickness (EDS equivalent thickness of 26 ± 2 nm) enable the detection of the silicon and $SiO_2$ from the substrate.

After 140s etching, the surface contaminants and the unreacted precursor are removed. Then the film-substrate interface is reached.

As presented in previous chapter 3 for standard PE-ALD, we have investigated the three satellites in order to discriminate the metallic oxidation state of silver to the oxidation phase.

Firstly, the presence of the resonance plasmon peak in all HR Ag 3d spectra (Figure 92) confirms the presence of Ag as metal for as-deposited and post-treated films. However, when comparing the satellite peak characteristic of the metallic phase for as-deposited and post-treated Ag films, we observe that its intensity is lower after plasma post-treatment, on the surface. In this case, even if the main contribution of Ag is metallic, a part is also attributed to oxidized Ag. This could explain the increase of oxygen in the elemental composition.

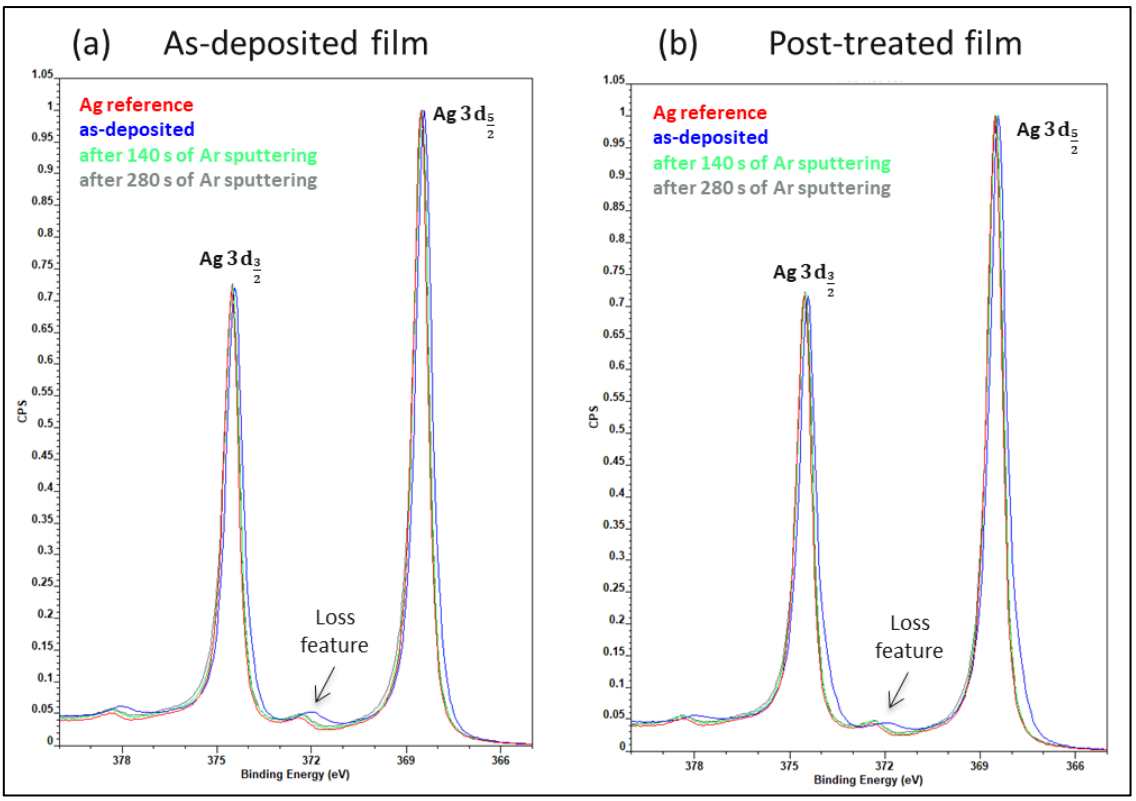


Figure 92: High resolution Ag 3d spectra of (a) as-deposited and (b) post-treated Ag thin films. Each spectrum, compared with the Ag reference (red line), was recorded at t=0 (in blue) and after Ar sputtering (two different times, t= 140 s in green and t= 280 s in grey)

This oxidation of the surface for post-treated film is also confirmed by the form of the Auger peak (Figure 93). Indeed, we observe a slightly distorted spectrum for HR Ag MNN (left part). However, in all cases, metallic Ag is obtained after etching.

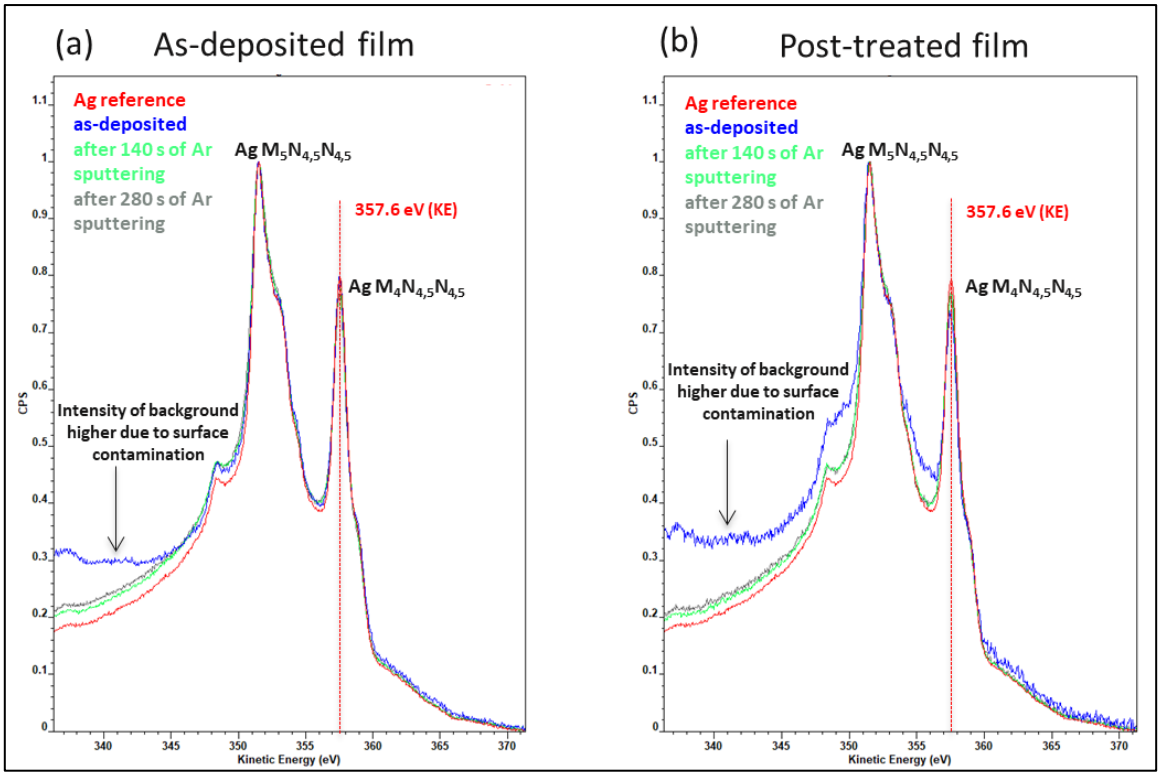


Figure 93: High resolution Ag MNN spectra of (a) as-deposited and (b) post-treated Ag thin films. Each spectrum, compared with the Ag reference (red line), was recorded at t=0 (in blue) and after Ar sputtering (two different times, t= 140 s in green and t= 280 s in grey)

The third signature is the value of the modified Auger parameter α' (Figure 94). The lower Auger parameter before sputtering is an indication of the remaining precursor for the as-deposited film, or the oxidized silver surface for post-treated film. In the bulk (after 140 and 280s Ar etching), the as-deposited film is already made of metallic silver nanoparticles, even if it is non-electrically conductive, proving that a first reduction reaction occurred before the production of the particles. The plasma post-treatment slightly enhances the metallic nature of Ag, which, along with a lower amount of fluorine in the elemental analysis, highlights the removal of unreacted precursor on the particle surface.

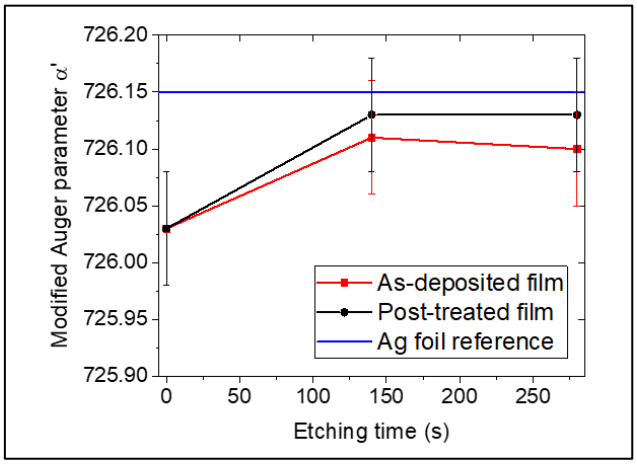


Figure 94: Modified Auger parameter (α') of Ag for different etching times for as-deposited (red squares) and post-treated (black disks) layers. The blue line corresponds to a reference Ag foil. The error bars correspond to the experimental error linked to the spectra acquisition step size.

Another hypothesis to explain the increase of oxygen content in post-treated films could be that the remaining unreacted Ag precursor present on the surface before post-treatment, prevents Ag from oxidation while after PT, the surface is “more metallic” (less precursor residues) thus more easily oxidizable. The HR C1s peak presented in Figure 95 confirms this hypothesis by the presence of the precursor on the surface before plasma post-treatment through the existence of C-$F_2$ and C-$F_3$ groups which are absent after post-treatment.

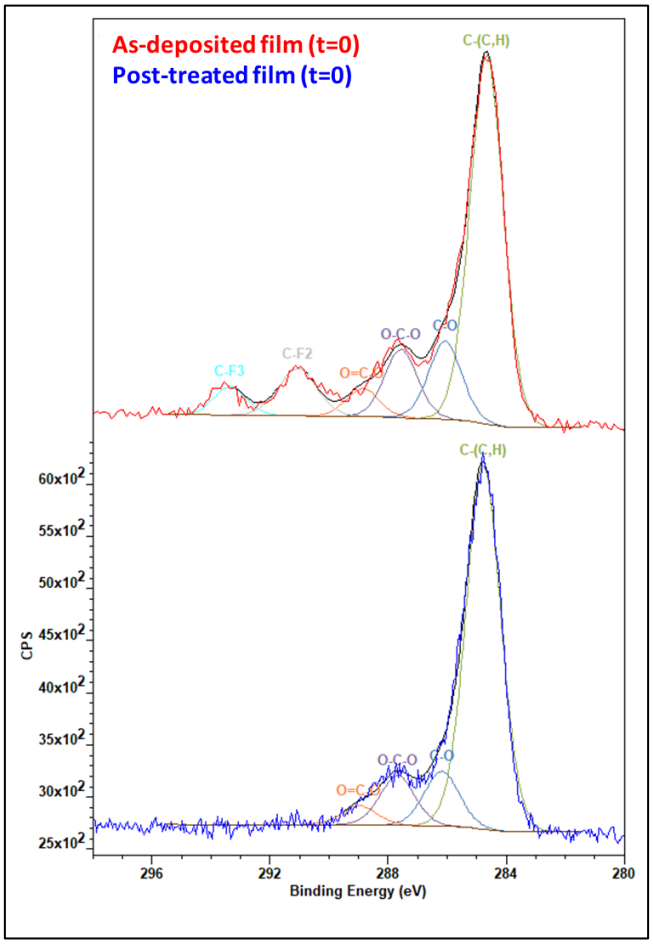


Figure 95: High resolution of C 1s peak of Ag thin film measured by XPS on the surface (t=0 s of Ar sputtering) for (a) as-deposited (in red) and (b) post-treated (in blue) Ag thin films. Deconvolution of C 1s peak has been performed neglecting the presence of C-$CF_2$/C-$CF_3$ (situated between C-(C,H) and C-O) as well as C-F (same position as O=C-O)

ToF-SIMS analyzes have been also performed in order to understand which part of the precursor is remaining to validate this hypothesis. (Figure 96)

The strong decrease of $AgPC_6H_{15}^+$ and $PC_6H_{16}^+$ fragments combined with the increase of silver in the form of several clusters ($Ag^+$, $Ag_2^+$, $Ag_3^+$, $Ag_4^+$, $Ag_5^+$ and $Ag_7^+$) confirms the reduction reaction giving pure silver films. However, in the negative mode, the presence of $C_4O_2F_7^-$ and $C_3F_7^-$ highlights the remaining Ag precursor on the surface. Based on the fragments $PO_2^-$, $PO_3^-$ and $PO_2F_2^-$, one hypothesis could be that the phosphine group has been removed or oxidized during deposition, and fluorine group is remaining. On the other hand, the presence of anions $Cl^-$ and $AgCl_2^-$ in the Ag deposition spectra confirms that it is coming from contamination of the deposition reactor since they are not present in the monomer spectrum.

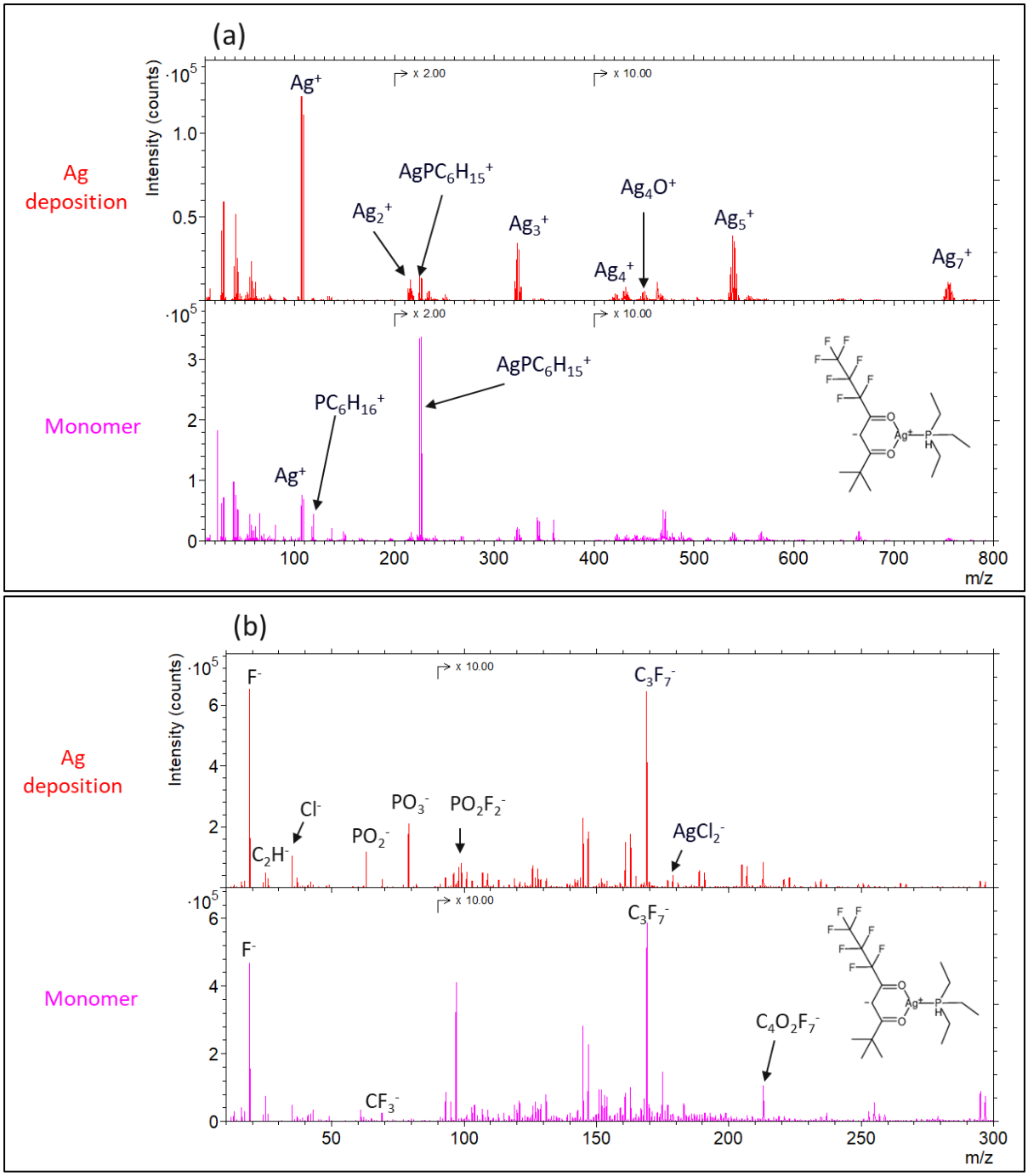


Figure 96: ToF-SIMS spectrogram (intensity as a function the atomic mass m/z) measured (a) in the positive mode (only positive ions are collected) and (b) in the negative mode (only negative ions are collected) for as-deposited Ag (without plasma post-treatment) as well as for the silver precursor Ag(fod)($PEt_3$) (in magenta, chemical formula in the inset).

### V.2.2. Crystalline structure

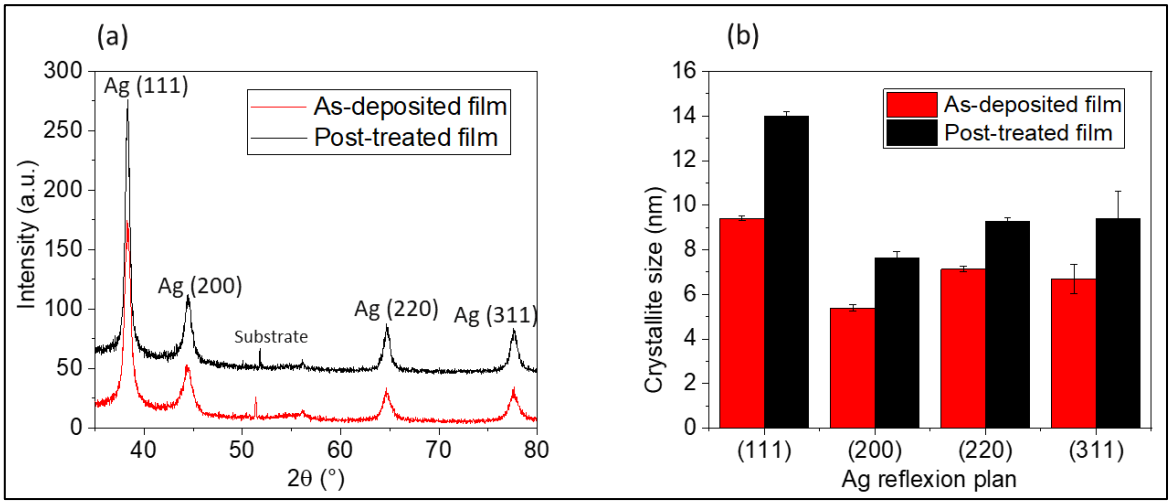


Figure 97: (a) X-ray diffraction spectrogram of Ag thin films synthetized on silicon substrate (EDS equivalent thickness of 61 ± 3 nm) corresponding to as-deposited (in red) and post-treated (in black) films. (b) Crystallite size extracted from (111), (200), (220) and (311) diffraction peaks in (a) of as-deposited (in red) and post-treated (in black) films.

The XRD diffractogram (Figure 97 (a)) shows that the as-deposited film already consists of polycrystalline face centered cubic (fcc) silver ($Fm\bar{3}m$) (JCPDS 04-0783) and exhibits (111), (200), (220) and (311) typical reflections. No signature of other phases, such as silver oxide, are observed. The microscopic crystalline structure is slightly affected by the plasma post-treatment. Indeed, the main difference between the two products remains in the crystallite size, as determined by the analysis of the peak width using a Lorentzian fitting function and the Debye–Scherrer equation [203, 204] (Figure 97 (b)). It increases for post-treated film, with a preferential growth in the (111) direction.

Until now, we have shown that the as-deposited film made of compact NPs exhibited poor electrical conductivity due to the presence of remaining unreacted Ag precursor on the surface. By sintering the compact NPs, the PT removes the remaining precursor and confers competing electrical properties to sputter-deposited thin films.

In the next sections, we describe the main parameters influencing the new processing conditions, both for the deposition of compact nanoparticles as well as for the post-treatment. The main difference as compared to the standard PE-ALD process is the continuous exposure of the precursor during the plasma pulse. The cycling only requires two steps, (i) a first step where the precursor reacts with the substrate without the need of plasma (section V.3.), and (ii) a second step with a plasma pulse, during which the precursor is still exposed, but react both with the plasma and the substrate (section V.4.).

The main criterion for validating the process is the morphology of the resulting film, which must be made of a compact film of nanoparticles (see Figure 85 (d)) rather than isolated islands as observed for the standard PE-ALD process (see Figure 85 (c)). The uniformity of this morphology is also an important criterion. For the films after post-processing, the important criterion is the conductivity of the film.

## V.3. Investigation of the deposition parameters in order to understand the growth mechanism

### V.3.1. Influence of the deposition parameters with continuous silver precursor exposure

We have investigated the deposition conditions in order to obtain a uniform new morphology made of compact nanoparticles. The investigated parameters and their range of investigation are described in Table 26. We first study the influence of these parameters on the deposition and then propose a model for the growth mechanism of Ag compact films.

| Parameters | Symbol | Units | Range | Optimum |
|---|---|---|---|---|
| Chamber temperature | $T_{ch}$ | °C | 130, 150 | 150 |
| Hot source temperature | $T_{hs}$ | °C | 100, 130 | 130 |
| **Argon flow in the plasma head** | $Ar_{pl}$ | sccm | 100, 300 | 300 |
| **Argon flow in the process lines** | $Ar_{pr}$ | sccm | 100, 300 | 300 |
| Argon flow in the chamber | $Ar_{ch}$ | sccm | - | 100 |
| Hydrogen flow in the plasma head | $H_{2pl}$ | sccm | - | 20 |
| Pulse time 1 of Ag precursor | $t_{pr}$ | s | Constant | constant |
| **Pulse time 2 of plasma** | $t_{pl}$ | s | 0, 1, 3, 5, 10 | 3 |
| Purge time 1 after Ag pulse | $t_{pu1}$ | s | Constant | constant |
| **Purge time 2 after plasma pulse** | $t_{pu2}$ | s | 0, 1, 10, 50, 100 | 10 |
| **Distance substrate-grid** | $d$ | cm | 1, 2.5, 4 | 2.5 |
| **RF plasma power** | $P_{dep}$ | W | 20, 50, 100 | 50* |

Table 26: List of experimental parameters and investigated studied for the optimization of the first step of the two-step processing. For the study, we focus on the five parameters written in red. The other parameters are fixed and based on the previous results, except if defined otherwise in the caption of the figure. *: these two parameters need to be correlated in order to have the same efficiency of the plasma source.

#### V.3.1.1 Influence of the plasma conditions: RF plasma power $P_{dep}$ and distance grid-substrate $d$

One of the main parameters that we identified as critical for obtaining a uniform deposition of a film with the new morphology is the “plasma density”, which is influenced by the RF power, the distance between the grid and the substrate, the Ar flows.

The SEM images of the film obtained in different conditions and at variable RF plasma powers is shown at two position in Figure 98. At high RF power of 100 W (Figure 98 (a)), the morphology in the middle of the wafer (10 cm) is very similar to the standard ALD process. At a RF power of 50 W (Figure 98 (b) and (d)), the morphology at 5 cm is the expected one for the new process, while the result at 10 cm is still disconnected islands. At the lowest RF plasma power of 20 W (Figure 98 (d)), the morphology of compact nanoparticles is observed at both positions on the wafer. It is clear that the lower RF power favors the morphology with compact nanoparticles. We note that, in the absence of plasma (RF power set to zero), no deposition occurs, as demonstrated previously for standard PE-ALD in chapter 3. The plasma is thus still important in order to make the precursor react with the surface. We note as well that the lowest RF plasma power achievable in our system strongly depends on the history of the reactor, as in certain conditions powers lower than 50 W give strong fluctuations of the plasma conditions, and no deposition.

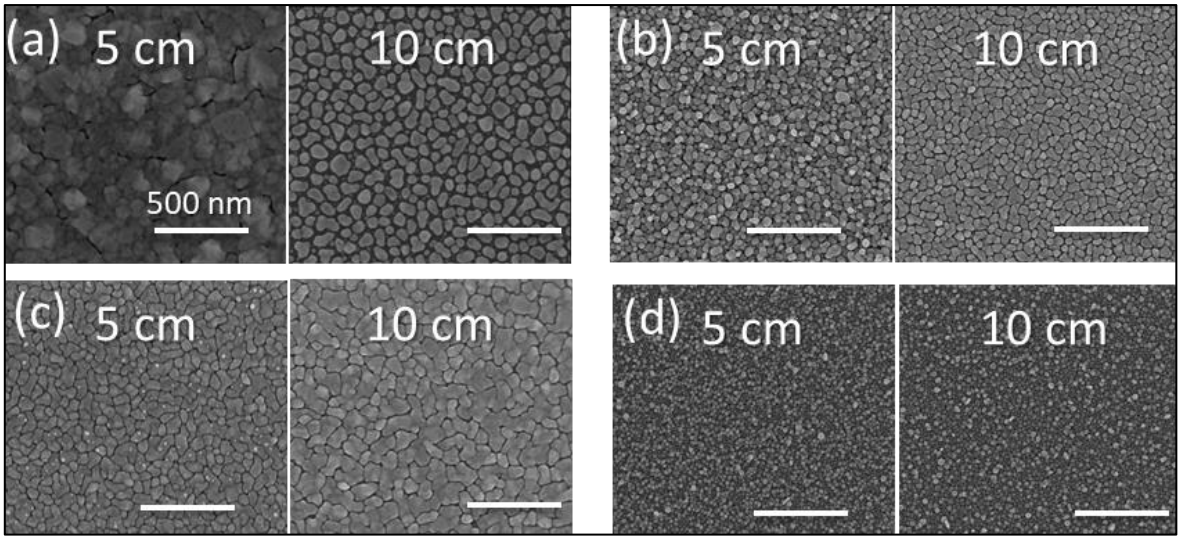


Figure 98: Scanning Electron Micrographs of films deposited at various RF power $P_{dep}$ for 3 different conditions and at two positions on the wafer (5 cm and 10 cm, as indicated on the images). (a-b) distance grid-substrate d = 1 cm, with RF plasma power of (a) 100 W and (b) 50 W. (c-d) distance grid-substrate d = 4 cm, with RF plasma power of (c) 50 W and (d) 20 W. The other deposition parameters are the optimum ones exposed in Table 26 for 400 cycles, except $T_{ch}$ = 130°C and $T_{hs}$ = 100°C. The scale bars correspond to 500 nm.

In the remote plasma conditions used during the processing, another parameter influencing the concentration of radicals interacting with the sample surface is the **distance between the grid and the sample**. Two distances have been investigated, 1 cm and 4 cm, as shown in Figure 99. The larger plasma distance seems to favor a more compact film as compared to the lower plasma distance, which seems to lead to separated islands. We note however that, in both case for the RF plasma power of 50 W, compact nanoparticles are mainly obtained at the inlet, and islands are still observed in the center. The influence of the plasma distance is thus not as important as the one of the RF plasma power.

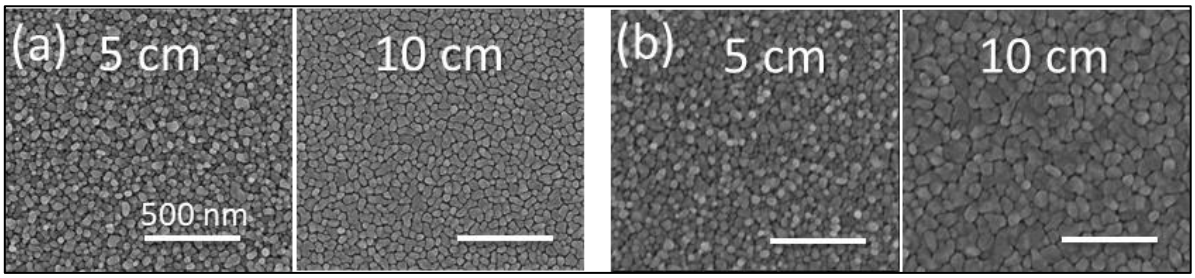


Figure 99: Scanning Electron Micrographs of films deposited at various distances *d* between the grid and the substrate of (a) 1 cm and (b) 4 cm, and at two positions on the wafer (5 cm and 10 cm, as indicated on the images). The RF plasma power is fixed at 50 W. The other deposition parameters are the optimum ones exposed in Table 26 for 400 cycles, except $T_{ch}$ = 130°C and $T_{hs}$ = 100°C. The scale bars correspond to 500 nm.

The conclusion of this part is that the new morphology is first due to the continuous exposure of the silver precursor during the plasma pulse, but also that mild plasma conditions are required. The mild plasma conditions are obtained by using low RF power or high distance between the grid and the sample. Optimum conditions then achieve a deposition of ultra-thin compact film made of Ag nanoparticles over the entire 200 mm wafer, as shown in Figure 100.

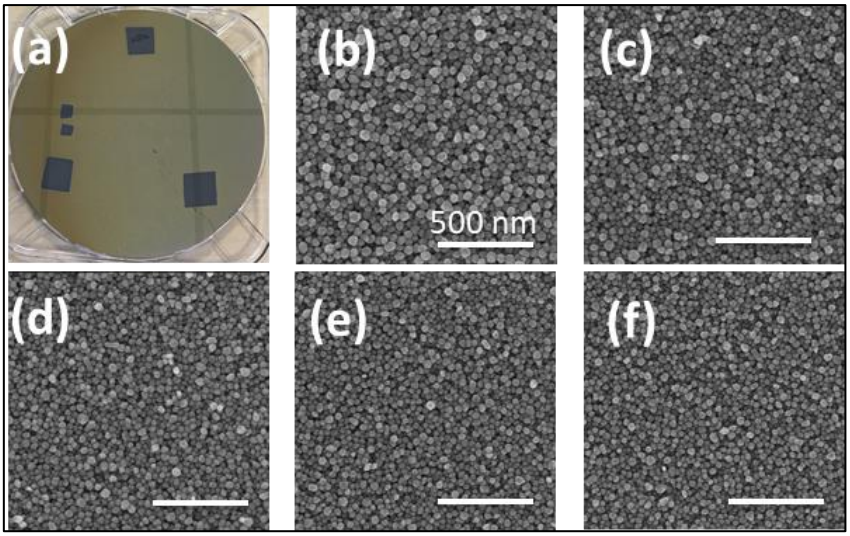


Figure 100: (a) Optical image of the 200 mm Si substrate (black squares are due to presence of small samples during deposition) and (b-f) Scanning Electron Micrographs of the film obtained at different positions on the Si 200 mm wafer substrate in the new processing conditions. Distance from the inlet of the reactor: (b) 5 cm, (c) 7.5 cm, (d) 10 cm, (e) 12.5 cm and (f) 15 cm. Deposition parameters are the optimum ones exposed in Table 26 for 400 cycles. The scale bars correspond to 500 nm.

### V.3.1.2. Influence of the chamber and hot source temperatures: $T_{ch}$ and $T_{hs}$

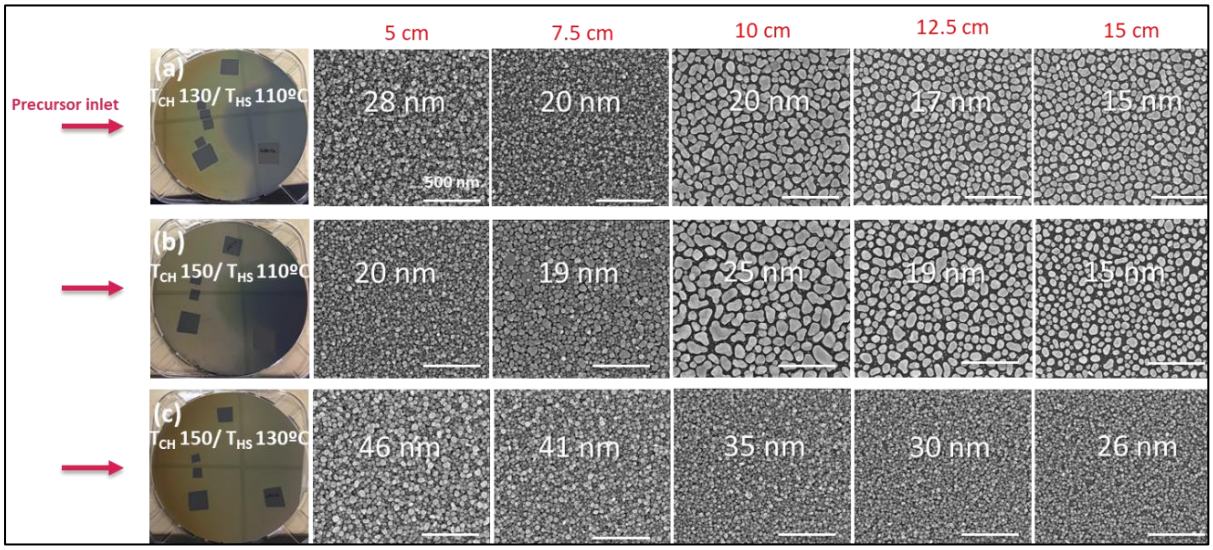


Figure 101: Optical images (left) and scanning electron micrographs (right) at different positions on the 200 mm Si wafer as compared to the inlet of the reactor, indicated above the images. The deposition temperatures are (a) $T_{ch}$ = 130°C and $T_{hs}$ = 110°C, (a) $T_{ch}$ = 150°C and $T_{hs}$ = 110°C and (c) $T_{ch}$ = 150°C and $T_{hs}$ = 130°C. The other deposition parameters are the optimum ones exposed in Table 26 for 400 cycles. The inlet of the reactor is indicated by the pink arrow. The scale bars correspond to 500 nm. The darker squares on the Si wafer mark the positions of glass samples used for electrical measurements.

The chamber temperature $T_{ch}$ controls the substrate temperature which influences directly the rates of the chemical reactions (precursor with the surface, and reduction) and the mobility of the reactants on the surface and the hot source temperature, $T_{hs}$ influences the amount of precursor exposed in the reactor as it is linked to the evaporation rate of the precursor.

The couple of temperatures $T_{ch}$/$T_{hs}$ plays a critical role on the uniformity of the deposition. Figure 101 shows images of the wafer and SEM pictures for three different temperature conditions. The best uniformity is obtained when both the precursor and the chamber temperatures are increased to $T_{ch}$ 150°C/ $T_{hs}$ 130°C, see Figure 101 (c). An increase of the chamber temperature alone (Figure 101 (b)) does not show a significant improvement as compared to the deposition performed at lower temperature (Figure 101 (a)). A proposed explanation is given in the next section.

#### V.3.1.3. Influence of the plasma pulse time and purge time after the plasma pulse: $t_{pl}$ and $t_{pu2}$

We have investigated the influence of the plasma pulse time and of the purge time between the plasma pulses on the uniformity of the morphology of the silver film. The plasma pulse time is responsible of the creation of the hydrogen radicals and during the purge time, Ag precursor fills the reactor.

In all cases presented here, the obtained morphology is a compact film of nanoparticles. However, Figure 102 already shows that the pulse and purge times strongly impact the uniformity of the film, i.e. by changing the observed color on the wafer. The color is related to the thickness, but also to the morphology, i.e. a yellowish color is obtained for compact NPs whereas a silver color is produced for separated islands. Indeed, for a given plasma pulse time $t_{pl}$, the purge time $t_{pu2}$ does not change a lot the uniformity of the deposition. In contrast, a change of $t_{pl}$ at a constant $t_{pu2}$, gives a very high uniformity variation. The best uniformity is obtained for a pulse time as short as 3 s but a too short $t_{pl}$ gives reduced deposition. Figure 103 highlights that the uniformity variation is directly correlated to a change in film morphology. A higher plasma pulse time gives two different morphologies, compact NPs at the left side of the 200mm Si wafer and islands on the right side whereas 3s-pulse gives compact NPs all along the substrate.

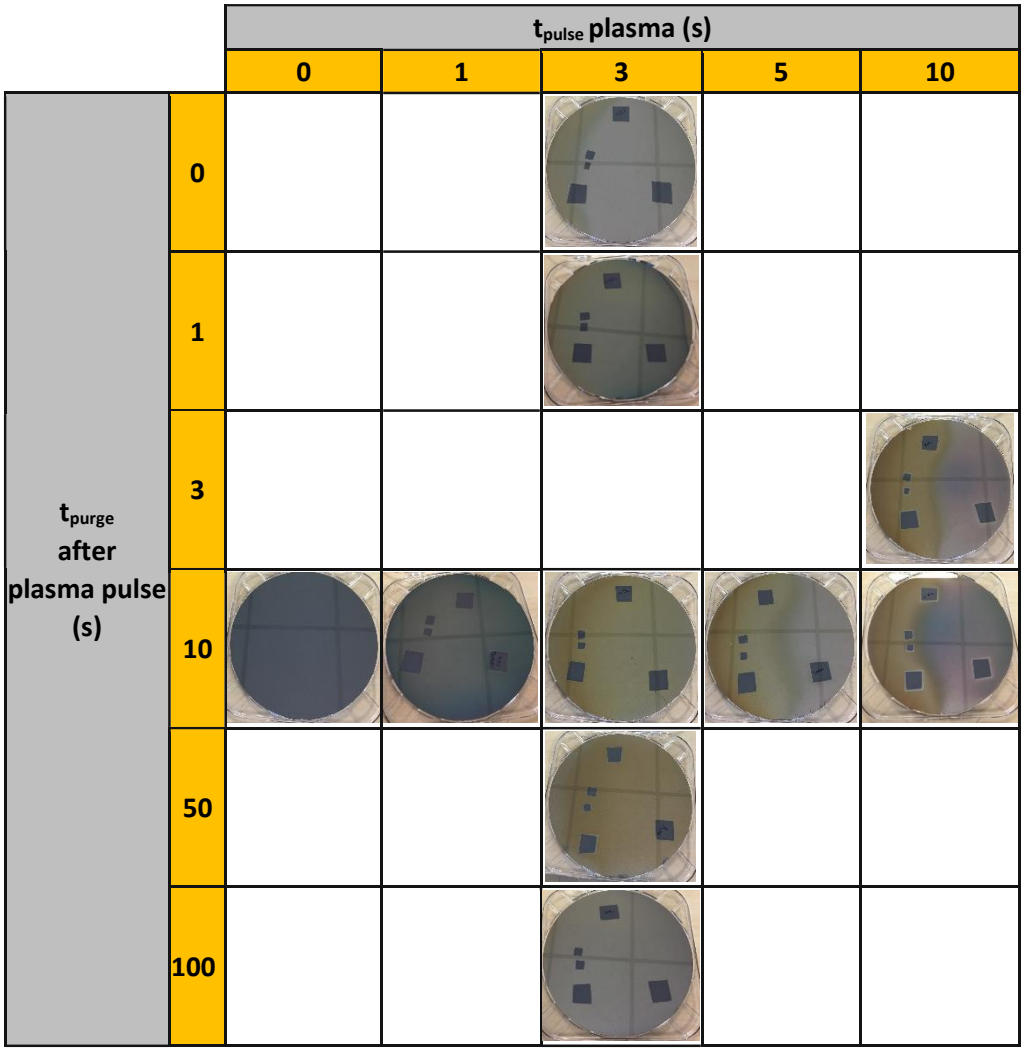


Figure 102: Optical images of 200 mm wafer after deposition of 400 cycles of silver using the continuous exposure of Ag precursor and before the plasma post-processing step (black squares are due to presence of small samples during deposition). The change of color of the surface is directly correlated with the change of the film thickness and morphology. The other deposition parameters are the optimum ones exposed in Table 26 for 400 cycles.

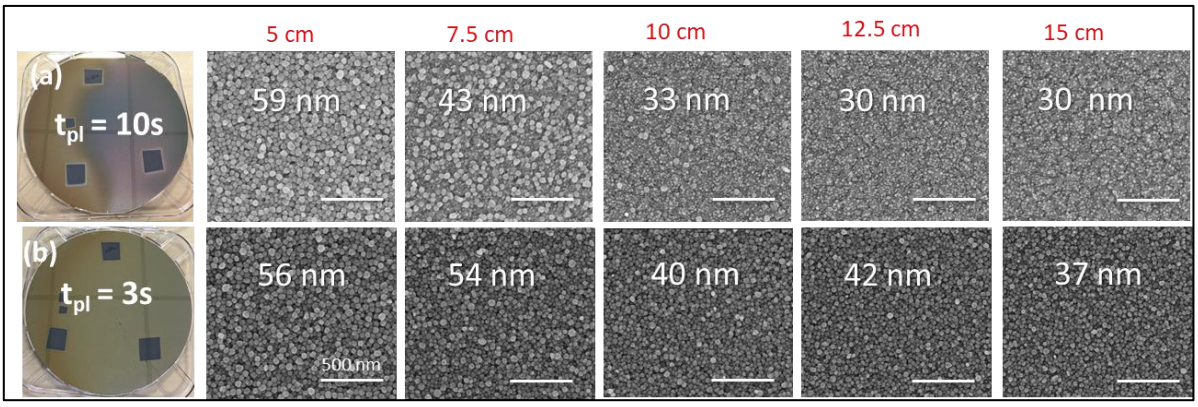


Figure 103: Influence of the plasma pulse time $t_{pl}$ (a) 10 s and (b) 3 s at a given purge time ($t_{pu2}$ = 10 s), on the uniformity of the deposition. Optical images (left) and scanning electron micrographs (right) at different positions on the 200 mm Si wafer as compared to the inlet of the reactor, indicated above the images. The other deposition parameters are the optimum ones exposed in Table 26 for 400 cycles. The scale bars correspond to 500 nm. The darker squares on the Si wafer mark the positions of glass samples used for electrical measurements.

### V.3.1.4. Influence of the argon flows: $Ar_{pr}$ and $Ar_{pl}$

The flow of carrier gas, i.e. the **Ar process flow $Ar_{pr}$** is expected to influence the amount of precursor carried to the reactor. As seen on the optical images of the Si wafer and SEM images in Figure 104, a low Ar process flow leads to a strong non-uniformity both of the thickness (color of the wafer in the optical image and EDS thickness) and the film morphology: a thicker film made of close NPs at the inlet and disconnected islands which decrease in coverage from the center to the outlet. However, when increasing $Ar_{pr}$, even if a variation of the thickness of 50% is observed, the film is made of compact NPs all along the 200 mm substrate.

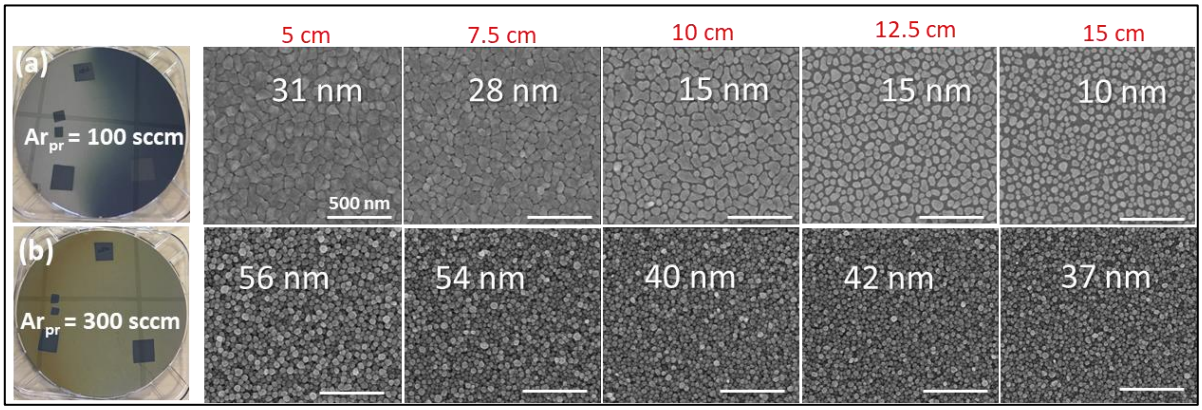


Figure 104: Influence of the Ar process flow $Ar_{pr}$ (a) 100 sccm and (b) 300 sccm on the uniformity of the deposition. Optical images (left) and scanning electron micrographs (right) at different positions on the 200 mm Si wafer as compared to the inlet of the reactor, indicated above the images. The other deposition parameters are the optimum ones exposed in Table 26 for 400 cycles. The scale bars correspond to 500 nm. The darker squares on the Si wafer mark the positions of glass samples used for electrical measurements.

The **Ar flow in the plasma head $Ar_{pl}$**, is expected to influence the amount of radicals arriving on the substrate for the reduction reaction. For Ar plasma flow, as shown in Figure 105, we observe the same compact NPs morphology and good uniformity for the two sets of measurements. However, the thickness is different with a thick film obtained for higher $Ar_{pl}$ flow.

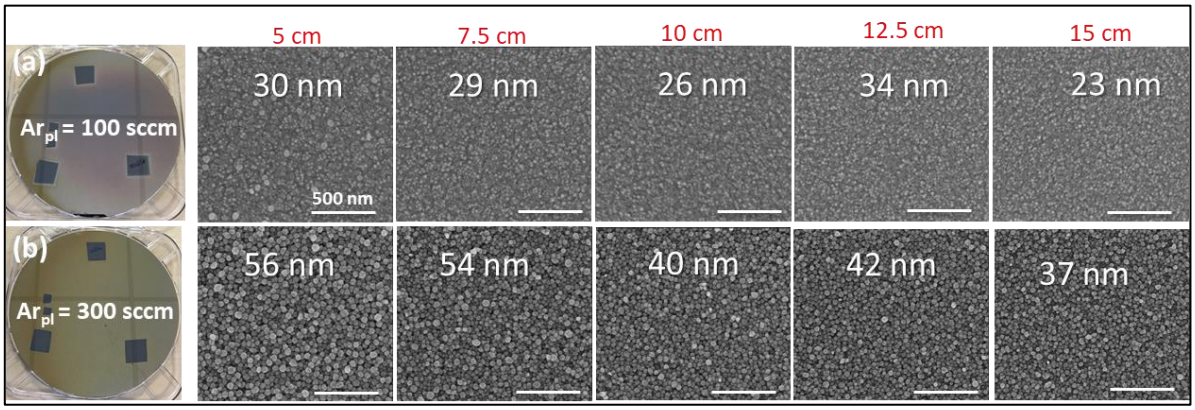


Figure 105: Influence of the Ar plasma flow $Ar_{pl}$ (a) 100 sccm and (b) 300 sccm on the uniformity of the deposition. Optical images (left) and scanning electron micrographs (right) at different positions on the 200 mm Si wafer as compared to the inlet of the reactor, indicated above the images. The other deposition parameters are the optimum ones exposed in Table 26 for 400 cycles. The scale bars correspond to 500 nm. The darker squares on the Si wafer mark the positions of glass samples used for electrical measurements.

### V.3.2. Discussion of a proposed model for the growth mechanism of silver compact films

We have established an hypothesis regarding the new process giving Ag compact NPs speculating that we not only have a surface reaction but also a gas-phase reaction. In order to validate this hypothesis, the previous results have been used to create a model for the growth mechanism, as illustrated in Figure 106.

Based on these results obtained regarding the **influence of the plasma conditions**, we give an hypothesis on the role of the plasma conditions (Figure 106 (a)). It is obvious from previous analysis that mild plasma conditions favor the deposition of the new morphology (compact nanoparticles) as compared to the morphology already identified in the standard PE-ALD process (disconnected islands). We make an hypothesis on the deposition mechanism that may explain this observation. Here we speculate that the new morphology is obtained due to the reaction of the silver precursors with radicals in the gas phase, rather than on the substrate surface as expected for the standard ALD process. The non-uniform deposition from the inlet to the outlet of the reactor may be explained by the cross-flow of the gas carrying the precursor (from the inlet to the outlet) and the flow of gas carrying the radicals (vertically from the top to the substrate surface). Then it is easy to understand that the new morphology is obtained more favorably at the inlet rather than at the outlet. In case of strong plasma conditions, this mechanism consumes the total amount of incoming precursor at the inlet. This has been demonstrated by performing a continuous deposition with both the precursor and the plasma activated continuously, i.e. in a chemical vapor deposition (CVD mode). In this case, deposition occurs only at the inlet. With a continuous precursor flow and the pulsed plasma (process investigated here), the mechanism alternates between the CVD mode at the inlet, and the ALD mode at the outlet, since the precursor reaches the outlet only when the plasma is off. This could explain why the compact nanoparticles are observed at the inlet, and that the morphology at the outlet is close to the one observed for the standard ALD. At last, with mild plasma conditions, the radicals only activate the precursor without consuming it fully at the inlet, and the activated precursor can then cover the full surface with the new compact morphology.

During the **purge time**, we have only the continuous exposure of the Ag precursor which gets into the reactor and start to fill it, but no chemical reaction is taking place (Figure 106 (a)). When the **plasma pulse** is activated, the Ag precursor continues to be exposed but at the same time, the radicals created by the plasma arrive at the top (Figure 106 (b)). When $t_{pl}$ **is too short,** we have a gas-phase reaction but no film deposition on the substrate since we do not have a reducing agent to react with the adsorbed Ag precursor. On the contrary, when $t_{pl}$ **is too long**, we have enough hydrogen radicals for reacting with the silver precursor and thus a gas-phase reaction only takes place at the inlet of the wafer because it stops the precursor arrival and prevent it to reach the outlet. Consequently, at the outlet, we have a surface reaction since the precursor adsorbed on the surface is reduced by the $H_2$ plasma. This explains why we observed compact NPs at the inlet versus disconnected islands at the outlet. Finally, at **optimum plasma pulse time**, there is not enough $H_2$ plasma to react with the adsorbed Ag precursor in such a way that only a gas-phase reaction can take place in all position of the wafer and compact NPs are obtained. We used this model in order to understand the other parameters.

The other parameter that influences the growth mechanism is the **temperatures**, both of the chamber and the hot source (Figure 106 (c)). $T_{ch}$ controls the substrate temperature and thus the chemical reactions: the surface reaction and the reduction reaction. $T_{hs}$ controls the injected amount of precursor and the evaporation rate: when $T_{hs}$ increases, the propagation speed of precursor increases too. When $T_{hs}$ is higher than $T_{ch}$, we observe a condensation of the Ag precursor in the precursor driving line and thus no film deposition. A higher $T_{ch}$ than $T_{hs}$ is needed. At the standard temperatures $T_{ch}$ 130°C/ $T_{hs}$ 110°C, we observe the same effect than the one when using a too long plasma pulse time: gas-phase reaction at the inlet part and surface reaction at the outlet. When increasing $T_{ch}$ to 150°C while keeping $T_{hs}$ at 110°C, we observe the same non-uniformity. The primordial criterion to explain the change of morphology and uniformity is thus the hot source temperature. When it is increased to 130°C, the precursor flow increases too and we obtained the best film uniformity and a gas-phase reaction occurring on the entire substrate surface, giving compact NPs.

The **Ar process flow** controls the precursor exposure and is thus directly correlated with the effect of $T_{hs}$: the higher the **Ar process flow** $\boldsymbol{Ar_{pr}}$, the more the precursor amount exposed, leading to a uniform gas phase reaction (Figure 106 (d)). A too-low $Ar_{pr}$ causes a gas-phase reaction only at the inlet and a surface reaction at the outlet. For the **Ar plasma flow** $\boldsymbol{Ar_{pl}}$ (Figure 106 (e)), the morphology and uniformity remain constant but a difference in thickness is noticed. We need an equilibrium where enough $Ar_{pl}$ is injected in order to obtain enough hydrogen radicals arrival in the reactor and a better reaction efficiency.

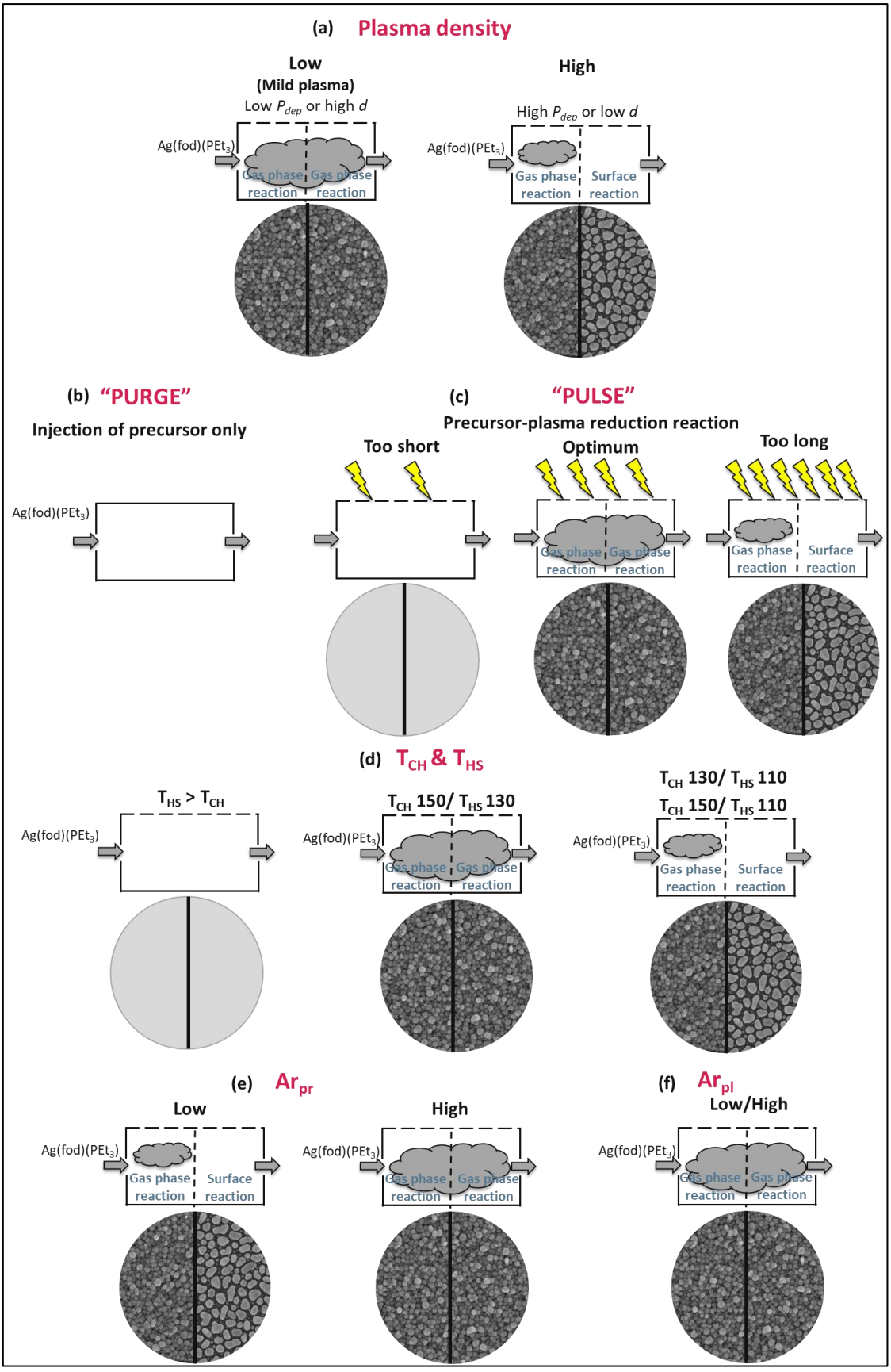


Figure 106: Schemes representing the influence on the Ag deposition morphology of (a) plasma density based on Figure 98 and Figure 99 (b) purge time $t_{pu2}$ after plasma pulse based on Figure 102 and Figure 103, (c) plasma pulse time $t_{pl}$ based on Figure 102 and Figure 103, (d) couple of temperatures $T_{ch}/T_{hs}$ based on Figure 101, (e) Ar process flow $Ar_{pr}$ based on Figure 104 and (f) Ar plasma flow $Ar_{pl}$ based on Figure 105.

### V.3.3. Conclusion

This part has been dedicated to the investigation of the deposition parameters for obtaining a thin compact silver film which represents the first stage of the two-step approach. We have first observed that, by exposing the precursor during the plasma pulse, a silver thin film made of dense and compact nanoparticles is deposited by using mild plasma conditions, i.e. low RF power or high distance between the grid and the sample. Higher deposition temperatures and Ar flows have shown to strongly improve the morphology and uniformity of the deposition.

Based on the experimental results, we have proposed a model for the growth mechanism of Ag compact films. This model highlights that, during the first deposition step which consists of a modified PE-ALD process, the precursor is exposed into the chamber also during the plasma pulse, thus making the reaction not only on the surface but also in the gas phase.

The as-deposited films are however weakly conductive. The second step consisting of a further plasma post-treatment in order to sinter the particles, resulting in a highly conductive ultra-thin film, is the object of the next section.

## V.4. Investigation of the post-processing of silver films made of compact nanoparticles

As explained in the principle of the two-step process (section V.1.1.), the post-treatment step is required in order to provide films with high conductivity by merging the particle and form a percolated film (Figure 85 (e)). This post-treatment step involves hydrogen plasma treatment during a given period, without precursor exposure and the parameters that have been investigated are described in Table 27.

| Parameters | Symbol | Units | Range |
|---|---|---|---|
| **$H_2$ flow in the plasma head** | $H_{2pl}$ | sccm | 0, 20, 40 |
| **Ar flow in the plasma head** | $Ar_{pl}$ | sccm | 140, 300 |
| **Ar process flow** | $Ar_{pr}$ | sccm | 50, 300 |
| **Time of post-treatment** | $t_{post}$ | s | 60-2430 |
| **Distance substrate-grid** | $d$ | cm | 1, 4 * |
| **RF plasma power** | $P_{post}$ | W | 100, 150, 200, 250 |

Table 27: List of parameters studied for the optimization of the plasma-post treatment process. * in the direct post-treatment configuration, the grid has been removed.

As presented in chapter 2, it is important to note that, for plasma post-processing, we have used a remote capacitively coupled plasma (RF, 13.56 MHz) placed on top of the reactor. A grid serves as a ground electrode and defines the plasma chamber. This leads to a decrease of flux and energy of the ions towards the substrate but also to a somewhat reduced radical density flowing into the reactor. In order to enhance the efficiency of the plasma by promoting the hydrogen radical's density, we have also studied the effect of removing the grid and thus creating a direct contact with the active plasma. These two configurations, named arbitrary "direct PT" for PT performed in the absence of the grid and "indirect PT" for PT performed in the presence of the grid, are indicated systematically as the results are presented.

### V.4.1 Influence of the post-processing on the morphology

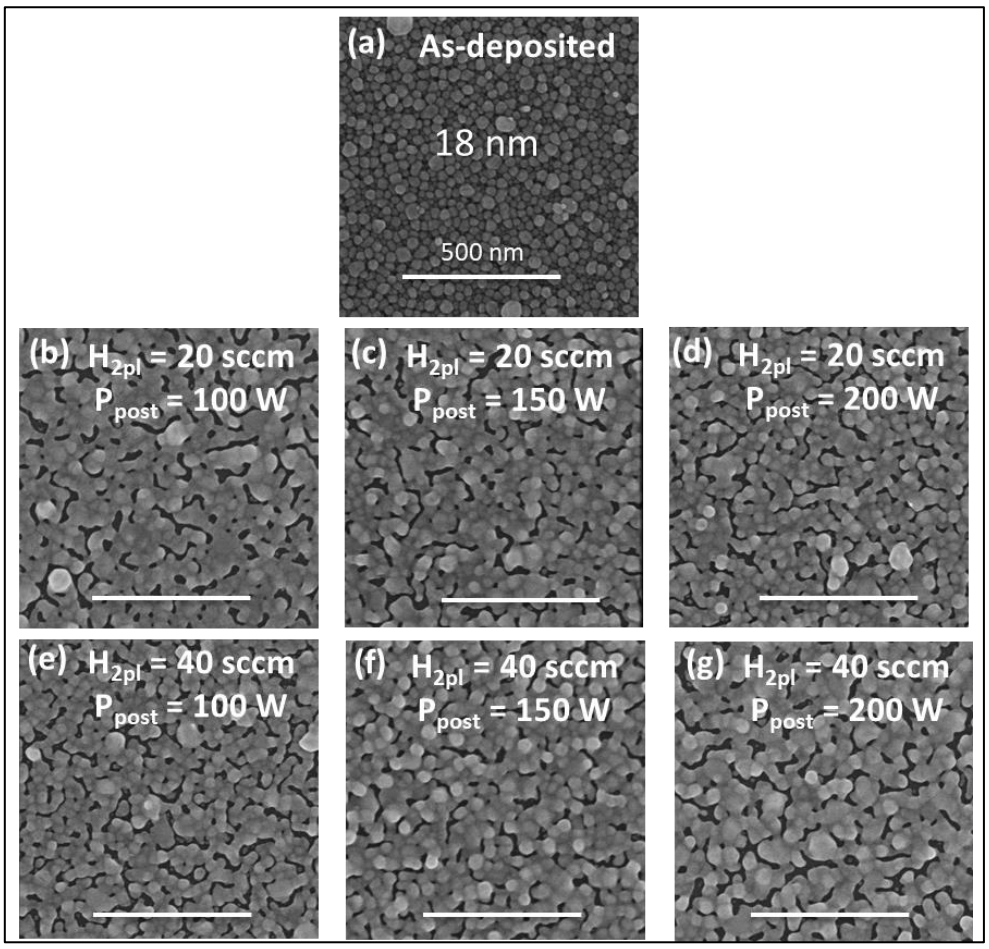


Figure 107: Scanning electron micrographs of silver films deposited on Si (with native oxide) at $T_{ch}$ = 110°C before (a) and after (b-g) 600 s of plasma post-treatment done with the presence of the grid (indirect PT) at *d* = 1 cm, $Ar_{pl}$ = 300 sccm and $Ar_{pr}$ = 300 sccm and showing different morphologies regarding the studied parameters ($H_{2pl}$ flow plasma head and plasma power $P_{post}$): (a) as-deposited silver film, (b) for $H_{2pl}$ = 20 sccm/ $P_{post}$ = 100 W, (c) for $H_{2pl}$ = 20 sccm/ $P_{post}$ = 150 W, (d) for $H_{2pl}$ = 20 sccm/ $P_{post}$ = 200 W, (e) for $H_{2pl}$ = 40 sccm/ $P_{post}$ = 100 W, (f) for $H_{2pl}$ = 40 sccm/ $P_{post}$ = 150 W and (g) for $H_{2pl}$ = 40 sccm/ $P_{post}$ = 200 W. The values present on the images refer to the thickness of the films determined by EDS. The scale bars correspond to 500 nm.

In this part, we study the influence of the different plasma post-treatment conditions exposed in Table 27 on the morphology of the silver films, with the aim to obtain a continuous film.

Figure 107 reveals the scanning electron micrographs of silver films deposited on Si and post-treated under **different $H_2$ flow injected in the plasma head $H_{2pl}$** and **RF plasma power $P_{post}$**. After silver deposition, the film is made of dense and compact nanoparticles (Figure 107 (a)). When we apply a hydrogen-based plasma post-processing, the particles sinter together, giving more continuous Ag films in all the cases studied and a gentle decrease of the rms roughness from 5.23 ± 0.24 nm for as-deposited film to 4.44 ± 0.23 nm after 600 s of PT performed at 100 W is observed (Figure 107 (b)). On the other hand, slight changes in the morphology are noticed as a function of the ratio between hydrogen flow and plasma power. At $P_{post}$ of 100 W and 150 W, the increase of $H_{2pl}$ from 20 sccm (Figure 107 (b) and Figure 107 (c), respectively) to 40 sccm (Figure 107 (e) and Figure 107 (f), respectively) leads to a lower degree of coalescence of the particles whereas at 200 W, a higher degree of coalescence is obtained for the highest $H_{2pl}$ (Figure 107 (g)). At 20 sccm of $H_{2pl}$, increasing $P_{post}$ leads

to less sintered nanoparticles (Figure 107 (b-d) but at 40 sccm of $H_{2pl}$, the highest plasma power gives the most percolated film (Figure 107 (g)). Both hydrogen flow and plasma power are responsible of the density of the bombardment of energetic hydrogen radicals on the substrate. In order to obtain the highest degree of coalescence of the particles, a post-treatment with an optimum ratio of plasma power/hydrogen flow is needed to promote enough hydrogen radical's density while preventing film dewetting.

Figure 108 reveals the scanning electron micrographs of silver films deposited on Si and post-treated in the **presence** of **$H_2$ flow injected in the plasma head** ***$H_{2pl}$*** under different **argon flows** ***$Ar_{pr}$/$Ar_{pl}$*** (300 sccm/300 sccm and 50 sccm/140 sccm). The morphology of films post-treated in the **absence of** ***$H_{2pl}$,*** i.e. using argon-based post-processing are also shown.

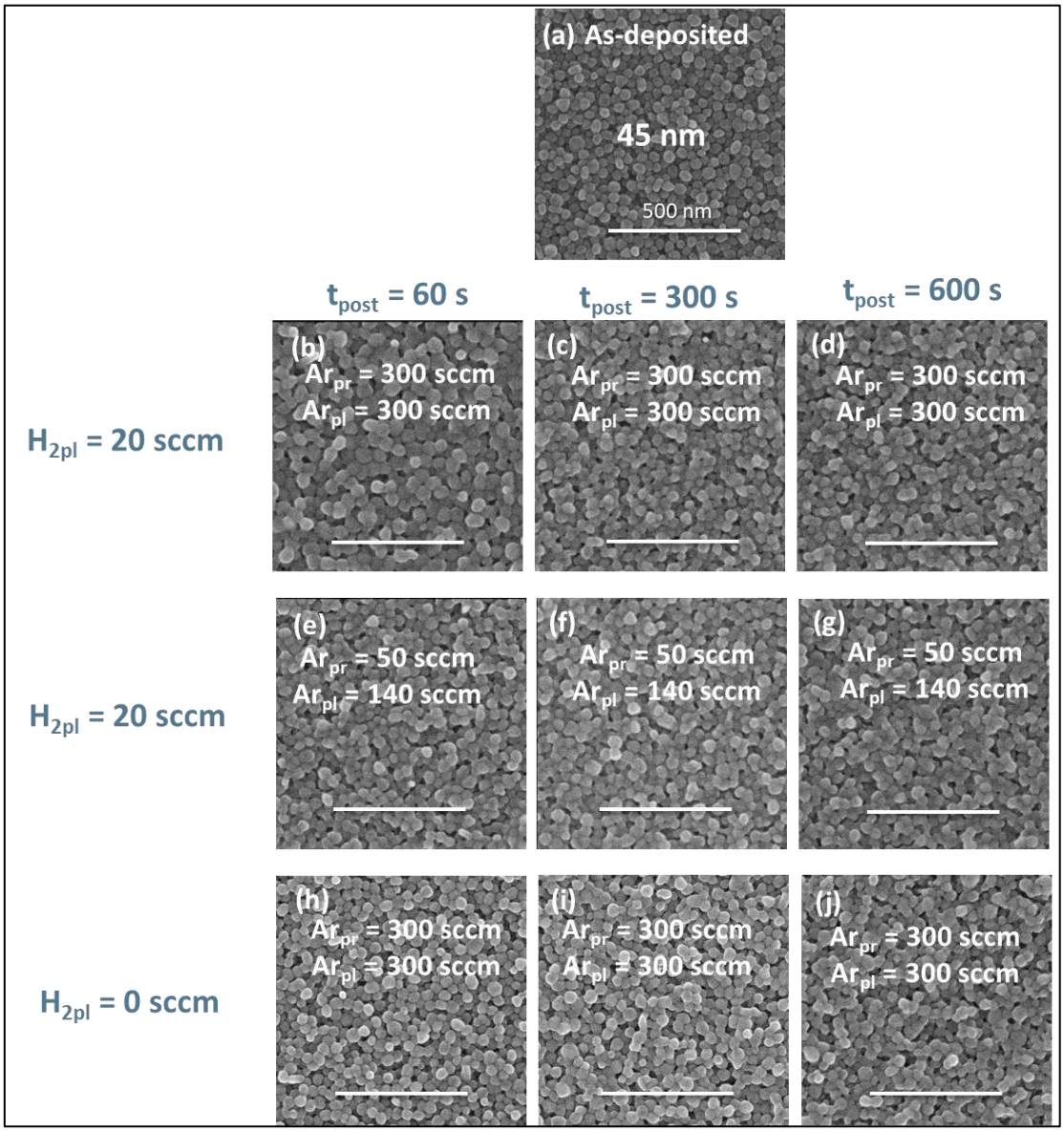


Figure 108: Scanning electron micrographs of silver films deposited on Si (with native oxide) at $T_{ch}$ = 110°C before (a) and after (b-j) plasma post-treatment done with the presence of the grid (indirect PT) at d = 1 cm, $P_{post}$ = 100 W, at different duration of post-processing $t_{post}$: (b-e-h) 60 s, (c-f-i) 300s and (d-g-j) 600 s. The post-treatment have been performed in the presence of 20 sccm of $H_2$ flow (b-g) either with (b-d) $Ar_{pr}$ = 300 sccm / $Ar_{pl}$ = 300 sccm or (e-g) $Ar_{pr}$ = 50 sccm / $Ar_{pl}$ = 140 sccm and in the absence of $H_{2pl}$ (h to j). The value on the image (a) refers to the EDS thickness of the films. The scale bars represent 500 nm.

The role of the chemical nature of the plasma gas, and thus the **nature of the radicals** created by the glow discharge, has been tested by comparing post-processing performed under $Ar/H_2$ vs. under Ar flows injected in the plasma head in Figure 108 (b-d) and Figure 108 (h-j), respectively. Higher degree of coalescence is obtained using hydrogen-based plasma as compared to argon-based plasma. This observation is independent of the plasma post treatment duration time $t_{post}$. The explanation is the higher reactivity of H radicals as compared to Ar radicals.

Due to the geometry of the reactor, i.e. the cross-flow delivery system of the argon carrier gas $Ar_{pr}$ coming from the inlet to the outlet and the **flow of argon $Ar_{pl}$** carrying the radicals vertically from the top to the substrate surface, the amount of radicals hydrogen radicals arriving on the substrate is then impacted. When comparing high $Ar_{pl}$ of 300 sccm in Figure 108 (b-d) to lower one of 140 sccm in Figure 108 (e-g), no obvious differences in film morphology are extracted, even at larger $t_{post}$. It is important to note that the $Ar_{pr}$ has been fixed in order to not disturb the gas symbiosis. As a conclusion, the Ar flow used during post-processing is a parameter not as important as expected.

The **distance *d* between the grid and the substrate** also plays a role on the hydrogen radicals density flowing into the reactor and their energy. The higher the distance, the less dense and less energetic hydrogen radicals when arriving on the surface. When comparing two films presenting roughly the same initial morphology and thickness but post-treated with the grid placed at two different distances (Figure 109), we see that morphology of the film post-treated with the lower *d* (Figure 109 (b)), presents a mosaic-like structure and a higher degree of coalescence as compared to higher *d* ((Figure 109 (d)). The plasma is thus more efficient when the grid is placed close to the substrate, promoting a higher amount of reactive species. The next study exposes post-treatments performed in the direct mode, i.e. in the absence of the grid in order to enhance the efficiency of the plasma.

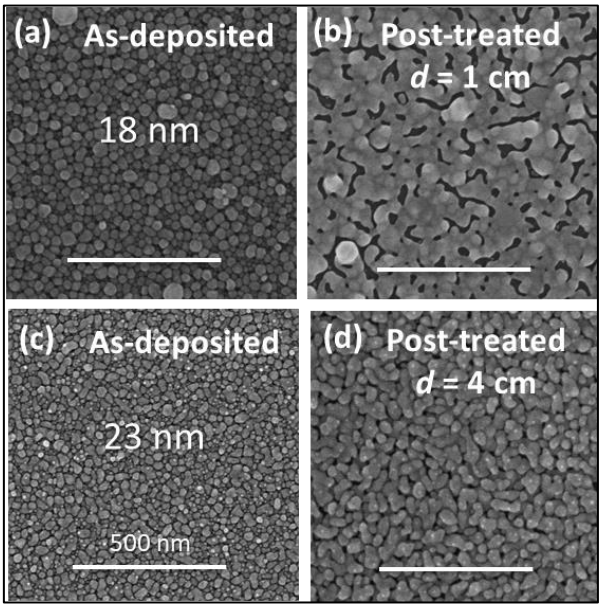


Figure 109: Scanning electron micrographs of silver films deposited on Si (with native oxide) before (a and c) and after (b and d) plasma post-treatment done at $P_{post}$ = 100 W during $t_{post}$ = 600 s under 20 sccm of $H_2$ flow, $Ar_{pl}$ = 300 sccm, $Ar_{pr}$ = 300 sccm with the presence of the grid (indirect PT) placed at (b) *d* = 1 cm and (d) *d* = 4 cm from the substrate.

Figure 110 shows the scanning electron micrographs of silver films deposited on Si after a fine tuning of the **time of plasma post-treatment $t_{post}$**. The 17-nm-thick as-deposited Ag film is made of

compact film morphology composed of multiple layers of particles (Figure 110 (a)) which partially merge after 5 s of post-processing (Figure 110 (b)). Then, the film coverage decreases with the increased $t_{post}$ leading to the presence of gaps and a mosaic-like structure (Figure 110 (c-d)). As shown in the cross-section images, prolonged plasma exposure time generates the spreading of the film on the substrate (Figure 110 (d)) and after the final post-treatment exposed in Figure 110 (e), the layer dewetting is taking place due to the high efficiency of the active species of the plasma.

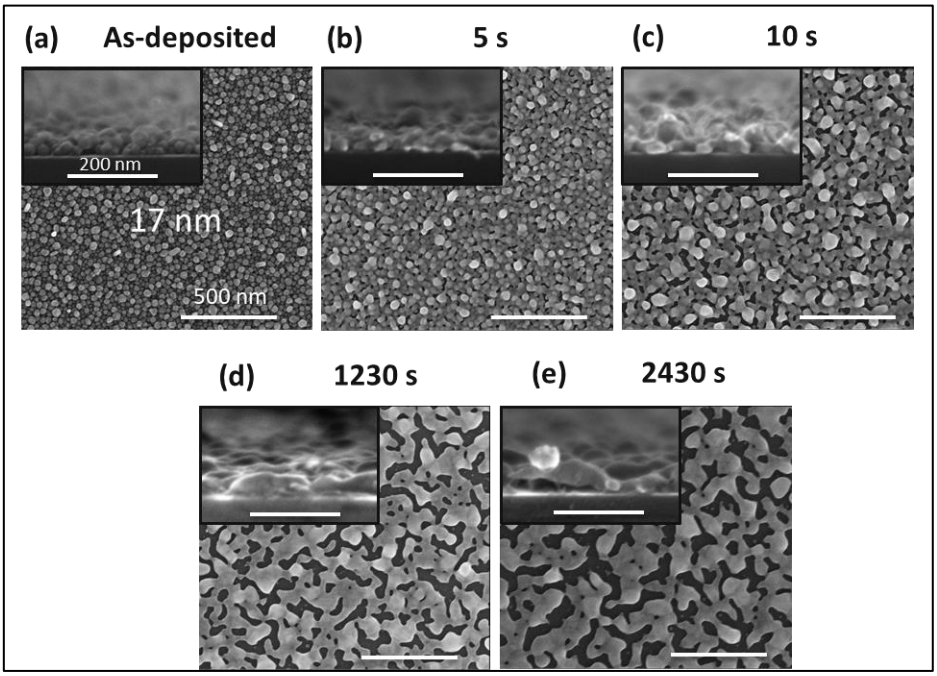


Figure 110: Scanning electron micrographs in top view and cross section (inset) of a 17-nm-thick silver films deposited on Si (with native oxide) at $T_{ch}$ = 140°C before (a) and after (b-e) plasma post-treatment done at $P_{post}$ = 100 W, $Ar_{pl}$ = 300 sccm and $Ar_{pr}$ = 300 sccm under 20 sccm of $H_2$ flow in the plasma head without the grid (direct PT) and showing different morphologies regarding the studied parameter (time of post-treatment $t_{post}$): (a) as-deposited silver film, (b) $t_{post}$ = 5 s, (c) $t_{post}$ = 10 s, (d) $t_{post}$ = 1230 s and (e) $t_{post}$ = 2430 s (1230 s at $P_{post}$ = 100 W + 1230 s at $P_{post}$ = 100 W). The value on the image (a) refers to the EDS thickness of the films. The scale bars represent 500 nm for the top view images and 200 nm for the cross views.

### V.4.2. Influence of the post-processing on the electrical properties

In this subsection, we study the effect of both the plasma post-treatment processing power ($P_{post}$) and its duration ($t_{post}$) on the electrical properties of the silver films as they are the more significant parameters to judge the efficiency of the post-processing and have the higher influence on the film morphology.

#### V.4.2.1. RF plasma power $P_{post}$ of plasma post-treatment

Figure 111 presents the dependence of the sheet resistance of silver films on the RF plasma power $P_{post}$ used during post-treatment. The as-deposited silver film presents a very high sheet resistance (or very low electrical conductivity) due to the presence of unreacted silver precursor and lack of connection between particles, as already mentioned in previous section. Increased plasma power yields to more energetic radicals' bombardment thus the film sheet resistance decreases with the RF plasma power, demonstrating a sheet resistance of $9.23\times10^{1}$ Ω/□ (conductivity of $2.85\times10^{3}$ S/cm) for a 20-nm- thick silver film. This conclusion is in agreement with the study of the films'

morphology and it demonstrates that the post-processing power improves the electrical conductivity of silver films by increasing the connectivity between particles.

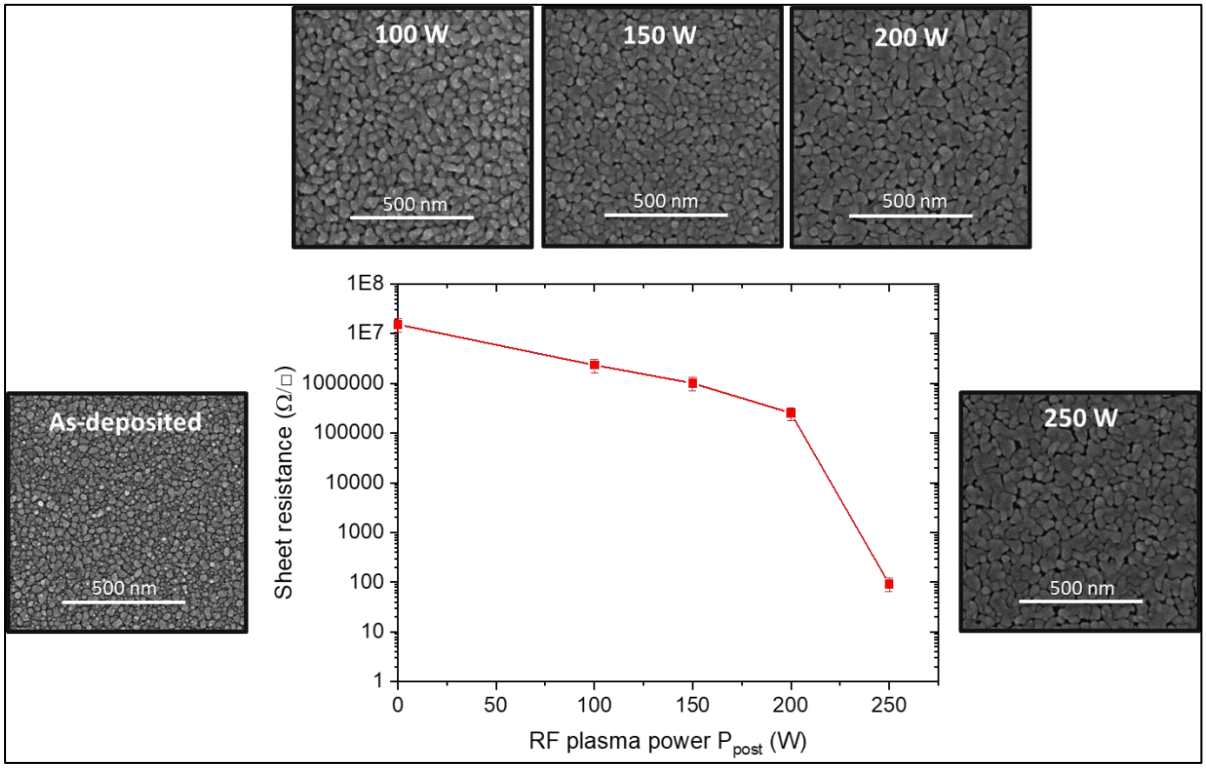


Figure 111: Influence of the RF plasma power $P_{post}$ used during 600 s of post-processing on the sheet resistance of a 20-nm-thick Ag film deposited on glass substrate at $T_{ch}$ = 130°C with the presence of the grid (indirect PT) at $d$ = 4 cm, $Ar_{pl}$ = 300 sccm and $Ar_{pr}$ =300 sccm under 20 sccm of $H_2$ flow in the plasma head and corresponding scanning electron micrographs showing different morphologies regarding the studied parameter (RF plasma power $P_{post}$): from left to right: as-deposited silver film and for $P_{post}$ = 100 W, $P_{post}$ = 150 W, $P_{post}$ = 200 W and $P_{post}$ = 250 W. The scale bars correspond to 500 nm.

By applying a post-treatment in the absence of the grid, i.e. in the direct PT configuration, on a 40-nm-thick Ag film, the initial sheet resistance of $2.75\times10^7$ Ω/□ (conductivity of 9.10 mS/cm) decreases drastically to 15 Ω/□ (conductivity of $1.67\times10^4$ S/cm) already after 50 W performed during 10 min. This proves the higher efficiency of the post-treatment in this configuration.

### V.4.2.2. Time of plasma post-treatment $t_{post}$

We have tried to find a correlation between the film morphology and the electrical properties of Ag film with a fine tuning of the plasma post-treatment time $t_{post}$ with the more efficient configuration, i.e. in the absence of the grid (direct PT). The plot of the sheet resistance as a function of $t_{post}$ exposed in Figure 112 highlights the presence of different regimes. In the first regime ($t_{post}$ < 5 s, green region), a sharp decrease of the sheet resistance by severale orders of magnitude is observe while the film morphology remaines the same as for as-deposited film and made of well-defined compact nanoparticles. This change in electrical properties is probably due to the removal of the Ag precursor from the surface, as already proved by the chemical analyses in section V.2.. After that, in the second regime (5 s < $t_{post}$ < 30 s, blue region), the sheed resistance still decreases but at much lower rates. This corresponds to the transition from compact NPs to partial sintering of the NPs. In the third regime ($t_{post}$ > 30 s, pink region), a total sintering of the NPs gives a stable sheet resistance. After this plateau, we observe no more variation of the Rs but only a decrease of the film coverage.

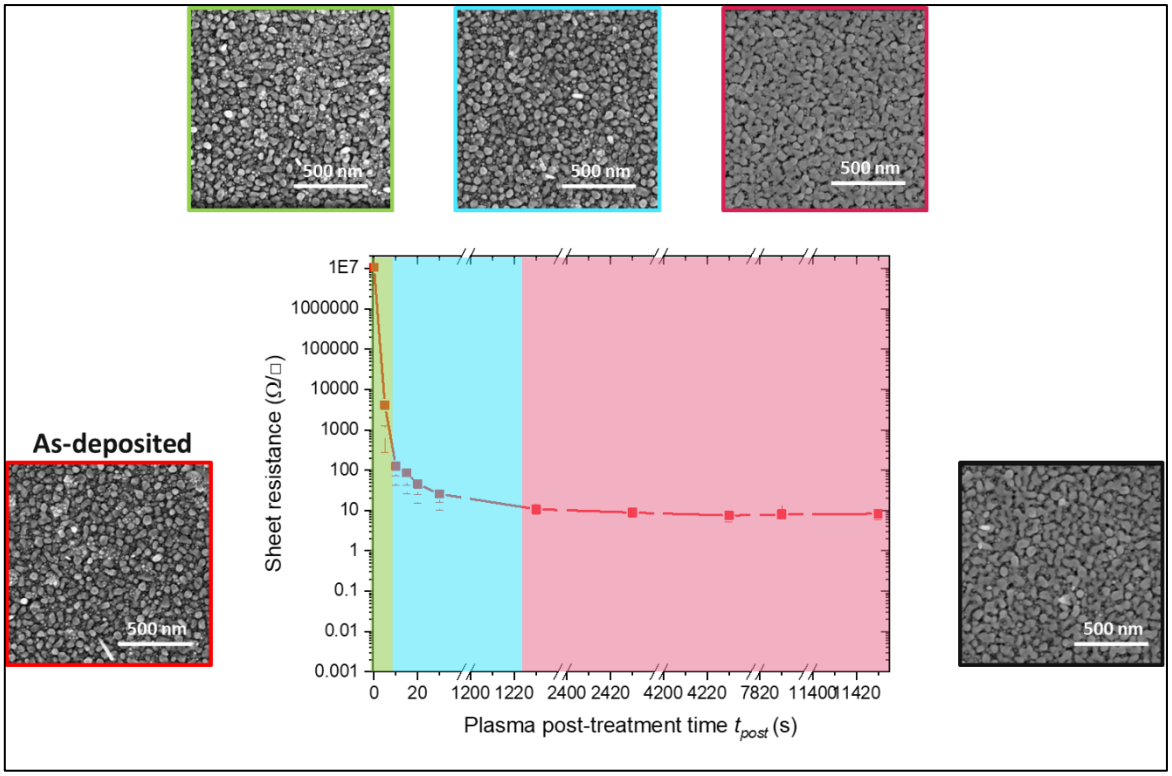


Figure 112: Influence of the plasma post-treatment time $t_{post}$ (direct PT) at $Ar_{pl}$ = 300 sccm and $Ar_{pr}$ = 300 sccm under 20 sccm of $H_2$ flow in the plasma head on the sheet resistance of a 40-nm-thick Ag film deposited on glass substrate with different colored zones corresponding to different regimes and Scanning electron micrographs outlined with the corresponding colored zones of the graph (from left to right): red outline: as-deposited film, green outline: $t_{post}$ = 5s / $P_{post}$ = 100 W, blue outline: $t_{post}$ = 20 s / $P_{post}$ = 100 W, pink outline: $t_{post}$ = 1230 s / $P_{post}$ = 100 W, black outline: $t_{post}$ = 1230 s / $P_{post}$ = 100 W + $t_{post}$ = 1200 s / $P_{post}$ = 150 W + $t_{post}$ = 5400 s / $P_{post}$ = 200 W + $t_{post}$ = 3600 s / $P_{post}$ = 250 W. The scale bars of SEM images represent 500 nm.

### V.4.2.3. Supplementary results

As supplementary results, when Ag depositions have been performed in the absence of hydrogen flow in the plasma head ($H_{2pl}$ set to 0 sccm), i.e. only in the presence of argon bombardment, we interestingly obtained the compact NPs morphology. However, the films were totally insulating, even after the hydrogen-based plasma post-processing. This is in agreement with the explanation of higher reactivity of H radicals as compared to Ar radicals.

In previous section, we have demonstrated the principle of the deposition of ultra-thin Ag films made of compact nanoparticles, and the post-processing step in order to merge the particle for producing a conductive film. An important conclusion is the apparent finite depth treated by the post-processing step, which is expected since the post-treatment is a surface processing step.

In order to provide films with arbitrary thicknesses using this two-steps processing (deposition of compact nanoparticles followed by a post-processing step), we have proposed a processing scheme involving both steps in a super-cycle, as described in Table 28. The number of cycles $N_1$ = 20 is evaluated for a deposition of 1 nm thick film, and the number $N_2$ enables us to investigate various thicknesses.

| Step | | Time | Repetitions | |
|---|---|---|---|---|
| **1** | Precursor pulse | $t_1$ = 10 s | $N_1$ = 20 | $N_2$ = 10, 20 |
| **2** | Plasma + precursor pulse | $t_2$ = 3 s | | |
| **3** | Purge | $t_3$ = 20 s | 1 | |
| **4** | Plasma post-treatment | $t_4$ = 1 min | | |

Table 28: Description of the super-cycles used for the deposition of Ag thin films.

For both depositions, the morphology is a compact silver film. We however observe a non-uniformity in the center of the wafer, where the film is thinner and still has the morphology of the films without post-treatment. We point out that the super-cycle was not fully optimized, in particular concerning the periodicity of the post-treatment. This non-uniformity might also be due to non-uniformity of the plasma in the chamber.

Regarding the electrical properties obtained by the super-cycle, we manage to reach a critical thickness as low as 25 ± 1 nm giving a conductivity of $1.41\times10^4$ S/cm (sheet resistance of 29 Ω/□) with the 10x20 super-cycle process and 50 ± 1 nm for the 20x20 super-cycle process giving a conductivity of $1.32\times10^5$ S/cm (sheet resistance of 1.5 Ω/□). The conductivity observed with this new processing scheme is close to the one demonstrated in previous section for the two-step process after plasma post-treatment. Nevertheless, no real improvement has been obtained. We note however that the process sequence has not been fully optimized, in particular concerning the periodicity of the super-cycle (value of $N_2$) and the post-treatment time (1 min) which have been estimated from assumptions on the deposition process with continuous precursor exposure and the post-treatment tests.

### V.4.3. Conclusion

The investigation of the hydrogen-based post-processing parameters performed on Ag films made of compact nanoparticles has been achieved regarding their influence on both the film morphology and the electrical properties. The sintering of the silver nanoparticles enhances the electrical conductivity of silver films by increasing the connectivity between particles. The plasma parameters (RF plasma power $P_{post}$ and time of plasma post-treatment $t_{post}$) highlight the presence of higher density of energetic radicals created by an increase of plasma power and prolonged plasma exposure time. This leads to a higher degree of coalescence of the particles.

## V.5. Conclusion

In this chapter, we have exposed a new process based on a two-step approach, which represents the most promising alternative to obtain ultra-thin continuous Ag films. We have optimized the deposition parameters and tried to understand the growth mechanism depending on these parameters.

We have first observed that, by exposing the precursor during the plasma pulse, i.e. by pulsed plasma-enhanced CVD, we deposit a silver thin film made of dense and compact nanoparticles, due to reaction occurring not only on the surface but also in the gas phase. This morphology is very interesting as it allows us to demonstrate an ultra-thin percolated film. The as-deposited films are however weakly conductive, with resistivity larger than 10 Ω·cm, most probably due the weak electrical connections between particles. However, a major issue that has been encountered during

the investigation of the deposition parameters is the lack of long-term reproducibility of the Ag deposition among different process session. This lack or reproducibility seems to be related to changes of the deposition reactor after changing the configuration and/or making the maintenance of the system. The origin of this lack of reproducibility is not yet fully understood. However, it does not seem to affect the plasma conditions, as the post-treatment conditions did not show such strong changes. Then, the observed change is mostly attributed to the silver precursor exposure. Several hypotheses can be mentioned, including variation of the silver precursor quality, small leakages induced by the change of configuration and/or the maintenance of the tool, or modification of the reactor after a large number of depositions. A real process optimization would then require a better control of the precursor exposure.

Through the investigation of the process parameters and the results obtained in terms of uniformity of the peculiar compact NPs morphology, a qualitative model of growth has been built. This morphology was obtained with mild plasma conditions and continuous Ag precursor exposure. It was also found that, a longer plasma pulse time, the use of higher temperatures as well as higher argon flows both in the process and in the plasma head, favor the uniformity of the compact NPs morphology. The explanation given by the qualitative model was that the reaction of the silver precursors with hydrogen radicals is taking place in the gas phase rather than on the substrate surface. This reaction is thus responsible of the obtention of the peculiar compact NPs.

A second breakthrough result presented here is the demonstration that a plasma post-treatment performed on the peculiar compact NPs morphology, sinters the nanoparticles, resulting in a highly conductive ultra-thin film. A quasi-continuous conducting coating with resistivity and critical thickness close to the values obtained by line-of-sight deposition techniques has been obtained, i.e. 15 nm and a sheet resistance of 1.6 Ω/□ for a 40 nm-thin film, corresponding to a resistivity of 6.4 μΩ.cm. A better unreacted-precursor removal and an enhancement of the metallic nature of polycrystalline Ag have also been proved after post-treatment. By studying the plasma post-processing parameters, a higher density of the bombardment of energetic hydrogen radicals on the substrate has shown to lead to a higher degree of merger of the particles. This was dependent on the RF plasma power, hydrogen plasma flow, plasma exposure time as well as distance between the grid and the substrate and an optimum ratio of RF plasma power/hydrogen flow is needed to favor enough H radicals and avoid dewetting of Ag film. Moreover, the plasma exposure time was shown to influence the electrical properties of the films and different regimes correlated with the film morphology have been found. A sharp decrease of the film resistivity by several orders of magnitude while keeping the compact but well-defined NPs morphology has been first obtained and explained by a removal of the unreacted precursor from the surface. The partial merger of the particles leads to still a decrease of the film resistivity but at much lower rate and the total sintering gives a stable value of the film resistivity.

Finally, a processing scheme including both the deposition and plasma post-treatment in an optimized way (super-cycle) has been presented. The preliminary results demonstrated highly conductive films deposited on large scale using this method, although further process optimizations are needed for over-passing the results obtained by the standard two-step processing.

Due to the very encouraging results and the potential use of Ag films deposited by the novel approach in a broad range application, in the following chapter, we compare the standard PE-ALD process and this new two-step processing regarding their functional properties.

# Chapter 6

# Comparison of the two different silver deposition processes

In the fabrication of microelectronic devices, which include Dynamic Random-Access Memory (DRAM) capacitors, transistors, and back-end-of line (BEOL) interconnects, copper films are widely studied. However, in this field, silver is of particular interest due to its low electrical resistivity and low residual stress compared to Cu. Moreover, a downscaling to less than 100 nm is possible without a considerable increase in resistivity. [19] All these arguments impose Ag as a potential replacement of Cu for contacts and interconnects. Besides microelectronics field, its visible and infrared reflectivity make it a good choice for optical instruments including mirrors and lenses. It has a strong plasmonic effect which makes it effective for plasmonic devices including sensors. Its chemical reactivity is used in catalysis and antibacterial surfaces. More and more of these applications require a conformal growth of ultra-thin silver layers, which represents a challenge for most deposition methods. Silver requires also to be deposited not only on silicon substrate but also on conducting and insulating oxides, [9] or on high aspect ratio structures for diverse applications. For the optical functional devices, a concrete example is low-emissivity windows used in automotive or smart buildings, where transparent conductive oxides (TCOs) are added as index matching optical layers to the stack made of TCO/Ag/TCO. For silver to be most effectively used in these applications, it is necessary to maintain a high degree of control over the morphology of the final deposition and to be able to ensure an extremely pure layer, independently of the sublayer. [228] In this chapter, a direct comparison of the standard PE-ALD processes and the new two-step approach for Ag deposition is made. The deposition on complex substrates using complex lateral high aspect ratio structures (LHAR) as well as the influence of the underlayer are presented in a first part. For the latter, in addition to study oxides exhibiting different surface energies, the differences between the underlayers are also investigated in terms of surface wettability which was quantified by the value of the water contact angle (WCA), and correlated to the surface hydroxyl groups density. As already exposed in the state-of-the-art, the optical properties of Ag films are highly dependent on their morphology. The second part of the chapter thus focuses on the influence of the silver film morphology on the optical properties. Therefore, we first see how the nanostructures affect the optical behavior in visible and near infrared ranges. Then, the following subsection is dedicated to silver films deposited by the two-step approach. We show the optical properties both before post-treatment processing leading to Ag compact nanoparticles and after PT giving highly covering percolated films. We see how the plasma post-processing duration affects the optical properties of the deposited Ag films.

---

This chapter is based on the publication *S. Wack, P. Lunca Popa, N. Adjeroud, C. Vergne, R. Leturcq,* Two-Step Approach for Conformal Chemical Vapor-Phase Deposition of Ultra-Thin Conductive Silver Films, *ACS Appl. Mater. Interfaces*, **2020**, 12, 32, 36329–36338.

## VI.1. Comparison of the two different processes on complex substrates

### VI.1.1. Conformality

The need in the field of microelectronics is the miniaturization of semiconductor devices which introduces more complex 3D geometries with complex shapes. One of the main challenges is to be able to fill silver in these 3D shapes. As expressed in the motivation of the chapter, the deposition of silver has been performed by line-of-sight methods such as PVD. It gives the best quality of ultrathin film, i.e. with highest conductivity, in particular for film with critical thickness lower than 20 nm (see chapter 5). However, it remains some issues with the uniformity and conformality on non-flat substrates (Figure 113 (a)). Ag is also deposited by non-line-of-sight techniques such as chemical vapor-phase deposition (CVD/ALD). These techniques enable the growth of uniform and conformal films in 3D structures with complex shapes (Figure 113 (b)), even if they usually produce non-electrically conductive ultra-thin films (for thickness below 20-50 nm) due to the islands growth mode.

For this purpose, we have investigated the conformal synthesis of Ag thin films on 3D structures with lateral high aspect ratio (LHAR) from PillarHall® technology, already used for this purpose in several works. [34, 229, 230, 231, 232, 233] (see II.1. Experimental section). While ALD is the most promising technique for conformal deposition, the PE-ALD of Ag thin film suffers from the recombination of plasma species (radicals) on the surfaces, which prevents the growth deeper into such structure. [2, 47, 229]

The same LHAR structure with high aspect ratio (AR of 100) has been used as substrate for silver films deposition using two different processes: our new approach after post-processing step (Figure 113 (c-e)) and standard PE-ALD (Figure 113 ((f-h)). We demonstrate in Figure 113 (c-e) that we manage to produce Ag thin layers extremely conformal on top, bottom and at the back of an LHAR with an AR of 100. In contrast, the Ag film synthetized with standard PE-ALD process show poor uniformity at the entrance of the trench and we observe no film deposition at the back of the cavity (Figure 113 (h)). It is probably due to the limited lifetime of hydrogen radicals required by the PE-ALD.

The morphology of the Ag percolated film on the sidewalls of a micro via hole is very uniform even in the lateral directions (Figure 114 (a) and (b)), making the process a good candidate for conducting interconnects in microelectronics. [234] At last, we exhibit the conformal deposition on silicon pillars (Figure 114 (c)), which is of interest for optical nanoantennas [235] and thanks to the pillars' high surface to volume ratios, applications as optical biosensing may be aimed. [236, 237] The analysis of conformality has been performed on such kind of structures (lateral, sidewall or pillars) for mainly platinum-group metals. [232, 238, 239] However, to the best of our knowledge, this is the first time for Ag films since usually only vertical structures are studied. [29, 139, 140] We present Ag deposited in vertical structures in Figure 115. For the two different processes, we have calculated the step coverage, i.e. the ratio of the film thickness at the bottom of the trench to the one at the top of the structure. [34] We succeeded in reaching a step coverage of 97% with our new approach against 72% for the standard PE-ALD process, which proves again the better conformality with the two-step process. In the literature, it was found that the film thickness, the density and size of the grains reduce with the penetration depth, leading to quasi no deposition at the bottom of the trench for Ag deposited by PE-ALD. [139, 140] However, higher AR have been studied (60, 33 and 8) and they explained that by the hydrogen radicals recombination during the plasma pulse, an insufficient Ag precursor exposure and complex flow dynamics associated with an aspect ratio that changes with

each PE-ALD cycle. [139] In our case, we did not go in depth in the study of vertical structures since LHAR features expose already results well beyond the state-of-the-art of Ag conformal deposition.

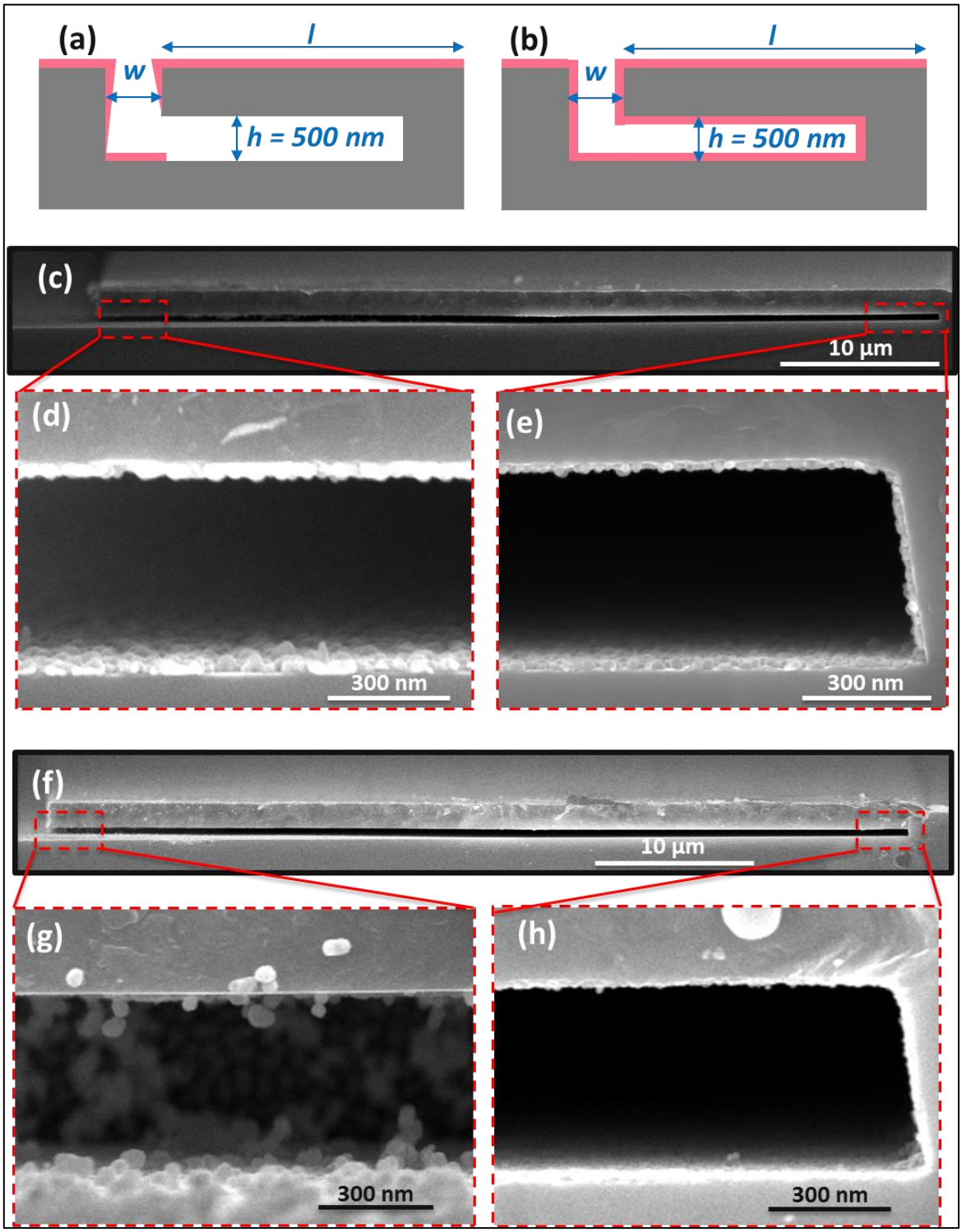


Figure 113: (a) and (b) Schemes of an expected thin film deposition on a lateral high aspect ratio structure by (a) line-of-sight technique and (b) non-line-of-sight technique. (c) to (e) Scanning Electron Micrographs (cross sections) of post-treated Ag thin layers deposited on LHAR structure (AR of 100) by pulsed-PECVD using our novel approach: (c) Low magnification SEM cross section, (d-e) High magnification SEM cross-sections of the structure shown in (c), taken (d) at the entrance and (e) at the back of the LHAR structure. (f) to (h) Scanning Electron Micrographs (cross sections) of Ag thin films obtained on LHAR structure (AR of 100) by standard PE-ALD process on (f) the same structure as (c) with a zoom in of the entrance (g) and back (h) of the cavity.

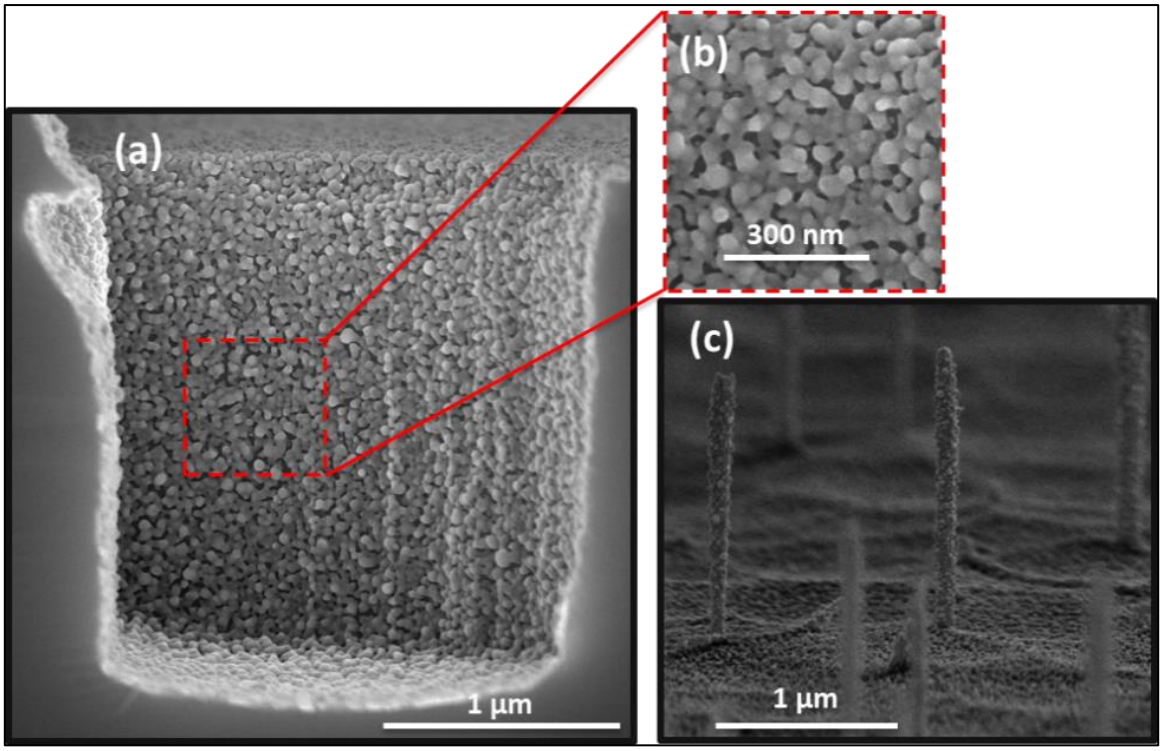


Figure 114: (a) and (b) Scanning Electron Micrographs (cross sections) of post-treated Ag thin films grown on the sidewalls of a micro via hole (zoom in (b)). (c) SEM image of Ag thin layer after PT deposited on silicon pillars.

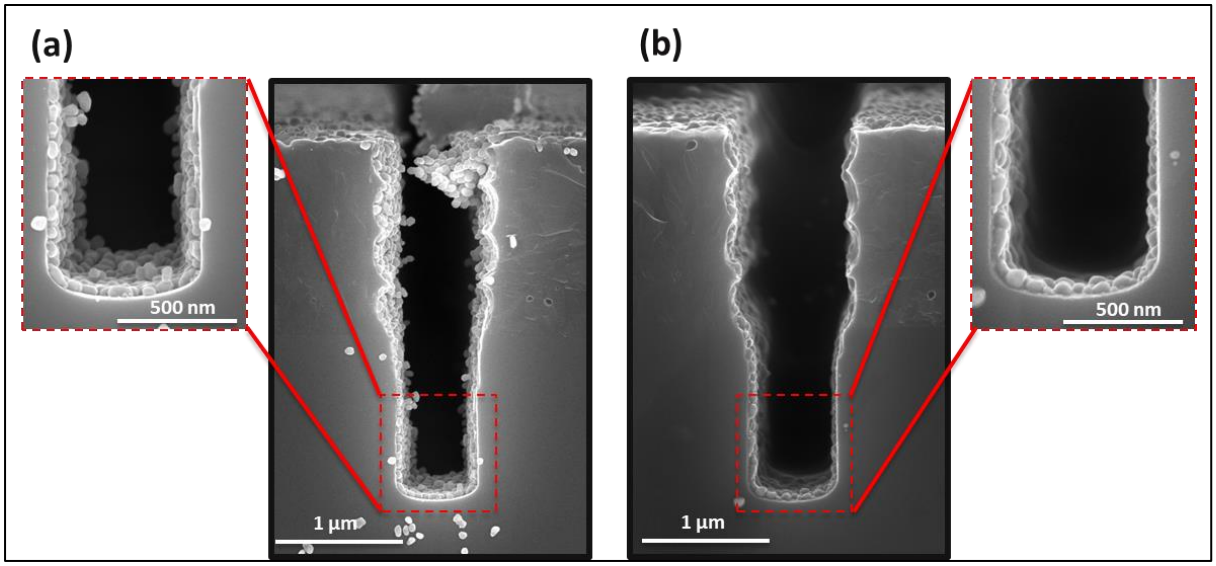


Figure 115: Scanning Electron Micrographs (cross sections) of Ag films deposited on vertical structure with an aspect ratio of 4 by (a) standard PE-ALD process (zoom of the bottom of the trench on the left) and (b) two-step process after post treatment (zoom of the bottom of the trench on the right).

In order to quantify the degree of conformality, thickness profiles of Ag film deposited into a "quasi-infinite trench" with a high AR of 10000 (opening width *w* of 100 µm, lateral gap width *l* of 5000 µm and gap height *h* of 500 nm) have been plotted to get rid of the depth effect [229, 230] (Figure 116 (a)). The thickness (determined by EDS) and the penetration depth have been measured after removing the top membrane of the LHAR structure (see II.2. Experimental section). The profiles show that standard PE-ALD process follows an exponential decrease, $t = Ae^{-x/B}$. This is explained by the

recombination of hydrogen radicals on the surfaces. [2] In contrast to this result, the Ag thin layer formed by the new approach follows the thin film solution of the diffusion law equation, $t = Ae^{-x^2/B}$, characterized by the presence of a plateau up to a penetration depth of 5 µm (AR = 10), followed by an exponential decrease. This behavior may be explained by deposition limited by the diffusion of precursors into the structure. [240] For both as-deposited and post-treated films, our novel approach gives a thickness variation of less than 10% for AR up to 12, and less than 50% for AR up to 40. This is 4 to 5 times larger than those measured for the standard PE-ALD method (10% variation for AR < 3 and 50 % for AR < 8).

The SEM images of Ag as-deposited and post-treated films and the ones of PE-ALD deposited in LHAR at different penetration depth are exposed in Figure 116 (b-g) and Figure 116 (h-j), respectively. We manage to deposit connected Ag films deeply into the trench using our two-step approach. The main morphological characteristics of the film, i.e. compact particles for the as-deposited film, and the merged particles after the post-treatment, are both preserved deep into the structure, showing that both steps are used efficiently in high aspect ratio structures. The layers remain connected until a penetration depth of 9 µm, after which the thickness becomes lower than the critical thickness (see chapter 5), with film morphology becoming disconnected. This value covers largely the requirements of the current microelectronic applications. In contrast, Ag deposited by standard PE-ALD shows a decrease of the NPs size and their coverage with the increase of the penetration depth. This is due to the H radicals' recombination with the walls of the trench and their inability to reach the back. We point out that the plasma post-treatment used for the two-step process seems to be more effective than the PE-ALD process in reaching structures with large aspect ratio, despite the fact that the plasma conditions are similar. This difference may be due to different doses used in the two processes, since the post-treatment is applied once during a long time, while the PE-ALD process is using multiple short plasma pulses, which may enable a better diffusion of the plasma species into the trench. But the involved mechanism and required species may also be very different in both processes.

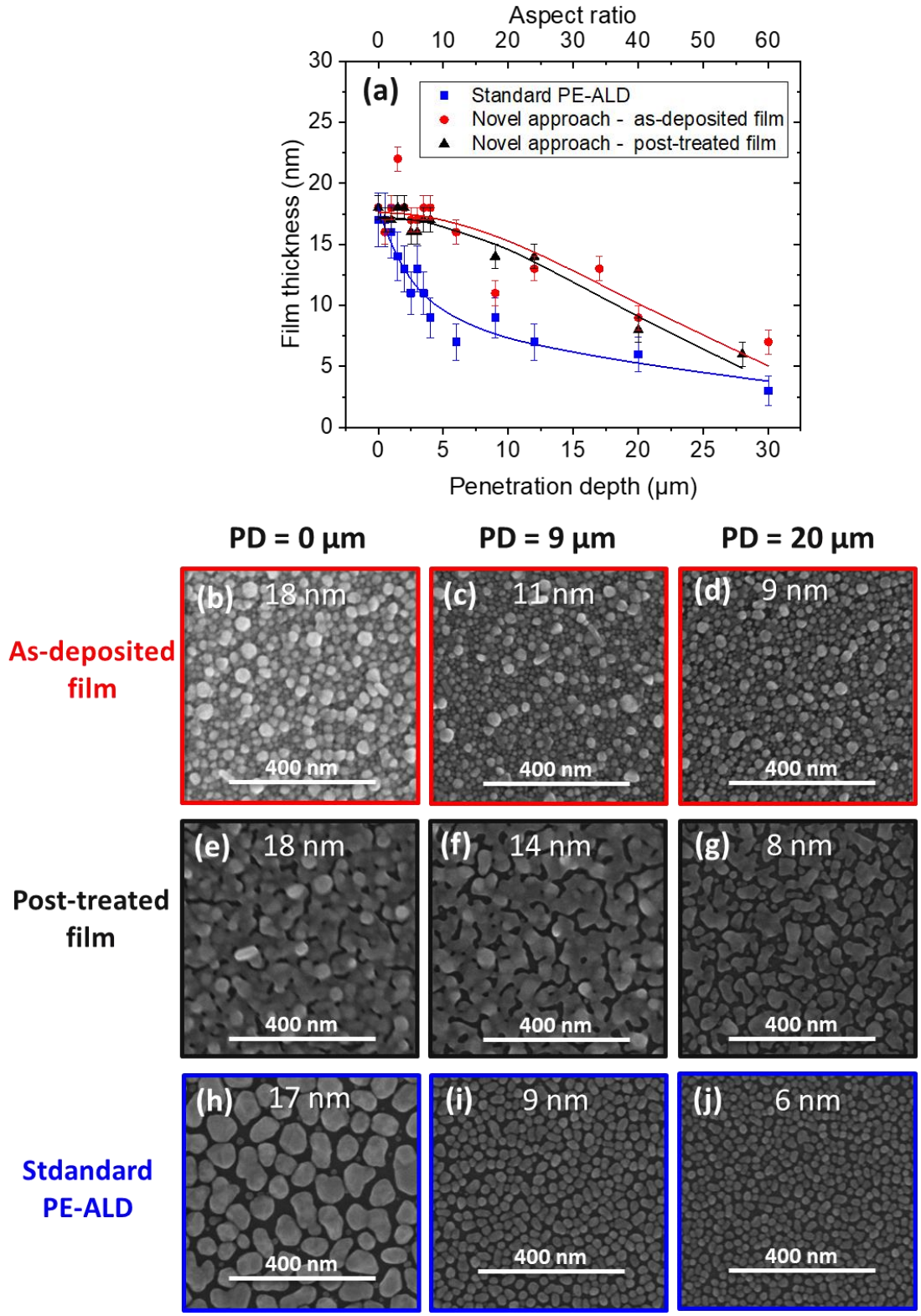


Figure 116: (a) Thickness profiles measured on a LHAR structure with an AR of 10000 (w of 100 µm, l of 5000 µm and h of 500 nm) of Ag films deposited with standard PE-ALD process (blue) and with our novel approach before (red) and after (black) plasma post-treatment. The thickness has been measured by EDS after removing the top membrane of the LHAR structure. The fits are an exponential dependence for the standard PE-ALD method, and a diffusion law for the novel approach (see main text). (b-j): Scanning Electron Micrographs (top view) of Ag thin films (b-g) deposited by the two-step process (b-d) before and (e-g) after post-treatment step and (h-j) deposited by standard PE-ALD process. All Ag films have been synthetized in the same structure as (a) at a penetration depth (PD) of (b-e-h) 0, (c-f-i) 9 and (d-g-j) 20 µm. The values on the middle of the images correspond to the EDS equivalent thickness of the Ag layer. The scale bars represent 400 nm.

As seen previously, with standard PE-ALD process, we observe the inefficiency of the plasma deeply in the trench due to H radicals which recombine with the walls of the trench and no H radicals are efficient in the bottom of the trench. However, it remains one question: what gives the efficiency of the PT until the bottom of the trench in the two-step process, in other words, what avoids the radical's recombination and what enhances the radical's penetration depth during the plasma post-treatment?

In order to try to answer to this question, we have performed the same Ag deposition in LHAR structure and then tested two different kind of plasma post-treatment. The first one is an indirect or remote PT, i.e. the remote plasma configuration where we keep the grid which serves as a ground electrode and defines the plasma chamber. This allows the elimination of all ionic species before their arrival on the substrate and let only radical flows in the reactor. (see the experimental methods in chapter 2) The second one is a direct PT where we removed the grid. In this case, the substrate holder acts as a ground electrode which leads to a superior plasma chamber (10 cm) as compared to remote plasma as well as the presence of all ionic species in addition to radical species. Figure 117 exposes the obtained results.

The direct PT gives a slightly better reduction reaction with a more channel-like network (Figure 117 b) as compared to indirect PT (Figure 117 c) but in both cases, we have a good effect of the PT very deep into the trench. However, it is quite tricky to quantify the efficiency of the PT as a function of the PD since, even without post-treatment (Figure 117 (a)) the deeper you go into the trench, the more nanoparticulate the film, since it becomes much thinner. Overall, the penetration depth of the post-treatment is equivalent for both direct and indirect PT, it is not only the fact to have a direct PT which avoids the radical's recombination by creating radicals on-site of the trench.

Maybe the limitation of radical's penetration is directly correlated with the plasma pulse time. Indeed, in our standard PE-ALD process, we used a very short plasma pulse time (3 s) which may be too short to have the diffusion of the radicals into the total depth of the trench, contrary to longer time used during the post-treatment of the two-step approach. By using Monte Carlo simulation for investigate the influence of surface recombination of radicals during PE-ALD, Knoops *et al.* [241] proved that a longer plasma exposure time must be employed in order to achieve conformal deposition in this recombination limited regime for PE-ALD of alumina. It was also confirmed by Dendooven *et al.* [242] However, the deposition of conformal film made of well-separated Ag NPs was not the aim of this PhD thesis since thermal-ALD already exhibits good achievements. [44, 48]

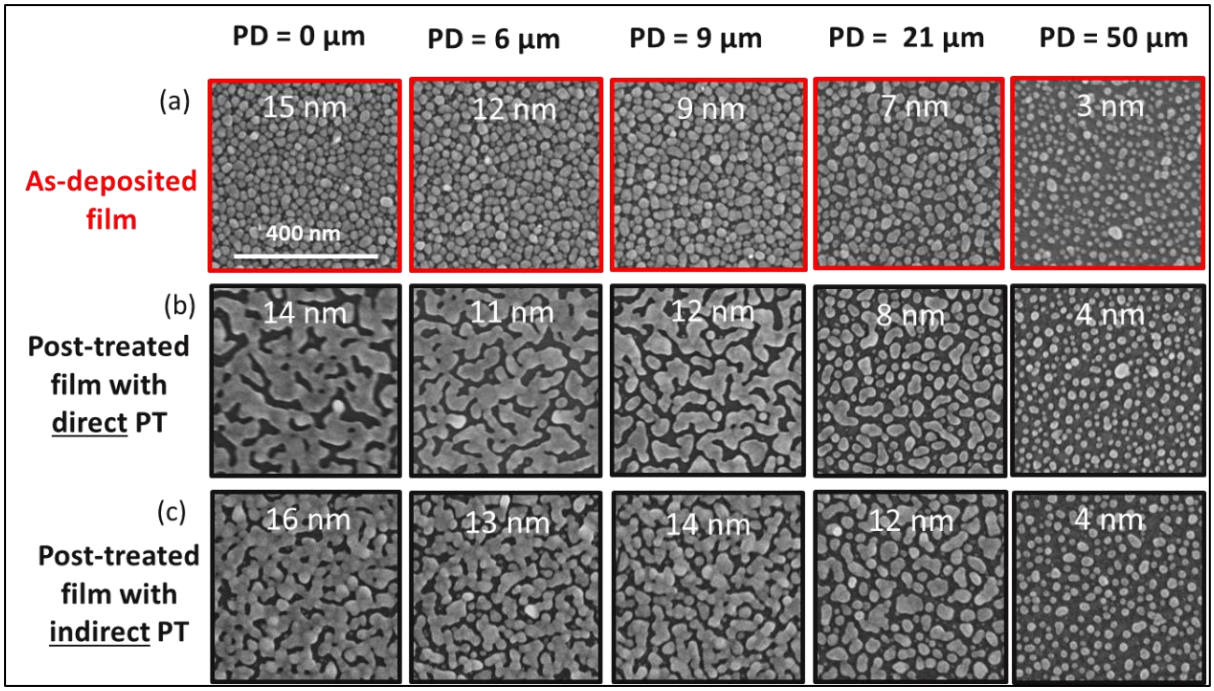


Figure 117: Scanning Electron Micrographs (top view) of Ag thin films deposited by the two-step process (a) before post-treatment (first line) and (b) after post-treatment step with direct post-treatment using $P_{post}$ = 100W, $t_{post}$ = 30 s and (c) after post-treatment step with indirect post-treatment using $P_{post}$ = 150W, $t_{post}$ = 10 min in LHAR structure with AR of 100 at different penetration depth (PD). The values on the middle of the images correspond to the EDS equivalent thickness of the Ag layer. The scale bars represent 400 nm.

### VI.1.2. Influence of the underlayer

Up to now, the previous investigation has been performed either on oxidized silicon wafer or cleaned glass substrates, depending on the analyses performed. In this section, we extend the investigation to other materials with the aim to highlight the quasi substrate-independency of silver films chemical-vapor phase deposited using both standard ALD and our two-step approach. This represents a key factor for the synthesis of metal films in a broad range of applications requiring weakly-interacting film/substrate systems, e.g. in optoelectronic and catalytic devices. [243]

In the background section of chapter 2, we have shown that silver films have been reported to have a nanocrystalline morphology and potentially uncoalesced and nanoparticulated morphologies at early stages of the growth before growing into a film. This is explained by the Volmer Weber growth mode which occurs since the adatoms have a strong affinity with each other instead of with the substrate, due to the high surface energy of metals. Based on that, as mentioned before (see chapter 1 section I.4.), underlayers have been used to reduce the migration of silver atoms in order to form a continuous film. Contrary to line-of-sight techniques which demonstrate a strong improvement for the growth of ultra-thin Ag continuous films, among the few studies dealing with the substrate influence on silver deposited by ALD, [19, 48, 146] only non-continuous films [48] with potentially a slight enhancement of the coverage but still non-continuous morphology [19] were observed. Researchers have studied underlayers exhibiting either higher surface energy than Ag itself (nickel, cobalt, tungsten, titanium, molybdenum), or lower one with oxide (e.g. $Al_2O_3$, $SiO_2$) and nitride (e.g. TiN). [19, 146] The aim of our investigation is thus to confirm and try to explain the weak influence of

the underlayers known in the literature for obtaining ultra-thin silver films by ALD, by supplementing the study with a higher number of oxides of different surface energies but also of different roughness (from 0.05 nm up to 86 nm) and of different morphology and crystallinity (amorphous vs polycrystalline). In addition, the differences between the underlayers are also investigated in terms of surface wettability which is quantified by the value of the water contact angle (WCA) and correlated to the surface hydroxyl groups density.

As already exposed in chapter 1, according to the work of Duan *et al.* on the thermal CVD of Ag, [183] both the morphology of the films deposited, and the efficiency of the deposition depend on the type of substrate and surface chemical functionality used to react with the precursor. Therefore, we have performed preliminary studies by testing different surface preparation of silicon substrate (pre-treatment by UV/$O_3$, plasma-activated $O_2$ or HF-etching, washing with the cleaning procedure of chapter 1 section I.1.4.2.) with a view of removing organic species present at the substrate surface or in order to change the surface chemical functionality of a ZnO underlayer (terminated either with $H_2O$ pulse or DEZ pulse giving respectively Zn–OH or Zn–H termination). However, no clear conclusions could have been extracted, probably because the substrates were exposed to air prior to subsequent Ag deposition on top of those. This is explained by the fact that we did not have the option to perform in-situ characterization but only ex-situ ones.

Mameli *et al.* [146] found a better Ag wetting on $H_2/N_2$ plasma pre-treated molybdenum substrate as compared to non-pre-treated one presenting a native $MoO_3$.The explanation was a removal of the low surface energy native Mo oxide on the surface which blocks the Ag coalescence (see section I.4.1.2.). Based on this work, we have also studied the effect of an in-situ $H_2$-plasma pre-treatment of silicon substrate in order to remove the native oxide $SiO_2$ before Ag deposition. However, no influence has been noticed when compared with non-pre-treated substrates. That is the reason why, in this study, we are not using this pre-treatment prior to Ag deposition on top of the subsequent substrates covered with different underlayers, and also in order to not deteriorate them. It is also worth mentioning that all substrates covered with different underlayers used in the following parts were exposed to air before Ag deposition. The main reasons are that, for some of the underlayers, their synthesis has been performed with other deposition techniques (wet chemistry for ZnO nanorods) and because the reactor was opened between their synthesis and the deposition of Ag in order to have the same experimental conditions for the metal deposition. It is also worth mentioning that only the glass substrates have been cleaned using the protocol presented in chapter 1 section I.1.4.2.

**VI.1.2.1. Properties of the underlayer**

As already mentioned in section I.2.1., by replacing the substrate with another one exposing higher surface energy than the deposited material, one could expect, in theory, the formation of a continuous metal film. We have selected underlayers with different surface energies coated on silicon substrate. Table 29 shows the theoretical value of the surface energy of the different underlayers used for the investigation. However, the surface energy is not a direct measure of the wettability as the former depends also on the physical condition of the surface, e.g. its crystalline structure, surface roughness or the amount of adsorbed impurities. [244] Therefore, the wettability of the surface, i.e. the ability of a liquid to maintain contact with a solid surface, has been characterized and quantified by the value of the water contact angle (WCA) and summarized in Table 30 in addition to the

experimental conditions of synthesis for each underlayer and their morphological properties (rms roughness, crystallinity). Figure 118 shows the corresponding SEM and AFM images.

| Underlayer | Theoretical surface energy (J/m²) | Reference |
|---|---|---|
| ZnO (100) | 1.6 | [245] |
| Ag | 1.25 | [225] |
| α-$Al_2O_3$ | 0.97 | [246] |
| $SiO_2$/Si (100) | 0.75 | [226] |
| Glass | 0.31 | [247] |

Table 29: List of theoretical surface energy value of the different underlayers used for the investigation.

| Material | Synthesis method | Thickness (nm) | Temperature of deposition (°C) | Rms roughness (nm) | Crystallinity | WCA $\theta$ (°) |
|---|---|---|---|---|---|---|
| ZnO coated silicon | Thermal ALD | 10 | 130-150 | 0.15 ± 0.01 | amorphous | 97.1 ± 0.4 |
| | | 90-110 | 130-150 | 2.7 ± 0.40 | polycrystalline | 105.2 ± 0.6 |
| $Al_2O_3$ coated silicon | Thermal ALD | 40 | 150 | 0.05 ± 0.01 | amorphous | 87 ± 1 |
| | | 110-130 | 130 | 0.11 ± 0.01 | | 88 ± 1 |
| ZnO nanorods coated ZnO on silicon | Wet chemistry | / | RT | 86 ± 37 | / | 116 ± 8 |
| Glass | From Guardian | / | / | 0.12 ± 0.03 | amorphous | 5 ± 1 |
| $SiO_2$/Si | From Siegert Wafer | 2-3 * | / | 0.05 ± 0.02 | polycrystalline | 38 ± 3 |

Table 30: Summary of the experimental conditions of synthesis and the properties of the silicon and glass substrates as well as underlayers coated silicon substrates used in the study of the influence of the underlayers. * thickness of the silica native oxide.

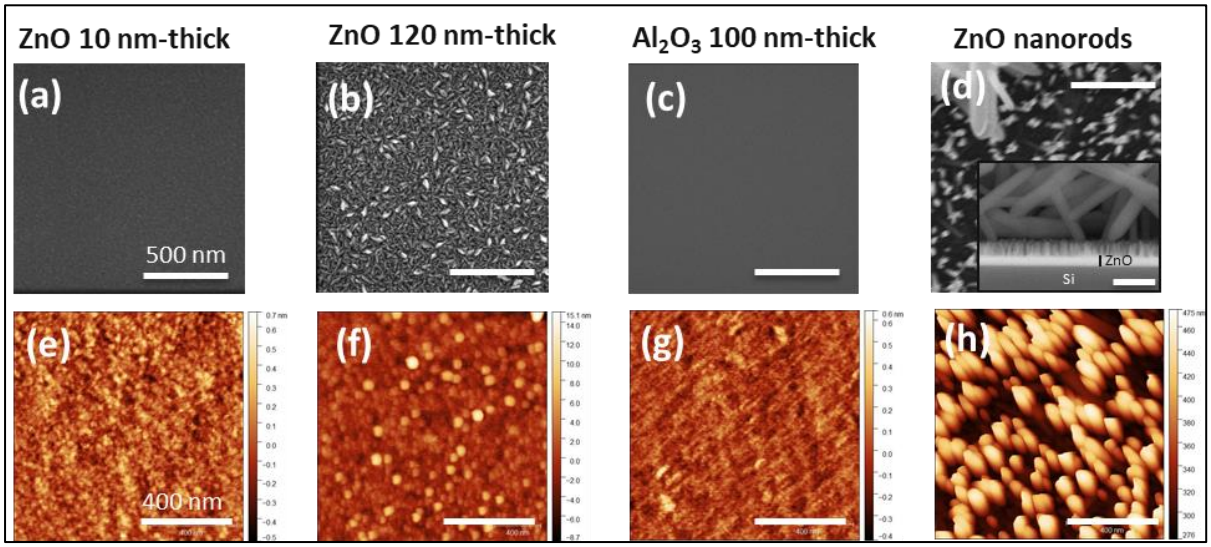


Figure 118: (a-d) Scanning electron micrographs and (e-h) atomic force micrographs of the different underlayers deposited on silicon with a silica native oxide ($SiO_2$/Si) substrate and used for the investigation. (a-b and e-f) ZnO films of different thicknesses, (c and g) $Al_2O_3$, and (d and h) ZnO nanorods deposited on ZnO layer (inset represents a cross section view). The scale bars represent 500 nm for SEM and 400 nm for AFM images.

ZnO coated silicon substrate have been selected since it exposes higher surface energy than silver itself (1.6 vs 1.25 J/m$^2$, respectively) and, as already discussed in chapter I, section I.4.1.2., this oxide is also known for being a good wetting layer for Ag deposited by physical vapor deposition. During this investigation, ZnO has been deposited with two different thicknesses in order to study the film morphology, amorphous and continuous for a 10-nm-thick film (Figure 118 (a,e)), and polycrystalline with a needle-like morphology for thicker ZnO films (120 nm-thick, Figure 118 (b,f)). On the contrary, $Al_2O_3$ ( Figure 118 (c,g)), silicon covered with native oxide silica ($SiO_2$/Si) and glass exhibit lower surface energy than silver.

The WCA values obtained experimentally (Table 30) do not follow the trend of the theoretical surface energy (Table 29). Indeed, glass substrate exhibits the lowest WCA of 5° due to the cleaning procedure already exposed in chapter 2, which removes the carbon surface contamination and thus enhances the presence of more hydroxyl nucleation groups needed for the chemisorption. [248, 249] The higher hydrophilicity (lower contact angle) of alumina compared to zinc oxide is also understood in terms of density of surface hydroxyl adsorption groups. Indeed, ZnO crystalline orientation is temperature-dependent. At a temperature of 130-140°C, ZnO presents a crystalline structure with a preferential growth on the (100) reflection plan which is known to be hydrophobic due to the unpolar character of the surface. [250, 251, 252] On the contrary, aluminium oxide is known to be polar and reacting well with water molecule and thus creating –OH functional groups. [48, 253] This explains our experimental results of an hydrophilic surface with a WCA lower than 90° for alumina and hydrophobic one for zinc oxide with WCA higher than 90°. When comparing alumina and $SiO_2$/Si underlayer, the water contact angles of, respectively 87° vs 38° is understood by lower hydroxyl groups on alumina as well as, due to the $Al_2O_3$ ALD synthesis, there could also be some remaining methyl surface groups coming from TMA precursor that reduce the wetting.

On the other hand, it is also known in the literature that the contact angle is influenced by both the surface roughness and the surface energy. [244, 249] This explains the higher WCA of 105° for polycrystalline rough ZnO as compared to 97° for smooth amorphous ZnO. All the previous five substrates (ZnO thin and thick, glass, $SiO_2$/Si, $Al_2O_3$) exhibit quite low rms roughness, no more than 3 nm. Therefore, in order to study the influence of rough substrates on the morphology of Ag film, we have used rough ZnO nanorods (rms roughness of 86 ± 37 nm) deposited via wet chemistry on top of 110-nm thick ZnO film. Polycrystalline ZnO film has been used as a catalyst and the roughness of the ZnO film creates nucleation centers enhancing the germination of ZnO NRs. We observe a first layer made of homogeneous and regular carpet of nanorods and a second layer on top of it made of bigger nanorods. (Figure 118 (d,h)) The hydrophobicity of the surface is confirmed by a high WCA of 116° due to the non-polar single crystal ZnO nanorods.

The different small substrates covered with the above mentioned underlayers were placed on top of a silicon wafer in the ALD reactor. In order to be only dependent on the effect of the underlayer on the silver film morphology, we have then deposited silver of different thicknesses on top of these underlayers using either standard PE-ALD process (Ag deposited after 100, 200, 400 and 800 cycles) or the two-step approach (Ag deposited after 200, 400, 600 and 800 cycles), with the optimized parameters already presented in chapters 3-4 and 5, respectively. The corresponding scanning electron micrographs of Ag thin films after a varying number of cycles are exposed in Figure 119 for standard PE-ALD and in Figure 121 and Figure 122 for the two-step process.

**VI.1.2.2. Silver films deposited by standard PE-ALD**

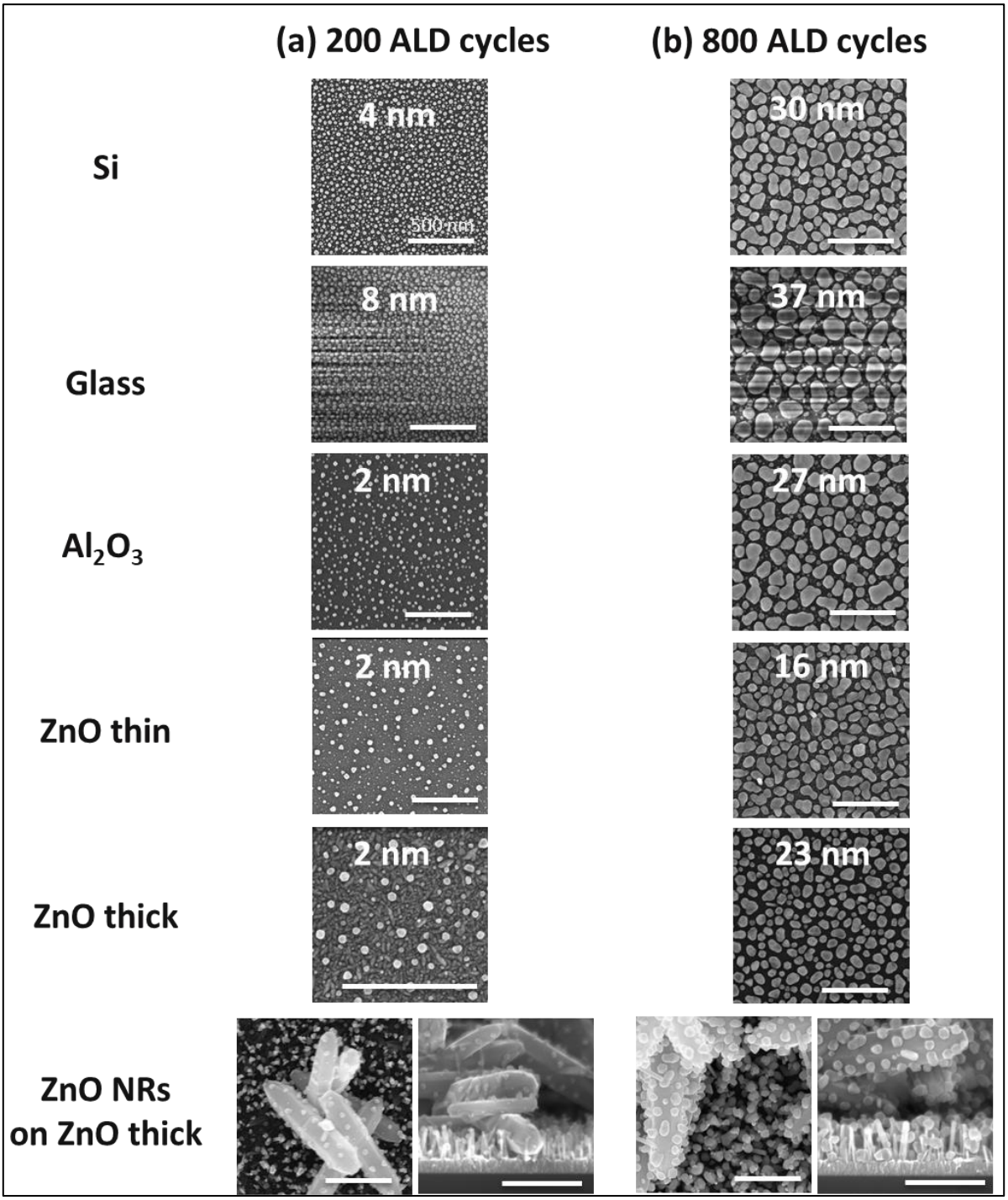


Figure 119: Scanning electron micrographs of Ag thin films deposited by standard PE-ALD on the different underlayers (study of surface energy and film morphology) after a varying number of cycles (a) 200 cycles and (b) 800 cycles. The values at the center of the images correspond to EDS thickness of the film. The scale bars represent 500 nm. The studies were performed at the optimum temperatures $T_{ch}$ = 130°C/$T_{hs}$ = 100°C.

The scanning electron micrographs of Ag thin films deposited on the different underlayers by standard PE-ALD after a varying number of cycles are shown in Figure 119. Interestingly, for silver deposited by standard PE-ALD process, for the same amount of material deposited, all the underlayers lead to the typical silver islands formation, even for the ZnO substrates exposing higher surface energy

than Ag itself. In order to quantify these observations, the influence of the number of cycles on different morphological parameters is examined in Figure 120. The Volmer-Weber mechanism is highlighted by, first, a linear increase of the EDS thickness (Figure 120 (a), average nanoparticle diameter (Figure 120 (b)-(e)) and coverage (Figure 120 (d)-(g)) and second, the exponential decrease of the nanoparticle density (Figure 120 (c)-(f)) due to the coalescence phenomenon.

However, slight differences are extracted regarding the growth rate. For a given number of ALD cycles, higher thickness is deposited when glass is used as substrate (Figure 119). The Ag deposition rate is thus much faster on glass (GPC of 0.048 ± 0.001 nm/cycle) as compared to the other underlayers, demonstrated by a higher slope of the thickness as function of number of cycles (Figure 120 (a)) and a higher nanoparticle size (Figure 119 and Figure 120 (b)). Si and $Al_2O_3$ lead to a moderate growth rate (GPC of respectively 0.026 ± 0.008 nm/cycle and 0.020 ± 0.008 nm/cycle) and ZnO films, both thick and thin, lead to a slower Ag deposition rate (GPC of respectively 0.019 ± 0.007 nm/cycle and 0.015 ± 0.003 nm/cycle). This slower deposition rate is also observed on the film morphology in Figure 119. After 800 ALD cycles, Ag films deposited on zinc oxide layers present the smallest diameter of particles as compared to, silicon, alumina and glass. Moreover, a slower start of the deposition is occurring for both ZnO underlayers and $Al_2O_3$ as compared to Si and glass but interestingly, no nucleation delay was obtained. This is seen by the presence of a plateau from 100 to 200 cycles in Figure 120 (a) for Ag thickness and (Figure 120 (b) for NP average diameter.

Several investigations have highlighted the relationship between the wettability of a substrate and the surface –OH groups. [248, 249, 254] Lower contact angles and thus higher wettability is found with the increase of surface hydroxyl groups density. On the other hand, the importance of hydroxyl groups uniformly covering the surface and enhancing the nucleation of the noble metal in chemical vapor-phase deposition processes is known in the literature. This has been proven for noble metals deposited by ALD, for instance Cu, [153] Ru, [171, 173] Ir, [172] Pt and Pd. [169] For Ag deposition, has presented in the state-of-the-art section, the hypothesis of surface reaction of Ag precursor presented by Duan *et al.* [183], Masango *et al.* [48] and Golrokhi *et al.* [29] highlight the importance of hydroxyl groups for precursor adsorption. (see chapter 1, section I.4.1.).

Overall, the link between the growth rate and the wettability seems then to be the density of –OH surface groups. A higher hydroxyl surface density enhances both the Ag precursor chemisorption and thus the metal loading on the surface as well as the wettability of the substrate.

Therefore, based on Figure 120 (a-d), the enhanced deposition rate on glass and $SiO_2$/Si is understood by a lower WCA (WCA of 5° and 38°, respectively) compared to higher hydrophobicity for ZnO and $Al_2O_3$ (WCA of, at least 87°, see Table 30) presenting lower growth rate. Another possible reason for the slower growth rate as function of the hydroxyl groups density may also be due to the bulkiness of Ag(fod)($PEt_3$) and its ligands which blocks nucleation sites caused by the steric hindrance effect, as also seen in the work of Masango *et al.* [48]. All these observations confirm the role of –OH groups on the precursor reaction with the surface. They also support that both the WCA and the deposition depend on many parameters, not only surface energy. However, the surface energy still plays a weaker role as it is highlighted in the next paragraph.

Another way to analyze the data is to plot the quantitative parameters as a function of the EDS thickness rather than the number of ALD cycles. It provides a better understanding of the deposition mechanism since we get rid of the growth speed. At a given thickness, for depositions performed on ZnO underlayers, Ag NPs are larger (Figure 120 (e)). This seems to indicate that Ag particles better wet ZnO substrates, as it was theoretically predictable due to the higher surface energy of ZnO. The amorphous zinc oxide substrate, i.e. the thinner one, is more favorable that the polycrystalline one. Indeed, already after 15 nm of Ag, the film deposited on ZnO 10-nm-thick underlayer exhibits an average NP diameter of 70 nm and covering at 80% the surface combined with a low density (Figure 120 (e-g)). From these observations, it seems that the deposition rate is correlated with the water wettability, i.e. lower contact angle and higher hydroxyl groups give larger growth rate, but the morphology depends less on the contact angle, and may demonstrate some weak influence of the surface energy.

We have finally completed the study by using a higher rms roughness underlayers, i.e. ZnO nanorods deposited on ZnO thick layer-covered silicon substrate. As shown in Figure 119, we managed to deposit Ag on these 3D structures. We obtained the same morphology made of separated islands increasing in size with the ALD cycles. This confirms that the Ag deposition is possible on substrates exhibiting high rms roughness. However, it was difficult to extract a quantitative measurement in order to compare the results obtained with the previous underlayers due to the non-planar morphology on the nanorods.

In summary, even if the investigated underlayers present significant difference in terms of surface energy and rms roughness, the morphology of silver on oxide layers is very similar. The higher growth rate seems to be related to the lower contact angle, potentially due to difference in density of –OH surface groups. The absence of difference in morphology is obtained when analyzing the morphology vs. deposited thickness, although a weak increase of particle size is observed for ZnO, which has the highest surface energy.

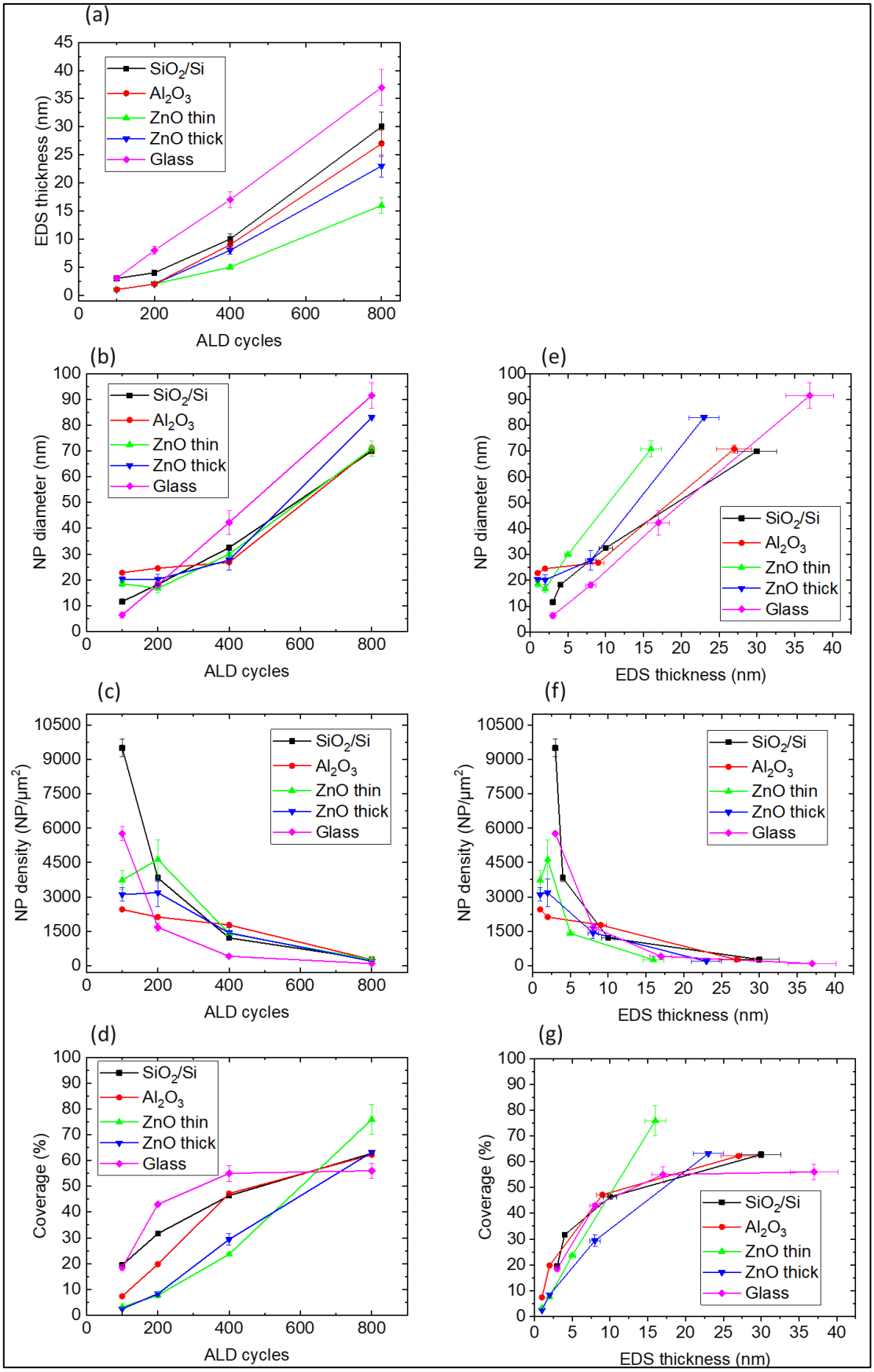


Figure 120: (a-d) Influence of the number of cycles on (a) the EDS equivalent thickness, (b) the nanoparticle size, (c) the NP density and (d) the film coverage and (e-g) Influence of the EDS thickness on (e) the nanoparticle size, (f) the NP density and (g) the film coverage. The Ag films have been deposited standard PE-ALD.

### VI.1.2.3. Silver films deposited by the two-step approach

When it comes to the two-step process, it was more difficult to give a quantitative analysis of the morphology related to the films. Indeed, as seen in Figure 121 (upper part of (a) and (b)), a similar film morphology made of compact nanoparticles with coverage close to 100% is obtained for all the substrates already after 200 cycles, contrary to separated islands previously exposed for standard PE-ALD process. Since we did not find a reliable way to quantify the degree of compactness of our Ag films, we focused our analysis on qualitatively comparing the Ag morphology based on SEM images. This weak influence of the underlayer on the Ag film morphology is confirmed in cross section views (Figure 122 a-e). We demonstrate that the film is rather composed of multiple layers of particles for all the underlayers. Since the particle size is directly related to the quantity of Ag material deposited, we have plotted its dependency as function of the number of cycles in Figure 122 (f). Overall, all the underlayers show the same growth rate, with an exception for glass which shows a faster growth, as already observed for PE-ALD, and probably due to the enhanced hydroxyl groups nucleation sites numbers created by the cleaning procedure. Contrary to Ag deposition performed with standard PE-ALD, no slower start of the deposition is occurring for ZnO and $Al_2O_3$ underlayers as compared to Si, but all these substrates exposing the same growth speed. The explanation could come from the fact that the growth mechanism linked to Ag deposited with our novel approach involved the competition between two mechanisms: a gas-phase reaction and a surface reaction. Therefore, not only the surface reaction plays a role on the growth mechanism, as it was the case for standard PE-ALD. At last, Ag have been synthetized on ZnO nanorods deposited on ZnO thick layer-covered silicon substrate (Figure 121). Due to the peculiar morphology of these 3D structures, it was not possible to determine the Ag thickness. However, we see on the SEM images that the same compact nanoparticle morphology as the one previously observed on the different underlayers have been obtained on the first layer made of homogeneous and regular carpet of nanorods whereas separated Ag islands have been achieved on bigger nanorods on top of it. An explanation could be that the deposition rate might be even lower on the sides of the rods which are purely non-polar, since the rods are single crystal ZnO.

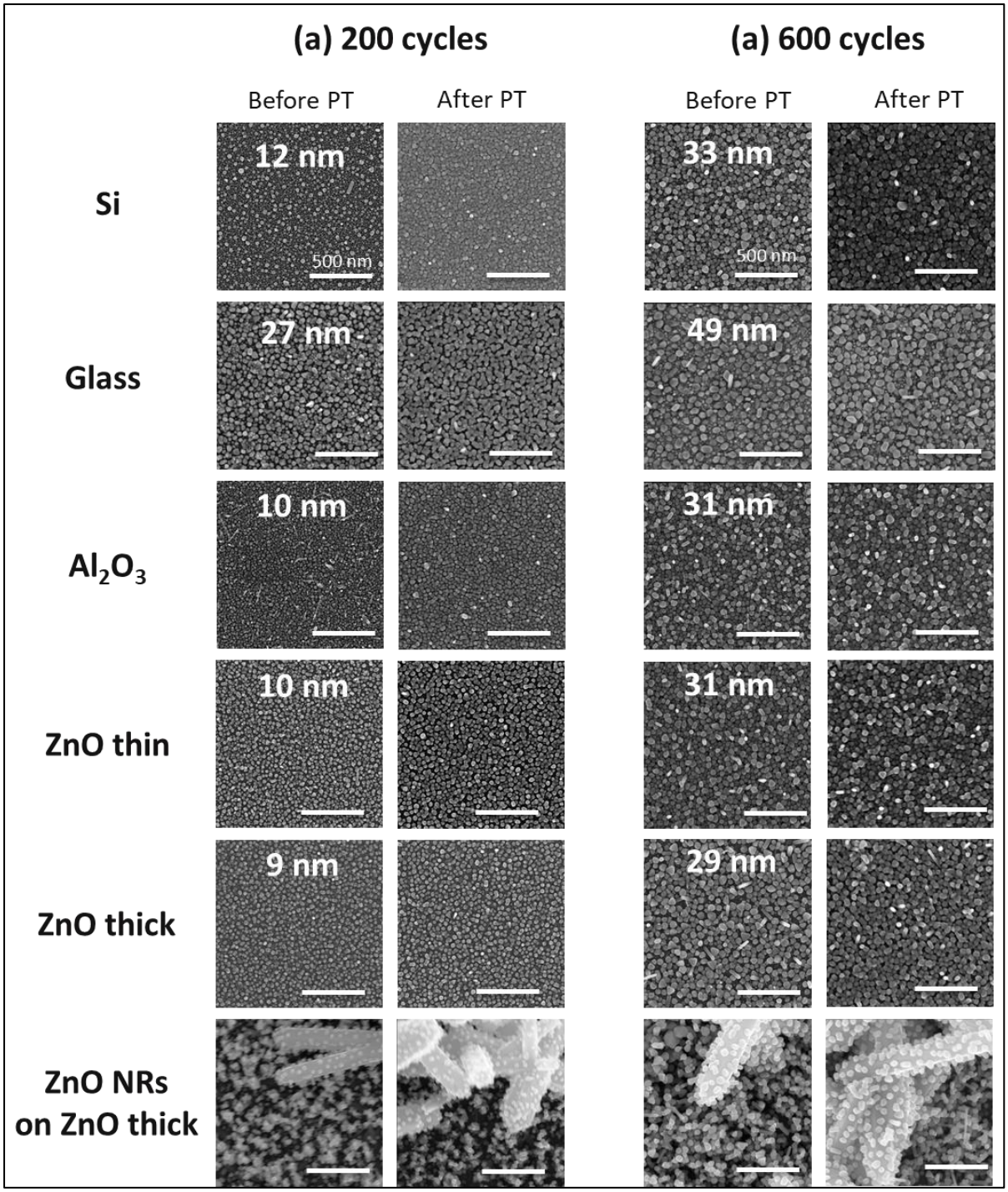


Figure 121: Scanning Electron Micrographs of Ag thin films deposited by the two-step approach on the different underlayers coated silicon after a varying number of cycles (a) 200 cycles and (b) 600 cycles, both before plasma post-treatment (upper part of (a) and (b)) and after plasma post-treatment with $t_{post}$ = 60 s at $P_{post}$ = 100 W (lower part of (a) and (b)). The values at the center of the images correspond to EDS thickness of the film. The scale bars represent 500 nm. The studies were performed at the optimum temperatures $T_{ch}$ = 150°C/$T_{hs}$ = 130°C.

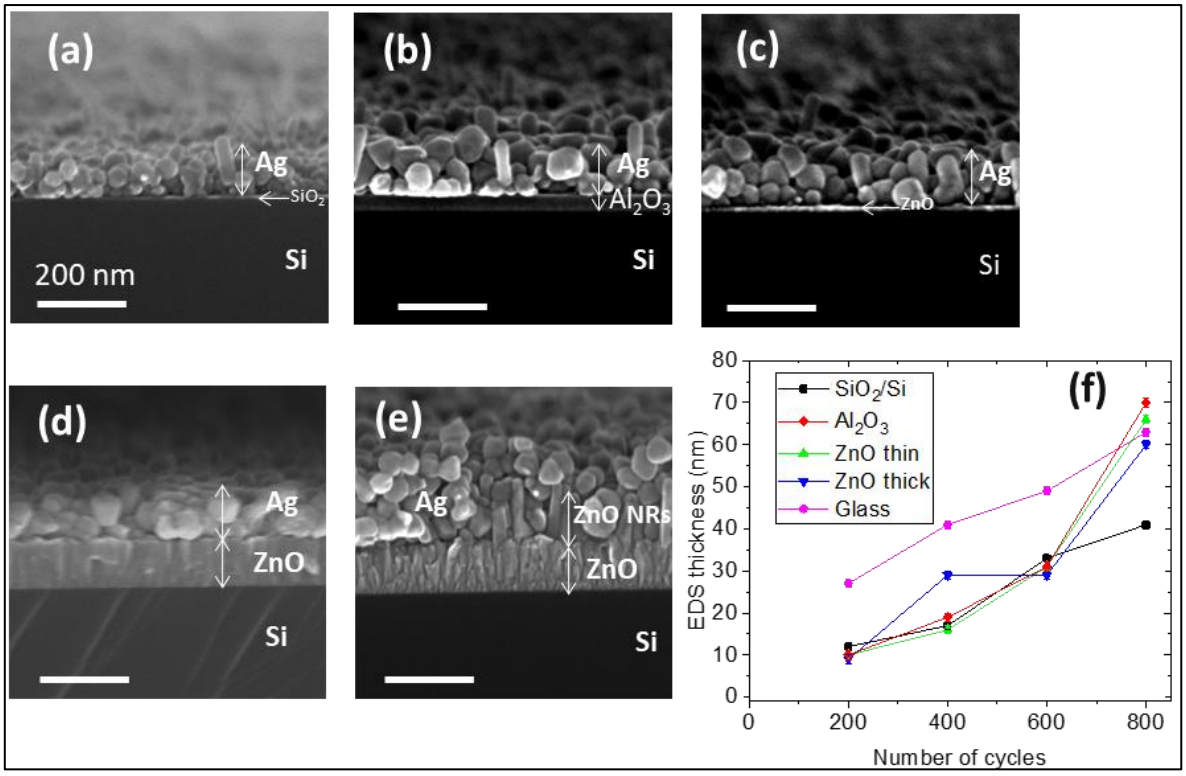


Figure 122: (a-e) Scanning Electron Micrographs in cross-section view of Ag thin films deposited by the first step of the two-step approach (i.e. before post-treatment) on the different underlayers coated silicon after 800 cycles (approximately 45 nm-thick): (a) Si with native oxide (b) $Al_2O_3$ (c and d) ZnO and (e) ZnO nanorods deposited on ZnO. The scale bars represent 500 nm. (f) Influence of the number of cycles on the EDS equivalent thickness of Ag deposited on the different underlayers. The studies were performed at the optimum temperatures $T_{ch}$ = 150°C/$T_{hs}$ = 130°C.

Next, in order to investigate the influence of the underlayers on the electrical properties of Ag films deposited by the two-step process, we have studied the sheet resistance of the films as a function of the plasma post-treatment duration. Ag deposited on underlayers coated glass have been used to measure the sheet resistance of the films in order to get rid of the leakage current influence in the case where conducting silicon substrate is used. We have checked that the morphology of Ag films remains unchanged between underlayers coated glass and underlayers coated silicon employed for SEM images to avoid charging effect caused by non-conductive substrates.

Figure 123 exhibits the dependence of the sheet resistance of Ag deposited after 600 cycles on the different underlayer materials as a function of the plasma post-treatment duration. The plasma post-treatment reduces significantly the Rs of Ag films by at least four orders of magnitude for all the underlayers (within error bars), already after $t_{post}$ = 15 s. This is due to the removal of the precursor on the surface, even if the films do not present any merger of the compact particles (Figure 121 (b), lower part), as already proved by the chemical properties in chapter 5. After 60 s, all Ag films exhibit close Rs values (ranging from 13 Ω/□ to 18 Ω/□), except for deposition performed on ZnO thick films. The higher sheet resistance of 35 Ω/□ is justified by the higher roughness of the ZnO underlayer, which is fully consistent with the work of Kato *et al.* [255] for defective Ag. For Ag films deposited on ZnO NRs, the absence of conduction at 600 cycles confirms that the substrate roughness plays a role on the electrical properties and film continuity. In this case, Ag film exhibited an electrical conduction only above 1200 cycles, with a value as low as 4.7 Ω/□ after 60 s of plasma PT, probably due to the fact that the large amount of Ag material has filled-in the gaps between particles. On the other hand, the

slightly lower sheet resistance of film synthetized on glass substrate is explained by the larger Ag film thickness deposited at 600 cycles, due to higher growth rate.

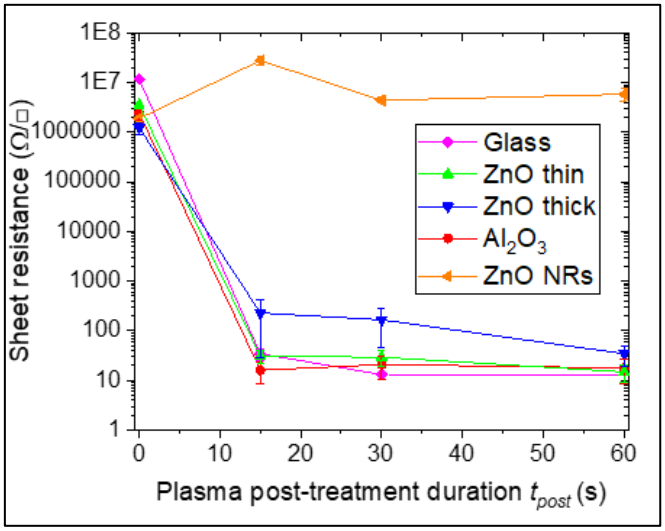


Figure 123: Dependence of Ag sheet resistance deposited after 600 cycles on the underlayer material as a function of the plasma post-treatment $t_{post}$ duration (0 s corresponds to as-deposited film, before the plasma post-treatment step). Direct PT has been used at $P_{post}$ = 100 W.

In summary, as for PE-ALD deposited films, similar Ag film morphology is obtained independently of the underlayer used. The deposition of silver exhibits similar growth rate in all cases, only excepted for glass substrates for which the higher hydroxyl group density promotes the growth speed. When following the electrical properties of Ag deposited on top of the underlayers, the plasma post-treatment decreases significantly the sheet resistance of the films, but the film roughness impairs the electrical conduction.

## VI.2. Optical properties of thin films deposited by the two different processes

### VI.2.1. Silver films deposited by standard PE-ALD

In chapter 4, we have shown that it was possible to tune the morphological properties of the deposited nanoparticles, i.e. the NP size, EDS and morphological thicknesses, aspect ratio, density and covered area by controlling the deposition parameters (temperatures, argon flows, precursor sequence times). In this section, we investigate the dependence of the optical properties on the Ag NPs morphology. We also prove the modulation of the transmittance (%T) and reflectance (%R) properties in the near infrared (NIR) region suitable for applications for optics and thermal mitigation, as well as the absorbance (%A) properties in the visible range useful for plasmonic effects, sensors or energy harvesting.

Two main factors are influencing the light reflectance, transmittance and absorbance by silver nanoparticles. The first one is related to the volume of Ag passed by light, i.e. the film thickness and the NP size with bigger volumes leading to increased light absorbance. The second one might be related to the morphology of the layer on the glass substrate, i.e. the film coverage. It is thus possible to modulate the optical properties of the film by changing the nanoparticle morphology.

We have studied the influence of the number of ALD cycles on the optical properties of Ag nanoparticle film with a coverage lower than 70%. All the depositions have been performed in the

same experimental conditions in order to follow only the influence of a change in nanoparticle morphology. The optical spectra with the corresponding scanning electron micrographs are shown in Figure 124 and the associate morphological parameters are presented in Table 31. As already explained in chapter 4, the growth follows the Volmer-Weber mode with a morphology made of small and spaced nanoparticles which get bigger, closer, and increasingly irregular in shape with increasing numbers of cycles, whereas the nanoparticle density decreases due to the merging of the NPs (see insets in Figure 124 and associated quantitative analysis in Table 31). For example, a film deposited after 100 ALD cycles presents an average nanoparticle size of 7 nm which cover 26 % of the surface, whereas 69% of the surface area is covered by nanoparticles with an average diameter up to 60 nm after 800 ALD cycles. We present in Figure 125 deposition giving higher surface coverage than 70%. At a coverage of 83%, NPs are very close with an average diameter of 120 nm. For a surface covered at 94%, a quasi-continuous film is obtained, with an electrical conductivity of $9.21\times10^{4} \pm 9.05\times10^{2}$ S/cm due to the merger of the particles.

In the visible/NIR region (for wavelength greater than 500 nm), except for the quasi-continuous film, we observe a transition from high reflectance and low transmittance at lower wavelength to low reflectance and high transmittance at larger wavelength. The wavelength where R = T (black arrow) shifts to higher value when the particle size and surface coverage increase, going to infinite when the film becomes continuous. Qualitatively, this transition is understood the following way. At lower wavelength, electrons move freely in the Ag particles, behaving as free electrons, i.e. with high %R and low %T. This corresponds to the Drude theory, as shown in the first chapter of the thesis work, section I.5.2.1. At higher wavelength, the electrons are bound to the particle size, thus behaving as bound electrons and following the oscillator model, with high %T and low %R (see section I.5.2.2.). When the particles size increases, the transition is redshifted due to the larger dipole size, going to infinite when the film becomes continuous (infinite particle size). The transition from discontinuous film (Figure 124 and Figure 125 (a)) to quasi-continuous film is highlighted by the almost constant high infrared reflection and low transmission (Figure 125 (b)), in accordance with Drude's theory. Moreover, the visible reflectance increases with the number of ALD cycles and therefore the thickness of the Ag films (Figure 124 and Figure 125). The higher visible reflectance is obtained for the film with the highest coverage (Figure 125 (b)).

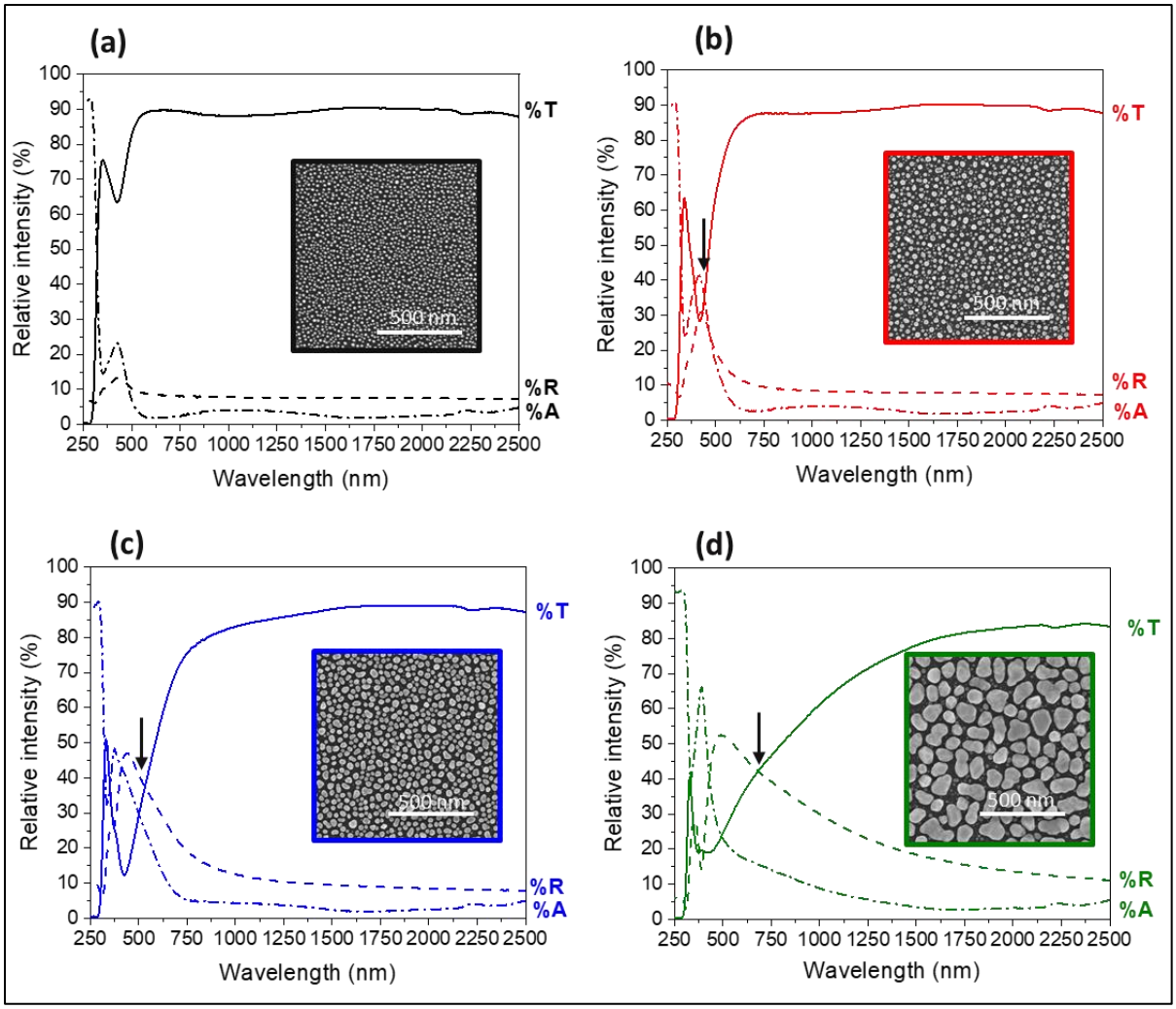


Figure 124: Influence of the number of cycles on the optical properties of Ag films on glass substrate for coverage lower than 70%: Transmittance (%T in solid lines), reflectance (%R in dash lines) and calculated absorbance (%A = 100-%R-%T in dash-dot lines) spectra as a function of light wavelength after a varying number of ALD cycles (a) 100 (b) 200 (c) 400 and (d) 800 ALD cycles. The black vertical arrows indicate the wavelength where %R = %T. The insets correspond to scanning electron micrographs (taken on silicon substrate close to the glass sample used for optical properties measurement) of the film investigated and the scale bars represent 500 nm.

| Sample | EDS thickness (nm) | Coverage (%) | Morphological thickness (nm) | NP size (nm) | Density NP/µm² |
|---|---|---|---|---|---|
| 100 ALD cycles | 3 | 26 | 12 | 6.7 | 7390 |
| 200 ALD cycles | 4 | 37 | 11 | 11.1 | 3837 |
| 400 ALD cycles | 10 | 48 | 21 | 19.7 | 1560 |
| 800 ALD cycles | 23 | 69 | 33 | 59.5 | 252 |

Table 31: Morphological parameters (EDS and morphological thicknesses, film coverage, nanoparticle size, nanoparticle density and aspect ratio) corresponding to the films presented in Figure 124 and Figure 126.

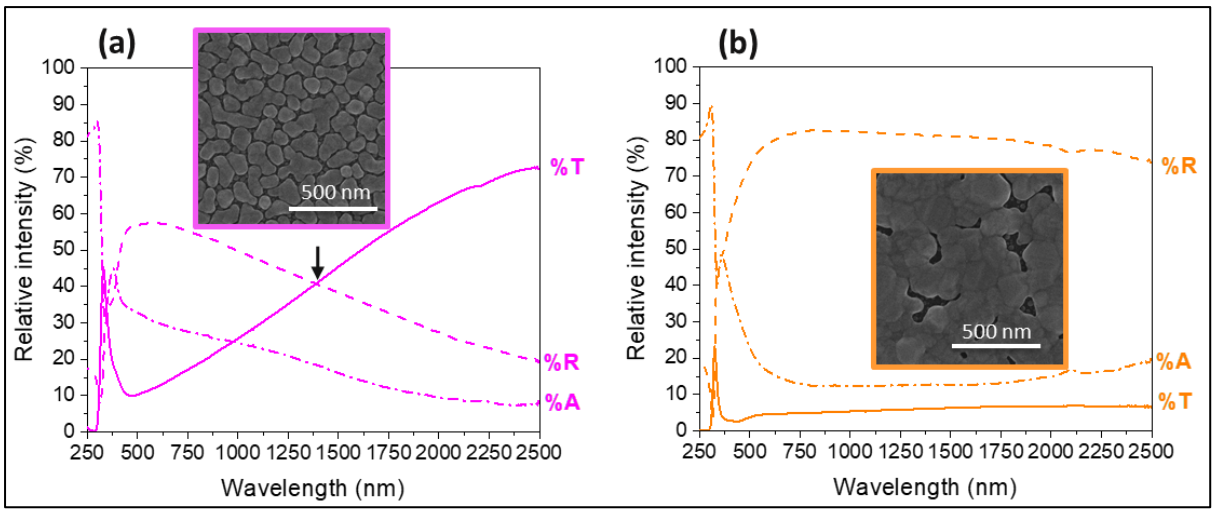


Figure 125: (a-b) Optical properties of Ag films on glass substrate for coverage higher than 70%: Transmittance (%T in solid lines), reflectance (%R in dashed lines) and calculated absorbance (%A = 100-%R-%T in dash-dotted lines) spectra as a function of light wavelength for film coverage higher than 70%, (a) 83% and (b) 94%. The insets correspond to scanning electron micrographs (taken on silicon substrate close to the glass sample used for optical properties measurement) of the film investigated and the scale bars represent 500 nm.

We observe a maximum absorbance peak in the visible region at a wavelength of around 400-430 nm (Figure 124 and Figure 125 (a)) corresponding to the localized surface plasmon resonance due to the metallic nanoparticle. For a surface covered at 94% exhibiting a quasi-continuous morphology, the LSPR here is due to the presence of defects in the film , i.e. non-uniform morphology made of gaps, as seen in the SEM image in Figure 125(b).

These LSPR peaks are zoomed in Figure 126. For film with coverage lower than 70% (Figure 126 (a)), we observe an enhancement of the magnitude of the peak and a blueshift of the peak along with the change in the film morphology, i.e. increase of particle size, film thickness and coverage while a decrease of particle density. Regarding the higher absorbance peak intensity with increase of the number of cycles, it is explained by the fact that the volume of Ag passed by light is affected by the film thickness and the NP size with bigger volumes leading to increased visible light absorbance. Second, it is important to notice that the shift of the absorbance peak to lower wavelength is observed even for almost continuous film (Figure 126 (b)). It was found in the literature that the LSPR optical response (spectral position, intensity and width of the absorbance peak) depends on the morphology of the nanoparticle and the covered area, and a redshift is generally observed when the particle size increases, as exposed in chapter 1, section I.5.3.. [25] In our study, the potential explanation for the blueshift is that the localized surface plasmon resonance is due to the surface defects/grain boundaries rather than directly to NP size and shape, at least for large particles and quasi-continuous film. [255, 256] The LSPR shifted to shorter wavelength is also observed by Haynes *et al.* when the lattice spacing of the array of Ag and Au nanoparticles synthetized by electron beam lithography is decreased. [257]

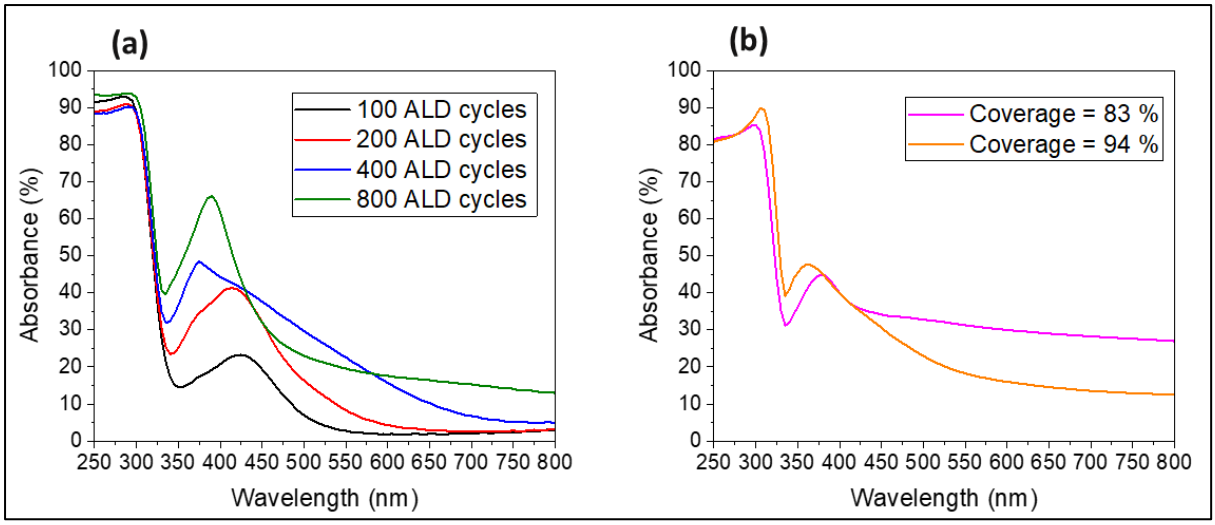


Figure 126: (a) Zoom in of the absorbance in the visible range corresponding to (a) the Ag films presented in Figure 124 deposited after a varying number of ALD cycles with coverage lower than 70% and (b) the Ag films presented in Figure 125 with coverage higher than 70%.

## VI.2.2. Silver films deposited by the two-step approach

### VI.2.2.1. Optical properties of Ag films before and after post-treatment

We have further investigated the optical properties of the silver films deposited by the two-step approach, as ultra-thin Ag films can be used for optical coatings in windows, lenses [21] or mirrors. [20] In order to investigate the functional properties of films synthesized using the new suggested process, we perform optical analysis of the as-deposited and post-treated Ag films. The optical properties of a 15 ± 1 (i.e. close to the critical thickness) and 42 ± 2 nm-thick Ag film deposited on glass substrate are shown in Figure 127 (a,c) and Figure 127 (b,d), respectively.

Before plasma post-treatment, the optical behavior of the Ag film made of compact nanoparticles is very similar to the one obtained for separated NPs using standard PE-ALD. For the thinner film (Figure 127 (a) in red), we observe the same transition: at lower wavelength, a high reflectance and low transmittance which, respectively decreases and increases at higher wavelength. However, the as-deposited film presents a stronger and broader absorbance peak ranging from the visible to NIR range (300-1300nm, Figure 127 (c) in red) compared to LSPR of well-separated Ag NPs shown in the previous section. This behavior is typical for a film of aggregated nanoparticles, were the plasmon resonance of small silver particles [27] is broadened by the strong dipolar interaction between particles. [258] Indeed, due to the compact particle morphology, the NPs are very close to each other and thus highly interacting between them. For the thicker film (Figure 127 (b) in red), the same transition from high %R/low %T at lower wavelength to low %R/high %T at higher wavelength is noted. However, the transition where R=T is shifted to higher wavelength, highlighting that the NPs are higher in size or more coupled. The plasmon peak followed by a peak shoulder giving stronger and broader absorbance is also caused by the dipolar interaction between particles due to the compact morphology (Figure 127 (d) in red).

After plasma post-treatment, for the thicker film (Figure 127 (b,d) in black), the reflectance strongly increases and reaches up to 97% in the infrared region while the transmittance and the absorbance are strongly reduced in the NIR region. This is explained by the widen conduction paths (free electrons in metal layers) due to the quasi-continuous film morphology, confirming thus the good long-range

electrical conduction properties obtained after PT. The absorbance of the post-treated film does not show any signature of aggregated nanoparticles, i.e peak broadening, that is the sign of a good sintering of the particles. As it was the case for a quasi-continuous film with a coverage of 94% deposited by standard PE-ALD (Figure 125(b)), the residual absorbance of the post-treated film in the visible region might be related to defects in the silver coatings, either due to holes or to the roughness of the deposit (rms roughness of 10.7 ± 0.2 nm for the as-deposited film and 8.9 ± 0.6 nm for post-treated film, see chapter 5). When it comes for the thinner film ((Figure 127 (a) in black), due to lower thickness of Ag layer and the existence of higher non-covered areas (presence of more gaps) in the film morphology, the spectrum presents a lower reflectance and a higher transmittance as compared to the thicker film. However, contrary to what was observed for as-deposited films, we observe quasi-constant reflectance and transmittance with a presence of a plateau when increasing wavelength. This is the signature of the transition from nanoparticle film to quasi-continuous film. The high and quasi uniform visible/NIR absorbance (Figure 127 (c) in black) confirms the strong dissipation due to the presence of defaults in the film, as already demonstrated for defective thin Ag films deposited by sputtering. [255]

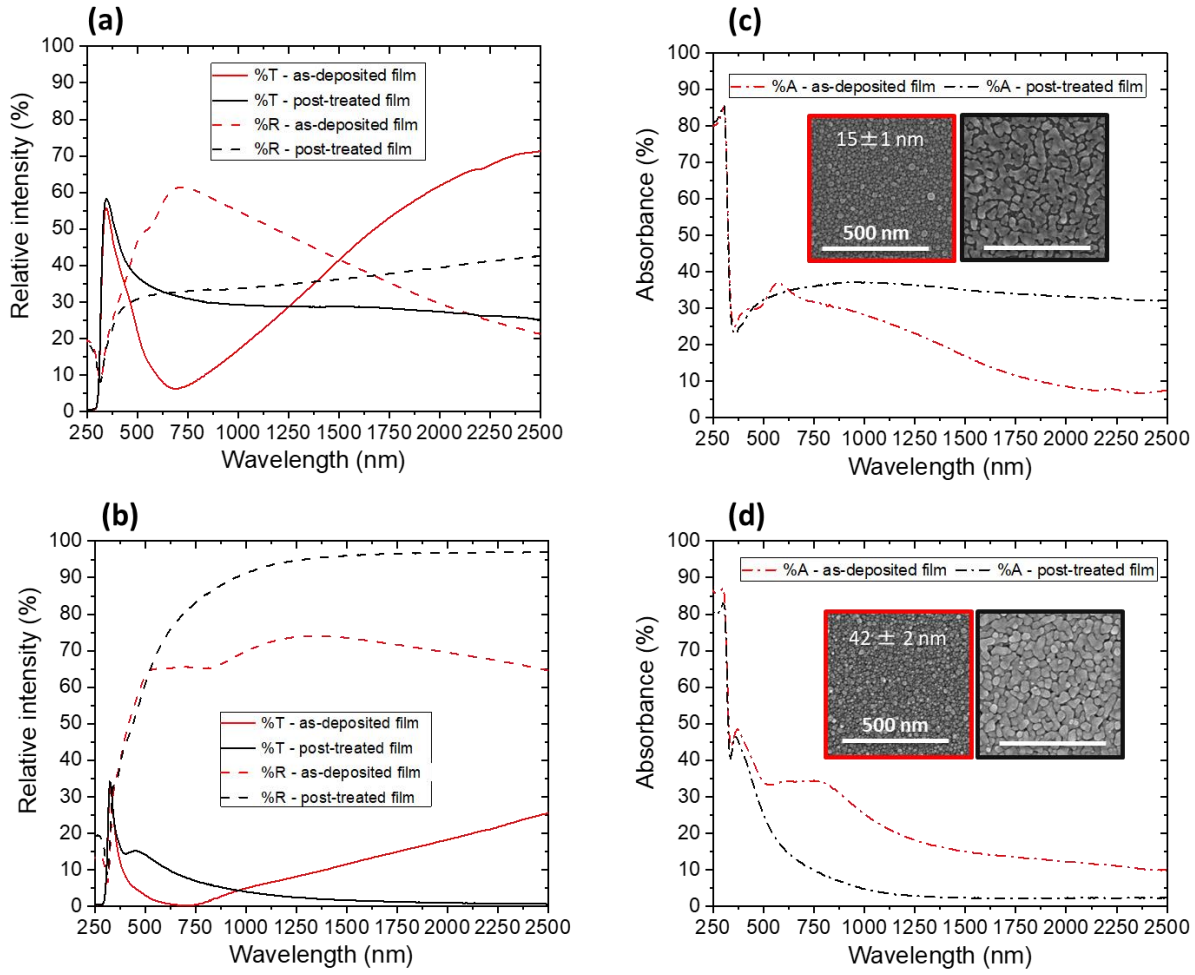


Figure 127: Optical properties of Ag thin films on glass substrates: (a-b) Transmittance (%T in solid lines), reflectance (%R in dash lines) and (c-d) calculated absorbance (%A = 100-%R-%T in dash-dot lines) spectra as a function of light wavelength corresponding to as-deposited (in red) and post-treated with indirect PT for $t_{post}$ = 600s and $P_{post}$ = 250W (in black) Ag thin layer. The insets in (c) and (d) correspond to SEM images for as-deposited (red outline) and post-treated (black outline) and the scale bars represent 500 nm. The EDS equivalent thickness is (a-c) 15 ± 1 nm and (b-d) 42 ± 2 nm.

### VI.2.2.2. Influence of the plasma post-treatment duration on the optical properties of Ag films

The effect of the plasma post-treatment with a fine tuning of its duration $t_{post}$ on the optical properties of Ag thin films has been studied deeper in Figure 128. The results are directly correlated with the sheet resistance of the layers and the corresponding morphology presented in Figure 129. We compare a 27 nm-thick Ag film deposited after 200 cycles and a 41 nm-thick Ag film deposited after 400 cycles, before (as-deposited) and after PT. As already highlighted in the previous section, the effect of the PT is clearly seen by a change in the optical spectra.

For the thinner film, already after the first PT of 5s, we observe the transition from nanoparticle film to percolated film both on the SEM images in Figure 129 and on the optical behavior of the film in Figure 128. First, the high visible/low IR reflectance is translated to a lower visible/higher IR reflectance with a uniform value after PT (Figure 128 (b)). We do not observe an increase of the reflectance as it was presented in chapter 1 for continuous film due to the fairly high films resistivity. Second, the low visible/high IR transmittance changes to a quasi-constant transmittance with a presence of a plateau when increasing wavelength after PT (Figure 128 (a)). Third, contrary to a decrease of the absorbance which is expected after PT (Figure 127 (d)), we observe in Figure 128 (c) a high and quasi uniform visible/NIR absorbance, as already demonstrated for the thin film in Figure 127 (c). This confirms again the strong dissipation due to the presence of defaults in the film, in accordance with the work of Kato *et al.* [255]. Even if we notice a high degree of coalescence of particles, no clear distinction of the effect of post-treatment duration on the optical spectra (%R, %T and %A) are noted. This might be due to the fact that the films remain highly resistive even after long $t_{post}$ of 11430 s of post-treatment at different plasma power (PT4), i.e. $4\times10^6$ Ω/□ after PT 4 (Figure 129). This is understood by the fact that the film is almost discontinuous (close to percolation).

For the thicker film deposited after 400 cycles, already after 5s of post-treatment, we observe the same transition as for thinner film on the optical properties of the film, from nanoparticle film with low visible/high IR %T and high visible/low %R to percolated film with almost constant %T and %R and %A from visible to IR regions. We do not obtain a lower value of the IR %A for post-treated films as compared to as-deposited ones, as it was the case in the previous section (Figure 127 (d)). This is due to the much lower value of IR %R (50-60% vs. 97%), probably caused by a lower film quality (higher resistivity of 30.8 μΩ.cm as compared to 6.7 μΩ.cm for the previous film). On the other hand, the shape of the visible %A peak of the post-treated Ag film after the two first PT (5 s and 10s) is very similar to the one of as-deposited film (Figure 128 (f)). Indeed, we see the presence of a strong and broad absorbance peak ranging from the visible to NIR range, typical for a film of aggregated nanoparticles. [27, 258] This is seen on the SEM images in Figure 129 for which the presence of well-defined connected particles is still noticed even after PT. Despite the absence of modification of the film morphology, we observe a drop of the sheet resistance value of 3 and 5 orders of magnitude after 5s (PT 1) and 20s (PT 2), respectively, probably due to the removal of the precursor on the surface (see chemical properties in chapter 5). For longer PT time (1230s at 100 W for PT3 and 11430s at different plasma power for PT 4), when increasing $t_{post}$, the IR absorbance decreases which is directly linked to the increasing IR reflectance (Figure 128 (e). This is due to the still decrease of the sheet resistance but at much lower rates (10.7 Ω/□ to 8.4 Ω/□). This is in accordance of the work of Kato et *al.* who found a decrease of the IR %A with the increase of the film conductivity. [255] We observe a good coalescence of the particle (see SEM in Figure 129) which is translated by a tighter visible absorbance peak for the two last post-treatments.

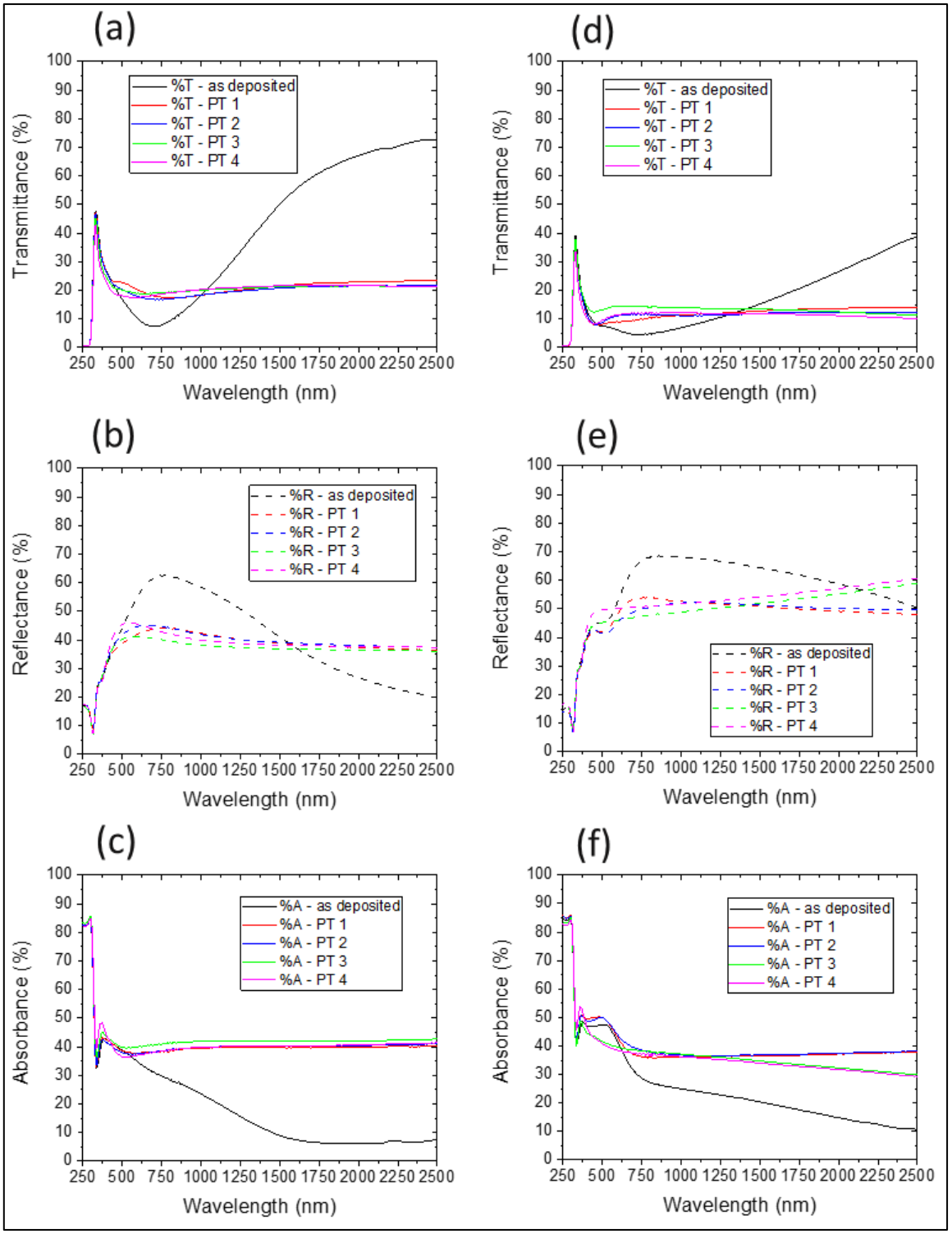


Figure 128: Influence of the direct plasma post-treatment time $t_{post}$ on the optical properties (transmittance %T (a-d), reflectance %R (b-e) and calculated absorbance %A = 100-%R-%T (c-f)) of Ag films deposited on glass substrate after 200 cycles giving a 27 nm-thick film (a-c) and after 400 cycles giving a 41 nm-thick film (d-f). The different parameters for the plasma post-treatment (PT) are: for PT 1, $t_{post}$ = 5s / $P_{post}$ = 100 W; for PT 2 $t_{post}$ = 20 s / $P_{post}$ = 100 W; for PT 3 $t_{post}$ = 1230 s / $P_{post}$ = 100 W and for PT 4 $t_{post}$ = 1230 s / $P_{post}$ = 100 W + $t_{post}$ = 1200 s / $P_{post}$ = 150 W + $t_{post}$ = 5400 s / $P_{post}$ = 200 W + $t_{post}$ = 3600 s / $P_{post}$ = 250 W. The electrical properties and morphology corresponding to each film are found in Figure 129.

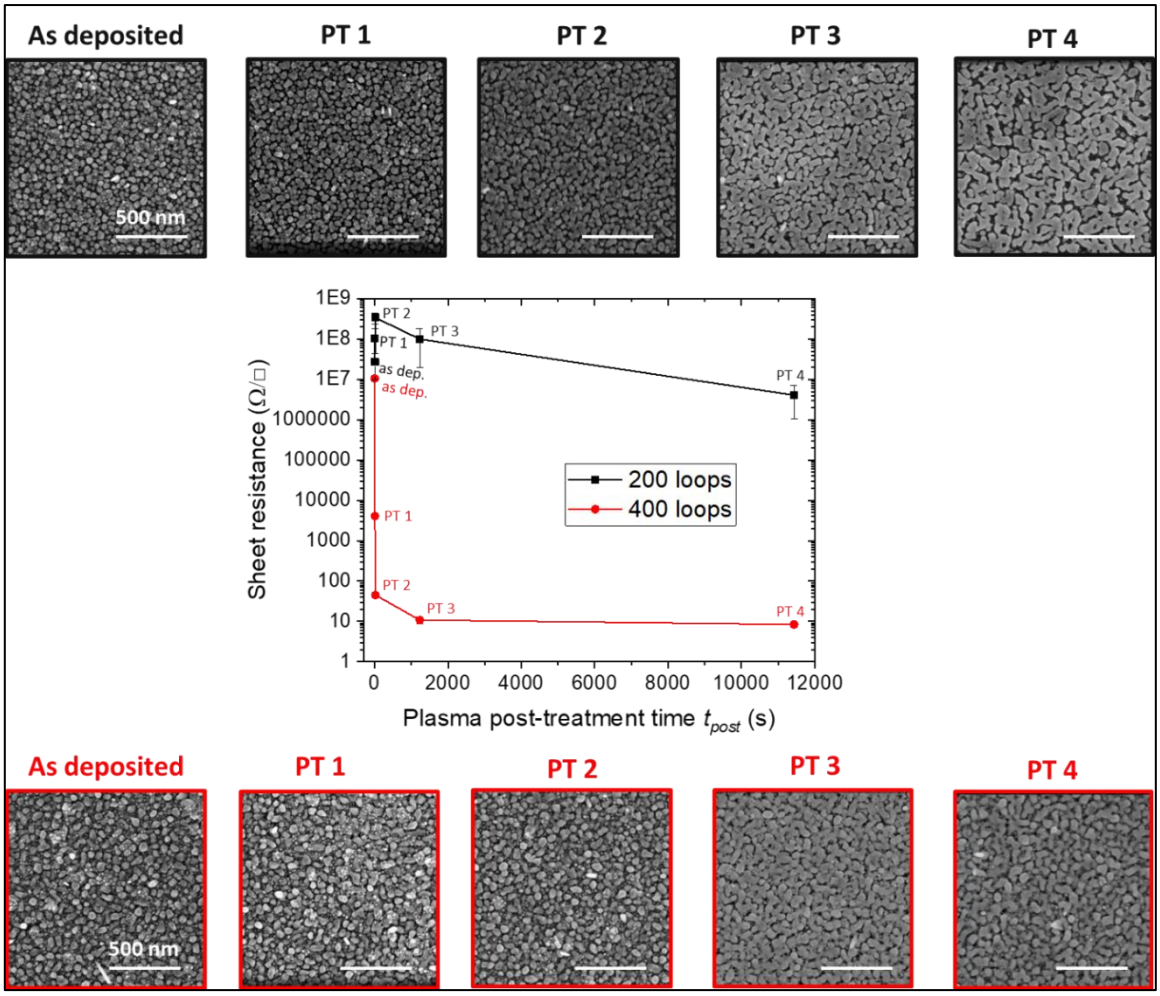


Figure 129: Influence of the direct plasma post-treatment time $t_{post}$ on the sheet resistance of Ag films deposited on glass substrate after 200 cycles giving a 27 nm-thick film (black) and 400 cycles giving a 41 nm-thick film (red) and corresponding scanning electron micrographs. The different parameters for the plasma post-treatment (PT) are: for PT 1, $t_{post}$ = 5s / $P_{post}$ = 100 W; for PT 2 $t_{post}$ = 20 s / $P_{post}$ = 100 W; for PT 3 $t_{post}$ = 1230 s / $P_{post}$ = 100 W and for PT 4 $t_{post}$ = 1230 s / $P_{post}$ = 100 W + $t_{post}$ = 1200 s / $P_{post}$ = 150 W + $t_{post}$ = 5400 s / $P_{post}$ = 200 W + $t_{post}$ = 3600 s / $P_{post}$ = 250 W. The scale bars of SEM images represent 500 nm. The optical properties corresponding to each film are found in Figure 128.

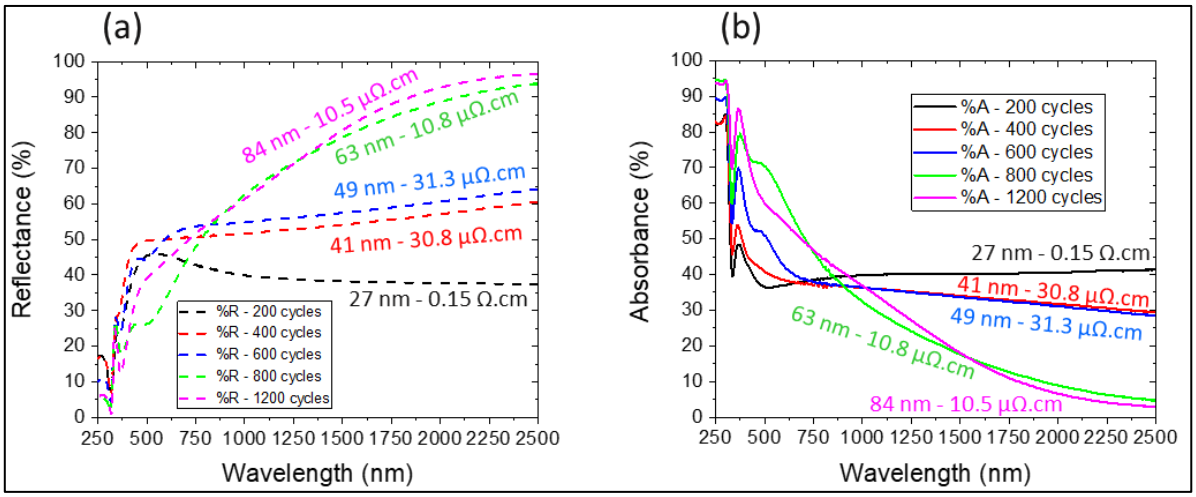


Figure 130: Influence of the number of cycles (and thus the film thickness) and electrical properties (resistivity) of post-treated Ag thin films on glass substrates on the optical properties of the film: (a) reflectance %R and (b) calculated absorbance %A = 100-%R-%T.

As we have highlighted that the optical properties are influenced by the electrical properties of Ag films, we have investigated the correlation between electrical and optical properties on Ag films in a broader range of thicknesses. We used post-treated Ag films after 11430 s of post-treatment at different plasma power (PT4) exhibiting connected morphology with thicknesses ranging from 27 nm to 84 nm and resistivity respectively from 0.15 Ω.cm to 10.5 μΩ.cm (Figure 130). We clearly see that an increase of the film resistivity leads to an increase of IR absorbance (Figure 130 (b)) while decreasing the IR reflectance (Figure 130 (a)). This has already been observed in the work of Kato *et al.* [255]. In the free electron model, the imaginary part of the dielectric constant $\varepsilon_2$ is proportional to the d.c. resistivity of the metal (see chapter 1 and e.g. [199]), thus the higher %A are directly linked to the higher d.c. resistivity of our films. The increase of the absorbance may also be due to the dissipation caused by surface plasmon polaritons (surface plasmon excited by electro-magnetic wave) on rough Ag surface as it was highlighted by Kato *et al.* [255].

## VI.3. Conclusion

In terms on **conformality**, we have seen that the standard PE-ALD gives a poor film conformality due to the plasma species recombination. On the contrary, the new two-step approach enables to obtain a highly-conformal Ag deposition, even for lateral high aspect ratio structures, which are impossible to fill in with line-of-sight methods. In addition to SEM morphologies, the results have been highlighted by studying the thickness profiles into a quasi-infinite trench for both processes. An exponential decrease of the Ag film thickness confirms the recombination of hydrogen radicals on the surfaces for standard PE-ALD which prevents the growth deeper into the structure. On the contrary, the gas-phase reaction occurring during the first step of the new process follows a diffusion law, which confirms the high degree of conformality obtained by means of our novel approach. We have also seen that the morphology obtained with the novel approach is preserved far into the lateral structure, both for as-deposited and post-treated films. The layers remain connected until the thickness becomes lower than the critical thickness. With a view to understanding what avoids the radical's recombination and what enhances the radical's penetration depth during the plasma post-treatment, we have performed the same Ag deposition in LHAR structure and then tested two different kind of post-processes, i.e. indirect (in the presence of the grid) and direct PT. Since the penetration depth of the post-treatment is equivalent for both direct and indirect PT, it was concluded that it was not only the fact to have a direct PT that gives the efficiency of the PT until the bottom of the trench. One hypothesis of this enhancement of conformality for the post-treatment could be that the limitation of radical's penetration is directly correlated with the plasma pulse time, which is longer during the plasma post treatment of pulsed PE-CVD deposited film compared to very short one for standard PE-ALD deposited film (3 s). Further investigations are still needed in order to validate this hypothesis, even though the deposition of conformal film made of well-separated Ag NPs was not the aim of this PhD thesis since thermal-ALD already exhibits good achievements. Overall, Ag deposited by our novel approach covers largely the requirements of the current microelectronic applications in terms of film conformality and Ag could be a good candidate for conducting interconnects in microelectronics.

Noble metal films supported on (metal) oxide and high aspect ratio substrates have also an interest for applications in microelectronics or smart windows market for continuous smooth layers and in optical coatings sensors for Ag nanoparticle film. Weakly-interacting film/substrate systems

represent a key factor for these applications. In this section, we have seen that the **underlayers** has a weak influence on the morphology of silver films deposited with both processes. Even for zinc oxide, which exhibits higher surface energy than silver itself, no continuous Ag films but rather a morphology of discrete islands have been obtained by standard PE-ALD, while the morphology made of Ag compact nanoparticles is preserved for pulsed PE-CVD deposited Ag films. We have used surface wettability quantified by the value of the water contact angle to compare the different underlayers and made a correlation with the surface hydroxyl groups density. We found that the Ag film growth rate was highly dependent on the –OH surface density which promoted the Ag precursor chemisorption and thus the metal loading. This higher growth rate was correlated to the lower contact angle values, presumably due to higher surface hydroxyl species. Since the standard PE-ALD involves only a surface-limited reaction whereas a gas-phase reaction and a surface reaction are taking place for pulsed PE-CVD, this effect was more pronounced in the first case. Indeed, for film deposited via the two-step approach, no slower start of the deposition is occurring for ZnO and $Al_2O_3$ underlayers as compared to Si, but all these substrates exposed the same growth rate. In addition, for this novel approach, when following the dependence of the electrical properties of Ag deposited on top the different underlayers and as a function of the post-treatment duration, for all films deposited after 600 cycles, a sharp decrease of the Ag films sheet resistance was noticed. However, the films roughness was found to increase the film resistivity due to the defects and almost insulating Ag deposition have been obtained on zinc oxide nanorods.

Finally, we have highlighted the interaction of the **optical properties** and the morphology of Ag films. The synthesis of discrete islands by standard PE-ALD is underlined by the presence of localized surface plasmon resonance absorbance peak in the visible region. We showed that the LSPR optical response (spectral position, intensity and width of the absorbance peak) was dependent on the morphology of the nanoparticle and the covered area. Contrary to what is usually observed in the literature, we observed a blueshift with the increase NP size and film coverage which might be explained either by the surface defects/grain boundaries rather than directly to NP size and shape for large particles/quasi-continuous films obtained after higher ALD cycles or by a decrease of the lattice spacing of the array of Ag. The second signature of nanoparticle films is the transition from a ‘continuous like’ optical behavior at low wavelengths, understood by Drude’s model and highlighted by a high reflectance/low transmittance, to the ‘particle-like’ behavior at higher wavelengths, understood by the oscillator model and highlighted by a low reflectance/high transmittance. When it comes to the two-step process, for Ag compact NPs film obtained before post-treatment, the same transition of reflectance and transmittance as PE-ALD deposited nanoparticle is observed as function of wavelength. The main difference relies on the presence of a broader absorbance peak which is linked to the interaction between particle due to the aggregated nanoparticle morphology. When plasma-post processing is applied, we noticed an optical behavior close to an ideal continuous film, with a strong increase of IR reflectance and strong decrease of both NIR absorbance and transmittance. However, the presence of defects in the film, either due to gaps or to the roughness of the deposit, cause a strong dissipation observed by a residual visible absorbance of the silver films. Finally, we proved that the electrical properties of Ag films deposited by the two-step approach affect the optical spectra. We have observed an increasing IR absorbance correlated to a decreasing IR reflectance when Ag film resistivity have increased. This may be due to the dissipation caused by surface plasmon polaritons (surface plasmon excited by electro-magnetic wave) on rough Ag surface.

# Conclusion and Perspectives

In this chapter, the important achievements of the thesis are presented in order to respond to the challenges of the work. Several outlooks arise from this PhD work. Therefore, preliminary studies giving encouraging results for potential future applications are highlighted and presented as proof of principle.

# General conclusion and outlook

## 1. Conclusion

This doctoral thesis focused on the deposition of ultra-thin silver films using chemical vapor-phase deposition, the film characterization and the growth mechanism comprehension. In order to overcome the physical limit of line-of-sight deposition, i.e. lack of film conformality on complex substrates, ALD-based processes were used. The state-of-the-art of chemical gas-phase processing of silver films highlights that the major challenge is to find a suitable metal precursor presenting both a thermal stability and a high vapor pressure. Moreover, another drawback is that the ALD of metal nanoparticles, and in particular silver, is still weakly understood in terms of growth mechanism and suffer from a lack of uniformity over large-area substrates. Using this method, we have seen that it is also quite challenging to obtain continuous Ag films, because, as for all noble metals, the growth mechanism leads to a nanoparticle morphology for low thickness.

Having these challenges in mind, this thesis work has followed **two different routes** to tackle them.

The **first route** is the deposition of Ag through standard PE-ALD using Ag(fod)($PEt_3$) as silver precursor and $H_2$ plasma as reducing agent. During the development of the process, it was found that, for low thickness, typically below 60 nm, the obtained silver layers are made of silver particles distributed on the surface, as expected from the growth of metal layers on oxide surfaces. As usually observed for most of ALD processes, the process parameters (i.e. temperatures, argon flows, plasma conditions and sequence times) play a critical role in the film synthesis. The aim was to achieve an ALD self-saturated regime which has been quantified by a systematic analysis of the film thickness uniformity over a large surface area (8-inch substrate) depending on the experimental conditions. We have proved a deficiency of the precursor injection system, creating a leak and continuous exposure of Ag precursor. This has been upgraded through modification of the geometry of the gas-valving system, and one of the major consequences of this upgrade was the strong improvement of the uniformity of the deposition. In a **preliminary investigation**, the chamber temperature was identified as the most critical parameter giving an optimum chamber temperature ranging from 100 to 140°C. The Ag precursor temperature, controlling its evaporation, needs to be at least 10°C lower than the chamber temperature in order to avoid condensation of the precursor on the reactor. The argon flows have been investigated, both in the process lines, to control the amount of precursor exposed into the chamber, and in the plasma head, to regulate the exposure of radicals created by the plasma. It was found that these parameters had a stronger influence at a lower chamber temperature due to the challenging control of the ALD parameters at this low temperature. Under selected parameters and reduced temperatures, quasi-continuous layers can be obtained. However, depositions made at such low temperatures were strongly non-reproducible due to the non-appropriate evaporation conditions of the Ag precursor. Using this preliminary approach as a starting point, a **fine development** of the PE-ALD of Ag highlighted that the ALD sequence times played a major role in order to ensure a saturation of the substrate surface. In optimum conditions, the Ag precursor pulse length $t_{pr}$ was 5 s, while the hydrogen plasma pulse $t_{pl}$ was 3 s. The purge length after the metal precursor $t_{pu1}$ was 5 s and 10 s after the plasma exposure $t_{pu2}$. The consequence of a deviation as compared to these times is a decrease of the uniformity of the film thickness, i.e. a change in the deposition regime with CVD-like

behavior when the purge time is too low, and an under-saturated regime when the pulse time is not high enough. The plasma conditions also highly influenced the deposition and, highlighted by chemical analyses, reactive hydrogen radical species were found to be mandatory in order to obtain pure silver in metallic state. We have also confirmed that lower temperatures ($T_{ch}$ = 110°C / $T_{hs}$ = 90°C) favored the formation of a quasi-continuous film but with a lack of reproducibility and higher temperatures ($T_{ch}$ = 130°C / $T_{hs}$ = 100°C) revealed a film made of nanoparticles which are separated. This effect might be related to the migration of metal atoms on the surface, which is reduced at low temperatures. The electrical conductivity of the films has been evaluated for both regimes. At low temperatures, the values were very low (e.g. conductivity of $7.12\times10^{-2}$ S/cm for a silver film of 22 nm). At high temperatures, low electrical conduction was obtained for thick films (conductivity of $2.46\times10^{-5}$ S/cm for a film thickness of 47 nm).

The parameters mentioned above have also been used in order to more carefully study the **growth mechanism** based on the particle morphology and demonstrate the large-scale uniform deposition of Ag NPs. By means of an original methodology, we have investigated deeper the uniformity of the deposition and quantified it in terms of film morphology. For that, we have reported the value of the morphological criteria (morphological and EDS film thickness, size, density and aspect ratio of Ag NPs, film coverage) both at the center position of an 8-inch substrate and, more originally, the gradient over a 10 cm distance on the substrate. We have demonstrated that the full analysis of the morphology and the gradient provided more information than the more commonly investigated average thickness alone. The analysis of the large-scale deposition, and thus the gradient, was very useful as it has demonstrated the limited process temperature window ranging from 130 to 140 °C, which is not anticipated by investigating the deposition rate alone. The control of the growth mode and ALD parameters remained crucial to obtain uniform NPs with tailored morphology. In the process window, we have demonstrated that appropriate pulse and purge times can produce films with less than 5% gradient of the thickness and NP size over 10 cm length. Regarding the plasma conditions, we proved that the maximum quantity of radicals arriving on the substrate with a reduced travelling distance gave the higher plasma efficiency needed for the reduction reaction of the precursor and favored a more uniform cross-flow between the lateral flow of silver precursor and the vertical flow of hydrogen radicals. When it comes to the uniformity at the atomic scale, according to *X-ray diffraction*, *time-of-flight secondary ion mass spectrometry* and *X-ray photoemission spectroscopy* performed on the whole silicon wafer, the deposited material was found to be made of uniformly deposited polycrystalline pure metallic Ag, with a low amount of impurities emanating from the precursor, showing the completeness of the reduction reaction. When varying the number of ALD cycles, a deposition process driven by surface reactions, as expected for ALD, have been obtained with an average growth per cycle of 0.017 ± 0.004 nm/cycle. A more detailed study on the morphological criteria were undertaken within the first deposition stages (first 800 ALD cycles). It was concluded that the observed trends were not consistent with a single growth mechanism. For that, an empirical model with a view to understanding the Ag NP growth mechanism on a surface has been proposed. The minimal combination that reproduces the experimental results was reaction and deposition, on top of a silver nanoparticle already adsorbed on the surface, on the triple point (interface between the substrate, deposited silver and gas) and material transfer. The growth mode involved both, deposition of Ag particles related to the Volmer-Weber mechanism, i.e. three-dimensional growth, and material transfer between particles, presumably via a 'surface Ostwald ripening' like process (larger particle growth at the expense of smaller ones). The material transfer mechanism mainly occurred during the plasma pulse, allowing us to tune the NP size while keeping the average thickness constant. However,

a deeper investigation is still needed regarding this material transfer mechanism, particularly by better distinguishing the competition between Ostwald ripening and particle migration and coalescence (Smoluchowski ripening).

Regarding the **second route**, we have demonstrated an alternative two-step process regime, which is more promising for continuous ultra-thin silver film deposition. A first step of pulsed plasma-enhanced CVD with continuous exposure of Ag precursor and pulse only of the plasma gave a peculiar morphology made of compact and highly covering nanoparticles, that is usually not achieved at low thickness with CVD or ALD methods. This process led to a typical growth per cycle of 0.065 ± 0.02 nm/cycle, corresponding to a growth rate of 0.27 nm/min, which is more than six times higher than the one obtained by standard PE-ALD (0.044 nm/min). However, the films remain almost insulating (sheet resistance of 6 MΩ/□ for a 25-nm-thick film). In order to make the deposit conductive, a second step of hydrogen-based plasma post-processing sintered these NPs, and highly conductive and almost continuous ultra-thin films have been obtained (sheet resistance of 6 Ω/□ for a 25-nm-thick film). A percolation threshold as low as 15 ± 1 nm (sheet resistance of 1.2 ± 0.1 kΩ/□ after post-treatment) and an electrical conductivity up to $3.9\times10^5$ S/cm for a 40-nm-thick post-treated Ag films have been achieved. These results are very close to the one obtained by physical vapor phase deposition and well beyond the one obtained by standard PE-ALD process deposited in the same temperature range (critical thickness of 63 ± 5 nm). Moreover, a mean-free path equals to 26 ± 2 nm and very close to sputtered Ag film proved the good quality of the film with a conductivity limited by the surface scattering rather than grain boundaries. Highlighted by chemical analyses, the originality of the two-step approach is that it is different from previous investigations, where a first deposition of a metal oxide is followed by a reduction step. Using the novel approach, the as-deposited film is already in metallic state even if it is non electrically conductive, and it exhibits all the typical diffraction plans of Ag with no signature of silver oxide phase. The further post-processing removes the unreacted Ag precursor from the surface and enhances the growth by an increase of crystallite size preferred on the (111) direction, explaining the increase in electrical conductivity.

The investigation of the **deposition parameters** of silver compact NP film has been used in order to understand the growth mechanism and also to propose a **qualitative model of growth**. It was found that mild plasma conditions (i.e. low RF power or high distance between the grid and the sample) favors the apparition of the peculiar morphology made of compact Ag NPs. The plasma pulse time has a higher influence on the film uniformity (in terms of the presence of compact morphology) as compared to the purge time between plasma pulses and the optimum conditions were $t_{pl}$ 3 s / $t_{pu2}$ 10 s. It was also found that the use of high temperatures, typically $T_{ch}$ 150°C and $T_{hs}$ 130°C and high Ar flows, typically 300 sccm both in the process and plasma head, strongly enhances the uniformity of the deposition and the obtention of compact films. Based on the experimental results of the obtained film morphology vs. process parameters, the qualitative model proposed in this thesis gives an hypothesis speculating that the new morphology is obtained due to the reaction of the silver precursors with hydrogen radicals in the gas phase, rather than on the substrate surface, as expected for the standard ALD process.

The investigation of the **plasma-post-processing parameters** performed on this peculiar morphology showed that, regarding its influence on the film morphology, a higher degree of coalescence of the particles was obtained with a higher density of the bombardment of energetic hydrogen radicals on the substrate. This depended mainly on hydrogen flow, RF plasma power, grid-substrate distance and plasma exposure time. In order to obtain the highest degree of coalescence of

the particles, a post-treatment with an optimum ratio of plasma power/hydrogen flow is needed to promote enough hydrogen radical's density while preventing film dewetting. The influence of the post-treatment on the electrical properties of the film with a fine tuning of its duration and power was achieved. By increasing the time of post-processing, an improvement of the electrical conductivity of silver films was obtained by, first, a removal of the unreacted silver precursor from the surface, which gave a sharp decrease of the film resistivity, then a partial sintering of the nanoparticles accompanying by still a decrease of the film resistivity, but at much lower rate, and finally an increase of the connectivity between particles with a total sintering giving a stable value of resistivity.

Although the process is new and the deposition mechanism is still largely non understood, this PhD work gave some hints on the potential reasons for the obtained film morphology. A deeper optimization of the process parameters is still needed in order to better understand the growth mechanism occurring mainly through the gas phase.

**Both processes**, i.e. standard PE-ALD and the novel two-step approach, have been compared regarding their **functional properties**.

In terms of **conformal deposition**, while ALD is the most promising technique for conformal deposition, the PE-ALD of Ag thin film suffers from the recombination of plasma species on the surfaces, which prevents the growth deeper into such structure. By using original lateral high aspect ratio structures, our new two-step process leads to a much better conformal deposition than PE-ALD, with better coverage than the one reported up to now for ALD of silver, i.e. a thickness variation of less than 10% for an aspect ratio (AR) up to 12:1 (versus 10% for AR < 3 for PE-ALD). This is understood by the gas-phase reaction occurring during the first step of the new process which follows a diffusion law, as compared to the surface-limited reaction in standard PE-ALD following an exponential decrease linked to radical's species recombination. Moreover, regarding the two-step process, both morphologies, i.e. compact nanoparticle for as-deposited film and connected film for the post-treated film, are preserved far into the structure until an AR of 18:1, after which the film thickness becomes lower than the critical thickness and leads to discontinuous films.

Interestingly, for both processes, a weak influence of the **underlayers** on the morphology of silver films deposited on top of them have been obtained. We have studied oxide underlayers exhibiting different surface energies, either higher than silver itself (zinc oxide) with a view to obtaining the formation of a continuous metal film, or lower ones (alumina, glass and silicon). The differences between the sublayers were also investigated in terms of surface wettability which was quantified by the value of the water contact angle (WCA) and correlated to the surface hydroxyl groups density. The study was completed by high rms roughness underlayers made of zinc oxide nanorods. It was found that the growth rate was highly dependent on the surface hydroxyl groups, which enhanced the Ag precursor chemisorption. The higher growth rate was related to the lower contact angle, potentially due to the higher density of –OH surface groups. This effect was more pronounced for standard PE-ALD, probably due to the surface-limited reaction, whereas the growth mechanism linked to Ag deposited with our novel approach involved the competition between two mechanisms: a gas-phase reaction and a surface reaction. On the other hand, the morphology remained unchanged for both processes, independent of the nature of the underlayer. Indeed, we still observed Ag made of well-defined islands for standard process and compact NPs for the two-step approach. Regarding the novel approach, we have additionally followed the dependence of the electrical properties of Ag deposited above the different underlayers and as a function of the post-treatment duration. All films deposited after 600 cycles exhibited close values of electrical conduction

after post-processing, but the roughness of the film was found to increase its resistivity, and almost insulating deposition have been obtained on zinc oxide nanorods. In this case, Ag film exhibited an electrical conduction only above 1200 cycles.

In the last part of the thesis, the close interaction between **optical behavior in visible and near infrared ranges and silver film morphology** has been presented. One signature of the films made of separated metal islands synthetized by standard PE-ALD is the presence of localized surface plasmon resonance absorbance peak in the visible region at a wavelength of around 400-430 nm, which depends on the nanoparticle morphology, i.e. size and shape. The other feature is the transition from a 'continuous like' optical behavior at low wavelengths, understood by Drude's model and highlighted by a high reflectance/low transmittance, to the 'particle-like' behavior at higher wavelengths, understood by the oscillator model and highlighted by a low reflectance/high transmittance. Before plasma post-treatment, the optical behavior of the Ag film made of compact nanoparticles is very similar to the one obtained for separated NPs using standard PE-ALD and followed the same transition as function of the wavelength. However, a broader absorbance peak, typical of aggregated nanoparticles causing interaction between them, is obtained. After the post-processing step, a strong increase of IR reflectance and strong decrease of both NIR absorbance and transmittance are achieved. The presence of the residual absorbance of the post-treated film in the visible region might be related to defects in the silver coatings, either due to holes or to the roughness of the deposit. The optical properties are influenced by the electrical properties of Ag films and, for film exhibiting electrical conduction, an increase of the film resistivity leads to an increase of IR absorbance while decreasing the IR reflectance. The higher absorbance is directly linked to both the higher d.c. resistivity of our films and the dissipation caused by surface plasmon polaritons of rough Ag surfaces. Our Ag depositions still need to be improved in terms of film quality. Indeed, for the nanoparticle synthetized by standard PE-ALD, the surface defects/grain boundaries are responsible for the LSPR blueshift rather than directly to NP size and shape. A fine tuning of the nanoparticle morphology could be interesting for sensors based on surface enhanced Raman spectroscopy (SERS) in order to exploit the local exaltation of the Raman signal of molecules located near the surface of metallic nanoparticles for the detection of chemical and biological species (detection of pollutants, explosives, food contaminants or biomarkers of disease in biological media). [259] Regarding the novel approach, for post-treated silver percolated film, the presence of defaults in the film, either due to holes or to the roughness of the deposit, cause a strong dissipation observed by a strong absorbance peaks in the UV-visible range. In order to be used as, for instance, low emissive coating in the field of automotive or smart buildings, these features need to be improved.

## 2. Outlook

During this thesis work, we have highlighted a conformal and connected ultra-thin silver films deposited by the two-step approach. An outlook could be to **understand even more the process and try to confirm the hypothesis of the occurrence of a gas-phase reaction** by an understanding of the diffusion process which is taking place during the Ag growth. For that, we could take benefit from the original lateral high aspect ratio structures. A future investigation can be to vary the experimental parameters (sequence times, temperatures, argon flows, plasma power) and follow the saturation profile of the Ag deposition in order to see their effect on the film conformality, into different aspect ratio structures, as it was done by Dendooven *et al.* [242] for alumina deposition. We can also implement this study by adding a theoretical model based on the diffusion–reaction model developed by Ylilammi *et al*. [240] and used also by Yim *et al.* [260].

A **completely different approach to obtain conformal and continuous silver thin-films** could be to deposit Ag by means of thermal ALD, which is a much more promising technique for conformal deposition as compared to PE-ALD, since no radical recombination affects the conformality. Even if thermal ALD generally produces Ag films made of separated island morphology, we have highlighted in the state-of-the art section that only one work has obtained a better-connected deposit. Indeed, Golrokhi *et al.* [46] have produced a planar film-like morphology exhibiting a critical thickness as low as 9 nm by means of direct liquid injection thermal ALD using (hfac)Ag(1,5- COD) as silver precursor and tertiary butyl hydrazine (TBH) as reducing agent. Here, substituted hydrazine ($^{t}BuHNNH_2$) was used rather than hydrazine ($H_2NNH_2$) due to the hazards (explosive and poisonous) of the un-substituted component. The reactivity of TBH on the surface has created however the formation of hydrazine in-situ, which can still present safety issue when upscaling. Therefore, the process conditions need to be adapted, e.g. by employing an adapted pumping system on the deposition equipment in order to prevent the emission of the toxic species into the atmosphere, but the cost of the process will be higher. In comparison with standard thermal ALD which usually uses alcohol as reducing agent, TBH was selected due to the lower pKa value (8.1) as compared to alcohols (e.g. 16.1 for propanol). Therefore, TBH is more acidic and more favorable proton donor. This higher reactivity explained also why lower deposition temperatures could be used and thus produced continuous Ag film by reducing Ag atoms migration. Based on this study, one future path could be to use the process of the work of Golrokhi *et al.* and see if it is possible to obtain a conformal deposition on high aspect ratio structures, in addition to the continuous film morphology. Another approach could be to combine this TBH reducing agent with the Ag precursor employed in this PhD work (Ag(fod)($PEt_3$)), but having in mind that hazardous products are created in-situ, and see if it is possible to reduce the critical thickness obtained with (hfac)Ag(1,5- COD) precursor. A last route could be to find a reducing agent which exhibits the same high reactivity as TBH but without the hazardous character of this specie.

Regarding the **growth mechanism taking place in both processes employed in this thesis work**, i.e. standard PE-ALD and the novel two-step approach, even if this PhD work gave some hints on the understanding, there is still a lack on the underlaying deposition mechanism. More precisely, the ligand-exchange reaction occurring during the nucleation phase, needs to be analyzed more deeply. For that, in-situ analyses could bring important information. In-situ *quartz crystal microbalance* (QCM) studies have been used by Masango *et al.* and enable to understand the nucleation of Ag NPs with (hfac)Ag($PMe_3$) during thermal ALD and the surface reaction taking place. [48] Combined with XPS analyses, they thus managed to discriminate between the removal of the $PMe_3$ ligand from the surface rather than the hfac group. In this PhD work, even if the QCM signal can be impacted by the plasma, this analysis could be envisioned. Another interesting approach could be to follow the released species in the reactor during the reaction by in-situ chemical analysis like *residual gas mass spectroscopy* (RGA). It could also be envisioned to investigate each half ALD reaction taking place on the surface and check what are the terminal surface groups and quantify them by in-situ *Fourier Transform Infrared Spectroscopy* (FTIR). For the two-step processing, by in-situ FTIR, an interesting study could be to follow the removal of the Ag precursor from the surface as a function of the plasma post-treatment duration and/or RF plasma power, and evaluate the amount and nature of organic species removed during the post-processing. This could be effective in confirming the removal of the precursor from the surface and correlate it with the change on the electrical properties of the Ag film. Ma *et al.* [195] followed the elimination of gum arabic capping surface polymer through this analysis.

# Future applications and proofs of concept

In this last part of the conclusion, preliminary studies giving encouraging results for potential future applications of Ag films developed in this PhD work are presented.

## 1. Proof of concept of low emissive coating

Infrared reflective (IRR) coatings play an important role in the heat management of glazing products by avoiding heat to be transferred. [261] Ultra-thin silver film embedded in metal oxides has currently exhibited the highest performances. [262]

As proof of principle, we have grown an ultra-thin silver layer (targeted thickness below 20 nm) using our novel two-step approach between two aluminum-doped zinc oxide (AZO) layers (thicknesses of 45 nm, see Figure 131 (a)), the full stack being deposited in the same reactor, thus avoiding the influence of the environment. The resulting stack exhibits the typical wavelength dependence for an IRR coating, with a broad transmittance peak in the visible range and a high reflectance in the NIR range. [262] To our knowledge, this is the first IRR coating fully made by ALD. The transmittance and reflectance spectra have been simulated using a parametric model for the optical constant of the Ag thin film, and optical constant determined separately for the AZO films deposited by ALD. The best fit is obtained using a film thickness of 12 nm and the optical constants shown in Figure 131 (b).

As compared to reference Ag films deposited by evaporation (dashed lines in Figure 131 (b)), [263] the main difference is the higher imaginary part of the dielectric constant $\varepsilon_2$ for the two- step process, by a factor 2 to 3. In the free electron model, $\varepsilon_2$ is proportional to the d.c. resistivity of the metal (see chapter 1 and e.g. [199]), thus this higher value is directly linked to the higher d.c. resistivity of our films as compared to more continuous films, as already shown in chapter 5. The additional peak observed below 500 nm can be explained by localized surface plasmon resonance due to morphological defects in the film.

The synthesis performed on a flat 10 cm × 10 cm glass substrate presents a good optical uniformity for the IRR coatings, with a standard deviation of less than 20% on the optical transmittance and reflectance, the span being mostly due to the deposition gradient along the non-optimized 200 mm diameter reactor. This has also been obtained for a reflective thick coating made of a 40-nm-thick silver film deposited on glass substrate (see chapter 6, section VI.2.2.1.).

At last, we prove in Figure 131 (c) and (d) that the optical films can be uniformly formed on complex substrate shapes, here a glass sample of 10 cm x 10 cm bent over two perpendicular directions, which is an important challenge for line-of-sight methods. The uniform silver coating is clearly visible on these pictures for the both kinds of stacks, the transparent IRR coating in Figure 131 (c) and the reflecting thick silver film in Figure 131 (d). It opens an interesting path for low-emissivity or infrared reflective windows in the field of automotive or smart buildings. However, for this IRR stack, the performances of the stack do not fulfil entirely the industrial requirement. The physical reason for this weak performance seems to be related to strong absorbance of the silver film, above 30 % over the full spectral range, in addition to absorbance peaks in the UV-VIS range, which still need to be improved.

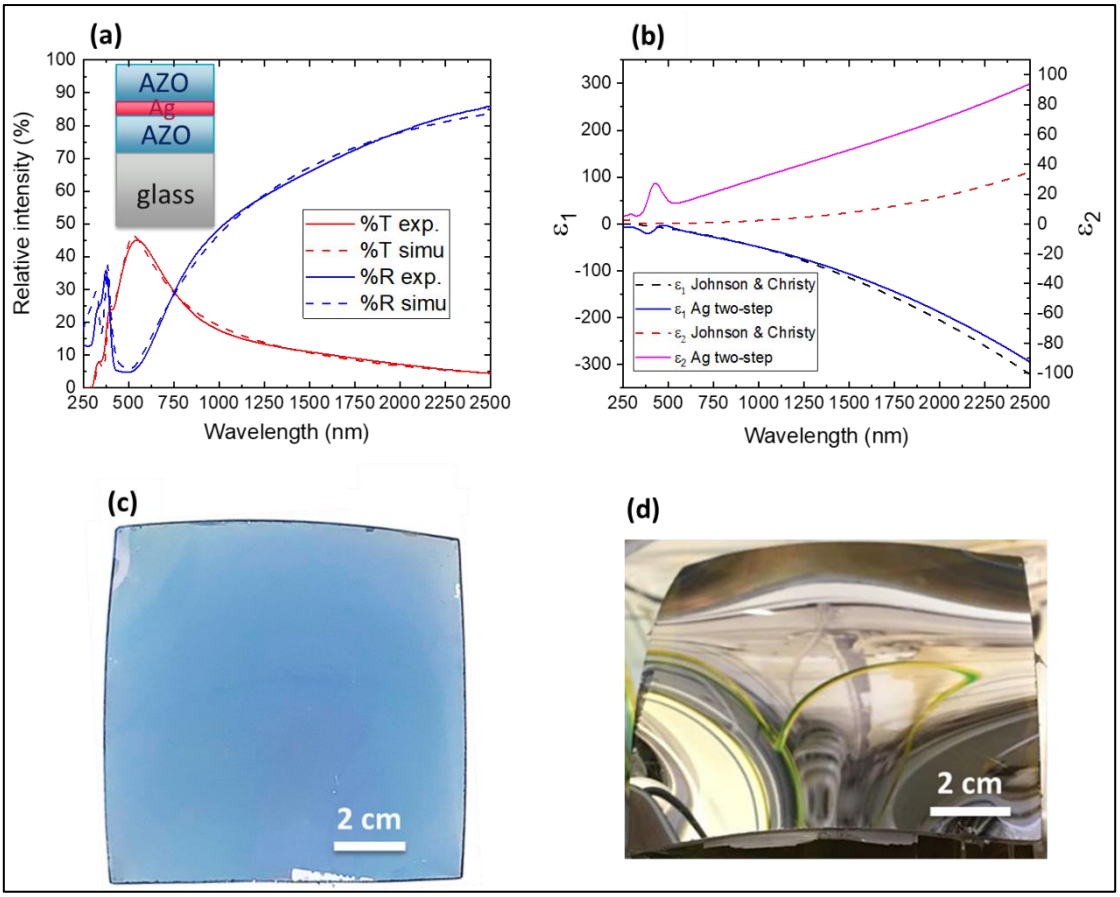


Figure 131: Optical properties of Ag thin films on glass substrates and application as infrared reflective (IRR) coating. (a) Transmittance (%T in red) and reflectance (%R in blue) spectra as a function of light wavelength for an IRR stack based on a Ag thin layer (targeted thickness below 20 nm) embedded in AZO matrix (45 nm for each layer). The inset represents a scheme of the multi-layers stack. Plain lines correspond to the measured spectra and dashed lines correspond to the calculated spectra using, for the Ag film, the optical constants represented in panel (b) and a thickness of 12 nm. (b) Real part ($\varepsilon_1$) and imaginary part ($\varepsilon_2$) of the dielectric constant used for modelling the silver film in the calculation in panel (a). The model used for simulating the experimental data (plain line, using the software CODE from Wolfgang Theiss) is compared to the optical constants for evaporated Ag thin film determined by Johnson and Christy. [263] (c) Picture of the same kind of stack as (a) deposited on 2-sided-bent glass substrate of 10 cm x 10 cm. (d) Picture of a bent glass substrate of 10 cm x 10 cm coated with 45 nm (thickness determined by ellipsometry) AZO and targeted 40 nm Ag thin film. Glass thickness is 2 mm.

We have also investigated IRR stack where the silver layer is based on disconnected silver nanoparticles (Ag NPs). The use of AZO as index matching layer allows us to increase the visible transmittance. However, a simple layer of Ag-NPs embedded in two AZO layers did not show competitive IRR performances, due to (1) gaps between the nanoparticles that reduce the near infra-red reflectance and (2) surface plasmon resonance that strongly enhances the absorbance (and decrease the transmittance) in the visible range (black lines in Figure 132 (b) and (c)). For these reasons, we have investigated a more original nanolaminated structure combining thin layer of Ag NPs and metal-oxide (MOx) ultra-thin films, embedded in AZO matrix (see scheme in Figure 132 (a)). The role of the MOx nanolayer placed in-between two Ag-NP layers is to (1) decouple successive depositions of Ag-NPs, with the aim of reducing the gaps and increase the near infrared reflectance, and (2) provide electrical connection between successive Ag-NP layers in order to reduce the surface plasmon resonance and increase the visible transmittance. The benefits of the ZnO interlayer are clearly demonstrated by an increased reflectance and decreased transmittance in the NIR region, while the transmittance peak in the visible region is almost not affected. The highest reflectance and

lowest transmittance in the NIR are obtained for a 1.2 Å-thick metal-oxide layer, which also demonstrate a reduction of the absorbance peak in the visible range.

Some applications could be envisioned for this nanolaminated stack. One of the main difference of IRR coatings based on Ag-NPs/MOx nanolaminates as compared to the currently used IRR based on continuous Ag films is the absence of long-range conduction within the film, which makes it transparent to radiation of large wavelength (typically in the far IR and microwave range). We emphasize that this original concept leads to a weakly conductive IRR with large IR transmittance, starting from the mid-IR spectral region, which can be of use for IRR coatings that remain potentially transparent to thermal wavelengths (e.g. for thermal imaging), microwave and terahertz radiation (e.g. for radar) and radio-frequencies (e.g. for mobile communications). Moreover, the surface plasmon resonance can be tuned by the nanoparticle size and the embedding material, which can be used to control the apparent color of the coating.

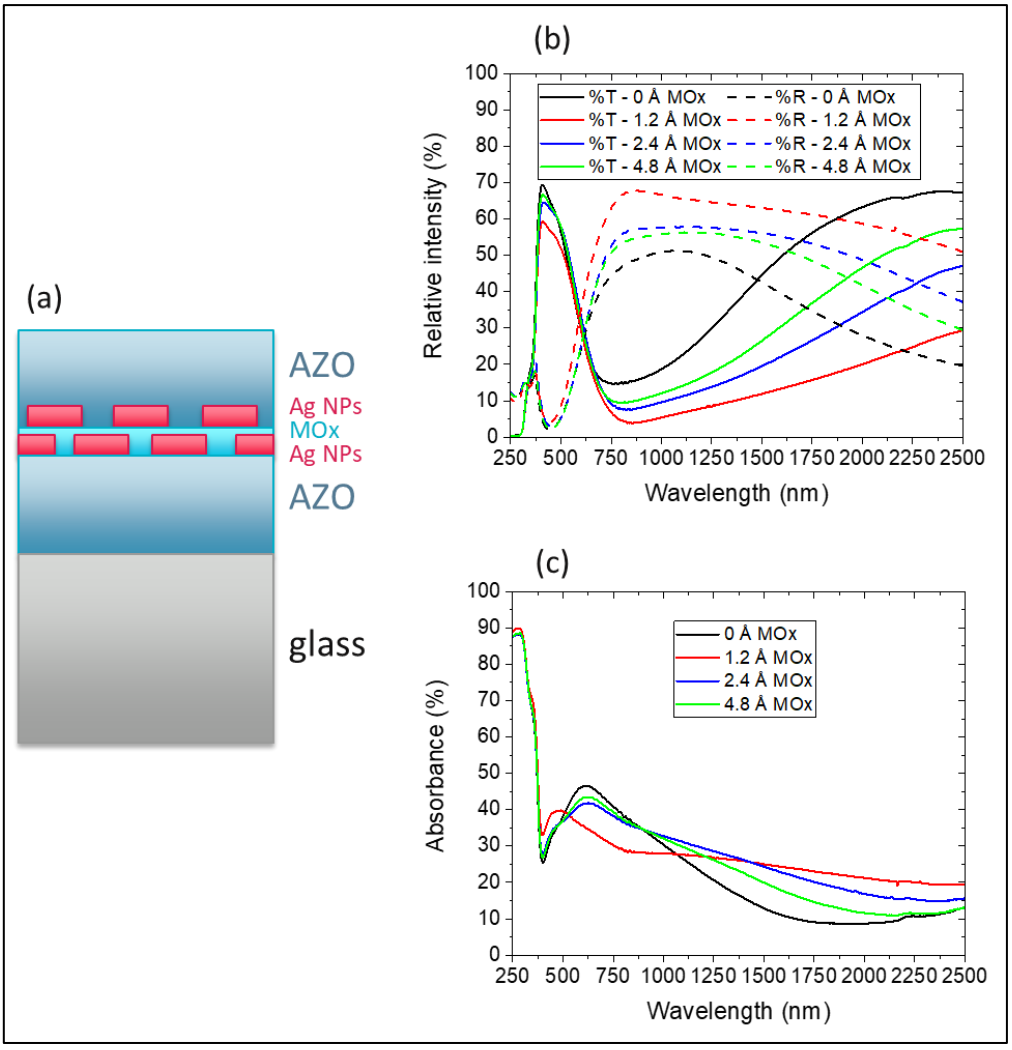


Figure 132: Optical properties of Ag thin films made of Ag NPs on glass substrates and application as infrared reflective (IRR) coating. (a) Scheme of a nanolaminated stack made by alternating Ag nanoparticle film and metal-oxide MOx nanolayer, embedded in AZO matrix. (b) Transmittance (%T in solid lines) and reflectance (%R in dash lines) spectra as a function of light wavelength for a nanolaminated stack based on Ag nanoparticle film (targeted thickness of 20 nm) and MOx thin layer of different thickness (from 0 Å to 4.8 Å) embedded in AZO matrix (45 nm for each layer). (c) Absorbance spectra as a function of light wavelength for the IRR stack presented in (a). The stack corresponding to 0 Å MOx is made of one Ag nanoparticle layer with targeted thickness of 40 nm embedded in AZO matrix.

## 2. Test of the photocatalytic properties

### 2.1. Principle of photocatalysis and interest of metal-oxide heterostructure

The principle of photocatalysis is based on the initiation of the degradation reaction of an organic compound using a material excited by light. Under the effect of a light excitation, the absorption of a photon, whose energy is higher than the gap between the valence band and the conduction band (band gap), will form electrons (e-)/holes (h+) pairs in the photocatalytic material (photocatalyst). There is emission of an electron e- at the conduction band and formation of a hole h+ at the valence band. This electron has reducing properties and the hole has oxidizing properties. If these carriers manage to migrate to the surface of the catalyst and enter into contact with a water or oxygen molecule, then redox reactions can take place: water and oxygen can be reduced to $O_2^{\cdot -}$ by electrons and oxidized to $OH^{\cdot}$ radicals by holes. [251]

The mainly used photocatalysts are semiconductors (SC) with a large band gap. This is the case of ZnO or $TiO_2$ for which the band gap is about 3.2 eV corresponding to a wavelength of 375 nm. Therefore, they display photocatalytic behavior limited to the UV range of sun light, i.e. only 3% of the solar spectrum is involved in a photocatalytic degradation reaction. [264] Another drawback of metal oxide semiconductor is the low stability and fast recombination of the photo-generated carriers. [265] In order to expand the light absorption and thus the photocatalytic activity in visible range and improve the charge carrier separation, hybrid system based on metal-oxides with plasmonic noble metal nanoparticles represent an interesting strategy. [266] When exposing this heterostructure assembly to UV light, e- of the semiconductor valence band are elevated to the conduction band and then transported to the Fermi level of the metal (lower than the one of the SC) which engenders the electrons/holes pairs separation through the formation of a Schottky barrier at the metal-semiconductor interface acting as an electron trap. When exposing the hybrid system to visible irradiation, the absorption of the light creates charge carriers in the metal through excitation of LSPR which are injected to the semiconductor conduction band and thus enhanced the photocatalytic activity.

Various combinations of plasmonic noble metal nanoparticles (Ag, Au, Cu) of different shapes and sizes (nanocubes, nanospheres, nanowires) with conventional photocatalyst materials as ZnO or $TiO_2$ in the form of NPs, NRs, films and other configuration are reported in the literature. [266] For example, Whang *et al.* [267] compared the photocatalytic degradations of methylene blue (MB) solutions under visible-light range of Ag doped ZnO and ZnO nanoparticles photocatalysts. They prove a notable improvement in the degradation efficiency of Ag/ZnO catalysts compared to ZnO with rate constant of, respectively $5.47\times10^{-3}$ and $1.37\times10^{-3}$ $min^{-1}$. Sangpour *et al.* [268] compared $Ag/TiO_2$ and $TiO_2$ catalysts deposited by magnetron sputtering. The presence of Ag nanoparticles enhanced the photodecomposition of MB in the presence of UV and visible light irradiation. Indeed, under UV irradiation, MB degradation rate of $1.9\times10^{-3}$ $min^{-1}$ for $TiO_2$ versus $7.1\times10^{-3}$ $min^{-1}$ for $Ag/TiO_2$ have been shown. When visible irradiation was used, $TiO_2$ catalyst exhibited a rate of degradation of $1.5\times10^{-3}$ $min^{-1}$ versus $4\times10^{-3}$ $min^{-1}$ for $Ag/TiO_2$. The best results were obtained using $Cu/TiO_2$ under UV irradiation (photodegradation rate of $17\times10^{-3}$ $min^{-1}$) and $Au/TiO_2$ under visible irradiation (photodegradation rate of $6.5\times10^{-3}$ $min^{-1}$).

## 2.2. Measurement method

The photocatalytic behavior of Ag films has been studied by following the absorbance of a probe molecule in solution at its absorption wavelength, using a UV/Visible spectrophotometer Infinite M1000 Pro from TECAN within a detection window from 400 to 700 nm. A six-well plate reactor from Thermo Scientific has been used as reactor, enabling the analysis of five samples at the same time (the last well being kept for control). As the plates used are not transparent in the UV range, photocatalytic degradation properties of our samples have been studied over the degradation of methylene blue (MB), absorbing in the visible range at 666 nm.

The photocatalysis process is rather simple. A 5mL solution of MB at a concentration of 5 mg/L is added to each six well. The plate is then shaken to homogenize the medium after which the samples are inserted into each well and left in the dark during the stabilization period (from 30 min to 2 hours). After that, an UV light (365 nm, 8 W) delivering a measured power of 2.28 mW/cm or Visible light (60 W) illuminates the sample from the top during the photocatalytic degradation phase. Every 30 minutes, samples are removed from the different wells, and the absorbance is measured with the UV/Visible spectrophotometer. By measuring the absorbance of the solution at the absorption wavelength of MB, we estimate its concentration during the photocatalytic process.

## 2.3. Results

As a preliminary test, we have deposited by our two-step process metallic Ag films after different cycles (and thus different thicknesses) made of highly covering compact nanoparticles in order to improve the specific surface of material on top of ZnO 100 nm-thick layers on planar glass substrates. Compact Ag NPs were also selected because they show a broadband absorption in the visible range as compared to well-separated islands obtained by standard PE-ALD. We have followed the photocatalytic degradation of methylene blue under visible and UV irradiation, and the results are presented in Figure 133 (a). Before lightening at time 0 min, the films have been left in the dark in presence of methylene blue (MB) solution, during 80 min before switching on UV light, and 60 min before switching on visible light. During this stabilization period, the absorption of MB on the surface of the samples induces a slight decrease of its concentration. After ignition of the lights, the decrease of the MB concentration followed a pseudo-first order kinetic law [251]: $ln(C_0/C) = kt$ with $C_0$ the initial concentration of reactant, $C$ the concentration of the reactant at time $t$ and $k$ the reaction constant. The slope of the linear fit of the plot $ln(C_0/C)$ as a function of time (Figure 133 (b)) corresponds to the degradation rate $k$. Table 32 summarizes the first order rate constant $k$ normalized to the surface exposed.

Unfortunately, we obtained similar rate constants in UV-visible region with and without the deposition of Ag on top of ZnO films. Indeed, in the Visible range, a rate constant of $5.23\times10^{-4}$ $min^{-1}.cm^{-2}$ versus $4.18\times10^{-4}$ $min^{-1}.cm^{-2}$ has been obtained for ZnO layer and Ag deposited after 400 ALD cycles on top of ZnO film, respectively. Therefore, no enhancement of the photocatalytic degradation of MB has been noticed in presence of Ag nanoparticles. The major problem of the experiments under visible irradiation could come from the use of a too powerful lamp (60 W) since also the control sample (MB without any catalyst) abnormally decreases as a function of the irradiation time. Another explanation could be the non-effective carriers' separation due to the contamination at the interface between Ag NPs and ZnO film coming from the fact that ZnO films were exposed to air prior to Ag NPs

deposition on top of them. It was also found that the area of semiconductor photocatalyst covered by metallic nanoparticles needs to be well controlled. The Ag NPs coverage should be high enough in order to promote a sufficient electron transfer between the semiconductor and Ag, but also controlled since a too high coverage leads to an inhibited photocatalytic activity by the reduced photocatalyst surface exposed to MB and limited radicals' generation. [269] In order to enhance the results obtained in our experiments, a solution could be to reduce the plasmonic Ag NPs coverage on the ZnO surface. Another option can be to use high surface ratio to volume substrate rather than planar one used in this investigation, in order to increase the specific surface of Ag, for example microporous glass fibers membranes which are widely used in the photocatalytic area. [270]

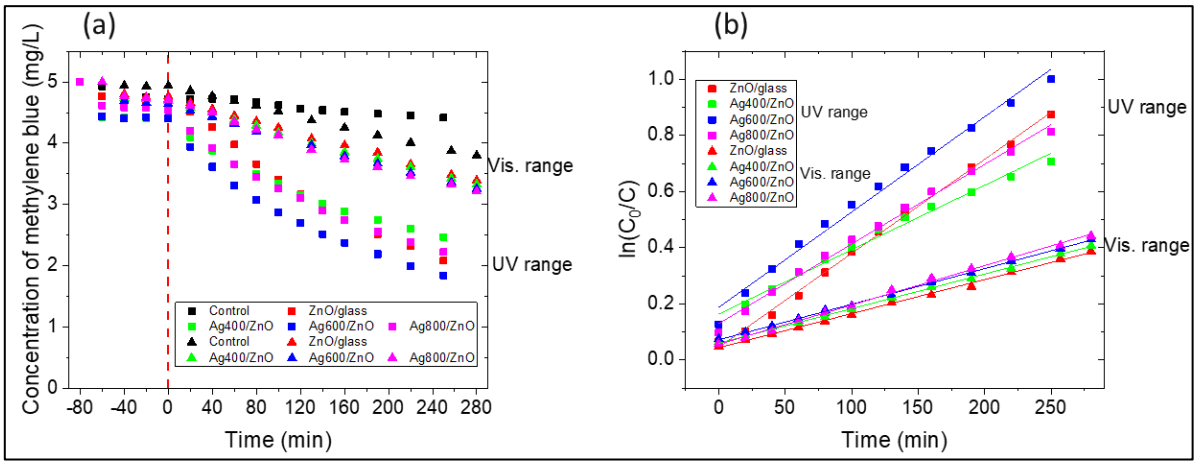


Figure 133: (a) Photocatalytic degradation of methylene blue under visible light (triangle symbol, 365 nm - 8W) and UV light (square symbol, 60 W) over ZnO/glass and Ag/ZnO/glass stacks with Ag deposited after 400, 600 and 800 ALD cycles. The time 0 min corresponds to the ignition of the lights. (b) Plot of $ln\ (C_0/C)$ as a function of the exposure time $t$ and the solid lines are the linear fitting results.

| | Visible range | | UV range | |
|---|---|---|---|---|
| **Samples** | **First order rate constant *k*** | **First order rate constant *k* normalized to the surface exposed** | **First order rate constant *k*** | **First order rate constant *k* normalized to the surface exposed** |
| | $\times 10^{-4}$ ($min^{-1}$) | $\times 10^{-4}$ $min^{-1}.cm^{-2}$ | $\times 10^{-3}$ ($min^{-1}$) | $\times 10^{-4}$ ($min^{-1}.cm^{-2}$) |
| ZnO/glass | 1.21 | 5.23 | 3.35 | 14.5 |
| Ag400/ZnO/glass | 1.23 | 4.18 | 2.29 | 7.78 |
| Ag600/ZnO/glass | 1.27 | 3.61 | 3.40 | 9.66 |
| Ag800/ZnO/glass | 1.40 | 4.12 | 2.83 | 8.33 |

Table 32: First order rate constant $k$ extracted from the plot of $ln\ (C_0/C)$ as a function of the exposure time $t$ in (Figure 133 (b)) and normalized to the surface exposed.

## 3. Proof of concept of antimicrobial activity

### 3.1. Interest of silver

Silver has been extensively used for its antibacterial activity in medical and consumer products due to its broad-spectrum antimicrobial activities in pharmaceutics, medicine, and dentistry fields combined with a lower toxicity on human body compared to other bactericides. [3] More and more

products are using silver in the form of nanoparticles for its more effective bactericidal activity, which allows it to be used in smaller quantities. Thanks to their nanometer scale range size and large surface-to-volume ratio, Ag NPs can penetrate into the bacteria cell walls and leads to the cell death. [271] It was found that a decrease of NP size engenders an enhancement of the antimicrobial activity. [31]

### 3.2. Measurement method

The antibacterial properties of Ag thin films against *Escherichia coli* ATCC 8739 (*E. coli,* Gram-negative) bacteria have been investigated through the testing method based on the International Standard ISO 22196:2011. Briefly, 0.4 mL of inoculum of known concentration of the microorganism to be tested is deposited homogeneously on the surface of the tested samples. The microbial concentration of viable microorganisms is determined immediately after an incubation time of 24 h. Therefore, the activity value is determined by comparing the untreated specimens (silicon wafer coupons) count to treated specimens (Ag thin film on silicon wafer coupons) count. More precisely, the antibacterial activity $R$ can be determined as the difference in logarithm between the number of viable bacteria recovered from the untreated test specimens after incubation ($U_t$) and the number of viable bacteria recovered from the treated test specimens after incubation ($A_t$). In general, coatings and films are considered as efficient antimicrobial surfaces when a 3-log reduction is observed between the untreated and treated specimens, i.e. $R$ = 3 and 99.99 % of the bacteria are eliminated. [272]

### 3.3. Results

A preliminary test has been performed on a 17-nm thick film made of compact Ag nanoparticles films deposited on silicon substrate through the first step of the two-step approach. With antibacterial activity against *E. coli* higher than 4 ($R$ = 6.8), very encouraging results for the use of this Ag film as an effective antibacterial coating have been demonstrated. Thanks to the self-saturation of ALD which can ensure a very high control over the thickness, and a highly conformal coating reached with our novel approach (see Chapter 6), these Ag films can be used as coating on high aspect ratio medical devices such as indwelling catheters, wound dressings and stainless-steel orthopedic devices. [23] The underlying mechanism against *E. coli* is beyond the scope of this thesis work but could be of interest to understand.

**In conclusion**, due to the wide ranges of applications of thin metal films, and the challenge to provide methods for conformal deposition, we hope that our work will be of interest for the whole community of material scientists and will inspire many investigations. The described method can also be extended to other noble metals, in particular copper and gold, for which the deposition using chemical vapor-based methods is a very active field.

# References


[1] Mallick, B. C.; Hsieh, C.-T.; Yin, K.-M.; Ashraf Gandomi, Y.; Huang, K.-T. Review−On Atomic Layer Deposition: Current Progress and Future Challenges. *ECS J. Solid State Sci. Technol.* **2019**, *8*, N55–N78.

[2] Hagen, D. J.; Pemble, M. E.; Karppinen, M. Atomic Layer Deposition of Metals: Precursors and Film Growth. *Appl. Phys. Rev.* **2019**, *6*, No. 041309.

[3] Tran, Q. H.; Nguyen, V. Q.; Le, A.-T. Silver Nanoparticles: Synthesis, Properties, Toxicology, Applications and Perspectives. *Adv. Nat. Sci.: Nanosci. Nanotechnol.* **2013**, *4*, 033001.

[4] Ju-Nam, Y.; Lead, J. R. Manufactured Nanoparticles: An Overview of their Chemistry, Interactions and Potential Environmental Implications. *Sci. Total Environ.* **2008**, *400*, 396–414.

[5] Gupta, R.; Xie, H. Nanoparticles in Daily Life: Applications, Toxicity and Regulations. *J. Environ. Pathol. Toxicol. Oncol.* **2018**, *37,* 209–230.

[6] Rivero, P. J.; Urrutia, A.; Goicoechea, J.; Arregui, F. J. Nanomaterials for Functional Textiles and Fibers. *Nanoscale Res. Lett.* **2015**, *10*, 501.

[7] Vargas-Bernal, R. The Next Generation of Nanomaterials for Designing Analog Integrated Circuits; *Analog Circuits: Fundamentals, Synthesis and Performance;* Tlelo-Cuautle, E.; Fakhfakh, M.; de la Fraga, L. G. Eds.; First Edition, Nova Science Publishers, **2017**.

[8] Piszczek, P.; Radtke, A. Silver Nanoparticles Fabricated Using Chemical Vapor Deposition and Atomic Layer Deposition Techniques: Properties, Applications and Perspectives: Review. *Noble and Precious Metals - Properties, Nanoscale Effects and Applications, Chapter 9,* **2018**.

[9] Elam, J. W.; Zinovev, A.; Pellin, M. J.; Comstock, D. J.; Hersam, M. C. Nucleation and Growth of Noble Metals on Oxide Surfaces Using Atomic Layer Deposition. *ECS Trans.* **2007**, *3*, 271.

[10] Weber, M. J.; Mackus, A. J. M.; Verheijen, M. A.; van der Marel, C.; Kessels, W. M. M. Supported Core/Shell Bimetallic Nanoparticles Synthesis by Atomic Layer Deposition. *Chem. Mater.* **2012**, *24*, 2973–2977.

[11] Schultz, D. A. Plasmon Resonant Particles for Biological Detection. *Curr. Opin. Biotechnol.* **2003**, *14*, 13–22.

[12] O'Neal, D. P; Hirsch, L. R.; Halas, N. J.; Payne, J. D.; West, J. L. Photo-Thermal Tumor Ablation in Mice Using Near-Infrared Absorbing Nanoparticles. *Cancer Lett.* **2004**, *209*, 171–176.

[13] Khan, S. A. Metal Nanoparticles for Drug Delivery and Diagnostic Applications; *Micro and Nano Technologies*, Shah, M. R., Imran, M., Ullah, S., Eds.; Elsevier, **2020**.

[14] Hagen, D. J.; Connolly, J.; Povey, I. M.; Rushworth, S.; Pemble, M. E. Island Coalescence during Film Growth: An Underestimated Limitation of Cu ALD. *Adv. Mater. Interfaces* **2017**, *4*, 1700274.

[15] Guo, S.; Wang, E. Noble Metal Nanomaterials: Controllable Synthesis and Application in Fuel Cells and Analytical Sensors. *Nano Today* **2011**, *6*, 240–264.

[16] Ulaeto, S. B.; Rajan, R.; Pancrecious, J. K.; Rajan, T.P.D.; Pai, B. C. Developments in Smart Anticorrosive Coatings with Multifunctional Characteristics. *Prog. Org. Coat.* **2017**, *111*, 294–314.

[17] Hauder, M.; Gstöttner, J.; Hansch, W.; Schmitt-Landsiedel, D. Scaling Properties and Electromigration Resistance of Sputtered Ag Metallization Lines. *Appl. Phys. Lett.* **2001**, *78*, 838–840.

[18] Joret, L.; Prost, A. Vitrages à Isolation Thermique Renforcée. *Techniques de l'ingénieur, Sciences et Technologies du verre,* **1999**, base documentaire : TIB573DUO., fr.

[19] Amusan, A. A.; Kalkofen, B.; Gargouri, H.; Wandel, K.; Pinnow, C.; Lisker, M.; Burte, E. P. Ag Films Grown by Remote Plasma Enhanced Atomic Layer Deposition on Different Substrates. *J. Vac. Sci. Technol. A* **2016**, *34*, No. 01A126.

[20] Boccas, M.; Vucina, T.; Araya, C.; Vera, E.; Ahhee, C. Protected-Silver Coatings for the 8-m Gemini Telescope Mirrors. *Thin Solid Films* **2006**, *502*, 275–280.

[21] Szczyrbowski, J.; Dietrich, A.; Hartig, K. Evaluation and Control of the Properties of Thin Sputtered Silver Films for Spectrally Selective Coatings. *Sol. Energy Mater.* **1987**, *16*, 103–111.

[22] Grosse, P.; Hertling, R.; Müggenburg, T. Design of Low Emissivity Systems Based on a Three-Layer Coating. *J. Non-Cryst. Solids* **1997**, *218*, 38–43.

[23] Li, Y.; Leung, P.; Yao, L.; Song, Q. W.; Newton, E. Antimicrobial Effect of Surgical Masks Coated with Nanoparticles. *J. Hosp. Infect.* **2006**, *62*, 58–63.

[24] Piedade, A. P.; Vieira, M. T.; Martins, A.; Silva, F. In Vitro Behaviour of Nanocrystalline Silver-Sputtered Thin Films. *Nanotechnology* **2007**, *18*, 105103.

[25] Rycenga, M.; Cobley, C. M.; Zeng, J.; Li, W.; Moran, C. H.; Zhang, Q.; Qin, D.; Xia, Y. Controlling the Synthesis and Assembly of Silver Nanostructures for Plasmonic Applications. *Chem. Rev.* **2011**, *111*, 3669–3712.

[26] Minjauw, M. M.; Solano, E.; Sree, S. P.; Asapu, R.; Van Daele, M.; Ramachandran, R. K.; Heremans, G.; Verbruggen, S. W.; Lenaerts, S.; Martens, J. A.; Detavernier, C.; Dendooven, J. Plasma-Enhanced Atomic Layer Deposition of Silver Using Ag(fod)($PEt_3$) and $NH_3$-Plasma. *Chem. Mater.* **2017**, *29*, 7114–7121.

[27] Amendola, V.; Bakr, O. M.; Stellacci, F. A Study of the Surface Plasmon Resonance of Silver Nanoparticles by the Discrete Dipole Approximation Method: Effect of Shape, Size, Structure, and Assembly. *Plasmonics* **2010**, *5*, 85–97.

[28] Baburin, A. S.; Merzlikin, A. M.; Baryshev, A. V.; Ryzhikov, I. A.; Panfilov, Y. V.; Rodionov, I. A. Silver-Based Plasmonics: Golden Material Platform and Application Challenges. *Opt. Mater. Express* **2019**, *9*.

[29] Golrokhi, Z.; Chalker, S.; Sutcliffe, C. J.; Potter, R. J. Self-Limiting Atomic Layer Deposition of Conformal Nanostructured Silver Films. *Appl. Surf. Sci.* **2016**, *364*, 789–797.

[30] Evanoff, D. D. Jr.; Chumanov, G. Synthesis and Optical Properties of Silver Nanoparticles and Arrays. *Phys. Chem. Chem. Phys.* **2005**, *6*, 1221–1231.

[31] Raza, M. A.; Kanwal, Z.; Rauf, A.; Sabri, A. N.; Riaz, S.; Naseem, S. Size- and Shape-Dependent Antibacterial Studies of Silver Nanoparticles Synthesized by Wet Chemical Routes. *Nanomaterials* **2016**, *6*, 74.

[32] Banzai, K.; Naka, S.; Okada, H. $MoO_3$/Ag/$MoO_3$ Anode for Organic Light-Emitting Diodes and its Carrier Injection Property. *Jpn. J. Appl. Phys.* **2015**, *54*, No. 054101.

[33] Chen, W.; Thoreson, M. D.; Ishii, S.; Kildishev, V.; Shalaev, V. M. Ultra-thin Ultra-Smooth and Low-Loss Silver Films on a Germanium Wetting Layer. *Opt. Express* **2010**, *18*,5124–5134.

[34] Cremers, V.; Puurunen, R. L.; Dendooven, J. Conformality in Atomic Layer Deposition: Current Status Overview of Analysis and Modelling. *Appl. Phys. Rev.* **2019**, *6*, No. 021302.

[35] Yuan, Z.; Dryden, N. H.; Vittal, J. J.; Puddephatt, R. J. Chemical Vapor Deposition of Silver. *Chem. Mater.* **1995**, *7*, 1696–1702.

[36] Bahlawane, N.; Premkumar, P. A.; Brechling, A.; Reiss, G.; Kohse-Höinghaus, K. Alcohol-Assisted CVD of Silver Using Commercially Available Precursors. *Chem. Vap. Deposition* **2007**, *13*, 401–407.

[37] Oehr, C.; Suhr, H. Deposition of Silver Films by Plasma-Enhanced Chemical Vapour Deposition. *Appl. Phys. A* **1989**, *49*, 691–696.

[38] Gao, L.; Härter, P.; Linsmeier, Ch.; Gstöttner, J.; Emling, R.; Schmitt-Landsiedel, D. Metalorganic Chemical Vapor Deposition of Silver Thin Films for Future Interconnects by Direct Liquid Injection System. *Mater. Sci. Semicond. Process.* **2004**, *7*, 331–335.

[39] Puurunen, R. L. Surface Chemistry of Atomic Layer Deposition: A Case Study for the Trimethylaluminum/Water Process. *J. Appl. Phys.* **2005**, *97*, 121301.

[40] Niskanen, A.; Hatanpää, T.; Arstila, K.; Leskelä, M.; Ritala, M. Radical-Enhanced Atomic Layer Deposition of Silver Thin Films Using Phosphine-Adducted Silver Carboxylates. *Chem. Vap. Deposition* **2007**, *13*, 408–413.

[41] Kariniemi, M.; Niinistö, J.; Hatanpää, T.; Kemell, M.; Sajavaara, T.; Ritala, M.; Leskelä, M. Plasma-Enhanced Atomic Layer Deposition of Silver Thin Films. *Chem. Mater.* **2011**, *23*, 2901–2907.

[42] Gu, D.; Zhang, C.; Wu, Y.-K.; Guo, L. J. Ultrasmooth and Thermally Stable Silver-Based Thin Films with Subnanometer Roughness by Aluminum Doping. *ACS Nano* **2014**, *8*, 10343–10351.

[43] Yang, Y.; Song, W.; Ding, L. Dielectric/Ultrathin Metal/Dielectric Structured Transparent Conducting Films for Flexible Electronics. *Sci. Bull.* **2020**, 1324.

[44] Chalker, P. R.; Romani, S.; Marshall, P. A.; Rosseinsky, M. J.; Rushworth, S.; Williams, P. A. Liquid Injection Atomic Layer Deposition of Silver Nanoparticles. *Nanotechnology* **2010**, *21*, 405602.

[45] Mäkelä, M.; Hatanpää, T.; Mizohata, K.; Meinander, K.; Niinistö, J.; Räisänen, J.; Ritala, M.; Leskelä, M. Studies on Thermal Atomic Layer Deposition of Silver Thin Films. *Chem. Mater.* **2017**, *29*, 2040–2045.

[46] Golrokhi, Z.; Marshall, P. A.; Romani, S.; Rushworth, S.; Chalker, P. R.; Potter, R. J. The Influence of Tertiary Butyl Hydrazine as a Co-Reactant on the Atomic Layer Deposition of Silver. *Appl. Surf. Sci.* **2017**, *399*, 123–131.

[47] Dhakal, D.; Assim, K.; Lang, P.; Bruener, P.; Grehl, T.; Georgi, C.; Waechtler, T.; Ecke, R.; Schulz, S. E.; Gressner, T. Atomic Layer Deposition of Ultrathin $Cu_2O$ and Subsequent Reduction to Cu Studied by In Situ X-Ray Photoelectron Spectroscopy. *J. Vac. Sci. Technol. A* **2016**, *34*, No. 01A111.

[48] Masango, S. S.; Peng, L.; Marks, L. D.; Van Duyne, R. P.; Stair, P. C. Nucleation and Growth of Silver Nanoparticles by AB and ABC-Type Atomic Layer Deposition. *J. Phys. Chem. C* **2014**, *118*, 17655–17661.

[49] Van Bui, H.; Grillo, F.; Van Ommen, J. R. Atomic and Molecular Layer Deposition: Off the Beaten Track. *Chem. Commun.* **2017**, *53*, 45–71.

[50] El-Nour, K. M. M. A.; Eftaiha, A.; Al-Warthan, A.; Ammar, R. A. A. Synthesis and Applications of Silver Nanoparticles. *Arabian. J. Chem.* **2010**, *3*, 135–140.

[51] Hatanpää, T. Precursor Chemistry for Atomic Layer Deposition. Ph.D. thesis, University of Helsinki, **2019**.

[52] Hämäläinen, J. Atomic Layer Deposition of Noble Metal Oxide and Noble Metal Thin Films. Ph.D. thesis, University of Helsinki, **2013**.

[53] Schneider, N.; Donsanti, F. Atomic Layer Deposition (ALD) Principes Généraux, Matériaux et Applications. *Techniques de l'Ingénieur Nanomatériaux : Synthèse et Elaboration,* **2016**, base documentaire : TIB195DUO., fr.

[54] Mäkelä, M. Studies on Atomic Layer Deposition of Gold and Silver Thin Films. Ph.D. thesis, University of Helsinki, **2018**.

[55] Miikkulainen, V.; Leskelä, M.; Ritala, M.; Puurunen, R. L. Crystallinity of Inorganic Films Grown by Atomic Layer Deposition: Overview and General Trends. *J. Appl. Phys.* **2013**, *113*, No. 021301.

[56] Leskelä, M.; Ritala, M. Atomic layer deposition (ALD): From Precursors to Thin Film Structures. *Thin Solid Films* **2002**, *409*, 138–146.

[57] Profijt, H. B.; Potts, S. E.; Van de Sanden, M. C. M.; Kessels, W. M. M. Plasma-Assisted Atomic Layer Deposition: Basics, Opportunities, and Challenges. *J. Vac. Sci. Technol. A* **2011**, *29*, 050801.

[58] Puurunen, R. L. Growth per Cycle in Atomic Layer Deposition: Real Application Examples of a Theoretical Model. *Chem. Vap. Deposition* **2003**, *9*, 327–332.

[59] Kajikawa, Y. Roughness Evolution During Chemical Vapor Deposition. *Mater. Chem. Phys.* **2008**, *112*, 311–318.

[60] Venables, J. A.; Spiller, G. D. T.; Hanbücken, M. Nucleation and Growth of Thin Films. *Rep. Prog. Phys.* **1984**, *47*, 399–459.

[61] Greene, J. *Handbook of Deposition Technologies for Films and Coatings,* Third Edition, Martin, P. M., Ed.; William Andrew Publishing: Boston, **2010**.

[62] Feng Liu; Hohage, M.; Lagally, M. G. *Encyclopedia of Applied Physics*, Surfaces and Interfaces of Solids, Structure of; University of Wisconsin-Madison, Madison, Wisconsin, United States; Wiley-VCH.

[63] Campbell, C. T. Ultrathin Metal Films and Particles on Oxide Surfaces: Structural, Electronic and Chemisorptive Properties. *Surf. Sci. Rep.* **1997**, *27*, 1–111.

[64] Venables, J. A. Atomic Processes in Crystal Growth. *Surf. Sci.* **1994**, *299-300*, 798–817.

[65] Zhang, Z.; Lagally, M. G. Atomistic Processes in the Early Stages of Thin-Film Growth. *Science* **1997**, *276*, 377–383.

[66] Weber, M. J. Atomic Layer Deposition of Noble Metal Nanoparticles. Ph.D. thesis, Technische Universiteit Eindhoven, **2014**.

[67] Ratsch, C.; Venables, J. A. Nucleation Theory and the Early Stages of Thin Film Growth. *J. Vac. Sci. Technol. A: Vacuum, Surfaces, and Films* **2003**, *21*, S96–S109.

[68] Stoldt, C. R.; Jenks, C. J.; Thiel, P. A.; Cadilhe, A. M.; Evans, J. W. Smoluchowski ripening of Ag islands on Ag(100). *J. Chem. Phys.* **1999**, *111*, 5157–5166.

[69] Wynblatt, P.; Gjostein, N. A. Supported Metal Crystallites. *Prog. Solid State Chem.* **1975**, *9*, 21–58.

[70] Wynblatt, P.; Gjostein, N. A. Particle Growth in Model Supported Metal Catalysts–I. Theory. *Acta Metall.* **1976**, *24*, 1165–1174.

[71] Venables, J. A. *Introduction to Surface and Thin Film Processes*; Cambridge University Press, **2000**, 372.

[72] Zhu, L.; Lu, G.; Mao, S.; Chen, J.; Dikin, D. A.; Chen, X.; Ruoff, R. S. Ripening of Silver Nanoparticles on Carbon Nanotubes. *Nano* **2007**, *2*, 149–156.

[73] Weiss, J.; Canceliere, C.; McClements, D. J. Mass Transport Phenomena in Oil-in-Water Emulsions Containing Surfactant Micelles: Ostwald Ripening. *Langmuir* **2000**, *16*, 6833–6838.

[74] Tang, J.; Photopoulos, P.; Tserepi, A.; Tsoukalas, D. Two-dimensional Nanoparticle Self-Assembly Using Plasma-Induced Ostwald Ripening. *Nanotechnology* **2011**, *22*.

[75] Fukamori, Y.; König, M.; Yoon, B.; Wang, B.; Esch, F.; Heiz, U.; Landman, U. Fundamental Insight into the Substrate-Dependent Ripening of Monodisperse Clusters. *ChemCatChem* **2013**, *5*, 3330–3341.

[76] Grillo, F.; Van Bui, H.; Moulijn, J. A.; Kreutzer, M. T.; Van Ommen, J. R. Understanding and Controlling the Aggregative Growth of Platinum Nanoparticles in Atomic Layer Deposition: An Avenue to Size Selection. *The J. Phys. Chem. Lett.* **2017**, *8*, 975–983.

[77] Mackus, A. J. M.; Verheijen, M. A.; Leick, N.; Bol, A. A.; Kessels, W. M. M. Influence of Oxygen Exposure on the Nucleation of Platinum Atomic Layer Deposition: Consequences for Film Growth, Nanopatterning, and Nanoparticle Synthesis. *Chem. Mater.* **2013**, *25*, 1905–1911.

[78] Goulas, A.; Van Ommen, J. R. Atomic Layer Deposition of Platinum Clusters on Titania Nanoparticles at Atmospheric Pressure. *J. Mater. Chem. A* **2013**, *1*, 4647–4650.

[79] Sun, S.; Zhang, G.; Gauquelin, N.; Chen, N.; Zhou, J.; Yang, S.; Chen, W.; Meng, X.; Geng, D.; Banis, M. N.; Li, R.; Ye, S.; Knights, S.; Botton, G.A.; Sham, T.-K.; Sun, X. Single-atom Catalysis Using Pt/Graphene Achieved through Atomic Layer Deposition. *Sci. Rep.* **2013**, *3*.

[80] Hämäläinen, J.; Puukilainen, E.; Sajavaara, T.; Ritala, M.; Leskelä, M. Low Temperature Atomic Layer Deposition of Noble Metals Using Ozone and Molecular Hydrogen as Reactants. *Thin Solid Films* **2013**, *531*, 243–250.

[81] Grillo, F.; Van Bui, H.; La Zara, D.; Aarnink, A. A. I.; Kovalgin, A. Y.; Kooyman, P.; Kreutzer, M. T.; Van Ommen, J. R. From Single Atoms to Nanoparticles: Autocatalysis and Metal Aggregation in Atomic Layer Deposition of Pt on $TiO_2$ Nanopowder. *Small* **2018**, *14*.

[82] Mackus, A. J. M.; Weber, M. J.; Thissen, N. F. W.; Garcia-Alonso, D.; Vervuurt, R. H. J.; Assali, S.; Bol, A. A.; Verheijen, M. A.; Kessels, W. M. M. Atomic Layer Deposition of Pd and Pt Nanoparticles for Catalysis: On the Mechanisms of Nanoparticle Formation. *Nanotechnology* **2015**, *27*, 034001.

[83] Dendooven, J.; Ramachandran, R. K.; Solano, E.; Kurttepeli, M.; Geerts, L.; Heremans, G.; Rongé, J.; Minjauw, M. M.; Dobbelaere, T.; Devloo-Casier, K.; Martens, J. A.; Ventomme, A.; Bals, S.; Portale, G.; Coati, A.; Detavernier, C. Independent Tuning of Size and Coverage of Supported Pt Nanoparticles Using Atomic Layer Deposition. *Nat. Commun.* **2017**, *8*.

[84] Solano, E.; Dendooven, J.; Ramachandran, R. K.; Van de Kerckhove, K.; Dobbelaere, T.; Hermida-Merino, D.; Detavernier, C. Key role of surface oxidation and reduction processes in the coarsening of Pt nanoparticles. *Nanoscale* **2017**, *9*, 13159–13170.

[85] Van den Bruele, F. J.; Smets, M.; Illiberi, A.; Creyghton, Y.; Buskens, P.; Roozeboom, F.; Poodt, P. Atmospheric Pressure Plasma Enhanced Spatial ALD of Silver. *J. Vac. Sci. Technol. A* **2015**, *33*, No. 01A131.

[86] Duan, Y.; Rani, S.; Newberg, J. T.; Teplyakov, A. V. Investigation of the Influence of Oxygen Plasma on Supported Silver Nanoparticles. *J. Vac. Sci. Technol. A* **2018**, *36*, 01B101.

[87] Zhang, S.; Cargnello, M.; Cai, W.; Murray, C. B.; Graham, G. W.; Pan, X. Revealing Particle Growth Mechanisms by Combining High-Surface-Area Catalysts Made with Monodisperse Particles and Electron Microscopy Conducted at Atmospheric Pressure. *J. Catal.* **2016**, *337*, 240–247.

[88] Peroulis, D. Capacitive MEMS Switches; *Encyclopedia of Nanotechnology*, Bhushan, B., Ed.; First Edition Springer, **2012**.

[89] Swift, K. G.; Booker, J. D. In *Manufacturing Process Selection Handbook*; Swift, K., Booker, J., Eds.; Butterworth-Heinemann: Oxford, **2013**.

[90] Pierson, H. O. In *Handbook of Chemical Vapor Deposition (CVD)* Principles, Technology, and Applications, Book, Second Edition; Pierson, H. O., Ed.; William Andrew Publishing: Norwich, NY, **1999**.

[91] Chuprakov, I. S.; Martin, J. D.; Dahmen, K. H. New Flash-Evaporation Feeder for Chemical Vapor deposition. *J. Phys. IV France,* **1999**, *9*, 901–908.

[92] Haase, T.; Kohse-Höinghaus, K.; Bahlawane, N.; Djiele, P.; Jakob, A.; Lang, H. CVD with Tri-$^{n}$butylphosphine Silver(I) Complexes: Mass Spectrometric Investigations and Depositions. *Chem. Vap. Deposition* **2005**, *11*, 195–205.

[93] Abourida, M.; Guillon, H.; Jimenez, C. Decams. J. M.; Weiss, F.; Valet, O. Doppelt, P. Silver Thin Films Deposited by Injection MOCVD. *In Proceedings of the 203$^{rd}$ Meeting of the Electrochemical Society*; Paris, France, August **2003**, 938–945.

[94] Gao, L.; Härter, P.; Linsmeier, Ch.; Wiltner, A.; Emling, R.; Schmitt-Landsiedel, D. Silver Metal Organic Chemical Vapor Deposition for Advanced Silver Metallization. *Microelectron. Eng.* **2005**, *82*, 296–300.

[95] Zanotto, L.; Benetollo, F.; Natali, M.; Rossetto, G.; Zanella, P.; Kaciulis, S.; Mezzi, A. Facile Synthesis and Characterization of New β-Diketonate Silver Complexes. Single-Crystal Structures of (1,1,1,5,5,5-Hexafluoro-2,4-pentadionato)(2,2'-bipyridine)silver(I) and (1,1,1,5,5,5-Hexafluoro-2,4-pentadionato)(N,N,N',N'-tetramethylethylenediamine)silver(I) and Their Use as MOCVD Precursors for Silver Films. *Chem. Vap. Deposition* **2004**, *10*, 207–213.

[96] Samoilenkov, S.; Stefan, M.; Wahl, G.; Paramonov, S.; Kuzmina, N.; Kaul, A. Low Temperature MOCVD of Conducting, Micrometer-Thick, Silver Films. *Chem. Vap. Deposition* **2002**, *8*, 74–78.

[97] Dryden, N. H.; Vittal, J. J.; Puddephatt, R. J. New Precursors for Chemical Vapor Deposition of Silver. *Chem. Mater.* **1993**, *5*, 765–766.

[98] Chi, K.-M.; Chen, K.-H.; Peng, S.-M.; Lee, G.-H. Synthesis and Characterization of (β-Diketonato)silver Vinyltriethylsilane Compounds and Their Application to CVD of Silver Thin Films. Crystal Structure of the (2,2-Dimethyl-6,6,7,7,8,8,8-heptafluoro-3,5-octanedionato)silver Vinyltriethylsilane Dimer. *Organometallics* **1996**, *15*, 2575–2578.

[99] Chi, K.-M.; Lu, Y. MOCVD of Silver Thin Films from the (1,1,1,5,5,5-Hexafluoro-2,4-pentanedionato)-silver[bis(trimethylsilyl)acetylene] Complex. *Chem. Vap. Deposition* **2001**, *7*, 117–120.

[100] Szłyk, E.; Piszczek, P.; Grodzicki, A.; Chaberski, M.; Goliński, A.; Szatkowski, J.; Błaszczyk, T. CVD of $Ag^{I}$ Complexes with Tertiary Phosphines and Perfluorinated Carboxylates–A New Class of Silver Precursors. *Chem. Vap. Deposition* **2001**, *7*, 111–116.

[101] Yuan, Z.; Dryden, N. H.; Li, X.; Vittal, J. J.; Puddephatt, R. J. Chemical Vapour Deposition of Copper or Silver from the Precursors [M(hfac)(C≡NMe)] [M = Cu, Ag; hfac = $CF_3C(O)CHC(O)CF_3$]. *J. Mater. Chem.* **1995**.

[102] Piszczek, P.; Szłyk, E.; Chaberski, M.; Taeschner, C.; Leonhardt, A.; Bała, W.; Bartkiewicz, K. Characterization of Silver Trimethylacetate Complexes with Tertiary Phosphines as CVD Precursors of Thin Silver Films. *Chem. Vap. Deposition* **2005**, *11*, 53–59.

[103] Piszczek, P.; Lewandowska, Z.; Radtke, A.; Jędrzejewski, T.; Kozak, W.; Sadowska, B.; Szubka, M.; Talik, E.; Fiori, F. Biocompatibility of Titania Nanotube Coatings Enriched with Silver Nanograins by Chemical Vapor Deposition. *Nanomaterials* **2017**, *7*.

[104] Szymańska, I.; Piszczek, P.; Szczęsny, R.; Szłyk, E. Thermal and MS Studies of Silver(I) 2,2-dimethylbutyrate Complexes with Tertiary Phosphines and Their Application for CVD of Silver Films. *Polyhedron* **2007**, *26*, 2440–2448.

[105] Szłyk, E.; Piszczek, P.; Łakomska, I.; Grodzicki, A.; Szatkowski, J.; Błaszczyk, T. $Au^{I}$ and $Ag^{I}$ Complexes with Tertiary Phosphines and Perfluorinated Carboxylates as Precursors for CVD of Gold and Silver. *Chem. Vap. Deposition* **2000**, *6*, 105–108.

[106] Eisenbraun, E. T.; Klaver, A.; Patel, Z.; Nuesca, G.; Kaloyeros, A. E. Low Temperature Metalorganic Chemical Vapor Deposition of Conformal Silver Coatings for Applications in High Aspect Ratio Structures. *J. Vac. Sci. Technol. B* **2001**, *19*, 585–588.

[107] Shapiro, M. J.; Lackey, W. J.; Hanigofsky, J. A.; Hill, D. N.; Carter, W. B.; Barefield, E. K. Chemical Vapor Deposition of Silver Films for Superconducting Wire Applications. *J. Alloys Compd.* **1992**, *187*, 331–349.

[108] Voorhoeve, R. J. H.; Merewether, J. W. Selective Deposition of Silver on Silicon by Reaction with Silver Fluoride Vapor. *J. Electrochem. Soc.* **1972**, *119*, 364–368.

[109] Jeffries, P. M.; Wilson, S. R.; Girolami, G. S. Crystal Structure of $[CF_3CFC(CF_3)Ag]_4$ and its Use as a Chemical Vapor Deposition Precursor for Silver Films. *J. Organomet. Chem.* **1993**, *449*, 203–209.

[110] Serghini-Monim, S.; Yuan, Z.; Griffiths, K.; Norton, P. R.; Puddephatt, R. J. Low-Temperature Chemical Vapor Deposition of Silver on Ag(111) Using $((CH_3)_3CCOCHCOC_3F_7)AgPEt_3$. *J. Am. Chem. Soc.* **1995**, *117*, 4030–4036.

[111] Lin, W.; Warren, T. H.; Nuzzo, R. G.; Girolami, G. S. Surface-Selective Deposition of Palladium and Silver Films from Metal-Organic Precursors: A Novel Metal-Organic Chemical Vapor Deposition Redox Transmetalation Process. *J. Am. Chem. Soc.* **1993**, *115*, 11644–11645.

[112] Itsuki, A.; Uchida, H.; Satou, M.; Ogi, K. Properties of a New Organo Silver Compound for MOCVD. *Nucl. Instrum. Methods Phys. Res. B* **1997**, *121*, 116–120.

[113] Lu, Y. F.; Takai, M.; Nagatomo, S.; Kato, K.; Namba, S. Direct Writing of Ag-Lines on Mn-Zn Ferrite by Laser-Induced Thermal Decomposition by $CH_3COOAg$. *Appl. Phys. A,* **1992**, 54, 51–56.

[114] Lu, Y. F.; Takai, M.; Shiokawa, T.; Aoyagi, Y. Growth of Ultrathin Silver Films by Excimer-Laser-Induced Decomposition of Silver Acetate in Air. *Jpn. J. Appl. Phys.* **1994**, *33*, 1313–1315.

[115] Edwards, D. A.; Harker, R. M.; Mahon, M. F.; Molloy, K. C. Aerosol-Assisted Chemical Vapour Deposition (AACVD) of Silver Films from Triphenylphosphine Adducts of Silver β-diketonates and β-diketoiminates, including the structure of [Ag(hfac)($PPh_3$)]. *J. Mater. Chem* **1999**, *9*, 1771–1780.

[116] Edwards, D. A.; Harker, R. M.; Mahon, M. F.; Molloy, K. C. Aerosol-Assisted Chemical Vapour Deposition (AACVD) of Silver Films from Triorganophosphine Adducts of Silver Carboxylates, Including the Structure of [Ag($O_2CC_3F_7$)($PPh_3$)$_2$]. *Inorg. Chim. Acta* **2002**, *328*, 134–146.

[117] Edwards, D. A.; Mahon, M. F.; Molloy, K. C.; Ogrodnik, V. Aerosol-Assisted Chemical Vapour Deposition of Silver Films from Adducts of Functionalised Silver Carboxylates. *J. Mater. Chem.* **2003**, *13*, 563–570.

[118] Edwards, D. A.; Mahon, M. F.; Molloy, K. C.; Ogrodnik, V. Silver(I) Aryloxide–triphenylphosphine Complexes. An Assessment of their Potential as CVD Precursors and the Structure of [Ag($OC_6H_4$Me-2)($PPh_3$)$_3$]·2-Me$C_6H_4$OH·$C_6H_5$Me. *Inorg. Chim. Acta* **2003**, *349*, 37–44.

[119] Xu, C.; Hampden-Smith, M. J.; Kodas, T. T. Aerosol-Assisted Chemical Vapor Deposition (AACVD) of Silver, Palladium and Metal Alloy ($Ag_{1-x}Pdx$, $Ag_{1-x}Cu_x$ and $Pd_{1-x}Cu_x$) Films. *Adv. Mater.* **1994**, *6*, 746–748.

[120] Brook, L. A.; Evans, P.; Foster, H. A.; Pemble, M. E.; Steele, A.; Sheel, D. W.; Yates, H. M. Highly Bioactive Silver and Silver/Titania Composite Films Grown by Chemical Vapour Deposition. *J. Photochem. Photobiol. A* **2007**, *187*, 53–63.

[121] Yates, H. M.; Brook, L. A.; Sheel, D. W. Photoactive Thin Silver Films by Atmospheric Pressure CVD. *Int. J. Photoenergy* **2008**, *2008*.

[122] Sheel, D. W.; Brook, L. A.; Yates, H. M. Controlled Nanostructured Silver Coated Surfaces by Atmospheric Pressure Chemical Vapour Deposition. *Chem. Vap. Deposition* **2008**, *14*, 14–24.

[123] Hansen, B. N.; Hybertson, B. M.; Barkley, R. M.; Sievers, R. E. Supercritical Fluid Transport-Chemical Deposition of Films. *Chem. Mater.* **1992**, *4*, 749–752.

[124] Baum, T. H.; Comita, P. B. Chemical Vapor Deposition of Gold and Silver; *The Chemistry of Metal CVD, Chapter 6;* Toivo T. Kodas, T. T.; Hampden-Smith, M. J. Eds.; Wiley, **1994**.

[125] Grodzicki, A.; Łakomska, I.; Piszczek, P.; Szymańska, I.; Szłyk, E. Copper(I), Silver(I) and Gold(I) Carboxylate Complexes as Precursors in Chemical Vapour Deposition of Thin Metallic Films. *Coord. Chem. Rev.* **2005**, *249*, 2232–2258.

[126] Bahlawane, N.; Kohse-Höinghaus, K.; Premkumar, P. A.; Lenoble, D. Advances in the Deposition Chemistry of Metal-Containing Thin Films Using Gas Phase Processes. *Chem. Sci.* **2012**, *3*, 929–941.

[127] Hampden-Smith, M. J.; Kodas, T. T. Chemical vapor deposition of metals: Part 1. An overview of CVD processes. *Chem. Vap. Deposition* **1995**, *1*, 8–23.

[128] Serghini-Monim, S.; Yuan, Z.; Griffiths, K.; Norton, P. R.; Puddephatt, R. J. Direct Evidence for Silver Film Deposition below Room Temperature on Pt(111) from the((($CH_3$)$_3$CCOCHCO$C_3F_7$)AgP$Et_3$ Precursor. *J. Phys. Chem.* **1995**, *99*, 9230–9235.

[129] Bailey, A.; Corbitt, T. S.; Hampden-Smith, M. J.; Duesler, E. N.; Kodas, T. T. Synthesis and Characterization of 1,1,1,5,5,5-Hexafluoroacetylacetonato-(1,5-Cyclooctadiene)Silver(I) Dimer. An Unusual β-Diketonate Coordination Mode. *Polyhedron* **1993**, *12*, 1785–1792.

[130] Burleva, L. P.; Andreev, V. M.; Boldyrev, V. V. Thermal Decompositions of Silver Carboxylates. *J. Therm. Anal.* **1988**, *33*, 735–739.

[131] Chi, K.-M.; Lin, C.-T.; Peng, S.-M.; Lee, G.-H. Synthesis and Characterization of New Silver Complexes of Alkynes. Single-Crystal Structures of (1,1,1,5,5,5-Hexafluoro-2,4-pentanedionato)- (diphenylacetylene)silver and Tetrakis(1,1,1,5,5,5- hexafluoro-2,4-pentanedionato)bis(4-octyne)tetrasilver. *Organometallics* **1996**, *15*, 2660–2663.

[132] Chi, K.-M.; Chen, K.-H.; Lin, H.-C.; Lin, K.-J. Synthesis and Characterization of (β-diketonato)silver Complexes of 7-*tert*-butoxynorbornadiene. Single-crystal structures of (hfac)(7-$Bu^t$-O-NBD)Ag and [(hfac)$_2$(7-$Bu^t$-O-NBD)$Ag_2$]$_n$. *Polyhedron* **1997**, *16*, 2147–2154.

[133] Paramonov, S. E.; Kuzmina, N. P.; Troyanov, S. I. Synthesis and Crystal Structure of Silver(I) Carboxylate Complexes, $Ag(P^nBu_3)[C(CH_3)_3COO]$ and $Ag(Phen)_2[CF_3COO]\cdot H_2O$. *Polyhedron* **2003**, *22*, 837–841.

[134] Römbke, P.; Schier, A.; Schmidbaur, H.; Cronje, S.; Raubenheimer, H. Mono- and Bimetallic Gold(I) and Silver(I) Pentafluoropropionates and Related Compounds. *Inorg. Chim. Acta* **2004**, *357*, 235–242.

[135] Ngo, S. C.; Banger, K. K.; Toscano, P. J.; Welch, J. T. Synthesis and Physical and Structural Characterization of Ag(I) Complexes Supported by Non-Fluorinated β-Diketonate and Related Ancillary Ligands. *Polyhedron* **2002**, *21*, 1289–1297.

[136] Decams, J.-M.; Guillon H.; Doppelt, P. US Patent. 7608099B2, **2009**.

[137] Baum, T. H.; Larson, C. E.; Reynolds, S. K. US Patent, 5096737A, **1992**.

[138] Boysen, N.; Hasselmann, T.; Karle, S.; Rogalla, D.; Theirich, D.; Winter, M.; Riedl, T.; Devi, A. An N-Heterocyclic Carbene Based Silver Precursor for Plasma-Enhanced Spatial Atomic Layer Deposition of Silver Thin Films at Atmospheric Pressure. *Angew. Chem. Int. Ed.* **2018**, *57*, 16224–16227.

[139] Cleveland, E.; Glembocki, O.; Prokes, S.M. Plasma Enhanced Atomic Layer Deposition of Silver Thin Films for Applications in Plasmonics and Surface Enhanced Raman Scattering. In *Proceedings of SPIE, Nanoepitaxy: Materials and Devices IV;* Kobayashi, N. P.; Talin, A. A.; Islam M. S. Eds.; San Diego, California, United States, October **2012**, Vol. *8467*.

[140] Kariniemi, M.; Niinistö, J.; Vehkamäki, M.; Kemell, M.; Ritala, M.; Leskelä, M.; Putkonen, M. Conformality of Remote Plasma-Enhanced Atomic Layer Deposition Processes: An Experimental Study. *J. Vac. Sci. Technol. A* **2012**, *30*, No. 01A115.

[141] Prokes, S. M.; Glembocki, O. J.; Cleveland, E. Novel Optical Properties of Ag Films Deposited by Plasma Enhanced Atomic Layer Deposition (PEALD), In *Proceedings of SPIE, United States, October, 2012*; Kobayashi N. P.; Talin A. A.; Islam M. S., Eds.; Nanoepitaxy: Materials and Devices IV, **2012**; Vol. *8467*.

[142] Prokes, S. M.; Glembocki, O. J.; Cleveland, E.; Caldwell, J. D.; Foos, E.; Niinistö, J.; Ritala, M. Spoof-Like Plasmonic Behavior of Plasma Enhanced Atomic Layer Deposition Grown Ag Thin Films. *Appl. Phys. Lett.* **2012**, *100*, No. 053106.

[143] Prokes, S. M.; Glembocki, O. J.; Livenere, J. E.; Tumkur, T. U.; Kitur, J. K.; Zhu, G.; Wells, B.; Podolskiy, V. A.; Noginov, M. A. Hyperbolic and Plasmonic Properties of Silicon/Ag Aligned Nanowire Arrays. *Opt. Express* **2013**, *21*, 14962–14974.

[144] Prokes, S. M.; Glembocki, O. J.; Self Assembled Metamaterials Formed via Plasma Enhanced ALD of Ag Thin Films. *ECS Trans.* **2014**, *64*, 279–289.

[145] Caldwell, J. D.; Glembocki, O. J.; Bezares, F. J.; Kariniemi, M.; Niinistö, J. T.; Hatanpää, T.; Rendell, R. W.; Ukaegbu, M.; Ritala, M.; Prokes, S. M.; Hosten, C. M.; Leskelä, M.; Kasica, R. Large-Area Plasmonic Hot-Spot Arrays: Sub-2 nm Interparticle Separations with Plasma-Enhanced Atomic Layer Deposition of Ag on Periodic Arrays of Si Nanopillars. *Opt. Express* **2011**, *19*, 26056–26064.

[146] Mameli, A.; Van den Bruele, F. J.; Ande, C. K.; Verheijen, M. A.; Kessels, W. M. M.; Roozeboom, F. On The Growth, Percolation and Wetting of Silver Thin Films Grown by Atmospheric-Plasma Enhanced Spatial Atomic Layer Deposition. *ECS Trans.* **2016**, *75*, 129–142.

[147] Ko, C.-T.; Yang, P. S.; Han, Y.-Y.; Wang, W.-C.; Huang, J.-J.; Lee, Y.-H.; Tsai, Y.-J.; Shieh, J.; Chen, M.-J. Atomic-Layer-Deposited Silver and Dielectric Nanostructures for Plasmonic Enhancement of Raman Scattering from Nanoscale Ultrathin Films. *Nanotechnology* **2015**, *26*, 265702.

[148] Compton, R.; Prokes, S. M.; Glembocki, O. J.; Pala, I. R.; Gerardi, H. K.; Owrutsky, J. C. Observation of Coherent Oscillations in Plasma-Enhanced Atomic Layer Deposition Ag Films. *Appl. Phys. Lett.* **2014**, *104*, No. 073101.

[149] Devlin-Mullin, A.; Todd, N. M.; Golrokhi, Z.; Geng, H.; Konerding, M. A.; Ternan, N. G.; Hunt, J. A.; Potter, R. J.; Sutcliffe, C.; Jones, E.; Lee, P. D.; Mitchell, C. A. Atomic Layer Deposition of a Silver Nanolayer on

Advanced Titanium Orthopedic Implants Inhibits Bacterial Colonization and Supports Vascularized de Novo Bone Ingrowth. *Adv. Healthc. Mater.* **2017**, *6*, 1700033.

[150] Senkevich, J. J.; Tang, F.; Rogers, D.; Drotar, J. T.; Jezewski, C.; Lanford, W. A.; Wang, G.-C.; Lu, T.-M. Substrate-Independent Palladium Atomic Layer Deposition. *Chem. Vap. Deposition* **2003**, *9*, 258–264.

[151] Kim, H. Characteristics and Applications of Plasma Enhanced-Atomic Layer Deposition. *Thin Solid Films* **2011**, *519*, 6639–6644.

[152] Vallee, C. ALD assistée par plasma (PEALD). *Techniques de l'Ingénieur Nanomatériaux : Synthèse et Elaboration,* **2016**, base documentaire : TIB195DUO., fr.

[153] Li, Z.; Rahtu, A.; Gordon, R. J. Atomic Layer Deposition of Ultrathin Copper Metal Films from a Liquid Copper(I) Amidinate Precursor. *J. Electrochem. Soc.* **2006**, *153*, C787–C794.

[154] Martensson, P.; Carlsson, J.-O. Atomic Layer Epitaxy of Copper Growth and Selectivity in the Cu(II)-2,2,6,6-tetramethyl-3,5-heptanedionate/$H_2$ Process. *J. Electrochem. Soc.* **1998**, *145*, 2926–2931.

[155] Shrestha, P.; Gu, D.; Tran, N.; Tapily, K.; Baumgart, H.; Namkoong, G. Investigation of Volmer-Weber Growth during the Nucleation Phase of ALD Platinum Thin Films and Template Based Platinum Nanotubes. *ECS Trans.* **2010**, *33*, 127–134.

[156] Choi, B. H.; Lee, J. H.; Lee, H. K.; Kim, J. H. Effect of Interface Layer on Growth Behavior of Atomic-Layer-Deposited Ir Thin Film as Novel Cu Diffusion Barrier. *Appl. Surf. Sci.* **2011**, *257*, 9654–9660.

[157] Kim, S. K.; Han, S.; Han, J. H.; Hwang, C. S. Effect of Crystalline Structure of $Tio_2$ Substrates on Initial Growth of Atomic Layer Deposited Ru Thin Films. *Appl. Surf. Sci.* **2011**, *257*, 4302–4305.

[158] Puurunen, R. L.; Vandervorst, W. Island Growth as a Growth Mode in Atomic Layer Deposition: A Phenomenological Model. *J. Appl. Phys.* **2004**, *96*, 7686–7695.

[159] Kim, S. K.; Han, J. H.; Kim, G. H.; Hwang, C. S. Investigation on the Growth Initiation of Ru Thin Films by Atomic Layer Deposition. *Chem. Mater.* **2010**, *22*, 2850–2856.

[160] Yim, S.-S.; Lee, D.-J.; Kim, K.-S.; Kim, S.-H.; Yoon, T.-S.; Kim, K.-B. Nucleation Kinetics of Ru on Silicon Oxide and Silicon Nitride Surfaces Deposited by Atomic Layer Deposition. *J. Appl. Phys.* **2008**, *103*, 113509.

[161] Kukli, K.; Aarik, J.; Aidla, A.; Uustare, T.; Jõgi, I.; Lu, J.; Tallarida, M.; Kemell, M.; Kiisler, A.-A.; Ritala, M.; Leskelä, M. Structure and Morphology of Ru Films Grown by Atomic Layer Deposition from 1-ethyl-1'-methyl-ruthenocene. *J. Cryst. Growth* **2010**, *312*, 2025–2032.

[162] Egorov, K. V.; Lebedinskii, Y. Y.; Soloviev, A. A.; Chouprik, A. A.; Azarov, A. Y.; Markeev, A. M. Initial and Steady-State Ru Growth by Atomic Layer Deposition Studied by *In Situ* Angle Resolved X-Ray Photoelectron Spectroscopy. *Appl. Surf. Sci.* **2017**, *419*, 107–113.

[163] Wu, L.; Eisenbraun, E. Integration of Atomic Layer Deposition-Grown Copper Seed Layers for Cu Electroplating Applications. *J. Electrochem. Soc.* **2009**, *156*, H734–H739.

[164] Wu, L.; Eisenbraun, E. Effects of Hydrogen Plasma Treatments on the Atomic Layer Deposition of Copper. *Electrochem. Solid-State Lett.* **2008**, *11*, H107–H110.

[165] Aaltonen, T.; Ritala, M.; Tung, Y.-L.; Chi, Y.; Arstila, K.; Meinander, K.; Leskelä, M. Atomic Layer Deposition of Noble Metals: Exploration of The Low Limit of The Deposition Temperature. *J. Mater. Res.* **2004**, *19*, 3353–3358.

[166] Aaltonen, T.; Ritala, M.; Arstila, K.; Keinonen, J.; Leskelä, M. Atomic Layer Deposition of Ruthenium Thin Films from $Ru(thd)_3$ and Oxygen. *Chem. Vap. Deposition* **2004**, *10*, 215–219.

[167] Aaltonen, T.; Ritala, M.; Sajavaara, T.; Keinonen, J.; Leskelä, M. Atomic Layer Deposition of Platinum Thin Films. *Chem. Mater.* **2003**, *15*, 1924–1928.

[168] Feng, J.-Y.; Minjauw, M. M.; Ramachandran, R. K.; Daele, M. V.; Poelman, H.; Sajavaara, T.; Dendooven, J.; Detavernier, C. The Co-Reactant Role during Plasma Enhanced Atomic Layer Deposition of Palladium. *Phys. Chem. Chem. Phys.* **2020**, *22*, 9124–9136.

[169] Lu, J.; Elam, J. W.; Stair, P. C. Atomic Layer Deposition Sequential Self-limiting Surface Reactions for Advanced Catalyst "bottom-up" Synthesis. *Surface Science Reports* **2016**, *71*, 410–472.

[170] Aaltonen, T. Atomic Layer Deposition of Noble Metal Thin Films. Ph.D. thesis, University of Helsinki, **2005**.

[171] Aaltonen, T.; Alén, P.; Ritala, M.; Leskelä, M. Ruthenium Thin Films Grown by Atomic Layer Deposition. *Chem. Vap. Deposition* **2003**, *9*, 45–49.

[172] Aaltonen, T.; Ritala, M.; Sammelselg, V.; Leskelä, M. Atomic Layer Deposition of Iridium Thin Films. *J. Electrochem. Soc.* **2004**, *151*, G489–G492.

[173] Park, K. J.; Terry, D. B.; Stewart, S. M.; Parsons, G. N. In Situ Auger Electron Spectroscopy Study of Atomic Layer Deposition: Growth Initiation and Interface Formation Reactions during Ruthenium ALD on Si–H, $SiO_2$, and $HfO_2$ Surfaces. *Langmuir* **2007**, *23*, 6106–6112.

[174] Chaukulkar, R. P.; Thissen, N. F. W.; Rai, V. R.; Agarwal, S. Low Temperature Hydrogen Plasma-Assisted Atomic Layer Deposition of Copper Studied using In Situ Infrared Reflection Absorption Spectroscopy. *J. Vac. Sci. Technol. A* **2014**, *32*, No. 01A108.

[175] Guske, J. T.; Brown, J.; Welsh, A.; Franzen S. Infrared Surface Plasmon Resonance of AZO-Ag-AZO Sandwich Thin Films. *Opt. Express.* **2012**, *20*, 23215–23226.

[176] West, G. T.; Kelly, P.; Bradley, J. A Comparison of Thin Silver Films Grown Onto Zinc Oxide via Conventional Magnetron Sputtering and HiPIMS Deposition. *IEEE Trans. Plasma Sci.* **2010**, *38*, 3057–3061.

[177] Ni, C.; Shah, P.; Sarangan, A. M. Effects of Different Wetting Layers on the Growth of Smooth Ultra-Thin Silver Thin Films. In *Proceedings of SPIE, Nanoengineering: Fabrication, Properties, Optics, and Devices XI*; Campo, E. M.; Dobisz, E. A.; Eldada, L. A., Eds.; International Society for Optics and Photonics: San Diego, California, United States, August 2014 Vol. *9170*.

[178] Lazzari, R.; Jupille, J. Silver Layers on Oxide Surfaces: Morphology and Optical Properties. *Surf. Sci.* **2001**, *482-485*, 823–828.

[179] Stefaniuk, T.; Wróbel, P.; Trautman, P.; Szoplik, T. Ultrasmooth Metal Nanolayers for Plasmonic Applications: Surface Roughness and Specific Resistivity. *Appl. Opt.* **2014**, *53*, B237–B241.

[180] Formica, N.; Ghosh, D.; Carrilero, A.; Chen, T.; Simpson, R. E.; Pruneri, V. Ultrastable and Atomically Smooth Ultrathin Silver Films Grown on a Copper Seed Layer. *ACS Appl. Mater. Interfaces* **2013**, *5*, 3048–3053.

[181] Alvarez, R.; González, J. C.; Espinós, J. P.; González-Elipe, A. R.; Cueva, A.; Villuendas, F. Growth of Silver on ZnO and $SnO_2$ Thin Films Intended for Low Emissivity Applications. *Appl. Surf. Sci.* **2013**, *268*, 507–515.

[182] Zhang, C.; Kinsey, N.; Chen, L.; Ji, C.; Xu, M.; Ferrera, M.; Pan, X.; Shalaev, V. M.; Boltasseva, A.; Guo, L. High-Performance Doped Silver Films: Overcoming Fundamental Material Limits for Nanophotonic Applications. *Adv. Mater.* **2017**, *29*, 1605177.

[183] Duan, Y.; Rani, S.; Zhang, Y.; Ni, C.; Newberg, J. T.; Teplyakov, A. V. Silver Deposition onto Modified Silicon Substrates. *J. Phys. Chem. C* **2017**, *121*, 7240–7247.

[184] Kato, K.; Omoto, H.; Takamatsu, A. Optimum Structure of Metal Oxide Under-Layer Used in Ag-Based Multilayer. *Vacuum* **2008**, *83*, 606–609.

[185] Elam, J. W.; Zinovev, A.; Han, C. Y.; Wang, H. H.; Welp, U.; Hryn, J. N.; Pellin, M. J. Atomic Layer Deposition of Palladium Films on $Al_2O_3$ Surfaces. *Thin Solid Films* **2006**, *515*, 1664–1673.

[186] Waechtler, T.; Oswald, S.; Roth, N.; Jakob, A.; Lang, H.; Ecke, R.; Schulz, S. E.; Gessner, T.; Moskvinova, A.; Schulze, S.; Hietschold, M. Copper Oxide Films Grown by Atomic Layer Deposition from Bis(tri-

*n*-butylphosphane)copper(I)acetylacetonate on Ta, TaN, Ru, and $SiO_2$. *J. Electrochem. Soc.* **2009**, *156*, H453–H459.

[187] Waechtler, T.; Roth, N.; Mothes, R.; Schulze, S.; Schulz, S. E.; Gessner, T.; Lang, H.; Hietschold, M. Copper Oxide ALD from a Cu(I) β-Diketonate: Detailed Growth Studies on $SiO_2$ and TaN. *ECS Trans.* **2009**, 25, 277–287

[188] Waechtler, T.; Ding, S.-F.; Hofmann, L.; Mothes, R.; Xie, Q.; Oswald, S.; Detavernier, C.; Schulz, S. E.; Qu, X.-P.; Lang, H.; Gessner, T. ALD-Grown Seed Layers for Electrochemical Copper Deposition Integrated with Different Diffusion Barrier Systems. *Microelectron. Eng.* **2011**, *88*, 684–689.

[189] Li, Z.; Gordon, R. G. Thin, Continuous, and Conformal Copper Films by Reduction of Atomic Layer Deposited Copper Nitride. *Chem. Vap. Deposition* **2006**, *12*, 435–441.

[190] Huang, J.; Liu, X.; Lu, Y.; Zhou, Y.; Xu, J.; Li, J.; Wang, H.; Fang, J.; Yang, Y.; Wang, W.; Tan, R.; Song, W. Seed-Layer-Free Growth of Ultra-Thin Ag Transparent Conductive Films Imparts Flexibility to Polymer Solar Cells. *Sol. Energy Mater. Sol. Cells* **2018**, *184*, 73–81.

[191] Raut, N. C.; Al-Shamery, K. Inkjet Printing Metals on Flexible Materials for Plastic and Paper Electronics. *J. Mater. Chem. C,* **2018**, *6*, 1618–1641.

[192] Mo, L.; Guo, Z.; Yang, L.; Zhang, Q.; Fang, Y.; Xin, Z.; Chen, Z.; Hu, K.; Han, L.; Li, L. Silver Nanoparticles Based Ink with Moderate Sintering in Flexible and Printed Electronics. *Int. J. Mol. Sci.* **2019**, *20*, 2124.

[193] Reinhold, I.; Hendriks, C. E.; Eckardt, R.; Kranenburg, J. M.; Perelaer, J.; Baumann, R. R.; Schubert, U. S. Argon Plasma Sintering of Inkjet Printed Silver Tracks on Polymer Substrates. *J. Mater. Chem.* **2009**, *19*, 3384–3388.

[194] Bromberg, V.; Ma, S.; Egittob, F. D.; Singler, T. J. Highly Conductive Lines by Plasma-Induced Conversion of Inkjet-Printed Silver Nitrate Traces. *J. Mater. Chem. C* **2013**, *1*, 6842–6849.

[195] Ma, S.; Bromberg, V.; Liu, L.; Egitto, F. D.; Chiarot, P. R.; Singler, T. J. Low Temperature Plasma Sintering of Silver Nanoparticles. *Appl. Surf. Sci.* **2014**, *293*, 207–215.

[196] Stenzel, O. *The Physics of Thin Film Optical Spectra, An Introduction,* Second Edition Springer, **2016**.

[197] Shalaev, V. M. Optical Properties of Nanostructured Random Media, Springer, **2010**.

[198] Bulír, J.; Novotný, M; Lynnykova, A; Lančok, J.; Bodnár, M.; Škereň, M. Preparation of Nanostructures Ultrathin layer. In *Proceedings of SPIE, Nanostructured Thin Films III;* Martin-Palma, R. J.; Jen, Y.-J.; Lakhtakia A. Eds.; San Diego, California, United States, August **2010**, Vol. *7766*.

[199] Doremus, R. H. Optical Properties of Thin Metallic Films in Island Form. *J. Appl. Phys.* **1966**, *37*, 2775–2781.

[200] Crêpellière, J.; Menguelti, K.; Wack, S.; Bouton, O.; Gérard, M.; Popa, P. L.; Pistillo, B. R.; Leturcq, R.; Michel, M. Spray Deposition of Silver Nanowires on Large Area Substrates for Transparent Electrodes. *ACS Appl. Nano Mater.* **2021**, *4*, 1126–1135.

[201] Caicedo, N.; Thomann, J.-S.; Leturcq, R.; Lenoble, D. Aspect ratio improvement of ZnO nanowires grown in liquid phase by using step-by-step sequential growth. *CrystEngComm* **2016**, *18*, 5502–5511.

[202] Crêpellière, J. Metalorganic Chemical Vapour Deposition of p-type Delafossite $CuCrO_2$ Semiconductor Thin Films: Characterization and Application to Transparent p-n Junction. Ph.D. thesis, Université du Luxembourg, **2016**.

[203] Birkholz, M.; Fewster, P. F.; Genzel, C. *Thin Film Analysis by X-Ray Scattering*; Wiley-VCH, Weinheim, **2006**.

[204] de Keijser, T. H.; Langford, J. I.; Mittemeijer, E. J.; Vogels, A. B. P. Use of The Voigt Function in a Single-Line Method for the Analysis of X-Ray Diffraction Line Broadening. *J. Appl. Crystallogr.* **1982**, *15*, 308–314.

[205] Goldstein, J. L.; Newbury, D. E.; Michael, J. R.; Ritchie, N. W.; Scott, J. H. J.; Joy, D. C. *Scanning Electron Microscopy and X-Ray Microanalysis*; 3rd ed.; Springer: New-York, **2003**.

[206] Kyser, D. F.; Murata, K. Quantitative Electron Microprobe Analysis of Thin Films on Substrates. *IBM J. Res. Dev.* **1974**, *18*, 352–363.

[207] Murata, K.; Kotera, M.; Nagami, K. Quantitative Electron Microprobe Analysis of Thin Films on Substrates with a New Monte Carlo Simulation. *J. Appl. Phys.* **1983**, *54*, 1110–1114.

[208] Murata, K.; Sugiyama, K. Quantitative Electron Microprobe Analysis of Ultrathin Gold Films on Substrates. *J. Appl. Phys.* **1989**, *66*, 4456–4461.

[209] Campos, C. S.; Vasconcellos, M. A. Z.; Llovet, X.; Salvat, F. Thickness Determination of Ultra-Thin Films on Si Substrates by EPMA. *Microchim. Acta* **2004**, *145*, 13–17.

[210] Drouin, D.; Hovington, P.; Gauvin, R. CASINO: A New Monte Carlo Code in C Language for Electron Beam Interactions–Part II: Tabulated Values of the Mott Cross Section. *Scanning* **1997**, *19*, 20–28.

[211] Hovington, P.; Drouin, D.; Gauvin, R. CASINO: A New Monte Carlo Code in C Language for Electron Beam Interaction–Part I: Description of the Program. *Scanning* **1997**, *19*, 1–14.

[212] Waldo, R. A.; Militello, M. C.; Gaarenstroom, S. W. Quantitative Thin-Film Analysis with an Energy-Dispersive X-ray Detector. *Surf. Interface Anal.* **1993**, *20*, 111–114.

[213] Pauly, N.; Yubero, F.; Tougaard, S. Quantitative Analysis of Satellite Structures in XPS Spectra of Gold and Silver. *Appl. Surf. Sc.* **2016**, *383*, 317–323.

[214] Bates, C. W.; Wertheim, G. K.; Buchanan, D. N. E. Nature of the 3.8 eV Plasmon in X-Ray Photoemission from Silver. *Phys. Lett. A* **1979**, *72*, 178–180.

[215] Gaarenstroom, S. W.; Winograd N. Initial and Final State Effects in the ESCA Spectra of Cadmium and Silver Oxides. *J. Chem. Phys.* **1977**, *67*, 3500–3506.

[216] Kaushik, V. K. XPS Core Level Spectra and Auger Parameters for Some Silver Compounds. *J. Electron Spectros. Relat. Phenomena* **1991**, *56*, 273–277.

[217] Ferraria, A. M.; Carapeto, A. P.; Botelho do Rego, A. M. X-Ray Photoelectron Spectroscopy: Silver Salts Revisited. *Vacuum* **2012**, *86*, 1988–1991.

[218] Schön, G.; Tummavuori, J.; Lindström, B.; Enzell, C.; Swahn, C.-G. ESCA Studies of Ag, $Ag_2O$ and AgO. *Acta Chem. Scand.* **1973**, *27*, 2623–2633.

[219] Gao, X.-Y.; Wang, S.-Y.; Li, J.; Zheng, Y.-X.; Zhang, R.-J.; Zhou, P.; Yang, Y.-M.; Chen, L.-Y. Study of Structure and Optical Properties of Silver Oxide Films by Ellipsometry, XRD and XPS Methods. *Thin Solid Films* **2004**, *455-456*, 438–442.

[220] Lützenkirchen-Hecht, D. Electrochemically Grown Silver Oxide ($Ag_2O$) by XPS. *Surf. Sci. Spectra* **2011**, *18*, 96–101.

[221] Mikhlin, Y. L.; Vishnyakova, E. A.; Romanchenko, A. S.; Saikova, S. V.; Likhatski, M. N.; Larichev, Y. V.; Tuzikov, F. V.; Zaikovskii, V. I.; Zharkov, S. M. Oxidation of Ag Nanoparticles in Aqueous Media: Effect of Particle Size and Capping. *Appl. Surf. Sci.* **2014**, *297*, 75–83.

[222] Moulder, J. F.; Stickle, W. F. Sobol, P. E.; Bomben K. D. *Handbook of X-ray Photoelectron Spectroscopy*; Chastain, J., Ed.; Physical Electronics Division; Perkin-Elmer Corporation: Eden Prairie, Minnesota, USA, **1995**.

[223] Bartha, J.; Knaut, M.; Junige, M.; Geidel, M.; Albert, M. In situ Monitoring for ALD Process Control. *Proceedings of the AVS 11th International Conference on Atomic Layer* Deposition, Cambridge, Massachusetts, USA, June 26−29,**2011**.

[224] Elers, K.-E.; Blomberg, T.; Peussa, M.; Aitchison, B.; Haukka, S.; Marcus, S. Film Uniformity in Atomic Layer Deposition. *Chem. Vap. Deposition* **2006**, *12*, 13–24.

[225] Kumikov, V. K.; Khokonov, K. B. On the Measurement of Surface Free Energy and Surface Tension of Solid Metals. *J. Appl. Phys.* **1983**, *54*, 1346–1350.

[226] Gilman, J. J. Direct Measurements of the Surface Energies of Crystals. *J. Appl. Phys.* **1960**, *31*, 2208.

[227] Lienhart, R. FR Patent. 015113, **2015**.

[228] Adjeroud, N. Promoting the LIST Centre of Excellence in Atomic Layer Deposition. *Impact* **2021**, *2021*, 33–35.

[229] Arts, K.; Vandalon, V.; Puurunen, R. L.; Utriainen, M.; Gao, F.; Kessels, W. M. M.; Knoops, H. C. M. Sticking probabilities of $H_2O$ and $Al(CH_3)_3$ during Atomic Layer Deposition of $Al_2O_3$ Extracted from their Impact on Film Conformality. *J. Vac. Sci. Technol. A* **2019**, *37*, No. 030908.

[230] Arts, K.; Utriainen, M.; Puurunen, R. L.; Kessels, W. M. M.; Knoops, H. C. M. Film Conformality and Extracted Recombination Probabilities of O Atoms during Plasma-Assisted Atomic Layer Deposition of $SiO_2$, $TiO_2$, $Al_2O_3$, and $HfO_2$. *J. Phys. Chem. C* **2019**, *123*, 27030–27035.

[231] Gao, F.; Arpiainen, S.; Puurunen, R. Microscopic Silicon-Based Lateral High-Aspect-Ratio Structures for Thin Film Conformality Analysis. *J. Vac. Sci. Technol. A:* **2015**, *33*, No. 010601.

[232] Mattinen, M.; Hämäläinen, J.; Gao, F.; Jalkanen, P.; Mizohata, K.; Räisänen, J.; Puurunen, R.; Ritala, M.; Leskelä, M. Nucleation and Conformality of Iridium and Iridium Oxide Thin Films Grown by Atomic Layer Deposition. *Langmuir* **2016**, *32*, 10559–10569.

[233] Kim, K.; Yong, K. Highly Conformal Cu Thin-Film Growth by Low-Temperature Pulsed MOCVD. *Electrochem. Solid-State Lett.* **2003**, *6*, C106–C108.

[234] Kikuchi, H.; Yamada, Y.; Ali, A.; Liang, J.; Fukushima, T.; Tanaka, T.; Koyanagi, M. Tungsten Through-Silicon via Technology for Three-Dimensional LSIs. *Jpn J. Appl. Phys.* **2008**, *47*, 2801–2806.

[235] Song, M.; Wang, D.; Peana, S.; Choudhury, S.; Nyga, P.; Kudyshev, Z. A.; Yu, H.; Boltasseva, A.; Shalaev, V. M.; Kildishev, A. Colors with Plasmonic Nanostructures: A Full-Spectrum Review. *Appl. Phys. Rev.* **2019**, *6*, No. 041308.

[236] Gudur, A.; Ji, H.-F. Bio-Applications of Nanopillars. *Front. Nanosci. Nanotechnol.* **2016**, *2*, 1–10.

[237] Choudhury, B. D.; Casquel, R.; Bañuls, M. J.; Sanza, F. J.; Laguna, M. F; Holgado, M.; Puchades, R.; Maquieira, A.; Barrios, C. A.; Anand, S. Silicon Nanopillar Arrays with $SiO_2$ Overlayer for Biosensing Application. *Opt. Mater. Express* **2014**, *4*, 1345–1354.

[238] Dong, H.; Hinestroza, J. P. Metal Nanoparticles on Natural Cellulose Fibers: Electrostatic Assembly and In Situ Synthesis. *ACS Appl. Mater. Interfaces* **2009**, *1*, 797–803.

[239] Vaish, A.; Krueger, S.; Dimitriou, M.; Majkrzak, C.; Vanderah, D. J.; Chen, L.; Gawrisch, K. Enhancing the Platinum Atomic Layer Deposition Infiltration Depth Inside Anodic Alumina Nanoporous Membrane. *J. Vac. Sci. Technol. A* **2015**, *33*, No. 01A148.

[240] Ylilammi, M.; Ylivaara, O. M. E.; Puurunen, R. L. Modeling Growth Kinetics of Thin Films Made by Atomic Layer Deposition in Lateral High-Aspect-Ratio Structures. *J. Appl. Phys.* **2018**, *123*, 205301.

[241] Knoops, H. C. M.; Langereis, E.; van den Sanden, M. C. M.; Kessels, W. M. M. Conformality of Plasma-Assisted ALD: Physical Processes and Modeling. *J. Electrochem. Soc.* **2010**, *157*, G241–G249.

[242] Dendooven, J.; Deduytsche, D.; Musschoot, J.; Van Meirhaeghe, R. L.; Detavernier, C. Conformality of $Al_2O_3$ and AlN Deposited by Plasma-Enhanced Atomic Layer Deposition. *J. Electrochem. Soc.* **2010**, *157*, G111–G116.

[243] Jamnig, A.; Sangiovanni, D. G.; Abadias, G.; Sarakinos, K. Atomic-Scale Diffusion Rates During Growth of Thin Metal Films on Weakly-Interacting Substrates. *Sci. Rep.* **2019**, *9*, 6640.

[244] Wenzel, R. N. Resistance of Solid Surfaces to Wetting by Water. *Ind. Eng. Chem.* **1936**, *28*, 988–994.

[245] Jiang, X.; Jia, C. L.; Szyszka, B. Manufacture of Specific Structure of Aluminum-Doped Zinc Oxide Films by Patterning the Substrate Surface. *Appl. Phys. Lett.* **2002**, *80*, 3090–3092.

[246] Tavakoli, A. H.; Maram, P. S.; Widgeon, S. J.; Rufner, J.; van Benthem, K.; Ushakov, S.; Sen, S.; Navrotsky, A. Amorphous Alumina Nanoparticles: Structure, Surface Energy, and Thermodynamic Phase Stability. *J. Phys. Chem. C* **2013**, *117*, 17123–17130.

[247] Rhee, S. K. Surface Energies of Silicate Glasses Calculated from their Wettability Data. *J. Mater. Sci.* **1977**, *12*, 823–824.

[248] Takeda, S.; Yamamoto, K.; Hayasaka, Y.; Matsumoto, K. Surface OH Group Governing Wettability of Commercial Glasses. *J. Non-Cryst. Solids* **1999**, *249*, 41–46.

[249] Takeda, S.; Fukawa, M. Role of Surface OH Groups in Surface Chemical Properties of Metal Oxide Films. *Mater. Sci. Eng. B* **2005**, *119*, 265–267.

[250] Zeng, J. H.; Jin, B. B.; Wang, Y. F. Facet Enhanced Photocatalytic Effect with Uniform Single-Crystalline Zinc Oxide Nanodisks. *Chem. Phys. Lett.* **2009**, *472*, 90–95.

[251] Rogé, V. Etude, Fabrication et Caractérisation de Nanostructures Catalytiques de Type $ZnO/SnO_2$ Intégrées à des Membranes Modèles pour la Dépollution de l'Eau. Ph.D. thesis, Université de Strasbourg, **2015**.

[252] Rogé, V.; Bahlawane, N.; Lamblin, G.; Fechete, I.; Garin, F.; Dinia, A.; Lenoble, D. Improvement of the Photocatalytic Degradation Property of Atomic Layer Deposited ZnO Thin Films: The Interplay Between Film Properties and Functional Performances. *J. Mater. Chem. A* **2015**, *3*, 11453–11461.

[253] Lu, J.; Elam, J. W.; Stair, P. C. Synthesis and Stabilization of Supported Metal Catalysts by Atomic Layer Deposition. *Acc. Chem. Res.* **2013**, *46*, 1806–1815.

[254] Bannwarth, M. B.; Klein, R.; Kurch, S.; Frey, H.; Landfester, K.; Wurm, F. R. Processing and Adjusting the Hydrophilicity of Poly(oxymethylene) (Co)polymers: Nanoparticle Preparation and Film Formation. *Polym. Chem.* **2015**, *7*, 184–190.

[255] Kato, K.; Omoto, H.; Tomioka, T.; Takamatsu, A. Visible and Near Infrared Light Absorbance of Ag Thin Films Deposited on ZnO Under Layers by Magnetron Sputtering. *Sol. Energy Mater. Sol. Cells* **2011**, *95*, 2352–2356.

[256] Smith, G. B.; Earp, A. A. Metal-in-Metal Localized Surface Plasmon Resonance. *Nanotechnology* **2010**, *21*, No. 015203.

[257] Haynes, C. L.; McFarland, A. D.; Zhao, L.; Van Duyne, R. P.; Schatz, G. C.; Gunnarsson, L.; Prikulis, J.; Kasemo, B.; Käll, M. Nanoparticle Optics: The Importance of Radiative Dipole Coupling in Two-Dimensional Nanoparticle Arrays. *J. Phys. Chem. B* **2003**, *107*, 7337–7342.

[258] Drachev, V. P.; Perminov S. V.; Rautian, S. G. Safonov, V. P. Nonlinear Optical Effects and Selective Photomodification of Colloidal Silver Aggregates. *Top. Appl. Phys.* **2002**, *82*, 113–148.

[259] Guillot, N.; Lamy De la Chapelle, M. Lithographied Nanostructures as Nanosensors. *J. Nanophotonics* **2012**, *6*, 4506–4507.

[260] Yim, J.; Ylivaara, O. M. E.; Ylilammi, M.; Korpelainen, V.; Haimi, E.; Verkama, E.; Utriainen, M.; Puurunen, R. L. Saturation Profile Based Conformality Analysis for Atomic Layer Deposition: Aluminum Oxide in Lateral High-Aspect-Ratio Channels. *Phys. Chem Chem. Phys.* **2020**.

[261] Granqvist, C. G. Transparent Conductors as Solar Energy Materials: A Panoramic Review. *Sol. Energy Mater. Sol Cells* **2007**, *91*, 1529–1598.

[262] Butt, M. A.; Fomchenkov, S. A.; Kazanskiy, N. L.; Ullah, A.; Ali, R. Z.; Habib, M. Infrared Reflective Coatings for Building and Automobile Glass Windows for Heat Protection. In *Proceedings of SPIE Optical Technologies in Telecommunications*; International Society for Optics and Photonics, Samara, Russian Federation, April 2017; **2016**, Vol. *10342*.

[263] Johnson, P. B.; Christy, R. W. Optical Constants of the Noble Metals. *Phys. Rev. B* **1972**, *6*, 4370–4379.

[264] Ishchenko, O. Elaboration of Plasmonic Nano-Composites and Study of their Specific Catalytic Activities. Ph.D. thesis, Université de Strasbourg, **2016**.

[265] Hoffmann, M. R.; Martin, S. T.; Choi, W.; Bahnemann, D. W. Environmental Applications of Semiconductor Photocatalysis. *Chem. Rev.* **1995**, *95*, 69–96.

[266] Kochuveedu, S. T.; Jang, Y. H.; Kim, D. H. A Study on the Mechanism for the Interaction of Light with Noble Metal-Metal Oxide Semiconductor Nanostructures for Various Photophysical Applications. *Chem. Soc. Rev.* **2013**, *42*, 8467–8493.

[267] Whang, T.-J.; Hsieh, M.-T.; Chen, H.-H. Visible-Light Photocatalytic Degradation of Methylene Blue with Laser-Induced Ag/ZnO Nanoparticles. *Appl. Surf. Sci.* **2012**, *258*, 2796–2801.

[268] Sangpour, P.; Hashemi, F.; Moshfegh, A. Z. Photoenhanced Degradation of Methylene Blue on Cosputtered M:$TiO_2$ (M = Au, Ag, Cu) Nanocomposite Systems: A Comparative Study. *J. Phys. Chem. C* **2010**, *114*, 13955–13961.

[269] He, Y.; Basnet, P.; Murph, S. E. H.; Zhao, Y. Ag Nanoparticle Embedded $TiO_2$ Composite Nanorod Arrays Fabricated by Oblique Angle Deposition: Toward Plasmonic Photocatalysis. *ACS Appl. Mater. Interfaces* **2013**, *5*, 11818–11827.

[270] Rogé, V.; Didierjean, J.; Crêpellière, J.; Arl, D.; Michel, M.; Fechete, I.; Dinia, A.; Lenoble, D. Tuneable Functionalization of Glass Fibre Membranes with ZnO/$SnO_2$ Heterostructures for Photocatalytic Water Treatment: Effect of $SnO_2$ Coverage Rate on the Photocatalytic Degradation of Organics. *Catalysts* **2020**, *10*, 733.

[271] Yin, I. X; Zhang, J.; Zhao, I. S.; Mei, M. L.; Li, Q.; Chu, C.-H. The Antibacterial Mechanism of Silver Nanoparticles and Its Application in Dentistry. *Int. Journal Nanomedicine* **2020**, *15*, 2555–2562.

[272] Website, https://www.epa.gov/pesticide-registration/interim-guidance-expedited-review-products-adding-residual-efficacy-claims.

[273] Garner, W. E.; Reeves, L. W. The Thermal Decomposition of Silver Oxide. *Trans. Faraday Soc.* **1954**, *50*, 254–260.

# Appendices

**Annex 1**: Correspondence between general and structural formulae of complexes used for Ag deposition by CVD

| Name of the complex | General formula | Nature of coordinated compound |
|---|---|---|
| Ag β-diketonates | [Ag(β-dik)L] | ▪ β-dik = acac, dpm, tfac, hfac,fod, tmeda, bipy,Btfac, Ttfac<br>▪ β -diketoiminates = hfacNhex, hfacNchex<br>▪ L = VTES, BTMSA, BTMSE, BDMESA, ATMS, COD<br>▪ L' = $PMe_3$, $PEt_3$, $PPh_3$ |
| Ag β-diketonates phosphine adducts | [Ag(β-dik)L'] | |
| Ag β-diketoiminates | [Ag(β-diketoim)L] | |
| Ag β-diketoiminates phosphine adducts | [Ag(β-diketoim)L'] | |
| Ag carboxylates | [Ag($O_2$CR)] | ▪ R = Me, $^t$Bu, $C(CH_3)_3$, 2,4,6-$Me_3C_6H_2$<br>▪ Rf = $CF_3$, $C_2F_5$, $C_3F_7$, $C_6F_{13}$, $C_7F_{15}$, $CF_3$, $C_2F_5$, $C_3F_7$, $C_8F_{17}$, $C(CH_3)CCH_3H$, $(CH_2)C_6H_5$<br>▪ R' = Me, Ph, n-Bu |
| Ag fluorocarboxylates | [Ag($O_2$CRf): | |
| Ag carboxylates phosphine adducts | [Ag($O_2$CRPR'$_3$)] | |
| Ag fluorocarboxylates phosphine adducts | [Ag($O_2$CRf)PR'$_3$] | |
| Ag aryloxide-triphenylphosphine | [Ag(OR)($PPh_3$)$_2$] | ▪ R = $C_6H_2Cl_3$-2,4,6, $C_6H_4$Me-2, $C_6H_2(CH_2NMe_2)_3$-2,4,6 |
| | [Ag(OR)($PPh_3$)$_3$].ROH | ▪ R = Ph, $C_4H_4$Me-2 |

# Work done in conjunction with others

All of the experiment and analytical works presented in this thesis were carried out by the author, with the following exceptions:

- The X-ray photoelectron spectroscopy measurements (XPS) were performed by Dr Jérôme Guillot and Christèle Vergne at LIST;
- The Energy dispersive X-ray Spectroscopy (EDS) measurements, only on glass substrates, were performed by Jean-Luc Biagi;
- The Time-of-Flight Secondary Ion Mass Spectrometry (ToF-SIMS) analyzes were performed by Dr Jérôme Bour and Dr. Gilles Frache;
- X-ray Reflectivity measurements (XRR) were performed in coordination with Dr Tony Schenk;
- The thermogravimetry analysis (TGA) was performed by Régis Vaudemont;
- The water contact angle (WCA) measurements were performed in coordination with Dr Bianca Rita Pistillo and Jonathan Crêpellière;
- The antibacterial properties measurements were performed by Delphine Collard at LIST;
- The photocatalytic properties were performed in coordination with Dr Vincent Rogé at LIST;
- Zinc oxides nanorods substrates were procured by Rutuja Busari.

# Scientific outputs

## Publications

- *J. Crêpellière, K. Menguelti, S. Wack, O. Bouton, M. Gérard, P. Lunca Popa, B. R. Pistillo, R. Leturcq, M. Michel*, Spray Deposition of Silver Nanowires on Large Area Substrates for Transparent Electrodes, *ACS Appl. Nano Mater.*, **2021**, https://doi.org/10.1021/acsanm.0c02763.
- *S. Wack, P. Lunca Popa, N. Adjeroud, C. Vergne, R. Leturcq* Two-Step Approach for Conformal Chemical Vapor-Phase Deposition of Ultra-Thin Conductive Silver Films, *ACS Appl. Mater. Interfaces*, **2020**, 12, 32, 36329–36338.
- *S. Wack, P. Lunca Popa, N. Adjeroud, J. Guillot, B. R. Pistillo, R. Leturcq* Large-Scale Deposition and Growth Mechanism of Silver Nanoparticles by Plasma-Enhanced Atomic Layer Deposition, *J. Phys. Chem. C,* **2019**, 123, 44, 27196–27206.

## Patent

- WO/2018/115369, *R. Leturcq, N. Adjeroud, S. Wack* "Method for Depositing Alumina by Atomic Layer Deposition"

## Conference presentations

1. **MRS Spring Meeting 2021 Virtual Meeting** | April, 17–23, 2021 – *S. Wack, P. Lunca Popa, N. Adjeroud, C. Vergne, R. Leturcq* "Novel Approach for Conformal Chemical Vapor-Phase Deposition of Ultra-Thin Conductive Silver Films", *oral presentation*.
2. **ALD/ALE 2020 Virtual Meeting** | June, 29 – July, 1, 2020 – *S. Wack, P. Lunca Popa, N. Adjeroud, C. Vergne, R. Leturcq* "Novel Approach for Conformal Chemical Vapor-Phase Deposition of Ultra-Thin Conductive Silver Films", *poster presentation*.
3. **MRS Fall Meeting 2019** | December, 1–6, 2019, Boston, United-States – *S. Wack, P. Lunca Popa, N. Adjeroud, C. Vergne, R. Leturcq* "Novel Approach for Conformal Chemical Vapor-Phase Deposition of Ultra-Thin Conductive Silver Films", *oral presentation*.
4. **MRS Fall Meeting 2019** | December, 1–6, 2019, Boston, United-States – *S. Bhudia, S. Wack, N. Adjeroud, J. Guillot, R. Leturcq* "Atomic Layer Deposition of Zinc-Doped Alumina at Room-Temperature for Organic Opto-Electronics", *oral presentation*.
5. **Luxembourg Institute of Science and Technology (LIST) annual PhD Day 2019** | November, 26, 2019, Belvaux, Luxembourg – *S. Wack, P. Lunca Popa, N. Adjeroud, C. Vergne, J. Guillot, G. Frache, B. R. Pistillo, R. Leturcq* "Chemical Vapor-Phase Deposition of nanostructured silver layers", *oral presentation*.
6. **EuroCVD 22 – Baltic ALD 16** | June, 24–28, 2019, Luxembourg – *S. Wack, P. Lunca Popa, N. Adjeroud, J. Guillot, G. Frache, B. R. Pistillo, R. Leturcq* "Growth Mechanism of Uniform Silver Nanoparticles by Plasma-Enhanced Atomic Layer Deposition", *oral presentation*.

7. **Luxembourg Institute of Science and Technology (LIST) annual PhD Day 2018** | November, 15, 2018, Belvaux, Luxembourg – *S. Wack, P. Lunca Popa, N. Adjeroud, J. Guillot, G. Frache, B. R. Pistillo, R. Leturcq* "Properties of Thick Silver Films Grown by Plasma Enhanced Atomic Layer Deposition", *oral presentation*.
8. **E-MRS Fall Meeting 2018** | September, 17–20, 2018, Warsaw, Poland – *S. Wack, P. Lunca Popa, R. Leturcq* "Controlling the Morphology of Silver Nanoparticles Deposited by Plasma-Enhanced Atomic Layer Deposition for Plasmonic Applications", *2 oral presentations*.
9. **E-MRS Fall Meeting 2018** | September, 17–20, 2018, Warsaw, Poland – *S. Wack, S. Bhudia, N. Adjeroud, J. Guillot, R. Leturcq* "Alumina Layers Grown at Room Temperature by Atomic Layer Deposition for Organic Electronics", *oral presentation*.
10. **E-MRS Spring Meeting 2018** | June, 18–22, 2018, Strasbourg, France – *S. Wack, P. Lunca Popa, N. Adjeroud, J. Guillot, G. Frache, B. R. Pistillo, R. Leturcq* "Properties of Thick Silver Films Grown by Plasma Enhanced Atomic Layer Deposition", *oral presentation*.
11. **E-MRS Spring Meeting 2018** | June, 18–22, 2018, Strasbourg, France – *S. Wack, N. Adjeroud, J. Guillot, R. Leturcq* "Zinc-Doped Alumina Thin-Layers Grown at Room Temperature by Atomic Layer Deposition for Organic Electronics", *oral presentation*.

## Workshops

- 6ème workshop, évènement virtuel, Réseau d'acteurs français de l'ALD (RAFALD), | November, 2020.
- Project Management: From Theory to Practice - European summer school | July, 2019, Prague, Czech Republic.
- 8th French-speaking conference on electron spectroscopy (ELSPEC) 2018 | June, 2018, Biarritz, France.
- ALD for Industry - 2nd Workshop and Tutorial | March, 2018, Dresden, Germany.
- Belux 3 Training School – Chemistry of ALD | March, 2018, Luxembourg Institute of Science and Technology (LIST), Belvaux – Luxembourg.